



HAL
open science

Cycle de l'uranium et évolution tectono-métamorphique de la ceinture orogénique Pan-Africaine du Lufilien (Zambie)

Aurélien Eglinger

► **To cite this version:**

Aurélien Eglinger. Cycle de l'uranium et évolution tectono-métamorphique de la ceinture orogénique Pan-Africaine du Lufilien (Zambie). Sciences de la Terre. Université de Lorraine, 2013. Français. NNT : 2013LORR0306 . tel-01750652

HAL Id: tel-01750652

<https://hal.univ-lorraine.fr/tel-01750652>

Submitted on 29 Mar 2018

HAL is a multi-disciplinary open access archive for the deposit and dissemination of scientific research documents, whether they are published or not. The documents may come from teaching and research institutions in France or abroad, or from public or private research centers.

L'archive ouverte pluridisciplinaire **HAL**, est destinée au dépôt et à la diffusion de documents scientifiques de niveau recherche, publiés ou non, émanant des établissements d'enseignement et de recherche français ou étrangers, des laboratoires publics ou privés.



AVERTISSEMENT

Ce document est le fruit d'un long travail approuvé par le jury de soutenance et mis à disposition de l'ensemble de la communauté universitaire élargie.

Il est soumis à la propriété intellectuelle de l'auteur. Ceci implique une obligation de citation et de référencement lors de l'utilisation de ce document.

D'autre part, toute contrefaçon, plagiat, reproduction illicite encourt une poursuite pénale.

Contact : ddoc-theses-contact@univ-lorraine.fr

LIENS

Code de la Propriété Intellectuelle. articles L 122. 4

Code de la Propriété Intellectuelle. articles L 335.2- L 335.10

http://www.cfcopies.com/V2/leg/leg_droi.php

<http://www.culture.gouv.fr/culture/infos-pratiques/droits/protection.htm>



Université de Lorraine, GeoRessources-CREGU
UMR 7359, Vandœuvre-lès-Nancy, 54506 Nancy, France
Ecole doctorale RP2E (Ressources, Procédés, Produits et Environnement)
Collegium Sciences et Technologies

THESE

Présentée pour l'obtention du titre de
Docteur de l'Université de Lorraine
en **Géosciences**
par

Aurélien Eglinger

Cycle de l'uranium et évolution tectono- métamorphique de la ceinture orogénique Pan-Africaine du Lufilien (Zambie)

Soutenance publique le 13/12/2013

Membres du jury :

Rapporteurs :	Ph. Muchez	Professeur, Université catholique de Louvain, Belgique
	B. De Waele	Professeur, Western Australia University, Australie
Examineurs :	P. Barbey	Professeur, Université de Lorraine, France
	M. Cuney	Directeur de recherche CNRS-GeoRessources-CREGU
	M. Jébrak	Professeur, Université de Québec à Montréal, Canada
	M. Pagel	Professeur, Université Paris-Sud, Paris
Directeurs de thèse :	A.-S. André-Mayer	Professeur, Université de Lorraine, France
	O. Vanderhaeghe	Professeur, Université de Lorraine, France
Invités :	A. Tarantola	Maître de conférences, Université de Lorraine, France
	M. Brouand	Géologue, AREVA Mines, Paris La Défense

Résumé: L'uranium, du fait de ses propriétés chimiques (lithophile, incompatible) représente un traceur de choix dans le suivi de la formation et de l'évolution de la croûte continentale. Il peut être utilisé pour discuter des différents modèles de formation, de croissance et d'évolution de la croûte continentale débattus ces dernières décennies. Ce travail de thèse, ciblé sur la ceinture Pan-Africaine du Lufilien en Zambie, s'appuie sur une approche multi-méthodes combinant géologie structurale, pétro-géochimie, géochronologie et inclusions fluides dans le but de caractériser le cycle de l'U et les minéralisations uranifères pour ce segment de croûte continentale. Les séries silicoclastiques/évaporitiques de la ceinture du Lufilien, encaissant les minéralisations uranifères, se sont déposées en contexte de rift (bassin du Roan) lors de l'amincissement lithosphérique et de la dislocation du supercontinent Rodinia au Néoproterozoïque inférieur. Les âges U-Pb des grains de zircon détritique de ces séries métasédimentaires soulignent une source principalement Paléoproterozoïque. Ces mêmes grains de zircon présentent des signatures isotopiques ϵ_{Hf} inférieures au CHUR (entre 0 et -15) et des âges modèles $T_{\text{DM}} \text{ Hf}$, compris entre ~2.9 et 2.5 Ga. Ces données suggèrent donc la formation d'une croûte continentale précoce, et donc une extraction mantellique de l'uranium dès la fin de l'Archéen (< 2.5 Ga) puis une remobilisation par déformation et métamorphisme au cours du Protérozoïque. L'uranium aurait donc été remobilisé et re-concentré au cours d'orogènes successives jusqu'au cycle Pan-Africain. Durant ce cycle Pan-Africain, la datation U-Pb et la signature REY (REE et Yttrium) des cristaux d'uraninite caractérisent un premier événement minéralisateur, daté vers 650 Ma, associé à la circulation de fluides de bassin expulsés des évaporites du Roan, circulant à l'interface socle/couverture, dans ce contexte de rift continental. Un second événement minéralisateur, daté vers 530 Ma et contemporain du pic métamorphique ($P=9\pm 3$ kbar ; $T=610\pm 30$ °C), est assuré par des fluides métamorphiques issus de la dissolution des évaporites, en contexte de subduction/accrétion continentale. Quelques remobilisations tardives de l'uranium sont observées lors de l'exhumation des roches métamorphiques et leur accrétion tectonique dans la zone interne de la ceinture orogénique du Lufilien. L'analyse pétrographique indique que durant ces interactions fluides/roches syn- à tardi-métamorphiques, l'uranium est lessivé des minéraux hôtes (allanite, monazite), des gneiss formant le socle de la série du Katanga remobilisé et partiellement fondu au cours de l'orogène Pan-Africain.

Abstract: Uranium is an incompatible and lithophile element, and thus more concentrated in silicate melt produced by the partial melting of the mantle related to continental crust formation. Uranium can be used as a geochemical tracer to discuss the generation and the evolution of continental crust. This thesis, focused on the Pan-African Lufilian belt in Zambia, combines structural geology, metamorphic petrology and thermobarometry, fluid inclusions, geochemistry and geochronology in order to characterize the uranium cycle for this crustal segment. Silici-clastic and evaporitic sediments have been deposited within an intracontinental rift during the dislocation of the Rodinia supercontinent during the early Neoproterozoic. U-Pb ages on detrital zircon grains in these units indicate a dominant Paleoproterozoic provenance. The same zircon grains show subchondritic ϵ_{Hf} (between 0 and -15) and yield Hf model ages between ~2.9 and 2.5 Ga. These data suggest that the continental crust was generated before the end of the Archean (< 2.5 Ga) associated with uranium extraction from the mantle. This old crust has been reworked by deformation and metamorphism during the Proterozoic. Uranium has been remobilized and re-concentrated during several orogenic cycles until the Pan-African orogeny. During this Pan-African cycle, U-Pb and REY (REE and Yttrium) signatures of uranium oxides indicate a first mineralizing event at ca. 650 Ma during the continental rifting. This event is related to late diagenesis hydrothermal processes at the basement/cover interface with the circulation of basinal brines linked to evaporites of the Roan. The second stage, dated at 530 Ma, is connected to metamorphic highly saline fluid circulations, synchronous to the metamorphic peak of the Lufilian orogeny ($P=9\pm 3$ kbar ; $T=610\pm 30$ °C). These fluids are derived from the Roan evaporite dissolution. Some late uranium remobilizations are described during exhumation of metamorphic rocks and their tectonic accretion in the internal zone of the Lufilian orogenic belt. During these synmetamorphic fluid-rock interactions, uranium has been leached from U-bearing minerals such as allanite or monazite hosted by the reworked and partially molten gneissic basement.

REMERCIEMENTS

Mon arrivée au pays de la « minette » remonte en 2009 dans le but d'intégrer la deuxième année du Master «*Ressources minérales*». Chose faite ! C'est à cette période et, plus précisément, durant mon stage de recherche en laboratoire que j'ai porté un intérêt pour la recherche, intérêt grandement suscité par la présence d'Alex. Alexandre Tarantola, mon directeur de master qui est devenu un collègue de travail, puis mon « mentor » durant mes trois années de thèse et surtout un ami. Merci beaucoup de m'avoir fait partager ton expérience et ta sagesse dès le stage de M2 et merci également de m'avoir fait une place dans ton bureau où l'ambiance studieuse était en harmonie avec la bonne humeur (c'est grâce à toi que j'ai développé une ouïe fine sur les pas de chacun des chercheurs du sixième étage) ! Bref, un grand merci à toi car sans ton soutien et ta confiance, je ne serais probablement pas en train d'écrire ces remerciements !

Evidemment, mes remerciements se portent vers Anne-Sylvie André-Mayer et Olivier Vanderhaeghe, mes deux directeurs de thèse, et j'ai envie de dire la doublette parfaite pour un encadrement de thèse idéal et complémentaire aussi bien sur le plan scientifique, administratif mais surtout humain. Merci Anne-Sylvie pour ton énergie tout au long de la thèse et ton expertise métallogénique ! J'ai envie de dire «*Wunderbar* » ! Olivier, je te remercie pour ton esprit critique et constructif sur la vision en 3 dimensions des orogènes ! Para- ou ortho-dérivée, moi je dis : on s'en fout, c'est une migmatite ! Merci pour tout, merci pour votre suivi irréprochable et j'espère pouvoir continuer à travailler avec vous sur de futurs projets !

Je remercie le jury qui a accepté d'évaluer ce travail. Merci aux rapporteurs Philippe Muechez et Bert De Waele d'avoir fait ce voyage pour l'occasion et pour ces échanges scientifiques sur la ceinture du Lufilien. Michel Cuney, Michel Jébrak et Maurice Pagel, je vous remercie d'avoir examiné cette thèse, je suis très heureux que nous ayons partagé ce temps ensemble, entre métallogénistes ! Merci à Marc Brouand de m'avoir soutenu et accompagné au cours de cette troisième année. Enfin merci Mr le Président, Pierre Barbey, d'avoir apprécié la qualité et l'apport pour la connaissance scientifique de ce travail de thèse.

Ce travail a également été le fruit de nombreuses collaborations, notamment avec mes amis Cyril Durand et Philippe Goncalves ! Cyril, qui n'aurait pas parié un *kopeck* sur ma poursuite d'études à l'issue de ma première année de fac! Voilà que tu te retrouves impliqué pour trois années dans mon projet de thèse ! Merci pour ces échanges scientifiques et pour ton temps partagé aussi bien au cœur de la savane Zambienne (où on a cru à une piqure de mouche Tsé-tsé !) qu'autour d'une bonne Triple Karmeliet (où là ce sont les lendemains matins qui piquaient !). Merci à Philippe pour sa formation, déjà universitaire dès la licence 3, et ensuite de m'avoir initié aux modélisations *P-T* qu'est la pseudosection ! J'ai bien dit « initié » car j'ai encore du chemin à faire pour me considérer en tant que géothermobaro-magicien ! Un réel plaisir de vous avoir retrouvé et d'avoir travaillé avec vous deux durant ces trois années ! Merci !

Merci à Armin Zeh, Jean-Louis Paquette et Etienne Deloule pour leur investissement et de m'avoir fait partagé leur expérience pour la géochronologie ! Merci à Michel Cuney de toujours avoir gardé sa porte ouverte à toute discussion et de m'avoir fait partager sa passion (oui oui on peut le dire) pour la métallogénie de l'Uranium ! Une grande partie de ce travail, je vous le dois !

A tous les partenaires scientifiques de la société AREVA, notamment et surtout Jean-Pierre Milesi et Jean-Louis Feybesse (paix à son âme) qui ont initié ce projet, à Marc Brouand qui a pris le relai, je leur en suis reconnaissant ! Merci également au support logistique de la compagnie Barrick Limited pour leur accueil sur le terrain !

Merci à toute l'équipe bretonne, et je pense à Marc, Philippe, Benoît, Nathan, Dédé, et surtout Romich et Jeanne pour votre accueil chaleureux lors de mes visites en pays celtiques (alors du coup la limite des pays celtiques, elle passe par où ?). Un grand merci à toi Sophie, je te considère désormais comme intégrée à la grande famille des chapeaux ronds (je parle bien des chapeaux, hein ? pas de confusion !). Merci à toi d'avoir fait de notre collaboration une belle rencontre scientifique et amicale par ta motivation et ta sympathie !

Merci à Mr. Bonnetti, mon compagnon de galère ! En fait, j'ai plutôt bien vécu ces trois années de thèse, je parlerais donc plus de compagnon de croisière ! Avec comme équipage Mr. Belgodère, Mr. Salardon et Mr. Jouanny ! Bien entendu, je vois bien comme capitaine Mr.

Bonnetti, longue vue à la main à scruter l'horizon (héhé) ! Merci à vous les chefs aussi bien pour tous les *Wine & Gastro* que les parties de belotte, et j'en passe !

Bien entendu, cette croisière a été agréable et sans trop de houle, grâce à la bonne ambiance du laboratoire et je pense notamment à Laurent, Merca, Antonin, frère Toé, Philippe, Mathieu, Stéphanie, Lucille, Sandrine (courage à toi pour la dernière ligne droite), Moussa, Anthony, Manu, Max, Vanessa et Julien ! J'ai pu bénéficier de leurs conseils ! Merci à toute l'équipe GeoRessources, techniciens, chercheurs, enseignants-chercheurs, secrétaires et ingénieurs de m'avoir intégré ! Je tiens à remercier plus personnellement Patrick Lagrange, Olivier Rouer et Sandrine Mathieu pour tous les coups de pouce apportés tout au long de cette thèse et Zira pour son éternel enthousiasme ! Je tiens aussi à remercier les étudiants de master qui ont contribué à ce travail de thèse, je pense à Clément Ferraina, François Turlin, François Frémont et Romain Dalleu ! Merci également aux étudiants côtoyés durant ces trois années, notamment : Céline, Jen, P-A, Arnaud et ceux que j'oublie !

Une pensée aussi pour mes collègues promotionnels Bisontins : Barny, Bolloche, Bonnet Vert, Clairon (alias Sacoche), Flavien (alias Machine), Flo, Jean-Charles, Pad, Rudix et surtout Tutu (le fanfaron de service)! J'ai juste envie de dire : Géols Motivés !

Cette thèse n'aurait été possible aussi sans le soutien de mes amis belfortains, ma deuxième famille en quelque sorte ! Merci d'avoir toujours été là, certains depuis la maternelle, d'autres depuis le collège ou encore la fac ! Bref, depuis de nombreuses années ! Et c'est en grande partie grâce à vous que je suis devenu le Glinglin que vous connaissez. Je prends le temps de vous remercier un à un (dans l'ordre alphabétique pour pas faire de jaloux !) : Bou et sa moitié Djoulinette, Cam, Cla, Crevette et sa petite femme Crevettine, Mama, Momo, Morinski, Milou, Peerz, Pusch, Ragoman et sa petite famille Manon et Lina, Ramzy, Roro, Skyman, Ticketman, Tom et Vio. Bon je n'ai pas intérêt à en avoir oublié un sinon...

Je remercie également toute ma famille et notamment mes parents de m'avoir soutenu et d'avoir toujours cru en moi depuis bien des années ! Vous m'avez toujours permis de réaliser mes souhaits ! Sans vous rien de tout cela n'eut été possible ! Cette thèse est aussi pour vous ! Et aussi

pour toi frangin ! Quelle idée de s'être expatrié outre-Atlantique, ça va qu'il y a quelques congrès au Québec pour te rendre plus souvent visite ! Tu me manques !

Je complimente enfin Caro, le meilleur pour la fin, pour ces cinq années (et oui déjà !) passées à tes côtés ! Grâce à toi, les moments difficiles sont déjà oubliés ! Tu es pour beaucoup dans l'aboutissement de ce travail (et notamment pour la partie biblio) ! Mille mercis (ça fait beaucoup quand même) !

SOMMAIRE

INTRODUCTION	15
1. Thématique et problématique.....	17
2. Objectifs de la thèse	18
3. Organisation du manuscrit	21
PARTIE I: CROISSANCE ET ÉVOLUTION DE LA CROÛTE CONTINENTALE	23
CHAPITRE 1: Les continents, leur croissance et leur concentration en uranium	25
1. La croûte continentale: définition	25
2. La croûte continentale archéenne et protérozoïque : distribution et composition	27
3. Modèles de croissance, remobilisation et recyclage de la croûte continentale.....	29
4. Concentration en éléments radioactifs dans la croûte continentale : cas de l'uranium	33
5. Cycle de l'uranium de l'Archéen jusqu'à l'actuel.....	36
CHAPITRE 2: Crustal evolution of basement inliers in the internal zone of the orogenic Lufilian belt: U-Pb coupled with Hf isotopes of zircon and whole-rock Sm-Nd isotopic data (Domes region, Zambia)	39
Abstract	40
1. Introduction.....	41
2. Geological background: Previous geochronology, geochemistry and isotopic data	42
2.1. The Congo-Kasai craton.....	42
2.2. The Bangweulu block.....	44
2.3. The Kibaran belt.....	45
2.4. The Irumide belt.....	45
2.5. The Lufilian-Zambezi belt.....	46
3. Geological setting and description of the sampled lithologies	47
3.1. Solwezi dome	48
3.2. Mwombezhi dome.....	51
4. Methodology	52
4.1. Geochemistry	52
4.2. LA-MC-ICPMS U-Pb and Lu-Hf isotope analyses of zircon	53
4.3. Sm-Nd isotopes analyses of whole rock.....	53
5. Whole rock geochemistry: major and trace elements.....	54
5.1. Solwezi dome	54
5.2. Mwombezhi dome.....	57
6. Isotopic results	59
6.1. Solwezi dome	59
6.2. Mwombezhi dome.....	65
7. Discussion.....	72
7.1. Intrusion and deposition ages	72
7.1.1. Solwezi basement inliers	72
7.1.2. Mwombezhi basement inliers	74
7.2. Implication for crustal evolution from Archean to Mesoproterozoic	75
PARTIE II : FORMATION DES CEINTURES OROGÉNIQUES PAN-AFRICAINES	117
CHAPITRE 3: Le cycle orogénique Pan-Africain.....	119
1. Cycle orogénique: définition.....	119
2. Le supercontinent Rodinia	120
3. Le supercontinent Gondwana.....	123
4. Qu'entend-t-on par continent West Gondwana?.....	124
5. Les ceintures orogéniques du West Gondwana.....	126

5.1. Les ceintures orogéniques précoces à cycle long (1000-600 Ma)	126
5.2. Les ceintures orogéniques récentes à cycle court (600-520 Ma).....	127
5.3. Chronologie des évènements associés à l'assemblage du West Gondwana.....	127
5.4. Présentation de la ceinture du Damara-Lufilien-Zambezi.....	128

CHAPITRE 4: Tectonic evolution of the internal orogenic zone of the Pan-African Lufilian belt (Zambia): Structural, petrologic, thermobarometric and U-Pb-Th, Lu-Hf and Sm-Nd isotopic constraints..... 131

Abstract	132
1. Introduction.....	133
2. Regional geology	134
3. Analytical procedures	138
3.1. Geochemical analyses of whole rocks and minerals	138
3.2. Sm-Nd isotopes analyses of whole rock.....	138
3.3. Lu-Hf isotope dilution analyses of garnet and whole rock.....	139
3.4. LA-MC-ICPMS U-Pb and Lu-Hf isotope analyses of zircon	140
4. Mantling rocks: micaschists and magmatic rocks.....	141
4.1. Sampling	141
4.2. Whole rock geochemistry.....	145
4.3. Petrography and mineral chemistry.....	149
4.4. Geochronology.....	150
4.5. Geothermobarometry	153
5. Core rocks: Garnet amphibolites and kyanite-garnet amphibolites.....	156
5.1. Sampling	156
5.2. Whole rock geochemistry.....	156
5.3. Petrography and mineral chemistry.....	158
5.4. Geochronology	159
5.5. Geothermobarometry	160
6. Discussion.....	162
6.1. Pre-collisional divergence.....	162
6.2. Syn-collisional convergence.....	166
6.3. Pre- to syn-collisional geodynamic evolution of the Lufilian belt	170

PARTIE III: IMPLICATIONS MÉTALLOGÉNIQUES: SOURCE, TRANSPORT, DÉPÔT DE L'URANIUM 189

CHAPITRE 5: Geochemical signatures of uranium oxides in the Lufilian belt: from unconformity-related to syn-metamorphic uranium deposits during the Pan-African orogenic cycle..... 191

Abstract	192
1. Introduction.....	193
2. Geological setting	195
2.1. Lithostratigraphy of the Katanga sequence	196
2.2. Tectonic evolution of the Lufilian belt.....	199
3. Uranium mineralization	200
3.1. External fold-and-thrust belt uranium occurrences	201
3.2. Domes region uranium occurrences	201
4. Materials and methods	203
5. Results.....	204
5.1. Description of the samples investigated and chemical composition for the major elements determined by EMP	204
5.1.1. Uranium oxides dated at ca. 650 Ma in the External fold-and-thrust belt	204
5.1.2. Uranium oxides dated at ca. 530 Ma in the External fold-and-thrust belt	206
5.1.3. Uranium oxides dated at ca. 530 Ma in the Domes region	206
5.2. Rare Earth Element (REE) analyses by LA-ICPMS	206
5.3. Yttrium (Y) content measured by EMP and LA-ICPMS	209

6.	Discussion.....	211
6.1.	Interpretation of the geochemical uranium oxide signatures from the U occurrences in the Lufilian belt	211
6.2.	Comparison between uranium occurrences of the Pan-African Lufilian belt and worldwide uranium deposits.....	214
7.	Conclusion.....	220

CHAPITRE 6: Hypersaline fluids generated by high-grade metamorphism of evaporites: fluid inclusion study of uranium occurrences in the Western Zambian Copperbelt 227

	Abstract.....	228
1.	Introduction.....	229
2.	Regional geology.....	232
2.1.	Lithostratigraphy of the Katanga sequence.....	233
2.2.	Tectonic evolution of the Lufilian belt.....	234
2.3.	Synmetamorphic U mineralizations.....	235
3.	Analytical methods.....	238
3.1.	Petrography and mineral chemistry.....	238
3.2.	Microthermometry.....	238
3.3.	Raman spectroscopy.....	239
3.4.	LA-ICPMS.....	239
4.	Results.....	241
4.1.	Mineral paragenesis.....	241
4.1.1.	Lolwa occurrence.....	241
4.1.2.	Mitukuluku occurrence.....	243
4.2.	Quartz vein microstructures and fluid inclusion petrography.....	246
4.2.1.	Quartz vein microstructures.....	246
4.2.2.	Fluid inclusion petrography.....	247
4.3.	Fluid inclusion geochemistry.....	248
4.3.1.	Lolwa occurrence.....	248
4.3.2.	Mitukuluku occurrence.....	252
5.	Discussion.....	255
5.1.	Deformation and fluid circulation.....	255
5.2.	Chemistry and source of fluids.....	258
5.3.	Geodynamic context, fluid circulations and uranium mineralization.....	264
6.	Conclusion.....	266

CHAPITRE 7: Uranium mobilization by fluids associated with Ca-Na metasomatism: a P-T-t record of fluid-rock interactions during Pan-African metamorphism (Western Zambian Copperbelt)..... 274

	Abstract.....	275
1.	Introduction.....	276
2.	Regional geology.....	278
2.1.	Lithostratigraphy of the Katanga Supergroup in the internal and external zones of the Lufilian belt	279
2.2.	Tectonic evolution of the Lufilian belt.....	282
2.3.	Synmetamorphic uranium mineralizations.....	283
3.	Sampling and analytical procedures.....	285
3.1.	Sampling.....	285
3.2.	Electronic Microprobe.....	286
3.3.	Laser Ablation Inductively Coupled Plasma Mass Spectrometry (LA-ICPMS).....	287
3.4.	Ion microprobe.....	287
4.	Petrography and geochemistry.....	287
4.1.	Base of the metasedimentary cover of the Solwezi dome: the Lower Roan Group.....	287
4.2.	The pre-Katanga gneissic-migmatitic basement exposed in the core of the Solwezi dome.....	291
5.	Geochronological constraints.....	296
5.1.	Th-Pb on monazite from the kyanite micaschists.....	296
5.2.	U-Pb on uraninite from the kyanite micaschists.....	297
6.	P-V-T-X properties of the fluids.....	298

7.	Discussion.....	300
7.1.	Geochronological constraints on uranium mineralizations during the tectonic evolution of the Lufilian belt	300
7.2.	P-T-t-fluid/rock interactions.....	302
7.3.	Uranium mass balance	305
8.	Conclusion	307
	Appendix 1: Simplifications of the different chemical systems for fluid inclusion isochores.....	309
	Complementary data.....	321
	Thermometry on accessory minerals associated with uraninite.....	321
	Geochronology on uraninite grains.....	322
	CONCLUSIONS GENERALES	327
1.	Croissance crustale et nature de l'héritage de l'Archéen au Mésoprotérozoïque.....	328
2.	Evolution <i>P-T-t</i> de la ceinture orogénique du Lufilien	329
3.	Cycle de l'uranium et genèse des minéralisations uranifères du Lufilien	331
	RÉFÉRENCES BIBLIOGRAPHIQUES.....	335
	LISTE DES FIGURES	379
	LISTE DES TABLEAUX.....	389

INTRODUCTION

1. Thématique et problématique

Les principaux gisements primaires d'uranium sont situés dans des segments de croûte continentale formée dès l'Archéen (Witwatersrand, Afrique du Sud) jusqu'au Protérozoïque, notamment dans les ceintures orogéniques paléoprotérozoïques datées à 2.1 Ga (Francevillien, Eburnéen, Transamazonien) et à 1.8 Ga (Transhudsonien) et dans les ceintures néoprotérozoïques datées à 0.5 Ga (Pan-Africain). Cette corrélation entre gisements uranifères et ceintures orogéniques suggère un lien génétique entre ces deux objets.

Des interrogations subsistent quant à la relation entre la création et l'évolution géodynamique des fragments de croûte continentale au Protérozoïque et leur relation avec la métallogénie d'éléments lithophiles tels que l'uranium. L'uranium, en tant qu'élément incompatible, se trouve préférentiellement concentré dans la croûte continentale. Cependant, les modalités de redistribution de l'uranium en relation avec les processus qui affectent la croûte continentale, notamment au cours des orogénèses, restent encore à déterminer. Il s'agit dans ce projet de savoir en quoi les processus géodynamiques de création et de déformation de croûte continentale au Protérozoïque ont pu influencer l'extraction et la (re-)mobilisation de cet élément chimique, à intérêt économique, à partir de réservoirs qui sont à déterminer. Il est donc essentiel de comprendre le cycle métallogénique des concentrations uranifères protérozoïques en identifiant l'influence des processus géologiques impliqués dans la **mobilisation**, le **transport** et le **dépôt** de ce métal, tout en intégrant la notion de **formation**, de **croissance** et d'**évolution** de ces segments de croûte continentale. Il convient à ce propos de définir les mécanismes de formation, de croissance et d'évolution de la croûte continentale :

- (i) Un fragment de croûte continentale « **juvénile** » (angl. **juvenile**) est la part de croûte qui est directement issue de la fusion partielle du manteau, plus ou moins enrichi ;
- (ii) Un fragment de croûte continentale « **recyclée** » (angl. **recycled**) est la part de croûte retournée dans le manteau par la subduction ou la délamination ;
- (iii) Un fragment de croûte continentale « **remobilisée** » (angl. **reworked**) est la part de croûte soumise à la déformation et au métamorphisme au cours des orogénèses. Cette remobilisation peut affecter soit directement les marges de cratons et/ou les sédiments issus de l'érosion des cratons.

Deux modèles extrêmes s'opposent quant à la formation, la croissance et l'évolution de la croûte continentale et, en corollaire, pour la concentration de l'uranium :

- (i) **Extraction précoce** de la croûte continentale et de l'uranium lors de la différenciation primaire de la Terre (Armstrong, 1968; Fyfe, 1978; Reymer and Schubert, 1986). Ce stock initial est ensuite remobilisé en relation avec les processus de surface et les processus métamorphiques, métasomatiques et magmatiques lors d'orogénèses successives ou recyclé dans le manteau dans les zones de convergence de plaques ;

- (ii) **Extraction progressive** de la croûte continentale et de l'uranium dans les zones de convergence de plaques par fusion partielle de la plaque plongeante (basaltes ± sédiments) et du manteau en supra-subduction (Hurley and Rand, 1969). Dans ce cas également, la croûte continentale juvénile est susceptible d'être affectée par remobilisation ou recyclage.

Des modèles intermédiaires entre ces deux modèles extrêmes de formation de la croûte continentale s'accordent sur le fait qu'environ 60 à 80% du volume des continents actuels ait été extrait du manteau dès la fin de l'Archéen, il y a 2.5 Ga (Taylor and McLennan, 1985 ; Belousova et al., 2010 ; Hawkesworth et al., 2010).

2. Objectifs de la thèse

L'évaluation de la pertinence de ces modèles passe par la définition d'un cadre tectonique où des minéralisations uranifères sont décrites et en étroite relation spatiale et temporelle avec la formation de ceintures orogéniques d'âge Protérozoïque en marge de noyaux cratoniques d'âge Archéen. Pour se faire, l'Afrique australe constitue une cible de premier choix pour tester ces modèles. De fait, le cadre tectonique retenu pour ce projet de thèse est un segment de croûte continentale faisant partie intégrante de la ceinture orogénique **Néoprotérozoïque** du **Damara/Lufilien/Zambèze**.

La ceinture orogénique du **Damara/Lufilien/Zambèze** s'est formée au cours de l'orogénèse Pan-Africaine datée à 0.5 ± 0.3 Ga, entre les cratons du Congo et du Kalahari (Figure 1). Dans sa partie Ouest, en Namibie, la ceinture du Damara est caractérisée par des minéralisations uranifères, d'une importance économique mondiale (exemple : Rössing mine), associées à des intrusions granitiques tardi- à post-collision datées entre ca. 520-480 Ma (Toé, 2012). Ces intrusions minéralisées sont liées aux phases de relaxation thermique et d'effondrement gravitaire subséquentes à l'épaississement crustal de l'orogène dans un contexte de convergence de plaques (Toé et al., 2013). A l'instar de la thèse de Wilfried Toé qui portait sur la genèse des minéralisations uranifères dans la ceinture du Damara en Namibie, cette thèse se focalisera sur la genèse des minéralisations uranifères de la ceinture du Lufilien, en Zambie.

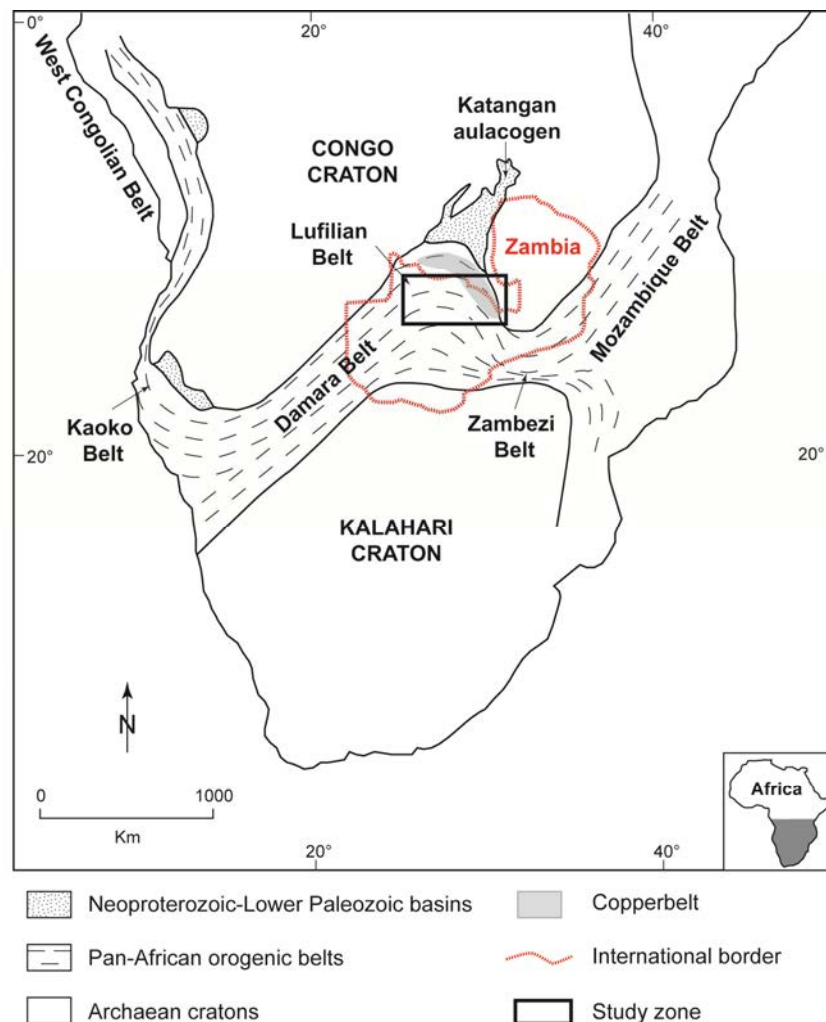


Figure 1: Localisation du projet de thèse dans son contexte géologique simplifié

L'intérêt scientifique de cette ceinture **Pan-Africaine** est double. D'une part, d'un point de vue géodynamique, il s'agit d'un domaine poly-orogénique qui permettra donc de caractériser les contributions relatives de la croissance, de la remobilisation et du recyclage de la croûte continentale depuis l'Archéen jusqu'au Néoprotérozoïque. D'autre part, cette ceinture présente de nombreuses occurrences uranifères encaissées par les séries néoprotérozoïques métasédimentaires du Katanga, décrites aussi bien en Zambie qu'en République démocratique du Congo. Ainsi, il sera donc possible de caractériser et de discuter des relations entre les **processus géologiques** (magmatisme, déformation, métamorphisme, métasomatisme) et la mobilisation, le transport et le dépôt de l'**uranium**.

Afin de réaliser ces travaux de thèse, **une approche multi-méthodes combinant géologie structurale, pétrologie, géochimie, géochronologie et inclusions fluides** a été élaborée. Plus spécifiquement, cette approche est requise pour:

- (i) Déterminer la **nature** de l'**héritage** de croûte **Archéenne** à **Mésoprotérozoïque** (sédiments issus de l'érosion des cratons ou bien blocs crustaux incorporés tectoniquement dans les ceintures orogéniques) ;
- (ii) Reconstruire l'**évolution P-T-t** de la ceinture du Lufilien-Zambèze et définir la nature du contact avec la bordure des cratons Archéens ;
- (iii) Caractériser la **typologie** et la **chronologie** des **minéralisations uranifères** décrites dans la ceinture du Lufilien ;
- (iv) Evaluer l'impact des **circulations de fluides** sur les **transferts** élémentaires, notamment celui de l'**uranium**.

L'originalité de cette thèse est en premier lieu d'aborder la métallogénie de l'uranium dans le cadre de la croissance et de l'évolution de la croûte continentale en considérant les différents modèles débattus à l'heure actuelle. De plus, l'approche pluridisciplinaire à différentes échelles depuis celle de la ceinture orogénique jusqu'à celle du minéral dépasse le cadre classique de l'étude métallogénique ciblée sur le gisement.

3. Organisation du manuscrit

L'essentiel de ce travail de recherches porte sur la zone interne de l'orogénèse du Lufilien, en Zambie. Ce manuscrit de thèse est organisé en **trois grandes parties**, comprenant chacune différents chapitres.

La **première partie (partie I)** porte sur la croissance et l'évolution de la croûte continentale en intégrant le cycle de l'uranium de l'Archéen au Protérozoïque. Cette partie couple deux chapitres (**chapitres 1 & 2**). Le **chapitre 1** permet de définir (i) l'état de l'art sur les modèles de croissance et d'évolution de la croûte continentale et (ii) l'évolution de l'uranium au cours des temps géologiques. Le **chapitre 2** est un article en préparation pour soumission au journal *Precambrian Research*. Il présente des données géochronologiques et isotopiques permettant de discuter l'évolution crustale de la zone interne de la ceinture orogénique du Lufilien, de l'Archéen au Mésoproterozoïque.

La **seconde partie (partie II)** de ce manuscrit s'intéresse plus particulièrement à l'évolution des ceintures orogéniques Pan-Africaines. Cette partie s'articule également en deux chapitres (**chapitres 3 & 4**). Le **chapitre 3** permet de présenter la distribution spatiale et temporelle des ceintures Pan-Africaines. Le **chapitre 4** étudie l'évolution de la ceinture du Lufilien au Néoproterozoïque en intégrant la notion de cycle de Wilson. Les résultats, présentés également sous forme d'un article en préparation pour soumission à *Journal of African Earth Sciences*, sont basés essentiellement sur une étude géochronologique et isotopique couplée à une étude géothermobarométrique permettant de reconstruire l'évolution *P-T-t* de la ceinture du Lufilien.

La **troisième partie (partie III)** est consacrée aux implications métallogéniques pour l'uranium, en s'appuyant sur le paradigme source-transport-dépôt. Cette partie s'articule sous forme de trois chapitres (**chapitres 5, 6 & 7**), représentant trois articles (i) publié en Octobre 2013 dans la revue *Ore Geology Reviews*, (chapitre 5, dépôt des minéralisations uranifères), (ii) accepté en Octobre 2013 dans le journal *Contributions to Mineralogy and Petrology* (chapitre 6, transport de l'uranium) et soumis dans la revue *Chemical Geology* (chapitre 7, interaction fluides-roches). Le **chapitre 5** introduit la typologie des minéralisations uranifères du Lufilien en intégrant principalement des données géochimiques sur uraninite. Le **chapitre 6** étudie la

distribution et la chimie des fluides impliqués dans le transport de l'uranium dans la zone interne du Lufilien, au cours du métamorphisme Pan-Africain. Enfin, le **chapitre 7**, essentiellement basé sur des données pluridisciplinaires, est ciblé sur l'enregistrement des interactions fluide-roche observées sur le terrain depuis l'échelle du minéral jusqu'à l'échelle de l'affleurement voire de la région. Ce chapitre propose également une quantification de ces interactions fluide-roche en termes de lessivage et mobilisation de l'élément uranium.

Ce manuscrit se conclut par une **discussion-conclusion** qui intègre les résultats obtenus et présentés sous forme de publications dans chacune des trois parties. Nous portons une réflexion globale sur les processus d'évolution de la croûte continentale Protérozoïque dans la ceinture du Lufilien. Cette discussion permet également de considérer le cycle de l'uranium à cette période, en intégrant cet élément dans un modèle géodynamique cohérent et original.

Toutes les références bibliographiques citées dans les différents chapitres sont regroupées à la fin du manuscrit afin d'en faciliter sa lecture. Les données présentées sous forme de tableaux sont fournies en annexe de chaque chapitre.

Cette thèse a reçu le support scientifique et financier de plusieurs organismes : (i) la société minière AREVA, dont une des thématiques **R&D** s'intitule « **Potentiel métallogénique de la croûte continentale** », (ii) le CNRS via son programme national NEEDS ((Nucléaire, énergie, environnement, déchets, société) et (iii) la compagnie minière Barrick Limited apportant un support logistique et technique à Lumwana, en Zambie.

Ce projet, de par sa multi-disciplinarité, implique la collaboration de différentes équipes de recherche dont les laboratoires GeoRessources (Nancy), CRPG (Nancy), Géosystèmes (Lille), Chrono-Environnement (Besançon), Institut für Geowissenschaften (Frankfurt), Magmas et Volcans (Clermont-Ferrand) et Géosciences (Rennes) avec la participation du Musée Royal de l'Afrique Centrale (Tervuren).

PARTIE I: CROISSANCE ET EVOLUTION DE LA CROUTE CONTINENTALE

CHAPITRE 1: Les continents, leur croissance et leur concentration en uranium

1. La croûte continentale: définition

Classiquement, les continents sont définis comme de vastes continuités géographiques émergées entourées par des océans. Cette notion n'a pas évolué depuis l'antiquité et correspond à la vision de tout un chacun. Cependant, outre cette définition géographique, il existe aussi et surtout une définition géologique, plus précise, qui intègre des observations mais aussi des interprétations liées à des décennies d'études. Dans un premier temps, les continents ne se limitent pas à une surface émergée mais possèdent une partie immergée tels que le talus continental ou encore le plateau continental. Les plateaux continentaux marquent la transition progressive entre croûte continentale et océanique, et définissent alors la notion de marge passive. Actuellement, la distribution de la croûte est bimodale, c'est-à-dire que l'on distingue une croûte océanique dont l'altitude moyenne est de -3800 m, et une croûte continentale, dont la l'altitude moyenne est de +837 m (Figure 2). La notion de continents n'intègre donc pas qu'une simple vision en 2D, considérés comme des surfaces, mais une vision en 3D, c'est-à-dire que l'on considère les continents en tant que volume. En effet, le géologue prend en compte les parties profondes et parlent alors de masses continentales. Ce n'est qu'au début du XX^{ème} siècle que l'Allemand Alfred Wegener prête attention à la disposition des continents et souligne le fait que la côte Est de l'Amérique du Sud semble s'emboîter parfaitement dans la côte Ouest de l'Afrique (Figure 2). D'autres bien avant lui s'en étaient aperçus mais sans proposer, à partir de cette observation, une théorie de dérive des continents. Il est maintenant acté que les limites de continents sont régies par la tectonique des plaques qui permet d'en comprendre leur répartition géographique, leur formation et leur évolution (Windley, 1986). La tectonique des plaques s'inscrit dans le schéma classique du cycle de Wilson (Wilson, 1966), c'es-à-dire que la formation de montagnes (orogénie ou orogénèse) est le produit de l'ouverture puis de la fermeture d'un océan. La fin d'un cycle orogénique est marquée par la collision de deux masses continentales, ce qui entraîne la création de relief à la limite de plaques.

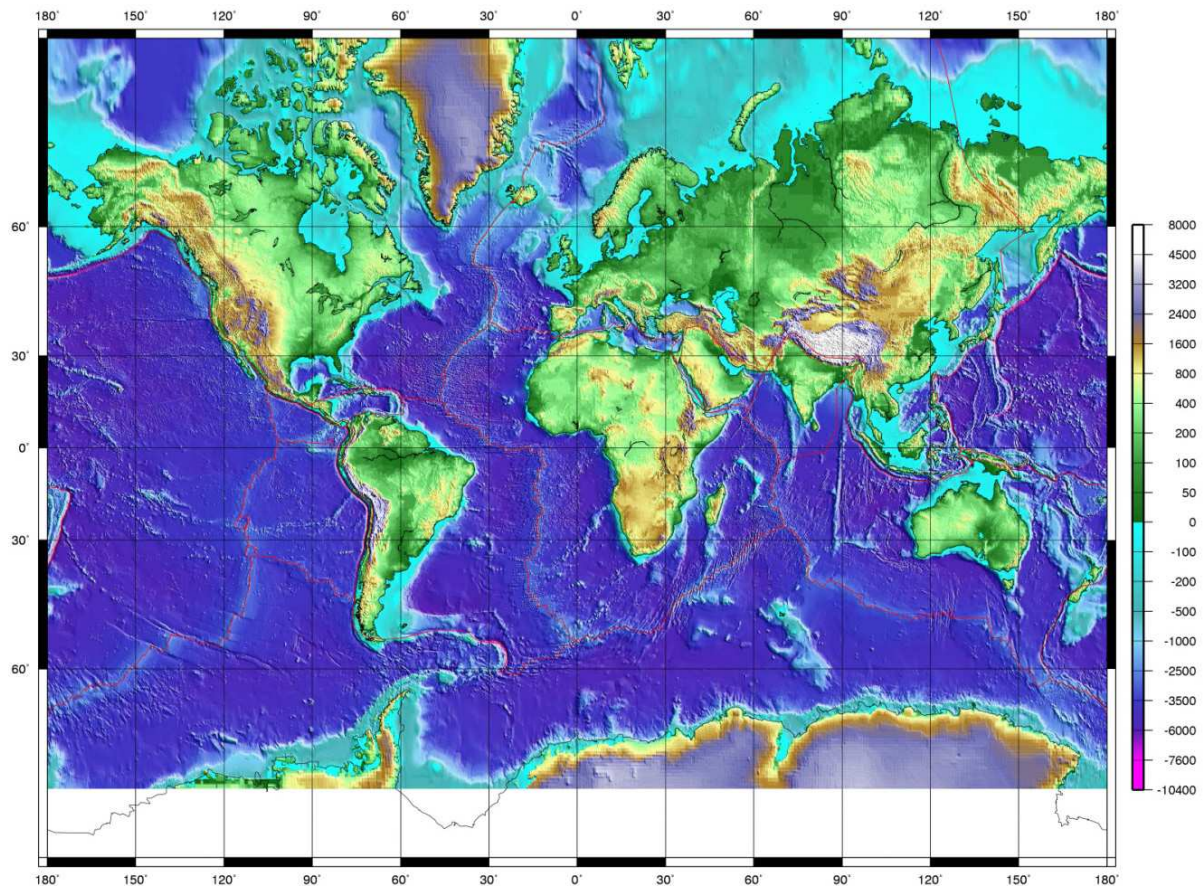


Figure 2: Planisphère terrestre représentant la distribution des altitudes (en mètres, échelle de droite) par rapport au niveau de la mer (par référence égale à zéro). Les lignes rouges indiquent les limites des différentes plaques tectoniques (carte tirée du SERC : Science Education Ressource Center du Carleton College).

La croûte continentale « flotte » sur le manteau asthénosphérique du fait de leur différence rhéologique. Ainsi, il est important d'introduire la notion de lithosphère. La lithosphère est l'ensemble constituée de la croûte terrestre (continentale ou océanique) et de la partie supérieure du manteau. Cette unité a un comportement rigide alors que l'asthénosphère sous-jacente est ductile. L'état rhéologique d'un solide dépend étroitement de sa température et par conséquent, le manteau asthénosphérique peut se transformer en manteau lithosphérique par refroidissement. La différence principale entre la lithosphère et l'asthénosphère correspond donc à une limite rhéologique liée à l'isotherme 1300 °C même si ces deux portions de manteau ont aussi très probablement des compositions différentes.

2. La croûte continentale archéenne et protérozoïque : distribution et composition

Les principaux continents, dans leur configuration actuelle, sont constitués de noyaux cratoniques d'âge essentiellement archéen autour desquels sont disposés de manière concentrique des ceintures orogéniques datées depuis le Protérozoïque (Hoffman, 1978 ; Artemieva, 2006 ; Figure 3).

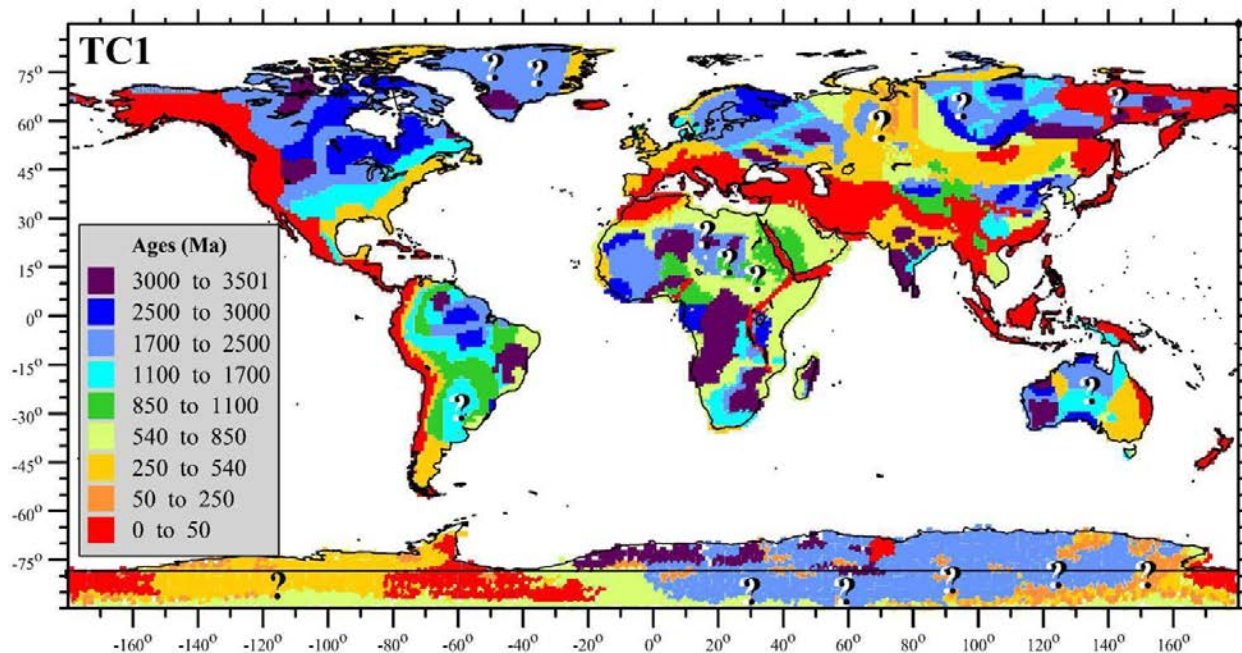


Figure 3: Répartition des âges de la croûte continentale à la surface de la Terre (Artemieva, 2006).

Les cratons archéens sont des blocs continentaux dont leur partie plus ancienne forme les boucliers. Ils représentent 15% des terrains précambriens (Goodwin, 1981) et constituent les nucleus des continents actuels. Le terme de craton définit donc une croûte continentale qui, après de longues périodes actives, a atteint un état stable. La cratonisation est donc un stade tardif de l'évolution des terrains archéens, qui permet la préservation (partielle) des épisodes tectoniques, magmatiques et métamorphiques majeurs (Pollack, 1986) ainsi que l'accumulation de grandes couvertures sédimentaires peu déformées. Ces noyaux cratoniques sont constitués par :

- (i) Des complexes magmatiques (90 à 95 % de la surface des cratons Archéens) constitués de Tonalite, Trondhjémite et Granodiorite (TTG). Ce sont des roches cristallines grenues, riches en quartz, feldspath plagioclase, biotite et parfois amphibole mais pauvres en feldspath potassique (Condie, 1998 ; Moyen and Van Hunen, 2012) ;

- (ii) Des ceintures de roches vertes (5 à 10 % de la surface des cratons Archéens) composées de laves ultrabasiqes, appelées komatiites, et de laves basiques intercalées avec des sédiments. Les komatiites se forment à des températures de 1600 à 1650 °C, contrairement aux basaltes actuels (1250-1350 °C). Ces ceintures sont également caractérisées par la présence de niveaux riches en quartz et magnétite (Banded-Iron Formation : BIF) dont le dépôt est lié à l'atmosphère réductrice qui régnait à la surface de la Terre jusqu'à 2,2 Ga.

La structure interne de ces noyaux cratoniques souligne des alternances de dômes à cœur de roches cristallines et de bassins comprenant les roches vertes (Van Kranendonk et al., 2004). Bien que des éclogites aient été reconnues localement dans les noyaux cratoniques (Moyen et al., 2006), le métamorphisme est essentiellement dans le faciès des schistes verts pour les ceintures de roches vertes mais atteint le faciès des granulites impliquant un gradient géothermique élevé (Brown, 2007).

Les ceintures orogéniques accrétées autour de ces noyaux cratoniques comprennent :

- (i) Des complexes magmatiques aux caractéristiques pétrologiques et géochimiques allant de calco-alkalin à péralumineux en passant par alcalin ;
- (ii) Des séries sédimentaires à dominante silicoclastique mais aussi des carbonates.

Ces ceintures comprennent également des successions de dômes et bassins mais avec un alignement préférentiel qui suggère l'influence d'un raccourcissement horizontal plus important en bordure du craton (Cagnard et al., 2007). Le métamorphisme des séries métasédimentaires couvre un spectre plus large que celui des roches des noyaux cratoniques avec d'une part des assemblages de minéraux traduisant un métamorphisme de Haute-Température allant du faciès des schistes verts à celui des granulites mais aussi des reliques de métamorphisme de Haute-Pression/Basse-Température dans le faciès des éclogites (Brown, 2007).

Il est à noter que l'attribution chronologique de ces ceintures a été initialement basée essentiellement sur des arguments stratigraphiques. Si les relations de recoupements et le principe

de superposition ne sont pas à remettre en cause, la pertinence des reconstructions stratigraphiques basées sur la succession de séquences lithologiques dans les domaines internes des ceintures orogéniques affectés par une déformation et un métamorphisme polyphasés intense est discutable. Plus récemment, les données géochronologiques sont venues compléter les arguments stratigraphiques dans l'attribution des âges aux ceintures orogéniques et aux roches impliquées. La datation de roches magmatiques combinée à leurs signatures pétrologiques et géochimiques permet de contraindre des événements d'accrétion magmatique. Cependant, ces données sont également à considérer avec attention, notamment lorsqu'il s'agit de la datation de roches magmatiques ou de migmatites témoignant de la fusion de matériel continental. En effet, dans ce cas, l'héritage de minéraux détritiques, en particulier le zircon, est courant. L'élaboration d'un modèle géodynamique cohérent pour la formation et l'évolution de ces ceintures au cours du Protérozoïque requiert de prendre en compte l'ensemble des données structurales, pétrologiques, géochimiques et géochronologiques. Les points clés à clarifier sont la chronologie et la nature des structures marquant les transitions entre marge active/marge passive en bordure de craton. L'implication relative de domaines océaniques et de marges continentales dans la formation de ces ceintures orogéniques est également à déterminer. Enfin, la contribution relative de magmas juvéniles et de magmas issus de la fusion partielle des roches accrétées dans les ceintures orogéniques doit être évaluée.

3. Modèles de croissance, remobilisation et recyclage de la croûte continentale

La préservation de la croûte archéenne n'a été que partielle au cours de temps géologiques. En effet, comme précisé dans le paragraphe précédent, l'archéen n'affleure que très peu, 15 % des terrains précambriens, et pourtant ce pourcentage est peu révélateur de la quantité de croûte juvénile produite à cette période, c'est-à-dire directement extraite d'un réservoir mantellique, par opposition à la croûte recyclée.

Différents modèles de formation et d'évolution de la croûte continentale ont été proposés dans la littérature depuis une extraction précoce avant 4 Ga lors de la différenciation de la Terre primitive (Armstrong, 1968; Fyfe, 1978; Reymer and Schubert, 1986; Figure 4) jusqu'à une formation plutôt tardive (Hurley and Rand, 1969). Cependant, ce dernier modèle qui prônait cette origine tardive de la croûte continentale était fondé sur des analyses isotopiques Rb-Sr et K-Ar

sur roches totales. A la lumière de données isotopiques et géochimiques plus récentes, les auteurs s'accordent à dire que plus de 60% du volume actuel de la croûte continentale a été produit dès la fin de l'Archéen (Fyfe, 1978 ; Reynet and Schubert, 1984 ; Taylor and McLennan, 1985 ; Armstrong, 1991 ; Belousova et al., 2010 ; Hawkesworth et al., 2010).

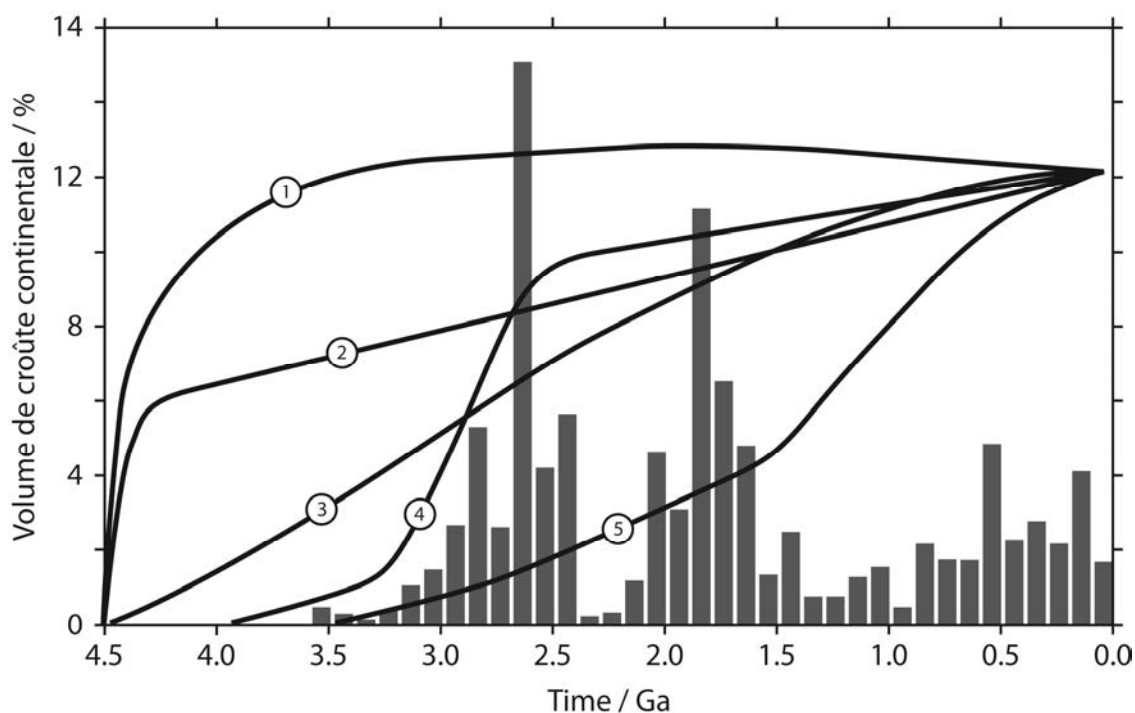


Figure 4: Histogramme de la distribution volumique de croûte continentale juvénile depuis la formation de la Terre (modifié d'après Condie, 2005). Cette distribution basée sur une compilation des âges U-Pb sur zircons et des âges modèles Nd met en avant le mode épisodique de la croissance continentale. Les modèles de croissance de croûte continentale sont aussi reportés (1 : Fyfe, 1978 ; 2 : Reynet and Schubert, 1984 ; 3 : Armstrong, 1991 ; 4 : Taylor and McLennan, 1985 ; 5 : Hurley and Rand, 1969).

Si les discussions sur la formation et l'évolution dans le temps de la croûte continentale sont encore aujourd'hui ouvertes, les modèles génétiques, c'est-à-dire géodynamiques, à l'origine de la création de croûte continentale, restent également sujet à débat. En effet, deux modèles opposés sont évoqués pour expliquer la formation de la croûte continentale primaire (Albarède, 1998 ; Artemieva, 2009 ; Windley, 2003) : le modèle de subduction et le modèle de panaches mantelliques. Selon les auteurs, le premier modèle, modèle de subduction, repose sur l'analogie avec l'actuel, où la croûte juvénile se crée principalement dans une tectonique dite horizontale, avec la formation d'arcs magmatiques à l'aplomb de zones de subduction par fusion du coin de

manteau (Condie, 2007). En effet, la composition moyenne de la croûte continentale est identique à celles des marges actives (Taylor and McLennan, 1985) ce qui tend à montrer que les zones de subduction participent activement à la croissance des masses continentales (Taylor, 1967). La fusion partielle de la croûte océanique dans la zone de subduction contribue aussi à la production de magma juvénile. Ce modèle propose donc une formation et une évolution progressive de la croûte continentale au cours des temps géologiques (Taylor and McLennan, 1985). Un des arguments les plus convaincants pour ce modèle intermédiaire est que la pétrogenèse des TTG correspond bien à ce type de contexte. De plus, la structuration en ceintures combinant des complexes magmatiques et des roches sédimentaires silico-clastiques et carbonatées suggère une accréation tectonique d'arcs magmatiques et de bassins associés autour de noyaux continentaux préexistants en relation avec des mouvements horizontaux significatifs (Vanderhaeghe et al., 1998 ; Moyen et al., 2006). Cependant, les mécanismes de formation de ces ceintures protérozoïques présentées comme résultant de mouvements horizontaux sont également discutées. L'interprétation de ces ceintures en termes de chaînes intracratoniques par fermeture de rifts avortés est favorisée par l'analyse des données stratigraphiques et structurales des avant-pays mais est également appuyée par la signature alcaline d'une partie des roches magmatiques associées à ces sédiments. Cependant, les signatures calco-alcalines d'une autre partie des roches magmatiques suggèrent plutôt la formation d'arcs magmatiques en marge des cratons. Enfin, l'identification de roches basiques affectées par un métamorphisme en faciès Eclogite a permis d'élaborer des modèles impliquant la fermeture de domaines océaniques.

A l'opposé, certains auteurs proposent un second modèle pour expliquer la formation de la croûte continentale, le modèle de panaches mantelliques, impliquant une croissance de la croûte continentale épisodique en relation avec l'activité cyclique de superplumes mantelliques dont le corollaire serait la formation de supercontinents (Condie, 1982 ; Anderson, 1994). Cette cyclicité est bien exprimée dans la distribution et la répartition des âges de cristallisation U-Pb des grains de zircon (Condie, 1998, 2005). En effet, les pics d'âges pourraient être interprétés comme des pics de croissance et d'activité du manteau avec multiplication de plumes, supportant le modèle de panache. Ce modèle de point chaud invoque que des remontées de panaches mantelliques fondent et forment des plateaux océaniques puis des croûtes de composition granitique. Ce second modèle pourrait être également appuyé par la structuration en dômes et bassins des

noyaux cratoniques archéens. En effet, ces structures peuvent être interprétées comme résultant d'instabilités gravitaires au sein d'une croûte constituée de roches basiques surmontant des roches plus différenciées, voire des magmas. Ces caractéristiques souligneraient un mode de genèse crustal par fusion partielle de larges plateaux océaniques mis en place à l'aplomb d'un panache mantellique (Kroner and Layer, 1992). Cette croissance verticale peut également intervenir dans le cas de sous-plaquage (*underplating*) de magmas d'origine mantellique en base de croûte d'arc ou de croûte continentale (Jahn, 2004) en réponse à la rupture du panneau plongeant. Le flux de chaleur généré permet la fusion de la croûte inférieure et la production de magmas plus ou moins siliceux et caractérisés par une contamination par l'encaissant et par une composante juvénile mantellique. Les injections d'origine asthénosphérique peuvent aussi se mettre en place directement dans les niveaux supérieurs, voire superficiels de la croûte.

Les caractéristiques géophysiques du manteau sous-continental des cratons archéens indiquent deux types de racines lithosphériques qui pourraient refléter la formation de ces premiers noyaux continentaux d'une part en relation avec l'activité de plumes mantelliennes et d'autre part en relation avec la subduction (Artemieva and Mooney, 2001). Dans tous les cas, la formation de la croûte continentale est liée à l'extraction d'un liquide magmatique issu initialement de la fusion partielle du manteau. En contrepartie, une partie de la croûte continentale est recyclée dans le manteau sous formes de sédiments dans les zones de subduction (Veizer and Jansen, 1985 ; Von Huene and Scholl, 1991).

Depuis le Paléoproterozoïque et l'installation d'une tectonique des plaques dite moderne, le volume de croûte généré au niveau des zones de subduction est de $2.8 \text{ km}^3/\text{an}$ alors que le taux de recyclage de la croûte continentale est estimé à $3.2 \text{ km}^3/\text{an}$ (Scholl and Von Huene, 2009). Cette compensation entre le volume de croûte juvénile et le volume de croûte recyclée permet d'expliquer la relative stabilité du volume total de croûte continentale depuis 3.0-2.5 Ga. Ainsi, les marges actives représentent non seulement des sites de production de croûte juvénile mais aussi des sites de recyclage de la croûte continentale. Il est important de noter que ces taux sont estimés sur une large période et à l'échelle planétaire.

En conclusion, de nombreuses études opposent différents modèles dont les extrêmes seraient : croissance verticale *versus* croissance horizontale. Le débat reste ouvert ! Les travaux récents, basés sur l'analyse couplée de plusieurs systèmes isotopiques sur zircon (Nd-Hf-O), permettent de dynamiser la recherche sur la croissance crustale. L'utilisation de l'hafnium sur grains de zircon, développée par Patchett en 1982, permet de combiner datation et traçage primordial (i.e. croûte *versus* manteau). Les avancées techniques de l'analyse par ablation laser couplée à un ICP-MS permettent d'obtenir dans une même zone, au sein d'un même grain de zircon, l'âge U-Pb (cristallisation), la signature en Hf (mantellique ou crustal) et l'âge modèle (extraction du matériel depuis son réservoir mantellique). Afin d'intégrer les données globales de croissance crustale, il faut d'abord documenter et discuter régionalement les données. C'est dans cette optique que le chapitre 2 présente une ébauche d'article qui propose une application de ce couplage traçage-datation sur zircon (Lu-Hf et U-Pb).

4. Concentration en éléments radioactifs dans la croûte continentale : cas de l'uranium

En normalisant les éléments traces au manteau primitif, et en les classant du plus incompatible au moins incompatible (dans les conditions de la fusion partielle du manteau), les continents montrent un net enrichissement en éléments incompatibles et une décroissance non-linéaire vers les moins incompatibles et même vers les éléments compatibles, à partir de de l'Al (Figure 5 ; Hofmann, 1988). L'élément chimique uranium se classe dans la famille des éléments dits incompatibles (ou hygromagmatophile) du fait de sa faible affinité avec les réseaux cristallins des silicates. Cette faible affinité est due à sa forte valence de charge combinée à un rayon ionique élevé. Il fait partie du groupe *High Field Strength Elements* (HFSE) au même titre que le thorium (Rollinson, 1983). Les éléments hygromagmatophiles ont un coefficient de partage K_D minéral-liquide silicaté inférieur à 1 et, de ce fait, sont préférentiellement concentrés dans les liquides silicatés lors des processus de fusion partielle ou lors de la cristallisation des magmas. Ainsi, la croûte continentale se trouve enrichie en éléments incompatibles dont l'uranium, extrait du manteau par fusion partielle (Hofmann, 1988 ; Shaw and Sturchio, 1992). En termes de concentration par rapport au manteau primitif (U = 21 ppb) dont l'uranium est extrait, la croûte continentale inférieure (U = 1.0-1.4 ppm) montre un enrichissement d'un facteur 47 à 66 fois supérieur alors que la croûte continentale supérieure (U = 2.7 ppm) présente un enrichissement

130 fois supérieur. La subduction de la croûte océanique et des sédiments permet de recycler l'uranium et d'autres éléments incompatibles d'origine continentale dans le manteau, par rapport au thorium et donc ce processus entraîne une diminution continue du rapport Th/U, généralement déterminé à partir du rapport $^{232}\text{Th}/^{238}\text{U}$ (kappa). Elliot et al. (1999) ont estimé que le rapport Th/U d'un manteau supérieur source des MORB (avec 0.01 ppm de Th) peut être abaissé de 4.0 à 2.6 pendant un intervalle de 1.8 Ga. Ce processus est appelé le recyclage post-Archéen de l'uranium (PURE : *Post archean Uranium REcycling*).

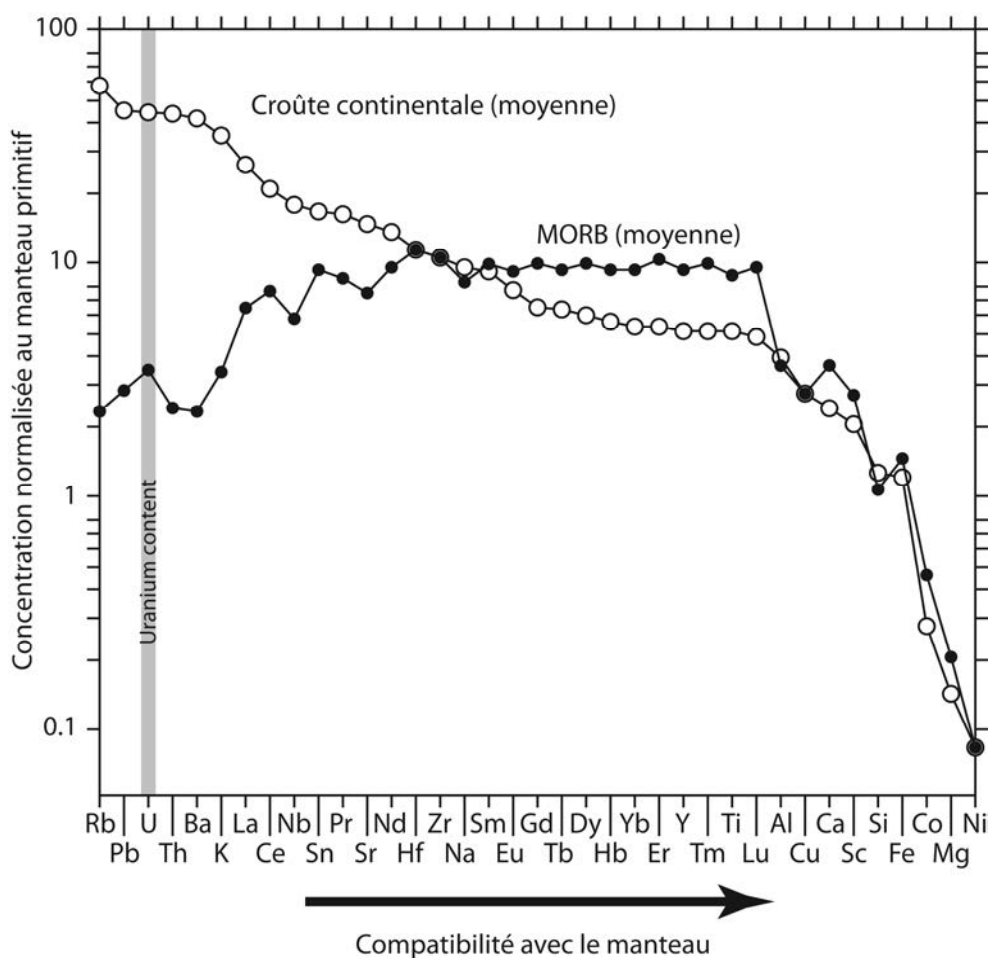


Figure 5: Présentation des concentrations moyennes normalisées au manteau primitif des éléments chimiques dans la croûte continentale en comparaison avec les valeurs pour les MORB (modifiée d'après Hofmann, 1988).

Les propriétés chimiques (valence et rayon ionique élevés) font que cet élément sera préférentiellement incorporé dans les minéraux lourds tels que le zircon, la monazite, l'uraninite, thorianite/thorite par substitutions avec le Zr, les terres rares ou encore le thorium du fait de leur

valence et rayon ionique voisins (Cuney and Friedrich, 1987). Cet élément présente également l'intérêt d'être radioactif ce qui lui confère, outre le fait qu'il génère de la chaleur dans la croûte continentale, toutes les propriétés d'un géochronomètre permettant de dater les processus géologiques. En conclusion, c'est donc grâce à ces nombreuses propriétés physiques et chimiques que l'uranium peut-être considéré comme un traceur géochimique de la différenciation, de la croissance, de l'évolution et de la remobilisation de la croûte continentale au cours des temps géologiques (Figure 6). En effet, cet élément est aussi bien mobilisé durant des processus géologiques profonds (magmatisme, métamorphisme et interactions fluide-roche) que de processus de surface (altération, érosion, transport et dépôt).

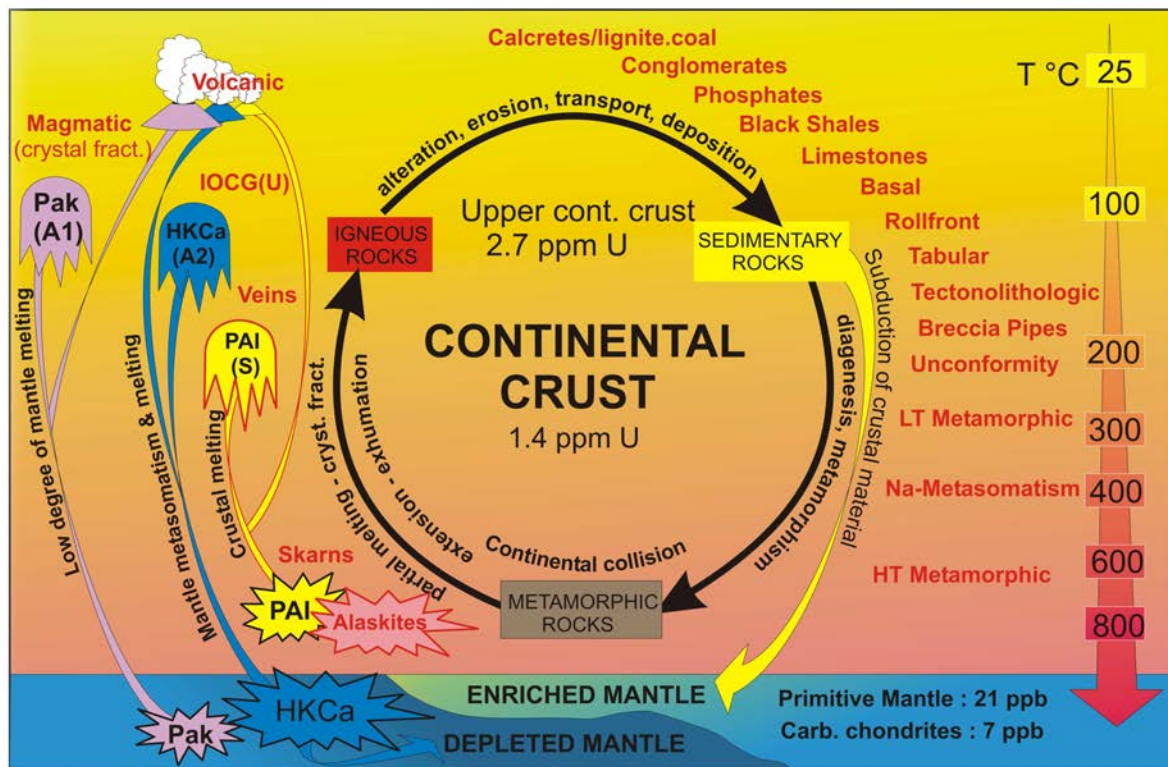


Figure 6: Cycle de l'uranium dans les différents contextes de gisements en relation avec les principaux processus de fractionnement au cours d'un cycle géologique (Cuney, 2009). Les réservoirs représentés sont le manteau et la croûte continentale. Les types de gisements sont les caractères rouges gras ; les mécanismes métallogéniques sont en caractères noirs gras. KCa = magma Calco-alcalin potassique ; Pak = magma Peralcalin ; Pal = magma Peralumineux.

5. Cycle de l'uranium de l'Archéen jusqu'à l'actuel

La typologie des gisements d'uranium est également un marqueur des processus impliqués dans la formation des premiers continents et de leur évolution (Cuney, 2010). Cuney (2010) propose quatre périodes d'évolution majeures pour les concentrations d'uranium à travers les temps géologiques.

La première période s'étale depuis les premiers stades d'accrétion terrestre jusqu'à 3.2 Ga. Cette période est caractérisée par la formation de la première croûte continentale principalement composée de basaltes et de séries TTG avec une concentration très faible en uranium (quelques ppm au maximum). L'uranium est principalement porté par des phases réfractaires et aucune concentration économique n'est connue, même dans les séries les plus différenciées. La seconde période est marquée par l'apparition de granites enrichis en uranium datés dès 3.1 Ga. Ces granitoïdes riches en éléments incompatibles, et en particulier en uranium et thorium, sont associés à une période de forte croissance crustale s'étalant de 3.2 à 2.2 Ga. L'uranium est essentiellement fractionné par des processus magmatiques donnant lieu à la production de magmas fortement potassique permettant de concentrer et de précipiter l'uranium sous forme d'uraninite (UO_2). Pour exemple, ces granites ultra-potassiques, avec des affinités calco-alcalines, sont décrits dans le craton du Kaapval-Kalahari en Afrique du Sud (Robb et al., 1990). L'érosion de ces granites pré-concentrés en uranium conduit à la formation des premières concentrations uranifères dans les bassins sédimentaires clastiques sous forme de conglomérats à galets de quartz à or-uranium du Witwatersrand en Afrique du Sud, la première concentration économique sur terre dont les dépôts les plus anciens du Dominion Reef sont datés à environ 3.08 Ga (Robb and Meyer, 1990). Les uraninites dans ce type de gisement sont d'origine détritique mais aussi remobilisées localement dans des plans de cisaillement. Les accumulations détritiques ne sont possibles qu'en l'absence d'oxygène car l'uraninite est très facilement soluble en conditions oxydantes.

La seconde période, allant de l'Archéen au Paléoprotérozoïque supérieur, est marquée par l'apparition de deux grands types de granites porteurs d'uranium : (i) les granites métalumineux fortement fractionnés et enrichis en potassium, ainsi que les pegmatites associées à ces processus et (ii) les leucogranites peralumineux fortement différenciés résultant de la fusion partielle des

métasédiments (Cuney and Friedrich, 1987 ; Cuney, 2009). Les granites métalumineux sont connus dans la plupart des cratons archéens tel que le craton du Yilgarn (Champion and Smithies, 2007) et le socle de East Alligator River Uranium district en Australie, la Province du Supérieur au Canada, le craton Amazonien au Brésil (Tallarico et al., 2005), les cratons de Dharwar (Jayayanda et al., 1995) et Singhbum en Inde (Sarangi and Singh, 2006) ou encore au sein du bouclier Baltique. Ces granites métalumineux où des uraninites ont été décrites sont datés entre 3.1 et 2.5 Ga. Les granites peralumineux, capable également de cristalliser de l'uraninite, commencent à apparaître vers 2.7 Ga (Cuney, 2009). Ces granites sont généralement enrichis en uranium, mais appauvris en éléments incompatibles tels que le thorium, en raison de la faible solubilité des minéraux accessoires porteurs de ces éléments (Cuney and Friedrich, 1987). Pendant cette période, les degrés les plus élevés de fractionnement magmatique sont atteints. Tel est l'exemple des pegmatites peralumineuses à éléments des terres rares (ETR) de Tanco dans le Manitoba, qui ont réussi à cristalliser une uraninite pauvre en Th-ETR (Duhamel et al., 2009). Il est intéressant de souligner que le fractionnement des magmas très peralumineux offre l'unique mécanisme capable de produire un enrichissement en uranium par rapport au thorium.

La troisième période s'étalant du Paléoproterozoïque supérieur au Néoproterozoïque est marquée par le phénomène d'oxyatmoversion ou *Great Oxidation Event* (GOE) à environ 2.3 Ga (Holland, 2002 ; Farquhar and Wing, 2003 ; Bekker et al., 2004). Cet événement marque une augmentation spectaculaire de la fugacité en oxygène de l'atmosphère et donc un changement irréversible dans les modes de transfert et de dépôt de l'uranium. Ainsi, l'uranium mis alors en contact avec les eaux superficielles oxydantes, passe en solution sous forme de complexes de carbonates d'uranyle (sous la valence U^{6+}). L'uranium facilement lessivable provient des accumulations de type paléo-placers formées avant 2.3 Ga et soumises aux circulations de fluides météoriques. Les autres sources d'uranium possibles sont les uraninites provenant des granites très fractionnés, les silicates d'uranium métamictes, les oxydes présents dans les roches plutoniques ou sédimentaires ou encore les verres volcaniques facilement altérables (Cuney, 2009). A la même période, d'énormes quantités de matières organiques ont été accumulées dans les sédiments de plateau et les milieux des mers épicontinentales. Pour exemple, des concentrations uranifères élevées sont décrites dans les séries de schistes noirs dans le bassin de Franceville au Gabon (Mossman et al., 1998). Cette période marque donc l'apparition de

concentrations uranifères hydrothermales et l'incorporation de cet élément dans les séries sédimentaires de plateforme continentale. Ces formations seront par la suite remobilisées durant des phases orogéniques plus tardives. La fusion partielle de ces séries métasédimentaires pré-enrichies en uranium permettra la genèse de pegmatites enrichies en uraninite le long de ces ceintures orogéniques d'âge Protérozoïque. Ces minéralisations sont décrites comme des sources potentielles pour la genèse des gisements de type discordance (*unconformity-related deposits*) ou encore de type métasomatique (*sodic metasomatic deposits*). Les cratons archéens et protérozoïques seront remobilisés au cours d'événements orogéniques successifs durant le Méso- et Néoprotérozoïque (Cuney, 2009).

Enfin, la dernière période d'évolution majeure pour les concentrations uranifères proposée par Cuney (2009) s'étend depuis l'Ordovicien, environ 0.45 Ga, jusqu'à l'actuel. La métallogénie est soumise alors à l'apparition des plantes vasculaires qui a pour conséquence de créer d'épaisses séquences sédimentaires silicoclastiques continentales réduites dans lesquelles l'uranium peut être piégé. Ces pièges peuvent fournir des concentrations actuellement économiques tels que les bassins intracontinentaux Mésozoïque à Cénozoïque au Niger (Pagel et al., 2005) ou encore en Asie Centrale (Munara, 2012 ; Bonnetti, 2013).

CHAPITRE 2: Crustal evolution of basement inliers in the internal zone of the orogenic Lufilian belt: U-Pb coupled with Hf isotopes of zircon and whole-rock Sm-Nd isotopic data (Domes region, Zambia)

Aurélien Eglinger¹ ; Olivier Vanderhaeghe¹ ; Anne-Sylvie André-Mayer¹ ; Armin Zeh² ; François Frémont¹ ; Cyril Durand³ ; Marc Poujol⁵ ; Jean-Louis Paquette⁶ ; Mike Richards⁷

Article en préparation pour *Precambrian Research*

¹GeoRessources, UMR 7359, CNRS-CREGU-Université de Lorraine, Nancy, France

²Institute of Geosciences, Johann Wolfgang Goethe-University, Frankfurt am Main, Germany

³Géosystèmes, Université de Lille 1, Lille, France

⁴CRPG, UMR 7358 CNRS-Université de Lorraine, Nancy, France

⁵Laboratoire Magmas et Volcans, UMR 6524, CNRS-Université Blaise Pascal, Clermont-Ferrand, France

⁶Géosciences Rennes, UMR 6118 CNRS-Université de Rennes 1, Rennes, France

⁷Barrick Limited, Lumwana, Zambia

Abstract

The Lufilian orogenic belt, formed between the Congo-Kasai and the Zimbabwe-Kaapvaal cratons during the Pan-African orogeny, comprises some basement inliers outcropping as tectonic windows interleaved with high-grade metasediments of the Neoproterozoic Katanga sequence. This area is known as the Domes region and these basement inliers are classically interpreted as undifferentiated Paleoproterozoic crust. Our U-Pb coupled Lu-Hf on zircon grain and whole-rock Sm-Nd isotopic investigations, focused on the Solwezi and Mwombezhi domes, highlight that these Pre-Katanga rocks have recorded a long history from Archean to Mesoproterozoic eons. U-Pb crystallization ages present different modes at ca. 1.92, 1.89, 1.71, 1.19 and 1.11 Ga and could be related to several peaks of magmatic activity described at the regional scale: the Usagaran (2.05-1.93 Ga), the Ubendian (1.88-1.85 Ga), the Lukamfwa (1.65-1.55 Ga) and the Irumide (1.05-0.95 Ga) phases. The T_{DM} model ages calculated for these rocks are mainly ranging from ca. 2.9 to 2.5 Ga which indicates a preponderant Neoproterozoic source. The contribution of a cryptic Archean crust is corroborated by detrital zircon grains dated up to ca. 2.69 Ga. The corresponding ϵ_{Hf} values plot mainly within the subchondritic reservoir between 0 and -15. These isotopic results demonstrate a long history of an Archean continental crust reworking with minor juvenile mantle input between the Paleo- and Mesoproterozoic eons. These results are in good agreement with the Proterozoic episodic crustal reworking within the Irumide belt interpreted as the southern metacratonic boundary of an Archean Bangweulu block. In conclusion, the basement inliers exposed in the Domes region have witnessed multiple metacratonization events and we propose that the Domes region represents the southwestern metacratonic boundary of the Bangweulu block, in continuation with the Mesoproterozoic Irumide belt. The Bangweulu block might have been the metacratonic margin of a larger Archean craton, as the Tanzania or Congo craton.

Keywords: Domes region, Lufilian belt, crustal reworking, Archean source, metacraton, Bangweulu block

1. Introduction

The Lufilian belt is known for its world-class copper-cobalt deposits (Mendelsohn, 1961; Unrug, 1983; Key et al., 2001; Cailteux et al., 2005; Dewaele et al., 2006) but also for its uranium occurrences (Meneghel, 1981; Decrée et al., 2011; Eglinger et al., 2013; 2014; submitted). Most of these mineralizations are hosted by the basal silico-clastic sequence of the Neoproterozoic Katanga Supergroup, designated as the Lower Roan Group. Different metallogenic models involve the basement rocks as the source of these elements (Koziy et al., 2009; Eglinger et al., 2013). However, basement rocks are poorly exposed in the Lufilian belt and, subsequently, poorly characterized in terms of geochemical and geochronological constraints. Gneissic rocks attributed to the pre-Katanga basement are nevertheless exposed in the core of the Kabompo, Mwombezi, Solwezi, Luiswishi domes and of the Kafue Anticline in the Lufilian belt. Recent geochemical and geochronological data obtained on gneisses from the core of the Kafue Anticline indicate crystallization ages of calc-alkaline magmatic rocks between 1.99 and 1.87 Ma (Rainaud et al., 2005). The western part of the Domes region, which is the focus of this paper, has been comparatively less studied. Previous works comprise a Rb-Sr whole rock age of 1220 Ma, a Rb-Sr muscovite age of 744 ± 8 Ma and K-Ar ages on micas ranging between 710 and 510 Ma (Cosi et al., 1992) and only sparse U-Pb zircon ages of 1884 ± 10 Ma and 1874 ± 9 Ma (John, 2001). Based on these data, these basement inliers have been interpreted to represent a pre-Katanga basement composed of orthogneisses with a Paleoproterozoic protolith age.

New analytical development of improved techniques for the *in-situ* analysis of U-Pb and Lu-Hf isotopes have recently brought fresh perspectives on (i) the crust-mantle differentiation and (ii) the origin and evolution of the continental crust. The current-day composition and structure of the continents reflects the relative contribution of (i) magmatic versus tectonic accretion of juvenile magmas and of (ii) reworking versus recycling of existing continental crust. Reworking can occur by deformation and metamorphism directly at the margin of a cratonic nucleus or after a cycle of erosion of the pre-existing continents and deposition in intracratonic or oceanic basins (Hawkesworth et al., 2010). Crustal recycling is potentially mainly achieved by subduction (Cloos, 1993) although it has been proposed that it also occurs by delamination of the lower crust.

In this study, we present (i) new combined U-Pb and Lu-Hf isotope data obtained on zircon grains from magmatic and metasedimentary rocks sampled in the Solwezi and the Mwombeshi basement inliers, and (ii) whole-rock Sm-Nd data acquired on mafic rocks intrusive in the metasedimentary sequence. These data indicate a record of magmatic and metamorphic events spreading from the Neoproterozoic to the Mesoproterozoic and point to the contribution of a juvenile-depleted mantle and a reworked older crust in the sources of the magmatic rocks. The significance of these ages and their geographical distribution serves to discuss the evolution of the crust forming the Bangweulu block and the internal zone of the Lufilian belt from the Archean to the Mesoproterozoic.

2. Geological background: Previous geochronology, geochemistry and isotopic data

The Lufilian belt forms an arcuate structure straddling the eastern part of Angola, the southern Democratic Republic of Congo (D.R.C.) and northwestern Zambia. It formed between the Kalahari and Congo cratons during amalgamation of the Gondwana supercontinent (Unrug, 1983; John et al., 2004; Johnson et al., 2005). The southern boundary of the Lufilian belt is marked by the sinistral Mwembeshi dislocation shear zone (MBZ) between the Lufilian and the Zambezi belts (De Swardt et al., 1965; Hanson et al., 1993). This shear zone has been interpreted to represent a lithospheric-scale weakness zone of Paleoproterozoic age (Porada and Berhorst, 2000), a transform-type plate boundary or a suture (Coward and Daly, 1984; Daly, 1986). The Pan-African Lufilian belt is localized in between the Congo-Kasai craton to the west and northwest, and the Zimbabwe craton to the south, and reworks the Kibaran orogenic belt to the northwest, the Bangweulu block to the northeast and the Irumide orogenic belt to the southeast (Figure 7).

2.1. The Congo-Kasai craton

This craton consists of a complex of granulite, gneiss, granite and amphibolite, gabbro-norite and gabbro-charnockite and migmatitic rocks. Granitic rocks yield Rb-Sr model ages between 3.49 and 3.33 Ga (Delhal and Ledent, 1973; Cahen et al., 1984). Sm-Nd and Rb-Sr isochron ages on TTG (Tonalite, Trondjemite, Granodiorite) suites, exposed in the northern part of the Congo-Kasai craton, give ages ranging between 2.8 and 2.9 Ga (Tchameni et al., 2000; Shang et al.,

2004). T_{DM} Nd model ages suggest that these rocks are derived from a late Mesoarchean crust. Younger whole-rock Rb-Sr ages are described in the northern and southern part of the craton, where late-granites are dated at around 2.6 Ga (Delhal et al., 1976; Caen-Vachette et al., 1988; Tchameni et al., 2000). Key et al. (2001) reported zircon U-Pb crystallization ages of 2561 ± 10 and 2538 ± 10 Ma for granitic gneisses from northwestern Zambia. These authors reported also a zircon crystallization age of 2058 ± 7 Ma for a porphyritic granite intruding these Archean gneisses.

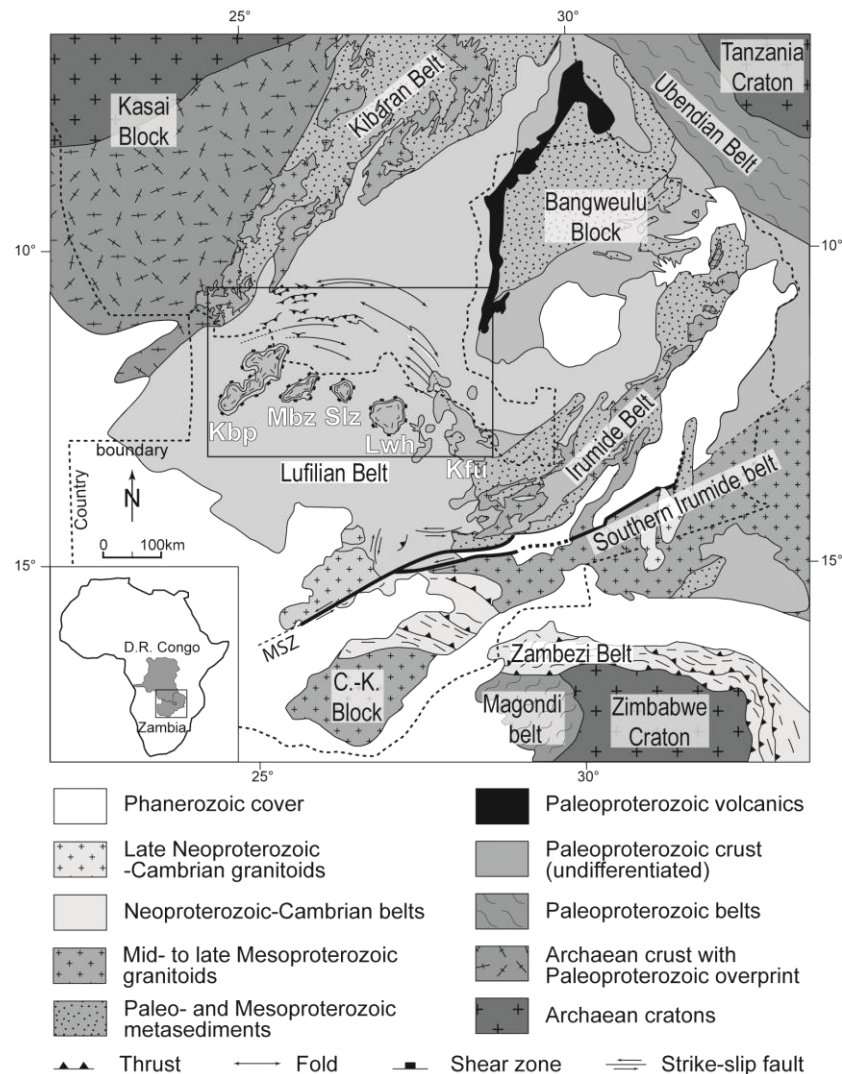


Figure 7: Tectonic map of central and southern Africa showing the location of the Lufilian-Zambezi belt in relation to the surrounding Archean cratons and Paleo- to Mesoproterozoic belts (modified after De Waele et al., 2008). Abbreviations: Kbp = Kabompo dome; Mbz = Mwombezhi dome; Slz = Solwezi dome; Lwh = Luswishi dome; Kfu = Kafue Anticline; C.-K. = Choma Kalomo block; MSZ = Mwembeshi Shear Zone; Ky = Kyanite; Tlc = Talc. The black rectangle represents the study area enlarged in Figure 8.

2.2. *The Bangweulu block*

The Bangweulu block consists of Archean and Paleoproterozoic crust on which a Paleoproterozoic continental-margin arc developed (Brewer et al., 1979; Andersen and Unrug, 1984; Kabengele et al., 1991; Figure 7). The presence of a cryptic Archean basement, named the Likasi terrane, is indirectly supported by the presence of Mesoarchean xenocrystic zircon (ca. 3.2 Ga) within a ca. 1.8 Ga tuff from the Katanga sequence (Rainaud et al., 2003). One granite gneiss along the southern boundary of the Bangweulu block yielded a zircon U-Pb crystallization age of 2736 ± 36 Ma, which is the only direct evidence of Archaean crust in the region (De Waele, 2005; De Waele et al., 2006a, b). This block comprises different lithotectonic units including high-grade granitic rocks and schists sequences, dated between 2.09 and 1.93 Ga (Ring et al., 1997; Rainaud, 2005; Rainaud et al., 2003; 2005; Vrana et al., 2004; De Waele, 2005) and plutono-volcanic rocks, dated between 1.88 and 1.82 Ga with T_{DM} Nd model ages ranging from 2.9 and 2.5 Ga (Brewer et al., 1979; Schandelmeier, 1980, 1983; Kabengele et al., 1991; Ngoyi et al., 1991; John, 2001; De Waele, 2005; Rainaud et al., 2005; De Waele et al., 2006). This calc-alkaline plutono-magmatic event was initially interpreted as a magmatic arc related to subduction to the northwest of the Bangweulu block (Brewer et al., 1979; Andersen and Unrug, 1984; Kabengele et al., 1991). Lenoir et al. (1994) used similarities in age between tectonothermal events in the Usagaran and Ubendian belts to suggest a long-lasting active continental margin along the southern margin of the Tanzania and Congo cratons, terminated by transpressive shear along the Ubendian belt and intrusion of the ca. 1.8 Ga plutono-volcanic suite. More recently, Hanson (2003) proposed that this magmatic suite is a result of late- to post-collisional anatexis of overthickened crust marking the end of Ubendian tectonism. This magmatic sequence is overlain by a supracrustal Paleoproterozoic metasedimentary sequence, known as the Mporokoso Group (Andrews-Speed, 1980; Andersen and Unrug, 1984; De Waele and Fitzsimons, 2007). The maximum age of this metasedimentary sequence is provided by a concordant age on detrital zircon at 1829 ± 19 Ma and minimum age is constrained by the emplacement of the Lusenga syenite at ca. 1.15 Ga within the Mporokoso Group (Brewer et al., 1979). Detrital zircon ages suggest the predominance of a local source for magmatic rocks exposed in the Ubendian belt and in the Bangweulu block (De Waele and Fitzsimons, 2007). Some younger metasediments have been described and derived from the reworking of the Mporokoso Group with a maximum age deposition at 1434 ± 13 Ma (Andersen and Unrug, 1984; De Waele and Fitzsimons, 2007).

2.3. *The Kibaran belt*

This Mesoproterozoic orogenic belt is located between the Tanzania craton/Bangweulu block to the east and the Congo-Kasai craton to the west (Figure 7). Two major magmatic-tectonic events were described in this belt. The first magmatic event is related with voluminous granitoids emplacement during a short period of time between 1.37 and 1.38 Ga (Tack et al., 2002, 2007; Kokonyangi et al., 2004). These granitoids are represented by peraluminous S-type in the north and by intermediate-felsic I-type in the south (Kokonyangi et al., 2004). According to Kokonyangi et al. (2004), this magmatic-thermal event is related to underplating of arc mafic magmas at the base and within the crust, which caused an increase in temperature and partial melting of metasedimentary rocks (Kokonyangi et al., 2004). A second tectonic event, affecting both metasedimentary rocks and granitoids, is recorded at ca. 1.08 Ga and reached metamorphism up to amphibolite-grade, with P - T conditions estimated at 6.0-6.5 kbar and 740-780 °C (Kokonyangi et al., 2004).

2.4. *The Irumide belt*

The Mesoproterozoic Irumide belt is located along the southern margin of the Bangweulu block. This belt includes a deformed basement, folded metasedimentary units and voluminous granitoid intrusions (De Waele et al., 2008). Deformed basement is dated by U-Pb on magmatic zircon grains and yielded crystallization ages mainly between 2.05 and 1.92 Ga (De Waele et al., 2006). These rocks yielded T_{DM} Nd model ages between 3.2 and 3.1 Ga (De Waele et al., 2006). The oldest rocks within the Irumide belt, are exposed in its southwestern part, were dated at 2726 ± 36 Ma by U-Pb on magmatic zircon grains (De Waele, 2005; De Waele et al., 2006). This gneissic basement is overlain by Paleoproterozoic metasedimentary sequences, referred as the Manshya River and Kamona Group. The maximum ages of deposition is given by concordant U-Pb age on detrital zircon grains at 1882 ± 30 Ma and 1953 ± 15 Ma, respectively (De Waele and Fitzsimons, 2007) and the minimum ages are given by the ages of granitoids intruding these sequences, respectively, dated at 1610 ± 26 Ma and 1664 ± 6 Ma by U-Pb on magmatic zircon grains (De Waele, 2005; De Waele et al., 2006). These granitoids present T_{DM} Nd model ages of 3.2 and 2.8 Ga, and the difference between the T_{DM} model ages and the crystallization ages imply significant crustal reworking (De Waele, 2005; De Waele et al., 2006). Detrital signatures of the Manshya River and Kamona Group sequences are similar to the Mporokoso Group with

dominant modes around 2000 and 1850 Ma, but with a larger detrital input at ca. 1.85 Ga for the Mporokoso Group (De Waele and Fitzsimons, 2007). Basal intrusive volcanic units in these metasediments yield crystallization ages between ca. 1.88 and 1.86 Ga and T_{DM} model ages ranging from 2.8 and 2.2 Ga (De Waele et al., 2006). Most granitoid rocks in the Irumide belt were emplaced during the Irumide orogeny, with U-Pb crystallization ages on zircon ranging from ca. 1.05 and 0.95 Ga (De Waele et al., 2006). The majority of these granitoids are subalkaline and peraluminous. Two samples were analyzed for Nd isotopes and give T_{DM} Nd model ages of 3.3 and 2.6 Ga (De Waele et al., 2006). The peak metamorphism is constrained at between ca. 1.02 and 1.01 Ga through U-Pb dating of low U/Th zircon overgrowths (De Waele, 2005).

2.5. The Lufilian-Zambezi belt

Neoproterozoic extension along the southern margin of the Congo craton is recorded both in the Lufilian and Zambezi belts as two-distinct rift-related volcano-sedimentary and passive margin sequences. The first continental rifting in the Lufilian-Zambezi belt started at ca. 880 Ma, resulting in the deposition of the Roan Group sediments in the Lufilian belt. Early extensional stages of continental rifting are well illustrated by the emplacement of Neoproterozoic granitoids exhibiting WPG (A-type) affinities (Katongo et al., 2004) and dated between ca. 880 (Nchanga granite: 883 ± 10 Ma; Armstrong et al., 2005) and ca. 820 Ma (Ngoma gneiss: 820 ± 7 Ma; Hanson et al., 1988). Volcanic rocks were also associated with this magmatism and present consistent U-Pb ages at ca. 880 Ma (Johnson et al., 2007a). These rocks present negative $\epsilon Nd(t)$ isotope ratios indicating that they were generated by mixing/assimilation of juvenile material with older basement gneisses (Johnson et al., 2007a). Porada and Berhorst (2000) proposed that these plutonic-volcanic felsic rocks mark the dislocation of the Rodinia supercontinent at ca. 880 Ma. Alternatively, Kröner and Cordani (2003) have argued that this part of Africa was not part of the Rodinia supercontinent. The second rifting event is marked by the extrusion of the Luakela volcanics of the Mwashya Subgroup, which stratigraphically overlies the Roan Group in the Lufilian belt. These volcanic rocks are dated at 765 ± 5 Ma by U-Pb on zircon (Key et al., 2001). Additional evidence for magmatic activity at this period is expressed by the gabbroic intrusions, within Katanga carbonate sediments of Solwezi area, dated at 745 ± 8 Ma and 753 ± 9 Ma by U-Pb on zircon (Barron, 2003; Barron et al., 2003). In the Lufilian belt, these mafic rocks hosted by

the Upper Roan Group and the Mwashya Subgroup display continental-within-plate and tholeiitic geochemical signatures (Tembo et al., 1999). The authors concluded based on geochemical data that rifting did not progress beyond the continental rift stage in the Lufilian belt. However, eclogite, metagabbro and gabbro characterized by N-MORB geochemical signatures are interpreted to be vestiges of an oceanic crust in the Lufilian-Zambezi belt (John et al., 2003).

A minimum age for the onset of subduction is recorded by Eclogite facies metamorphism, dated at ca. 595 Ma by Sm-Nd whole-rock and garnet isochron on mafic boudins in the Zambezi belt (John et al., 2003). Subduction and exhumation of crustal units under a low geothermal gradient to form the accretionary orogenic belt is depicted by *P-T* estimates of kyanite-bearing eclogites with temperatures of 590-750 °C at a minimum pressure of 20 kbar (John et al., 2003). Phengite-bearing eclogites equilibrated at a temperature between 720 and 755 °C and a pressure between 20 and 28 kbar (John et al., 2003). Crustal tectonic accretion is followed by an increase in the geothermal gradient recorded by intermediate-pressure/intermediate-temperature conditions (Barrovian metamorphism) with a pressure around 13 ± 1 kbar and a temperature of 750 ± 25 °C dated at 529 ± 2 Ma, by U-Pb on monazite grains from kyanite-talc micaschist in the Kabompo, Mwombezi and Solwezi domes (John et al., 2004). ^{40}Ar - ^{39}Ar thermochronology on biotite and Rb-Sr dating on muscovite and biotite yield ages ranging from 510 to 463 Ma that are interpreted to represent post-orogenic cooling of the metamorphic rocks in the Lufilian belt (Cosi et al., 1992; John et al., 2004; Rainaud et al., 2005).

3. Geological setting and description of the sampled lithologies

The Lufilian belt has been subdivided in five lithotectonic units: (i) the Katanga aulacogen, previously called Golfe du Katanga, acted as the foreland during the northward thrusting in the external zone, (ii) the External-fold-and-thrust belt, (iii) the Domes region, (iv) the synclinorial belt and (v) the Katanga high (Unrug, 1988). The latter two lithotectonic units are poorly exposed and thus poorly known. The Katanga high is interpreted as the southern margin of the basin, the hinterland of the belt (Kampunzu and Cailteux, 1999). In this paper, according to the Pan-African metamorphic isogrades described by François and Cailteux (1981) and Cosi et al. (1992), we define two major orogenic units: (i) an external zone characterized by biotite±chlorite±sericite metamorphic paragenesis (Greenschist facies) and (ii) an internal zone characterized by

garnet+kyanite metamorphic paragenesis (Amphibolite facies). The external zone comprises the Katanga (External fold-and-thrust belt) and Zambian (Kafue anticline) Copperbelt. This zone comprises a Neoproterozoic sedimentary and metasedimentary sequence, the Katanga Supergroup, composed from the bottom to the top of the Roan, Nguba and Kundelungu Groups presumably deposited on top of a pre-Katanga basement (Figure 7). This low grade metasedimentary sequence of the external zone is affected by folds and thrusts. The internal zone corresponds to the Domes region and comprises the Kabompo, Mwombezhi, Solwezi and Luswishi domes. It is marked by a higher metamorphic grade ranging from upper Greenschist to upper Amphibolite facies affecting a complexly folded nappe pile made of metasedimentary rocks interleaved with migmatitic-gneisses deformed in low-amplitude dome-shaped structures (Mendelsohn, 1961; Cosi et al., 1992; Porada and Berhorst, 2000; John et al., 2004). This study is focused on two basement inliers, Solwezi and Mwombezhi domes, outcropping in the internal orogenic belt (Figure 8).

3.1. Solwezi dome

The basement rocks are represented by gneisses more or less migmatitic, and minor amphibolites. Five gneissic-migmatitic rocks (*ZM-10-09*, *ZM-10-13*, *ZM-10-17*, *ZM-10-38* and *ZM-10-53*), described as the Gneiss Formation in the literature, were sampled within the core of the Solwezi dome, outcropping in the northern and western part (Figure 8). These samples show flat-lying foliation outlined by variation in the proportions of mineral phases. Foliation is marked by the alternation of biotite-rich layers and quartz-feldspar layers. Feldspar minerals are plagioclase (oligoclase) and K-feldspar (orthoclase and microcline). Secondary muscovite grains, described in the samples *ZM-10-09*, *ZM-10-13* and *ZM-10-17*, are also delineating the foliation. Late epidote and scapolite poikiloblasts overprint the main foliation. Samples *ZM-10-09*, *ZM-10-13*, *ZM-10-17* and *ZM-10-53* are characterized by the presence of centimetric feldspar recrystallized porphyroclasts, wrapped in the foliation (Figure 9a, b, c). These four rocks present characteristics of augen gneiss and could be interpreted as ortho-derived. In the western part of the dome, a coarse-grained and sheared granite was sampled (*ZM-10-66*). This igneous rock is characterized by an assemblage of quartz, orthose, microcline, plagioclase, biotite and muscovite. Foliation is mainly underlined by phyllosilicate and elongated quartz grains. Minor epidote and scapolite grains are also found as xenoblastic grains. One migmatitic sample was sampled in the

south part of the dome. This sample is characterized by syn-migmatitic foliation and by discordant granitic veins (Figure 9d, e). The granitic fraction shows some garnet porphyroblasts. The matrix is dominated by quartz, microcline, muscovite and biotite. One amphibolite (ZM-10-51) was collected in the western part of the dome. Amphibolite occurs as metric boudins transposed within gneissic foliation (Figure 9f). This amphibolite is characterized by large amphibole (pargasite) and rutile grains with a matrix dominated by plagioclase (andesine-labradorite), epidote, biotite and minor feldspar (orthoclase).

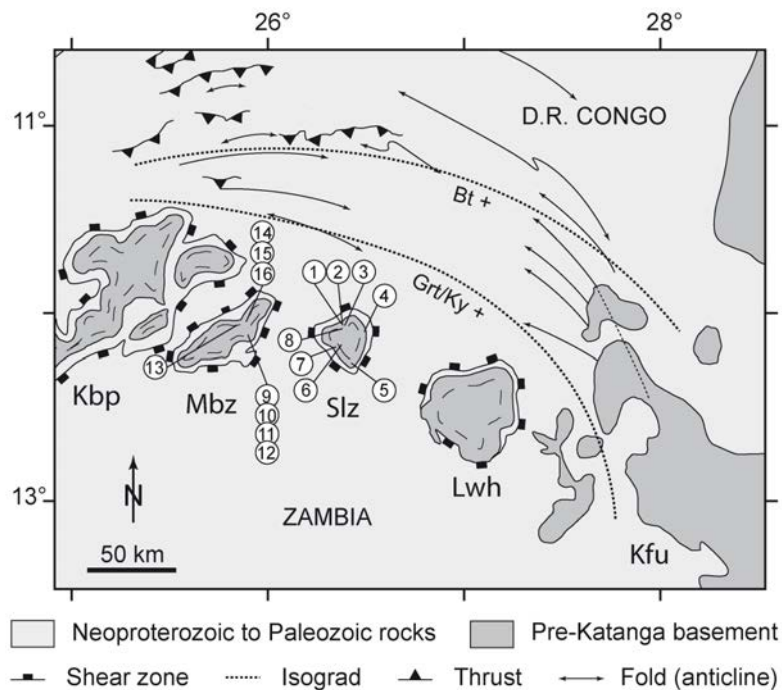


Figure 8: Simplified geological map of the internal and external zones of the Lufilian belt and sample location. References to studied samples: n°1-2-3 = orthogneiss (ZM-10-09, ZM-10-13 and ZM-10-17); n°4 = granite (ZM-10-66); n°5 = paragneiss (ZM-10-62); n°6 = amphibolite (ZM-10-51); n°7 = orthogneiss (ZM-10-53); n°8 = paragneiss (ZM-10-38); n°9 = paragneiss (ZM-39-01); n°10 = amphibolite (ZM-39-04); n°11 = paragneiss (ZM-62-05); n°12 = paragneiss (ZM-66-08); n°13 = orthogneiss (ZM-12-07); n°14 = amphibolite (ZM-12-13); n°15 = amphibolite (ZM-12-16); n°16 = granite (ZM-12-25). Details are in Table 1. Abbreviations: Kbp = Kabompo dome; Mbz = Mwombezhi dome; Slz = Solwezi dome; Lwh = Luswishi dome; Kfu = Kafue Anticline; Bt = Biotite; Grt = Garnet; Ky = Kyanite.

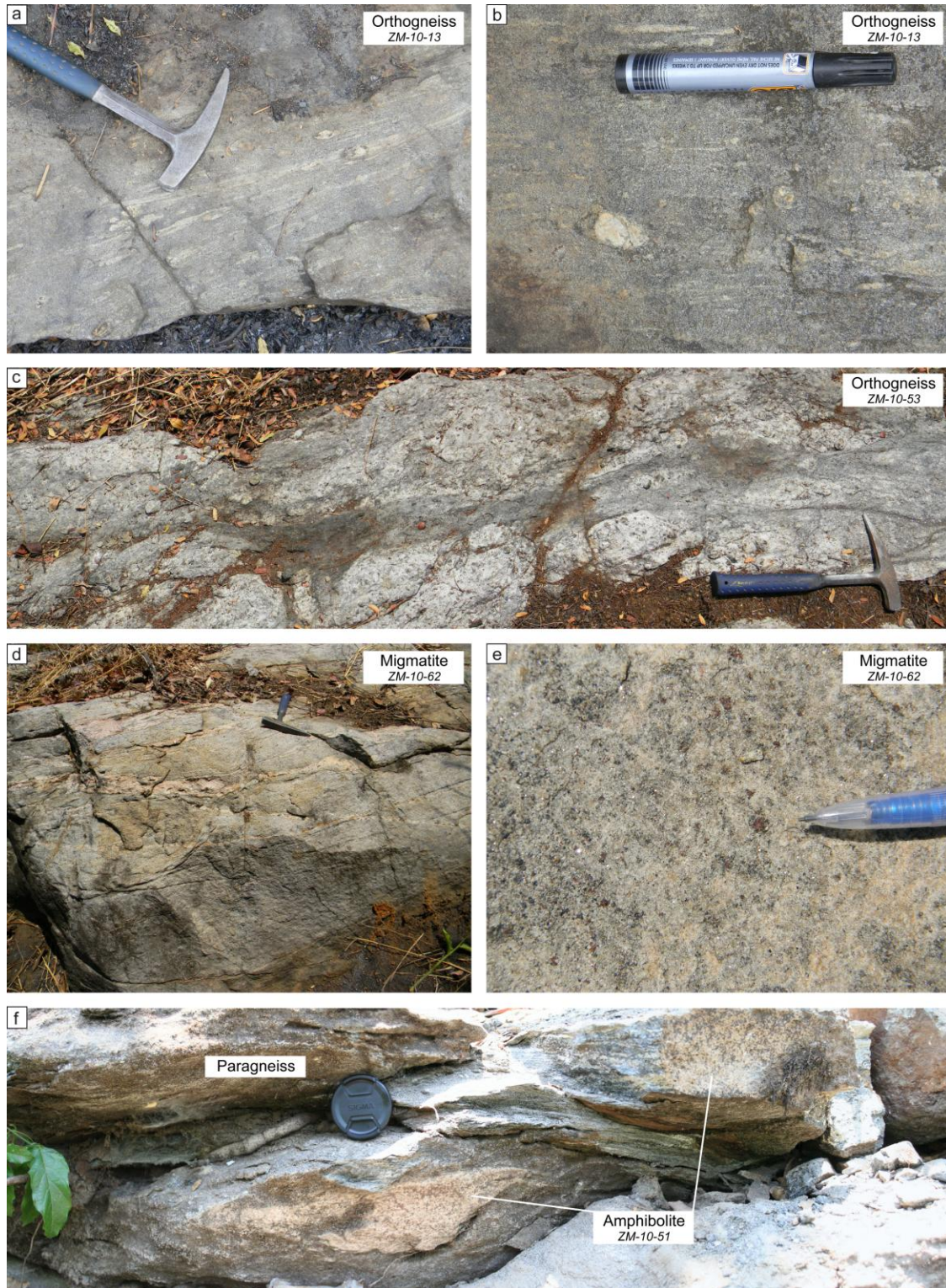


Figure 9: Outcrop pictures from the Solwezi dome. a, b, c: Partially migmatitic orthogneiss with feldspar porphyroclasts transposed within foliation. d: Migmatitic paragneiss with concordant syn-migmatitic foliation and discordant granitic veins. e: Garnet porphyroblast within grainitic fraction. f: Amphibolite boudins hosted by paragneiss and transposed within the foliation.

3.2. *Mwombezhi dome*

The basement rocks of Mwombezhi dome consist of schists, gneisses more or less migmatitic and minor amphibolite. Samples were collected from drill cores, *ZM-39-01*, *ZM-39-04*, *ZM-62-05* and *ZM-66-08* in the Chimiwungo area, from outcrops in the open pit, *ZM-12-13*, *ZM-12-16*, *ZM-12-25* in the Malundwe mine and one from an outcrop, *ZM-12-07*, localized in the western part of the dome. Samples *ZM-39-01* and *ZM-62-05* are two pink paragneisses characterized by quartz, feldspar (microcline) and biotite. Some K-feldspar porphyroclasts present a sigmoid shape and are transposed to the foliation. Minor kyanite grains are wrapped in the biotite-rich bands. Accessory minerals are represented by hematite, magnetite, muscovite, epidote and scapolite. Different mafic rocks (*ZM-39-04*) were sampled within these pink gneisses. These metabasites are characterized by biotite, amphibole (tschermakite), plagioclase (oligoclase-albite) and quartz with late scapolite, titanite, epidote and minor apatite. Sample *ZM-66-08* is characterized by a schistosity marked by the abundance of oriented biotite grains, associated with feldspar and quartz. Accessory allanite grains were observed.

Sample *ZM-12-07* is characterized by feldspar porphyroclasts and by shear bands marked by biotite (Figure 10a, b). Two basic rocks (*ZM-12-13* and *ZM-12-16*) are exposed as decimetric to metric boudins which are transposed into the foliation of migmatites (Figure 10c). These two mafic rocks are characterized by garnet (almandine) and amphibole (tschermakite) assemblage. Matrix is dominated by plagioclase (andesine), quartz, biotite, ilmenite and rutile. One granitic vein concordant to the syn-migmatitic foliation was also sampled (*ZM-12-25*; Figure 10c) and interpreted as the granitic fraction formed by partial melting. This rock presents a granular texture and is characterized by a quartz and plagioclase assemblage with minor secondary mica, chlorite and epidote grains.

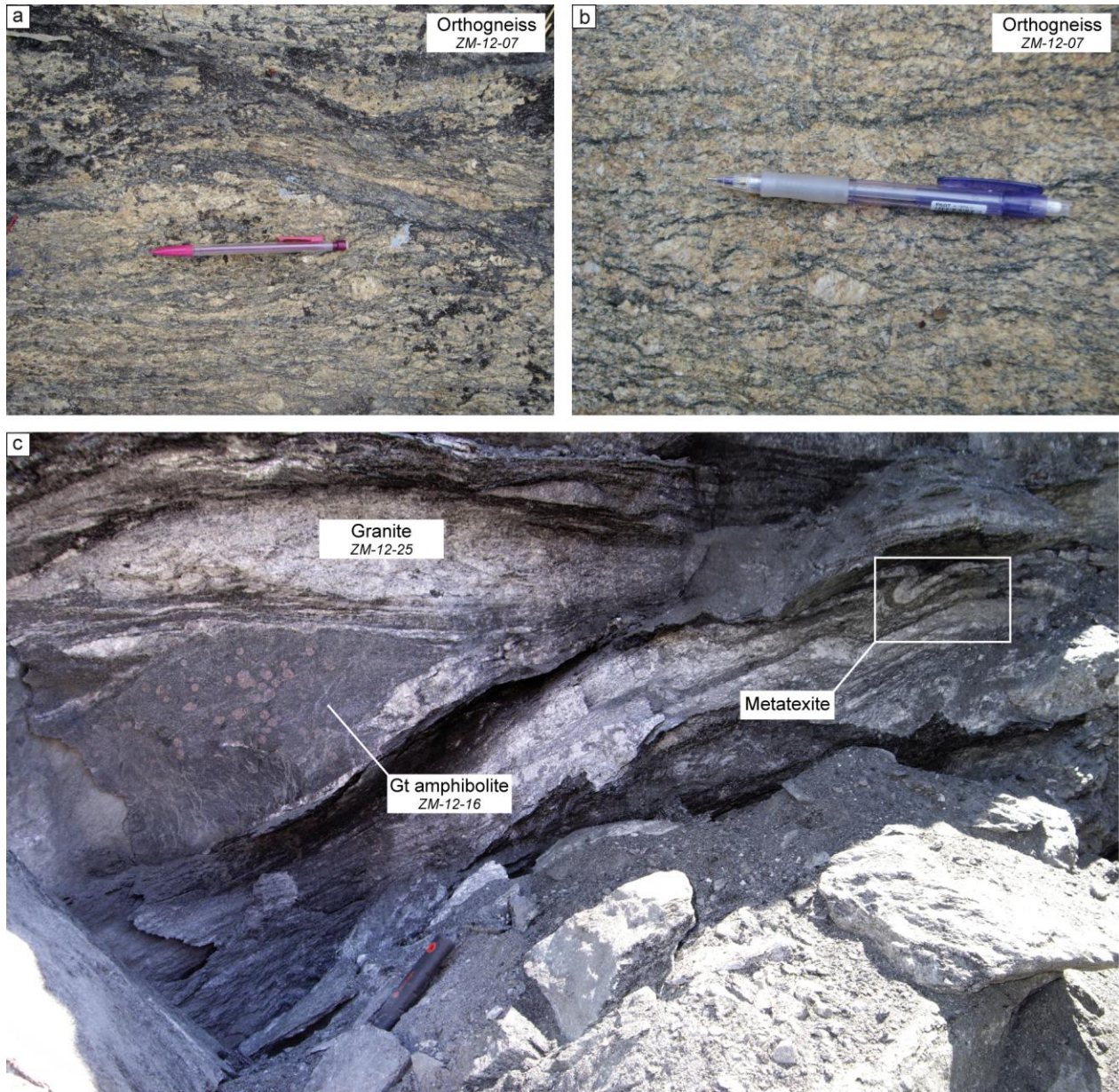


Figure 10: Outcrop pictures from the Mwombezhi dome. a, b: Orthogneiss with feldspar porphyroclasts transposed within shear bands. c: Garnet amphibolite boudins transposed within syn-migmatitic foliation.

4. Methodology

4.1. Geochemistry

Major and trace elements were determined by ICP-AES and ICP-MS at the Service d'Analyse des Roches et des Minéraux, Nancy (SARM, CRPG-CNRS, France) on 16 whole-rock samples collected in the Solwezi and Mwombezhi basement inliers. Sample preparation, analytical

conditions and limits of detection are detailed in Carignan et al. (2001). Major and trace element compositions are given in Table 2 and Table 3.

4.2. LA-MC-ICPMS U-Pb and Lu-Hf isotope analyses of zircon

Rock samples were crushed following successive stages using, respectively, a jaw crusher and a roller mill. Zircon grains were concentrated using (i) density separation with suitable liquids such as bromoform (density = 2.84 g/cc) and diiodomethane (density = 3.31 g/cc) and (ii) magnetic separation with the Frantz isodynamic separator. Zircon grains were handpicked out individually, mounted in epoxy blocks and polished for analysis. External form and internal texture were imaged using combined cathodoluminescence (CL) and secondary electron microscopy (SEM) techniques in a JEOL JSM-6490 instrument with Gatan MiniCL at the Goethe University of Frankfurt (Germany). U-Pb and Lu-Hf isotopes analyses of zircon grains from all rocks were carried out by laser ablation-inductively coupled plasma mass spectrometry (LA-ICPMS), also at the Goethe University of Frankfurt (Germany). Methods and instruments were described by Gerdes and Zeh (2006; 2009), with modifications explained in Zeh and Gerdes (2012). In addition, U-Pb isotope data of zircon grains from two samples were obtained by LA-ICPMS at the Laboratoire Magmas et Volcans in Clermont-Ferrand (France), using the method described in Hurai et al. (2010). Laser spots for Lu-Hf (squared spots with an edge length of 40 μm) were placed mostly directly “on-top” of the U-Pb laser spots (19-26 μm in diameter), or within the same zone characterized by CL imaging. The results of U-Pb and Lu-Hf isotope analyses are shown from the Table 5 to Table 26.

4.3. Sm-Nd isotopes analyses of whole rock

Sm–Nd isotopic values were determined on crushed whole-rock samples by isotope dilution. All analyses were carried out at the Geosciences Rennes Laboratory at the University of Rennes 1. Samples were spiked with a ^{150}Nd – ^{149}Sm mixed solution and dissolved in HF–HNO₃. REE elements were separated using BioRad AG 50W \times 8 H+ 200–400 mesh cationic resin. Sm and Nd were separated and collected by passing the solution through a further set of ion exchange columns loaded with Ln spec Eichrom resin. Sm and Nd were loaded with HNO₃ reagent on to double Re filaments and analysed in a Finnigan MAT262 multicollector mass spectrometer in static mode. In each analytical session, the unknowns were analysed together with the Ames

$^{143}\text{Nd}/^{144}\text{Nd}$ standard, which during the course of this study yielded an average of 0.511964 (standard deviation = 7.23×10^{-6}). All analyses of the unknowns are adjusted to a nominal $^{143}\text{Nd}/^{144}\text{Nd}$ value of 0.511850 for the La Jolla standard. Mass fractionation was monitored and corrected using the value $^{146}\text{Nd}/^{144}\text{Nd} = 0.7219$. Procedural blanks analyzed during the period of these analyses were ~ 190 pg and are considered to be negligible compared to the total quantity of Nd in the samples. The results of Sm-Nd are shown in the Table 4.

5. Whole rock geochemistry: major and trace elements

5.1. Solwezi dome

(i) Felsic units

Orthogneiss ZM-10-09, ZM-10-13 and ZM-10-17

Major element chemical characteristics of gneissic rocks with feldspar porphyroclasts indicate homogeneous SiO_2 and Al_2O_3 contents, ranging from 66.40 to 68.35 wt.% and from 14.56 to 15.17 wt.%, respectively, with FeO_T/MgO ratios between 3.21 and 3.73. In the normative classification diagram, these gneisses plot in the field for granodiorite (Figure 11; Table 2). They have an alumina saturation index between 0.93 and 1.07 and thus, they are metaluminous to peraluminous. However, secondary muscovite grains were observed in these gneisses and we interpret the peraluminous composition as a consequence of late alteration processes during Pan-African metamorphism (Eglinger et al., submitted). The $\text{K}_2\text{O}/\text{Na}_2\text{O}$ ratios are ranging from 0.78 to 1.05. In the Y versus Nb diagram (Pearce et al., 1984), these granodioritic gneisses plot in the field of volcanic arc or syn-collisional origins. These granodioritic gneisses have similar REE patterns showing LREE-enrichment and low negative Eu anomalies ($0.78 < \text{Eu}^* < 1.01$) (Figure 11). In the primitive mantle-normalized spidergram, these rocks are characterized by enrichment in such large ion lithophile elements (LILE) as Rb, Ba, Th and U, but low negative anomalies in Sr and high depletion in such high fields strength elements (HFSE) as Nb and Ta. This is a common pattern of trace element partition for continental crust (Rudnick, 1995; Hofmann, 1997; Barth et al., 2000; Rudnick and Gao, 2003) that is usually assumed to originate from the geochemical evolution of island arc magmas (Arculus, 1999).

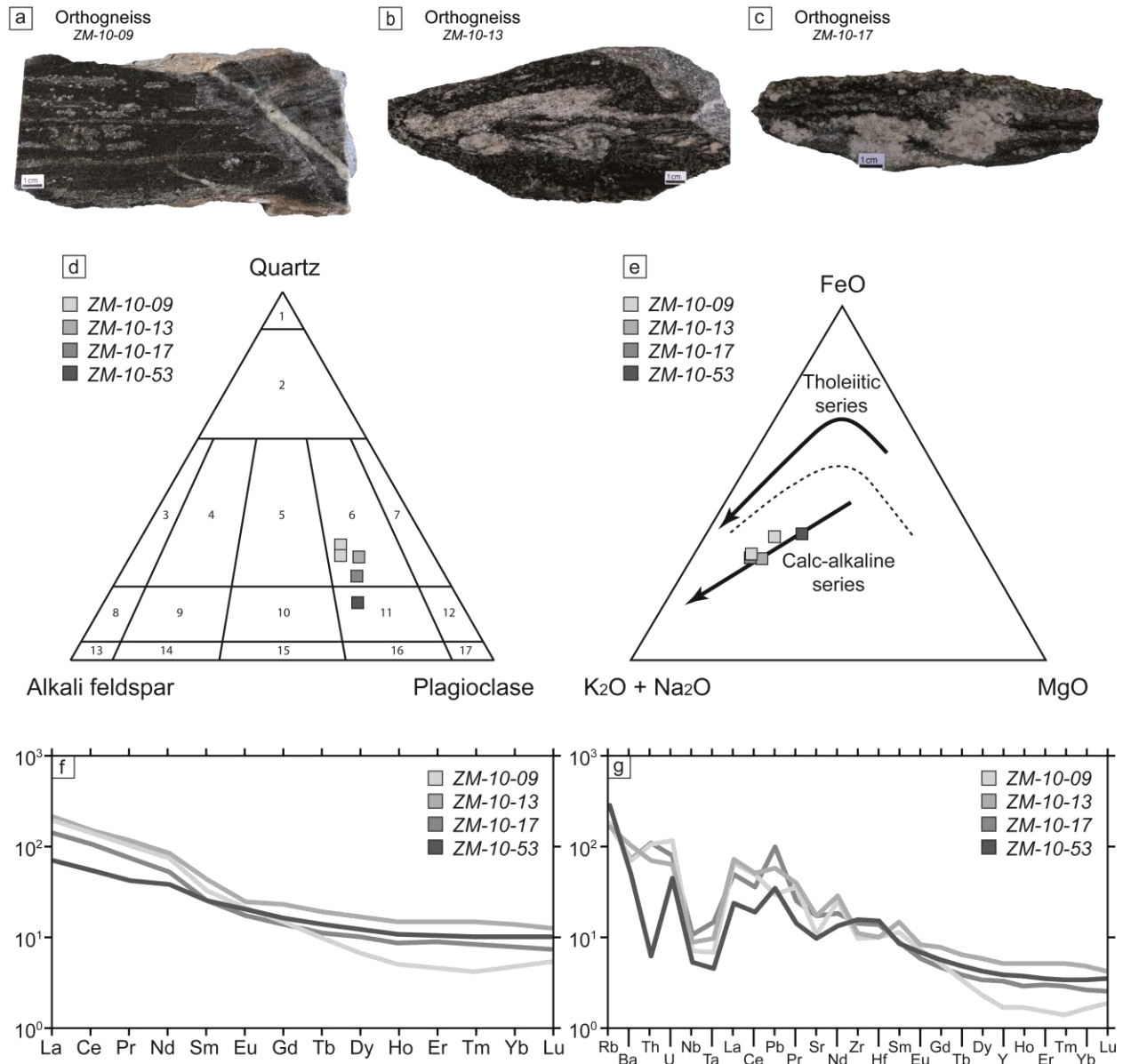


Figure 11: Macroscopic pictures, major and traces elements for the orthogneissic rocks from the Solwezi dome.

Orthogneiss ZM-10-53

Major element analyses of sample ZM-10-53 show moderate SiO₂ (67.07 wt.%) and high Al₂O₃ (17.16 wt.%) contents with a FeO_T/MgO ratio of 1.38. In the Q-A-P normative classification diagram, this granitoid plots in the field for quartz monzodiorite (Figure 11; Table 2). This rock sample has an alumina saturation index of 1.11, indicating a peraluminous composition, also probably due to the late alteration, and the ratio K₂O/Na₂O of 0.74 reflects an alkali monzodiorite. In the Y versus Nb diagram, this quartz monzodiorite plots in the field of volcanic arc or syn-collisional origins. The REE abundances are 10-70 times chondrite and REE pattern

displays no negative Eu anomaly ($Eu^* = 0.99$). In the primitive mantle-normalized spidergram, these rocks are characterized by enrichment in such LILE as Rb, Ba, and U, but low negative anomalies in Sr and high negative depletion in HFSE as Nb and Ta. This is a common pattern of trace element partition for continental crust that is usually assumed to originate from the geochemical evolution of island arc magmas (Arculus, 1999).

Paragneiss ZM-10-38

This rock displays a high SiO_2 content of 71.37 wt.%, a moderate Al_2O_3 content of 14.86 wt.% and a Fe_2O_3 , CaO, Na_2O and K_2O , contents of 3.87, 1.16, 2.00 and 3.70 wt.%, respectively (Table 2). The REE pattern shows a very high positive Ce anomaly ($Ce^* = 2.40$), a low Eu anomaly ($Eu^* = 0.71$) and light REE abundances are 40 times and heavy REE about 8 times the values of chondritic meteorites. The multi-element diagram displays a depletion in Nb and Ta and positive anomalies in Ce, Pb, Zr and Hf. This is a common pattern of trace element partition for continental crust that is usually assumed to originate from the geochemical evolution of island arc magmas (Arculus, 1999).

Granite ZM-10-66

Major element analyses of show high SiO_2 (72.46 wt.%) and Al_2O_3 (13.80 wt.%) contents with a FeO_T/MgO ratio of 3.30 (Table 2). In the Q-A-P normative classification diagram, this granitoid plots in the field for monzogranite. This rock sample has an alumina saturation index of 1.06, indicating a peraluminous composition and the ratio K_2O/Na_2O of 2.11 reflects a potassic monzogranite. In the Y versus Nb diagram, this monzogranite plots in the field of volcanic arc or syn-collisional origins. The REE abundances are 10-502 times chondrite and REE pattern displays a negative Eu anomaly ($Eu^* = 0.47$). The LREE display a fractionated pattern ($La_N/Sm_N = 5.6$), while the HREE are marked by sub-flat pattern with Gd_N/Yb_N of 3.6. The primordial-mantle-normalized pattern of this monzogranite shows negative anomalies for Ba, Nb-Ta, Ce, Sr, Eu and Zr-Hf.

(ii) Mafic units

Amphibolite ZM-10-51

Whole-rock analyses show sub-alkaline basaltic composition, with silica contents content of 45.48 wt.% and K₂O contents of 4.89 wt.% (Table 2). In the diagram FeO*/MgO vs. SiO₂ diagram, they plot in the high-Fe field, with Mg number of 0.48. They have Cr and Ni contents of 181 and 82 ppm, respectively. TiO₂ content is high, 2.39 wt.%, with a high Ti/V ratio of 51. Chondrite normalized REE contents show relatively flat patterns, slightly enriched in LREE (La_N/Yb_N = 4.7; Gd_N/Yb_N = 1.5), with slight negative Eu anomalies of 0.93. This REE pattern is parallel to the typical N-MORB pattern but enriched in REE, with abundance 38 to 123 times the one of chondrite. Trace elements normalized to the primitive mantle show negative Nb-Ta anomaly with a low Nb/La ratio (0.47).

5.2. Mwombezhi dome

(i) Felsic rocks

Paragneiss ZM-39-01 and ZM-62-05

These rocks display homogeneous SiO₂ contents ranging from 70.00 to 70.56 wt.%, Al₂O₃ from 13.15 to 13.72 wt.%, K₂O from 5.09 and 5.09 wt.% and Fe₂O₃ from 4.15 to 4.75 wt.% (Table 3). They have a variable MgO, CaO and Na₂O contents ranging from 0.56 to 2.41 wt.%, from 0.69 to 1.63 wt.% and from 0.80 to 3.24 wt.%, respectively. Relative to chondritic meteorites, these paragneiss have about 100 to 400 times the light REE and about 15 to 55 times the heavy REE content. Their REE patterns show a small negative Eu anomaly (0.48 < Eu* < 0.59). The multi-element diagrams show similar trends characterized by small Ba anomalies, depletion in Nb and Ta and strong negative anomalies in Sr. This feature could be reflect the provenance of these sediments, probably from the calc-alkaline series.

Paragneiss ZM-66-08

This rock displays an intermediate SiO₂ content of 60.83 wt.%, a moderate to high Al₂O₃ content of 16.22 wt.% and a Fe₂O₃, CaO, Na₂O and K₂O, contents of 5.83, 3.19, 4.86 and 2.74 wt.%, respectively (Table 3). The REE pattern shows a very low Eu anomaly (Eu* = 0.89) and light REE abundances are 100 to 200 times and heavy REE about 10 times the values of chondritic meteorites. The multi-element diagram displays a negative anomaly in Nb and Ta, with no significant Sr anomaly.

Orthogneiss ZM-12-07

Major element analyses of sample ZM-12-07 show moderate SiO₂ (63.34 wt.%) and high Al₂O₃ (15.98 wt.%) contents with a FeO_T/MgO ratio of 2.70 (Table 3). In the Q-A-P normative classification diagram, this granitoid plots in the field for granodiorite. This rock sample has an alumina saturation index of 1.18 and a ratio K₂O/Na₂O of 1.1. In the Y versus Nb diagram, this granodiorite plots in the field of volcanic arc or syn-collisional origins. The light REE abundances are 300 times chondrite and heavy REE 10 times. REE pattern displays a negative Eu anomaly (Eu* = 0.44). In the primitive mantle-normalized spidergram, these rocks are characterized by enrichment in such LILE as Rb, Ba, Th, U, but low negative anomalies in Sr and high negative depletion in HFSE as Nb and Ta. This is a common pattern of trace element partition for continental crust that is usually assumed to originate from the geochemical evolution of island arc magmas (Arculus, 1999).

(ii) Mafic rocks

Garnet amphibolites ZM-12-13 and ZM-12-16

Garnet amphibolites whole-rocks analyses show alkaline basaltic compositions (Table 3), with silica contents ranging from 54.28 to 54.96 wt.% and K₂O contents from 0.78 to 1.68 wt.%. In the diagram FeO*/MgO vs. SiO₂ diagram, they plot in the medium-Fe field, with Mg numbers ranging from 0.50 to 0.59. Their Cr and Ni contents vary, respectively, from 164 to 196 ppm and from 47 to 82 ppm. TiO₂ content is moderate, ranging from 1.54 and 1.60 wt.%, with a Ti/V ratio between 35 and 45. Chondrite normalized REE contents show fractionated patterns ($1.1 < La_N/Yb_N < 4.1$; $0.5 < Gd_N/Yb_N < 1.2$), with slight Eu anomalies ($0.84 < Eu^* < 1.07$).

Amphibolite ZM-39-04

Whole-rock analyses show sub-alkaline basaltic composition, with silica content of 45.48 wt.% and K₂O content of 4.89 wt.% (Table 3). In the diagram FeO*/MgO vs. SiO₂ diagram, they plot in the high-Fe field, with Mg number of 0.48. They have Cr and Ni contents of 181 and 82 ppm, respectively. TiO₂ content is high, 2.39 wt.%, with a high Ti/V ratio of 51. Chondrite normalized REE contents show relatively flat patterns, slightly enriched in LREE (La_N/Yb_N = 4.7; Gd_N/Yb_N = 1.5), with slight negative Eu anomalies of 0.93. Trace elements normalized to the primitive mantle show negative Nb-Ta anomaly with a low Nb/La ratio (0.47).

6. Isotopic results*6.1. Solwezi dome***(i) Felsic units***Orthogneiss ZM-10-09*

Zircon grains (80-350 µm) extracted from this gneissic rock exhibit subeuhedral to subrounded shape and growth zoning (Figure 12). Some grains show cores differentiated from their rims by geometrically irregular surfaces which truncate internal zoning. These features are interpreted as deep resorption of the early zircon phase mantled by newly grown magmatic zircon (Corfu et al., 2003). The zircon grains are characterized by an average Th/U ratio of 0.42 (n=42). Discordia line gives an upper intercept at 1904 ± 43 Ma with a MSWD of 1.8 (n=42; Figure 13a; Table 5). Similar ages between xenocrystic cores and rims observed on CL images reflect that resorption occurs during the same magmatic event. The Lu-Hf isotope analyses of these zircon grains yield homogeneous ¹⁷⁶Hf/¹⁷⁷Hf_i ratios ranging between 0.281417 and 0.281572, which correspond to εHf_i ranging from -7.5 to -3.4. Two-stage Hf model ages (T_{DM}) for these zircon grains are ranging between 2.78 and 2.65 Ga (n=6; Table 17).

Orthogneiss ZM-10-13

Zircon grains (100-400 µm) extracted from this gneissic rock exhibit subeuhedral to subrounded shape and oscillatory zoning (Figure 12). These zircon grains are characterized by an average Th/U ratio of 1.08 (n=23). Discordia line gives an upper intercept at 1889 ± 7 Ma with a MSWD

of 1.1 (n=23 with concordance > 95 %; Figure 13b; Table 6). The Lu-Hf isotope analyses of these zircon grains yield homogeneous $^{176}\text{Hf}/^{177}\text{Hf}_t$ ratios ranging between 0.28143 and 0.28148, which correspond to ϵHf_t ranging from -5.9 to -3.4 (n=21). Two-stage Hf model ages (T_{DM}) for these zircon grains are mostly ranging between 2.67 and 2.78 Ga (n=21; Table 18).

Orthogneiss ZM-10-53

Zircon grains (100-250 μm) extracted from this gneissic rock exhibit subeuhedral to subrounded shape (Figure 12). All grains have an oscillatory zoned core and regular growth is interrupted by textural discontinuities along which the original zoning is resorbed. These zones are characterized by a high luminescence. These features are interpreted as resorption of the early magmatic zircon phase. All zircon grains are surrounded by a rim characterized by a patchy luminescence interpreted as an overgrowth. Zircon grains with oscillatory zoning are characterized by an average Th/U ratio of 0.85 (n=17). Discordia line gives an upper intercept at 1849 ± 7 Ma with a MSWD of 0.7 (n=17 with concordance > 95 %; Figure 13c; Table 7). The Lu-Hf isotope analyses of these zircon grains yield homogeneous $^{176}\text{Hf}/^{177}\text{Hf}_t$ ratios ranging between 0.28152 and 0.28160, which correspond to ϵHf_t ranging from -3.9 to -0.4. Two-stage Hf model ages (T_{DM}) for these zircon grains are ranging between 2.63 and 2.47 Ga (n=17; Table 19).

Granite ZM-10-66

Zircon grains (100-300 μm) from sample ZM-10-06 are characterized by sub-euhedral to euhedral shape and are usually highly fractured (Figure 12). Zircon grains are generally characterized by oscillatory zoning on cathodo-luminescence (CL) images. Some resorption and re-crystallization features are also observed and could probably reflect a complex crystallization during magma evolution or to chemical modification post-crystallization during a metamorphic event (Corfu et al., 2003). Zircon grains are mostly concordant and present an average Th/U ratio of 0.53 (n=28) and an average $^{176}\text{Lu}/^{177}\text{Hf}$ ratio of 0.00084 (n=15). All zircon grains yield a Concordia age of 1109 ± 6 Ma (n=28; MSWD=1.2; Figure 13d; Table 8). The Lu-Hf isotope analyses of these zircon grains yield homogeneous $^{176}\text{Hf}/^{177}\text{Hf}_t$ ratios ranging between 0.28171 and 0.28176, which correspond to $\epsilon\text{Hf}(t)$ ranging from -13.3 to -11.3. Two-stage Hf model ages (T_{DM}) for these zircon grains are ranging between 2.60 and 2.50 Ga (n=15; Table 20).

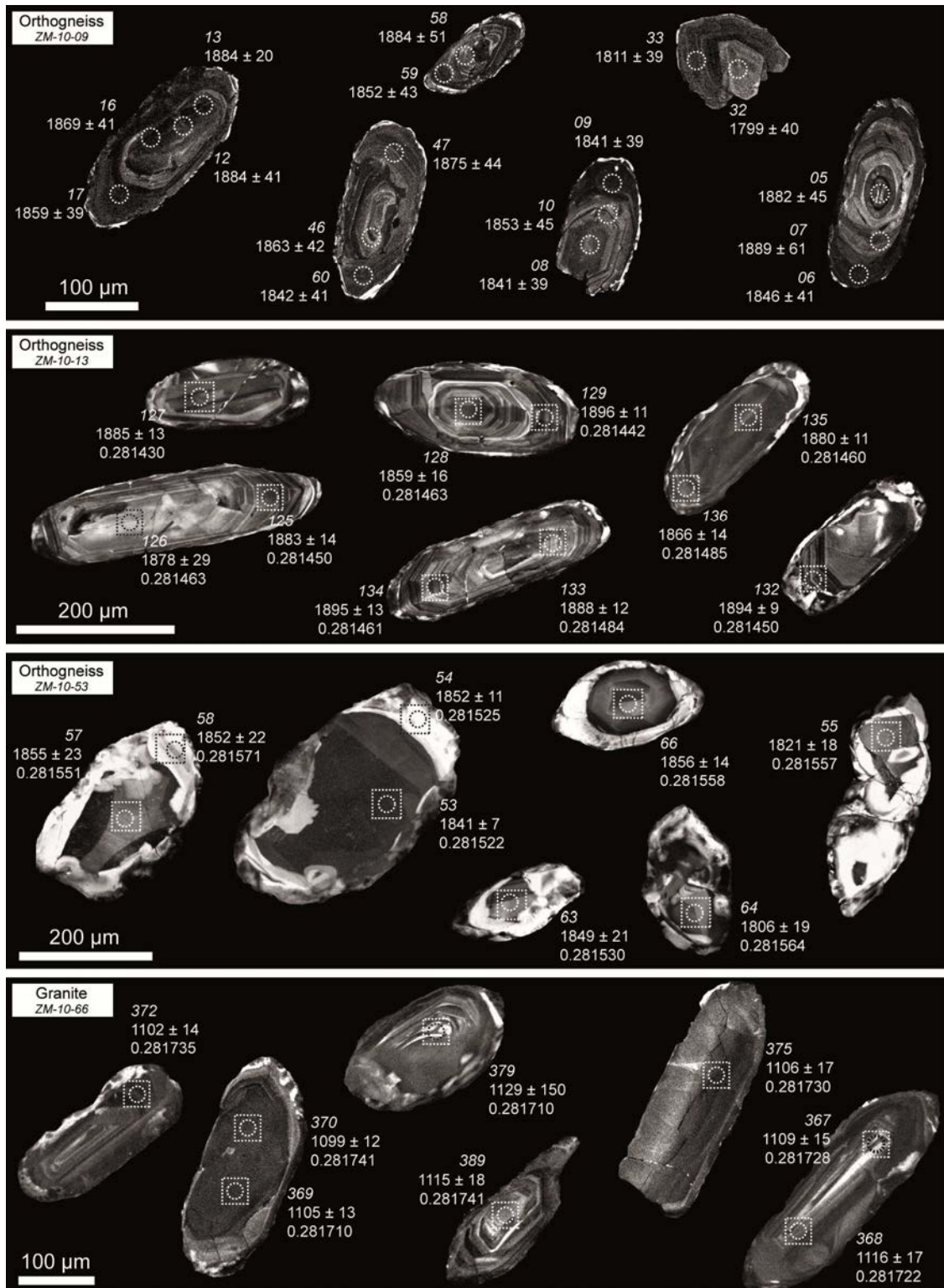


Figure 12: Cathodoluminescence images of some analyzed zircon grains of the orthogneissic and granitic rocks from the Solwezi dome. Dotted circles represent the points of analyses. Italic numbers are the referees label (see table X) and regular numbers are the $^{207}\text{Pb}/^{206}\text{Pb}$ ages with concordance >95% and the $^{176}\text{Hf}/^{177}\text{Hf}(t)$ ratio.

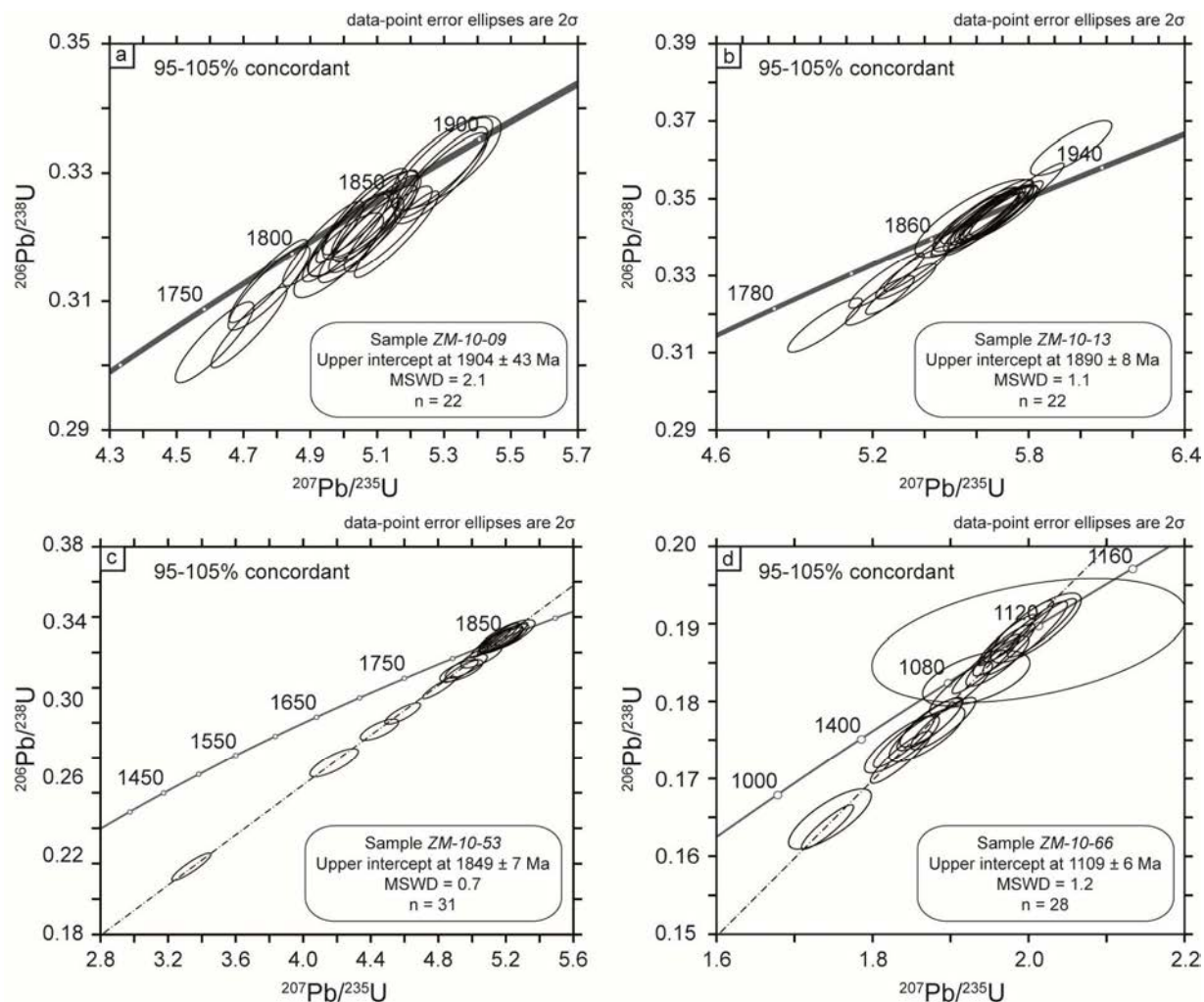


Figure 13: U-Pb concordia diagram for the orthogneissic and granitic rocks from the Solwezi dome.

Paragneiss ZM-10-38

Zircon grains (50-200 μm) from sample ZM-12-38 mostly present a sub-rounded to rounded shape SEM/CL images reveal zircon grains with both complex internal structure due to different degree of recrystallization and oscillatory zoning. Some zircon grains present xenocrystic cores, often characterized by a high luminescence, mantled by newly oscillatory zoning. Some xenocrystic cores also preserve an oscillatory zoning (Figure 14). The U-Pb isotope data obtained from zircon grains show different range of ages with modes at 2.05, 2.01, 1.93 and 1.87 Ga (Figure 15a, b; Table 9). The youngest zircon grain with magmatic zoning and a concordance $> 95\%$ yielded a $^{207}\text{Pb}/^{206}\text{Pb}$ age of 1822 ± 19 Ma (grain 268; Table 9). Zircon grains with modes at

2.05, 2.01, 1.93 and 1.87 Ga show subchondritic ϵHf_t down to -27.6, except few grains showing superchondritic ϵHf_t up to +1.4 (Table 21).

Migmatitic paragneiss ZM-10-62

Zircon grains from the *ZM-12-62* migmatitic sample present low Th/U (0.13-0.34) rim overgrowths dated at 1245 ± 24 Ma, 1210 ± 27 Ma and 1155 ± 24 Ma ($^{207}\text{Pb}/^{206}\text{Pb}$ ages with concordance > 95%). Age modes ranging between 1780 and 1355 Ma from this sample represent mostly partial dissolution and recrystallization areas of zircon grains (Figure 14; Figure 15c, d; Table 10). The youngest zircon grain yielded a $^{207}\text{Pb}/^{206}\text{Pb}$ age of 1474 ± 80 Ma (grain 19) with concordance > 95% (Table 10).

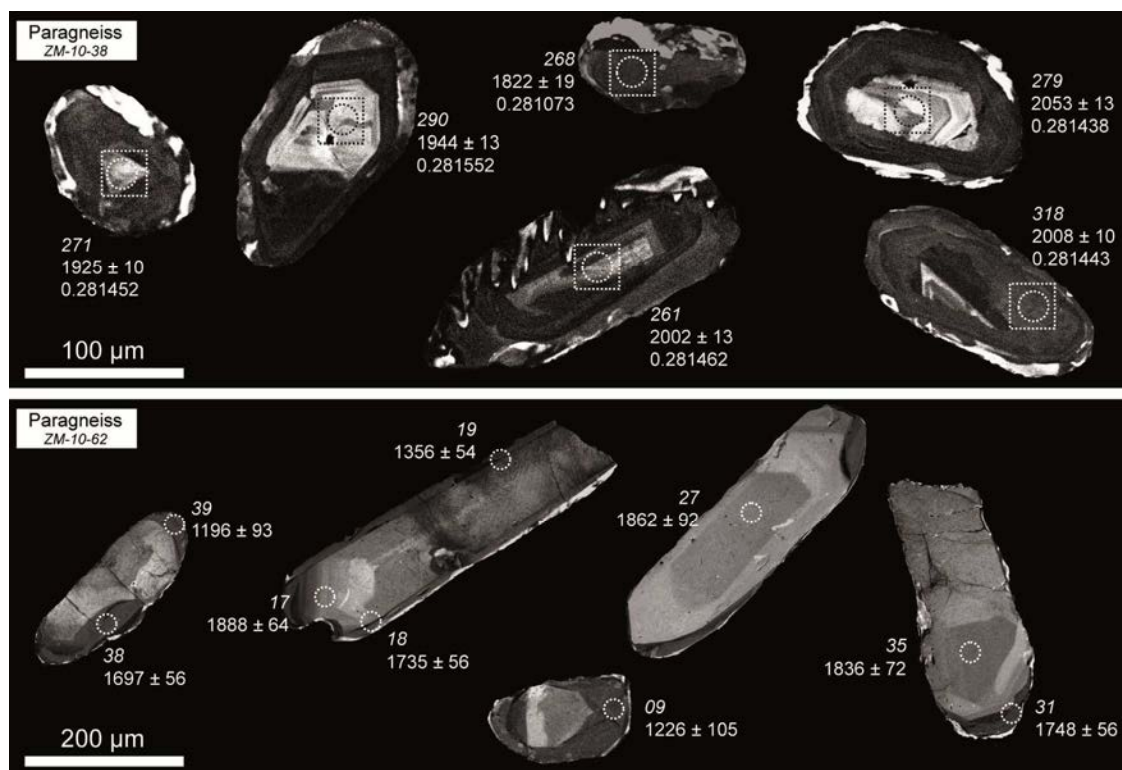


Figure 14: Cathodoluminescence images of some analyzed zircon grains of the paragneissic rocks from the Solwezi dome. Dotted circles represent the points of analyses. Italic numbers are the referees label (see complementary data) and regular numbers are the $^{207}\text{Pb}/^{206}\text{Pb}$ ages with concordance >95% and the $^{176}\text{Hf}/^{177}\text{Hf}(t)$ ratio.

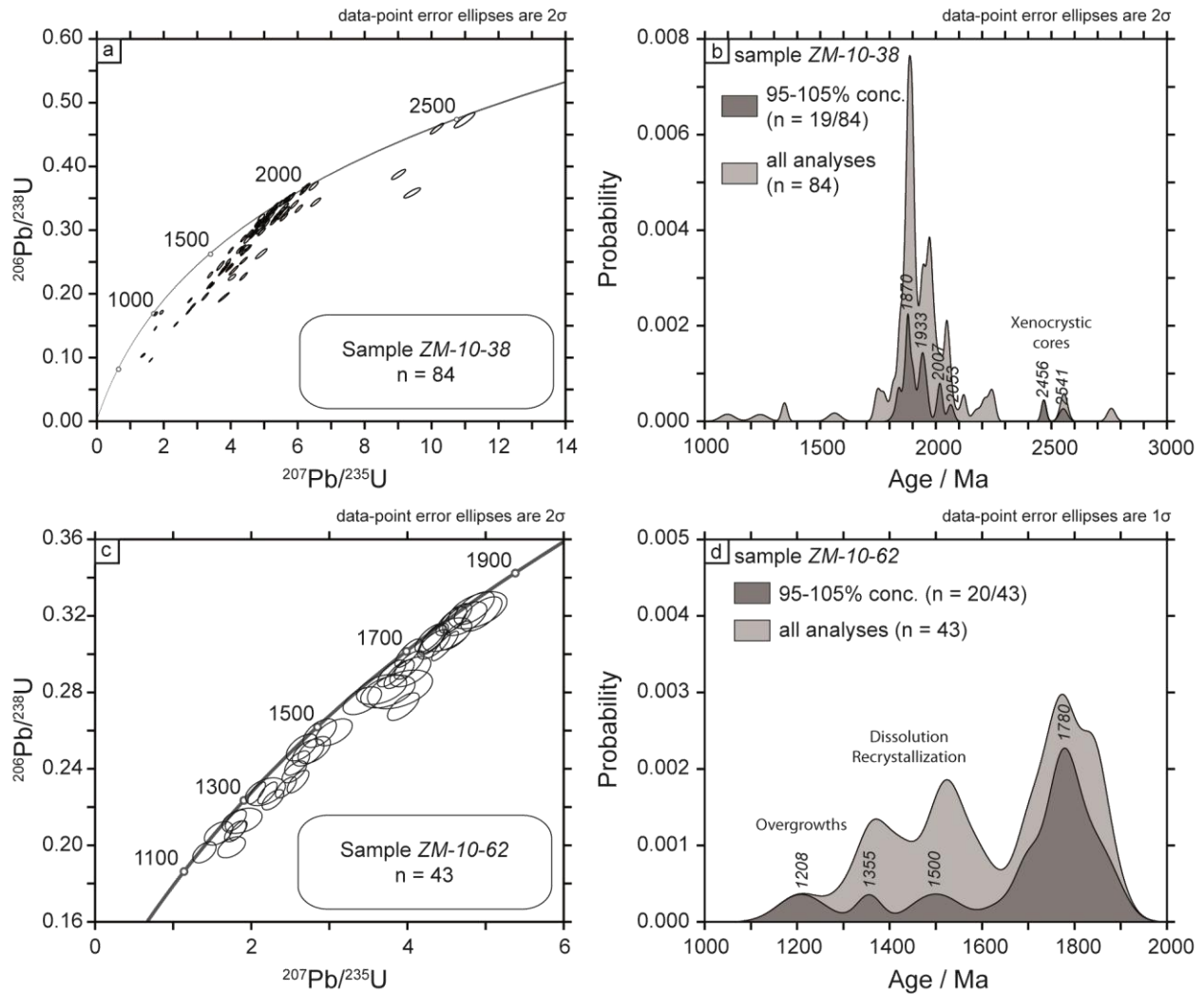


Figure 15: U-Pb concordia diagram and probability density plot for the paragneissic rocks from the Solwezi dome.

(ii) Mafic units

Amphibolite ZM-10-51

Nd isotopic composition shows $\epsilon\text{Nd}_{(1900)}$ value, compared to the Chondritic Uniform Reservoir (CHUR; Wasserburg et al., 1981), of -2.95 (Table 4). Nd model age, relative to the Depleted Mantle (T_{DM}), is calculated at 2.62 Ga.

6.2. Mwombezhi dome

(i) Felsic units

Paragneiss ZM-39-01

Zircon grains (200-500 μm) from sample ZM-39-01 are either squat or elongated with sub-euhedral shape. SEM/CL images reveal large zircon grains with oscillatory zoning and some of them are affected by dissolution-precipitation processes. Different zircon types can be distinguished: (i) partially re-crystallized zircon with patchy luminescence and (ii) oscillatory zoning zircon. Some zircon grains are surrounded by a thin overgrowth rim, with a low luminescence, crosscutting the oscillatory zoning (Figure 16). Zircon grains with minor dissolution/precipitation are mostly concordant and present a Th/U ratio with an average at 1.64 (n=62) and an average $^{176}\text{Lu}/^{177}\text{Hf}$ ratio of 0.00081 (n=18). Rims are characterized by lower Th/U ratios ranging from 0.00 to 0.07 (n=7) and lower average $^{176}\text{Lu}/^{177}\text{Hf}$ ratio of 0.00058 (n=6), compared to zircon with oscillatory zoning. The U-Pb isotope data obtained from zircon grains with a concordance > 95 % show different range of ages with a dominant mode at 1.71 Ga and minor modes between 1.61 and 1.43 Ga (Figure 17a, b; Table 11). The youngest zircon grain with magmatic zoning and a concordance > 95% yielded a $^{207}\text{Pb}/^{206}\text{Pb}$ age of 1515 ± 64 Ma (grain 190). Probably due to the limited number of analyses, the youngest populations are not well constrained. However, this sample shows similar age modes that the sample ZM-62-05. $^{207}\text{Pb}/^{206}\text{Pb}$ ages of the zircon rims in the sample ZM-39-01 are ranging from 1191 ± 39 Ma and 1113 ± 43 (with a concordance between 97 and 100%). The $\epsilon\text{Hf}(t)$ of the zircon grains is ranging from -6.9 to -1.9, reflecting a subchondritic reservoir. Zircon overgrowths yield $^{176}\text{Hf}/^{177}\text{Hf}(t)$ between 0.28166 and 0.28213 with $\epsilon\text{Hf}(t)$ between -13.4 and +3.7 which correspond to variable T_{DM} ranging from 2.66 to 1.73 Ga (Table 22).

Paragneiss ZM-62-05

Zircon grains (200-500 μm) extracted from ZM-62-05 are either squat or elongated with sub-euhedral shape and are usually fractured. SEM/CL images reveal a large diversity of complex internal structures, which reflect different degree of dissolution-recrystallization. Different zircon types can be distinguished: (i) strongly re-crystallized zircon with a low luminescence and (ii) partially re-crystallized with relic of magmatic zoning with a patchy luminescence (Figure 16).

Most zircon grains are surrounded by a thin overgrowth rim, with a low luminescence, crosscutting the oscillatory zoning and the patchy re-crystallized zones. Zircon grains strongly re-crystallized yield mostly discordant analyses and are characterized by variable Th/U and $^{176}\text{Lu}/^{177}\text{Hf}$ ratios (Table 12; Table 23). The U-Pb isotope data obtained from zircon grains with a concordance > 95 % show different range of ages with modes at 1.71, 1.59 and 1.48 Ga (Figure 17c, d). The youngest zircon grain with magmatic zoning and a concordance > 95% yields a $^{207}\text{Pb}/^{206}\text{Pb}$ age of 1475 ± 36 Ma (grain 277). Owing to the limited number of analyses, the younger populations are not statistically well constrained. Zircon grains with modes at 1.71, 1.58 and 1.47 Ga show subchondritic ϵHf_t down to -4.7, except for a few grains showing superchondritic ϵHf_t up to +6.8 (Table 23). Only two rims yielding a level of concordance > 95% were analyzed for U-Pb and Lu-Hf isotopes analyses. Rims are characterized by lower Th/U ratios of 0.02 and 0.04 (n=2) with $^{207}\text{Pb}/^{206}\text{Pb}$ ages at 1185 ± 18 and 1157 ± 20 Ma, respectively (with a concordance of 100). Their $^{176}\text{Lu}/^{177}\text{Hf}$ ratios are low, ranging between 0.00056 and 0.00061, compared to zircon partially or strongly re-crystallized. The two zircon rims yield $^{176}\text{Hf}/^{177}\text{Hf}(t)$ ratio of 0.28164 and 0.28202, which correspond to $\epsilon\text{Hf}(t)$ of -14.1 and -1.1 and T_{DM} of 2.70 and 1.97 Ga, respectively (Table 23).

Paragneiss ZM-66-08

Zircon grains from sample *ZM-66-08* are mostly small in size (150-300 μm) with a sub-rounded to sub-euhedral shape. SEM/CL images reveal zircon grains with both complex internal structure due to different degree of recrystallization and oscillatory zoning (Figure 16). The U-Pb isotope data obtained from zircon grains show different range of ages with a dominant mode at 1.91 Ga and minor modes at 1.87-1.86 Ga and 1.77-1.74 Ga (Figure 17e, f; Table 13). Probably due to the limited number of analyses, the minor populations are not well constrained. The youngest zircon grain with magmatic zoning and a concordance > 95% yielded a $^{207}\text{Pb}/^{206}\text{Pb}$ age of 1759 ± 25 Ma (grain 132). The mode at 1.15 Ga is characterized by a low Th/U ratio of 0.03 and could be related to metamorphic overgrowths (Table 13). Zircon grains with concordant ages plot mostly close to the chondritic uniform reservoir with $\epsilon\text{Hf}(t)$ ranging from -1.7 to +1.6 (Table 24).

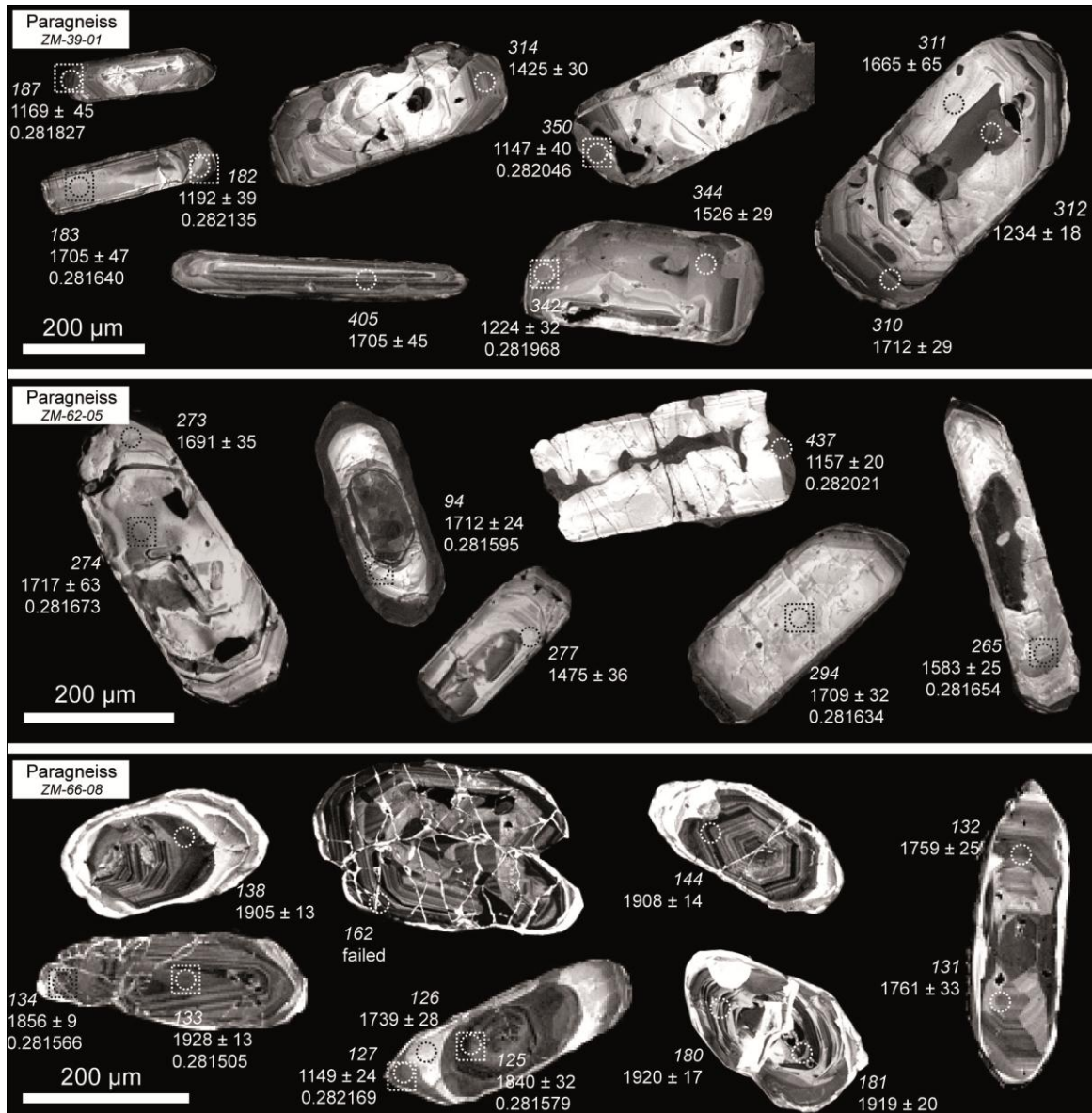


Figure 16: Cathodoluminescence images of some analyzed zircon grains of the paragneissic rocks from the Mwombezhi dome. Dotted circles represent the points of analyses. Italic numbers are the referees label (see complementary data) and regular numbers are the $^{207}\text{Pb}/^{206}\text{Pb}$ ages with concordance >95% and the $^{176}\text{Hf}/^{177}\text{Hf}(t)$ ratio.

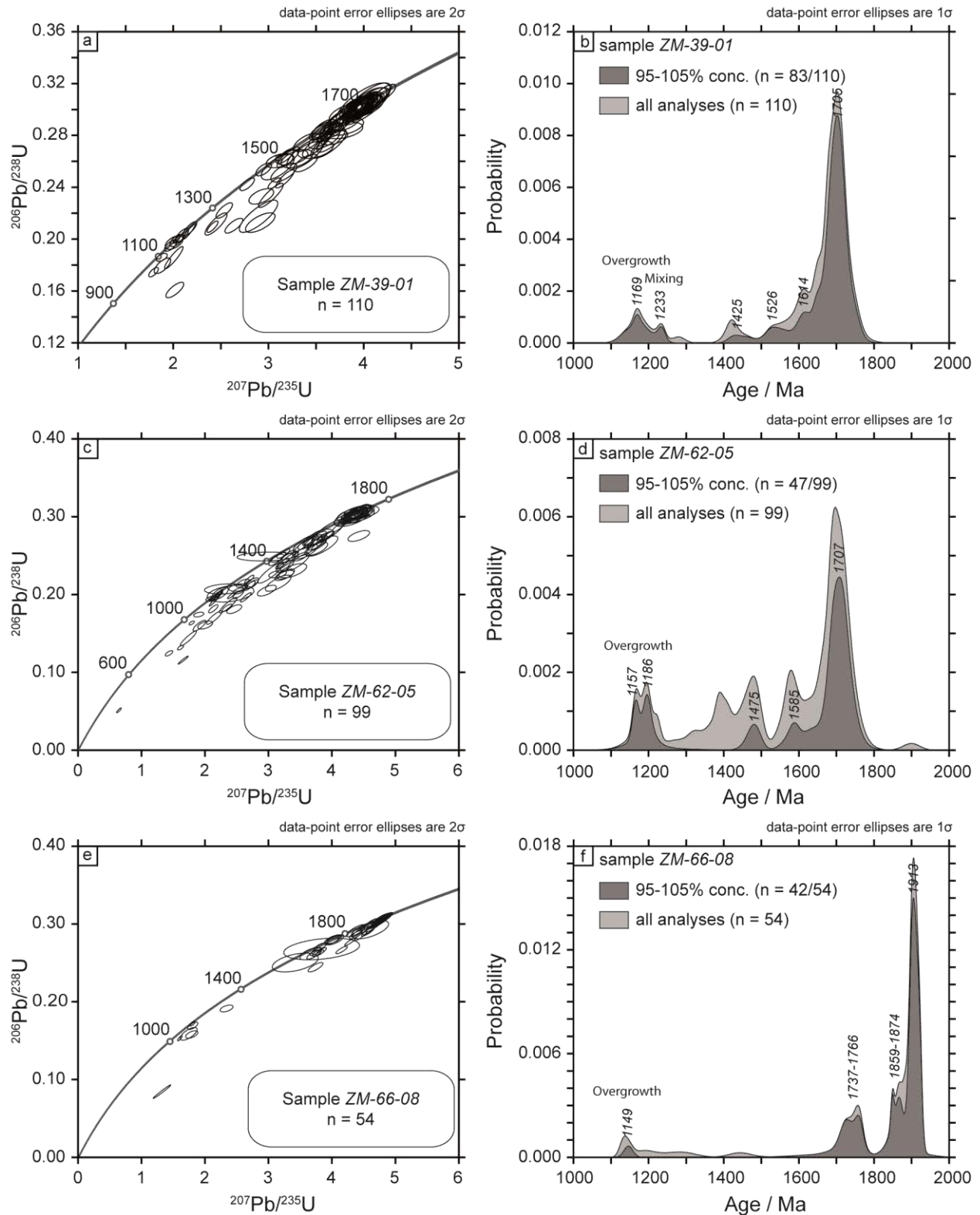


Figure 17: U-Pb concordia diagram and probability density plot for the paragneissic rocks from the Mwombezi dome.

Orthogneiss ZM-12-07

Zircon grains (100-500 μm) from sample *ZM-12-07* are either squat or elongated with sub-euhedral to euhedral shape. Zircon grains are generally characterized by growth zoning on cathodo-luminescence (CL) images, a feature consistent for zircon growth in igneous rocks. Some complex zircon grains present xenocrystic cores mantled by oscillatory zoning (Figure 18). Resorption and recrystallization features are also observed in some zircon grains probably related to complex crystallization during magma evolution or to chemical modification post-crystallization during a metamorphic event (Corfu et al., 2003). Zircon grains with minor dissolution/precipitation are mostly concordant and present variable Th/U ratios with an average at 0.28 (n=47) and an average $^{176}\text{Lu}/^{177}\text{Hf}$ ratio of 0.00103 (n=31). Preserved oscillatory zoning zircon grains (with concordance > 95%) yield a Concordia age of 1920 ± 8 Ma (n=47; MSWD=0.94; Figure 19a, b; Table 14). This age is consistent with concordant U-Pb age obtained on one magmatic monazite (U content ranging from 1595 and 3193 ppm with Th/U ratios comprised between 1.17 and 2.05) at 1918 ± 20 Ma (n=4; MSWD=0.001). The Lu-Hf isotope analyses of these zircon grains yield $^{176}\text{Hf}/^{177}\text{Hf}(t)$ ranging between 0.28110 and 0.28151, which correspond to $\epsilon\text{Hf}(t)$ ranging from -16.5 to -7.2. Two-stage Hf model ages (T_{DM}) for these zircon grains are ranging between 3.40 and 2.53 Ga (n=35 with an average at 2.80 Ga; Table 25). Xenocrystic cores present a wide range of $^{207}\text{Pb}/^{206}\text{Pb}$ ages ranging from 2.69 to 1.96 Ga. The oldest xenocrystic grain with a $^{207}\text{Pb}/^{206}\text{Pb}$ age at 2689 ± 10 Ma present a $^{176}\text{Hf}/^{177}\text{Hf}(t)$ ratio of 0.28137 with a $\epsilon\text{Hf}(t)$ of -6.8 and a calculated T_{DM} of 2.88 Ga.

Granite ZM-12-25

Zircon grains from sample *ZM-12-25* are small in size (100-200 μm) with a sub-rounded to sub-euhedral shape SEM/CL images reveal zircon grains with oscillatory zoning and some grains present dissolution/re-crystallization zones (Figure 18). The U-Pb isotope data obtained from zircon grains show different range of ages with a dominant mode at 1.35-1.12 Ga and minor modes at 1.90, 1.76 and 1.51 Ga (Figure 19c, d; Table 16). Grains from the dominant mode are characterized by low Th/U ratios ranging from 0.01 to 0.07 (n=34) and show a high degree of concordance (mostly > 95%). These zircon grains plot in the subchondritic reservoir with $\epsilon\text{Hf}(t)$ ranging from -12.8 to -9.0 and show T_{DM} model age ranging from 2.64 to 2.58 (n=8; Table 26). The youngest zircon grain with magmatic zoning and a concordance > 95% yielded a $^{207}\text{Pb}/^{206}\text{Pb}$

age of 1216 ± 22 Ma (grain 217). The oldest grain is also characterized by oscillatory zoning and by a higher Th/U ratio of 0.90 (grain 254). The $^{207}\text{Pb}/^{206}\text{Pb}$ crystallization age is calculated at 1928 ± 22 Ma (concordance = 100). This grain plots in the superchondritic reservoir with a $\epsilon_{\text{Hf}}(t)$ of +2.0 and gives a T_{DM} model age at 2.40 Ga (Table 26).

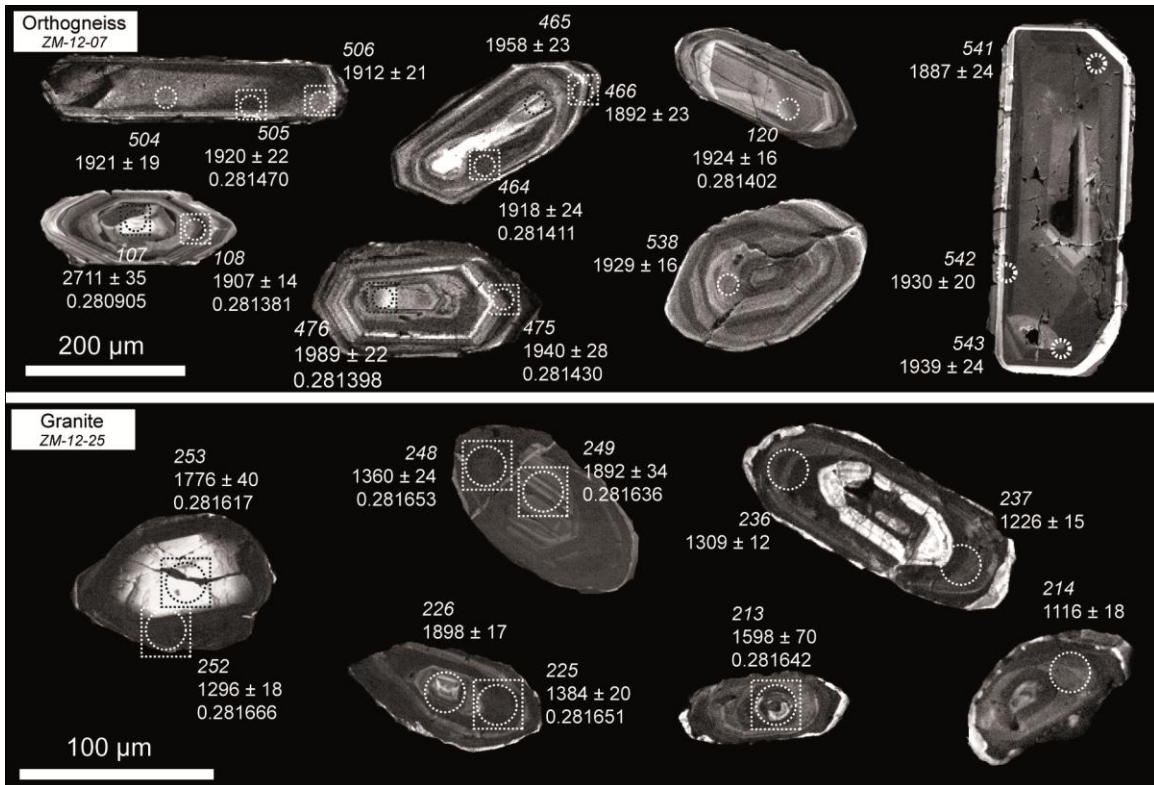


Figure 18: Cathodoluminescence images of some analyzed zircon grains of the paragneissic rocks from the Mwombeshi dome. Dotted circles represent the points of analyses. Italic numbers are the referees label (see complementary data) and regular numbers are the $^{207}\text{Pb}/^{206}\text{Pb}$ ages with concordance >95% and the $^{176}\text{Hf}/^{177}\text{Hf}(t)$ ratio.

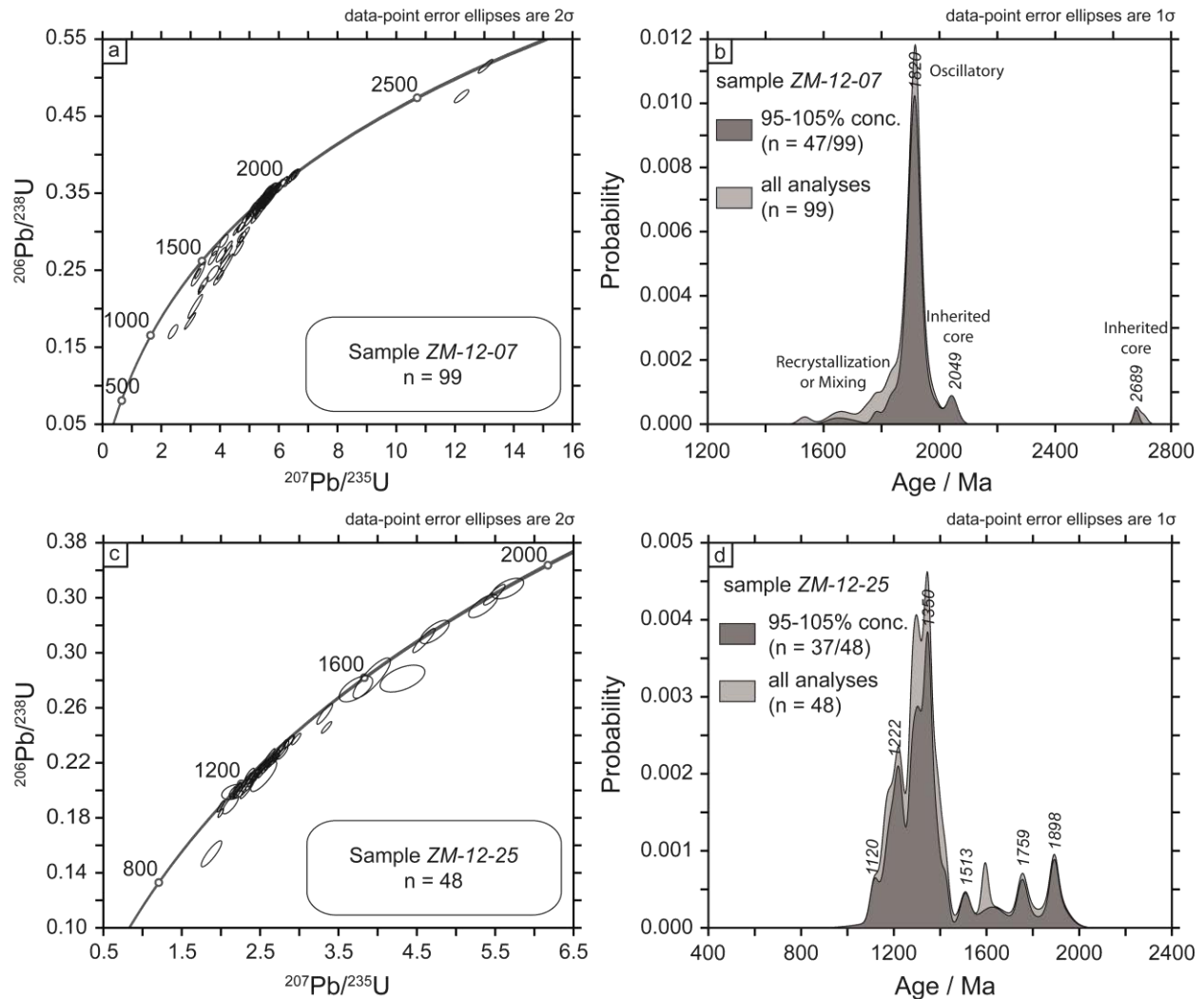


Figure 19: U-Pb concordia diagram for the orthogneissic and granitic rocks from the Mwombezi area.

(ii) Mafic units

Garnet amphibolites ZM-12-13, ZM-12-16 and amphibolite ZM-39-04

Nd isotopic composition shows $\epsilon\text{Nd}_{(1900)}$ values, compared to the Chondritic Uniform Reservoir (CHUR; Wasserburg et al., 1981), ranging from -1.28 to 1.53 (Table 4). Nd model ages, relative to the Depleted Mantle (T_{DM}), are in the range of 2.93 to 2.32 Ga.

7. Discussion

7.1. Intrusion and deposition ages

7.1.1. Solwezi basement inliers

Solwezi basement is mainly composed by gneissic and migmatitic rocks with some amphibolites, and the nature of this basement will be discussed using a combination of igneous crystallization and xenocrystic zircon ages. Three migmatitic orthogneisses (*ZM-10-09*, *ZM-10-13* and *ZM-10-53*) yield concordant ages at 1849 ± 7 Ma, 1889 ± 7 Ma and 1904 ± 43 Ma. These ages are in good agreement with zircon TIMS ages published by John (2001) for granitoid gneisses dated at 1874 ± 9 Ma, for Solwezi dome, and at 1884 ± 10 Ma for Kabompo dome. Ngoyi et al. (1991) and Rainaud et al. (2002) reported similar U-Pb zircon ages of 1882 ± 20 and 1873 ± 8 Ma for granitoids and metavolcanic rocks of the Luina dome. Magmatic activity at 1.90-1.85 Ga recorded by rocks exposed in the Solwezi dome is also recognized at a larger scale in the Bangweulu block (Brewer et al., 1979; Schandelmeier, 1980, 1983; Kabengele et al., 1991; Ngoyi et al., 1991; De Waele et al., 2006a) and in the Irumide belt (De Waele et al., 2006b). Voluminous calc-alkalic granitoids and co-genetic volcanic rocks were described with ages (U-Pb zircon and Rb-Sr whole-rock dating) ranging from 1.88 to 1.86 Ga in the Bangweulu block and from 1.88 to 1.85 Ga within the deformed Muva Supergroup in the Irumide belt (Brewer et al., 1979; Schandelmeier, 1980, 1983; Kabengele et al., 1991; Ngoyi et al., 1991; John, 2001; De Waele, 2005; Rainaud et al., 2005; De Waele and Fitzsimons, 2007). All these data suggest an extensive Paleoproterozoic magmatic arc, during the Ubendian orogeny, characterized by plutono-volcanic rocks with high-K calc-alkaline affinity, stretching from the Usagaran belt to the east to the Domes region, arguing in favour of a north-south oriented convergence during the Paleoproterozoic (De Waele et al., 2006). Considering the calc-alkaline affinity of these meta-igneous rocks and their U-Pb crystallization ages between 1.90-1.85 Ga, we propose that this Paleoproterozoic magmatic arc described in the Bangweulu block was extended to the west in the Domes region in Zambia. Rainaud et al. (2005) proposed that several magmatic arcs were formed episodically over a 200 million year period, between 2050 and 1850 Ma, and that these plutono-volcanic rocks were part of an extensive magmatic arc stretching from northern Zambia to northern Namibia, called the Bangweulu-Kamanjab terrane.

One sample in our study shows signs of inheritance of older zircons. Most zircon ages are ranging between 1830 and 2050, with a main mode at 1870 Ma (Figure 19b). Two xenocrystic cores yielded weighted mean $^{207}\text{Pb}/^{206}\text{Pb}$ ages of 2456 ± 10 Ma and 2541 ± 18 Ma. These oldest ages reveal the presence of crustal components as old as 2.54-2.45 Ga. These inherited zircons may be derived from the Kasai Craton in Congo, NE Angola and NW Zambia, where granites and migmatites have been dated at 2.56-2.54 Ga (Key and Armstrong, 2000) and where metasediments have been dated at ca. 2.40 Ga (Cahen et al., 1984). Inherited ages, but with much more diverse distribution, were described by Rainaud et al. (2003) in the Paleoproterozoic quartzite of the Kanona Group in the Zambian Copperbelt to the west. These ages define small cluster at 3.20, 3.03, 2.70, 2.50 and 2.40 Ga. The ages at 3.20 Ga could reflect a cryptic Mesoarchean terrane (Rainaud et al., 2003, 2005; Rainaud, 2005). De Waele et al. (2008) analyzed several metasedimentary sequences, both from the Bangweulu block and from the Irumide belt. $^{207}\text{Pb}/^{206}\text{Pb}$ ages distribution for the Kabweluma formation from metasedimentary basins in the Bangweulu block, shows similitude with the probability density distribution of the migmatitic paragneiss *ZM-10-38* from Solwezi dome. Kabweluma formation contains detrital zircon grains with 40% of ages are ranging between 1800 and 1900 Ma while another 40% ranges in age from 1950 to 2050 Ma (De Waele et al., 2008). The older zircons provide $^{207}\text{Pb}/^{206}\text{Pb}$ ages between 2160 and 2710 Ma. The youngest concordant analysis provides a maximum age of deposition at 1824 ± 19 Ma and thus this formation represents a Paleoproterozoic sedimentary sequence. In our case, for the paragneiss sample *ZM-10-38*, the youngest concordant $^{207}\text{Pb}/^{206}\text{Pb}$ at 1822 ± 19 Ma could represent the maximum age for the deposition of the sedimentary protolith of the migmatite and this migmatitic rock is interpreted as derived from a Paleoproterozoic sedimentary sequence, maybe a part of the Muva Supergroup. Zircon grains from the *ZM-10-62* migmatitic paragneiss present low Th/U (0.13-0.34) rim overgrowths dated at 1155 ± 24 Ma, 1210 ± 27 Ma and 1245 ± 24 Ma ($^{207}\text{Pb}/^{206}\text{Pb}$ ages with concordance > 95%). Age modes ranging between 1355 and 1500 from this sample represent partial dissolution and recrystallization areas of zircon grains and are not correlated to a magmatic-metamorphic event. A late Mesoproterozoic event is confirmed by the presence of inherited zircon grains dated at ca. 1.11 Ma in the peraluminous granite in the eastern part of the Solwezi dome. These Mesoproterozoic ages could be related to the collision phase during the Irumide orogeny.

7.1.2. *Mwombezhi basement inliers*

Mwombezhi dome is also composed by migmatitic-gneisses with minor mafic units. One orthogneiss yields a $^{207}\text{Pb}/^{206}\text{Pb}$ age at 1920 ± 8 . This crystallization age is confirmed by a concordant U-Pb age on one magmatic monazite grain at 1918 ± 20 Ma. Similar age was obtained on a potassic granodiorite, with calc-alkaline affinity, which yielded a zircon U-Pb age at 1927 ± 10 Ma and was collected from the basement in the northeastern Irumide belt, known as Luwalizi Granite Gneiss (De Waele, 2005). These granitoids could be part of the magmatic arc described by Rainaud et al. (2005) and De Waele et al. (2006). This meta-igneous rock contains xenocrystic zircon cores dated between 2.69 and 1.96 Ga. These oldest ages reveal the presence of Neoarchean crustal components as old as 2.69 Ga. It is in good agreement with inherited ages, ranging between 3.20 and 2.40 Ga, obtained by Rainaud et al. (2003) in the Kafue Anticline basement. Different schistose and gneissic rocks were dated during this study. Grey gneisses are characterized by different modes with a dominant mode at 1.91 Ga and two minor modes at 1.87-1.85 Ga and 1.76-1.73 Ga. A concordant $^{207}\text{Pb}/^{206}\text{Pb}$ magmatic zircon age at 1759 ± 25 Ma places the maximum age of deposition in the Paleoproterozoic era. Pink gneisses contain detrital zircon grains with a dominant mode ranging from 1.75 to 1.65 Ga and minor mode at ca. 1.58 and ca. 1.47 Ga. The youngest concordant analyses provide maximum $^{207}\text{Pb}/^{206}\text{Pb}$ ages of deposition at 1475 ± 36 Ma and at 1515 ± 64 Ma. Thus, these pink gneissic formations represent a metasedimentary sequence with a deposition age younger than the Mesoproterozoic.

All zircon grains from these gneissic metasedimentary sequences are surrounded by rims characterized by a low Th/U and interpreted as a metamorphic overgrowth dated at 1.19-1.15 Ga. This Mesoproterozoic event is consistent with metamorphism recorded by the migmatitic paragneiss from Solwezi dome, dated at 1.24-1.12 Ga and with the inherited zircon ages of the monzogranite from the Solwezi basement, dated at ca. 1.11 Ga. These ages could be related to the paroxysm of the Irumide orogeny during the formation of the Rodinia supercontinent. However, this age bracket is older than the metamorphic peak of the Irumide belt constrained at 1.02-1.01 Ga by De Waele et al. (2006).

7.2. Implication for crustal evolution from Archean to Mesoproterozoic

The oldest intrusions with crystallization age at 1.92 Ga present an average T_{DM} Hf model age of 2.80 Ga, suggesting a Meso- to Neoproterozoic source (Figure 20; Figure 21). This is in agreement with inherited zircon grains dated at 2.73 Ga reflecting derivation from a Neoproterozoic crust. The slightly younger granitoids group, dated at 1.85-1.89 Ga, is characterized by T_{DM} Hf ages ranging from ca. 2.80 to 2.50 Ga. As for the youngest intrusions dated at 1.11 Ga, T_{DM} Hf ages are distributed between 2.60 and 2.50 Ga (Figure 21). This Neoproterozoic to Neoproterozoic source is confirmed by T_{DM} Nd model ages ranging from 2.90 and 2.30 Ga on mafic units hosted by Paleo- and Mesoproterozoic metasedimentary sequences, suggesting a juvenile input at this period. Lu-Hf isotopic constraints presented in this paper indicate that all meta-igneous and metasedimentary rocks are derived from a unique Neoproterozoic to Neoproterozoic crust, reworked several times during magmatic and metamorphic events between the Paleoproterozoic (late Usagaran at ca. 1.92 Ga and Ubendian at ca. 1.90-1.85 Ga phases) and the Mesoproterozoic (ca. 1.24-1.11 Ga) without or minor juvenile input. This episodic crustal reworking is well reflected by old inherited zircon grains dated between 2.69 and 1.96 Ga and by ϵ_{Hf_t} data mostly plotting in the subchondritic uniform reservoir (Figure 20). Similar observations were published for the southern margin of the Bangweulu block and the Irumide belt by De Waele et al. (2006) and in the eastern part of the Domes region (Rainaud et al. 2003). Combining whole-rock geochemistry and Sr-Nd isotopic data, De Waele et al. (2006) proposed that the Irumide belt corresponds to the recurrently destabilized southern boundary of the Bangweulu block, whose preserved nucleus appears to be an Archean craton covered by Paleoproterozoic sediments. In this paper, the same scientific approach with Lu-Hf isotopes allows to propose that the basement inliers exposed in the internal orogenic Lufilian belt, referred as the Domes region, represent also the southwestern metacratonic boundary of the Bangweulu block.

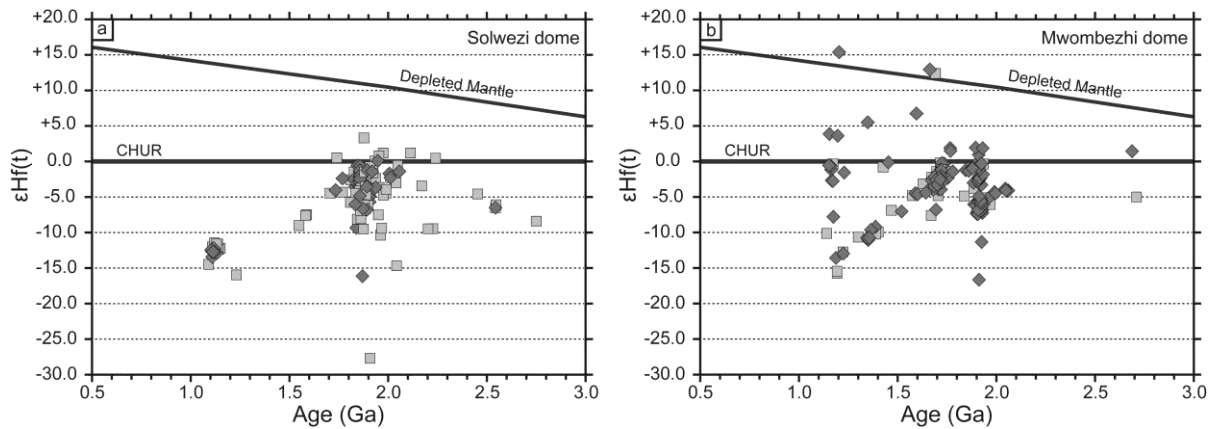


Figure 20: $\epsilon\text{Hf}(t)$ evolution diagram for all studied samples from (a) the Solwezi dome and (b) the Mwombezhi dome. Dark grey diamonds represent concordant ($> 95\%$) $^{207}\text{Pb}/^{206}\text{Pb}$ ages and light grey squares represent discordant ($< 95\%$) $^{207}\text{Pb}/^{206}\text{Pb}$ ages.

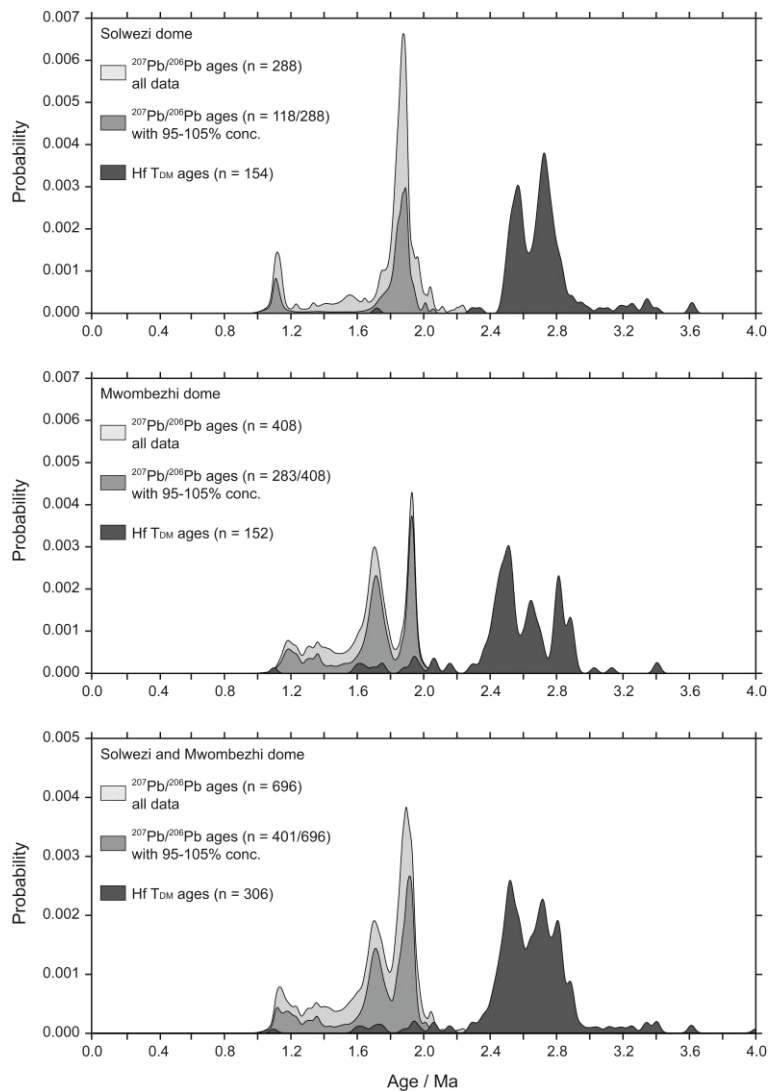


Figure 21: Probability density plots versus crystallization $^{207}\text{Pb}/^{206}\text{Pb}$ ages for studied samples.

Table 1: Sampling details. Abbreviations: Am = Amphibole, Ap = Apatite, Bt = Biotite, Cal = Calcite, Chl = Chlorite, Ep = Epidote, Kfs = Feldspar, Grt = Garnet, Ilm = Ilmenite, Mnz = Monazite, Ms = Muscovite, Ox = Iron oxide, Pl = Plagioclase, Qtz = Quartz, Rt = Rutile, Ttn = Titanite, Zrn = Zircon.

Number	Label	Sampling	Coordinates		Lithology	Mineralogy	
			North	East		Primary	Accessory
1	ZM-10-09	Outcrop	8648457	434886	Orthogneiss	Qtz, Pl, Bt, Kfs, Aln	Ep, Ap, Ms, Scp, Zrn
2	ZM-10-13	Outcrop	8648058	435164	Orthogneiss	Qtz, Pl, Bt, Kfs, Aln	Ep, Ap, Ms, Scp, Zrn
3	ZM-10-17	Outcrop	8647148	435744	Orthogneiss	Qtz, Pl, Bt, Kfs, Aln	Ep, Ap, Ms, Scp, Zrn
4	ZM-10-66	Outcrop	8643910	446350	Granite	Qtz, Mc, Pl, Bt, Ms	Zrn, Ox
5	ZM-10-62	Outcrop	8627213	440243	Paragneiss	Qtz, Bt, Mc, Grt, Ms, Mnz, Zrn	Aln, Ep, Ap
6	ZM-10-51	Outcrop	8636944	435271	Amphibolite	Am, Pl, Qtz, Bt, Ep	Rt, Ilm
7	ZM-10-53	Outcrop	8637043	435368	Orthogneiss	Qtz, Pl, Bt, Kfs	
8	ZM-10-38	Outcrop	8645761	435039	Paragneiss	Qtz, Pl, Kfs, Ms, Bt	Zrn
9	ZM-39-01	Drill core	Chimiwungo prospect		Paragneiss	Qtz, Kfs, Pl, Bt	Ox, Zrn, Cal, Ms, Hem, Ky, Ep
10	ZM-39-04	Drill core	Chimiwungo prospect		Amphibolite	Am, Pl, Qtz	Rt, Ilm
11	ZM-62-05	Drill core	Chimiwungo prospect		Paragneiss	Qtz, Fsp, Pl, Bt	Ox, Zrn, Ms
12	ZM-66-08	Drill core	Chimiwungo prospect		Paragneiss	Qtz, Pl, Bt, Ep	Aln, Ms
13	ZM-12-07	Outcrop	8643894	353483	Orthogneiss	Qtz, Kfs, Pl, Bt, Ms	Zrn
14	ZM-12-13	Outcrop	Malundwe open pit		Amphibolite	Gt, Am, Bt, Pl	Qtz, Rt, Ilm
15	ZM-12-16	Outcrop	Malundwe open pit		Amphibolite	Gt, Am, Bt, Pl	Qtz, Rt, Ilm
16	ZM-12-25	Outcrop	Malundwe open pit		Granite	Qtz, Bt, Pl	Chl, Ep

Table 2: Major element composition of whole-rock by ICP-OES samples from the Solwezi dome.

Location Lithology Sample	Solwezi dome							
	Orthogneiss				Paragneiss		Granite	Amphibolite
	ZM-10-09	ZM-10-13	ZM-10-17	ZM-10-53	ZM-10-38	ZM-10-62	ZM-10-66	ZM-10-51
<i>Oxides / wt.%</i>								
SiO ₂	67.07	66.40	67.76	61.56	71.37	70.09	71.68	44.52
TiO ₂	0.36	0.50	0.39	0.66	0.55	0.60	0.40	0.97
Al ₂ O ₃	14.56	15.17	15.34	15.76	14.86	12.98	13.65	20.55
Fe ₂ O ₃	4.14	3.78	3.37	6.37	3.87	6.17	2.68	11.61
MnO	0.05	0.05	0.03	0.05	0.03	0.14	0.02	0.18
MgO	1.93	2.16	1.64	4.15	1.32	0.31	0.73	4.38
CaO	3.54	3.64	2.85	2.15	1.16	2.13	1.53	13.33
Na ₂ O	2.77	3.87	3.95	4.19	2.00	1.61	2.57	2.49
K ₂ O	2.92	3.03	2.59	3.10	3.70	5.69	5.43	0.48
P ₂ O ₅	0.12	0.20	0.22	0.18	0.07	0.20	0.24	0.11
LOI	2.33	1.77	1.64	0.98	1.82	0.39	0.79	1.62
Total	99.79	100.56	99.77	99.13	100.74	100.30	99.71	100.24
<i>Trace / ppm</i>								
Cr	24.60	25.55	41.75	37.83	53.77	3.48	16.57	242.40
Co	24.76	24.14	16.24	19.85	10.96	4.45	5.72	19.96
Ni	18.83	17.56	15.24	24.54	26.08	0.00	10.03	62.21
Rb	115.70	105.00	113.70	181.70	154.70	120.80	218.90	10.88
Sr	227.10	369.80	367.20	208.10	193.20	201.40	211.10	753.30
Cs	1.45	1.50	1.58	2.42	1.54	0.67	0.97	0.22
Ba	487.20	714.30	511.60	350.20	904.90	2400.00	1022.00	57.52
Sc	-	-	7.86	21.74	-	14.16	-	-
V	71.08	61.42	51.72	100.10	54.51	4.16	33.32	205.10
Ta	0.28	0.40	0.61	0.19	0.66	1.32	0.88	0.46
Nb	5.07	6.25	7.68	3.85	9.70	20.71	15.49	8.43
Zr	107.40	124.00	162.30	175.10	156.70	730.00	303.00	203.00
Hf	3.09	3.14	4.23	4.72	4.52	18.59	8.26	5.80
Th	9.02	6.02	9.20	0.53	13.46	1.81	69.16	7.88
U	2.46	1.34	1.66	0.94	1.54	0.79	1.85	9.93
Y	7.63	23.36	15.17	17.49	7.04	70.13	20.68	49.95
La	45.79	50.03	33.59	16.53	10.50	55.18	119.00	48.03
Ce	86.85	91.84	64.71	33.61	54.12	119.30	256.60	91.00
Pr	9.87	10.95	7.05	3.94	2.92	15.95	26.86	10.71
Nd	34.63	39.53	24.64	17.86	10.13	69.09	90.27	40.65
Sm	5.03	6.55	3.88	3.84	2.18	15.45	13.76	8.35
Eu	1.22	1.41	0.99	1.16	0.45	4.08	1.57	4.35
Gd	3.06	4.67	2.80	3.37	1.69	14.20	7.73	8.19
Tb	0.36	0.71	0.42	0.52	0.26	2.21	1.02	1.35
Dy	1.71	4.26	2.52	3.14	1.55	12.99	4.75	8.62
Ho	0.28	0.84	0.48	0.62	0.30	2.55	0.74	1.72

Er	0.75	2.47	1.45	1.70	0.93	7.15	1.92	4.97
Tm	0.10	0.39	0.21	0.25	0.17	1.07	0.26	0.76
Yb	0.80	2.37	1.31	1.69	1.40	7.26	1.77	5.17
Lu	0.14	0.32	0.19	0.26	0.22	1.13	0.26	0.85
Cu	305.50	55.46	14.50	0.00	43.62	12.22	31.17	0.00
Zn	14.52	20.48	18.01	33.41	-	71.07	19.16	26.46
Pb	2.14	4.07	7.17	2.47	3.15	10.16	30.84	8.12

Table 3: Major element composition of whole-rock by ICP-OES samples from the Mwombezi dome.

Location Lithology	Mwombezi dome							
	Paragneiss			Granite	Orthogneiss	Amphibolite	Gt amphibolite	
Sample	ZM-39-01	ZM-62-05	ZM-66-08	ZM-12-25	ZM-12-07	ZM-39-04	ZM-12-13	ZM-12-16
<i>Oxides / wt. %</i>								
SiO₂	70.00	70.56	60.83	62.62	64.46	45.48	54.96	54.28
TiO₂	0.59	0.37	0.63	0.69	0.62	2.39	1.60	1.54
Al₂O₃	13.72	13.15	16.22	18.43	15.98	14.00	14.01	14.87
Fe₂O₃	4.15	4.75	5.83	3.48	5.04	16.39	14.33	11.68
MnO	0.03	0.03	0.05	0.02	0.05	0.18	0.27	0.19
MgO	0.56	2.41	2.73	1.82	1.68	6.42	6.04	7.17
CaO	1.63	0.69	3.19	2.68	1.89	6.15	6.30	4.88
Na₂O	3.24	0.80	4.86	7.35	3.67	1.24	1.01	1.73
K₂O	5.09	5.15	2.74	1.14	3.73	4.89	0.78	1.68
P₂O₅	0.21	0.13	0.31	0.19	0.10	0.39	0.23	0.05
LOI	1.07	1.98	1.28	1.11	2.04	2.04	1.03	2.28
Total	100.27	100.02	98.67	99.52	99.26	99.56	100.56	100.35
<i>Trace / ppm</i>								
Cr	6.00	4.76	29.32	104.40	39.23	181.60	195.90	163.80
Co	6.62	16.73	17.95	18.94	14.16	49.13	100.40	91.54
Ni	0.00	8.29	28.28	30.70	17.29	82.26	46.80	81.66
Rb	156.50	228.90	91.62	49.49	181.50	323.30	35.12	44.80
Sr	130.30	49.07	631.80	211.50	255.30	88.82	18.59	53.50
Cs	0.68	1.56	1.40	1.44	1.57	4.37	0.55	1.05
Ba	1317.00	663.50	670.00	123.50	674.80	600.60	52.37	157.00
Sc	9.68	8.46	10.56	5.97	12.80	35.25	35.05	44.80
V	18.93	17.81	87.52	86.17	54.44	279.60	214.70	262.20
Ta	2.31	2.26	0.55	0.64	0.78	0.94	1.21	0.74
Nb	37.78	27.91	9.49	5.86	16.74	13.73	16.15	10.30
Zr	626.40	376.30	139.70	166.80	284.10	235.80	200.50	120.10
Hf	14.47	10.03	3.35	4.51	7.54	5.76	5.28	3.28
Th	24.42	23.88	4.41	21.22	65.91	5.17	17.99	3.82
U	3.07	1.72	1.36	2.97	3.04	5.52	17.31	4.70
Y	86.60	20.79	20.82	16.25	23.51	44.76	50.37	57.93
La	100.70	22.55	43.72	47.63	74.60	29.14	28.72	13.10
Ce	221.80	56.63	89.24	93.66	172.70	65.29	63.28	27.93
Pr	27.06	6.31	10.38	11.31	21.22	8.32	7.55	3.85
Nd	92.46	24.09	39.01	41.13	77.04	35.09	29.57	16.69
Sm	18.38	5.12	6.38	7.62	15.97	8.12	6.85	4.60
Eu	3.25	0.73	1.57	1.61	1.85	2.44	1.92	1.78
Gd	15.45	4.29	4.58	5.88	10.40	7.90	7.20	5.60
Tb	2.51	0.65	0.63	0.79	1.37	1.27	1.32	1.07

Dy	15.05	3.55	3.49	3.88	6.30	7.74	8.50	7.85
Ho	3.02	0.67	0.66	0.58	0.91	1.57	1.74	1.87
Er	8.65	1.95	1.95	1.37	2.21	4.38	4.88	6.26
Tm	1.33	0.31	0.30	0.17	0.29	0.67	0.74	1.13
Yb	9.08	2.29	2.11	1.00	1.86	4.45	5.00	8.86
Lu	1.38	0.40	0.34	0.15	0.29	0.71	0.76	1.52
Cu	15.95	0.00	5.58	12.45	76.56	9.93	392.30	22.85
Zn	28.86	22.25	56.30	304.20	188.50	88.00	27.70	28.09
Pb	17.14	2.46	5.36	6.98	40.65	4.43	12.59	6.17

Table 4: Whole rock Nd and Sr isotopic data for samples from Solwezi and Mwombezi domes.

Sample	Loc.	Lithology	Age	$^{147}\text{Sm}/^{144}\text{Nd}$	$^{143}\text{Nd}/^{144}\text{Nd}$	Err.	$^{143}\text{Nd}/^{144}\text{Nd}(i)$	$\epsilon\text{Nd}(t)$	T_{DM}	$^{87}\text{Sr}/^{86}\text{Sr}$	$^{87}\text{Sr}/^{86}\text{Sr}(i)$
ZM-10-51	Slw.	Amphibolite	-	0.119237	0.511524	6×10^{-6}	-	-	-	0.716166	-
ZM-12-13	Mbz.	Gt amph.	-	0.134930	0.511922	4×10^{-6}	-	-	2.38	0.800163	-
ZM-12-16	Mbz.	Gt amph.	-	0.160221	0.512121	5×10^{-6}	-	-	2.93	0.756917	-
ZM-39-04	Mbz.	Amphibolite	-	0.134031	0.511937	5×10^{-6}	-	-	2.32	0.820484	-

Table 5: U-Pb isotope analyses of magmatic zircon grains from orthogneiss (*ZM-10-09; Solwezi Dome*)

Grain	$^{207}\text{Pb}^a$ (cps)	U ^b (ppm)	Pb ^b (ppm)	$\frac{\text{Th}^b}{\text{U}}$	$^{206}\text{Pbc}^c$ (%)	$\frac{^{206}\text{Pbd}}{^{238}\text{U}}$	$\pm 2s$	$\frac{^{207}\text{Pbd}}{^{235}\text{U}}$	$\pm 2s$	$\frac{^{207}\text{Pbd}}{^{206}\text{Pb}}$	$\pm 2s$	rho ^e	$\frac{^{206}\text{Pb}}{^{238}\text{U}}$	$\pm 2s$ (Ma)	$\frac{^{207}\text{Pb}}{^{235}\text{U}}$	$\pm 2s$ (Ma)	$\frac{^{207}\text{Pb}}{^{206}\text{Pb}}$	$\pm 2s$ (Ma)	conc. ^f (%)
05		55	22	0.90		0.3382	0.0069	5.3705	0.1319			0.83	1878	33			1882	45	100
06		235	79	0.21		0.3249	0.0065	5.0571	0.1131			0.89	1813	32			1846	41	98
07		174	34	0.31		0.1797	0.0039	2.8642	0.0949			0.66	1065	21			1889	61	56
09		293	103	0.42		0.3284	0.0065	5.0976	0.1089			0.93	1830	32			1841	39	99
10		83	33	1.03		0.3290	0.0067	5.1397	0.1257			0.83	1833	32			1853	45	99
11		350	126	0.59		0.3256	0.0064	5.2236	0.1110			0.93	1817	31			1901	39	96
12		389	75	0.69		0.1557	0.0031	2.4742	0.0554			0.89	933	17			1884	41	50
13		89	34	1.19		0.3094	0.0064	4.9182	0.1334			0.77	1738	32			1884	50	92
16		170	63	0.75		0.3265	0.0065	5.1462	0.1150			0.89	1822	32			1869	41	97
17		448	140	0.16		0.3035	0.0060	4.7571	0.1005			0.93	1709	30			1859	39	92
18		154	54	0.45		0.3234	0.0065	5.1988	0.1178			0.88	1806	31			1904	41	95
19		196	67	0.70		0.3023	0.0060	4.6489	0.1038			0.89	1703	30			1824	41	93
20		232	73	0.32		0.2991	0.0059	4.7291	0.1036			0.90	1687	29			1875	40	90
21		108	42	1.09		0.2982	0.0060	4.6395	0.1130			0.83	1682	30			1846	45	91
22		649	213	1.04		0.2759	0.0055	4.3993	0.0994			0.88	1571	28			1889	42	83
23		307	104	0.90		0.2915	0.0058	4.6622	0.1038			0.89	1649	29			1895	41	87
26		151	61	1.01		0.3358	0.0067	5.3657	0.1223			0.87	1866	32			1894	42	99
27		200	74	0.89		0.3158	0.0062	4.8119	0.1076			0.88	1769	31			1807	42	98
28		183	60	0.40		0.3038	0.0060	4.7662	0.1099			0.86	1710	30			1861	43	92
30		382	115	0.17		0.2945	0.0059	4.5510	0.1078			0.84	1664	29			1833	44	91
31		299	85	0.18		0.2764	0.0055	4.2774	0.1004			0.85	1573	28			1836	44	86
32		257	83	0.19		0.3171	0.0062	4.8100	0.1031			0.92	1776	30			1799	40	99
33		530	156	0.06		0.2941	0.0057	4.4907	0.0944			0.93	1662	29			1811	39	92
36		141	59	1.33		0.3368	0.0066	5.3666	0.1208			0.88	1871	32			1888	42	99
37		230	83	0.56		0.3293	0.0065	5.1519	0.1126			0.90	1835	31			1855	41	99
39		166	51	0.18		0.3020	0.0060	4.6883	0.1084			0.86	1701	30			1842	43	92
40		585	181	0.07		0.3087	0.0060	4.7480	0.1003			0.92	1734	30			1825	39	95
43		189	59	0.14		0.3059	0.0060	4.6374	0.1027			0.88	1721	30			1798	42	96
46		186	69	0.81		0.3284	0.0064	5.1595	0.1150			0.88	1831	31			1863	42	98

47	250	78	0.31	0.2968	0.0059	4.6948	0.1098	0.84	1676	29	1875	44	89						
48	268	93	0.73	0.3044	0.0060	4.8256	0.1112	0.86	1713	30	1879	43	91						
49	233	83	0.62	0.3265	0.0064	5.1955	0.1150	0.88	1822	31	1886	41	97						
50	244	86	0.62	0.3245	0.0063	5.1098	0.1125	0.88	1812	31	1867	41	97						
51	498	169	0.33	0.3239	0.0063	4.9862	0.1068	0.91	1809	31	1826	40	99						
53	317	97	0.15	0.3000	0.0059	4.6473	0.1080	0.85	1692	29	1837	44	92						
57	295	92	0.12	0.3081	0.0060	4.7538	0.1053	0.88	1731	29	1830	42	95						
58	242	101	1.07	0.3386	0.0069	5.3809	0.1462	0.75	1880	33	1884	51	100						
59	478	167	0.68	0.3113	0.0061	4.8625	0.1106	0.86	1747	30	1852	43	94						
60	255	88	0.30	0.3297	0.0064	5.1198	0.1126	0.88	1837	31	1842	41	100						
61	281	106	0.88	0.3218	0.0063	5.0374	0.1176	0.84	1799	31	1856	44	97						
62	160	59	0.62	0.3258	0.0064	5.0847	0.1203	0.83	1818	31	1851	44	98						
63	284	94	0.08	0.3256	0.0063	5.0829	0.1176	0.84	1817	31	1852	43	98						
Grain	$^{207}\text{Pb}^a$ (cps)	U ^b (ppm)	Pb ^b (ppm)	Th ^b U	$^{206}\text{Pb}^c$ (%)	$^{206}\text{Pb}^d$ ^{238}U	$\pm 2s$ (%)	$^{207}\text{Pb}^d$ ^{235}U	$\pm 2s$ (%)	$^{207}\text{Pb}^d$ ^{206}Pb	$\pm 2s$ (%)	rho ^e	^{206}Pb ^{238}U	$\pm 2s$ (Ma)	^{207}Pb ^{235}U	$\pm 2s$ (Ma)	^{207}Pb ^{206}Pb	$\pm 2s$ (Ma)	conc. ^f (%)
158	205675	2280	690	0.07	0.00	0.3116	1.9	4.8580	1.9	0.1131	0.5	0.97	1749	28	1795	16	1849	9	95
159	68729	707	220	0.56	b.d.	0.2810	1.6	4.4200	1.6	0.1141	0.5	0.96	1596	22	1716	14	1866	9	86
160	75607	756	230	0.15	0.01	0.3071	1.6	4.8660	1.8	0.1149	0.6	0.93	1726	25	1796	15	1878	12	92
161	42989	377	150	0.85	0.00	0.3425	1.7	5.4930	1.8	0.1163	0.6	0.93	1899	28	1899	16	1900	12	100
162	99217	2364	390	0.09	0.14	0.1652	10.9	2.2190	11.0	0.0974	1.9	0.99	986	100	1187	80	1575	35	63
163	36785	349	120	0.66	0.00	0.3099	1.7	4.8490	1.8	0.1135	0.5	0.95	1740	26	1793	15	1856	10	94

^aWithin run background-corrected mean ^{207}Pb signal in cps (counts per second). ^bU and Pb content and Th/U ratio were calculated relative to GJ-1 reference zircon. ^cPercentage of the common Pb on the ^{206}Pb . b.d. = below detection limit. ^dCorrected for background, within-run Pb/U fractionation (in case of $^{206}\text{Pb}/^{238}\text{U}$) and common Pb using Stacy and Kramers (1975) model Pb composition and subsequently normalised to GJ-1 (ID-TIMS value/measured value); $^{207}\text{Pb}/^{235}\text{U}$ calculated using $^{207}\text{Pb}/^{206}\text{Pb}/(^{238}\text{U}/^{206}\text{Pb}*1/137.88)$. ^eRho is the $^{206}\text{Pb}/^{238}\text{U}/^{207}\text{Pb}/^{235}\text{U}$ error correlation coefficient. ^fDegree of concordance = $^{206}\text{Pb}/^{238}\text{U}$ age / $^{207}\text{Pb}/^{206}\text{Pb}$ age x 100.

Table 6: U-Pb isotope analyses of magmatic zircon grains from orthogneiss (*ZM-10-13; Solwezi dome*)

Grain	$^{207}\text{Pb}^a$	U^b	Pb^b	Th^b	$^{206}\text{Pb}^c$	$^{206}\text{Pb}^d$	$\pm 2s$	$^{207}\text{Pb}^d$	$\pm 2s$	$^{207}\text{Pb}^d$	$\pm 2s$	rho^e	^{206}Pb	$\pm 2s$	^{207}Pb	$\pm 2s$	^{207}Pb	$\pm 2s$	conc.^f
	(cps)	(ppm)	(ppm)	U	(%)	^{238}U	(%)	^{235}U	(%)	^{206}Pb	(%)		^{238}U	(Ma)	^{235}U	(Ma)	^{206}Pb	(Ma)	(%)
120	24064	245	99	1.44	0.00	0.3074	1.5	4.7630	1.6	0.1124	0.6	0.93	1728	23	1778	14	1838	11	94
121	37326	385	140	0.32	0.06	0.3416	2.6	5.4640	2.7	0.1160	0.7	0.97	1894	42	1895	23	1896	12	100
122	24345	225	98	1.25	0.13	0.3405	1.5	5.4490	1.8	0.1161	0.9	0.86	1889	25	1893	15	1896	16	100
123	21002	212	92	1.70	0.00	0.3166	1.5	5.0440	1.7	0.1155	0.8	0.87	1773	23	1827	15	1888	15	94
124	24249	213	97	1.64	0.00	0.3407	1.5	5.4380	1.7	0.1158	0.8	0.89	1890	25	1891	15	1892	14	100
125	30065	288	120	1.14	0.00	0.3267	1.6	5.1870	1.7	0.1152	0.8	0.90	1822	25	1851	15	1883	14	97
126	21421	213	93	1.54	0.00	0.3393	2.2	5.3730	2.7	0.1148	1.6	0.81	1883	36	1881	24	1878	29	100
127	28297	263	110	1.26	0.00	0.3200	1.5	5.0890	1.7	0.1153	0.7	0.89	1790	23	1834	14	1885	13	95
128	24688	248	110	1.90	b.d.	0.3142	1.7	4.9240	1.9	0.1137	0.9	0.89	1761	26	1806	16	1859	16	95
129	37049	388	170	1.47	0.00	0.3418	1.5	5.4690	1.7	0.1161	0.6	0.93	1895	25	1896	14	1896	11	100
130	12091	127	49	1.32	0.00	0.2995	1.7	4.5350	2.0	0.1098	1.1	0.84	1689	25	1737	17	1796	20	94
131	27072	260	110	1.44	0.00	0.3059	1.7	4.8160	1.9	0.1142	0.7	0.92	1720	26	1788	16	1867	13	92
132	45977	417	170	0.99	b.d.	0.3394	1.4	5.4240	1.5	0.1159	0.5	0.94	1884	24	1889	13	1894	9	99
133	25506	229	99	1.32	0.00	0.3392	1.4	5.4050	1.6	0.1155	0.7	0.90	1883	23	1886	14	1888	12	100
134	30518	275	120	1.21	0.00	0.3410	1.5	5.4520	1.7	0.1160	0.8	0.89	1891	25	1893	14	1895	13	100
135	26693	253	110	1.71	b.d.	0.3301	2.0	5.2330	2.1	0.1150	0.6	0.95	1839	31	1858	18	1880	11	98
136	38714	371	140	1.03	b.d.	0.3247	1.6	5.1090	1.8	0.1141	0.8	0.91	1813	26	1838	15	1866	14	97
137	47364	437	170	1.35	0.00	0.2928	2.0	4.6910	2.1	0.1162	0.5	0.97	1656	29	1766	18	1898	9	87
138	151149	1288	400	0.08	0.06	0.3193	1.6	4.9270	1.7	0.1119	0.6	0.95	1786	25	1807	15	1831	10	98
139	36920	766	140	0.01	0.17	0.1967	1.6	2.2060	1.7	0.0813	0.6	0.94	1158	17	1183	12	1229	12	94
140	40851	373	160	1.12	0.00	0.3395	1.8	5.4120	2.0	0.1156	0.8	0.92	1884	30	1887	17	1889	14	100
141	32204	291	130	1.59	0.02	0.3227	1.5	5.1520	1.7	0.1158	0.7	0.92	1803	24	1845	14	1892	12	95
142	17127	155	68	1.22	0.01	0.3558	1.5	5.6650	1.8	0.1155	1.0	0.82	1962	25	1926	15	1887	18	104
143	25151	220	76	0.24	0.02	0.3400	1.6	5.4100	1.8	0.1154	0.7	0.92	1886	27	1886	15	1886	12	100
144	12598	112	50	1.51	b.d.	0.3396	1.5	5.4240	1.7	0.1159	0.8	0.87	1885	24	1889	14	1893	15	100
145	16671	161	50	0.26	b.d.	0.3045	1.5	4.8050	1.8	0.1144	0.9	0.85	1714	22	1786	15	1871	17	92

151	22633	218	87	0.92	0.00	0.3396	2.1	5.3970	2.3	0.1153	0.9	0.92	1885	35	1884	20	1884	16	100
152	24505	219	100	1.81	b.d.	0.3400	1.6	5.3920	1.8	0.1150	0.8	0.89	1887	26	1884	15	1880	15	100
153	49484	478	180	1.03	b.d.	0.3099	1.6	4.8150	1.9	0.1127	1.0	0.84	1740	24	1788	16	1843	18	94
154	29718	269	120	1.62	0.00	0.3169	1.8	5.0340	1.9	0.1152	0.7	0.94	1775	28	1825	16	1883	12	94
155	25866	215	97	1.57	0.09	0.3385	2.0	5.3800	2.1	0.1153	0.7	0.94	1879	32	1882	18	1884	13	100
156	20297	184	74	1.37	b.d.	0.3075	1.7	4.8690	1.9	0.1148	0.9	0.88	1728	26	1797	16	1877	16	92
157	13032	117	50	1.38	0.00	0.3386	1.7	5.3770	2.0	0.1152	1.0	0.85	1880	28	1881	17	1883	18	100

Table 7: U-Pb isotope analyses of magmatic zircon grains from orthogneiss (*ZM-10-53; Solwezi dome*)

Grain	$^{207}\text{Pb}^a$	U^b	Pb^b	Th^b	$^{206}\text{Pbc}^c$	$^{206}\text{Pbd}^d$	$\pm 2s$	$^{207}\text{Pbd}^d$	$\pm 2s$	$^{207}\text{Pbd}^d$	$\pm 2s$	rho^e	^{206}Pb	$\pm 2s$	^{207}Pb	$\pm 2s$	^{207}Pb	$\pm 2s$	^{207}Pb	$\pm 2s$	conc.^f
	(cps)	(ppm)	(ppm)	U	(%)	^{238}U	(%)	^{235}U	(%)	^{206}Pb	(%)		^{238}U	(Ma)	^{235}U	(Ma)	^{206}Pb	(Ma)	(Ma)	(%)	
51	13230	133	53	1.08	b.d.	0.3298	1.5	5.0830	1.8	0.1118	1.0	0.84	1837	25	1833	16	1829	18	100		
52	25705	282	110	0.67	0.10	0.3332	1.8	5.2060	2.0	0.1133	0.8	0.91	1854	29	1854	17	1853	15	100		
53	80484	753	290	0.84	0.00	0.3309	1.5	5.1350	1.6	0.1126	0.4	0.97	1843	25	1842	14	1841	7	100		
54	50211	502	180	0.40	0.00	0.3327	1.6	5.1960	1.7	0.1133	0.6	0.94	1852	26	1852	15	1852	11	100		
55	9883	103	38	0.93	0.00	0.3140	1.5	4.8190	1.8	0.1113	1.0	0.84	1760	23	1788	15	1821	18	97		
56	5855	69	22	0.95	b.d.	0.2565	1.7	3.7570	2.1	0.1062	1.4	0.77	1472	22	1584	17	1736	25	85		
57	9124	90	34	0.83	0.00	0.3235	1.5	5.0600	2.0	0.1134	1.3	0.76	1807	24	1829	17	1855	23	97		
58	12028	109	40	0.72	0.00	0.3183	1.6	4.9700	2.0	0.1133	1.2	0.80	1781	25	1814	17	1852	22	96		
59	5280	54	21	0.98	0.02	0.3159	1.5	4.9430	2.1	0.1135	1.5	0.71	1770	23	1810	18	1856	27	95		
60	11084	98	37	0.76	0.14	0.3330	1.8	5.2050	2.1	0.1134	1.2	0.82	1853	28	1853	18	1854	22	100		
61	39678	381	170	1.99	0.00	0.3072	1.6	4.8110	1.7	0.1136	0.7	0.91	1727	24	1787	15	1858	13	93		
62	3605	38	13	0.98	0.00	0.2679	2.2	4.1870	2.8	0.1134	1.7	0.80	1530	30	1672	23	1854	30	83		
63	11214	113	45	1.03	b.d.	0.3321	1.7	5.1770	2.0	0.1130	1.2	0.82	1849	27	1849	18	1849	21	100		
64	12632	141	51	1.00	0.00	0.3039	1.6	4.6260	1.9	0.1104	1.0	0.84	1711	24	1754	16	1806	19	95		
65	9469	165	43	0.70	0.06	0.2320	1.9	3.0640	2.4	0.0958	1.5	0.78	1345	23	1424	18	1543	28	87		
66	12857	119	46	1.00	0.03	0.3156	1.5	4.9400	1.7	0.1135	0.8	0.89	1768	23	1809	14	1856	14	95		
72	22570	230	68	0.57	b.d.	0.2618	2.3	4.1510	2.4	0.1150	0.7	0.96	1499	31	1664	20	1880	12	80		
73	15613	144	56	0.95	b.d.	0.3316	1.7	5.1770	2.0	0.1132	1.2	0.82	1846	27	1849	17	1852	21	100		

74	13164	115	39	0.70	0.00	0.2937	1.5	4.5940	1.9	0.1134	1.1	0.82	1660	22	1748	16	1855	19	89
75	11410	125	41	1.03	0.20	0.2645	1.7	3.9350	2.3	0.1079	1.5	0.76	1513	24	1621	19	1764	27	86
76	12617	120	46	1.02	0.18	0.3151	1.6	4.9980	1.9	0.1150	1.1	0.84	1766	25	1819	17	1880	19	94
77	11820	135	50	1.07	0.01	0.3087	1.6	4.5050	1.9	0.1059	1.1	0.82	1734	24	1732	16	1729	20	100
78	5954	72	22	0.69	0.04	0.2704	1.6	3.8860	2.2	0.1042	1.6	0.72	1543	22	1611	18	1701	29	91
79	5316	68	19	0.76	0.07	0.2396	1.7	3.2300	2.5	0.0978	1.9	0.67	1385	21	1464	20	1582	35	88
80	12475	131	49	1.17	b.d.	0.3041	1.5	4.6750	1.9	0.1115	1.2	0.78	1712	23	1763	16	1824	22	94
81	12230	126	30	0.47	0.00	0.2143	2.6	3.3380	2.9	0.1130	1.2	0.91	1251	30	1490	23	1848	22	68
82	7752	85	30	1.01	0.00	0.2852	1.6	4.4560	2.1	0.1133	1.4	0.73	1617	22	1723	18	1854	26	87
83	4047	36	14	0.80	0.04	0.3339	2.0	5.2150	2.6	0.1133	1.6	0.78	1857	33	1855	22	1853	29	100
84	15331	159	58	0.83	0.00	0.3140	1.8	4.9610	2.0	0.1146	1.0	0.87	1760	27	1813	17	1873	18	94
85	10126	110	39	0.73	0.03	0.3155	1.7	4.6940	2.1	0.1079	1.2	0.81	1768	27	1766	18	1764	23	100
86	17502	169	66	0.95	0.00	0.3315	2.2	5.1400	2.3	0.1125	0.9	0.93	1845	35	1843	20	1840	16	100

Table 8: U-Pb isotope analyses of magmatic zircon grains from granite (*ZM-10-66; Solwezi dome*)

Grain	$^{207}\text{Pb}^a$	U^b	Pb^b	Th^b	$^{206}\text{Pb}^c$	$^{206}\text{Pb}^d$	$\pm 2s$	$^{207}\text{Pb}^d$	$\pm 2s$	$^{207}\text{Pb}^d$	$\pm 2s$	rho^e	^{206}Pb	$\pm 2s$	^{207}Pb	$\pm 2s$	^{207}Pb	$\pm 2s$	conc.^f
	(cps)	(ppm)	(ppm)	U	(%)	^{238}U	(%)	^{235}U	(%)	^{206}Pb	(%)		^{238}U	(Ma)	^{235}U	(Ma)	^{206}Pb	(Ma)	(%)
367	18839	492	110	1.24	b.d.	0.1866	1.5	1.9690	1.6	0.0765	0.7	0.89	1103	15	1105	11	1109	15	99
368	18460	470	100	1.04	0.03	0.1852	1.4	1.9610	1.7	0.0768	0.9	0.85	1095	14	1102	11	1116	17	98
369	38616	991	180	0.21	0.00	0.1848	1.7	1.9460	1.8	0.0764	0.6	0.94	1093	17	1097	12	1105	13	99
370	39913	1047	190	0.24	0.00	0.1879	1.4	1.9730	1.6	0.0762	0.6	0.92	1110	15	1106	11	1099	12	101
371	22502	609	130	0.95	0.00	0.1800	1.5	1.9260	1.7	0.0776	0.6	0.93	1067	15	1090	11	1136	13	94
372	30311	930	190	0.52	0.10	0.1891	1.7	1.9880	1.9	0.0763	0.7	0.92	1116	18	1111	13	1102	14	101
373	17062	456	97	1.22	b.d.	0.1757	1.7	1.8700	2.1	0.0772	1.3	0.78	1043	16	1070	14	1126	26	93
374	47057	1333	230	0.27	0.00	0.1738	1.8	1.8680	1.9	0.0780	0.7	0.93	1033	17	1070	13	1146	14	90
375	57653	1433	250	0.07	0.55	0.1817	1.5	1.9140	1.7	0.0764	0.8	0.87	1077	15	1086	12	1106	17	97
376	18687	507	87	0.14	0.00	0.1772	1.5	1.8750	1.7	0.0768	1.0	0.83	1052	14	1072	12	1115	19	94
377	30217	776	130	0.23	0.01	0.1747	1.6	1.8400	1.7	0.0764	0.8	0.90	1038	15	1060	11	1106	15	94
378	41189	1039	170	0.13	0.01	0.1713	1.5	1.8360	1.6	0.0777	0.7	0.90	1019	14	1058	11	1140	15	89
379	39228	395	130	2.37	12.26	0.1879	3.5	2.0020	8.3	0.0773	7.5	0.42	1110	35	1116	58	1129	150	98
380	34475	902	190	1.12	0.00	0.1771	1.6	1.8910	1.8	0.0775	0.9	0.87	1051	15	1078	12	1133	18	93

381	81060	1926	340	0.13	1.10	0.1773	1.5	1.8560	2.1	0.0759	1.5	0.71	1052	15	1066	14	1093	30	96
382	33900	818	130	0.18	0.01	0.1636	1.4	1.7420	1.6	0.0772	0.7	0.91	977	13	1024	10	1127	13	87
388	48332	1345	210	0.06	b.d.	0.1647	1.9	1.7450	2.5	0.0769	1.6	0.78	983	18	1025	16	1117	31	88
389	14619	325	81	1.34	1.32	0.1830	1.6	1.9330	2.9	0.0766	2.4	0.55	1083	16	1093	20	1111	49	97
390	22226	571	130	1.06	0.00	0.1881	2.1	1.9960	2.2	0.0770	0.9	0.92	1111	21	1114	15	1121	17	99
391	23192	595	130	1.08	0.01	0.1770	1.6	1.8740	1.8	0.0768	0.9	0.87	1051	15	1072	12	1115	18	94
392	32593	725	140	0.40	2.11	0.1777	1.7	1.8530	3.1	0.0756	2.6	0.54	1054	16	1064	21	1085	53	97
393	12013	336	81	1.83	0.00	0.1788	1.5	1.9180	1.9	0.0778	1.2	0.79	1060	15	1087	13	1142	24	93
394	34768	951	210	1.14	0.69	0.1744	1.8	1.8380	2.1	0.0764	1.2	0.84	1036	17	1059	14	1106	24	94
395	23365	551	120	1.74	0.60	0.1895	1.9	2.0100	2.4	0.0769	1.4	0.81	1119	20	1119	16	1119	28	100
396	7328	194	53	2.15	0.00	0.1876	1.9	2.0140	2.6	0.0779	1.8	0.73	1108	20	1120	18	1143	36	97
397	64259	1362	240	0.29	1.49	0.1766	1.6	1.8040	2.6	0.0741	2.0	0.61	1048	15	1047	17	1043	41	100
398	18084	448	110	1.80	b.d.	0.1727	1.6	1.8370	1.7	0.0771	0.7	0.91	1027	15	1059	12	1125	14	91
399	32355	870	180	0.80	0.00	0.1895	1.6	2.0180	1.8	0.0772	0.8	0.91	1119	17	1121	12	1127	15	99

Table 9: U-Pb isotope analyses of detrital zircon grains from paragneiss (*ZM-10-38; Solwezi dome*)

Grain	$^{207}\text{Pb}^a$	U^b	Pb^b	Th^b	$^{206}\text{Pb}^c$	$^{206}\text{Pb}^d$	$\pm 2s$	$^{207}\text{Pb}^d$	$\pm 2s$	$^{207}\text{Pb}^d$	$\pm 2s$	rho^e	^{206}Pb	$\pm 2s$	^{207}Pb	$\pm 2s$	^{207}Pb	$\pm 2s$	conc.^f
	(cps)	(ppm)	(ppm)	U	(%)	^{238}U	(%)	^{235}U	(%)	^{206}Pb	(%)		^{238}U	(Ma)	^{235}U	(Ma)	^{206}Pb	(Ma)	(%)
260	73009	1512	280	0.49	0.10	0.1799	1.8	2.8450	1.9	0.1147	0.6	0.94	1066	18	1368	14	1875	11	57
261	27584	216	88	0.67	b.d.	0.3655	1.6	6.2060	1.8	0.1231	0.8	0.91	2008	28	2005	16	2002	13	100
262	74276	828	250	0.04	b.d.	0.3101	1.5	4.7980	1.7	0.1122	0.6	0.93	1741	24	1785	14	1836	11	95
263	42294	336	120	0.69	0.00	0.3390	1.7	5.4050	1.8	0.1156	0.5	0.95	1882	28	1886	16	1890	10	100
264	104356	1057	340	0.05	0.00	0.3288	1.4	5.1360	1.5	0.1133	0.5	0.95	1832	23	1842	13	1853	8	99
265	69128	659	230	0.81	b.d.	0.3171	1.4	5.2950	1.5	0.1211	0.5	0.95	1776	22	1868	13	1972	9	90
266	54011	647	160	0.20	0.00	0.2497	1.5	3.9100	1.7	0.1135	0.8	0.88	1437	19	1616	14	1857	14	77
267	65987	745	240	0.14	0.00	0.3311	1.5	5.2770	1.6	0.1156	0.6	0.92	1844	24	1865	14	1889	11	98
268	66848	809	250	0.08	0.00	0.3189	1.4	4.8980	1.7	0.1114	1.0	0.81	1784	22	1802	15	1822	19	98
268	71461	599	170	0.46	0.00	0.2517	1.9	4.3630	2.0	0.1257	0.6	0.95	1447	24	1705	17	2039	11	71
269	89183	929	280	0.05	b.d.	0.3064	1.4	4.8000	1.5	0.1136	0.6	0.93	1723	22	1785	13	1858	10	93
270	32962	918	150	0.72	0.13	0.1515	2.1	2.3500	2.2	0.1125	0.6	0.96	910	18	1228	15	1840	11	49
271	46652	393	140	0.26	0.03	0.3487	1.5	5.6710	1.6	0.1179	0.6	0.94	1929	25	1927	14	1925	10	100

272	60757	626	180	0.10	b.d.	0.2919	1.8	4.6410	1.8	0.1153	0.5	0.97	1651	26	1757	15	1885	8	88
273	44757	391	130	0.47	b.d.	0.3222	1.5	5.4210	1.6	0.1220	0.5	0.95	1800	23	1888	13	1986	9	91
274	43828	360	120	0.57	0.00	0.3138	1.5	5.2770	1.6	0.1220	0.6	0.92	1759	23	1865	14	1985	11	89
275	51933	468	170	0.30	0.00	0.3461	1.4	5.6520	1.5	0.1185	0.5	0.94	1916	24	1924	13	1933	9	99
276	62865	627	190	0.18	0.02	0.2991	1.5	4.8490	1.6	0.1176	0.6	0.92	1687	22	1793	14	1920	11	88
277	69120	673	170	0.34	0.31	0.2264	2.1	4.3610	2.2	0.1397	0.7	0.95	1316	25	1705	18	2223	12	59
278	22462	637	100	0.06	0.00	0.1677	1.6	1.7490	2.2	0.0756	1.6	0.72	999	15	1027	15	1085	31	92
278	42112	670	66	0.02	0.02	0.1024	2.6	1.3570	3.0	0.0961	1.4	0.88	629	16	871	18	1549	27	41
279	28947	238	100	1.03	b.d.	0.3695	1.5	6.4570	1.6	0.1267	0.8	0.89	2027	25	2040	15	2053	13	99
280	33685	345	96	0.45	b.d.	0.2704	1.8	4.3220	1.9	0.1159	0.8	0.91	1543	24	1698	16	1895	15	81
281	62772	517	180	0.44	0.00	0.3334	1.5	6.0150	1.6	0.1309	0.6	0.93	1855	25	1978	14	2110	11	88
282	71003	785	220	0.06	0.01	0.2943	1.7	4.5420	1.8	0.1120	0.6	0.94	1663	25	1739	15	1831	11	91
288	29286	276	91	0.43	b.d.	0.3125	2.1	4.9430	2.3	0.1147	1.0	0.91	1753	32	1810	20	1876	18	93
289	62051	853	260	0.44	0.44	0.3133	1.8	4.9010	2.0	0.1135	0.9	0.90	1757	28	1802	17	1855	16	95
290	22199	229	86	0.47	0.00	0.3510	1.7	5.7670	1.8	0.1192	0.7	0.92	1939	28	1941	16	1944	13	100
291	34317	298	110	1.03	0.00	0.3297	1.5	5.4990	1.7	0.1210	0.7	0.90	1837	24	1900	14	1971	13	93
292	124144	1341	430	0.31	b.d.	0.3213	1.5	5.0610	1.5	0.1142	0.4	0.97	1796	23	1830	13	1868	7	96
293	120372	940	280	0.70	0.00	0.2929	1.5	4.6570	1.6	0.1153	0.5	0.95	1656	22	1759	14	1885	9	88
294	62249	699	210	0.14	0.00	0.3105	1.5	4.7890	1.6	0.1119	0.5	0.94	1743	23	1783	13	1830	10	95
295	46392	512	140	0.14	0.00	0.2868	1.5	4.3630	1.6	0.1103	0.6	0.94	1626	22	1705	13	1805	10	90
296	67001	681	210	0.24	0.00	0.3188	1.5	5.0160	1.5	0.1141	0.5	0.94	1784	23	1822	13	1866	9	96
297	114546	636	280	0.54	b.d.	0.3873	1.7	9.0020	1.9	0.1686	0.9	0.88	2111	30	2338	17	2543	15	83
298	54597	510	180	0.72	0.00	0.3103	1.4	5.0560	1.6	0.1182	0.6	0.93	1742	22	1829	13	1929	10	90
299	32055	716	120	0.03	0.59	0.1702	1.5	1.9060	2.2	0.0812	1.7	0.66	1013	14	1083	15	1227	33	83
300	49481	712	130	0.04	0.00	0.1893	1.6	2.7720	1.8	0.1062	0.7	0.93	1118	17	1348	13	1735	12	64
301	37727	329	130	0.66	0.00	0.3444	1.7	5.5700	1.8	0.1173	0.6	0.94	1908	28	1912	15	1915	11	100
302	54892	486	150	0.37	0.00	0.2966	1.6	4.9120	1.8	0.1201	0.6	0.94	1674	24	1804	15	1958	11	86
303	53972	457	160	0.48	b.d.	0.3232	1.5	5.3700	1.5	0.1205	0.5	0.95	1805	23	1880	13	1964	8	92
304	45828	465	120	0.14	b.d.	0.2652	1.6	4.3630	1.8	0.1193	0.7	0.91	1516	22	1705	15	1946	13	78
305	120674	2649	370	0.13	b.d.	0.1454	1.8	1.7190	1.9	0.0858	0.6	0.94	875	15	1016	12	1332	12	66
306	90230	2001	200	0.14	0.00	0.0957	2.6	1.5860	2.7	0.1202	0.5	0.98	589	15	965	17	1960	8	30
307	67116	630	200	0.75	b.d.	0.2950	1.5	4.6570	1.6	0.1145	0.5	0.95	1666	22	1760	13	1872	8	89
308	73472	782	260	0.56	0.00	0.3144	1.5	4.9610	1.6	0.1144	0.5	0.94	1762	23	1813	14	1871	10	94

309	74760	778	230	1.17	0.00	0.2406	2.2	3.9300	2.2	0.1185	0.5	0.97	1390	27	1620	18	1933	10	72
310	54938	756	190	1.03	0.00	0.2378	2.0	3.7810	2.0	0.1153	0.5	0.97	1376	24	1589	16	1884	9	73
311	59766	793	140	0.56	b.d.	0.1723	2.6	2.7380	2.7	0.1152	0.6	0.97	1025	24	1339	20	1884	11	54
312	74722	704	250	0.46	0.00	0.3348	1.6	5.5910	1.7	0.1211	0.6	0.94	1862	26	1915	15	1973	11	94
313	55659	776	210	0.26	0.00	0.2675	1.5	3.9760	1.6	0.1078	0.6	0.92	1528	21	1629	13	1763	11	87
314	70728	585	130	0.13	0.00	0.2255	1.9	4.0160	2.3	0.1292	1.3	0.81	1311	22	1637	19	2087	24	63
315	118025	2250	660	0.35	0.00	0.2954	1.6	4.6930	1.7	0.1152	0.4	0.97	1668	24	1766	14	1883	7	89
316	50469	555	160	0.04	0.02	0.3038	2.0	4.8290	2.3	0.1153	1.2	0.86	1710	30	1790	20	1885	22	91
316	32796	100	56	0.77	0.00	0.4726	2.1	10.9700	2.4	0.1683	1.0	0.90	2495	44	2520	22	2541	18	98
317	59710	717	150	0.76	0.00	0.1952	2.5	3.2200	2.7	0.1196	0.8	0.96	1150	27	1462	21	1951	14	59
318	55627	465	180	0.58	b.d.	0.3631	1.7	6.1850	1.8	0.1235	0.6	0.95	1997	29	2002	16	2008	10	99
319	41899	475	130	0.46	0.00	0.2690	2.2	4.4100	2.8	0.1189	1.6	0.81	1536	31	1714	23	1940	29	79
319	150691	657	250	0.19	0.00	0.3579	1.8	9.4060	2.1	0.1906	1.0	0.87	1972	31	2378	20	2748	17	72
320	81232	918	290	0.25	b.d.	0.3211	1.9	5.1600	2.0	0.1166	0.6	0.95	1795	30	1846	17	1904	11	94
321	62380	843	190	0.87	0.00	0.2130	1.6	3.4220	1.7	0.1165	0.5	0.96	1245	19	1509	13	1904	9	65
322	77071	949	250	0.98	b.d.	0.2416	1.5	3.9820	1.6	0.1196	0.5	0.94	1395	18	1631	13	1950	10	72
323	97819	1090	320	0.61	0.00	0.2709	1.7	4.5030	1.9	0.1206	0.7	0.93	1545	24	1732	16	1965	12	79
324	29396	383	100	1.42	0.00	0.2433	2.5	3.6720	2.7	0.1095	0.9	0.94	1404	32	1565	22	1791	17	78
325	70273	1057	240	0.26	0.00	0.2292	1.7	3.3620	2.0	0.1064	0.9	0.88	1330	21	1496	16	1739	17	77
326	48989	278	140	0.46	0.14	0.4595	1.5	10.1400	1.6	0.1600	0.6	0.92	2437	30	2447	15	2456	10	99
327	76263	767	300	1.25	b.d.	0.3334	1.4	5.2690	1.6	0.1146	0.7	0.89	1855	23	1864	14	1874	13	99
333	44180	807	170	0.92	0.00	0.2128	1.9	3.3530	2.0	0.1143	0.5	0.96	1244	22	1493	16	1868	10	67
334	43927	546	160	0.16	0.00	0.2846	1.7	4.4710	1.9	0.1139	0.9	0.87	1615	24	1726	16	1863	17	87
335	50087	403	140	0.24	0.00	0.3396	1.6	5.8790	1.8	0.1256	0.6	0.93	1885	27	1958	15	2037	11	93
336	358930	2807	920	0.15	0.00	0.3255	1.5	5.6170	1.6	0.1252	0.5	0.96	1816	24	1919	14	2031	8	89
337	57516	445	120	0.29	b.d.	0.2624	2.6	4.8900	2.8	0.1352	1.1	0.93	1502	35	1801	24	2166	19	69
338	80772	651	160	0.65	0.00	0.2387	1.7	3.7750	1.8	0.1147	0.6	0.94	1380	21	1588	15	1875	12	74
339	39814	852	200	0.19	0.00	0.2359	2.5	4.0600	2.6	0.1249	0.7	0.96	1365	31	1646	22	2027	13	67
340	36286	362	120	0.28	0.00	0.3199	1.5	5.5640	1.6	0.1262	0.6	0.93	1789	23	1911	14	2045	10	87
341	49574	435	180	0.94	b.d.	0.3493	1.6	5.7500	1.7	0.1194	0.7	0.93	1931	27	1939	15	1947	12	99
342	191372	1524	310	0.39	b.d.	0.1941	3.2	3.7690	3.3	0.1408	0.7	0.98	1144	34	1586	27	2237	12	51
343	79659	753	250	0.09	0.00	0.3376	1.4	5.3240	1.5	0.1144	0.5	0.94	1875	23	1873	13	1870	9	100
344	77604	562	210	0.51	0.00	0.3434	1.6	6.5210	1.7	0.1377	0.7	0.91	1903	26	2049	15	2199	12	87

345	44035	390	160	1.30	0.00	0.3265	2.5	5.5590	2.6	0.1235	0.7	0.96	1821	40	1910	23	2007	13	91
346	85165	783	240	0.56	0.00	0.3167	1.4	5.0520	1.5	0.1157	0.4	0.95	1774	22	1828	13	1890	8	94
347	69907	865	210	0.26	0.00	0.2387	3.7	3.7820	3.8	0.1149	0.7	0.98	1380	46	1589	31	1878	13	73
348	62322	629	180	0.05	0.00	0.2935	1.5	4.6010	1.6	0.1137	0.6	0.93	1659	22	1750	14	1859	11	89
349	68339	807	210	0.19	0.00	0.2688	1.6	4.2430	1.9	0.1145	1.0	0.86	1535	22	1682	16	1872	17	82

Table 10: U-Pb isotope analyses of detrital zircon grains from paragneiss (ZM-10-62; Solwezi dome)

Grain	$^{207}\text{Pb}^a$ (cps)	U ^b (ppm)	Pb ^b (ppm)	Th ^b U	$^{206}\text{Pb}^c$ (%)	$^{206}\text{Pb}^d$ ^{238}U	$\pm 2s$	$^{207}\text{Pb}^d$ ^{235}U	$\pm 2s$	$^{207}\text{Pb}^d$ ^{206}Pb	$\pm 2s$	rho ^e	^{206}Pb ^{238}U	$\pm 2s$ (Ma)	^{207}Pb ^{235}U	$\pm 2s$ (Ma)	^{207}Pb ^{206}Pb	$\pm 2s$ (Ma)	conc. ^f (%)
05		13	2.8	0.15		0.2128	0.0054	2.5653	0.1765			0.37	1244	29			1369	131	91
06		41	9.3	0.34		0.2073	0.0047	2.4905	0.0922			0.61	1215	25			1363	71	89
07		14	3.7	0.73		0.2281	0.0058	2.8125	0.1747			0.41	1325	31			1412	118	94
08		22	6.2	0.55		0.2515	0.0058	3.2022	0.1353			0.55	1446	30			1474	80	98
09		25	5.2	0.34		0.2065	0.0050	2.3123	0.1244			0.45	1210	27			1226	105	99
10		11	3.6	0.98		0.2808	0.0070	4.1222	0.2369			0.44	1596	35			1739	105	92
11		21	5.9	0.54		0.2589	0.0060	3.3943	0.1452			0.54	1484	31			1529	81	97
12		23	6.2	0.52		0.2501	0.0058	3.3329	0.1412			0.55	1439	30			1560	80	92
15		99	32	0.29		0.3048	0.0064	4.7323	0.1151			0.86	1715	31			1841	44	93
16		13	4.1	0.77		0.2819	0.0082	4.2520	0.2855			0.43	1601	41			1789	123	89
17		18	6.7	0.75		0.3216	0.0072	5.1242	0.1804			0.64	1798	35			1888	64	95
18		34	11	0.51		0.2900	0.0063	4.2462	0.1287			0.71	1641	31			1735	56	95
19		66	15	0.33		0.2274	0.0048	2.7228	0.0759			0.75	1321	25			1356	54	97
22		12	4.6	1.25		0.3108	0.0073	4.7559	0.2117			0.53	1745	36			1815	81	96
25		35	7.4	0.13		0.2131	0.0046	2.4980	0.0883			0.61	1245	24			1316	69	95
26		49	12	0.17		0.2334	0.0049	3.1623	0.0964			0.69	1352	26			1591	58	85
27		8	3.4	1.14		0.3235	0.0078	5.0803	0.2570			0.48	1807	38			1862	92	97

28	42	13	0.52		0.2729	0.0059	4.2869	0.1386		0.67	1556	30		1863	59	84			
30	40	10	0.23		0.2433	0.0052	3.1572	0.1089		0.62	1404	27		1510	66	93			
31	41	13	0.45		0.2949	0.0062	4.3496	0.1309		0.70	1666	31		1748	56	95			
32	56	13	0.12		0.2277	0.0047	2.8349	0.0834		0.70	1322	25		1431	57	92			
35	16	6.2	1.08		0.3192	0.0071	4.9413	0.1928		0.57	1786	35		1836	72	97			
36	17	5.0	0.52		0.2594	0.0058	3.5477	0.1583		0.50	1487	30		1608	84	92			
37	23	6.4	0.62		0.2487	0.0056	3.2706	0.1407		0.52	1432	29		1535	82	93			
38	47	15	0.41		0.2904	0.0060	4.1659	0.1237		0.70	1643	30		1697	56	97			
39	31	6.2	0.23		0.1963	0.0044	2.1647	0.1004		0.48	1155	24		1196	93	97			
40	20	7.5	0.84		0.3246	0.0070	5.0479	0.1721		0.63	1812	34		1845	63	98			
41	44	14	0.46		0.3012	0.0061	4.3434	0.1170		0.75	1697	30		1707	51	99			
42	41	14	0.53		0.3086	0.0062	4.6152	0.1253		0.74	1734	31		1773	51	98			
46	18	6.5	1.04		0.2914	0.0065	4.3634	0.1755		0.55	1648	32		1776	75	93			
47	44	15	0.48		0.3079	0.0062	4.5973	0.1249		0.74	1730	30		1771	52	98			
48	29	6.0	0.16		0.1989	0.0046	2.4503	0.1233		0.46	1169	25		1412	98	83			
50	54	13	0.35		0.2302	0.0046	3.0301	0.0918		0.67	1336	24		1537	59	87			
51	42	14	0.64		0.3055	0.0063	4.6143	0.1446		0.66	1719	31		1792	59	96			
52	35	12	0.63		0.3193	0.0064	4.8444	0.1393		0.70	1787	31		1800	55	99			
55	37	13	0.59		0.3089	0.0062	4.5738	0.1301		0.70	1735	30		1755	54	99			
56	33	12	0.64		0.3177	0.0063	4.7996	0.1342		0.71	1779	31		1792	53	99			
57	37	13	0.74		0.3104	0.0062	4.8482	0.1375		0.70	1743	30		1853	54	94			
59	59	13	0.28		0.2078	0.0041	2.5261	0.0751		0.66	1217	22		1386	60	88			
60	35	9.3	0.63		0.2385	0.0048	3.1240	0.1049		0.60	1379	25		1528	66	90			
61	11	3.6	0.82		0.2819	0.0066	4.0572	0.2203		0.43	1601	33		1704	101	94			
62	37	9.1	0.51		0.2240	0.0045	2.8938	0.0973		0.60	1303	24		1502	66	87			
63	17	5.2	0.66		0.2758	0.0060	3.8505	0.1648		0.50	1570	30		1647	82	95			
Grain	²⁰⁷ Pb ^a	U ^b	Pb ^b	Th ^b	²⁰⁶ Pbc ^c	²⁰⁶ Pbd ^d	±2s	²⁰⁷ Pbd ^d	±2s	²⁰⁷ Pbd ^d	±2s	rho ^e	²⁰⁶ Pb	±2s	²⁰⁷ Pb	±2s	²⁰⁷ Pb	±2s	conc. ^f
	(cps)	(ppm)	(ppm)	U	(%)	²³⁸ U	(%)	²³⁵ U	(%)	²⁰⁶ Pb	(%)		²³⁸ U	(Ma)	²³⁵ U	(Ma)	²⁰⁶ Pb	(Ma)	(%)
400	20605	194	60	0.59	0.00	0.2828	1.5	4.3730	1.7	0.1121	0.7	0.90	1606	21	1707	14	1834	13	88
401	48227	3191	380	0.16	0.00	0.1200	2.4	1.8400	2.5	0.1112	0.8	0.95	731	16	1060	17	1819	14	40
402	18723	213	76	1.28	b.d.	0.2794	1.6	4.3160	1.8	0.1121	0.9	0.86	1588	22	1696	15	1833	17	87
403	12400	224	52	0.90	0.00	0.1973	1.6	2.4220	2.0	0.0891	1.3	0.78	1161	17	1249	15	1405	25	83

404	32620	488	130	0.33	0.01	0.2557	1.5	3.5600	1.6	0.1010	0.6	0.93	1468	20	1541	13	1642	11	89
405	99362	2509	410	0.16	0.00	0.1623	3.8	2.4840	3.8	0.1110	0.4	0.99	969	34	1267	28	1816	8	53
406	59014	2489	200	0.15	0.00	0.0787	2.1	1.1580	2.1	0.1068	0.6	0.96	488	10	781	12	1745	10	28
407	95574	1426	300	0.09	b.d.	0.2134	1.5	3.3410	1.5	0.1136	0.4	0.97	1247	17	1491	12	1857	7	67
408	36383	355	130	1.12	b.d.	0.2999	1.5	4.7190	1.6	0.1141	0.6	0.93	1691	22	1771	13	1866	11	91
409	23957	240	86	0.91	0.00	0.3077	1.5	4.8310	1.7	0.1139	0.7	0.89	1730	22	1790	14	1862	13	93
410	16829	160	57	0.54	b.d.	0.3319	1.5	5.1640	1.8	0.1128	1.0	0.83	1848	24	1847	15	1846	18	100
411	37722	327	130	1.00	0.00	0.3332	1.5	5.2330	1.6	0.1139	0.7	0.89	1854	24	1858	14	1862	13	100
412	35347	473	130	0.55	b.d.	0.2522	3.5	3.8780	3.5	0.1115	0.7	0.98	1450	45	1609	29	1825	12	79
413	1664	18	6.1	0.83	0.03	0.2941	1.9	4.4120	3.2	0.1088	2.6	0.58	1662	27	1715	27	1779	47	93
414	1693	25	6.6	0.59	0.11	0.2436	1.9	3.1220	3.0	0.0929	2.4	0.62	1406	24	1438	24	1487	45	95
415	2297	33	9.1	0.65	0.04	0.2464	1.8	3.2790	3.0	0.0965	2.3	0.62	1420	23	1476	23	1558	44	91
416	3054	29	11	1.14	0.00	0.3089	1.9	4.9020	2.6	0.1151	1.8	0.73	1735	28	1803	22	1881	32	92
417	2583	33	9.4	0.66	0.00	0.2592	1.8	3.6270	2.8	0.1015	2.1	0.64	1486	24	1555	22	1651	40	90
418	2102	23	8.4	1.15	b.d.	0.2994	1.9	4.4640	2.6	0.1082	1.9	0.71	1688	28	1724	22	1769	34	95
419	2221	22	8.1	0.86	0.00	0.3234	1.7	5.0550	3.0	0.1134	2.4	0.56	1806	26	1829	25	1854	44	97
420	2486	38	9.6	0.61	b.d.	0.2308	1.9	3.0770	3.0	0.0967	2.3	0.62	1339	22	1427	23	1561	43	86

Table 11: U-Pb isotope analyses of detrital zircon grains from paragneiss (ZM-39-01; Mwombezi dome)

Grain	$^{207}\text{Pb}^a$	U^b	Pb^b	Th^b	$^{206}\text{Pb}^c$	$^{206}\text{Pb}^d$	$\pm 2s$	$^{207}\text{Pb}^d$	$\pm 2s$	$^{207}\text{Pb}^d$	$\pm 2s$	rho^e	^{206}Pb	$\pm 2s$	^{207}Pb	$\pm 2s$	^{207}Pb	$\pm 2s$	^{207}Pb	$\pm 2s$	conc.^f
	(cps)	(ppm)	(ppm)	U	(%)	^{238}U	(%)	^{235}U	(%)	^{206}Pb	(%)		^{238}U	(Ma)	^{235}U	(Ma)	^{206}Pb	(Ma)	(%)	(%)	
182	2622	50	9.6	0.00	0.06	0.20290	2.1	2.232	2.9	0.07978	2.0	0.73	1191	23	1191	21	1192	39	100		
183	3480	37	14	1.60	1.31	0.28990	1.8	4.175	3.1	0.1045	2.5	0.57	1641	26	1669	26	1705	47	96		
184	6903	70	28	1.81	0.13	0.30180	1.7	4.355	2.2	0.1047	1.4	0.77	1700	26	1704	18	1708	26	100		
185	4851	45	20	2.86	0.58	0.29240	1.7	4.131	2.9	0.1025	2.4	0.59	1653	25	1660	24	1669	44	99		
186	11734	139	44	1.43	0.01	0.24650	2.2	3.45	2.6	0.1015	1.4	0.86	1421	29	1516	21	1652	25	86		
187	5797	110	21	0.08	0.63	0.19900	1.9	2.165	3.0	0.07888	2.3	0.64	1170	20	1170	21	1169	45	100		
188	2526	27	14	3.41	b.d.	0.29950	2.8	4.266	4.0	0.1033	2.9	0.70	1689	41	1687	33	1684	53	100		
189	7768	113	29	1.01	0.02	0.21040	2.2	2.846	3.0	0.09809	2.0	0.75	1231	25	1368	23	1588	37	78		
190	11503	161	50	1.16	2.84	0.26040	1.7	3.387	3.8	0.09436	3.4	0.44	1492	22	1501	30	1515	64	98		
191	3228	33	14	2.19	b.d.	0.30320	2.1	4.335	3.4	0.1037	2.7	0.61	1707	31	1700	29	1691	50	101		

192	7691	110	39	1.64	0.64	0.28550	2.0	3.912	2.8	0.09937	2.0	0.72	1619	29	1616	23	1612	36	100
193	4452	49	18	1.84	0.91	0.26330	1.9	3.535	4.4	0.09735	3.9	0.43	1507	25	1535	35	1574	74	96
199	3468	38	15	2.01	1.75	0.27470	2.1	3.709	3.4	0.09791	2.7	0.62	1565	30	1573	28	1585	50	99
200	12878	157	64	2.53	b.d.	0.27980	1.6	3.927	2.1	0.1018	1.3	0.77	1590	23	1619	17	1657	24	96
201	5257	55	24	2.46	b.d.	0.30040	1.9	4.31	2.5	0.1041	1.6	0.76	1693	29	1695	21	1698	30	100
202	48405	931	180	0.02	0.45	0.20010	1.3	2.174	1.6	0.07881	0.9	0.83	1176	14	1173	11	1167	17	101
203	88085	1069	220	0.02	3.84	0.19750	2.1	2.14	4.0	0.07855	3.4	0.53	1162	22	1162	28	1161	67	100
302	1703	19	9.9	3.87	0.38	0.26580	3.7	3.694	4.9	0.1008	3.2	0.75	1519	50	1570	40	1639	60	93
303	28960	333	100	0.21	0.10	0.30270	2.4	4.336	3.1	0.1039	1.9	0.78	1705	36	1700	26	1694	35	101
304	898	11	5.2	3.24	b.d.	0.30440	4.4	4.379	6.0	0.1043	4.1	0.73	1713	66	1708	51	1703	76	101
305	11395	131	49	1.31	b.d.	0.30330	2.3	4.363	2.6	0.1043	1.3	0.88	1707	35	1705	22	1703	23	100
307	3149	20	9.5	3.18	3.82	0.28410	1.9	4.137	4.7	0.1056	4.4	0.39	1612	27	1662	40	1725	80	93
308	10771	59	22	0.91	0.87	0.30560	1.8	4.428	3.4	0.1051	2.9	0.51	1719	27	1718	29	1716	54	100
309	11201	140	27	0.02	0.84	0.20040	1.4	2.194	2.0	0.07942	1.5	0.66	1177	15	1179	14	1183	30	100
310	23406	146	59	1.82	0.15	0.30290	1.8	4.379	2.4	0.1049	1.6	0.74	1705	27	1708	20	1712	29	100
311	11317	71	33	2.98	3.84	0.29660	2.1	4.18	4.0	0.1022	3.4	0.53	1674	31	1670	34	1665	63	101
312	12417	126	24	0.01	0.06	0.20610	2.4	2.316	2.6	0.08152	0.9	0.93	1208	26	1217	18	1234	18	98
313	29943	246	67	0.68	b.d.	0.24310	1.4	3.329	1.8	0.09932	1.2	0.75	1403	17	1488	15	1611	23	87
314	13430	126	34	0.71	0.25	0.24240	1.7	3.008	2.3	0.09	1.6	0.73	1399	21	1410	18	1425	30	98
315	5753	40	18	2.99	b.d.	0.26910	2.0	3.817	4.5	0.1029	4.1	0.44	1536	27	1596	37	1676	75	92
316	15681	96	38	1.53	0.77	0.30360	1.4	4.376	2.0	0.1045	1.5	0.68	1709	21	1708	17	1706	28	100
317	20276	139	53	1.80	0.10	0.28250	1.8	3.873	2.8	0.09945	2.1	0.66	1604	26	1608	23	1614	39	99
318	11025	66	27	2.11	0.35	0.28330	1.4	4.047	2.0	0.1036	1.4	0.72	1608	20	1644	16	1690	25	95
319	18501	107	45	2.04	0.12	0.30290	1.7	4.363	2.7	0.1044	2.1	0.63	1706	26	1705	23	1705	39	100
320	26521	168	66	1.61	b.d.	0.29960	1.7	4.331	2.0	0.1049	1.1	0.83	1689	25	1699	17	1712	21	99
321	3773	26	9.5	1.66	1.27	0.27720	2.3	3.914	3.8	0.1024	3.1	0.59	1577	32	1617	32	1669	57	95
322	20509	130	51	1.71	2.35	0.29910	1.8	4.256	3.0	0.1032	2.4	0.61	1687	27	1685	25	1683	44	100
323	3519	22	9.2	2.11	b.d.	0.29730	2.0	4.296	3.1	0.1048	2.3	0.66	1678	30	1693	26	1711	43	98
324	15101	91	36	1.61	b.d.	0.30150	1.7	4.313	2.1	0.1038	1.3	0.79	1699	25	1696	18	1692	24	100
325	24601	156	60	1.52	0.05	0.29990	1.8	4.274	2.1	0.1034	1.1	0.85	1691	27	1688	17	1686	20	100
326	96239	590	160	0.08	0.20	0.27670	1.5	3.922	1.6	0.1028	0.7	0.91	1575	21	1618	13	1675	12	94
327	8592	62	21	1.21	0.40	0.28390	1.9	3.883	2.6	0.0992	1.8	0.73	1611	27	1610	21	1609	33	100
333	11102	66	28	2.11	1.14	0.30790	2.4	4.488	3.5	0.1057	2.6	0.67	1730	36	1729	30	1727	48	100

334	10538	48	27	3.63	1.70	0.30250	2.3	4.377	4.5	0.1049	3.9	0.51	1704	35	1708	38	1713	72	99
335	13002	80	34	2.15	0.05	0.30350	1.7	4.389	2.2	0.1049	1.3	0.79	1709	26	1710	18	1713	25	100
336	10879	69	29	1.97	0.20	0.31270	1.8	4.629	2.4	0.1074	1.5	0.76	1754	28	1754	20	1755	28	100
337	12332	87	28	0.94	0.08	0.28230	1.6	3.874	2.1	0.09952	1.3	0.76	1603	22	1608	17	1615	25	99
338	33073	227	66	1.05	b.d.	0.23380	3.3	3.286	3.7	0.1019	1.8	0.87	1355	40	1478	29	1659	34	82
339	14486	70	23	0.50	0.83	0.30770	3.0	4.535	3.3	0.1069	1.4	0.90	1730	46	1737	28	1747	26	99
340	15252	88	31	0.83	0.15	0.30260	2.0	4.369	3.5	0.1047	2.9	0.57	1704	30	1706	29	1709	53	100
341	115188	573	150	0.11	0.00	0.27430	2.3	3.9	2.4	0.1031	0.8	0.95	1563	31	1614	19	1681	14	93
342	12767	123	26	0.21	0.84	0.20800	2.2	2.326	2.8	0.08112	1.6	0.81	1218	25	1220	20	1224	32	99
343	8186	60	19	1.22	b.d.	0.26210	2.1	3.592	4.2	0.09939	3.7	0.50	1501	28	1548	34	1613	68	93
344	19436	147	39	0.14	0.17	0.26440	1.7	3.459	2.3	0.09488	1.5	0.74	1512	23	1518	18	1526	29	99
345	17615	159	35	0.34	0.07	0.20940	1.7	2.591	2.1	0.08973	1.2	0.81	1226	19	1298	15	1420	23	86
346	28551	179	68	1.43	b.d.	0.30140	1.7	4.323	2.2	0.104	1.3	0.79	1698	26	1698	18	1697	25	100
347	3565	25	10	2.04	b.d.	0.28790	2.0	4.094	2.6	0.1031	1.7	0.75	1631	28	1653	22	1681	32	97
348	3866	25	12	2.77	b.d.	0.30460	2.0	4.431	3.2	0.1055	2.4	0.64	1714	30	1718	26	1723	45	99
349	5853	38	16	2.30	0.33	0.30100	1.9	4.334	2.6	0.1044	1.7	0.75	1696	29	1700	22	1704	32	100
350	9984	129	24	0.01	0.10	0.19500	1.9	2.097	2.8	0.07802	2.0	0.68	1148	20	1148	19	1147	40	100
351	3995	30	12	2.42	b.d.	0.25870	2.1	3.696	3.1	0.1036	2.3	0.68	1483	28	1570	25	1689	42	88
352	8983	59	23	1.84	0.52	0.29420	1.9	4.17	2.3	0.1028	1.3	0.82	1663	28	1668	19	1675	24	99
353	8996	59	25	2.11	b.d.	0.30190	2.2	4.324	2.7	0.1039	1.5	0.82	1701	33	1698	22	1694	28	100
354	34006	243	76	0.73	0.01	0.28340	2.4	3.959	2.6	0.1013	0.9	0.93	1609	35	1626	21	1648	17	98
381	3711	45	17	1.71	b.d.	0.29880	2.1	4.289	2.8	0.1041	1.9	0.74	1685	31	1691	24	1699	35	99
382	3132	33	15	2.69	1.00	0.30380	2.2	4.405	3.3	0.1052	2.5	0.66	1710	33	1713	27	1717	45	100
388	2556	27	9.6	1.52	1.16	0.27360	3.4	3.967	4.4	0.1051	2.8	0.77	1559	47	1627	36	1717	51	91
389	6179	72	25	1.53	0.74	0.26310	2.4	3.491	3.1	0.09623	1.9	0.79	1506	33	1525	25	1552	35	97
390	13266	139	50	1.08	0.32	0.30030	2.4	4.291	2.8	0.1036	1.4	0.86	1693	36	1692	23	1690	27	100
391	6836	69	24	0.87	0.20	0.30290	2.2	4.395	2.9	0.1053	1.9	0.75	1706	33	1711	24	1719	35	99
392	10075	91	34	2.72	1.46	0.21270	3.0	3.158	4.5	0.1077	3.3	0.67	1243	34	1447	35	1761	61	71
393	13251	155	61	1.43	b.d.	0.29870	1.8	4.256	2.2	0.1034	1.2	0.83	1685	27	1685	18	1685	23	100
394	22706	253	89	1.09	b.d.	0.29110	2.9	4.068	3.3	0.1014	1.6	0.87	1647	42	1648	27	1649	30	100
395	6931	89	31	1.15	b.d.	0.28900	2.7	4.009	3.0	0.1006	1.4	0.88	1637	39	1636	25	1635	27	100
396	4004	47	16	1.40	1.40	0.25140	2.4	3.44	3.7	0.09925	2.8	0.64	1446	31	1514	29	1610	52	90
397	10911	208	36	0.17	0.65	0.17430	1.7	1.897	2.4	0.07892	1.7	0.70	1036	16	1080	16	1170	34	89

398	10402	145	27	0.14	0.18	0.18560	3.9	2.135	4.2	0.08345	1.7	0.92	1097	39	1160	30	1280	32	86
399	10788	126	51	2.04	0.29	0.30430	2.0	4.404	2.5	0.105	1.6	0.78	1713	30	1713	21	1714	29	100
400	1794	19	9.1	2.99	0.83	0.30490	3.2	4.42	4.4	0.1051	3.0	0.72	1715	48	1716	37	1717	56	100
401	5327	66	27	1.90	0.11	0.30130	2.2	4.332	2.9	0.1043	1.9	0.75	1698	32	1699	24	1701	35	100
402	10629	166	34	0.94	b.d.	0.16060	3.1	2.147	4.1	0.09694	2.6	0.76	960	28	1164	29	1566	49	61
403	3661	54	15	1.16	0.23	0.21170	3.3	2.632	4.0	0.09017	2.2	0.83	1238	38	1310	30	1429	42	87
404	2449	26	12	2.89	b.d.	0.30360	2.7	4.393	3.8	0.105	2.7	0.71	1709	41	1711	32	1713	49	100
405	6050	58	27	2.66	b.d.	0.30160	2.1	4.345	3.2	0.1045	2.5	0.65	1699	31	1702	27	1705	45	100
406	8018	77	35	2.57	b.d.	0.30360	1.9	4.368	2.5	0.1043	1.6	0.78	1709	29	1706	21	1703	29	100
407	6039	73	28	1.30	b.d.	0.30460	2.1	4.409	2.6	0.105	1.6	0.79	1714	31	1714	22	1714	30	100
408	15688	227	66	0.33	0.11	0.28320	1.9	3.985	2.5	0.1021	1.6	0.75	1607	27	1631	20	1662	30	97
409	2773	25	11	2.59	2.51	0.28710	1.9	4.148	4.6	0.1048	4.2	0.42	1627	28	1664	39	1711	77	95
410	2350	23	11	2.70	2.45	0.30300	2.5	4.38	4.1	0.1048	3.3	0.60	1706	37	1709	35	1711	61	100
411	5405	130	25	0.33	b.d.	0.17940	2.8	2.001	4.0	0.08088	2.9	0.70	1064	27	1116	27	1219	56	87
412	4325	60	17	1.15	1.13	0.23280	2.1	3.172	3.9	0.09882	3.2	0.55	1349	26	1450	30	1602	60	84
413	27705	319	99	0.49	0.36	0.29180	2.8	4.147	3.0	0.1031	1.3	0.91	1650	40	1664	25	1681	23	98
414	8513	91	37	1.89	b.d.	0.30390	2.1	4.368	2.6	0.1043	1.7	0.78	1710	31	1706	22	1701	31	101
415	4871	56	23	1.74	b.d.	0.30250	2.7	4.38	3.1	0.105	1.5	0.87	1704	40	1709	26	1715	28	99
416	6207	74	28	1.82	0.01	0.27660	2.8	3.996	3.5	0.1048	2.1	0.80	1574	39	1633	28	1710	38	92
417	5500	61	24	1.67	0.07	0.30170	2.0	4.347	2.6	0.1045	1.7	0.76	1700	30	1702	22	1705	31	100
418	3540	38	16	1.86	b.d.	0.30440	2.4	4.427	3.7	0.1055	2.9	0.64	1713	36	1717	31	1722	53	99
419	9120	102	39	1.54	b.d.	0.30270	1.8	4.369	2.5	0.1047	1.8	0.72	1704	27	1706	21	1709	33	100
420	2791	52	18	0.83	0.28	0.30600	3.9	4.429	5.0	0.105	3.1	0.79	1721	60	1718	42	1714	57	100
426	1464	17	5.2	1.49	b.d.	0.21750	4.7	3.138	5.9	0.1047	3.5	0.80	1269	54	1442	46	1708	65	74
427	10149	168	36	0.03	0.85	0.22200	2.2	2.732	2.9	0.08924	1.9	0.77	1292	26	1337	22	1409	35	92
428	1853	26	9.2	1.80	b.d.	0.25560	3.2	3.367	4.7	0.09553	3.5	0.67	1467	42	1497	38	1539	66	95
429	12863	135	54	1.63	0.26	0.30420	2.1	4.408	2.5	0.1051	1.4	0.83	1712	31	1714	21	1716	26	100
430	4951	55	24	2.17	0.36	0.30520	1.8	4.424	2.8	0.1051	2.2	0.64	1717	27	1717	24	1716	40	100
431	9976	114	40	0.91	1.16	0.29660	2.4	4.25	3.0	0.1039	1.8	0.80	1674	35	1684	25	1695	33	99
432	11087	166	46	0.60	0.23	0.25370	1.6	3.201	2.4	0.0915	1.9	0.64	1457	20	1457	19	1457	36	100
433	4837	53	19	1.46	2.30	0.27830	1.6	4.035	3.3	0.1051	2.8	0.49	1583	22	1641	27	1717	52	92
434	5360	136	24	0.07	0.41	0.18610	1.4	1.993	2.6	0.07765	2.1	0.54	1100	14	1113	17	1138	43	97
435	3249	37	14	1.69	b.d.	0.27130	2.4	3.805	3.1	0.1017	1.9	0.79	1547	34	1594	25	1655	35	93

436 3186 41 15 1.54 b.d. 0.29960 2.1 4.329 3.1 0.1048 2.2 0.69 1689 32 1699 26 1711 41 99

Table 12: U-Pb isotope analyses of detrital zircon grains from paragneiss (ZM-62-05; Mwombezhi dome)

Grain	$^{207}\text{Pb}^a$	U^b	Pb^b	Th^b	$^{206}\text{Pbc}^c$	$^{206}\text{Pbd}^d$	$\pm 2s$	$^{207}\text{Pbd}^d$	$\pm 2s$	$^{207}\text{Pbd}^d$	$\pm 2s$	rho^e	^{206}Pb	$\pm 2s$	^{207}Pb	$\pm 2s$	^{207}Pb	$\pm 2s$	^{207}Pb	$\pm 2s$	conc. f
	(cps)	(ppm)	(ppm)	U	(%)	^{238}U	(%)	^{235}U	(%)	^{206}Pb	(%)		^{238}U	(Ma)	^{235}U	(Ma)	^{206}Pb	(Ma)	(%)		
89	27320	83	37	0.32	23.20	0.20160	4.3	2.402	12.6	0.08644	11.8	0.34	1184	46	1243	94	1348	228	88		
90	8098	74	58	8.26	0.00	0.30530	1.8	4.414	2.2	0.1049	1.4	0.79	1717	27	1715	19	1712	25	100		
91	2904	46	16	1.35	0.00	0.27070	3.3	3.732	3.9	0.09999	2.0	0.86	1544	46	1578	32	1624	37	95		
92	3407	34	14	2.03	b.d.	0.29780	1.7	4.342	2.7	0.1057	2.1	0.62	1680	25	1701	23	1727	39	97		
93	30104	382	82	0.27	4.04	0.18190	2.5	2.458	4.0	0.09799	3.1	0.62	1077	25	1260	29	1586	59	68		
94	5564	55	24	2.23	b.d.	0.30380	1.5	4.392	2.0	0.1048	1.3	0.75	1710	23	1711	17	1712	24	100		
95	40153	397	190	3.71	1.01	0.26400	2.1	3.789	2.5	0.1041	1.3	0.85	1511	28	1590	20	1698	24	89		
96	3662	39	16	2.19	0.00	0.30310	1.8	4.395	2.7	0.1052	2.0	0.67	1707	27	1711	23	1717	37	99		
97	18597	307	66	0.16	0.14	0.22000	2.0	2.692	2.4	0.08874	1.2	0.86	1282	24	1326	18	1399	24	92		
98	2224	22	9.5	2.31	b.d.	0.30290	1.9	4.39	3.3	0.1051	2.6	0.59	1706	29	1710	27	1716	49	99		
99	5423	61	22	1.14	1.26	0.30120	3.6	4.338	5.6	0.1045	4.3	0.64	1697	54	1701	47	1705	80	100		
257	4674	140	44	1.28	b.d.	0.23690	2.7	3.258	3.5	0.09974	2.3	0.76	1371	33	1471	28	1619	43	85		
258	3601	69	29	2.54	2.80	0.26250	4.1	3.838	5.3	0.106	3.3	0.78	1503	55	1601	43	1732	61	87		
259	27608	816	240	0.86	0.22	0.25300	2.0	3.228	2.5	0.09256	1.6	0.79	1454	26	1464	20	1479	30	98		
260	86428	1019	280	4.02	1.59	0.13220	1.7	1.611	2.5	0.08841	1.8	0.68	800	13	974	16	1391	35	58		
261	6841	184	68	1.83	0.90	0.26640	2.8	3.767	3.5	0.1025	2.0	0.81	1523	38	1586	28	1670	38	91		
262	5017	238	64	0.55	2.14	0.22680	1.6	3.139	3.7	0.1004	3.3	0.43	1318	19	1442	29	1631	62	81		
263	2731	88	26	1.31	b.d.	0.22880	4.8	3.037	5.4	0.09628	2.6	0.88	1328	58	1417	42	1553	48	85		
264	24062	686	180	0.55	0.35	0.24470	3.8	3.3	4.1	0.09781	1.7	0.91	1411	48	1481	33	1583	32	89		
265	11236	387	130	1.83	0.27	0.27060	2.2	3.649	2.6	0.0978	1.4	0.86	1544	31	1560	21	1583	25	98		
266	6670	250	72	1.41	1.49	0.21470	2.8	2.714	3.8	0.09169	2.5	0.75	1254	32	1332	28	1461	47	86		
267	9075	303	94	1.33	1.25	0.24870	2.7	3.29	3.3	0.09594	1.8	0.83	1432	35	1479	26	1547	35	93		
268	4104	107	36	1.86	1.74	0.24240	3.6	3.465	4.3	0.1037	2.3	0.84	1399	45	1519	34	1691	42	83		
269	5657	148	54	1.59	1.35	0.26560	3.0	3.543	3.7	0.09675	2.1	0.82	1519	41	1537	29	1562	40	97		
270	20525	1274	210	0.78	0.36	0.16360	1.3	1.782	1.9	0.07899	1.4	0.69	977	12	1039	12	1172	27	83		
271	11344	278	130	2.86	b.d.	0.29910	1.9	4.363	3.6	0.1058	3.1	0.52	1687	28	1705	30	1728	57	98		

272	50693	1325	370	0.71	0.13	0.24010	2.4	3.212	2.8	0.09704	1.3	0.88	1387	30	1460	22	1568	25	88
273	3797	100	42	1.99	b.d.	0.30180	3.8	4.313	4.2	0.1037	1.9	0.89	1700	57	1696	36	1691	35	101
274	2262	23	13	4.30	1.71	0.30610	2.3	4.439	4.1	0.1052	3.4	0.55	1722	35	1720	35	1717	63	100
275	6216	71	24	1.32	0.75	0.26280	4.4	3.629	5.7	0.1002	3.6	0.78	1504	60	1556	46	1627	66	92
276	7456	155	29	0.33	0.20	0.18200	2.2	2.129	2.8	0.08484	1.7	0.80	1078	22	1158	20	1312	33	82
277	5357	93	29	1.18	0.57	0.24590	2.9	3.131	3.5	0.09235	1.9	0.84	1417	37	1440	27	1475	36	96
278	3589	37	17	2.46	1.69	0.29660	1.8	4.195	3.2	0.1026	2.7	0.57	1675	27	1673	27	1671	49	100
279	1949	15	6.9	2.70	b.d.	0.28100	4.6	3.941	5.5	0.1017	3.0	0.83	1596	66	1622	46	1656	56	96
280	5147	41	16	2.31	2.21	0.26840	1.8	3.696	3.1	0.09987	2.5	0.60	1533	25	1571	25	1622	46	95
281	15760	142	42	1.17	0.26	0.24740	1.7	3.134	2.7	0.09186	2.1	0.63	1425	22	1441	21	1464	40	97
282	6814	58	21	1.03	4.67	0.30280	2.6	4.371	5.5	0.1047	4.9	0.47	1705	39	1707	47	1709	90	100
288	8038	59	23	2.41	0.03	0.27500	2.1	3.892	2.5	0.1026	1.4	0.83	1566	29	1612	20	1672	26	94
289	8598	125	28	0.73	0.79	0.20070	2.1	2.523	2.8	0.09117	1.8	0.76	1179	23	1279	21	1450	35	81
290	23439	331	54	0.21	0.41	0.16050	3.5	1.91	4.4	0.0863	2.6	0.81	960	32	1085	30	1345	50	71
291	3116	19	12	5.10	b.d.	0.30550	2.4	4.426	3.5	0.1051	2.4	0.71	1718	37	1717	29	1716	45	100
292	3443	22	9.9	2.68	b.d.	0.29980	2.3	4.273	2.9	0.1034	1.8	0.79	1690	34	1688	24	1686	33	100
293	45250	337	59	1.10	0.51	0.11620	3.8	1.655	3.9	0.1033	1.0	0.97	709	25	992	25	1685	18	42
294	4992	31	12	1.78	b.d.	0.30320	1.6	4.377	2.4	0.1047	1.8	0.67	1707	24	1708	20	1709	32	100
295	78273	175	38	1.48	1.37	0.05182	4.4	0.6411	5.0	0.08973	2.3	0.89	326	14	503	20	1420	44	23
296	35475	215	77	1.63	b.d.	0.27090	2.4	3.8	2.7	0.1017	1.1	0.90	1545	33	1593	22	1656	21	93
297	10365	105	24	0.52	1.43	0.20500	1.6	2.523	2.9	0.08924	2.4	0.55	1202	18	1279	22	1409	47	85
298	98926	532	120	0.56	0.13	0.19680	2.4	2.636	2.6	0.09713	1.1	0.90	1158	25	1311	19	1570	22	74
299	57977	455	82	0.03	1.36	0.16130	2.4	1.997	4.7	0.08982	4.1	0.52	964	22	1115	33	1422	77	68
300	6270	81	17	0.68	b.d.	0.17060	4.2	2.14	4.7	0.09097	2.2	0.89	1015	39	1162	33	1446	41	70
301	8986	99	24	0.72	0.32	0.21490	2.1	2.593	3.2	0.08753	2.4	0.66	1255	24	1299	23	1372	46	91
355	6946	80	31	1.60	0.10	0.29840	1.8	4.249	2.4	0.1033	1.6	0.76	1684	27	1684	20	1684	29	100
356	80947	1100	260	0.26	7.21	0.20940	1.8	2.518	4.9	0.0872	4.5	0.36	1226	20	1277	36	1365	88	90
357	2576	32	12	1.74	2.38	0.27730	2.0	3.839	3.7	0.1004	3.1	0.53	1578	27	1601	30	1632	58	97
358	50767	915	120	0.06	2.55	0.12480	2.4	1.429	3.6	0.08305	2.6	0.68	758	17	901	22	1270	52	60
359	17488	84	43	1.46	b.d.	0.30650	2.2	4.458	5.1	0.1055	4.6	0.43	1724	33	1723	43	1723	85	100
360	20634	238	83	1.28	0.40	0.28730	1.7	4.105	2.0	0.1036	1.0	0.86	1628	25	1655	17	1690	19	96
361	21147	492	91	0.03	0.03	0.19670	1.2	2.124	1.4	0.07829	0.8	0.85	1158	13	1157	10	1154	15	100
362	2810	32	11	1.40	1.50	0.25890	2.7	3.75	4.0	0.105	3.0	0.67	1484	36	1582	33	1715	55	87

363	34024	548	110	0.08	0.14	0.21160	2.3	2.696	2.8	0.09244	1.5	0.83	1237	26	1327	21	1476	29	84
364	16544	225	97	2.61	0.03	0.29680	1.7	4.222	2.2	0.1032	1.3	0.81	1675	26	1678	18	1682	23	100
365	8317	88	31	1.65	0.00	0.24940	1.8	3.509	2.5	0.102	1.7	0.73	1436	24	1529	20	1661	32	86
366	10804	257	50	0.17	1.28	0.19580	1.8	2.136	2.8	0.07913	2.2	0.64	1153	19	1160	20	1175	43	98
367	6895	51	17	3.47	12.58	0.20770	2.7	2.316	11.5	0.08088	11.2	0.23	1216	30	1217	85	1219	219	100
368	29884	474	94	0.06	3.49	0.19500	1.5	2.1	3.5	0.07811	3.1	0.43	1148	16	1149	24	1150	62	100
369	2214	24	11	2.54	b.d.	0.30450	3.1	4.388	3.8	0.1045	2.2	0.82	1714	47	1710	32	1706	40	100
370	11999	195	46	0.57	0.30	0.21390	2.1	2.737	2.7	0.09278	1.8	0.76	1250	24	1338	20	1483	33	84
371	2126	24	9.7	1.98	2.57	0.30280	2.1	4.36	4.1	0.1044	3.5	0.52	1705	32	1705	34	1704	64	100
372	8718	223	43	0.07	1.06	0.20160	1.3	2.219	2.3	0.07983	1.8	0.59	1184	15	1187	16	1193	36	99
373	2444	38	11	1.33	b.d.	0.21520	4.0	3.149	5.4	0.1061	3.6	0.75	1256	46	1445	42	1734	65	72
374	2335	23	9.7	2.12	0.70	0.30120	2.7	4.368	3.8	0.1052	2.7	0.70	1697	40	1706	32	1717	50	99
375	11325	150	52	1.43	0.56	0.27600	1.7	3.934	2.1	0.1034	1.1	0.84	1571	24	1621	17	1686	21	93
376	2639	29	12	1.68	b.d.	0.30510	2.0	4.411	3.4	0.1049	2.8	0.59	1716	30	1714	29	1712	51	100
377	4765	50	20	2.64	2.17	0.27570	2.0	4.418	3.2	0.1162	2.5	0.61	1570	27	1716	27	1899	45	83
378	33466	620	110	0.18	3.15	0.17480	1.4	1.898	3.6	0.07874	3.3	0.40	1038	14	1080	24	1166	65	89
379	3243	39	16	2.19	b.d.	0.30170	1.9	4.34	2.8	0.1043	2.0	0.68	1700	28	1701	23	1703	38	100
380	18882	339	66	0.06	0.44	0.20140	2.1	2.211	2.3	0.07959	1.1	0.89	1183	22	1184	16	1187	21	100
437	23129	499	92	0.02	0.04	0.19590	1.4	2.118	1.7	0.0784	1.0	0.82	1153	15	1155	12	1157	20	100
438	2008	28	7.5	0.73	0.68	0.22580	2.0	3.26	3.3	0.1047	2.6	0.61	1312	24	1472	26	1710	48	77
439	29572	590	110	0.12	0.14	0.19320	3.3	2.149	3.4	0.08065	0.9	0.97	1139	34	1165	24	1213	17	94
440	7211	77	17	0.46	1.26	0.20240	3.1	2.232	4.8	0.08	3.7	0.65	1188	34	1191	34	1197	72	99
441	3475	29	8.9	1.12	3.40	0.24900	1.9	2.957	12.7	0.08614	12.5	0.15	1433	24	1397	101	1341	242	107
442	6728	43	19	2.20	0.17	0.30460	1.5	4.404	2.8	0.1049	2.3	0.55	1714	23	1713	23	1712	42	100
443	7400	50	21	2.00	0.68	0.30670	2.3	4.459	3.4	0.1054	2.4	0.69	1724	36	1723	28	1722	45	100
444	7168	53	19	1.80	0.90	0.26540	2.2	3.591	3.0	0.09811	2.0	0.74	1518	30	1547	24	1589	37	96
445	3810	24	11	4.14	0.67	0.20520	2.8	2.968	4.2	0.1049	3.2	0.66	1203	31	1399	33	1713	58	70
446	27166	301	44	0.17	0.09	0.14380	5.5	1.733	5.9	0.08739	2.2	0.93	866	44	1021	39	1369	43	63
447	5640	45	14	1.29	1.30	0.24800	2.2	3.329	3.2	0.09738	2.4	0.67	1428	28	1488	25	1574	44	91
448	39890	446	86	0.11	0.18	0.19890	1.7	2.41	2.0	0.08785	0.9	0.89	1170	19	1245	14	1379	17	85
449	66540	540	100	0.30	0.68	0.18340	2.2	2.348	2.8	0.09284	1.8	0.77	1086	22	1227	20	1485	34	73
450	12256	170	57	1.46	3.11	0.25600	3.0	3.591	4.2	0.1017	2.9	0.72	1470	40	1548	34	1656	53	89
451	7148	49	22	2.66	3.47	0.30140	1.6	4.362	3.9	0.105	3.6	0.41	1698	24	1705	33	1714	66	99

452	12836	84	35	2.06	1.50	0.30020	1.7	4.321	2.5	0.1044	1.8	0.68	1692	25	1697	21	1703	34	99
453	3934	40	9.8	1.10	0.35	0.18660	4.4	2.358	4.8	0.09164	2.1	0.90	1103	45	1230	35	1460	40	76
454	2429	20	7.5	2.33	3.90	0.23110	3.2	3.379	5.2	0.1061	4.1	0.62	1340	39	1500	42	1733	76	77
455	7318	51	22	2.32	0.09	0.29880	1.6	4.29	2.3	0.1041	1.7	0.69	1686	24	1691	19	1699	31	99
456	4538	36	18	3.34	0.76	0.30530	2.5	4.405	3.7	0.1046	2.7	0.67	1717	37	1713	31	1708	50	101
457	35160	530	100	0.04	0.18	0.20190	2.0	2.214	2.2	0.07952	0.9	0.92	1186	22	1185	16	1185	18	100
459	38173	299	80	0.76	2.16	0.22550	2.7	3.247	3.9	0.1044	2.8	0.70	1311	32	1468	31	1705	51	77

Table 13: U-Pb isotope analyses of detrital zircon grains from paragneiss (ZM-66-08; Mwombezhi dome)

Grain	$^{207}\text{Pb}^a$	U^b	Pb^b	Th^b	$^{206}\text{Pb}^c$	$^{206}\text{Pb}^d$	$\pm 2s$	$^{207}\text{Pb}^d$	$\pm 2s$	$^{207}\text{Pb}^d$	$\pm 2s$	rho^e	^{206}Pb	$\pm 2s$	^{207}Pb	$\pm 2s$	^{207}Pb	$\pm 2s$	conc.^f
	(cps)	(ppm)	(ppm)	U	(%)	^{238}U	(%)	^{235}U	(%)	^{206}Pb	(%)		^{238}U	(Ma)	^{235}U	(Ma)	^{206}Pb	(Ma)	(%)
123	43214	336	140	1.10	0.02	0.34360	1.5	5.527	1.7	0.1167	0.7	0.90	1904	25	1905	15	1906	13	100
124	13500	113	46	1.48	0.12	0.32220	1.4	5.093	1.9	0.1146	1.2	0.77	1800	23	1835	16	1874	22	96
125	35875	300	120	0.86	0.20	0.32870	2.2	5.099	2.8	0.1125	1.8	0.77	1832	35	1836	24	1840	32	100
126	6833	65	24	1.25	0.23	0.29430	1.9	4.319	2.4	0.1064	1.5	0.78	1663	28	1697	20	1739	28	96
127	12990	283	52	0.03	0.10	0.19390	1.4	2.088	1.8	0.07809	1.2	0.75	1142	15	1145	13	1149	24	99
128	9411	90	38	2.26	0.11	0.29590	1.4	4.395	2.0	0.1077	1.5	0.69	1671	21	1711	17	1761	27	95
129	1958	18	7.8	2.07	0.06	0.31500	1.9	4.683	3.0	0.1078	2.4	0.62	1765	29	1764	26	1763	43	100
130	1845	26	6.2	0.65	0.39	0.21590	1.8	2.71	3.6	0.09107	3.1	0.50	1260	21	1331	27	1448	59	87
131	7580	69	30	2.04	0.00	0.31560	1.6	4.688	2.4	0.1077	1.8	0.66	1768	24	1765	20	1761	33	100
132	6511	58	24	1.94	b.d.	0.31460	1.5	4.667	2.0	0.1076	1.4	0.73	1763	23	1761	17	1759	25	100
133	99960	876	310	0.22	0.09	0.34490	1.7	5.617	1.8	0.1181	0.7	0.93	1910	28	1919	16	1928	13	99
134	39543	329	120	0.85	0.00	0.33250	1.3	5.204	1.4	0.1135	0.5	0.94	1851	21	1853	12	1856	9	100
135	25711	203	80	1.01	0.26	0.33550	1.5	5.308	1.7	0.1147	0.9	0.85	1865	24	1870	15	1876	16	99
136	5100	67	12	0.16	0.60	0.17940	4.4	2.02	6.3	0.08167	4.5	0.70	1064	43	1122	43	1238	88	86
137	36380	291	120	0.99	0.01	0.34210	1.4	5.519	1.6	0.117	0.8	0.87	1897	23	1904	14	1911	14	99
138	40613	318	130	1.38	0.05	0.34340	1.5	5.522	1.7	0.1166	0.7	0.91	1903	25	1904	14	1905	13	100

139	29723	227	94	1.36	0.59	0.34400	1.8	5.538	2.2	0.1168	1.2	0.82	1906	29	1907	19	1907	22	100
140	60154	495	180	0.40	0.02	0.34020	1.6	5.55	1.7	0.1183	0.6	0.94	1888	26	1908	14	1931	10	98
141	51396	379	150	0.87	0.13	0.34600	1.7	5.631	1.9	0.118	0.7	0.93	1915	29	1921	16	1927	12	99
142	33038	274	110	0.92	b.d.	0.34590	1.9	5.612	2.2	0.1177	1.1	0.87	1915	32	1918	19	1921	19	100
143	35087	285	100	0.88	0.00	0.32010	1.8	5.174	1.9	0.1172	0.8	0.92	1790	28	1848	17	1915	14	94
144	43144	335	140	1.21	0.11	0.34080	1.6	5.488	1.7	0.1168	0.8	0.89	1890	26	1899	15	1908	14	99
145	54754	413	170	1.35	0.09	0.32670	1.6	5.31	1.8	0.1179	0.9	0.88	1822	25	1870	15	1924	16	95
151	27119	206	82	0.99	0.27	0.34510	1.7	5.556	2.0	0.1168	1.2	0.83	1911	28	1909	18	1908	21	100
152	28875	229	85	0.62	0.23	0.33930	1.5	5.374	1.7	0.1149	0.9	0.85	1883	24	1881	15	1878	16	100
153	23649	174	65	0.63	b.d.	0.34400	1.7	5.568	2.0	0.1174	1.1	0.84	1906	28	1911	18	1917	20	99
154	34581	275	98	0.41	0.17	0.33790	1.4	5.404	1.7	0.116	1.0	0.83	1876	23	1886	15	1896	17	99
155	47068	366	150	1.09	0.13	0.33650	1.4	5.447	1.6	0.1174	0.7	0.90	1870	23	1892	13	1917	12	98
156	6564	53	23	1.71	0.22	0.32960	3.3	5.352	5.3	0.1178	4.1	0.62	1836	53	1877	46	1923	74	96
157	46105	395	160	1.46	b.d.	0.32620	1.6	5.135	1.8	0.1142	0.9	0.88	1820	25	1842	16	1867	15	97
158	25584	220	83	1.16	b.d.	0.32390	2.3	5.061	2.6	0.1133	1.1	0.90	1809	37	1830	22	1853	20	98
159	2886	46	9.2	0.56	0.96	0.17840	2.4	2.074	4.2	0.08431	3.5	0.56	1058	23	1140	29	1300	68	81
160	1941	38	6.9	0.05	0.28	0.19070	2.3	2.094	3.5	0.07964	2.7	0.65	1125	24	1147	25	1188	53	95
161	9322	119	49	2.06	0.27	0.29520	2.4	4.26	3.9	0.1047	3.1	0.61	1668	35	1686	32	1708	56	98
162	25846	369	49	0.51	0.89	0.09568	8.3	1.526	8.5	0.1157	1.4	0.99	589	47	941	53	1891	26	31
163	37214	374	130	1.22	1.15	0.27550	2.0	4.35	2.5	0.1145	1.6	0.79	1569	28	1703	21	1872	28	84
164	35360	301	110	0.62	0.09	0.34480	2.1	5.555	2.3	0.1168	1.1	0.89	1910	34	1909	20	1908	19	100
165	13637	106	39	0.52	0.03	0.34180	1.3	5.512	1.8	0.117	1.2	0.74	1895	22	1902	16	1910	22	99
166	26259	228	81	0.95	0.23	0.30000	1.4	4.828	1.7	0.1167	0.9	0.84	1691	22	1790	15	1907	17	89
167	38128	320	120	1.06	0.05	0.31260	1.4	4.984	1.5	0.1156	0.7	0.91	1754	21	1817	13	1890	12	93
168	29529	250	100	1.16	0.13	0.34290	2.1	5.542	2.5	0.1172	1.3	0.85	1901	35	1907	22	1914	23	99
169	12285	274	45	0.03	0.08	0.17310	1.7	1.851	2.0	0.07753	1.0	0.85	1029	16	1064	13	1135	20	91
170	9590	90	35	1.60	0.42	0.30530	1.5	4.433	2.1	0.1053	1.4	0.73	1717	23	1718	18	1720	26	100
171	4962	23	12	4.56	1.64	0.28250	4.0	3.973	8.7	0.102	7.7	0.46	1604	58	1629	73	1661	143	97
172	9780	93	36	1.59	0.50	0.29810	1.6	4.356	2.0	0.106	1.3	0.79	1682	24	1704	17	1732	23	97
173	71016	575	240	1.28	0.18	0.34510	1.4	5.59	1.6	0.1175	0.7	0.89	1911	24	1915	14	1918	13	100
174	72327	706	290	1.29	0.68	0.33660	2.5	5.448	2.6	0.1174	0.9	0.93	1870	40	1892	23	1917	17	98
175	38644	351	140	0.99	0.11	0.34540	1.5	5.61	1.8	0.1178	1.0	0.83	1913	25	1918	16	1923	18	99
176	33513	257	100	1.24	0.06	0.32850	1.4	5.318	1.6	0.1174	0.8	0.86	1831	23	1872	14	1917	15	96

177	22072	203	66	0.62	0.25	0.29840	1.6	4.45	1.9	0.1082	1.0	0.85	1683	23	1722	16	1769	18	95
178	343419	1031	610	0.92	31.21	0.30200	4.2	4.458	12.7	0.107	12.0	0.33	1701	64	1723	111	1750	219	97
179	76020	634	250	1.11	0.03	0.34440	2.1	5.55	2.2	0.1169	0.5	0.97	1908	36	1908	19	1909	10	100
180	37619	308	130	1.59	b.d.	0.34420	1.5	5.581	1.7	0.1176	0.9	0.85	1907	24	1913	15	1920	17	99
181	28219	194	82	1.31	b.d.	0.34370	2.0	5.568	2.3	0.1175	1.1	0.87	1904	32	1911	20	1919	20	99

Table 14: U-Pb isotope analyses of magmatic zircon grains from orthogneiss (*ZM-12-07; Mwombezi dome*)

Grain	$^{207}\text{Pb}^a$	U^b	Pb^b	Th^b	$^{206}\text{Pb}^c$	$^{206}\text{Pb}^d$	$\pm 2s$	$^{207}\text{Pb}^d$	$\pm 2s$	$^{207}\text{Pb}^d$	$\pm 2s$	rho^e	^{206}Pb	$\pm 2s$	^{207}Pb	$\pm 2s$	^{207}Pb	$\pm 2s$	conc.^f
	(cps)	(ppm)	(ppm)	U	(%)	^{238}U	(%)	^{235}U	(%)	^{206}Pb	(%)		^{238}U	(Ma)	^{235}U	(Ma)	^{206}Pb	(Ma)	(%)
100	84156	590	200	0.03	b.d.	0.34640	1.5	5.585	1.8	0.1169	1.0	0.83	1917	25	1914	16	1910	18	100
101	41471	387	120	0.31	0.07	0.29690	2.6	4.838	2.8	0.1182	1.2	0.91	1676	38	1792	24	1929	21	87
107	60288	229	130	0.95	0.10	0.47620	1.5	12.24	1.7	0.1865	0.9	0.86	2511	30	2623	16	2711	14	93
108	42657	324	120	0.43	0.18	0.34470	1.4	5.548	1.6	0.1168	0.8	0.86	1909	22	1908	14	1907	14	100
109	74354	567	190	0.03	0.02	0.34670	1.5	5.622	1.7	0.1176	0.8	0.89	1919	25	1919	15	1920	14	100
110	30261	209	100	1.82	b.d.	0.37180	1.3	6.476	1.7	0.1263	1.2	0.73	2038	22	2043	15	2047	21	100
111	114371	377	210	0.19	0.04	0.51550	1.4	13.07	1.5	0.1839	0.6	0.92	2680	31	2685	15	2689	10	100
112	60773	490	170	0.62	0.00	0.34540	1.7	5.592	1.9	0.1174	1.0	0.87	1912	28	1915	17	1917	17	100
113	19617	126	58	1.23	0.10	0.37470	1.5	6.572	1.8	0.1272	1.0	0.84	2051	27	2056	16	2060	17	100
114	64538	485	160	0.11	0.01	0.34630	1.9	5.605	2.0	0.1174	0.7	0.94	1917	31	1917	17	1917	12	100
115	100763	709	300	1.50	0.08	0.34750	2.0	5.636	2.1	0.1176	0.6	0.96	1923	33	1922	18	1920	10	100
116	67153	513	180	0.16	0.04	0.34710	1.3	5.644	1.5	0.1179	0.8	0.86	1921	21	1923	13	1925	14	100
117	203562	732	240	0.64	0.01	0.32540	1.8	5.287	1.8	0.1178	0.4	0.98	1816	28	1867	16	1924	7	94
118	42120	322	110	0.11	0.00	0.33550	1.3	5.465	1.5	0.1181	0.7	0.89	1865	21	1895	13	1928	12	97
119	57186	431	150	0.74	0.38	0.34340	1.3	5.56	1.6	0.1174	0.9	0.83	1903	21	1910	14	1917	16	99
120	47299	365	120	0.11	b.d.	0.34660	1.5	5.634	1.7	0.1179	0.9	0.86	1918	25	1921	15	1924	16	100
121	142958	999	410	0.45	2.63	0.34450	1.8	5.582	2.6	0.1175	1.9	0.70	1908	30	1913	22	1919	33	99
122	56071	419	140	0.31	0.10	0.34570	1.3	5.617	1.5	0.1179	0.8	0.86	1914	21	1919	13	1924	13	99
460	72659	588	170	1.32	0.49	0.27900	2.7	4.645	3.0	0.1208	1.2	0.91	1586	39	1757	25	1967	22	81
461	25629	179	71	0.72	b.d.	0.35430	2.6	5.86	3.0	0.12	1.5	0.86	1955	43	1955	26	1956	27	100
462	31987	289	94	0.02	0.04	0.33610	2.8	5.406	2.9	0.1167	0.9	0.95	1868	45	1886	25	1906	16	98
463	37811	321	110	0.54	0.50	0.33070	2.4	5.301	2.7	0.1162	1.3	0.88	1842	39	1869	24	1899	24	97

464	49407	387	130	0.87	0.27	0.34570	2.3	5.599	2.6	0.1175	1.3	0.86	1914	37	1916	23	1918	24	100
465	69093	568	260	1.39	0.71	0.34930	3.9	5.785	4.1	0.1201	1.3	0.95	1931	65	1944	36	1958	23	99
466	61211	549	180	0.09	0.14	0.34260	2.6	5.47	2.9	0.1158	1.3	0.90	1899	43	1896	25	1892	23	100
467	38285	294	99	0.48	0.29	0.34150	1.9	5.471	2.2	0.1162	1.1	0.86	1894	31	1896	19	1898	20	100
468	41600	343	120	0.61	0.11	0.34390	1.8	5.535	2.1	0.1167	1.0	0.87	1905	30	1906	18	1907	19	100
469	59246	422	160	3.10	0.40	0.36150	2.4	6.11	2.7	0.1226	1.1	0.92	1989	42	1992	23	1994	19	100
470	33237	437	75	0.13	b.d.	0.17160	4.3	2.401	5.6	0.1015	3.5	0.77	1021	41	1243	41	1651	66	62
471	68226	442	170	1.12	0.25	0.37170	2.0	6.44	2.4	0.1257	1.3	0.85	2037	36	2038	21	2038	22	100
472	48439	504	150	0.06	0.03	0.30160	1.5	4.534	1.7	0.109	0.7	0.90	1699	22	1737	14	1783	13	95
473	44334	375	120	0.10	2.31	0.30700	1.7	4.713	2.5	0.1113	1.9	0.65	1726	25	1770	21	1821	35	95
474	126674	785	330	0.92	0.02	0.37310	2.0	6.487	2.1	0.1261	0.8	0.93	2044	34	2044	19	2044	14	100
475	29662	229	59	1.62	b.d.	0.24120	3.2	3.955	3.6	0.1189	1.5	0.90	1393	41	1625	29	1940	28	72
476	40120	302	130	1.39	0.18	0.36100	2.4	6.084	2.7	0.1222	1.2	0.89	1987	41	1988	24	1989	22	100
477	40930	322	110	0.26	0.29	0.34440	2.5	5.504	2.8	0.1159	1.3	0.89	1908	42	1901	25	1894	23	101
478	201271	855	230	0.47	0.65	0.25530	5.3	4.171	5.4	0.1185	1.1	0.98	1466	70	1668	45	1933	19	76
479	51912	385	140	1.33	1.16	0.33450	3.4	5.321	3.8	0.1154	1.7	0.89	1860	55	1872	33	1885	31	99
480	77660	659	230	1.25	0.05	0.28760	2.0	4.691	2.2	0.1183	0.9	0.91	1630	28	1766	18	1931	16	84
486	56784	438	150	0.11	0.13	0.34710	2.7	5.644	2.8	0.1179	1.0	0.94	1921	44	1923	25	1925	18	100
487	58942	451	150	0.38	0.26	0.34660	2.1	5.616	2.3	0.1175	1.0	0.89	1918	34	1919	20	1919	19	100
488	116754	766	210	0.87	0.11	0.27150	3.6	4.219	3.8	0.1127	1.1	0.96	1549	50	1678	31	1843	20	84
489	29555	314	71	0.07	b.d.	0.23230	3.7	3.435	4.2	0.1072	1.9	0.89	1347	45	1512	33	1753	34	77
490	44895	388	120	3.00	1.52	0.29390	1.9	4.752	2.6	0.1173	1.8	0.74	1661	28	1777	22	1915	32	87
491	23107	199	68	0.15	0.02	0.34260	1.9	5.493	2.2	0.1163	1.0	0.89	1899	32	1900	19	1900	18	100
492	53336	433	150	0.13	0.03	0.34400	2.0	5.569	2.3	0.1174	1.2	0.85	1906	32	1911	20	1917	22	99
493	45569	398	110	1.53	1.42	0.27080	2.8	4.044	3.3	0.1083	1.8	0.84	1545	38	1643	27	1771	33	87
494	11183	94	43	1.79	0.20	0.33180	5.0	5.426	5.2	0.1186	1.4	0.96	1847	81	1889	46	1935	26	95
495	16580	177	64	1.20	0.00	0.33960	1.3	5.392	1.6	0.1152	1.0	0.78	1885	21	1884	14	1883	18	100
496	10657	283	64	0.45	0.00	0.20440	6.2	3.162	6.6	0.1122	2.2	0.95	1199	69	1448	52	1835	39	65
497	30554	227	97	2.22	0.00	0.34570	1.8	5.586	2.0	0.1172	0.9	0.89	1914	30	1914	17	1914	16	100
498	19234	281	76	0.47	0.00	0.26210	3.3	4.165	3.6	0.1153	1.4	0.92	1501	44	1667	30	1884	26	80
499	55116	463	180	0.98	b.d.	0.33870	2.5	5.409	2.8	0.1158	1.2	0.91	1880	41	1886	24	1893	21	99
500	17016	300	72	3.50	0.03	0.24660	2.3	3.242	2.5	0.09537	1.1	0.91	1421	29	1467	20	1535	20	93
501	33300	316	110	2.91	b.d.	0.34780	2.4	5.649	2.8	0.1178	1.4	0.87	1924	40	1924	24	1923	25	100

502	49090	546	150	0.33	0.47	0.26700	2.7	3.767	3.2	0.1023	1.7	0.85	1525	37	1586	26	1667	31	92
503	41667	485	89	1.28	b.d.	0.18520	4.9	2.978	5.1	0.1167	1.5	0.96	1095	50	1402	40	1906	27	57
504	39930	316	110	0.23	0.04	0.34650	1.7	5.621	2.0	0.1177	1.1	0.85	1918	28	1919	17	1921	19	100
505	40432	316	110	0.22	b.d.	0.34620	2.3	5.613	2.6	0.1176	1.2	0.88	1916	38	1918	23	1920	22	100
506	61344	465	160	0.15	0.05	0.34340	3.7	5.544	3.9	0.1171	1.2	0.95	1903	61	1907	34	1912	21	100
507	36270	432	99	0.20	0.16	0.22600	2.2	3.348	2.4	0.1075	1.0	0.91	1313	26	1492	19	1757	18	75
508	40844	323	110	0.08	0.06	0.34580	2.0	5.619	2.3	0.1179	1.0	0.89	1915	34	1919	20	1924	19	100
509	33309	278	93	0.04	0.06	0.34340	1.7	5.531	2.0	0.1168	1.0	0.86	1903	28	1905	17	1908	18	100
510	35382	339	100	0.08	0.27	0.31360	3.6	4.806	3.8	0.1112	1.2	0.95	1758	55	1786	32	1818	21	97
511	15579	178	57	0.67	1.34	0.28910	2.3	4.135	3.0	0.1037	1.9	0.77	1637	33	1661	25	1692	35	97
512	72204	585	160	0.33	2.71	0.24660	3.4	3.748	4.5	0.1103	2.9	0.77	1421	44	1582	37	1804	52	79
513	16569	225	69	0.63	0.07	0.27600	1.8	3.835	2.4	0.1008	1.6	0.74	1571	25	1600	20	1638	30	96
518	50216	508	160	0.26	0.06	0.32250	1.9	5.004	2.1	0.1125	0.8	0.92	1802	30	1820	18	1841	15	98
520	59947	628	210	0.08	0.12	0.34470	3.1	5.584	3.3	0.1175	1.1	0.95	1909	52	1914	29	1918	19	100
521	49552	391	130	0.12	0.30	0.33370	1.6	5.5	2.0	0.1195	1.2	0.81	1856	25	1901	17	1949	21	95
522	66600	555	190	0.06	0.06	0.34720	2.3	5.662	2.6	0.1183	1.2	0.89	1921	38	1926	22	1930	21	100
523	42273	338	120	0.66	0.02	0.34890	2.7	5.67	3.0	0.1179	1.3	0.91	1929	46	1927	26	1924	23	100
524	50018	409	140	0.11	0.08	0.34620	3.2	5.584	3.4	0.117	1.1	0.95	1917	54	1914	30	1911	20	100
525	28738	346	110	0.60	b.d.	0.28150	2.0	4.291	2.3	0.1106	1.1	0.89	1599	29	1692	19	1809	19	88
526	32080	261	100	0.96	b.d.	0.34390	2.5	5.546	2.9	0.117	1.5	0.86	1905	42	1908	25	1910	27	100
527	24302	192	81	1.21	0.48	0.34540	1.8	5.575	2.4	0.1171	1.5	0.78	1912	31	1912	21	1912	26	100
528	18516	156	69	1.38	0.15	0.34440	2.5	5.581	3.0	0.1175	1.7	0.83	1908	42	1913	27	1919	30	99
529	35463	306	100	0.06	0.17	0.34360	2.8	5.529	3.0	0.1167	1.1	0.93	1904	47	1905	27	1906	20	100
530	35215	275	89	0.03	0.08	0.32960	2.9	5.381	3.1	0.1184	1.2	0.92	1836	46	1882	27	1933	22	95
531	48937	409	130	0.09	0.11	0.32790	2.8	5.066	3.0	0.112	1.1	0.93	1828	44	1830	25	1833	19	100
532	53980	419	150	0.17	0.23	0.34540	2.1	5.569	2.3	0.1169	1.1	0.89	1913	34	1911	20	1910	19	100
533	82736	640	230	0.29	0.01	0.34860	2.1	5.652	2.3	0.1176	1.1	0.89	1928	35	1924	20	1920	19	100
534	41763	408	140	0.21	b.d.	0.33520	2.4	5.245	2.6	0.1135	1.2	0.90	1864	38	1860	23	1856	21	100
535	43338	359	140	0.58	0.05	0.34420	2.7	5.531	3.0	0.1166	1.3	0.90	1907	44	1905	26	1904	24	100
536	9768	85	36	1.51	b.d.	0.34470	1.8	5.544	3.3	0.1166	2.7	0.55	1909	30	1907	29	1905	49	100
537	46095	491	170	0.53	b.d.	0.34630	2.0	5.632	2.7	0.118	1.7	0.76	1917	34	1921	23	1925	31	100
538	83674	738	270	0.52	b.d.	0.34360	2.3	5.598	2.4	0.1182	0.9	0.93	1904	38	1916	21	1929	16	99
539	50228	451	160	0.24	b.d.	0.34290	3.2	5.526	3.4	0.1169	1.2	0.94	1901	53	1905	30	1909	21	100

540	34690	344	110	0.52	0.03	0.31680	2.3	4.989	2.6	0.1142	1.3	0.87	1774	36	1817	22	1868	23	95
541	48238	431	160	0.62	0.10	0.33510	2.7	5.334	3.0	0.1155	1.3	0.90	1863	44	1874	26	1887	24	99
542	38543	333	140	1.01	0.01	0.34620	1.9	5.645	2.2	0.1183	1.1	0.86	1916	32	1923	19	1930	20	99
543	47802	399	160	0.65	b.d.	0.34940	2.6	5.726	2.9	0.1189	1.3	0.89	1932	43	1935	26	1939	24	100

Table 15: U-Pb isotope analyses of magmatic monazite grain from orthogneiss (*ZM-12-07; Mwombezhi dome*)

Grain	²⁰⁷ Pb ^a	U ^b	Pb ^b	Th ^b	²⁰⁶ Pb ^c	²⁰⁶ Pb ^d	±2s	²⁰⁷ Pb ^d	±2s	²⁰⁷ Pb ^d	±2s	rho ^e	²⁰⁶ Pb	±2s	²⁰⁷ Pb	±2s	²⁰⁷ Pb	±2s	conc. ^f
	(cps)	(ppm)	(ppm)	U	(%)	²³⁸ U	(%)	²³⁵ U	(%)	²⁰⁶ Pb	(%)		²³⁸ U	(Ma)	²³⁵ U	(Ma)	²⁰⁶ Pb	(Ma)	(%)
544	31992	1595	4300	2.05	0.05	0.34610	2.4	5.625	2.9	0.1179	1.6	0.83	1916	40	1920	25	1924	29	100
545	32544	2239	3500	1.45	0.22	0.34630	3.9	5.618	4.3	0.1177	1.8	0.91	1917	65	1919	37	1921	32	100
547	62795	3193	5100	1.17	0.10	0.34850	2.9	5.548	3.3	0.1155	1.4	0.90	1927	49	1908	28	1887	25	102
548	19586	3115	2700	1.06	0.80	0.24640	5.2	3.261	5.7	0.09599	2.4	0.90	1420	66	1472	45	1548	46	92
549	22671	2766	2500	1.53	1.99	0.34640	4.0	5.633	4.8	0.1179	2.7	0.83	1917	67	1921	43	1925	48	100

Table 16: U-Pb isotope analyses of magmatic zircon grains from granite (*ZM-12-25; Mwombezhi dome*)

Grain	²⁰⁷ Pb ^a	U ^b	Pb ^b	Th ^b	²⁰⁶ Pb ^c	²⁰⁶ Pb ^d	±2s	²⁰⁷ Pb ^d	±2s	²⁰⁷ Pb ^d	±2s	rho ^e	²⁰⁶ Pb	±2s	²⁰⁷ Pb	±2s	²⁰⁷ Pb	±2s	conc. ^f
	(cps)	(ppm)	(ppm)	U	(%)	²³⁸ U	(%)	²³⁵ U	(%)	²⁰⁶ Pb	(%)		²³⁸ U	(Ma)	²³⁵ U	(Ma)	²⁰⁶ Pb	(Ma)	(%)
204	61177	698	190	0.68	b.d.	0.24630	1.5	3.348	1.7	0.0986	0.7	0.90	1419	19	1492	13	1598	14	89
205	77034	956	230	0.21	0.03	0.23810	1.5	2.957	1.7	0.09005	0.8	0.89	1377	18	1397	13	1427	15	97
206	96588	783	170	0.02	b.d.	0.23010	2.5	2.748	2.6	0.08662	0.6	0.97	1335	31	1341	20	1352	11	99
207	71704	992	210	0.05	0.30	0.21820	2.1	2.59	2.3	0.08608	0.8	0.93	1272	25	1298	17	1340	16	95
208	71567	1022	230	0.08	0.21	0.23630	1.5	2.877	1.8	0.08829	1.0	0.84	1368	19	1376	14	1389	19	98
209	36247	1246	290	0.03	0.30	0.22940	2.7	2.758	3.0	0.08721	1.4	0.89	1331	32	1344	23	1365	27	98
210	43760	1775	340	0.03	b.d.	0.20410	2.1	2.343	2.6	0.08327	1.6	0.79	1197	23	1226	19	1276	32	94
211	35266	1506	310	0.02	b.d.	0.21560	2.0	2.497	2.4	0.084	1.4	0.81	1259	22	1271	18	1293	28	97
212	34477	1695	320	0.03	0.29	0.19900	1.9	2.212	2.2	0.0806	1.1	0.87	1170	21	1185	16	1212	21	97
213	47361	1200	350	0.43	0.06	0.27400	2.8	3.725	4.7	0.09861	3.8	0.60	1561	39	1577	38	1598	70	98
214	30992	1241	220	0.03	0.01	0.18900	1.8	2.001	2.0	0.07681	0.9	0.89	1116	18	1116	13	1116	18	100
215	31524	1066	200	0.02	0.07	0.19990	1.7	2.169	2.3	0.07871	1.6	0.75	1175	19	1171	16	1165	31	101

216	40921	1466	280	0.04	b.d.	0.20000	2.5	2.186	2.8	0.07926	1.3	0.88	1176	27	1177	20	1179	27	100
217	40910	922	180	0.03	0.05	0.21210	1.7	2.361	2.0	0.08076	1.1	0.84	1240	19	1231	15	1216	22	102
218	19363	1510	290	0.03	0.12	0.19940	2.2	2.165	5.7	0.07875	5.3	0.39	1172	24	1170	41	1166	105	101
219	36320	1387	260	0.02	0.14	0.20190	2.7	2.253	2.9	0.08094	0.9	0.95	1185	30	1198	21	1220	17	97
220	42321	1434	300	0.01	0.04	0.22100	2.0	2.624	2.1	0.0861	0.7	0.94	1287	23	1307	16	1340	13	96
221	31974	1473	290	0.01	0.01	0.21100	2.0	2.426	2.1	0.08337	0.7	0.94	1234	22	1250	15	1278	14	97
222	41238	1743	360	0.04	0.03	0.21820	2.2	2.544	2.4	0.08455	0.9	0.93	1272	26	1285	18	1305	17	97
223	22727	1068	330	0.58	b.d.	0.28200	4.2	3.92	5.0	0.1008	2.7	0.84	1601	59	1618	41	1639	49	98
224	54550	1740	370	0.01	0.01	0.22560	1.8	2.687	2.0	0.08639	0.9	0.89	1312	21	1325	15	1347	17	97
225	36935	1148	260	0.02	b.d.	0.23550	1.5	2.859	1.8	0.08807	1.0	0.82	1363	18	1371	14	1384	20	98
226	35673	699	270	0.82	b.d.	0.34290	1.8	5.49	2.0	0.1161	0.9	0.89	1901	29	1899	17	1898	17	100
227	33426	1245	240	0.02	0.02	0.20130	2.8	2.335	3.0	0.08412	1.1	0.93	1182	31	1223	22	1295	21	91
228	55700	1735	350	0.01	b.d.	0.21070	4.4	2.546	5.3	0.08765	3.0	0.82	1232	49	1285	39	1375	58	90
229	33383	1189	230	0.07	2.01	0.19040	2.9	2.123	3.7	0.08087	2.4	0.77	1124	30	1156	26	1218	47	92
230	20800	270	110	0.94	6.60	0.28170	2.8	4.316	5.4	0.1111	4.7	0.51	1600	39	1696	46	1818	85	88
231	3259	105	20	0.65	0.33	0.15450	4.9	1.877	5.6	0.0881	2.7	0.87	926	42	1073	38	1385	52	67
232	44529	1359	300	0.01	0.01	0.23140	2.1	2.771	2.2	0.08685	0.7	0.95	1342	25	1348	17	1357	14	99
233	49126	1467	360	0.07	b.d.	0.25590	2.4	3.323	2.6	0.09417	1.1	0.90	1469	31	1487	21	1512	21	97
234	49417	1576	330	0.01	0.01	0.22200	1.9	2.614	2.1	0.08539	0.8	0.92	1293	23	1305	16	1324	16	98
235	47399	1741	350	0.02	0.01	0.21510	1.8	2.478	2.0	0.08357	0.8	0.90	1256	20	1266	14	1283	16	98
236	39709	1407	290	0.01	0.02	0.21910	2.0	2.559	2.1	0.0847	0.6	0.95	1277	23	1289	16	1309	12	98
237	21683	936	180	0.05	0.02	0.20650	2.7	2.312	2.8	0.0812	0.8	0.96	1210	30	1216	20	1226	15	99
243	48585	1599	340	0.01	0.03	0.22200	1.9	2.655	2.2	0.08673	1.0	0.89	1292	22	1316	16	1355	19	95
244	25979	710	240	0.50	0.24	0.30950	2.3	4.59	2.6	0.1076	1.1	0.91	1738	36	1748	22	1759	19	99
245	35952	1574	330	0.02	0.00	0.22090	3.6	2.566	3.7	0.08424	0.9	0.97	1287	43	1291	28	1298	17	99
246	42491	1596	330	0.01	0.02	0.21810	3.2	2.579	3.3	0.08575	0.8	0.97	1272	38	1295	25	1333	15	95
247	37807	1430	280	0.01	0.07	0.21080	2.9	2.434	3.1	0.08377	0.9	0.95	1233	33	1253	22	1287	18	96
248	36501	1180	260	0.03	0.49	0.22320	1.8	2.677	2.2	0.087	1.3	0.81	1299	21	1322	16	1360	24	95
249	30454	629	240	0.62	1.13	0.33450	2.0	5.34	2.8	0.1158	1.9	0.73	1860	33	1875	24	1892	34	98
250	35142	1403	270	0.02	0.02	0.20140	2.0	2.206	2.2	0.07942	0.9	0.91	1183	21	1183	15	1183	18	100
251	27442	1462	250	0.05	0.02	0.18410	1.4	1.997	1.6	0.07869	0.9	0.85	1089	14	1115	11	1164	17	94
252	33639	1292	260	0.01	0.25	0.21010	1.9	2.438	2.1	0.08414	0.9	0.90	1229	21	1254	15	1296	18	95
253	2513	68	26	1.30	b.d.	0.31570	2.2	4.728	3.1	0.1086	2.2	0.71	1769	35	1772	27	1776	40	100

254	11172	206	83	0.90	2.71	0.34730	1.7	5.657	3.0	0.1181	2.4	0.58	1922	29	1925	26	1928	43	100
255	41031	1725	340	0.01	0.03	0.21010	2.1	2.377	2.3	0.08208	0.8	0.93	1229	24	1236	17	1247	16	99
256	33740	1257	270	0.05	b.d.	0.22780	1.6	2.787	1.9	0.08872	1.0	0.86	1323	20	1352	14	1398	19	95

Table 17: Lu-Hf isotope analyses of magmatic zircon grains from orthogneiss (ZM-10-09; Solwezi Dome)

Grain	$^{176}\text{Yb}/^{177}\text{Hf}$ ^a	$\pm 2s$	$^{176}\text{Lu}/^{177}\text{Hf}$ ^a	$\pm 2s$	$^{178}\text{Hf}/^{177}\text{Hf}$	$^{180}\text{Hf}/^{177}\text{Hf}$	Sig_{Hf} ^b (V)	$^{176}\text{Hf}/^{177}\text{Hf}$	$\pm 2s$ ^c	$^{176}\text{Hf}/^{177}\text{Hf}_{(0)}$ ^d	$e\text{Hf}_{(0)}$ ^d	$\pm 2s$ ^c	T_{DM2} ^e (Ga)	age ^f (Ma)	$\pm 2s$ ^c
158	0.0796	53	0.00287	16	1.46721	1.88673	13	0.281594	29	0.281494	-3.9	1.0	2.67	1849	9
159	0.0188	9	0.00077	3	1.46710	1.88656	9	0.281463	25	0.281436	-5.6	0.9	2.78	1866	9
160	0.0326	25	0.00133	11	1.46720	1.88670	12	0.281538	26	0.281491	-3.4	0.9	2.66	1878	12
161	0.0211	37	0.00083	15	1.46720	1.88671	9	0.281447	25	0.281417	-5.5	0.9	2.80	1900	12
162	0.0583	27	0.00256	13	1.46707	1.88627	13	0.281649	39	0.281572	-7.5	1.4	2.65	1575	35
163	0.0312	19	0.00122	7	1.46715	1.88660	10	0.281542	29	0.281499	-3.6	1.0	2.66	1856	10

^aThe $^{176}\text{Yb}/^{177}\text{Hf} = (^{176}\text{Yb}/^{173}\text{Yb})_{\text{true}} \times (^{173}\text{Yb}/^{177}\text{Hf})_{\text{meas}} \times (M^{173}(\text{Yb})/M^{177}(\text{Hf}))b(\text{Hf})$, $b(\text{Hf}) = \ln(^{179}\text{Hf}/^{177}\text{Hf}_{\text{true}} / ^{179}\text{Hf}/^{177}\text{Hf}_{\text{measured}}) / \ln(M^{179}(\text{Hf})/M^{177}(\text{Hf}))$, M =mass of respective isotope. The $^{176}\text{Lu}/^{177}\text{Hf}$ were calculated in a similar way by using the $^{175}\text{Lu}/^{177}\text{Hf}$ and $b(\text{Yb})$. ^bMean Hf signal in volt. ^cUncertainties are quadratic additions of the within-run precision and the daily reproducibility of the zircon GJ-1. Uncertainties for GJ-1 is 2SD (2 standard deviation). ^dInitial $^{176}\text{Hf}/^{177}\text{Hf}$ and $e\text{Hf}$ calculated using the apparent Pb-Pb age determined by LA-ICP-MS dating (see column f), and the CHUR parameters: $^{176}\text{Lu}/^{177}\text{Hf} = 0.0336$, and $^{176}\text{Hf}/^{177}\text{Hf} = 0.282785$ (Bouvier et al., 2008). ^eTwo stage model age in billion years using the measured $^{176}\text{Lu}/^{177}\text{Lu}$ and Pb-Pb age of each spot (first stage = age of zircon), a value of 0.0113 for the average continental crust (second stage), and a depleted mantle $^{176}\text{Lu}/^{177}\text{Hf}$ and $^{176}\text{Hf}/^{177}\text{Hf}$ of 0.03933 and 0.283294, see Blichert-Toft & Puchtel (2010). ^fApparent Pb-Pb age determined by LA-SF-ICP-MS.

Table 18: Lu-Hf isotope analyses of magmatic zircon grains from orthogneiss (*ZM-10-13; Solwezi Dome*)

Grain	$^{176}\text{Yb}/^{177}\text{Hf}$ ^a	$\pm 2s$	$^{176}\text{Lu}/^{177}\text{Hf}$ ^a	$\pm 2s$	$^{178}\text{Hf}/^{177}\text{Hf}$	$^{180}\text{Hf}/^{177}\text{Hf}$	Sig_{Hf} ^b (V)	$^{176}\text{Hf}/^{177}\text{Hf}$	$\pm 2s$ ^c	$^{176}\text{Hf}/^{177}\text{Hf}_0$ ^d	eHf_0 ^d	$\pm 2s$ ^c	T_{DM2} ^e (Ga)	age ^f (Ma)	$\pm 2s$ ^c
120	0.0206	11	0.00081	3	1.46713	1.88659	10	0.281474	25	0.281445	-5.9	0.9	2.77	1838	11
121	0.0138	12	0.00054	3	1.46716	1.88670	12	0.281493	26	0.281474	-3.6	0.9	2.69	1896	12
122	0.0164	49	0.00056	14	1.46713	1.88664	10	0.281457	27	0.281437	-4.9	0.9	2.76	1896	16
123	0.0291	4	0.00105	1	1.46719	1.88661	10	0.281507	26	0.281469	-3.9	0.9	2.70	1888	15
124	0.0233	11	0.00084	5	1.46716	1.88660	10	0.281504	25	0.281473	-3.7	0.9	2.69	1892	14
125	0.0235	6	0.00085	2	1.46717	1.88662	12	0.281481	27	0.281450	-4.7	0.9	2.74	1883	14
126	0.0427	76	0.00155	27	1.46716	1.88674	11	0.281518	25	0.281463	-4.4	0.9	2.72	1878	29
127	0.0208	7	0.00076	2	1.46713	1.88649	10	0.281457	27	0.281430	-5.4	1.0	2.78	1885	13
128	0.0328	22	0.00121	8	1.46718	1.88679	10	0.281506	28	0.281463	-4.8	1.0	2.73	1859	16
129	0.0192	7	0.00070	2	1.46712	1.88673	10	0.281467	27	0.281442	-4.7	1.0	2.75	1896	11
130	0.0299	5	0.00106	2	1.46712	1.88650	10	0.281496	26	0.281459	-6.4	0.9	2.76	1796	20
131	0.0243	30	0.00084	8	1.46718	1.88653	11	0.281470	30	0.281440	-5.4	1.1	2.77	1867	13
132	0.0256	6	0.00089	3	1.46716	1.88662	11	0.281482	25	0.281450	-4.5	0.9	2.73	1894	9
133	0.0281	11	0.00102	4	1.46715	1.88657	10	0.281521	24	0.281484	-3.4	0.8	2.67	1888	12
134	0.0215	5	0.00078	1	1.46718	1.88660	11	0.281489	24	0.281461	-4.1	0.9	2.71	1895	13
135	0.0370	10	0.00138	3	1.46719	1.88679	12	0.281510	22	0.281460	-4.4	0.8	2.72	1880	11
136	0.0154	5	0.00058	1	1.46718	1.88668	12	0.281505	25	0.281485	-3.9	0.9	2.68	1866	14
137	0.0552	44	0.00213	19	1.46718	1.88659	10	0.281532	29	0.281456	-4.2	1.0	2.72	1898	9
138	0.0499	19	0.00202	8	1.46722	1.88661	11	0.281428	26	0.281358	-9.2	0.9	2.94	1831	10
139	0.0420	31	0.00148	10	1.46718	1.88642	15	0.282172	26	0.282138	4.7	0.9	1.71	1229	12
140	0.0454	21	0.00163	8	1.46716	1.88659	9	0.281531	31	0.281472	-3.8	1.1	2.69	1889	14
141	0.0291	34	0.00105	11	1.46715	1.88660	9	0.281506	27	0.281468	-3.9	0.9	2.70	1892	12
142	0.0218	3	0.00081	1	1.46717	1.88672	10	0.281492	24	0.281463	-4.2	0.8	2.71	1887	18
143	0.0077	6	0.00031	2	1.46718	1.88676	12	0.281473	24	0.281462	-4.2	0.8	2.72	1886	12
144	0.0156	13	0.00058	4	1.46715	1.88656	10	0.281463	30	0.281442	-4.8	1.1	2.75	1893	15
145	0.0071	10	0.00031	4	1.46714	1.88657	11	0.281474	23	0.281463	-4.5	0.8	2.72	1871	17
151	0.0273	14	0.00101	5	1.46716	1.88669	10	0.281501	24	0.281465	-4.2	0.8	2.71	1884	16
152	0.0276	15	0.00101	5	1.46719	1.88661	8	0.281510	31	0.281474	-3.9	1.1	2.69	1880	15
153	0.0191	3	0.00071	1	1.46719	1.88659	12	0.281471	26	0.281446	-5.8	0.9	2.77	1843	18
154	0.0308	7	0.00111	2	1.46720	1.88673	10	0.281494	23	0.281455	-4.5	0.8	2.73	1883	12
156	0.0171	40	0.00066	15	1.46718	1.88652	10	0.281490	27	0.281466	-4.3	1.0	2.71	1877	16
157	0.0188	3	0.00071	1	1.46723	1.88665	10	0.281507	26	0.281482	-3.6	0.9	2.68	1883	18

Table 19: Lu-Hf isotope analyses of magmatic zircon grains from orthogneiss (*ZM-10-53; Solwezi Dome*)

Grain	$^{176}\text{Yb}/^{177}\text{Hf}^a$	$\pm 2s$	$^{176}\text{Lu}/^{177}\text{Hf}^a$	$\pm 2s$	$^{178}\text{Hf}/^{177}\text{Hf}$	$^{180}\text{Hf}/^{177}\text{Hf}$	Sig_{Hf}^b (V)	$^{176}\text{Hf}/^{177}\text{Hf}$	$\pm 2s^c$	$^{176}\text{Hf}/^{177}\text{Hf}_{(t)}^d$	$e\text{Hf}_{(t)}^d$	$\pm 2s^c$	T_{DM2}^e (Ga)	age^f (Ma)	$\pm 2s^c$
51	0.0294	11	0.00113	4	1.46714	1.88656	9	0.281561	26	0.281521	-3.4	0.9	2.63	1829	18
52	0.0243	18	0.00091	6	1.46721	1.88676	9	0.281569	28	0.281537	-2.3	1.0	2.58	1853	15
53	0.0510	81	0.00171	19	1.46718	1.88673	11	0.281581	30	0.281522	-3.1	1.1	2.62	1841	7
54	0.0279	21	0.00107	8	1.46721	1.88670	11	0.281563	24	0.281525	-2.8	0.9	2.61	1852	11
55	0.0180	11	0.00069	4	1.46718	1.88666	10	0.281580	29	0.281557	-2.4	1.0	2.56	1821	18
56	0.0244	26	0.00090	9	1.46725	1.88669	9	0.281727	28	0.281697	0.7	1.0	2.33	1736	25
57	0.0278	9	0.00107	4	1.46716	1.88659	10	0.281588	29	0.281551	-1.8	1.0	2.56	1855	23
58	0.0120	2	0.00049	1	1.46717	1.88659	11	0.281588	22	0.281571	-1.1	0.8	2.52	1852	22
59	0.0130	8	0.00048	4	1.46719	1.88645	10	0.281559	25	0.281542	-2.1	0.9	2.57	1856	27
60	0.0218	14	0.00083	6	1.46714	1.88650	11	0.281617	29	0.281588	-0.5	1.0	2.49	1854	22
61	0.0119	3	0.00047	1	1.46721	1.88669	10	0.281595	29	0.281578	-0.7	1.0	2.50	1858	13
62	0.0155	10	0.00060	4	1.46716	1.88660	10	0.281601	27	0.281580	-0.8	0.9	2.50	1854	30
63	0.0297	21	0.00109	8	1.46713	1.88662	9	0.281568	28	0.281530	-2.7	1.0	2.60	1849	21
64	0.0206	15	0.00082	6	1.46714	1.88648	9	0.281593	26	0.281565	-2.4	0.9	2.55	1806	19
65	0.0171	8	0.00066	3	1.46716	1.88645	9	0.281572	25	0.281553	-8.9	0.9	2.70	1543	28
66	0.0213	19	0.00084	7	1.46720	1.88691	9	0.281588	28	0.281558	-1.5	1.0	2.54	1856	14
73	0.0285	17	0.00109	7	1.46713	1.88647	10	0.281585	24	0.281547	-2.0	0.8	2.57	1852	21
74	0.0290	21	0.00101	6	1.46715	1.88638	10	0.281592	27	0.281557	-1.6	1.0	2.54	1855	19
75	0.0181	12	0.00065	3	1.46715	1.88657	10	0.281564	28	0.281542	-4.2	1.0	2.62	1764	27
76	0.0777	120	0.00217	30	1.46716	1.88665	10	0.281613	30	0.281536	-1.7	1.1	2.57	1880	19
77	0.0167	17	0.00066	6	1.46718	1.88658	11	0.281595	30	0.281573	-3.9	1.1	2.57	1729	20
78	0.0101	3	0.00040	1	1.46718	1.88668	10	0.281592	24	0.281579	-4.3	0.9	2.58	1701	29
79	0.0223	8	0.00087	3	1.46714	1.88676	9	0.281597	24	0.281571	-7.3	0.9	2.65	1582	35
80	0.0233	6	0.00088	2	1.46720	1.88669	9	0.281614	27	0.281583	-1.3	1.0	2.51	1824	22
81	0.0227	16	0.00089	7	1.46717	1.88669	9	0.281594	24	0.281562	-1.5	0.9	2.54	1848	22
82	0.0183	8	0.00069	2	1.46715	1.88675	9	0.281601	28	0.281577	-0.9	1.0	2.51	1854	26
83	0.0146	6	0.00055	2	1.46718	1.88670	10	0.281587	27	0.281567	-1.2	0.9	2.53	1853	29
84	0.0268	16	0.00101	5	1.46719	1.88668	10	0.281723	25	0.281687	3.5	0.9	2.28	1873	18
85	0.0169	5	0.00066	1	1.46722	1.88674	10	0.281619	22	0.281597	-2.2	0.8	2.51	1764	23
86	0.0231	12	0.00087	4	1.46718	1.88646	11	0.281628	28	0.281598	-0.4	1.0	2.47	1840	16

Table 20: Lu-Hf isotope analyses of magmatic zircon grains from granite (ZM-10-66; Solwezi Dome)

Grain	$^{176}\text{Yb}/^{177}\text{Hf}^a$	$\pm 2s$	$^{176}\text{Lu}/^{177}\text{Hf}^a$	$\pm 2s$	$^{178}\text{Hf}/^{177}\text{Hf}$	$^{180}\text{Hf}/^{177}\text{Hf}$	Sig_{Hf}^b (V)	$^{176}\text{Hf}/^{177}\text{Hf}$	$\pm 2s^c$	$^{176}\text{Hf}/^{177}\text{Hf}_{(0)}^d$	$e\text{Hf}_{(0)}^d$	$\pm 2s^c$	T_{DM2}^e (Ga)	age^f (Ma)	$\pm 2s^c$
366	0.0283	6	0.00095	2	1.46717	1.88665	12	0.281736	29	0.281716	-12.9	1.0	2.58	1112	6
367	0.0195	5	0.00067	2	1.46715	1.88661	11	0.281742	27	0.281728	-12.6	1.0	2.56	1109	15
368	0.0148	4	0.00052	1	1.46716	1.88661	12	0.281733	29	0.281722	-12.6	1.0	2.57	1116	17
369	0.0272	12	0.00093	3	1.46716	1.88669	13	0.281729	26	0.281710	-13.3	0.9	2.60	1105	13
370	0.0315	14	0.00109	6	1.46719	1.88664	15	0.281763	27	0.281741	-12.3	0.9	2.54	1099	12
372	0.0250	24	0.00091	9	1.46716	1.88668	14	0.281754	24	0.281735	-12.4	0.9	2.55	1102	14
371	0.0224	6	0.00077	2	1.46710	1.88630	12	0.281736	30	0.281719	-12.2	1.1	2.56	1136	13
373	0.0219	16	0.00074	5	1.46717	1.88675	11	0.281763	25	0.281747	-11.5	0.9	2.51	1126	26
374	0.0231	24	0.00079	7	1.46716	1.88651	14	0.281735	26	0.281718	-12.1	0.9	2.56	1146	14
375	0.0301	10	0.00108	3	1.46715	1.88660	16	0.281752	20	0.281730	-12.6	0.7	2.56	1106	17
377	0.0173	15	0.00062	6	1.46717	1.88647	13	0.281762	26	0.281749	-11.9	0.9	2.52	1106	15
379	0.0278	20	0.00106	11	1.46718	1.88654	12	0.281732	26	0.281710	-12.7	0.9	2.58	1129	150
380	0.0269	12	0.00093	4	1.46719	1.88650	11	0.281763	25	0.281744	-11.5	0.9	2.52	1133	18
389	0.0238	12	0.00082	3	1.46716	1.88663	10	0.281758	28	0.281741	-12.0	1.0	2.53	1111	49
391	0.0294	13	0.00103	4	1.46717	1.88679	11	0.281780	24	0.281758	-11.3	0.8	2.50	1115	18

Table 21: Lu-Hf isotope analyses of detrital zircon grains from paragneiss (ZM-10-38; Solwezi Dome)

Grain	$^{176}\text{Yb}/^{177}\text{Hf}^a$	$\pm 2s$	$^{176}\text{Lu}/^{177}\text{Hf}^a$	$\pm 2s$	$^{178}\text{Hf}/^{177}\text{Hf}$	$^{180}\text{Hf}/^{177}\text{Hf}$	Sig_{Hf}^b (V)	$^{176}\text{Hf}/^{177}\text{Hf}$	$\pm 2s^c$	$^{176}\text{Hf}/^{177}\text{Hf}_{(0)}^d$	$e\text{Hf}_{(0)}^d$	$\pm 2s^c$	T_{DM2}^e (Ga)	age^f (Ma)	$\pm 2s^c$
260	0.0528	25	0.00164	7	1.46715	1.88657	16	0.281609	26	0.281551	-1.3	0.9	2.55	1875	11
261	0.0255	8	0.00093	3	1.46715	1.88659	14	0.281498	24	0.281462	-1.5	0.9	2.66	2002	13
262	0.0340	17	0.00117	6	1.46711	1.88653	14	0.281144	31	0.281089	-4.4	1.1	3.16	2450	8
263	0.0381	35	0.00130	11	1.46715	1.88655	16	0.281596	24	0.281550	-1.0	0.9	2.54	1890	10
264	0.0384	50	0.00137	21	1.46714	1.88661	15	0.281520	24	0.281472	-4.6	0.9	2.71	1853	8
265	0.0381	13	0.00126	5	1.46714	1.88660	12	0.281444	24	0.281396	-4.6	0.9	2.80	1972	9
266	0.0397	12	0.00146	5	1.46709	1.88636	14	0.281462	31	0.281410	-6.7	1.1	2.83	1857	14
267	0.0304	27	0.00101	9	1.46717	1.88660	12	0.281429	25	0.281393	-6.6	0.9	2.85	1889	11
268	0.0200	8	0.00072	2	1.46718	1.88678	14	0.281101	24	0.281073	-14.5	0.8	3.40	2039	11
269	0.0359	30	0.00138	13	1.46713	1.88655	14	0.281427	26	0.281378	-7.9	0.9	2.89	1858	10

270	0.0361	13	0.00100	4	1.46716	1.88667	15	0.281422	26	0.281388	-7.9	0.9	2.88	1840	11
271	0.0308	43	0.00106	14	1.46719	1.88658	14	0.281491	25	0.281452	-3.7	0.9	2.71	1925	10
272	0.0295	21	0.00108	8	1.46712	1.88636	13	0.281493	28	0.281454	-4.5	1.0	2.73	1885	8
273	0.0270	6	0.00088	1	1.46722	1.88670	13	0.281444	27	0.281411	-3.7	1.0	2.77	1986	9
274	0.0261	18	0.00090	7	1.46716	1.88659	13	0.281429	28	0.281395	-4.3	1.0	2.80	1985	11
275	0.0395	42	0.00134	13	1.46714	1.88661	15	0.281502	26	0.281453	-3.5	0.9	2.71	1933	9
276	0.0495	32	0.00176	12	1.46719	1.88659	17	0.281583	27	0.281519	-1.4	1.0	2.59	1920	11
277	0.0289	9	0.00094	3	1.46716	1.88658	13	0.281140	31	0.281100	-9.3	1.1	3.26	2223	12
278	0.0184	10	0.00062	5	1.46715	1.88643	23	0.281706	34	0.281694	-14.3	1.2	2.63	1085	31
279	0.0306	17	0.00101	7	1.46718	1.88675	12	0.281478	23	0.281438	-1.2	0.8	2.68	2053	13
280	0.0105	5	0.00034	1	1.46718	1.88666	16	0.281419	24	0.281407	-6.0	0.9	2.82	1895	15
288	0.0269	6	0.00088	3	1.46715	1.88657	12	0.281451	26	0.281420	-5.9	0.9	2.80	1876	18
279	0.0257	29	0.00083	9	1.46722	1.88687	10	0.281515	24	0.281485	-3.3	0.9	2.67	1888	8
281	0.0287	16	0.00104	4	1.46713	1.88666	14	0.281517	22	0.281475	1.4	0.8	2.58	2110	11
282	0.0157	9	0.00051	2	1.46716	1.88668	18	0.281513	23	0.281496	-4.3	0.8	2.68	1831	11
289	0.0633	74	0.00169	18	1.46712	1.88634	16	0.281486	36	0.281427	-6.2	1.3	2.80	1855	16
291	0.0273	17	0.00097	6	1.46715	1.88671	13	0.281601	24	0.281565	1.4	0.9	2.47	1971	13
290	0.0457	32	0.00155	10	1.46721	1.88665	16	0.281609	23	0.281552	0.3	0.8	2.51	1944	13
292	0.0766	92	0.00197	23	1.46716	1.88661	16	0.281482	24	0.281412	-6.4	0.9	2.82	1868	7
293	0.0779	91	0.00188	21	1.46714	1.88659	17	0.281480	24	0.281413	-6.0	0.9	2.81	1885	9
294	0.0384	10	0.00119	3	1.46712	1.88633	12	0.281493	25	0.281452	-5.9	0.9	2.76	1830	10
295	0.0370	5	0.00133	2	1.46717	1.88655	18	0.281522	24	0.281477	-5.6	0.8	2.72	1805	10
296	0.0379	45	0.00114	14	1.46715	1.88656	15	0.281184	32	0.281144	-16.0	1.1	3.34	1866	9
297	0.0430	14	0.00147	4	1.46722	1.88663	11	0.281057	38	0.280985	-5.9	1.3	3.32	2543	15
298	0.0702	48	0.00241	19	1.46714	1.88657	12	0.281649	24	0.281561	0.3	0.9	2.50	1929	10
301	0.0380	27	0.00123	8	1.46714	1.88657	13	0.281572	25	0.281528	-1.2	0.9	2.57	1915	11
299	0.0173	20	0.00053	6	1.46714	1.88661	16	0.281573	23	0.281561	-15.8	0.8	2.83	1227	33
302	0.0302	21	0.00099	9	1.46709	1.88650	14	0.281284	24	0.281247	-10.2	0.9	3.10	1958	11
303	0.0283	25	0.00093	9	1.46716	1.88663	11	0.281306	32	0.281271	-9.2	1.1	3.05	1964	8
304	0.0135	14	0.00039	4	1.46719	1.88642	13	0.281350	33	0.281335	-7.3	1.2	2.93	1946	13
309	0.0350	18	0.00133	6	1.46719	1.88668	12	0.281538	27	0.281489	-2.2	1.0	2.64	1933	10
315	0.0555	67	0.00152	19	1.46714	1.88644	14	0.281456	31	0.281401	-6.4	1.1	2.83	1883	7
316	0.0198	7	0.00070	3	1.46715	1.88654	11	0.281009	33	0.280975	-6.3	1.2	3.34	2541	18
317	0.0325	17	0.00118	4	1.46714	1.88666	12	0.281485	28	0.281442	-3.5	1.0	2.72	1951	14
318	0.0404	29	0.00143	10	1.46716	1.88661	12	0.281498	23	0.281443	-2.1	0.8	2.69	2008	10
319	0.0204	18	0.00075	8	1.46713	1.88652	12	0.280825	24	0.280785	-8.2	0.9	3.61	2748	17

320	0.0261	4	0.00098	3	1.46711	1.88664	11	0.280828	37	0.280793	-27.6	1.3	3.99	1904	11
321	0.0388	26	0.00124	6	1.46718	1.88666	13	0.281599	32	0.281554	-0.5	1.2	2.53	1904	9
322	0.0281	13	0.00104	4	1.46720	1.88671	14	0.281606	30	0.281567	1.0	1.1	2.48	1950	10
335	0.0697	26	0.00233	8	1.46706	1.88659	13	0.281493	34	0.281403	-2.8	1.2	2.76	2037	11
334	0.0790	21	0.00272	9	1.46715	1.88654	14	0.281527	28	0.281431	-5.9	1.0	2.79	1863	17
336	0.0189	2	0.00069	0	1.46719	1.88670	12	0.281442	25	0.281416	-2.5	0.9	2.73	2031	8
337	0.0176	16	0.00061	5	1.46716	1.88646	12	0.281332	36	0.281307	-3.2	1.3	2.88	2166	19
340	0.0180	18	0.00065	6	1.46712	1.88659	10	0.281493	33	0.281468	-0.3	1.2	2.63	2045	10
342	0.0304	48	0.00081	12	1.46715	1.88645	14	0.281405	31	0.281371	0.7	1.1	2.72	2237	12
344	0.0182	11	0.00064	2	1.46714	1.88650	12	0.281142	40	0.281116	-9.3	1.4	3.24	2199	12
349	0.0156	12	0.00048	3	1.46719	1.88644	12	0.281345	25	0.281327	-9.3	0.9	2.98	1872	17

Table 22: Lu-Hf isotope analyses of detrital zircon grains from paragneiss (*ZM-39-01; Mwombezhi Dome*)

Grain	$^{176}\text{Yb}/^{177}\text{Hf}$ ^a	$\pm 2s$	$^{176}\text{Lu}/^{177}\text{Hf}$ ^a	$\pm 2s$	$^{178}\text{Hf}/^{177}\text{Hf}$	$^{180}\text{Hf}/^{177}\text{Hf}$	Sig_{Hf} ^b (V)	$^{176}\text{Hf}/^{177}\text{Hf}$	$\pm 2s$ ^c	$^{176}\text{Hf}/^{177}\text{Hf}_{(0)}$ ^d	$e\text{Hf}_{(0)}$ ^d	$\pm 2s$ ^c	T_{DM2} ^e (Ga)	age ^f (Ma)	$\pm 2s$ ^c
182	0.0061	3	0.00032	1	1.46718	1.88678	9	0.282142	29	0.282135	3.7	1.0	1.73	1192	39
183	0.0497	52	0.00164	17	1.46713	1.88697	6	0.281693	38	0.281640	-2.1	1.3	2.46	1705	47
187	0.0139	22	0.00054	6	1.46717	1.88658	10	0.281839	49	0.281827	-7.7	1.8	2.34	1169	45
185	0.0310	38	0.00104	11	1.46706	1.88678	6	0.281683	31	0.281650	-2.5	1.1	2.45	1669	44
190	0.0193	8	0.00075	2	1.46693	1.88736	6	0.281648	33	0.281626	-6.9	1.2	2.57	1515	64
191	0.0196	20	0.00068	7	1.46714	1.88672	7	0.281660	32	0.281638	-2.5	1.1	2.47	1691	50
201	0.0259	20	0.00090	7	1.46715	1.88701	7	0.281643	30	0.281614	-3.2	1.1	2.51	1698	30
202	0.0175	3	0.00085	1	1.46719	1.88683	10	0.281989	26	0.281971	-2.6	0.9	2.06	1167	17
203	0.0239	6	0.00112	2	1.46717	1.88684	13	0.282002	31	0.281977	-2.5	1.1	2.05	1161	67
321	0.0311	18	0.00102	6	1.46717	1.88653	12	0.281696	27	0.281664	-2.1	1.0	2.43	1669	57
322	0.0163	5	0.00059	2	1.46711	1.88687	16	0.281675	28	0.281656	-2.0	1.0	2.43	1683	44
323	0.0195	3	0.00065	1	1.46717	1.88679	11	0.281647	29	0.281626	-2.4	1.0	2.48	1711	43
324	0.0226	2	0.00079	1	1.46716	1.88675	16	0.281679	26	0.281653	-1.9	0.9	2.43	1692	24
342	0.0072	1	0.00031	0	1.46717	1.88678	17	0.281975	27	0.281968	-1.4	1.0	2.04	1224	32
349	0.0201	3	0.00067	0	1.46715	1.88676	12	0.281646	27	0.281624	-2.6	1.0	2.49	1704	32
351	0.0214	3	0.00073	1	1.46714	1.88678	12	0.281646	27	0.281622	-3.1	1.0	2.50	1689	42
347	0.0178	1	0.00062	1	1.46715	1.88675	13	0.281640	26	0.281621	-3.3	0.9	2.50	1681	32
350	0.0088	7	0.00034	3	1.46717	1.88664	20	0.282053	47	0.282046	-0.4	1.7	1.93	1147	40

348	0.0144	12	0.00047	3	1.46710	1.88671	13	0.281624	31	0.281609	-2.7	1.1	2.51	1723	45
352	0.0210	6	0.00068	1	1.46714	1.88681	15	0.281630	24	0.281609	-3.9	0.9	2.53	1675	24
309	0.0166	6	0.00067	1	1.46715	1.88698	9	0.281670	36	0.281656	-13.4	1.3	2.66	1183	30
382	0.0256	25	0.00087	9	1.46710	1.88665	6	0.281689	31	0.281661	-1.1	1.1	2.41	1717	45
388	0.0235	20	0.00083	7	1.46711	1.88678	6	0.281688	33	0.281661	-1.0	1.2	2.41	1717	51
394	0.0217	4	0.00078	1	1.46717	1.88676	8	0.281648	28	0.281623	-3.9	1.0	2.51	1649	30
399	0.0278	2	0.00097	2	1.46711	1.88665	8	0.281689	27	0.281657	-1.2	1.0	2.42	1714	29
400	0.0222	6	0.00077	2	1.46720	1.88657	6	0.281660	31	0.281635	-2.0	1.1	2.46	1717	56
401	0.0204	4	0.00069	2	1.46714	1.88682	7	0.281635	29	0.281613	-3.1	1.0	2.51	1701	35
409	0.0249	35	0.00086	12	1.46718	1.88686	6	0.281658	27	0.281631	-2.3	1.0	2.47	1711	77
415	0.0517	32	0.00169	10	1.46710	1.88682	5	0.281718	35	0.281663	-1.0	1.2	2.41	1715	28
426	0.0297	23	0.00098	8	1.46712	1.88687	6	0.281667	36	0.281635	-2.2	1.3	2.46	1708	65

Table 23: Lu-Hf isotope analyses of detrital zircon grains from paragneiss (ZM-62-05; Mwombeshi Dome)

Grain	$^{176}\text{Yb}/^{177}\text{Hf}$ ^a	$\pm 2s$	$^{176}\text{Lu}/^{177}\text{Hf}$ ^a	$\pm 2s$	$^{178}\text{Hf}/^{177}\text{Hf}$	$^{180}\text{Hf}/^{177}\text{Hf}$	Sig_{Hf} ^b (V)	$^{176}\text{Hf}/^{177}\text{Hf}$	$\pm 2s$ ^c	$^{176}\text{Hf}/^{177}\text{Hf}_{(0)}$ ^d	$\text{eHf}_{(0)}$ ^d	$\pm 2s$ ^c	T_{DM} ^e (Ga)	age^f (Ma)	$\pm 2s$ ^c
90	0.0317	38	0.00105	12	1.46717	1.88679	9	0.281648	36	0.281614	-2.8	1.3	2.50	1712	25
99	0.0272	10	0.00092	4	1.46709	1.88701	7	0.281657	30	0.281627	-2.5	1.1	2.48	1705	80
94	0.0215	9	0.00072	2	1.46713	1.88685	8	0.281608	30	0.281585	-3.9	1.1	2.56	1712	24
92	0.0326	37	0.00109	12	1.46711	1.88687	8	0.281665	30	0.281630	-1.9	1.1	2.46	1727	39
95	0.0638	57	0.00214	19	1.46709	1.88704	10	0.281639	36	0.281570	-4.7	1.3	2.59	1698	24
96	0.0314	17	0.00098	6	1.46708	1.88675	9	0.281666	35	0.281634	-2.0	1.3	2.46	1717	37
265	0.0225	5	0.00077	1	1.46717	1.88676	7	0.281677	29	0.281654	-4.4	1.0	2.49	1583	25
266	0.0329	46	0.00114	17	1.46715	1.88683	7	0.281696	40	0.281664	-6.8	1.4	2.52	1461	47
268	0.0423	24	0.00135	6	1.46717	1.88671	5	0.281712	31	0.281669	-1.4	1.1	2.40	1691	42
271	0.0483	59	0.00159	18	1.46716	1.88665	6	0.281728	35	0.281676	-0.2	1.2	2.37	1728	57
272	0.0270	11	0.00092	4	1.46717	1.88691	8	0.281681	31	0.281654	-4.7	1.1	2.49	1568	25
274	0.0243	16	0.00081	5	1.46715	1.88676	11	0.281699	28	0.281673	-0.6	1.0	2.39	1717	63
278	0.0253	7	0.00080	2	1.46715	1.88667	14	0.281683	27	0.281657	-2.2	1.0	2.44	1671	49
280	0.0266	27	0.00087	9	1.46714	1.88690	13	0.281692	26	0.281665	-3.1	0.9	2.44	1622	46
279	0.0488	6	0.00158	2	1.46716	1.88679	12	0.282146	29	0.282096	13.0	1.0	1.58	1656	56
293	0.0800	71	0.00241	23	1.46711	1.88677	16	0.282138	42	0.282062	12.4	1.5	1.64	1685	18
294	0.0369	46	0.00120	15	1.46715	1.88671	11	0.281673	28	0.281634	-2.2	1.0	2.46	1709	32
295	0.0390	85	0.00115	21	1.46712	1.88692	22	0.281893	30	0.281862	-0.7	1.1	2.16	1420	44

361	0.0224	10	0.00089	3	1.46723	1.88655	12	0.282057	38	0.282037	-0.6	1.3	1.94	1154	15
368	0.0296	12	0.00095	3	1.46713	1.88685	11	0.281656	52	0.281636	-14.9	1.8	2.72	1150	62
369	0.0178	4	0.00062	2	1.46716	1.88674	6	0.281634	31	0.281614	-3.0	1.1	2.50	1706	40
373	0.0228	22	0.00074	6	1.46715	1.88660	7	0.281666	32	0.281642	-1.3	1.1	2.44	1734	65
374	0.0203	13	0.00066	4	1.46725	1.88674	7	0.281678	30	0.281657	-1.2	1.1	2.42	1717	50
378	0.0212	10	0.00096	7	1.46700	1.88686	7	0.282059	39	0.282038	-0.3	1.4	1.93	1166	65
379	0.0314	42	0.00104	13	1.46713	1.88684	7	0.281679	33	0.281646	-1.9	1.2	2.44	1703	38
437	0.0139	6	0.00056	2	1.46713	1.88675	14	0.282033	26	0.282021	-1.1	0.9	1.97	1157	20
438	0.0300	15	0.00096	5	1.46707	1.88675	10	0.281723	28	0.281691	-0.1	1.0	2.35	1710	48
439	0.0225	12	0.00088	4	1.46712	1.88676	18	0.282213	33	0.282192	6.3	1.2	1.61	1213	17
440	0.0206	9	0.00075	2	1.46721	1.88671	13	0.282478	36	0.282461	15.4	1.3	1.09	1197	72
441	0.0178	3	0.00068	1	1.46722	1.88669	13	0.282107	35	0.282090	5.6	1.2	1.75	1341	242
443	0.0207	12	0.00070	3	1.46710	1.88680	12	0.281642	27	0.281619	-2.4	1.0	2.49	1722	45
444	0.0111	5	0.00046	1	1.46719	1.88660	13	0.281979	27	0.281965	6.8	1.0	1.87	1589	37
455	0.0242	13	0.00081	3	1.46713	1.88676	10	0.281620	30	0.281594	-3.8	1.1	2.55	1699	31
457	0.0177	3	0.00061	2	1.46714	1.88683	13	0.281650	27	0.281636	-14.1	1.0	2.70	1185	18
459	0.0176	8	0.00057	2	1.46713	1.88682	11	0.281644	31	0.281626	-2.6	1.1	2.48	1705	51

Table 24: Lu-Hf isotope analyses of detrital zircon grains from paragneiss (ZM-66-08; Mwombeshi Dome)

Grain	$^{176}\text{Yb}/^{177}\text{Hf}^a$	$\pm 2s$	$^{176}\text{Lu}/^{177}\text{Hf}^a$	$\pm 2s$	$^{178}\text{Hf}/^{177}\text{Hf}$	$^{180}\text{Hf}/^{177}\text{Hf}$	Sig_{Hf}^b (V)	$^{176}\text{Hf}/^{177}\text{Hf}$	$\pm 2s^c$	$^{176}\text{Hf}/^{177}\text{Hf}_{(t)}^d$	$e\text{Hf}_{(t)}^d$	$\pm 2s^c$	T_{DM2}^e (Ga)	age^f (Ma)	$\pm 2s^c$
123	0.0181	17	0.00075	7	1.46714	1.88701	8	0.281575	38	0.281548	-0.7	1.4	2.54	1906	13
124	0.0127	6	0.00048	2	1.46711	1.88695	8	0.281581	40	0.281564	-0.9	1.4	2.52	1874	22
125	0.0180	11	0.00071	2	1.46707	1.88681	8	0.281604	34	0.281579	-1.1	1.2	2.51	1840	32
127	0.0077	4	0.00041	2	1.46705	1.88694	7	0.282178	44	0.282169	4.0	1.6	1.68	1149	24
128	0.0589	14	0.00198	6	1.46709	1.88668	6	0.281784	34	0.281718	2.0	1.2	2.28	1761	27
129	0.0290	8	0.00099	4	1.46712	1.88666	6	0.281738	28	0.281705	1.6	1.0	2.30	1763	43
130	0.0045	1	0.00022	0	1.46715	1.88682	8	0.281870	31	0.281864	0.0	1.1	2.14	1448	59
133	0.0667	49	0.00218	17	1.46713	1.88686	17	0.281585	26	0.281505	-1.7	0.9	2.61	1928	13
134	0.0101	2	0.00037	1	1.46715	1.88693	9	0.281579	35	0.281566	-1.2	1.2	2.53	1856	9
135	0.0246	9	0.00092	5	1.46716	1.88687	12	0.281599	26	0.281566	-0.8	0.9	2.52	1876	16
142	0.0172	8	0.00065	4	1.46717	1.88691	11	0.281576	29	0.281552	-0.2	1.0	2.52	1921	19
151	0.0182	4	0.00067	2	1.46715	1.88675	12	0.281596	30	0.281572	0.2	1.1	2.49	1908	21
154	0.0075	9	0.00029	3	1.46717	1.88673	14	0.281565	26	0.281555	-0.2	0.9	2.52	1917	12

160	0.0120	7	0.00043	2	1.46715	1.88677	12	0.281609	26	0.281599	-15.3	0.9	2.77	1188	53
166	0.0182	3	0.00069	1	1.46716	1.88674	9	0.281606	27	0.281591	-15.6	1.0	2.79	1188	53
168	0.0549	98	0.00176	29	1.46711	1.88689	12	0.281660	29	0.281597	1.0	1.0	2.44	1907	17
169	0.0115	3	0.00043	1	1.46713	1.88687	16	0.281792	25	0.281783	-10.0	0.9	2.44	1135	20
170	0.0319	11	0.00101	1	1.46715	1.88673	13	0.281719	27	0.281686	-0.1	0.9	2.36	1720	26
178	0.0350	50	0.00118	16	1.46712	1.88678	12	0.281646	35	0.281607	-2.2	1.2	2.50	1750	219
179	0.0136	8	0.00050	3	1.46707	1.88690	19	0.281554	42	0.281536	-1.1	1.5	2.56	1909	10

Table 25: Lu-Hf isotope analyses of magmatic zircon grains from orthogneiss (*ZM-12-07; Mwombezi Dome*)

Grain	$^{176}\text{Yb}/^{177}\text{Hf}^a$	$\pm 2s$	$^{176}\text{Lu}/^{177}\text{Hf}^a$	$\pm 2s$	$^{178}\text{Hf}/^{177}\text{Hf}$	$^{180}\text{Hf}/^{177}\text{Hf}$	Sig_{Hf}^b (V)	$^{176}\text{Hf}/^{177}\text{Hf}$	$\pm 2s^c$	$^{176}\text{Hf}/^{177}\text{Hf}_{(t)}^d$	$e\text{Hf}_{(t)}^d$	$\pm 2s^c$	T_{DM2}^e (Ga)	age^f (Ma)	$\pm 2s^c$
107	0.0289	29	0.00099	14	1.46730	1.88666	8	0.280956	36	0.280905	-4.8	1.3	3.39	2711	14
108	0.0449	21	0.00160	10	1.46711	1.88706	9	0.281439	29	0.281381	-6.6	1.0	2.86	1907	14
109	0.0245	11	0.00083	6	1.46712	1.88681	9	0.281438	35	0.281408	-5.4	1.3	2.80	1920	14
100	0.0360	11	0.00144	7	1.46705	1.88711	9	0.281485	30	0.281433	-4.7	1.1	2.76	1910	18
101	0.0278	11	0.00096	5	1.46715	1.88694	10	0.281450	34	0.281415	-4.9	1.2	2.79	1929	21
110	0.0214	17	0.00074	7	1.46714	1.88670	8	0.281395	34	0.281366	-3.9	1.2	2.82	2047	21
112	0.0378	42	0.00136	15	1.46713	1.88713	8	0.281172	46	0.281102	1.7	1.6	3.02	2689	10
111	0.0094	14	0.00030	6	1.46715	1.88701	11	0.281381	32	0.281370	-6.8	1.1	2.88	1917	10
113	0.0297	20	0.00104	7	1.46716	1.88692	7	0.281399	34	0.281358	-3.9	1.2	2.83	2060	17
114	0.0264	21	0.00092	10	1.46702	1.88696	8	0.281414	33	0.281380	-6.4	1.2	2.86	1917	12
115	0.0682	93	0.00226	27	1.46703	1.88685	6	0.281481	30	0.281399	-5.7	1.1	2.82	1920	10
116	0.0086	8	0.00027	3	1.46709	1.88692	10	0.281375	35	0.281366	-6.7	1.3	2.88	1925	14
118	0.0164	23	0.00054	8	1.46709	1.88689	9	0.281375	27	0.281355	-7.0	1.0	2.90	1928	12
119	0.0423	26	0.00139	4	1.46710	1.88687	10	0.281422	29	0.281371	-6.7	1.0	2.88	1917	16
120	0.0298	25	0.00085	12	1.46710	1.88683	9	0.281433	37	0.281402	-5.5	1.3	2.81	1924	16
121	0.0491	49	0.00143	11	1.46706	1.88686	11	0.281462	36	0.281410	-5.3	1.3	2.80	1919	33
122	0.0353	56	0.00117	19	1.46706	1.88688	9	0.281447	36	0.281404	-5.4	1.3	2.81	1924	13
460	0.0252	20	0.00088	8	1.46715	1.88672	9	0.281395	27	0.281362	-5.9	0.9	2.87	1967	22
461	0.0281	22	0.00096	7	1.46715	1.88679	5	0.281429	36	0.281394	-5.0	1.3	2.81	1956	27
462	0.0267	4	0.00095	2	1.46715	1.88679	8	0.281399	31	0.281365	-7.2	1.1	2.89	1906	16
463	0.0242	17	0.00068	5	1.46709	1.88677	10	0.281395	38	0.281371	-7.2	1.4	2.89	1899	24
464	0.0303	26	0.00103	8	1.46721	1.88685	7	0.281449	34	0.281411	-5.3	1.2	2.80	1918	24
466	0.0387	9	0.00134	4	1.46712	1.88671	11	0.281455	36	0.281407	-6.0	1.3	2.82	1892	23

468	0.0303	10	0.00101	3	1.46715	1.88680	9	0.281450	27	0.281414	-5.5	1.0	2.80	1907	19
469	0.0095	7	0.00024	2	1.46712	1.88667	9	0.281399	26	0.281390	-4.3	0.9	2.80	1994	19
474	0.0195	3	0.00072	1	1.46719	1.88697	5	0.281404	32	0.281376	-3.6	1.1	2.81	2044	14
475	0.0258	13	0.00089	5	1.46714	1.88690	9	0.281430	30	0.281397	-5.3	1.1	2.81	1940	28
476	0.0395	10	0.00135	4	1.46711	1.88669	8	0.281449	33	0.281398	-4.1	1.2	2.79	1989	22
478	0.0385	25	0.00133	8	1.46710	1.88675	7	0.281595	33	0.281546	-0.2	1.2	2.53	1933	19
479	0.0192	31	0.00063	11	1.46715	1.88687	8	0.281440	28	0.281417	-5.8	1.0	2.80	1885	31
480	0.0410	18	0.00149	5	1.46712	1.88678	8	0.281423	26	0.281369	-6.5	0.9	2.87	1931	16
486	0.0430	27	0.00155	13	1.46713	1.88686	9	0.281436	29	0.281379	-6.2	1.0	2.86	1925	18
491	0.0279	44	0.00097	15	1.46710	1.88685	9	0.281410	33	0.281376	-7.0	1.2	2.88	1900	18
492	0.0482	59	0.00174	21	1.46716	1.88684	10	0.281468	34	0.281404	-5.5	1.2	2.81	1917	22
495	0.0355	34	0.00127	11	1.46714	1.88676	8	0.281550	27	0.281504	-2.8	1.0	2.63	1883	18
496	0.0331	21	0.00118	9	1.46711	1.88679	8	0.281523	36	0.281482	-4.7	1.3	2.70	1835	39
497	0.0398	30	0.00136	10	1.46708	1.88679	8	0.281552	31	0.281503	-2.1	1.1	2.62	1914	16
498	0.0310	26	0.00109	10	1.46717	1.88694	9	0.281519	29	0.281480	-3.6	1.0	2.68	1884	26
501	0.0589	104	0.00190	34	1.46703	1.88698	7	0.281539	42	0.281470	-3.1	1.5	2.68	1923	25
502	0.0373	29	0.00124	11	1.46712	1.88684	7	0.281553	40	0.281514	-7.4	1.4	2.72	1667	31
503	0.0311	27	0.00107	10	1.46711	1.88675	9	0.281519	37	0.281481	-3.1	1.3	2.67	1906	27
505	0.0477	58	0.00148	19	1.46715	1.88687	7	0.281524	29	0.281470	-3.1	1.0	2.68	1920	22
511	0.0252	38	0.00088	14	1.46717	1.88679	7	0.281549	36	0.281521	-6.6	1.3	2.69	1692	35
523	0.0216	15	0.00080	5	1.46715	1.88685	12	0.281271	29	0.281242	-11.2	1.0	3.12	1924	23
524	0.0142	12	0.00047	4	1.46718	1.88676	12	0.281118	27	0.281101	-16.5	1.0	3.40	1911	20
528	0.0362	24	0.00114	7	1.46717	1.88677	14	0.281542	28	0.281500	-2.1	1.0	2.62	1919	30
526	0.0461	15	0.00176	4	1.46711	1.88735	5	0.281560	34	0.281496	-2.5	1.2	2.64	1910	27
527	0.0339	9	0.00116	3	1.46718	1.88676	7	0.281548	28	0.281506	-2.1	1.0	2.62	1912	26
533	0.0205	44	0.00068	17	1.46715	1.88671	8	0.281442	32	0.281418	-5.0	1.1	2.78	1920	19
532	0.0331	34	0.00109	14	1.46716	1.88668	14	0.281459	28	0.281419	-5.2	1.0	2.79	1910	19
535	0.0186	9	0.00060	3	1.46717	1.88680	15	0.281517	28	0.281496	-2.6	1.0	2.64	1904	24
536	0.0171	4	0.00054	1	1.46716	1.88671	14	0.281529	26	0.281510	-2.1	0.9	2.61	1905	49

Table 26: Lu-Hf isotope analyses of magmatic zircon grains from granite (ZM-12-25; Mwombezhi Dome)

Grain	$^{176}\text{Yb}/^{177}\text{Hf}$ ^a	$\pm 2s$	$^{176}\text{Lu}/^{177}\text{Hf}$ ^a	$\pm 2s$	$^{178}\text{Hf}/^{177}\text{Hf}$	$^{180}\text{Hf}/^{177}\text{Hf}$	Sig_{Hf} ^b (V)	$^{176}\text{Hf}/^{177}\text{Hf}$	$\pm 2s$ ^c	$^{176}\text{Hf}/^{177}\text{Hf}_{(0)}$ ^d	$\text{eHf}_{(0)}$ ^d	$\pm 2s$ ^c	T_{DM2} ^e (Ga)	age^f (Ma)	$\pm 2s$ ^c
206	0.0466	40	0.00186	14	1.46715	1.88727	9	0.281675	33	0.281628	-10.6	1.2	2.64	1352	11
213	0.0344	28	0.00138	10	1.46705	1.88699	8	0.281683	41	0.281642	-4.5	1.5	2.50	1598	70
219	0.0411	10	0.00169	7	1.46716	1.88669	10	0.281688	37	0.281649	-12.8	1.3	2.66	1220	17
220	0.0408	8	0.00175	4	1.46701	1.88704	8	0.281679	30	0.281635	-10.6	1.1	2.63	1340	13
223	0.0579	22	0.00196	6	1.46699	1.88685	7	0.281682	32	0.281621	-4.2	1.1	2.52	1639	49
224	0.0320	12	0.00138	6	1.46708	1.88701	10	0.281657	34	0.281622	-10.9	1.2	2.66	1347	17
225	0.0376	4	0.00158	1	1.46708	1.88701	10	0.281692	28	0.281651	-9.0	1.0	2.58	1384	20
229	0.0399	35	0.00152	13	1.46718	1.88698	10	0.281692	31	0.281657	-12.6	1.1	2.65	1218	47
231	0.0236	26	0.00080	9	1.46710	1.88688	6	0.281642	33	0.281621	-10.1	1.2	2.64	1385	52
248	0.0436	11	0.00184	5	1.46710	1.88685	10	0.281701	34	0.281653	-9.5	1.2	2.59	1360	24
249	0.0435	40	0.00147	11	1.46712	1.88698	8	0.281689	35	0.281636	2.1	1.3	2.37	1892	34
252	0.0483	15	0.00207	7	1.46708	1.88701	10	0.281717	33	0.281666	-10.5	1.2	2.59	1296	18
253	0.0296	27	0.00122	14	1.46705	1.88676	6	0.281658	37	0.281617	-1.3	1.3	2.47	1776	40
254	0.0327	19	0.00124	4	1.46715	1.88673	7	0.281656	34	0.281610	2.0	1.2	2.40	1928	43
256	0.0472	26	0.00201	12	1.46713	1.88675	8	0.281674	30	0.281621	-9.8	1.1	2.63	1398	19

PARTIE II :
FORMATION DES
CEINTURES
OROGENIQUES PAN-
AFRICAINES

CHAPITRE 3: Le cycle orogénique Pan-Africain

1. Cycle orogénique: définition

Au cours des temps géologiques, les déplacements des masses continentales, sous l'influence des mouvements mantelliques, peuvent être décrits de manière cyclique. C'est en 1966 que J. T. Wilson propose que tout bassin océanique prenne naissance à l'intérieur d'un continent, d'un rift continental puis s'agrandit entre les marges continentales passives. Par la suite, la subduction de la lithosphère océanique, le long de l'une au moins des marges devenue active, induit la fermeture de ce domaine océanique jusqu'à la collision finale de deux masses continentales, entraînant la création de relief (orogénie ou orogénèse) à la limite de plaques. Seule une suture ophiolitique témoigne de la disparition d'ancien domaine océanique. Ainsi est né le cycle de Wilson qui se décompose donc en différents intervalles de temps reflétant différents contextes géodynamiques :

- Rifting continental
- Ouverture d'un domaine océanique
- Expansion de l'océan
- Subduction sous une marge continentale/océanique
- Collision

Chaque fin de cycle de Wilson est caractérisée par la réunification des ensembles continentaux en supercontinents. Chaque formation d'un supercontinent entraîne la disparition d'une portion de lithosphère océanique et, simultanément, permet la formation de terrains de haut-grade métamorphique dans les zones de collision. Après quelques millions d'années, ces supercontinents vont se fragmenter sous l'influence de plumes mantelliques gigantesques, ou superplumes. Parmi les supercontinents formés lors de l'histoire géologique de la Terre, on trouve le Columbia (~1.9 Ga), la Rodinia (~1.0 Ga) et le Gondwana (~0.5 Ga). Ainsi, les ceintures Pan-Africaines se sont formées suite à la fragmentation du supercontinent Rodinia lors de la formation du Gondwana.

2. Le supercontinent Rodinia

Durant les dernières décennies, les auteurs se sont accordés sur l'existence d'un supercontinent au Méso-Néoprotérozoïque (1000-725 Ma), connu sous le nom de Rodinia, du terme russe « rodit » qui signifie « donner naissance » (McMenamin and McMenamin, 1990). Une année plus tard, de nombreux travaux apportent des informations précieuses sur la géométrie et l'âge de ce supercontinent (Dalziel, 1991 ; Hofmann, 1991 ; Moores, 1991). Cependant, l'âge et la géométrie de ce supercontinent est encore un vaste sujet de discussion et les modèles de reconstitution ne cessent d'évoluer au fur et à mesure de l'acquisition de nouvelles données, principalement paléomagnétiques et géochronologiques. Un point commun aux différentes reconstitutions proposées dans la littérature est la juxtaposition de la marge Est du continent Laurentia (Amérique du Nord) avec les cratons d'Amazonie et Baltique, et la juxtaposition de la marge Ouest Laurentia avec le bloc Est Gondwana (Australie, Est Antarctique, Inde, Madagascar et Sri-Lanka). Le continent Laurentia est supposé rester au centre du Rodinia au cours de son évolution (Hofman, 1991). La consolidation du supercontinent Rodinia est marquée par un ensemble d'orogènes d'âge Mésoprotérozoïque à Néoprotérozoïque inférieur (~1400-900), dénommées sous le terme d'orogènes Grenvilliennes. La fragmentation du Rodinia est marquée par une extension crustale et la formation de bassins sédimentaires en Australie et Laurentia. La rupture du supercontinent Rodinia est principalement amorcée par l'ouverture de l'océan Paléo-Pacifique entre les continents Laurentia et East Antarctica-West Australia (Unrug, 1997 ; Cordani et al., 2003). L'ouverture de ce domaine océanique permettant la séparation en deux du supercontinent Rodinia est daté à 720 Ma, âge basé sur des données paléo-magnétiques (Powell et al., 1993). Cependant, ce modèle peut être sujet à discussion quant au regard du peu de données paléomagnétiques disponibles dans la littérature pour reconstruire le trajet de ces microcontinents (Meert and Torsvik, 2003). En ce qui concerne l'histoire du futur continent West Gondwana, la position du craton du Congo-Sao Francisco est sujette à débat. Certains auteurs suggèrent que ce craton n'ait jamais été associé au supercontinent Rodinia (Kröner and Cordani, 2003 ; Figure 22). D'autres auteurs soulignent que la présence de terrains d'âge Mésoprotérozoïque remobilisés au cours de l'orogène Grenvillienne le long de la chaîne des Irumides et de la marge du bloc de Rio de la Plata pourrait indiquer que ces masses continentales furent intégrées au sein du supercontinent Rodinia (De Waele et al., 2008 ; Fuck et al., 2008).

Dans cette configuration, le bloc Rio de la Plata serait probablement encastré entre le craton du Congo-Sao Francisco et la Laurentia (D'Agrella-Filho et al., 2004 ; Weil et al., 1998).

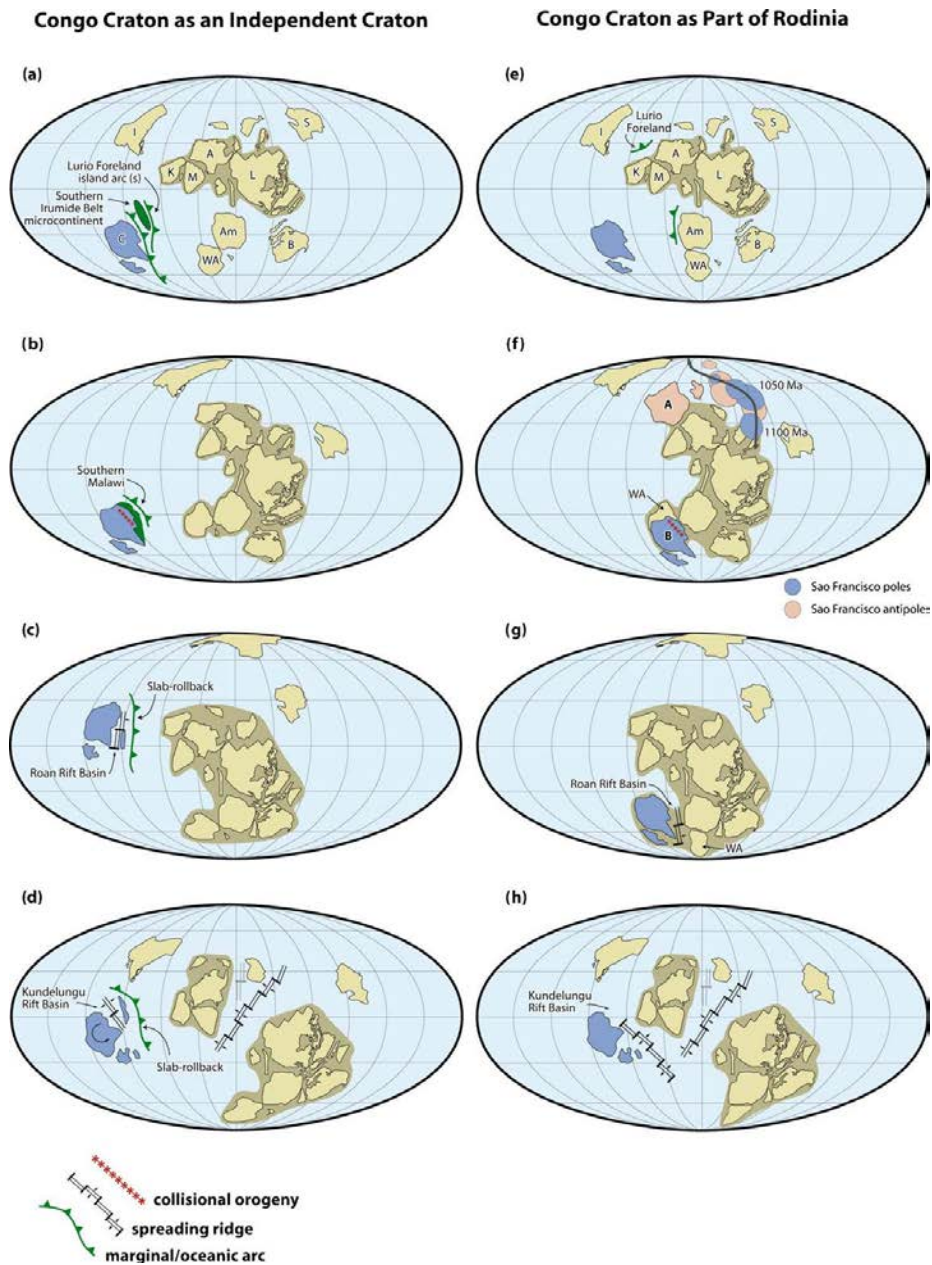


Figure 22: Reconstitutions paléo-géographiques, d'après De Waele et al. (2008) présentant deux modèles possibles de l'évolution du craton du Congo-Sao Francisco à différents intervalles de temps : à 1050 Ma (a et e), à 1020 Ma (b et f), à 880 Ma (c et g) et à 760 Ma (d et h). Abréviations : A = Australia ; Am = Amazonia ; B = Baltica ; C = craton Congo-Sao Francisco; I = India; K = Kalahari; L = Laurentia; M = Mawson Craton (Antarctique); S = Siberia; WA= West-Africa.

Quant à la place du bloc du Kalahari dans la configuration du Rodinia, sa position lors des reconstitutions est variable (Figure 23). Certains auteurs considèrent qu'il occupait une position équatoriale dans la configuration du Rodinia (Renne et al., 1990 ; D'Agrella-Filho et al., 1998) alors que d'autres proposent de la localiser dans l'hémisphère sud, relié au craton de Congo-Sao Francisco (Dalziel, 1992 ; Meert and Van Der Voo, 1997 ; Li et al., 2008) ou encore dans une position séparée (Weil et al., 1998).

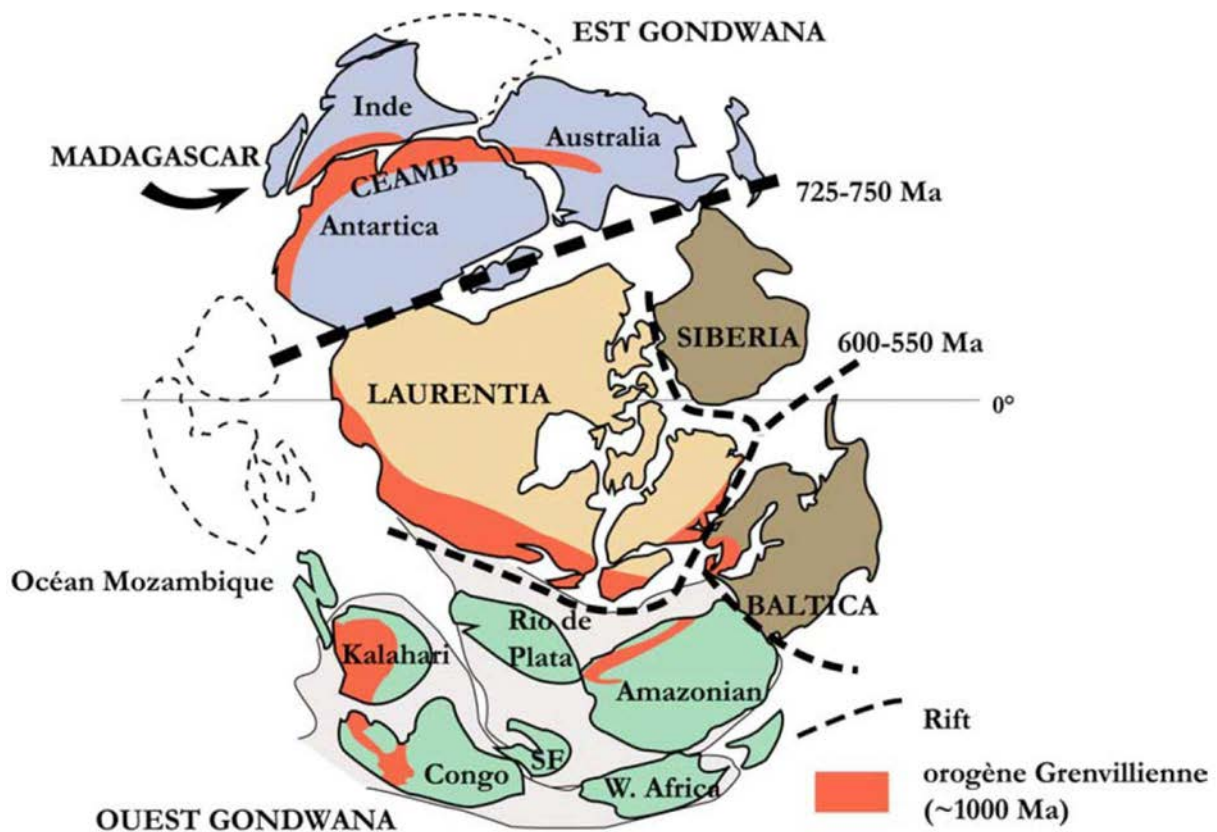


Figure 23: Reconstitution paléogéographique du supercontinent Rodinia à 750 Ma (Dalziel, 1997). Dans les reconstitutions plus récentes de Torsvik et al. (1996) le bloc West Gondwana est éclaté en plusieurs fragments et les cratons du Kalahari et Congo sont localisés approximativement à la jonction Antarctique-Laurentia (en pointillé sur la figure).

3. Le supercontinent Gondwana

L'existence et l'histoire du supercontinent Gondwana durant le Paléozoïque et sa fragmentation au cours du Mésozoïque à l'origine des continents Afrique, Amérique du Sud, Antarctique, Australie et Inde est désormais très bien établie (Figure 24). La formation du supercontinent Gondwana est également associée à des événements géodynamiques qui impliquent la fermeture de domaine océanique par subduction, impliquant des stades de collisions continentales d'anciens blocs crustaux datés de l'Archéen au Mésoprotérozoïque (Unrug, 1997). Les événements datés entre 1000 et 720 Ma, postérieurs à la formation du supercontinent Rodinia, mais antérieurs à sa dislocation totale, sont représentés par des manifestations magmatiques, type superplume (Dalziel, 1991, 1992 ; Trompette, 2000 ; Li et al., 2008), post-tectoniques accompagnées par la formation de rifts intracontinentaux (Unrug, 1997). La fragmentation du Rodinia et la fermeture de l'océan Mozambique aboutiraient à la consolidation du supercontinent Gondwana au Néoprotérozoïque (Hoffman, 1991 ; Powell et al., 1993 ; Meert and Van Der Voo, 1997). La chaîne du Mozambique correspondrait à une structure Nord-Sud qui s'étend depuis le Mozambique jusqu'au Kenya et Ouganda, relayée au nord par le bouclier Arabo-Nubien. Stern (1994) associe ces deux structures (Chaîne du Mozambique et bouclier Arabo-Nubien) sous le même nom d'Orogenèse Est Africaine, datée entre 800 et 650 Ma.

La vision que la formation finale du supercontinent Gondwana est matérialisée par la collision entre deux continents, West et East Gondwana (Shackleton, 1986) suite à la fermeture de l'océan Mozambique, est un peu simpliste (Meert, 2001). De nombreuses études basées sur des données paléo-magnétiques ont permis de prouver que certains blocs continentaux n'étaient encore pas accrétés au continent West Gondwana au milieu du Cambrien (Tohver et al., 2006). Par exemple, Meert (2003) décrit qu'il serait peut être plus judicieux de décrire la formation du Gondwana comme une amalgamation des continents Nord (cratons de Sao Francisco-Congo-India) et Sud (cratons Kalahari-Antarctica) Gondwana durant l'orogénèse du Kuunga (550-530 Ma). Dans la suite du manuscrit, nous considérons que la ceinture Damara-Lufilien-Zambezi fait partie intégrante du continent West Gondwana selon le modèle de Shackleton (1986).

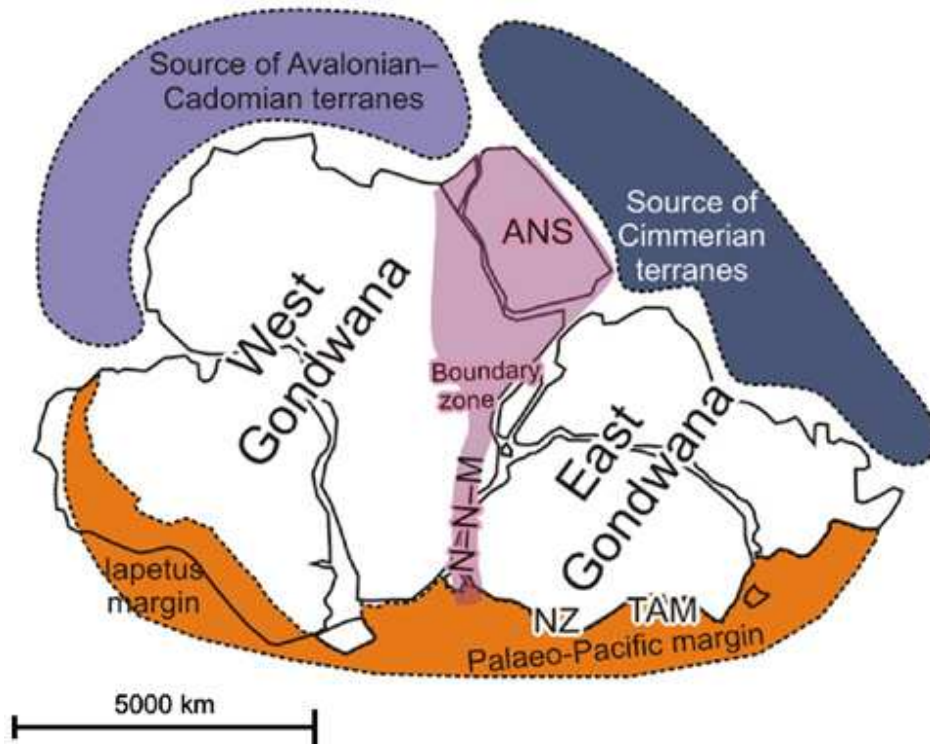


Figure 24: Reconstitution du supercontinent Gondwana (d'après Unrug 1997; Vaughan and Pankhurst, 2008). La partie grisée correspond à la limite entre les continents West et East Gondwana. Abréviations : NZ = Nouvelle-Zélande, TAM = Montagnes Trans-antarctiques, ANS = Bouclier Arabo-Nubien, N-N-M = Ceinture du Namaqua-Natal-Maud.

4. Qu'entend-t-on par continent West Gondwana?

Le continent West Gondwana est aujourd'hui représenté en Amérique du Sud, Arabie, Afrique et à l'est de l'Antarctique. Historiquement, cette différenciation entre West et East Gondwana a été proposée par Du Toit (1937). Ce continent est composé de boucliers d'âge Archéen, de cratons ou fragments cratoniques d'âge Archéen à Mésoprotérozoïque, de ceintures orogéniques mobiles d'âge Néoprotérozoïque-Cambrien et ainsi que des ceintures orogéniques plus tardives qui ont permis l'accrétion de terrains d'âge Paléozoïque à Mésozoïque (Unrug, 1997 ; Pankurst et al., 1998 ; Brito Neves et al., 1999 ; Vaughan and Storey, 2000 ; Murphy et al., 2004 ; Tohver et al., 2006). Les éléments cratoniques comprennent le craton Amazonia-West Africa, le craton Sao Francisco-Congo, le craton Kalahari-Grunehogna, le craton Rio de la Plata ainsi que le bouclier Arabian-Nubian (Tohver et al., 2006 ; Figure 25). Certaines zones décrites dans la littérature comme une « province remaniée » pourraient représentées un ensemble de

mini-cratons et de mini-chaînes, au NE du Brésil (Brito Neves and Cordani, 1991), ainsi que des vestiges d'un ancien craton parfois appelé métacraton du Sahara (Liégeois et al., 1994). Le terme Brasiliano/Pan-African belt a été proposé par Brito Neves et al. (1999) et est réservé pour les ceintures ayant permis la formation complète du continent West Gondwana. Au total, 19 ceintures orogéniques ont été décrites permettant cette formation continentale. La limite entre les continents West et East Gondwana étant matérialisée par la ceinture orogénique Est Africaine s'étendant, au nord, du bouclier Arabo-Nubien jusqu'au fragment cratonique East Antarctic, au sud (Stern, 1994).

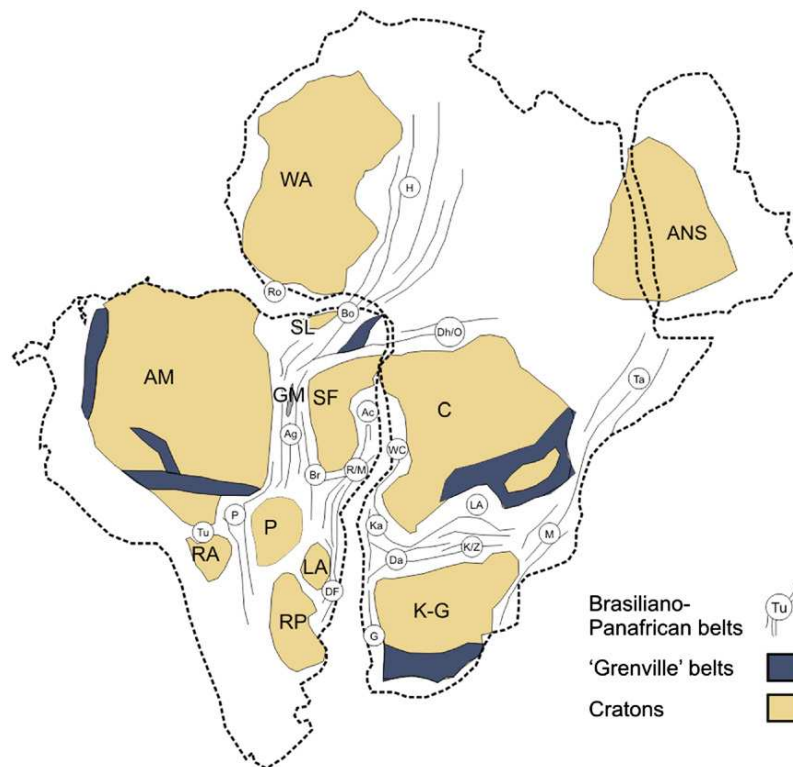


Figure 25: Reconstitution du continent West Gondwana (d'après Tohver et al., 2006; Vaughan and Pankhurst, 2008). Cette carte présente les différents cratons ainsi que les ceintures Brasiliano-Pan African. Les cratons sont représentés en jaune clair, on distingue : AM = Amazonia ; ANS = Bouclier Arabo-Nubien ; C = Congo ; GM = Massif du Goiás ; K-G= Kalahari-Grunchogna ; LA = Luis Alves ; P = Parana ; RA = Rio Apa ; SF = Sao Francisco ; SL = Sao Luis ; WA = West Africa. Les ceintures Bresilinao-Pan African sont représentés en traits fins : Ac = Araçuaí ; Ag = Araguaia ; Bo = Borborema ; Br = Brasília ; Da = Damara ; DF = Dom Feliciano ; Dh/O = Dahomeides/Oubangides ; G = Gariép ; H = Hoggar ou Trans-Sahara ; Ka = Kaoko ; K/Z = Katangan/Zambezi ; LA = Lufilian belt ; M = Mozambique ; P = Paraguay ; R/M = Ribeira/Mantequeira ; Ro = Rokelides ; Ta = Tanzania ; Tu = Tucavaca ; WC = West Congo.

5. Les ceintures orogéniques du West Gondwana

5.1. Les ceintures orogéniques précoces à cycle long (1000-600 Ma)

Ces ceintures ont été dénommées *old long-lived belts* ou ceintures de type O-LL et comprennent, sur le continent West Gondwana, les structures suivantes : les chaînes Trans-Saharienne ou Hoggar, Brasilia, Dom Feliciano, Gariep, Ribeira-Mantiqueira et Dahomeides-Oubanguide (Trompette, 1997 ; 2000), quant à la ceinture du Damara-Lufilian-Zambezi, initialement interprétée comme une chaîne intracontinentale (Porada and Wittig, 1983), fait probablement partie de cette catégorie de ceinture (Gray et al., 2006). La formation de ces ceintures orogéniques est associée à la fermeture de principaux domaines océaniques. Les zones de suture témoignant de la présence de paléo-océans sont identifiées sur la base des arguments suivants :

- (i) Présence de complexes mafiques et ultramafiques interprétés comme des sutures ophiolitiques. Ces complexes ont été identifiés dans les chaînes Brasilia (Drake, 1980) et Dahomeides-Oubanguide (Penaye et al., 1993 ; Poidevin, 1985). La ceinture amphibolitique du Matchless dans la chaîne du Damara témoignerait également la présence d'un paléo-océan (Kasch, 1983 ; Gray et al., 2006) ;
- (ii) Magmatisme calco-alcalin à l'aplomb des zones de subduction d'une croûte océanique. Ce type de magmatisme a été caractérisé pour les chaînes Trans-Saharienne ou Hoggar (Chikhaoui et al., 1980) et Dom Feliciano (Fernandez et al., 1992) ;
- (iii) Métamorphisme granulitique de haute pression, décrit dans les chaînes Trans-Saharienne ou Hoggar (Caby, 1987), de Gariep (Kröner, 1975) et Dahomeides-Oubanguide (Barbey et al., 1990 ; Nzenti et al., 1984 ; Poidevin, 1985) ;
- (iv) Anomalies gravimétriques et magnétiques soulignant la juxtaposition de portions lithosphériques distinctes. Ceci est le cas pour les chaînes Trans-Saharienne ou Hoggar (Bayer and Lesquer, 1978 ; Caby, 1987), Brasilia (Lesquer et al., 1981) et Dahomeides-Oubanguide (Regan and Marsh, 1982).

Ces différentes zones de suture permettent d'identifier quatre grands ensembles réunis dans le cadre de l'assemblage du West Gondwana constitués (i) des cratons West Africa-Ama-zonia et

Rio de la Plata, (ii) du craton de Congo-Sao Francisco, (iii) du bloc Kalahari et (iv) de la « Province Remaniée ». Le formation de ces ceintures a donc impliqué la fermeture de divers domaines océaniques dont l'océan Adamastor entre les cratons West Africa, Amazonia et le bloc du Rio de la Plata, d'une part, et le craton du Congo-Sao Francisco d'autre part, l'océan Damara ou Khomas entre les cratons du Kalahari et du Congo-Sao Francisco, l'océan Trans-Sahara entre le craton West Africa, Amazonia et le méta-craton du Sahara (Gray et al., 2008).

5.2. Les ceintures orogéniques récentes à cycle court (600-520 Ma)

Ces ceintures sont décrites principalement comme des chaînes intracontinentales, voire avec une océanisation très peu développée. Elles sont appelées young short-lived belts ou Y-SL. Elles peuvent être représentées par les chaînes Araçuaí ou encore Paraguay (Trompette, 2000). La fermeture de domaines intracontinentaux est spatialement et génétiquement liée aux chaînes de type O-LL. Elles seront parfois interprétées comme des structures précoces de rupture avortée du supercontinent Gondwana vers 600 Ma (Trompette, 1997). Ces ceintures orogéniques marquent une tendance générale à la dislocation de l'ensemble constitué des cratons West Africa-Amazonia et du bloc de Rio de la Plata en trois entités distinctes.

5.3. Chronologie des évènements associés à l'assemblage du West Gondwana

Les évènements d'accrétion et de collision qui ont abouti à la formation du continent West Gondwana sont datés dès 850 Ma et ce jusqu'à la fin du Cambrien, vers 490 Ma (Brito Neves et al., 1999). L'évènement majeur enregistré par le continent West Gondwana est la collision entre l'ensemble formé des cratons West Africa, Amazonia et le bloc du Rio de la Plata, d'une part, et le craton de Congo-Sao Francisco, d'autre part (Hofman, 1991). Cette collision permet de rassembler, avant 600 Ma (Trompette, 2000), deux entités initialement contigües dans la configuration du Rodinia séparées vers 900 Ma lorsque le craton de Congo-Sao Francisco s'est détaché de la Laurentia. La zone de collision entre le craton de Congo-Sao Francisco, le bloc du Kalahari et le bloc du Rio de la Plata est plus complexe et plus ancienne (Fernandez et al., 1992 ; Trompette, 1997). La déformation associée à cette collision est assez diachrone, datée à 630 Ma dans le sud de la chaîne de la ceinture Ribeira-Mantiqueira, 640-620 Ma et 700 Ma respectivement au nord et au sud de la chaîne Dom Feliciano, 550-600 Ma dans les ceintures de

Gariép et Malmesbury (Trompette, 1997). La collision entre le craton de Congo-Sao Francisco avec la province remaniée n'opère que quelques millions d'années après, entre 600 et 580 Ma (Caby and Arthaud, 1987 ; Pimentel and Fuck, 1992). L'âge de la collision à l'origine de la chaîne Damara est controversé. Martin and Porada (1977) proposent un âge Cambrien inférieur à moyen tandis que Kröner (1982) décrit une évolution polyphasée, avec une phase précoce, qui pourrait être située entre 675 et 575 Ma, sur la base d'âge Rb-Sr. L'accrétion de nouveaux blocs crustaux a été active durant toute la période d'amalgamation (Cawood, 2005) et est restée continue jusqu'aux derniers épisodes de dislocation du continent West Gondwana (Vaughan et al., 2002).

5.4. Présentation de la ceinture du Damara-Lufilien-Zambezi

Les ceintures orogéniques du Damara-Lufilien-Zambezi forment un ensemble linéaire, toutefois masqué par des sédiments d'âge Phanérozoïque, entre les ceintures du Damara, du Lufilien et du Zambezi. Ce segment orogénique délimite actuellement les cratons du Congo, au nord, et du Kalahari, au sud. Ces trois ceintures orogéniques ont permis l'amalgamation des cratons Congo-Sao Francisco et Kalahari suite à la fermeture d'un ou plusieurs domaines océaniques, connus sous les noms d'océan Khomas, ceinture du Damara (Gray et al., 2008), et Zambezi, ceintures du Lufilien-Zambezi (John et al., 2004).

L'histoire de ce cycle Pan-Africain commence par un rifting continental et une sédimentation, dominée par des séries silicoclastiques, datées vers 880 Ma pour le Lufilien (Lower Roan Group ; Porada and Berhorst, 2000)-Zambezi (Kafue Rhyolite formation ; Johnson et al., 2007) et 840 Ma pour le Damara (Etusis formation ; Tegtmeyer and Kröner, 1985). Il s'agit alors de la fragmentation intracontinentale du supercontinent Rodinia. Certains auteurs ont décrits ces ceintures orogéniques comme des rifts avortés, n'ayant pas évolué depuis le stade intracontinental en domaine océanique et décrivant alors une formation de chaîne dite intra-cratonique ou ensialique (Porada and Wittig, 1983). Cependant, à la lumière de données paléomagnétiques, Gray et al. (2008) confirme que les cratons du Congo et du Kalahari étaient séparés d'une latitude de 30° par un océan de dimensions inconnues, entre 780 et 740 Ma. Ceci permet de contredire la formation et le développement de chaînes intra-cratoniques tout au long du cycle Pan-Africain,

modèle évoqué pour la ceinture du Damara-Lufilien-Zambezi. Dans la ceinture Damara, la formation d'un océan est notamment confirmée par la présence d'une zone riche en amphibolite, caractérisée par une signature géochimique de type MORB, connue sous le nom de Matchless belt, et interprétée comme le vestige d'une croûte océanique (océan Khomas ; Killick, 2000). Dans la ceinture Zambezi, des données géochimiques sur des éclogites et des gabbros confirment une affinité géochimique de type MORB et témoignent également de la présence d'un océan (océan Zambezi ; John et al., 2003). Dans la ceinture du Lufilien, les quelques travaux effectués sur les gabbros et méta-gabbros affleurant au nord-ouest de la région n'ont pas permis d'identifier le stade d'océanisation (Tembo et al., 1999).

Cependant, les auteurs ne s'accordent pas sur le fait qu'il y ait eu un seul ou plusieurs domaines océaniques séparant les cratons du Congo-Sao Francisco et du Kalahari. De plus, la vergence de la subduction est également contradictoire impliquant pourtant la collision entre deux mêmes entités continentales aussi bien, à l'ouest, dans la ceinture du Damara qu'à l'est, dans la ceinture de Zambezi. Kasch (1983 ; Figure 26) propose une subduction vers le nord ou le nord-ouest du craton Kalahari sous le craton du Congo pour la ceinture du Damara alors que John et al. (2003) propose une subduction vers le sud du craton du Congo sous le craton du Kalahari pour la ceinture du Lufilien-Zambezi (Figure 27). Cependant, la convergence crustale due à la subduction entre ces deux entités cratoniques semble être synchrone, se déroulant entre 580 et 560 Ma dans la ceinture du Damara (Gray et al., 2006) et entre 600 et 570 Ma dans la ceinture du Lufilien-Zambezi (John et al., 2003). La fermeture complète du domaine océanique du Khomas par collision continentale se serait déroulée vers 540 Ma dans la zone centrale de la ceinture du Damara (Jacob et al., 2000) et vers 530 Ma dans la zone interne de la ceinture du Lufilien-Zambezi (John et al., 2004).

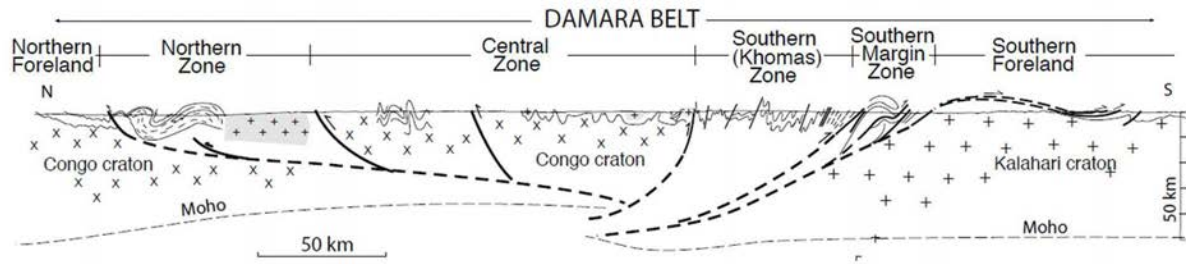
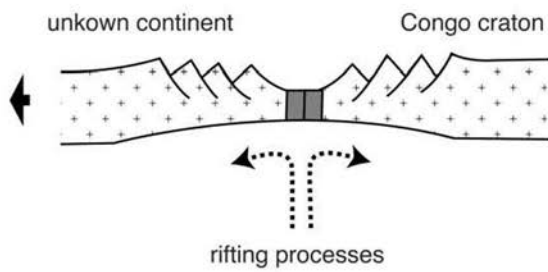
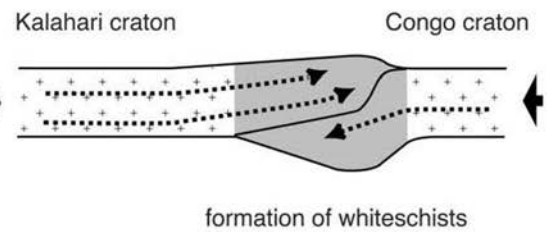


Figure 26: Coupe géologique au 1 : 500 000 de la ceinture du Damara (Miller and Grote, 1988).

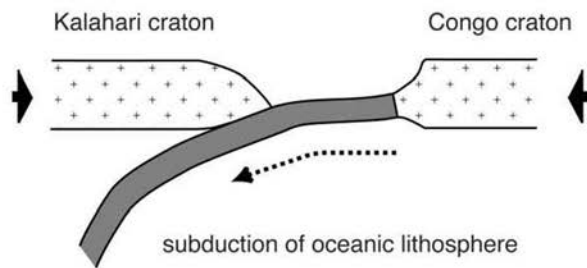
a) extension since ca. 880 Ma
- ocean floor formation



c) continental collision at ca. 530 Ma
- HP / LT metamorphism



b) convergence
- eclogite formation at ca. 600 Ma



d) cooling since 530 Ma
- uplift and erosion

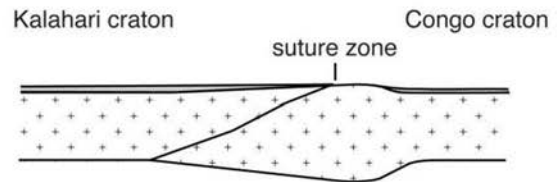


Figure 27: Illustration de l'évolution de la ceinture du Lufilien-Zambezi au cours du cycle Pan-Africain (John, 2001).

CHAPITRE 4: Tectonic evolution of the internal orogenic zone of the Pan-African Lufilian belt (Zambia): Structural, petrologic, thermobarometric and U-Pb-Th, Lu-Hf and Sm-Nd isotopic constraints

Aurélien Eglinger¹ ; Olivier Vanderhaeghe¹ ; Anne-Sylvie André-Mayer¹ ; Armin Zeh² ; Cyril

Durand³ ; Philippe Goncalves⁴ ; Marc Pujol⁵ ; Mike Richards⁶

Article en préparation pour *Journal of African Earth Sciences*

¹GeoRessources, UMR 7359, CNRS-CREGU, Université de Lorraine, Nancy, France

²Institute of Geosciences, Johann Wolfgang Goethe-University, Frankfurt am Main, Germany

³Géosystèmes, UMR 8217, Université de Lille 1, Lille, France

⁴Chrono-Environnement, UMR 6249, Université de Franche-Comté, Besançon, France

⁵Géosciences Rennes, UMR 6118 CNRS-Université de Rennes 1, Rennes, France

⁶Barrick Limited, Lumwana mine, Zambia

Abstract

The Lufilian-Zambezi belt formed during the Pan-African orogeny, at ca. 0.5 Ga, between the Congo and the Kalahari cratons. Several contrasting geodynamic models were published to explain the nature of this orogenic belt from the development of an intracratonic orogenic belt to the development of a collisional orogenic belt following an oceanic basin closure. The extensive occurrences of kyanite-talc micaschists (whiteschists) described in the Lufilian and the Zambezi belts require high P - T conditions, probably in agreement with a collision-type orogen. However, uncertainties remain regarding the evolution of the Lufilian belt compared to the Zambezi belt, the deformation style and the nature of the gneissic-migmatitic windows exposed in the Domes region of the Lufilian belt. This study is focused on the Mwombezi and the Solwezi domes in Zambia where gneissic-migmatitic windows surrounded by kyanite±talc micaschists were described and attributed to basement inliers. In this paper, we combine petrography, U-Pb and Lu-Hf geochronology, Hf and Nd isotopes analyses and geothermobarometry in order to (i) constrain the timing of the pre- to syn-collisional evolution of the Lufilian belt, (ii) discuss the relation between migmatitic-gneissic windows and the micaschist units and (iii) integrate their metamorphic evolution in a geodynamic model.

We propose that the south margin of the Congo-Bangweulu craton was boudinaged during the Rodinia dislocation up to ca. 720 Ma leading the formation of an intracratonic basin (Roan-Kundelungu basin), in the north, and an oceanic basin (Zambezi ocean) to the south. Plate convergence was first accommodated by oceanic subduction and was followed by continental subduction dated at ca. 555-525 Ma recorded by both migmatite-gneiss and kyanite±talc micaschist units with P - T conditions at ca. 9 kbar and 620 °C. Due to the low density of the continental crust, crustal basement inliers were exhumed during the final stage of the continental collision between ca. 510-470 Ma.

Keywords: Pan-African; P - T - t conditions; continental subduction; Domes region

1. Introduction

Contrasting geodynamic models have been proposed for the initial structure of lithosphere that separated the Congo-Kalahari cratons before the development of the Lufilian-Zambezi belts and, thus, several tectonic models have been proposed to explain the Pan-African orogeny in this region. Early tectonic models invoked the development of an intracratonic orogenic belt between the Congo and Kalahari cratons based on the apparent absence of an oceanic suture (Daly, 1986; Hanson et al., 1994). Accordingly, the Lufilian belt has been interpreted to represent an inverted rift characterized by the reworking of the Katanga sedimentary sequence typical of a rift environment (Tembo et al., 1999; Porada and Behorst, 2000). A same geodynamic evolution has been proposed for the Damara orogenic belt in Namibia (Porada and Wittig, 1983). More recently, opening of an oceanic realm has been argued on the basis of the presence of associations of mafic rocks with black shales such as the Khomas complex in the Damara belt (Kukla et al., 1991; Hoffmann et al., 2004) and in the Zambezi belt (John et al., 2003). The presence of an oceanic domain separating the Congo and Kalahari cratons is further corroborated by paleomagnetic data (Meert et al., 1995). The mafic rocks in the Zambezi belt have been affected by Eclogite facies metamorphism dated at ca. 600 Ma (Sm-Nd whole-rock and garnet isochron) implying burial by subduction (John et al., 2003). Furthermore, the invoked style of tectonic accretion is very different from one publication to the other. Authors that have been working mainly in the external zone of the Lufilian belt favor a tectonic style marked by rift inversion associated with thin-skin tectonics and decollement of the Katanga sedimentary cover relative to the pre-Katanga basement (Porada and Behorst, 2000). In contrast, authors that have studied the internal zone emphasize the complex ductile deformation and depict a complex nappe structure characterized by isoclinal folds and coeval high-pressure/low-temperature metamorphism (Cosi et al., 1984; Johnson and Oliver, 1998, 2002; John et al., 2004).

Accordingly, debated issues regarding the tectonic evolution of the internal zone of the Lufilian belt encompass (i) the nature (continental or oceanic) of the transitional crust between the Congo and the Kalahari cratons before development of the Lufilian belt, (ii) the significance of the current-day contact between the migmatitic gneisses coring the domes and the metasedimentary sequence mantling the domes, namely whether it represents a low-grade

decoulement reworking a former basement/cover unconformity or a complexly folded lithologic contact in a nappe pile.

To improve understanding of the Lufilian belt, from the pre- to syn-collisional stages, we sampled, in Domes region (Zambia), basal Neoproterozoic metasedimentary cover and some magmatic rocks associated with these metasediments in the Solwezi area (presented in this paper as the mantling rocks). We sampled also gneissic-migmatitic metasediments and amphibolites in the Mwombezhi area attributed to the basement (presented as the core rocks). We present here new whole-rock, trace element compositions, geochronological and isotopic data coupled with *P-T* estimates in order (i) to discuss the timing and the evolution of the rifting stage(s) and (ii) to integrate the *P-T-t* evolution recorded by the Neoproterozoic metasediments and the gneissic-migmatitic dome cores during the Pan-African orogeny.

2. Regional geology

The Lufilian belt is part of the Neoproterozoic-Cambrian Brasiliano-Pan-African belts (Brito Neves et al., 1999), associated with the amalgamation of the West Gondwana supercontinent. Brasiliano-Pan-African belts result from the collision of several continental blocks including the Arabian-Nubian shield, the Amazonia-West Africa, the Sao Francisco-Congo, the Kalahari-Grunehogna and the Rio de la Plata cratons (Tohver et al., 2006; Figure 28). More specifically, the Lufilian orogenic belt formed during the Pan-African orogeny between the Kalahari craton at South and the Congo craton at North (Unrug, 1983, 1997; John et al., 2004; Johnson et al., 2005). This belt forms an arc marking the transition between the Damara belt in Namibia and the Zambezi belt in Zimbabwe. The Damara-Lufilian-Zambezi orogen marks a Neoproterozoic suture, the site of a major ocean basin whose closure was an integral component of the assembly of West Gondwana (Johnson et al., 2005). The southern and eastern margins of the Congo craton comprise (i) different Archean blocks including the Angola-Kasai blocks and the Tanzania craton surrounded (ii) by Paleoproterozoic belts, the Ubendian belt and Bangweulu block, and (iii) by Mesoproterozoic belts, the Kibaran and Irumide belts (De Waele et al., 2008).

On the basis of paleomagnetic and isotopic data, insufficient evidence is available to support or deny the amalgamation of the Congo Craton during the Rodinia supercontinent formation

(Johnson et al., 2005; De Waele et al., 2008). The northern margin of the Kalahari craton is composed by the Zimbabwe and the Kaapvaal cratons surrounded by a Paleoproterozoic event, the Magondi belt, and a Mesoproterozoic event including the Choma Kalomo block (De Waele et al., 2006, 2008). The Kalahari craton was a component of the Rodinia supercontinent, associated with Australia, Antarctica and South China (e.g. Dalziel, 1997; Li et al., 2003; Loewy et al., 2003; Pisarevsky et al., 2003). The southern boundary of the Lufilian belt is marked by the sinistral Mwembeshi dislocation shear zone (MSZ) between the Lufilian and the Zambezi belts (De Swardt et al., 1965; Hanson et al., 1993). This shear zone is variably interpreted as a weakness zone in the lithosphere of Paleoproterozoic age (Porada and Berhorst, 2000), as a transform-type plate boundary, or as a suture (Coward and Daly, 1984; Daly, 1986).

The external zone of the Lufilian belt is characterized by a Neoproterozoic sedimentary and metasedimentary sequence, the Katanga Supergroup, composed from the bottom to the top of the Roan, Nguba and Kundelungu Groups presumably deposited on top of a pre-Katanga basement (Porada and Berhorst, 2000). This sedimentary sequence of the external zone is affected by folds and thrusts (Figure 28) and low grade metamorphism reaching the Lower Greenschist facies. This external zone is referred to as the External fold-and-thrust belt in the literature (De Swardt and Drysdal, 1964) and this style of deformation is illustrated by the traces of anticlinal axial planes in Figure 28. The internal zone of the Lufilian belt, comprising the Domes region, is marked by a higher metamorphic grade ranging from Upper Greenschist to Upper Amphibolite facies affecting a complexly folded nappe pile made up of Neoproterozoic metasedimentary rocks interleaved with migmatitic gneisses interpreted as basement inliers (Mendelsohn, 1961; Cosi et al., 1992; Porada and Berhorst, 2000; John et al., 2004). In the internal zone, regional scale lithological contacts and outcrop patterns are controlled by low-amplitude dome-shaped structures. Migmatitic gneisses outcropping in the core of these domes yielded U-Pb ages ranging between 1.92 and 1.11 Ga (Eglinger et al., to be submitted). The Hf model ages of magmatic and detrital zircon grains are ranging from late Mesoarchean to Neoproterozoic. Coupling U-Pb and Lu-Hf data, Eglinger et al. (to be submitted) suggest that these basement inliers represent the southwestern metacratonic boundary of the Bangweulu block represented by para- and orthogneissic rocks, in continuation with the Mesoproterozoic Irumide belt.

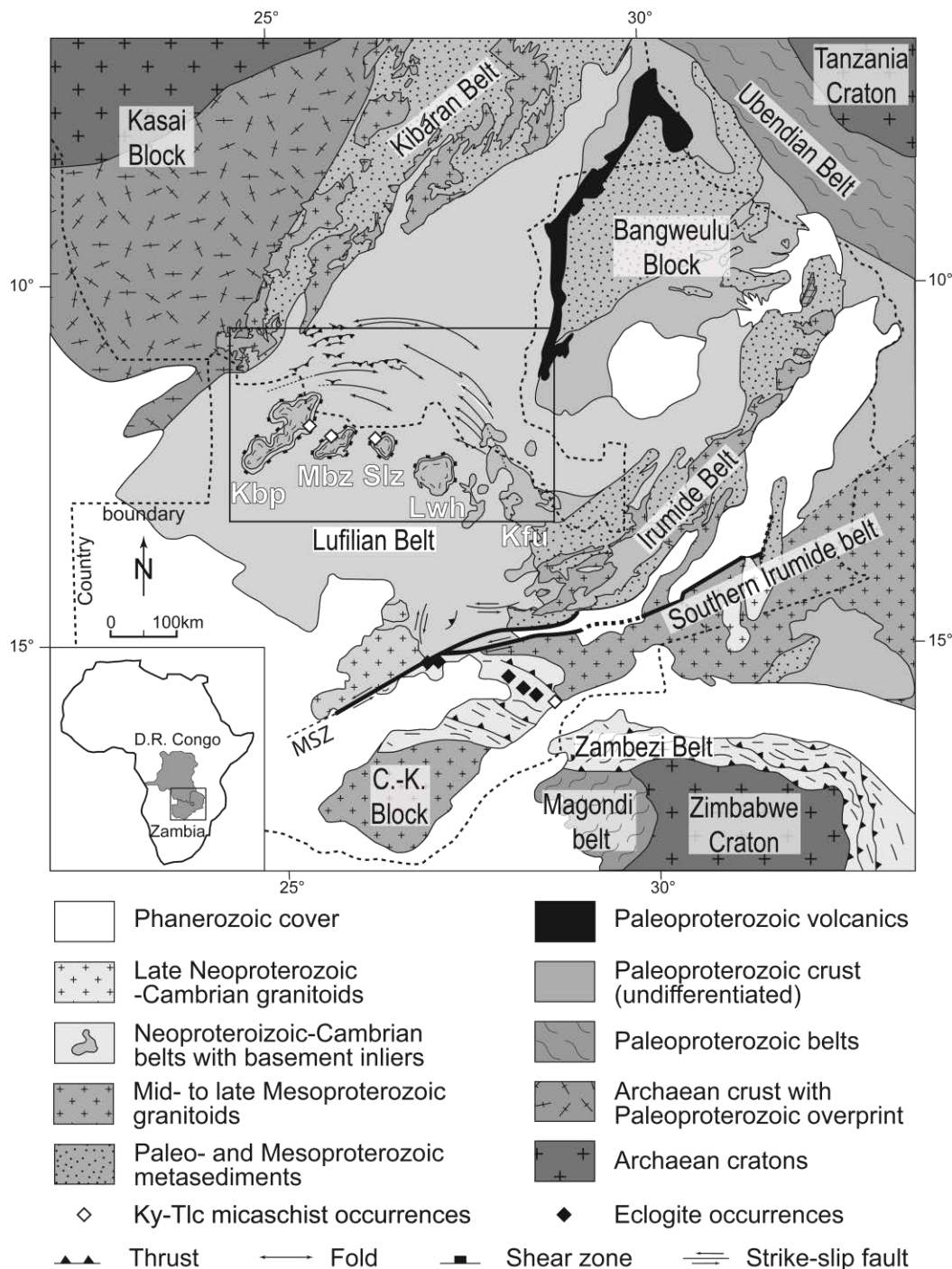


Figure 28: Tectonic map of central and southern Africa showing the location of the Lufilian-Zambezi belt in relation to the surrounding Archean cratons and Paleo- to Mesoproterozoic belts (modified after De Waele et al., 2008). Black and white diamonds represent the location of moderate to high pressure rocks (John et al., 2004; Vrana and Barr; 1972). Abbreviations: Kbp = Kabompo dome; Mbz = Mwombeshi dome; Slz = Solwezi dome; Lwh = Luswishi dome; Kfu = Kafue Anticline; C.-K. = Choma Kalomo block; MSZ = Mwembeshi Shear Zone; Ky = Kyanite; Tlc = Talc. The black rectangle represents the study area enlarged in Figure 29.

The lithostratigraphy of the Katanga Supergroup has been essentially reconstructed in the external zone of the Lufilian belt taking advantage of rather good outcrop conditions, a large number of drilled cores and open pits (see Kampunzu and Cailteux, 1999, for further descriptions of the lithostratigraphy of the Katanga sequence). In the internal zone, deformation and metamorphism have been much more intense and the reconstruction of the stratigraphy is thus more speculative, but is thought to be generally similar to the external zone (Cosi et al., 1992). Cosi et al. (1992) described, in the internal zone, a nappe pile composed of both gneissic-migmatitic layers interpreted as part of the pre-Katanga basement and of metasedimentary sheets attributed to the Katanga Supergroup (Figure 29). A distinct kyanite micaschist layer marks the transition between the gneissic-migmatitic core (basement rocks) of the domes and their metasedimentary mantle (cover rocks). This particularly Mg-rich layer (as evidence by the presence of phlogopite, talc and clinocllore; Eglinger et al., in press) has been interpreted as a metamorphosed equivalent of the Roan Group evaporites (Cosi et al., 1992). These rocks have preserved relics of sedimentary structures such as fluvial channels and cross-bedding stratification (Figure 30a, b). In summary, the geodynamic evolution of the Zambezi-Lufilian belt is constrained in the external zone by the evolution of sedimentary deposits and deformation into a fold and thrust belt, and in the internal zone by the structural and metamorphic evolution of the nappe pile. Rift basin opening (from 880 to 600 Ma) was followed by convergence (from 600 to 530 Ma) of the Congo and Kalahari cratons. The nature of the Lufilian-Zambezi basin was very controversial. Geochemical investigations of intrusive bodies, gabbros and metagabbros, within the Katanga sequence in the Lufilian belt were interpreted as an indication that the rifting probably did not significantly overstep a continental stage (Tembo et al., 1999) whereas geochemical data obtained from eclogites and gabbros in the Zambezi belt give evidence that they were formed at an oceanic spreading ridge (John et al., 2003). Transition from divergent to convergent tectonic regime is recorded by Eclogite facies metamorphism, dated at ca. 640-600 Ma by Sm-Nd whole-rock and garnet isochron on mafic boudins in the Zambezi belt (John et al., 2003). Subduction of crustal units under a low geothermal gradient to form the accretionary orogenic belt is depicted by *P-T* estimates of phengite-bearing eclogites with temperatures of 720-755 °C at pressures between 20 and 28 kbar (John et al., 2003). Intermediate-high pressure/intermediate-temperature conditions (Barrovian metamorphism) from the kyanite-talc micaschist in the Kabompo, Mwombezi and Solwezi domes records a pressure around 13 ± 1

kbar and a temperature of 750 ± 25 °C dated at 529 ± 2 Ma, by U-Pb on monazite grains that corresponds to a mid-pressure/mid-temperature Barrovian metamorphism interpreted as attesting for post-thickening thermal relaxation of the orogenic crust (John et al., 2004). ^{40}Ar - ^{39}Ar thermochronology on biotite and Rb-Sr dating on muscovite and biotite yield ages ranging from 510 to 463 Ma that are interpreted to represent post-orogenic cooling of the metamorphic rocks in the Lufilian belt (Cosi et al., 1992; John et al., 2004; Rainaud et al., 2005).

3. Analytical procedures

3.1. Geochemical analyses of whole rocks and minerals

Bulk compositions of samples from various lithologies were determined by ICP-OES using an Icap 6500 spectrometer at CRPG (Nancy, France). Sample preparation, analytical conditions and limits of detection are detailed in Carignan et al. (2001). These data are compared in the following sections and compared with previously published analyses. The geochemical compositions of the samples (Table 28; Table 29) will be used for equilibrium phase diagram modelling (PerpleX, Connolly, 1990). Major and trace elements for silicates were obtained by the EMP method using a Cameca PC-controlled SX-100 (GeoRessources, Nancy). During analysis, an accelerating voltage of 15kV, beam current of 12nA and peak counting time 10 to 20s were used.

3.2. Sm-Nd isotopes analyses of whole rock

Sm–Nd isotopic values were determined on crushed whole-rock samples by isotope dilution. All analyses were carried out at the Geosciences Rennes Laboratory at the University of Rennes1. Samples were spiked with a ^{150}Nd – ^{149}Sm mixed solution and dissolved in HF-HNO₃. REE elements were separated using BioRad AG 50W× 8 H+ 200–400 mesh cationic resin. Sm and Nd were separated and collected by passing the solution through a further set of ion exchange columns loaded with Ln spec Eichrom resin. Sm and Nd were loaded with HNO₃ reagent on to double Re filaments and analysed in a Finnigan MAT262 multicollector mass spectrometer in static mode. In each analytical session, the unknowns were analysed together with the Ames nNd-1 Nd standard, which during the course of this study yielded an average of 0.511964

(standard deviation = 7.23×10^{-6}). All analyses of the unknowns are adjusted to a nominal $^{143}\text{Nd}/^{144}\text{Nd}$ value of 0.511850 for the La Jolla standard. Mass fractionation was monitored and corrected using the value $^{146}\text{Nd}/^{144}\text{Nd} = 0.7219$. Procedural blanks analyzed during the period of these analyses were ~ 190 pg and are considered to be negligible compared to the total quantity of Nd in the samples.

3.3. Lu-Hf isotope dilution analyses of garnet and whole rock

Rock samples were processed in an agate mortar, preventing any pollution, and then sieved. From the 250–500 μm garnet fractions of 45–140 mg were handpicked under ethanol using a binocular microscope, to get pure garnet fractions (at least two fractions) excluding grains having visible inclusions. To selectively dissolve the garnet fractions while leaving potential zircon and rutile inclusions, as the main Hf-bearing contaminant intact, they were dissolved in closed Teflon® vials on a 120 °C hotplate rather than in high-pressure Parr® bombs (Lagos et al., 2007; Schmidt et al., 2008). After rinsing with Milli-Q H₂O, mineral separates were spiked with a mixed $^{176}\text{Lu}/^{180}\text{Hf}$ tracer for Lu and Hf concentration determinations, and then digested as follows: the minerals were decomposed in HF–HNO₃–HClO₄ and then 6M HCl, drying down at high temperature (fuming HClO₄) between the steps (Lagos et al., 2007). Separation of Lu and Hf was achieved on an ion-exchange column containing Eichrom Ln-Spec resin (Münker et al., 2001). Lutetium and Hf isotope ratios were measured on a Finnigan Neptune MC-ICPMS equipped with a Cetac ARIDUS™ sample introduction system at Goethe University Frankfurt. This instrumental setup ensured high sensitivity, enabling the precise measurement of Hf isotope compositions of samples having as little as 10 ng of Hf at a signal intensity of ~ 475 mV of ^{176}Hf for a 10 ppb Hf solution. Because only 50–80% of the Yb were separated from Lu with the purification technique employed here, a correction was necessary for the interference of ^{176}Yb on ^{176}Lu (Blichert-Toft *et al.*, 1997). The Yb interference was monitored by measuring two interference-free Yb isotopes (^{173}Yb and ^{171}Yb). Their ratio was used to apply an instrumental mass bias correction to measured $^{176}\text{Lu}/^{175}\text{Lu}$ values, assuming a $^{173}\text{Yb}/^{171}\text{Yb}$ of 1.129197 and the exponential law (Vervoort et al., 2004). This mass bias correction was also applied to the $^{176}\text{Yb}/^{171}\text{Yb}$ used for correcting the ^{176}Yb interference on ^{176}Lu . In-run statistics for the measured and corrected $^{176}\text{Lu}/^{175}\text{Lu}$ range from 0.031 to 0.037 % 2 S.E. Mass bias on the Hf isotope ratios was corrected using $^{179}\text{Hf}/^{177}\text{Hf} = 0.7325$ and the exponential law. The Hf solutions were virtually

free of any Yb and Lu, but contained various amounts of Ta and W. All isobaric interferences on Hf isotopes were monitored and corrected using the mass bias corrected $^{173}\text{Yb}/^{176}\text{Yb}$, $^{175}\text{Lu}/^{176}\text{Yb}$, $^{180}\text{Ta}/^{181}\text{Ta}$, and $^{183}\text{W}/^{180}\text{W}$ values. During the course of this study, the Lu standard yielded $^{176}\text{Lu}/^{175}\text{Lu}=0.026554\pm 11$ ($2\sigma\approx 0.04\%$, $n=4$) and the Hf Standard JMC-475 yielded $^{176}\text{Hf}/^{177}\text{Hf}=0.282155\pm 13$ ($2\sigma\approx 0.5\%$, $n=6$). In-run analytical uncertainty for $^{176}\text{Hf}/^{177}\text{Hf}$ was typically around $\pm 0.3\epsilon$ or better. For the calculation of the mineral isochrons the ISOPLLOT program (Ludwig, 2007) was used with a $^{176}\text{Lu}=1.867\times 10^{-11} \text{ a}^{-1}$ (Scherer et al., 2001; Söderlund et al., 2004). For the $^{176}\text{Hf}/^{177}\text{Hf}$ uncertainties we used quadratic additions of the reproducibility of the JMC-475 ($2\sigma=0.5\epsilon$) and the in-run precisions (2σ errors). Uncertainties on $^{176}\text{Lu}/^{177}\text{Hf}$ were propagated from the reproducibility of the Lu standard and the uncertainty in the spike calibration (0.15%), and multiplied by an error magnification factor that depends on the measured $^{176}\text{Lu}/^{175}\text{Lu}$. Resulting uncertainties for the $^{176}\text{Lu}/^{177}\text{Hf}$ values are 0.25-0.5%. Repeated blank measurements yielded < 29 pg for Hf, and < 5 pg for Lu.

3.4. LA-MC-ICPMS U-Pb and Lu-Hf isotope analyses of zircon

Rock samples were crushed following successive stages using, respectively, a jaw crusher and a roller mill. Zircon grains were concentrated using (i) density separation with suitable liquids such as bromoform (density = 2.84 g/cc) and diiodomethane (density = 3.31 g/cc) and (ii) magnetic separation with the Frantz isodynamic separator. Zircon grains were handpicked out individually, mounted in epoxy blocks and polished for analysis. External form and internal texture were imaged using combined cathodoluminescence (CL) and secondary electron microscopy (SEM) techniques in a JEOL JSM-6490 instrument with Gatan MiniCL at the Goethe University of Frankfurt (Germany). U-Pb and Lu-Hf isotopes analyses of zircon grains from all rocks were carried out by laser ablation-inductively coupled plasma mass spectrometry (LA-ICPMS), also at the Goethe University of Frankfurt (Germany). Methods and instruments were described by Gerdes and Zeh (2006; 2009), with modifications explained in Zeh and Gerdes (2012). Laser spots for Lu-Hf (squared spots with an edge length of 40 μm) were placed mostly directly “on-top” of the U-Pb laser spots (19-26 μm in diameter), or within the same zone characterized by CL imaging. The results of U-Pb and Lu-Hf isotope analyses are shown from Table 36 to Table 39.

4. Mantling rocks: micaschists and magmatic rocks

4.1. Sampling

The Neoproterozoic metasedimentary cover sequence, known as the Katanga Supergroup, is mainly composed by siliciclastic-evaporitic and carbonaceous rocks. Some meta-igneous rocks are described within this sequence. We sampled kyanite micaschists (*ZM-10-07*, *ZM-10-08*, *ZM-10-24* and *ZM-10-41*), along the tectonic contact between cover and basement and supposed to belong to the Roan Group, the basal unit of the Katanga Supergroup cover (Figure 29; Figure 30). The Mwombezi dome is mantled by a similar kyanite micaschist unit (Figure 29).

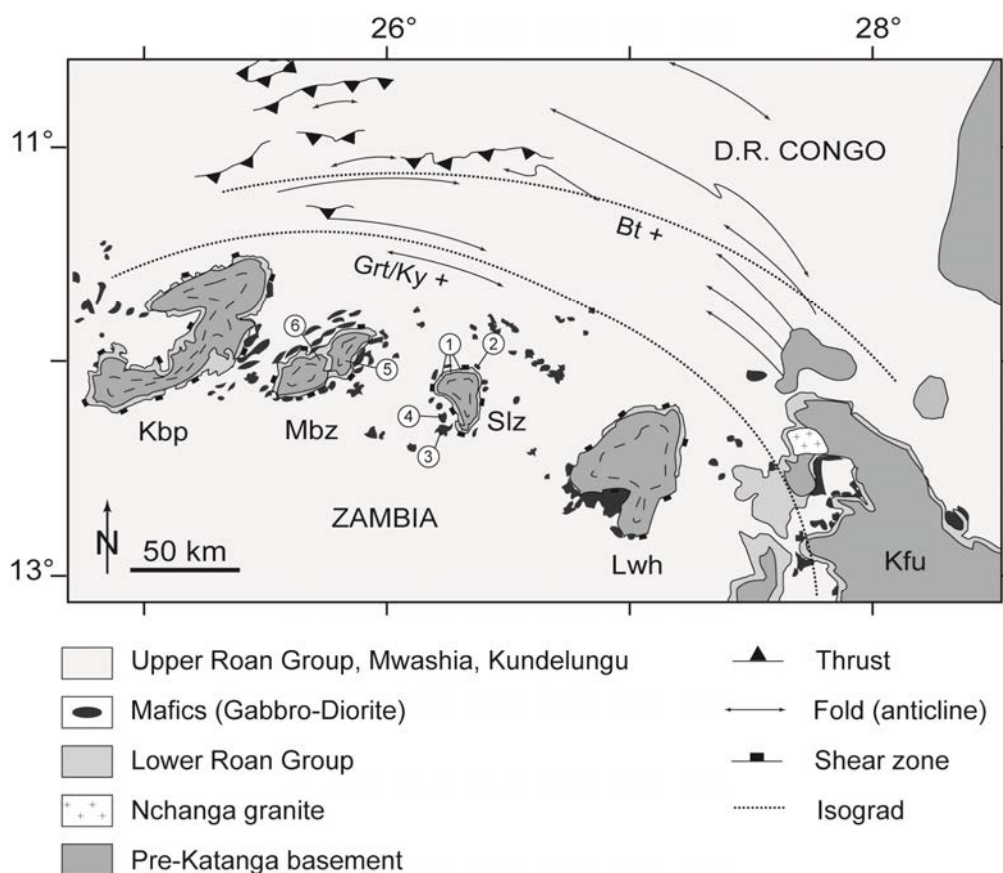


Figure 29: Simplified geological map of the internal and external zones of the Lufilian belt and sample location (modified after Barron, 2003). References to studied samples: n°1 = kyanite micaschists (*ZM-10-07*, *ZM-10-08*, *ZM-10-24* and *ZM-10-41*); n°2 = metagabbro (*ZM-10-21*); n°3 = metagabbro (*ZM-10-47*); n°4 = metadiorites (*ZM-10-45* and *ZM-12-18*); n°5 = garnet-kyanite amphibolite (*ZM-82-14*); n°6 = garnet amphibolites (*ZM-12-13* and *ZM-12-16*). Details are in Table 27. Abbreviations: Kbp = Kabompo dome; Mbz = Mwombezi dome; Slz = Solwezi dome; Lwh = Luswishi dome; Kfu = Kafue Anticline; Bt = Biotite; Gt = Garnet; Ky = Kyanite.

These micaschists, locally quartz-rich, are made of quartz, biotite, kyanite, hematite, rutile, chlorite with minor muscovite. These rocks preserved relics of sedimentary structures such as fluvial channels, cross-bedding stratification and conglomerate layers consisting of matrix-supported quartz pebbles (Figure 30a, b). This particularly Mg-rich layer has been interpreted as a metamorphosed equivalent of the Lower Roan Group evaporites (Cosi et al., 1992). Kyanite micaschists show a penetrative schistosity associated with shear bands defining sigmoid shaped microliths consistent with a top to the North sense of shear (Figure 30c). Locally, kyanite grains underline a N-S trending mineral lineation associated with a top to the North C/S fabric (Figure 30d).

Meta-igneous rocks consist of meta-gabbros and meta-diorites mostly intrusive within the Mwashia Subgroup and the Nguba Group, part of the Katanga cover. Intrusive rocks were sampled around the Solwezi dome, within calcite and dolomitic marbles, interpreted as part of the Upper Roan Group and within biotite schists, interpreted as part of the Mwashia Group. Metagabbros (*ZM-10-21* and *ZM-10-47*) and meta-diorites (*ZM-10-45* and *ZM-12-18*) were collected around the Solwezi dome (Figure 29; Figure 31). The distribution of magmatic rocks is well documented by aeromagnetic anomalies in the Solwezi and Mwombezhi areas. Only one metabasalt (sample *ZM-12-27*) was collected from the Mwombezhi area but not sampled directly from an outcrop and that is why its precise location is uncertain. All these rocks have been metamorphosed to Amphibolite facies and some of them are locally scapolitized. Mineralogy of mafic rocks is dominated by plagioclase, amphibole and Ti-Fe oxides. Mineralogy of felsic rocks is dominated by quartz, plagioclase with some biotite, amphibole and Fe-oxides.

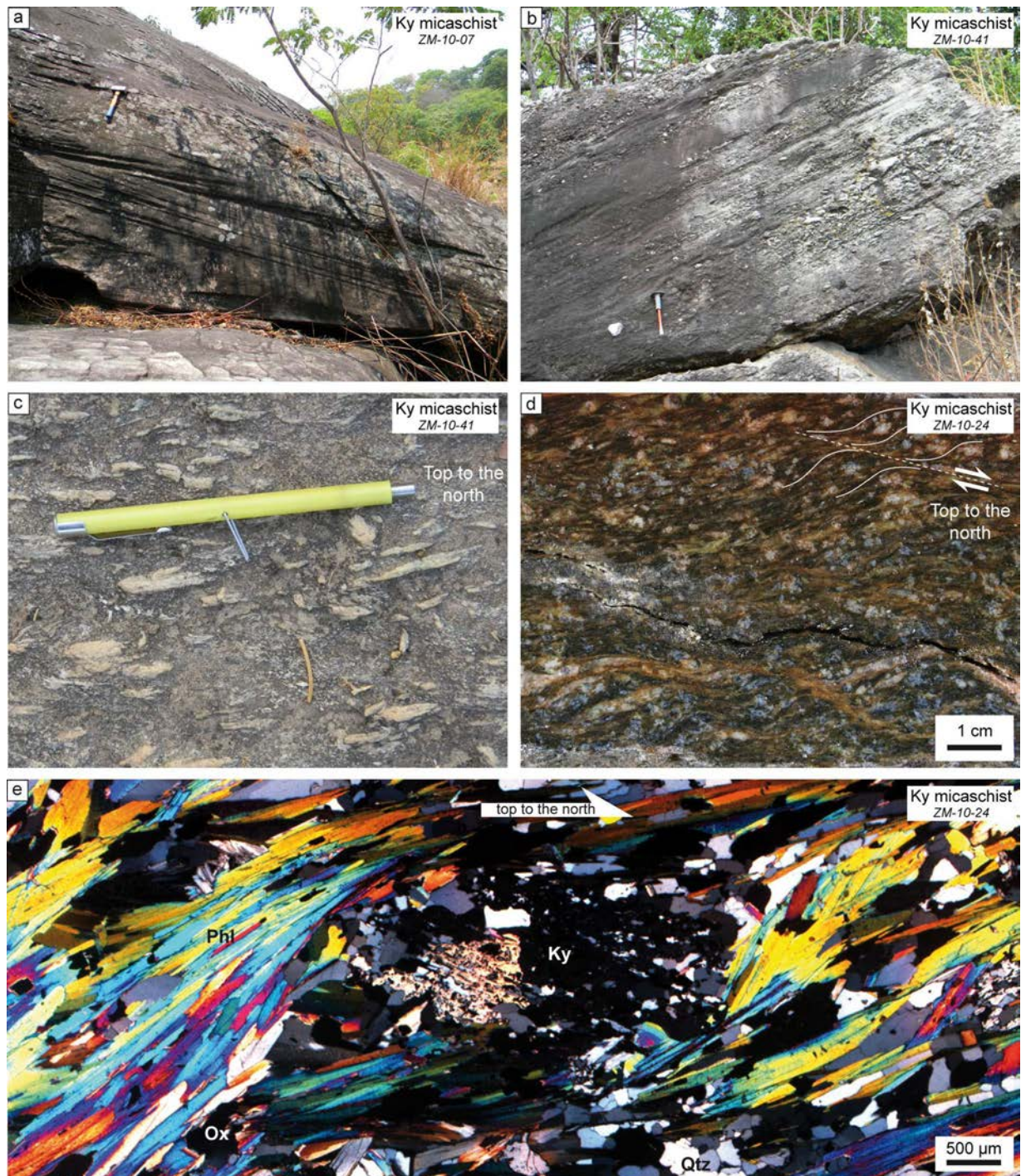


Figure 30: a: Parallel and cross-bedding structures in kyanite micaschist rimming the Pre-Katanga rocks of the Solwezi area. b: Monomictic conglomerate with quartzite pebbles and/or cobbles. c: Mineral lineation marked by kyanite (second generation: K2) porphyblasts. d: Kyanite micaschist showing C/S fabric. e: Kyanite poikiloblast grain (first generation: K1) wrapped into the schistosity (S_{n+1}) and containing oriented inclusions of quartz and iron oxide, defining an inherited schistosity (S_n).

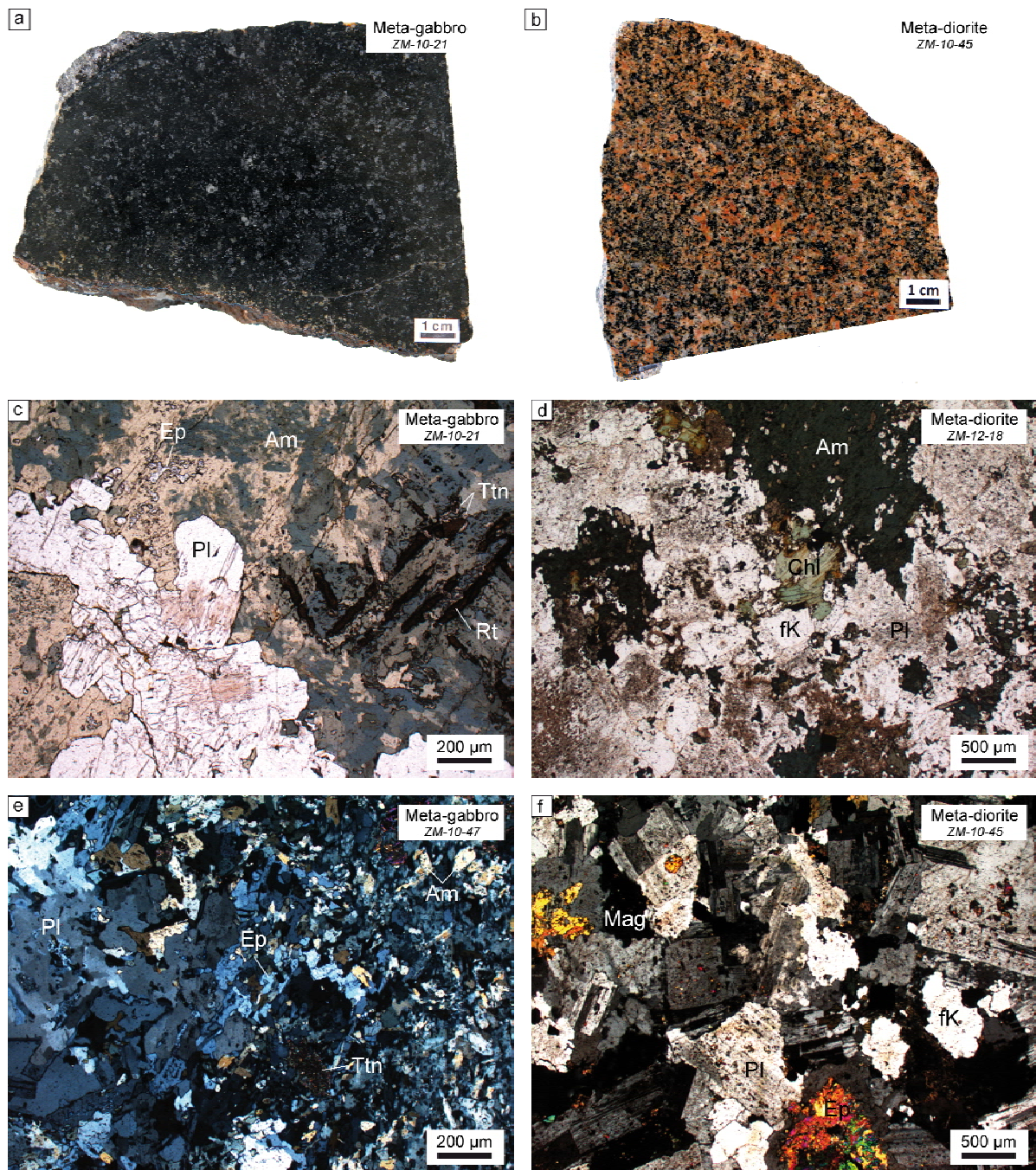


Figure 31: a, b: Granular and equant texture of metagabbro and metadiorite, respectively. c: Plagioclase-amphibole-epidote matrix of metagabbro showing recrystallized texture with amphibole subgrain formation and one skeletal rutile grain, maybe a pseudomorph of Ti-rich magnetite, surrounded by titanite within amphibole (plane-polarized light). d: K-feldspar-amphibole-plagioclase matrix of metadiorite showing irregular and interlobate boundaries between matrix minerals reflecting a ductile deformation (plane-polarized light). e: Plagioclase-amphibole-epidote

matrix of metagabbro showing recrystallized texture with plagioclase subgrains formation (cross-polarized light). f: Plagioclase-feldspar-epidote matrix of metadiorite with magnetite (cross-polarized light).

4.2. Whole rock geochemistry

The kyanite micaschists (*ZM-10-07, ZM-10-08, ZM-10-24 and ZM-10-41*) in the Solwezi dome are characterized by a high aluminous bulk compositions, above 16.01 wt.%. The MgO and Fe₂O₃ contents show a very wide range between 3.00 and 11.37 wt.% and 1.70 and 5.47 wt.%, respectively (Figure 32a; Table 28). The SiO₂ content ranges from 57.71 to 75.50 wt.%, correlating with locally quartz-rich mineralogy. In the Th-Hf-Co ternary diagram, samples plot between the upper and the lower continental crust composition fields (Figure 32b). This indicates two component mixing involving upper crustal material and a more mafic contribution. The REE patterns do not show negative Eu anomalies ($0.93 < \text{Eu}^* < 0.95$; Figure 32c). REE patterns were potentially disturbed during post deposition hydrothermal alteration.

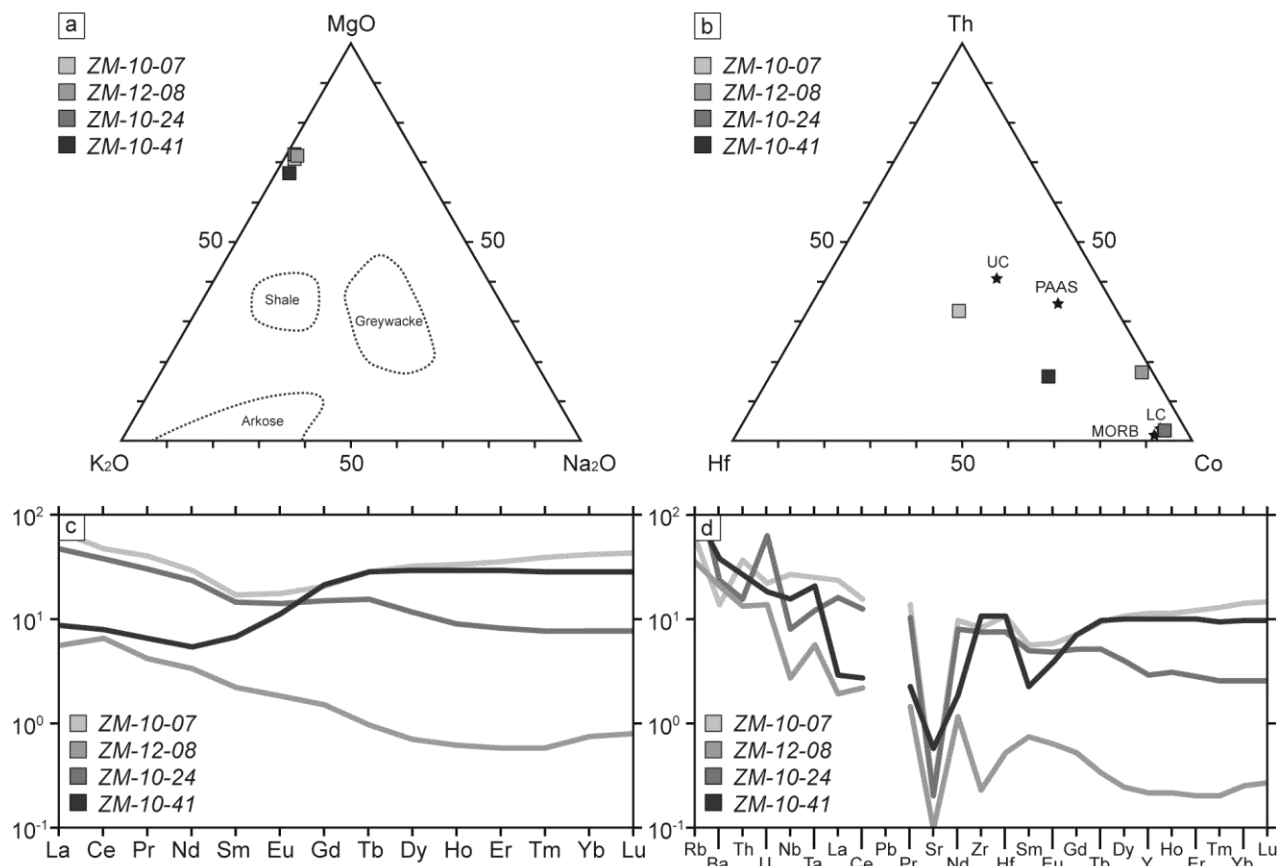


Figure 32: Major and trace elements geochemistry of the kyanite micaschists from the Solwezi area. Abbreviations: UC = Upper Crust; PAAS = Post Archean Australian shale; LC = Lower Crust; MORB = Mid-Ocean Ridge Basalt.

Meta-gabbro rocks (samples *ZM-10-21* and *ZM-10-47*; Figure 33a, b) show silica contents ranging from 45.60 to 47.16 wt.%, moderate Al₂O₃ (15.17-15.66 wt.%), K₂O (0.72-1.02 wt.%), high FeO_T/MgO ratio between 1.7 and 2.7 and high TiO₂ contents (2.02-2.76 wt.%; Table 28). In the Q-A-P normative classification diagram, these rocks plot in the field of gabbro (Figure 33a, b). The metabasalt sample (*ZM-12-27*) displays the same major element composition with a SiO₂ content of 45.78, Al₂O₃ of 14.82, K₂O of 0.97 and FeO_T/MgO ratio of 1.3. Calculated Ti/V ratio for these meta-gabbros ranges between 39 and 45, Zr/Y ratios ranging from 4.88 to 4.94, Ti/Y from 488 to 824 and Zr/Nb from 8.56 to 8.99. The metabasalt shows Ti/V ratio of 62, Zr/Y of 5.93, Ti/Y of 579 and Zr/Nb of 8.06. All these ratios indicate that these metabasic rocks are in the field of within-plate basalts. Cr and Ni contents range, respectively, from 27 to 216 ppm and from 39 to 95 ppm for the meta-gabbros. Meta-basalt shows Cr and Ni contents of 113 and 73 ppm, respectively. In the Zr/TiO₂ (0.004-0.006) vs. Nb/Y (0.54-0.74) plot, these rocks are

between the subalkaline and alkaline basalts fields. REE patterns are fractionated ($4.6 < \text{La}_N/\text{Yb}_N < 6.4$; $1.7 < \text{Gd}_N/\text{Yb}_N < 2.0$) showing a linear enrichment from HREE to LREE. Meta-gabbro REE patterns do not show negative Eu anomalies ($1.00 < \text{Eu}^* < 1.19$; Figure 33c), suggesting that magmatic evolution was not dominated by plagioclase fractionation. The Th/La ratios of the metabasic rocks, which are known to be controlled by the source components of the continental tholeiites (Hawkesworth and Gallagher, 1993), are low (0.12-0.32). A low ratio ($\text{Th}/\text{La} < 1$), with relative depletion of Th compared to lithospheric continental tholeiites, indicates the participation of an asthenospheric component. High field strength and heavy rare-earth elements are not fractionated, and confirm a possible spinel lherzolite source (Figure 33d). These metabasic rock types have $^{87}\text{Sr}/^{86}\text{Sr}$ initial ratios at 750 Ma (U-Pb on magmatic zircon; Barron et al., 2003) ranging from 0.70662 to 0.70841 for metagabbros, and equal to 0.70806 for metabasalt. Nd isotopic composition shows negative $\epsilon\text{Nd}_{(750)}$ values, compared to the Chondritic Uniform Reservoir (CHUR, Wasserburg et al., 1981), ranging from -1.4 to -0.3 for metagabbro and equal to -2.1 for metabasalt (Table 35). These rocks have a calculated $^{143}\text{Nd}/^{144}\text{Nd}$ initial ratio ranging between 0.511565 and 0.511655, compared to the Chondritic Uniform Reservoir (CHUR, Wasserburg et al., 1981). Nd model ages, relative to the Depleted Mantle (T_{DM}), are in the range of 1.54 to 1.38 Ga for all these metabasic rocks.

Meta-diorite rocks (samples *ZM-10-45* and *ZM-12-18*) show intermediate silica contents around 61.00 wt.%, high Al_2O_3 content ranging from 15.33 to 17.38 wt.% with FeO_T/MgO ratios between 5.71 and 10.91 (Table 28). In the Q-A-P normative classification diagram, these rocks plot in the field of quartz-diorite (Figure 33a, b). These rocks have an alumina saturation index ($\text{ASI} = \text{molecular ratio } \text{Al}_2\text{O}_3/(\text{CaO}+\text{Na}_2\text{O}+\text{K}_2\text{O})$) of 0.84-0.92, indicating a metaluminous composition and present low $\text{K}_2\text{O}/\text{Na}_2\text{O}$ ratios, ranging from 0.07 to 0.13. In the Y versus Nb diagram (Pearce et al., 1984), these meta-diorites plot in the field for within-plate granites. The REE patterns show an enrichment of the REE, with abundances 57-421 times chondrite (normalization values after McDonough and Sun, 1995) and relatively sublinear enrichment from HREE to LREE. The REE enrichment could be related to the presence of accessory phases as titanite and apatite described in these samples. The LREE display a slightly fractionated pattern ($\text{La}_N/\text{Sm}_N = 2.27\text{-}2.39$) and the HREE a sub-flat pattern ($\text{Gd}_N/\text{Yb}_N = 1.79\text{-}1.94$). In the multi-element diagram, strong Rb, Ba, Pb and Sr anomalies are probably correlated to post-magmatic

processes. Lithophile and HREE-LREE are more enriched in these evolved facies than in mafic facies, represented by metagabbros and metabasalt (samples *ZM-10-21*, *ZM-10-47* and *ZM-12-27*). Multi-element diagrams normalized to primitive mantle present an enrichment of Nb and Ta and negative Ba and Sr anomalies (Figure 33 d). These characteristics rule out the involvement of subduction related processes in their evolution (Rogers et al., 1985; Nelson and McCulloch, 1989; Zhao et al., 1995). This is because alkaline rocks in such settings tend to have strong negative Nb and Ta anomalies as is seen for the Yamato syenites, Mount Collins monzonite (Zhao et al., 1995) which are interpreted to have subduction related tectonic affinities. In contrast, multi-element patterns of rocks from rift or hot spot related tectonic setting like Victoria alkali basalts, in Australia (McDonough et al., 1985) are enriched in Nb and Ta which suggests a rift or hotspot related setting for the alkaline magmatism in the Lufilian belt. Furthermore, the high heavy rare-earth and high field strength elements content coupled to the very low Th/La ratio (0.096-0.097) also suggest that these granitoids are derived from an asthenospheric source, potentially by differentiation of a melt generated by partial melting of a spinel lherzolite source. These metadiorite rocks have a calculated $^{87}\text{Sr}/^{86}\text{Sr}$ initial ratio at 720 Ma of 0.70545. Nd isotopic composition shows positive $\epsilon\text{Nd}_{(720)}$ values of 1.4 and a calculated $^{143}\text{Nd}/^{144}\text{Nd}$ initial ratio of 0.511782, compared to the Chondritic Uniform Reservoir (CHUR, Wasserburg et al., 1981). Nd model age, relative to the Depleted Mantle (T_{DM}), is of 1.14 Ga. The relative homogeneous Sr-Nd isotope data for these alkaline rocks indicate that they were derived from one homogenous source.

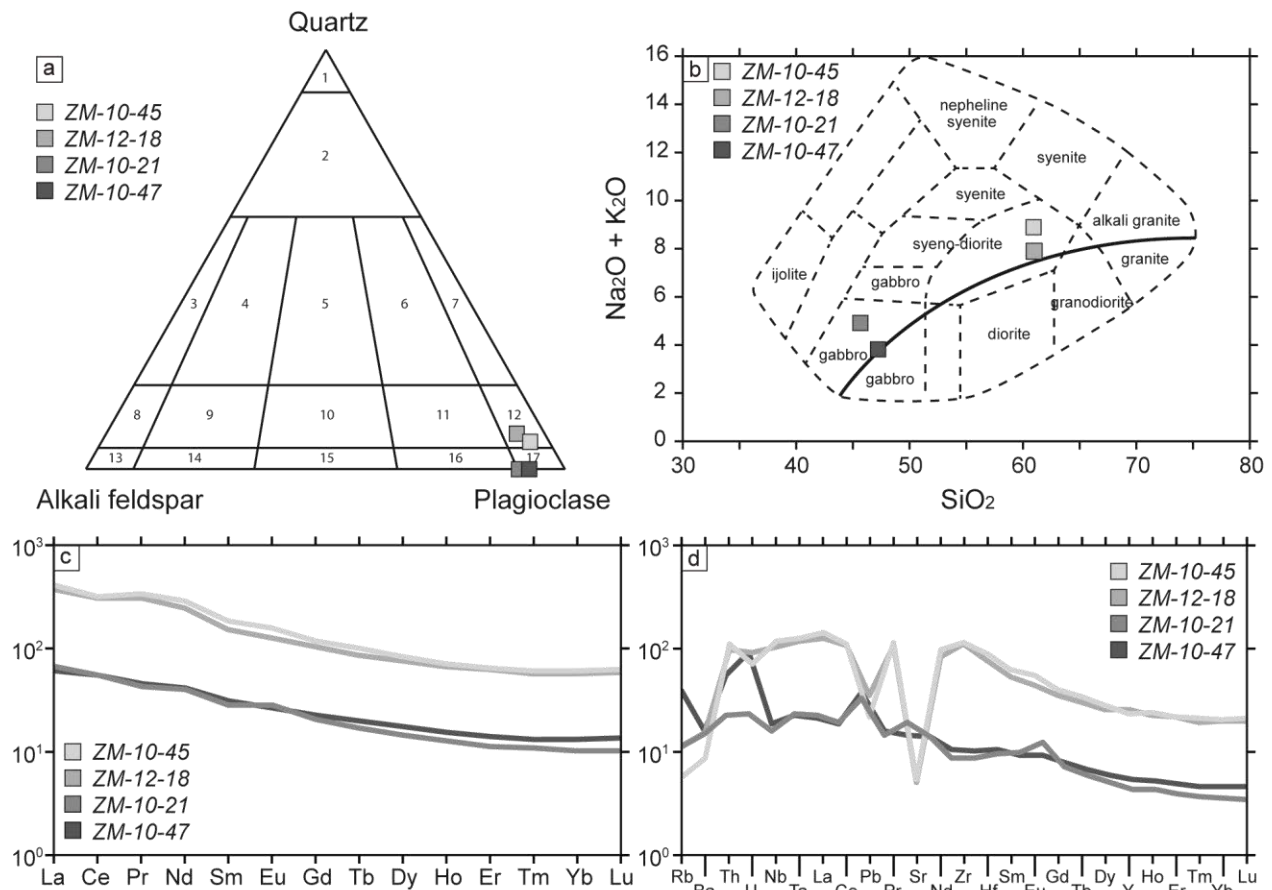


Figure 33: Major and trace elements geochemistry of the meta-gabbros and the meta-diorites from the Solwezi area. Reference numbers: 12 = quartz diorite/gabbro; 17 = diorite/gabbro.

4.3. Petrography and mineral chemistry

Kyanite micaschists rimming the core of the Solwezi dome show a grano-lepidoblastic texture with C/S fabric underlined by micas and sigmoidal-shape kyanite porphyroblasts (Figure 30). The matrix is dominated by quartz, rutile and hematite alternating with biotite layers that define the schistosity (S_{n+1}). Quartz grains boundaries are straight defining a polygonal fabric. Biotite grains are typically phlogopite with X_{Mg} ranging from 0.941 to 0.959 with a TiO_2 content ranging from 0.59 to 0.76 wt.% (Table 30). Monazite grains are mostly sub-automorphous and do not show any features such as a rounded shape or percussion marks that would indicate a detrital origin. Accordingly, these grains are interpreted to have grown *in-situ* during metamorphism. Monazite grains are mainly localized within the (001) cleavage plane of phlogopite blasts marking the C/S fabric in sample ZM-10-24 (Figure 71d), and mainly scattered in the matrix in

sample *ZM-10-07*. Syn- to post-tectonic chlorite grains are also observed. Chlorite grains are clinocllore with X_{Mg} ranging from 0.967 to 0.976 (Table 30). Kyanite crystals display two distinct structural positions relative to the S_{n+1} schistosity. Some kyanite grains are poikiloblasts wrapped into the schistosity (S_{n+1}) and contain inclusions of quartz and iron oxide, defining an inherited schistosity S_n . These grains are interpreted as pre-tectonic (pre- S_{n+1}) porphyroblasts (Figure 30e). The other generation is represented by sub-automorphous grains oriented parallel to the schistosity. They are interpreted as syn-tectonic porphyroblasts.

Metagabbroic rocks were thoroughly recrystallized during regional metamorphism, no relict of primary pyroxene grains was observed. Matrix is dominated by plagioclase-amphibole-epidote (Figure 31a, c, e). Some rare biotite, quartz and magnetite grains are described. Skeletal rutile grains are in inclusions within amphibole and are surrounding by titanite rims (Figure 31c). Amphibole composition lie in the compositional field of magnesian hastingsite (calcic amphiboles) and plagioclase composition is ranging from oligoclase to andesine ($0.20 < X_{An} < 0.38$). Most of the grains are characterized by crystalplastic deformation and show subgrain formations.

Metadioritic rocks are characterized by a plagioclase-rich matrix with K-feldspar, epidote and some quartz grains (Figure 31b, d, f). Plagioclase is exclusively represented by albite ($X_{An} < 0.01$). Rutile grains are mostly surrounding by titanite and iron oxides are represented by magnetite. Some apatite grains are also present. Samples *ZM-10-45* and *ZM-12-18* display two types of amphibole, respectively represented by actinolite (calcic amphiboles) and magnesian hastingsite (calcic amphiboles). Late chlorite grains are growing from amphibole grains.

4.4. Geochronology

Zircon grains (50-300 μm) from kyanite micaschists (sample *ZM-10-24*) mostly present a sub-rounded to rounded shape. SEM/CL images reveal zircon grains with complex internal structure due to different degree of re-crystallization and/or oscillatory zoning. The U-Pb isotope data obtained from zircon grains show different range of ages with two dominant modes at 1.88 and 1.88 Ga, and two minor modes at 1.72 and 1.28 Ga (Figure 34; Table 36). Owing to the

rather large spread of ages, these two last populations are not well constrained. The youngest zircon grain with magmatic zoning and a concordance $> 95\%$ yielded a $^{207}\text{Pb}/^{206}\text{Pb}$ age of 1282 ± 21 Ma (grain 251). Zircon grains with modes at 1.88, 181 and 1.72 Ga show subchondritic ϵHf_t ranging from -8.4 to -1.3 with two-stage Hf model ages (T_{DM}) between 2.96 and 2.64 Ga (Table 37). The youngest zircon grain shows a subchondritic ϵHf_t of -16.7 with a T_{DM} of 2.55 Ga. A large number of analyses are discordant indicating that the U/Pb has been perturbed in these zircon grains after their Paleo to Mesoproterozoic crystallization. However, the large dispersion of the analyses precludes the determination of a precise age for this perturbation event.

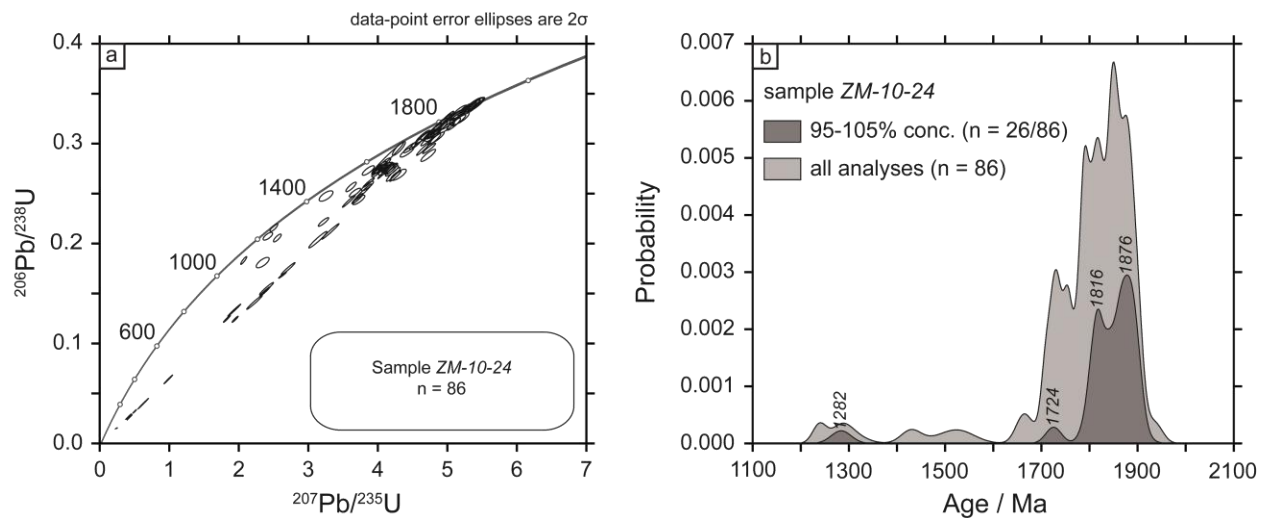


Figure 34: a. Concordia diagram for U-Pb isotope ratio (a) and probability density plot of $^{207}\text{Pb}/^{206}\text{Pb}$ ages (b) for detrital zircon grains from the kyanite micaschist (*ZM-10-24*).

Eglinger et al. (submitted) analyzed several monazite grains within kyanite micaschists from the Solwezi dome for U-Pb-Th isotopic dating (samples *ZM-10-07* and *ZM-10-24*). Nine monazite grains from *ZM-10-07* and six from sample *ZM-10-24* have been investigated for ^{232}Th - ^{208}Pb analyses and results are reported in Table X. X-ray maps of these monazite grains show patchy zoning patterns which correspond to distinct chemical domains and interpreted to partial dissolution/crystallization zones involving fluid-rock interactions. In some domains, the positive correlation between Ca and Th concentrations is interpreted as the consequence of cation substitutions toward the brabantite $(\text{U, Pb, Th})\text{Ca}(\text{PO}_4)_2$ end-member composition (Rose, 1980). This cationic substitution involves the following exchange: $2\text{REE}^{3+} \Leftrightarrow \text{Th}^{4+} + \text{Ca}^{2+}$ (Poitrasson et al., 2000). These ^{232}Th - ^{208}Pb ages are represented in Figure 35 where two clusters are identified.

One cluster present ages scattered between 539 ± 11 and 554 ± 13 Ma and second cluster between 451 ± 10 and 516 ± 11 Ma, correlated with the altered zone of monazite (high brabantite content).

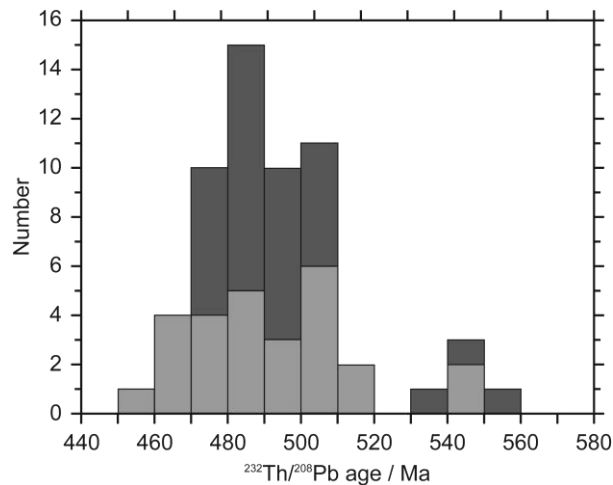


Figure 35: Histogram of Pan-African ^{232}Th - ^{208}Pb ages of monazite grains from the kyanite micaschists (dark grey bars => ZM-10-07 and light grey bars => ZM-10-24).

Zircon grains (100-300 μm) from sample ZM-10-45 are squat with sub-euhedral to euhedral shape and are usually fractured. Zircon grains are generally characterized by oscillatory zoning on cathodo-luminescence (CL) images, a feature consistent for zircon growth in igneous rocks (Figure 36). Some resorption and re-crystallization features are also observed and could probably reflect a complex crystallization during magma evolution or to chemical modification post-crystallization during a metamorphic event (Corfu et al., 2003).

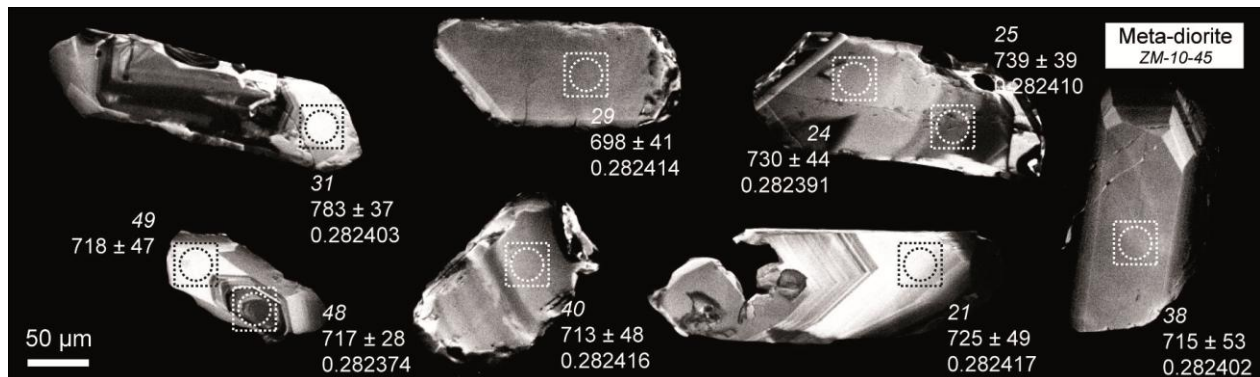


Figure 36: Cathodoluminescence images of zircon grains from the metadiorite sample (ZM-10-45). Dotted circles: location and size of laser spots used for U-Pb isotope analyses ($^{207}\text{Pb}/^{206}\text{Pb}$ ages). Dotted squares: location and size of laser spot used for Lu-Hf isotope analyses ($^{176}\text{Hf}/^{177}\text{Hf}_{(t)}$ ratios).

Zircon grains are mostly concordant ($> 95\% = 30/38$) with an average Th/U ratio of 0.80 ($n=38$) and a $^{176}\text{Lu}/^{177}\text{Hf}$ ratio ranging between 0.00055 and 0.00186 ($n=33$). All zircon grains yield a Concordia age of 720 ± 9 Ma ($n=30$; MSWD=0.37; Figure 37; Table 38). The Lu-Hf isotope analyses of these zircon grains yield homogeneous $^{176}\text{Hf}/^{177}\text{Hf}_t$ ratios ranging between 0.28237 and 0.28242, which correspond to $\varepsilon\text{Hf}(t)$ ranging from +1.1 to +3.1, in the superchondritic uniform reservoir. Two-stage Hf model ages (T_{DM}) for these zircon grains are ranging between 1.50 and 1.40 Ga ($n=33$; Table 39).

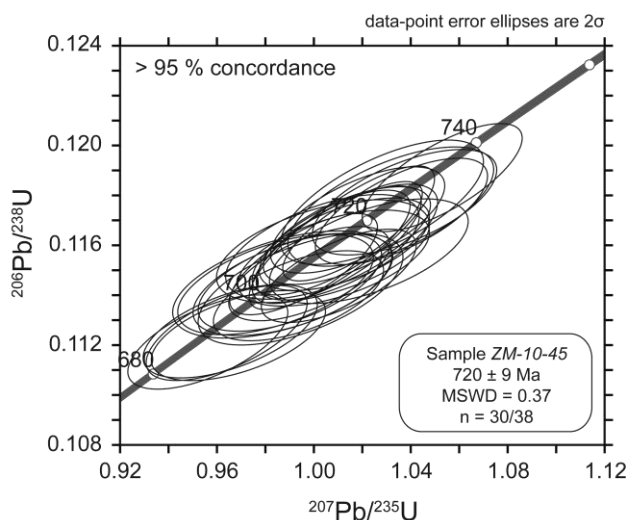


Figure 37: Concordia diagram for U-Pb isotope ratio of X individual zircon grains from the meta-diorite sample (ZM-10-45).

4.5. Geothermobarometry

To evaluate the peak metamorphic conditions of the Amphibolite facies rocks recorded by the mantling rocks, pseudosections were calculated using the whole-rock compositions of the kyanite micaschist (ZM-10-24) sample. These data were completed by conventional quantitative geobarometers as the aluminium-in-hornblende geobarometry for metagabbro rocks (ZM-10-21 and ZM-10-47).

This phase diagram was calculated in the KFMASH chemical system, i.e. excluding Ca-, Na- and Ti-bearing minerals because of the low concentration of these elements, and absence of Ca, Na and Ti in minerals in observed mineral assemblages. As this kyanite micaschist is mainly

composed by hydrate phases (phlogopite and chlorite), we supposed that the effect of H₂O understaruration on assemblages is negligible; we used a $X_{\text{H}_2\text{O}}$ of 1 wt.%. First mineral equilibrium modelling was calculated excluding the iron oxide phases. However, the Fe-Mg phase compositions predicted by this phase diagram were different than the observed mineral compositions.

For example, the predicted compositions for biotite and chlorite are shifted to more Fe-rich compositions than measured, although the relative Fe²⁺-Mg partitioning between the phases is the same. As the mineral assemblage reflecting the peak metamorphic is kyanite-biotite-chlorite-hematite-quartz, one possibility to explain this discrepancy is that the Fe³⁺ contents in the ferromagnesian minerals have been overestimated. This can be explained by the fact that the iron oxide phase, here hematite, has not been taken into account for phase equilibrium modelling. We calculated different *P-T* pseudosections with X_{Fe} step at 0, 20, 40, 60 and 80 % Fe as Fe³⁺ in order to fit the X_{Fe} isopleths of biotite and chlorite within the peak assemblage field. The best fit was obtained for X_{Fe} content of 80% and figure Xa shows the *P-T* pseudosection using the adjusted Fe content. The peak assemblage is predicted to be stable in a field from ~580 to 640 °C between ~5.5 and 12 kbars (Figure 38a). The second *T-X*_{Fe³⁺} pseudosection (Figure 38b) shows that for fixed *P-T* conditions (e.g. at 10 kbars and 650 °C), peak metamorphic assemblage could be kyanite-biotite-chlorite-quartz, kyanite-biotite-chlorite-hematite-quartz, kyanite-biotite-chlorite-talc-hematite-quartz or even kyanite-biotite-talc-hematite-quartz. This can be explained by a passive enrichment in MgO content due to an increase of the $X_{\text{Fe}^{3+}}$ content [$\text{Fe}_2\text{O}_3/(\text{FeO} + \text{Fe}_2\text{O}_3)$]. This is expressed by talc formation at the expense of chlorite.

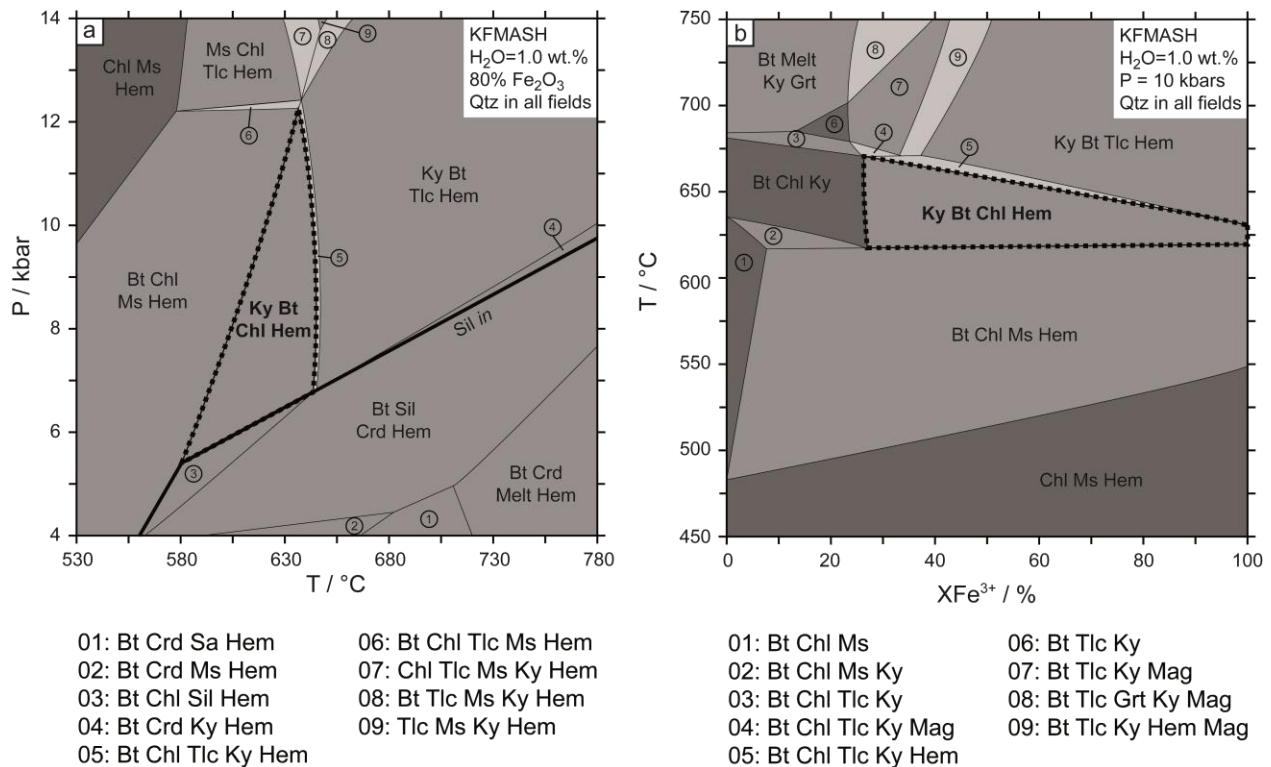


Figure 38: a: Mineral equilibria modelling results for the kyanite micaschist (*ZM-10-24*) rimming the Solwezi basement core. b: T - $X_{Fe^{3+}}$ pseudosection at 10 kbar. In both pseudosections, heavy dashed line underlines the field of the estimated peak assemblage represented by Kyanite-Biotite-Chlorite-Hematite+Quartz. Abbreviations: Bt = Biotite; Chl = Chlorite; Crd = Cordierite; Grt = Garnet; Hem = Hematite; Ky = Kyanite ; Mag = Magnetite ; Ms = Muscovite; Qtz = Quartz; Sa = Sanidine; Sil = Sillimanite ; Tlc = Talc.

For more reliable quantitative pressure estimation, the Al^{tot} (total amount of Al calculated anhydrous on a 23-oxygen) in hornblende barometers (Hammarstrom and Zen, 1986; Schmidt, 1992) were applied to the metagabbroic rocks, intrusive within the Katanga sequence. These geobarometers were calibrated for calc-alkaline intrusive rocks with the extensive buffering mineral assemblage: amphibole, plagioclase, K-feldspar, quartz, biotite, titanite, magnetite, ilmenite and epidote. Ague (1997) argued that the regional pressure gradients determined with the Al-in-hornblende barometers are valid, but the absolute values of P show an error of ± 1.5 kbar. The pressure estimates for the hornblende range from 8.5 to 9.9 kbar and from 8.2 to 9.5 kbar (Hammarstrom and Zen, 1986; $P = 5.03Al^{tot} - 3.92$ kbar; Schmidt, 1992; $P = 4.76Al^{tot} - 3.01$ kbar). The above P estimates are in agreement with the P - T field predicted by the kyanite-biotite-chlorite-quartz-hematite assemblage. The peak metamorphic conditions (i.e. 9 ± 1.5 kbar) correspond to burial depth of ca. 25-35 km.

5. Core rocks: Garnet amphibolites and kyanite-garnet amphibolites

5.1. Sampling

The Pre-Katanga basement inliers are composed by ortho- and paragneiss locally migmatitic and some amphibolites. Basement rocks are ranging in age from Paleoproterozoic to Mesoproterozoic (Cosi et al., 1992; John, 2001; Eglinger et al., to be submitted). Garnet amphibolites (*ZM-12-13* and *ZM-12-16*; Figure 39) were sampled within the gneissic-migmatitic rocks outcropping within the core of the Mwombezhi dome (Malundwe mine). Mineralogy of these rocks is dominated by amphibole, garnet, plagioclase and quartz with some Ti-Fe oxides. A garnet-kyanite amphibolite schist (*ZM-82-14*) was also sampled. Mineralogy is characterized by garnet, kyanite, amphibole, biotite, quartz and feldspar. All these rocks have also been metamorphosed to Amphibolite facies.

5.2. Whole rock geochemistry

Garnet amphibolites (samples *ZM-12-13* and *ZM-12-16*) whole-rocks analyses show sub-alkaline basaltic-andesitic compositions, with silica contents ranging from 54.28 to 54.96 wt.% and K₂O contents from 0.78 to 1.68 wt.% (Figure 40a; Table 29). In the FeO*/MgO vs. SiO₂ diagram, they plot in the medium-Fe field, with Mg numbers ranging from 0.50 to 0.59. Their Cr and Ni contents vary, respectively, from 164 to 196 ppm and from 47 to 82 ppm. TiO₂ content is moderate, ranging from 1.54 and 1.60 wt.%, with a Ti/V ratio between 35 and 45. Chondrite normalized REE contents show fractionated patterns ($1.1 < La_N/Yb_N < 4.1$; $0.5 < Gd_N/Yb_N < 1.2$), with slight Eu anomalies ($0.84 < Eu^* < 1.07$; Figure 40b). The kyanite-garnet amphibolite is characterized by a high Al₂O₃ content, above 18.41 wt%. TiO₂, MgO and Fe₂O₃ contents are respectively 1.01, 7.77 and 11.58 wt% (Table 29). In the Na₂O versus SiO₂ diagram, this sample shows intermediate composition between alkaline to sub-alkaline fields (Figure 40a). Chondrite normalized REE pattern show a positive anomaly in Eu ($Eu^* = 1.76$; Figure 40b). In the multi-element diagram, these three amphibolite samples show negative anomalies in Nb-Ta and Sr. They also show positive anomalies in Th-U (Figure 40c).

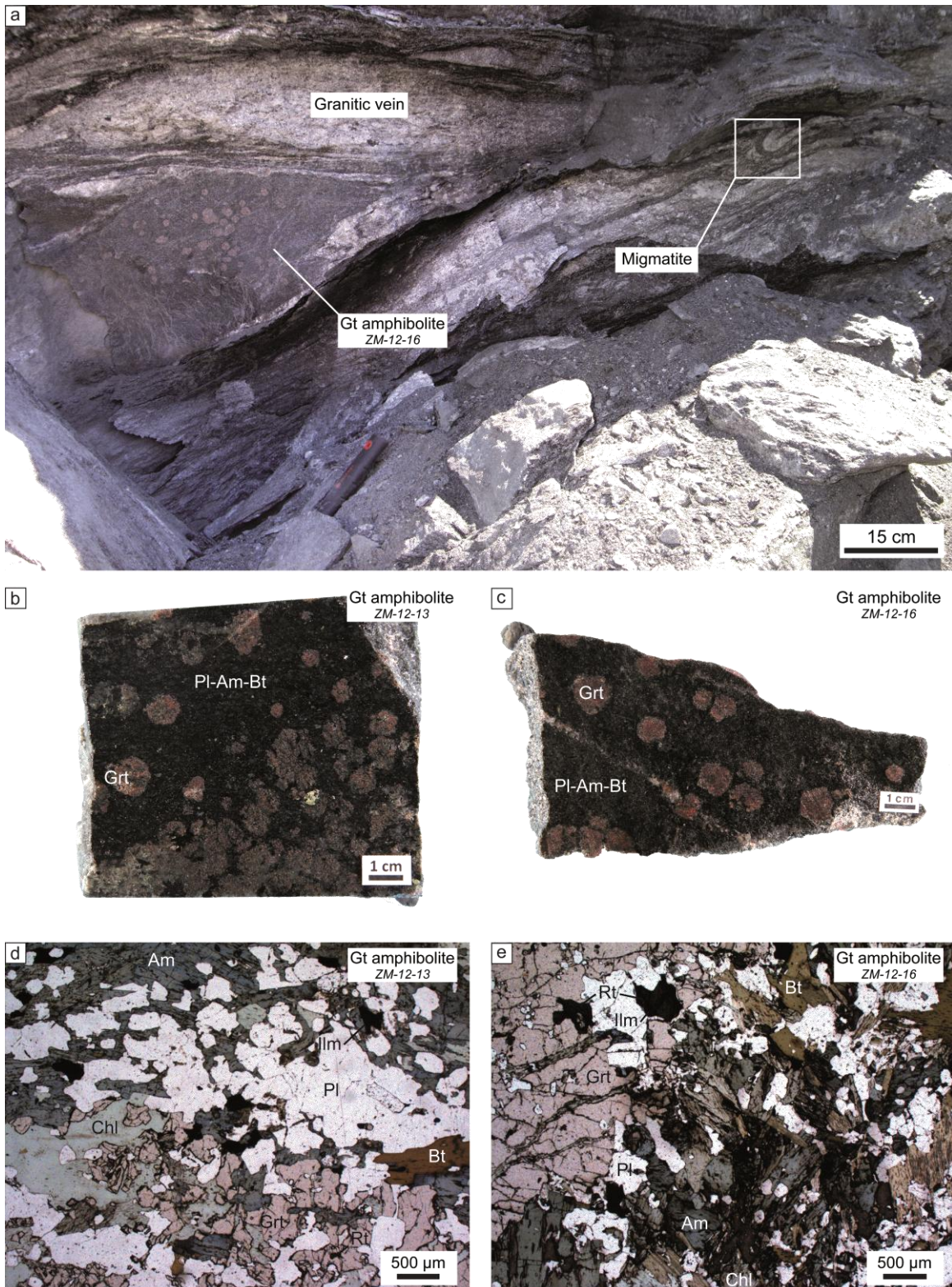


Figure 39: a: Garnet amphibolite boudins transposed into the metatexite foliation (ZM-12-16: Malundwe mine). b, c: Garnet porphyroblasts in amphibole-rich matrix (samples ZM-12-13 and ZM-12-16). d-e: Rutile inclusions within garnet porphyroblasts in plagioclase-amphibole-biotite matrix.

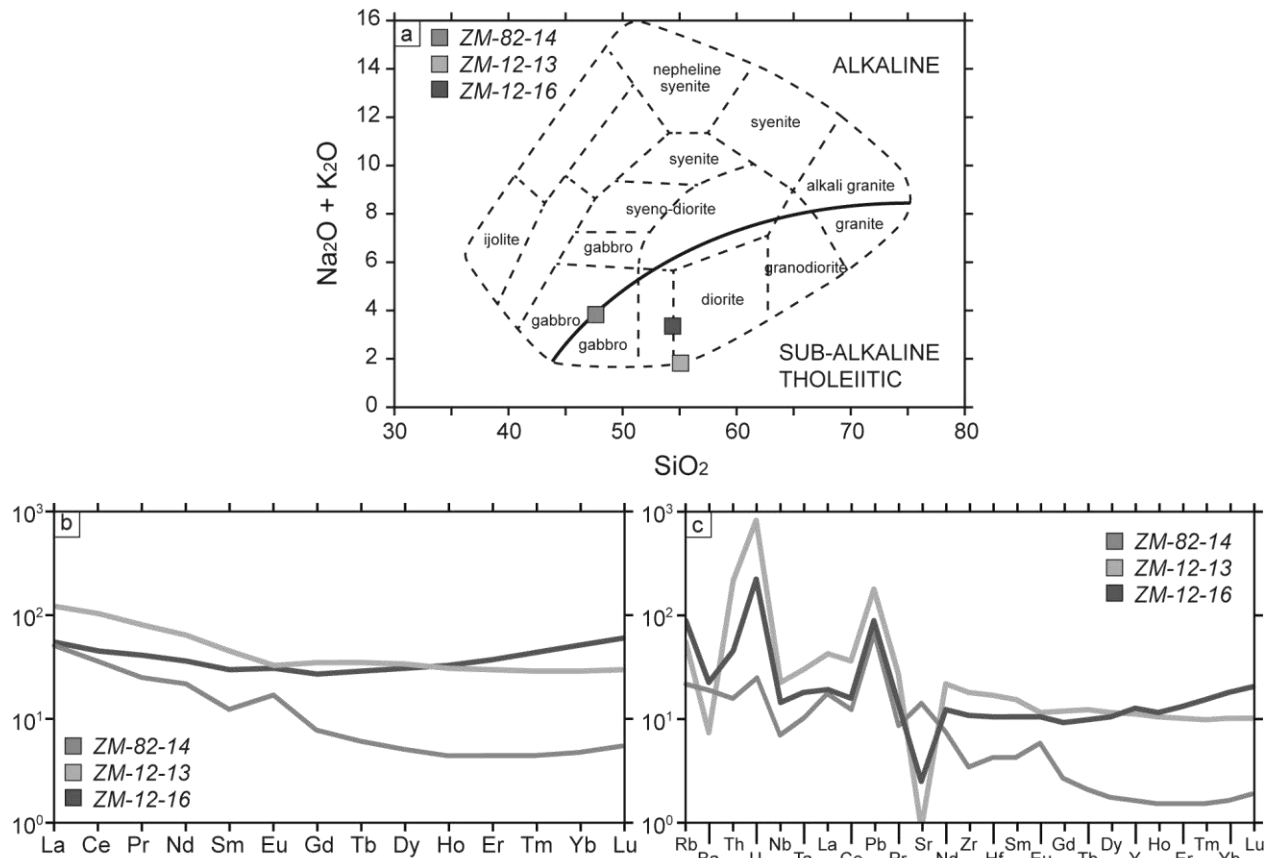


Figure 40: Major and trace elements geochemistry of the amphibolites from the Mwombezi area.

5.3. Petrography and mineral chemistry

Garnet amphibolites show a porphyroblastic texture characterized by the presence of garnet poikiloblasts (1-2 cm; Figure 39b, c). Matrix is dominated by amphibole, plagioclase, quartz, biotite and ilmenite. Rare rutile grains are included in the amphibole and/or garnet and locally within matrix minerals (Figure 31d, e). Some rutile grains are surrounding by ilmenite in the matrix. Amphibole and ilmenite define a discrete schistosity. Amphibole compositions from the matrix lie in the compositional field of tschermakite and plagioclase is dominated by andesine ($X_{\text{An}} 0.45-0.47$; Table 31; Table 32). Some plagioclase grains show higher Ca content characterized by labradorite composition ($X_{\text{An}} 0.56$). Neither amphibole nor plagioclase in this amphibolite sample show significant zoning across individual grains. Garnet grains do not show a strong zoning between core and rim but are characterized by a slight decrease in Ca with a slight increase in Mg and Fe from the core to the rim (core: $X_{\text{Grs}} 0.17-0.18$, $X_{\text{Prp}} 0.18$, $X_{\text{Alm}} 0.64-0.65$ and rim: X_{Grs}

0.20 X_{Prp} 0.17 X_{Alm} 0.63). These trends may represent relict growth zoning that has been extensively modified at high temperatures. Growth zoning in granoblastic garnet is usually homogenized at $T > 600$ °C. Garnet porphyroblasts contain almost all mineral phases of the matrix as inclusions, to the exception of ilmenite. The high X_{Fe} may correlate with high Fe content in the igneous precursor. Chlorite grains, represented by ripidolite (X_{Mg} 0.60), overprint the schistosity and are interpreted as post-tectonic minerals.

Garnet-kyanite amphibolites are characterized by a lepto-porphyroblastic texture marked by the presence of kyanite and garnet poikiloblasts (0.5-1 cm). Matrix is dominated by plagioclase, oligoclase and andesine (An 0.26-0.42), quartz, amphibole, biotite (X_{Mg} 0.69-0.70 and Ti content of 1.27-1.52 wt.%) and ilmenite (Table 33; Table 34). Two generations of amphibole are distinguished optically and by their heterogeneous compositions. The first generation is represented by tschermakite (calcic amphibole) and is mainly associated with matrix minerals. The second generation, represented by gedrite (ferro-magnesian amphibole), underlines the schistosity. Gedrite grains are affected by microboudinage. Garnet and kyanite poikiloblasts contain all matrix minerals and rutile is mostly included within kyanite grains. The composition of garnet is quite uniform between core (X_{Alm} 0.61 X_{Grs} 0.16 X_{Prp} 0.23) and rim (X_{Alm} 0.60 X_{Grs} 0.14-0.16 X_{Prp} 0.24-0.26). Some chlorite grains, represented by sheridanite (X_{Mg} 0.77), overprint the deformation and are interpreted as post-tectonic blasts.

5.4. Geochronology

We analyzed handpicked separates of garnet and the whole rock for Lu-Hf isochron dating (Figure 41). Hafnium contents of the whole rocks for samples *ZM-82-14* and *ZM-12-13* range, respectively, between 0.81 and 3.49 ppm and Lu contents between 0.1 and 0.6 ppm. Garnets exhibit variable Lu contents (from 1.1 up to 14 ppm) at moderate Hf concentrations between 0.11 and 0.50 ppm. The spread in $^{176}\text{Lu}/^{177}\text{Hf}$ ratios of the garnets ensured a robust isochron regression. We determined two multi-point isochrons: one for the garnet amphibolite (sample *ZM-82-14*; Figure 41a) at 530.0 ± 1.4 Ma with MSWD (mean square of weighted deviates) = 0.39 and one for the garnet-kyanite amphibolite (sample *ZM-12-13*; Figure 41b) at 532.8 ± 2.1 Ma with MSWD = 1.07.

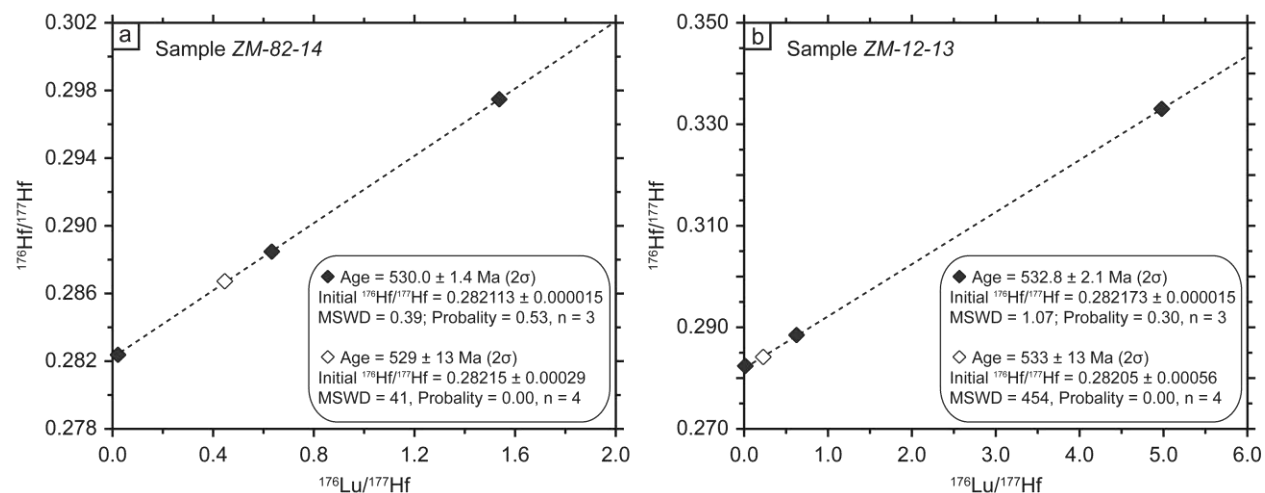


Figure 41: Lu-Hf garnet-whole rock isochrons for the garnet-kyanite amphibolite (a) and the garnet amphibolite (b) from the Mwombezi basement.

5.5. Geothermobarometry

To evaluate the peak metamorphic conditions of the Amphibolite facies rocks recorded by the core rocks, one pseudosection was calculated using the whole-rock compositions of the garnet amphibolite (*ZM-12-13*) sample.

This phase diagram was calculated in the TiNCKFMASH chemical system with H₂O-saturated conditions. As some relict rutile grains are included in amphibole and garnet and are largely replaced by ilmenite in the matrix, this garnet amphibolite is characterized by biotite-plagioclase-garnet-amphibole-rutile peak metamorphic assemblage. This peak assemblage is predicted to be stable in a large field from ~610 to 740 °C between ~7.5 and 13.5 kbars, within the rutile stability field, consistent with petrographic observations. As the garnet compositions are quite uniform between core and rim, we can plot the X_{Mg} , X_{Ca} and X_{Fe} isopleths to constraint the P - T conditions of the peak metamorphism. These isopleths intersect at high angles, providing unique intersection point with a good degree of confidence (Figure 42a, b, c). Garnet isopleths predict a P - T field from 620 to 640 °C between 8.9 and 9.7 kbars (Figure 42d).

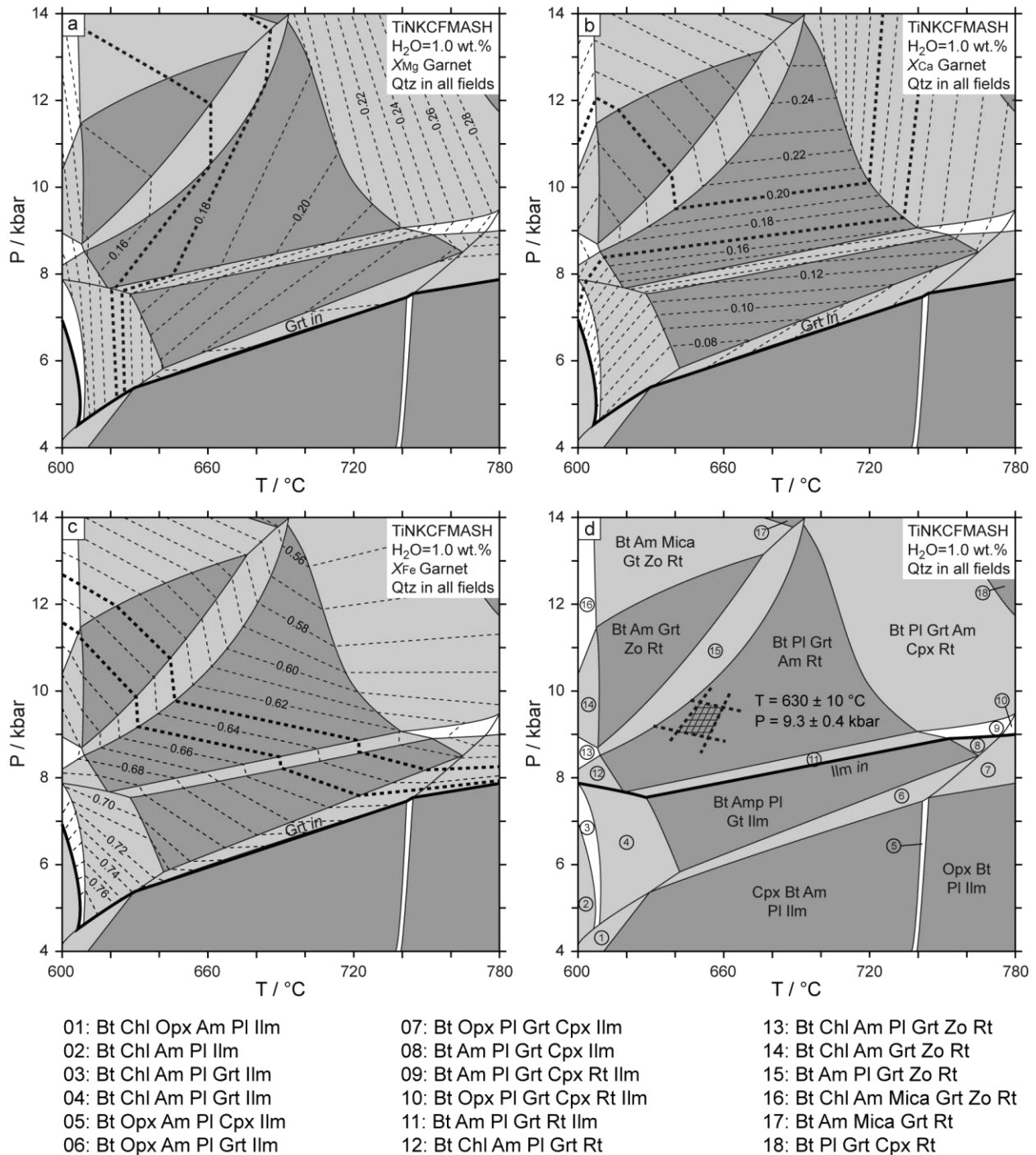


Figure 42: Mineral equilibria modelling for garnet amphibolite (ZM-12-13) outcropping in the Mwombezhi basement core. a to c: Pseudosections showing the calculated garnet isopleths modelling. Heavy dashed lines represent the calculated composition of garnet grains. Black heavy line represents the limit of the garnet stability field. d: Dashed heavy black lines show the intersection for the measured garnet composition within the field of the stable assemblage. Black heavy line represents the limit of the rutile stability field. Abbreviations: Am = Amphibole; Bt = Biotite; Chl = Chlorite; Cpx= Clinopyroxene; Grt = Garnet; Ilm = Ilmenite; Opx = Orthopyroxene; Pl = Plagioclase; Rt = Rutile; Zo = Zoisite.

6. Discussion

Pre- to syn-collisional context of the Pan-African Lufilian belt are discussed in the next sections based on results from this study and completed by data published in the literature.

6.1. Pre-collisional divergence

In the Lufilian belt, the Nchanga intrusion is dated at 883 ± 10 Ma (Armstrong et al., 1999; Armstrong et al., 2005) and exhibits WPG (A-type granite) affinities with high contents of ($\text{Na}_2\text{O} + \text{K}_2\text{O}$), Ga/Al, Zr, Y, Nb and low abundances of CaO and MgO (Katongo et al., 2004). On the basis of geochronological and geochemical data, Katongo et al. (2004) suggest that the Nchanga intrusion was emplaced during the earliest extensional stages of continental rifting (Figure 46a). This magmatic event marks the first continental rifting stage leading the dislocation of the Congo-Tanzania-Bangweulu Craton, at ca. 880 Ma forming the Roan basin (Porada and Berhorst, 2000). Similar granitoids and felsic volcanic rocks were described in the Zambezi belt and dated between ca. 879 Ma (Kafue metavolcanic rocks; Wilson et al., 1993) and ca. 820 Ma (Ngoma gneiss; Hanson et al., 1988). Detrital zircon grains, found within cross-bedded Lower Roan quartzite, dated at ca. 880 Ma by U-Pb (Armstrong et al., 2005) confirm the emplacement of the Roan Group detrital sediments after ca. 880 Ma. The Roan Group, described in the Lufilian belt and interpreted as a rift-to-drift sequence, is characterized by a basal siliciclastic unit, known as the Lower Roan Group (Binda, 1994). Two studies constrain the provenance of the Lower Roan Group metasediments in the eastern part of the internal orogenic belt, around the Kafue Anticline (Armstrong et al., 2005; Master et al., 2005). Detrital zircons ages, obtained by U-Pb TIMS *in-situ* analyses, indicate a mainly Paleoproterozoic provenance for the basal sequence of the Katanga Supergroup (Armstrong et al., 2005; Master et al., 2005). According to the data presented in this paper, detrital zircon ages from the kyanite micaschist (ZM-10-24) rimming the Solwezi dome and also interpreted as the Lower Roan Group, give the same Paleoproterozoic provenance. $^{207}\text{Pb}/^{206}\text{Pb}$ ages with a concordance above 95% are mostly ranging between 1895 ± 14 and 1724 ± 16 Ma (Figure 43). The youngest concordant analysis obtained on single zircon grain provides a maximum age of deposition at 1282 ± 21 Ma. This youngest age corresponds to the age of the late magmatic/metamorphic event recorded by the Solwezi and Mwombezi basement inliers, dated between 1.24 and 1.11 Ga (Eglinger et al., to be submitted).

Consequently, we consider that the Lower Roan sediments in the western part of the Domes region was deposited at the same time as the Lower Roan sequence in the eastern part, namely after ca. 880 Ma. Majority of these zircon grains with crystallization ages between ca. 1.89 and ca. 1.28 Ga (Table 36) shows subchondritic ϵ_{Hf} and have Hf model ages between ca. 2.9 and 2.5 Ga (Table 37) suggesting the remobilization of an old Neoproterozoic crust.

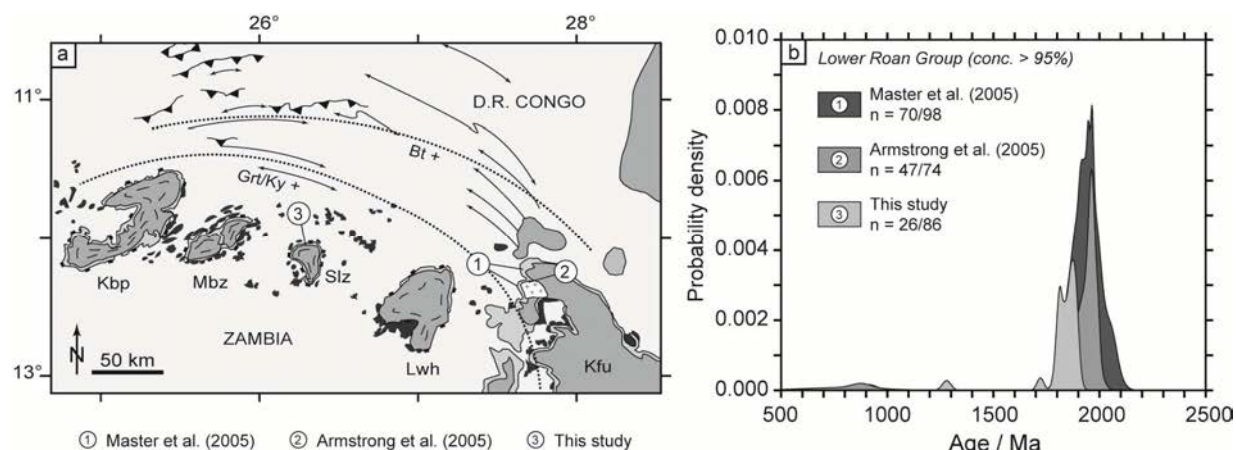


Figure 43: Provenance ages of the studied Lower Roan Group. a: Location of studied samples from literature and this study (ZM-10-24). b: Probability density plot of $^{207}\text{Pb}/^{206}\text{Pb}$ ages for detrital zircon grains of the Lower Roan Group.

The deposition of the Upper Roan Group, dominated by clastic metasediments and marble, occurred before the intrusion of numerous meta-gabbroic sills and dykes dated at ca. 750 Ma (Barron et al., 2003). This second pulse of magmatism is linked to a second rifting event forming the Mwashia-Kundelungu basin (Porada and Berhorst, 2000; Figure 46b). Volcanic activity related to this rifting is well expressed in both external and internal zones of the Lufilian orogenic belt. In the external zone, in DRC and NW Zambia, the Mwashia Group is characterized by a thick sequence of mafic volcanic rocks (Lwawu volcanics) deposited at 765 ± 5 Ma, age U-Pb on zircon (Key et al., 2001) which stratigraphically overlies the Roan Group. In the internal zone, several meta-gabbroic bodies were mapped and two of them, sampled in the Solwezi area, yielded U-Pb zircon ages of 745 ± 8 and 752 ± 9 Ma (Barron, 2003; Barron et al., 2003). In our study, the meta-gabbros from Solwezi (ZM-10-21 and ZM-10-47) and the meta-basalt from Mwombezi area display continental-within-plate and alkaline geochemical signature. They share a systematic low Th/La ratio (0.12-0.32) which is interpreted to trace continental tholeiites (Hawkesworth and Gallagher, 1993). A high ratio (> 1) indicates an enriched and purely

lithospheric source (spinel lherzolite). In contrast, a low Th/La ratio involves the contribution of an asthenospheric component. In the Lufilian belt, we suggest that tholeiitic basalts were generated by decompression of the continental lithosphere at the onset of continental extension. Metabasic rocks (*ZM-10-21*, *ZM-10-47* and *ZM-12-27*) from the Katanga cover described in this paper display similar petrographic and geochemical characteristics to the gabbros described by Tembo et al. (1999) in the eastern part of the Domes region, around the Luswishi dome and the Kafue Anticline. All these metabasic rocks of the Domes region have geochemical characteristics of basaltic rocks produced in a continental rift environment (e.g. the East African Rift system). Rifting did not progress beyond the continental stage in the Lufilian belt. Mafic rocks were also described in the Zambezi belt by John et al. (2003) but they are characterized by N-MORB chemistries and are interpreted to be vestiges of an oceanic crust (John et al., 2003).

A new U-Pb age at 720 ± 9 Ma on a meta-diorite, presented in this study, provides additional time constraints on the second rifting event related to the formation of the Mwashia-Kundelungu basin. The timing of this rifting was constrained by U-Pb zircon dating of two volcanic sequences dated between ca. 765 Ma and ca. 735 Ma, respectively (Key et al., 2001). These meta-diorites, plotting in the field of within-plate granites, are characterized by a very low Th/La ratio (0.096-0.097) and do not present Nb-Ta anomalies. The very low Th/La ratio points to a strong asthenospheric contribution in their source. The enrichment of the REE and HFS elements cannot be produced by any crystal fractionation mechanism from a parent magma depleted in these elements. The enrichment is also not due to crustal assimilation because REE abundances are higher than the bulk crust values, thus adding such crustal material would diminish the REE content of the rocks. Moreover, the Sr and Nd isotopic ratios do not show any mixing relationship. Hence, it can be argued that the enrichment of the HFS and REE elements is a characteristic of the source. The high $^{87}\text{Sr}/^{86}\text{Sr}$ and low $^{143}\text{Nd}/^{144}\text{Nd}$ measured ratios ranging from 0.707507 to 0.709975 and 0.511590 to 0.511782 are in agreement with an enriched mantle source (Dupre and Allegre, 1983; Figure 44). Such a reservoir could be related to an old subcontinental lithosphere. We conclude that these diorites were emplaced during late stages of continental lithospheric rifting of the south margin of Congo-Bangweulu craton, involving an asthenospheric component in the genesis of these metadiorites.

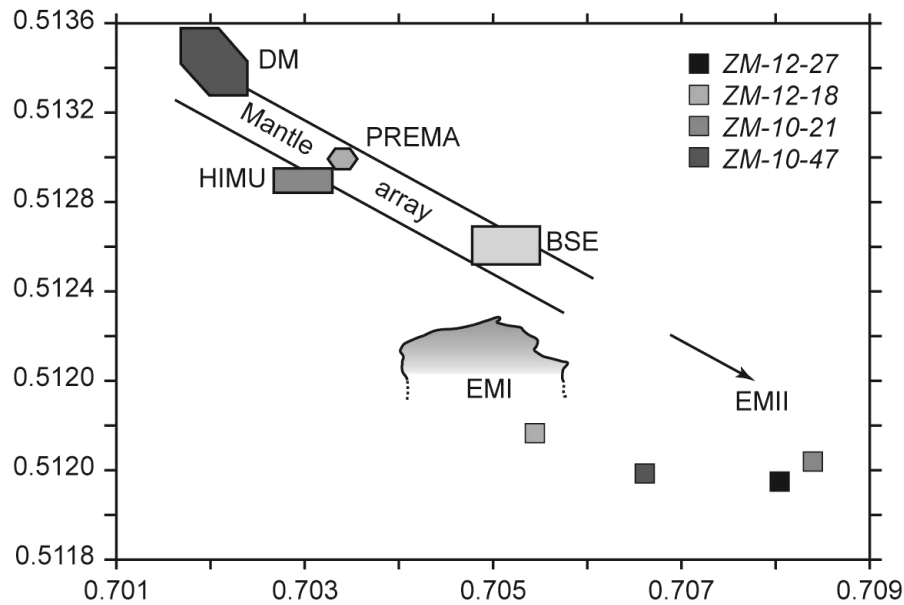


Figure 44: $^{143}\text{Nd}/^{144}\text{Nd}$ versus $^{87}\text{Sr}/^{86}\text{Sr}$ isotope correlation diagram showing the main oceanic mantle reservoirs of Zindler and Hart (1986) and the position of the Pan-African magmatic rocks (metagabbros *ZM-10-21* and *ZM-10-47*, metadiorite *ZM-12-18* and metabasalt *ZM-12-27*). Abbreviations: BE = Bulk Silicate Earth; DM = Depleted Mantle; EMI and EMII = Enriched Mantle; HIMU = Mantle with high U/Pb ratio; PREMA = PREvalent MANTle composition. The mantle array is defined by many oceanic basalts and a bulk Earth value of $^{87}\text{Sr}/^{86}\text{Sr}$ can be obtained from this trend.

Zircon crystallization ages recorded by mafic to intermediate intrusions in the Katanga sequence around the Solwezi dome are ranging between ca. 750 Ma (meta-gabbro; Barron et al., 2003) and ca. 720 Ma (meta-diorite; this study), representing a Neoproterozoic peak of magmatic activity. Whole rock Nd model ages for metagabbros (*ZM-10-21* and *ZM-10-47*) and zircon Hf model ages for meta-diorite (*ZM-10-45*) yield a similar range of T_{DM} from 1.38 to 1.54 Ga and from 1.40 to 1.50 Ga, respectively (Figure 45; Table 39). These model ages are calculated for samples which were extracted from a depleted mantle but if we consider that the source of these rocks is an enriched subcontinental mantle, these T_{DM} model ages have no significance. Another alternative to explain these Mesoproterozoic model ages could be related to the presence of an enriched mantle source by successive subduction whereby crustal material is injected into the mantle. In this case, the T_{DM} reflect a mixing age and not the age of the mantle extraction.

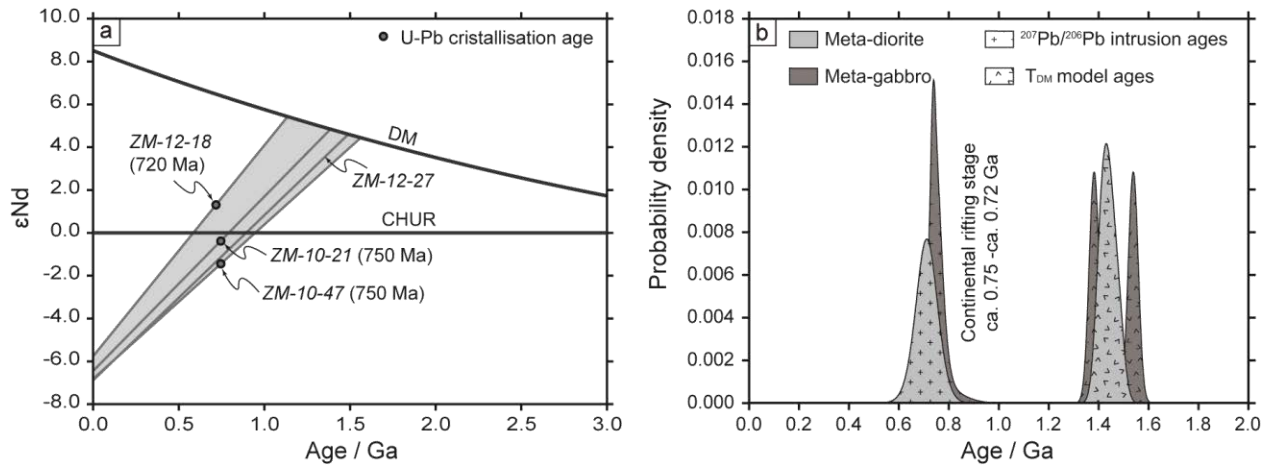


Figure 45: ϵ_{Nd} versus U-Pb ages and probability density plot of $^{207}\text{Pb}/^{206}\text{Pb}$ intrusion ages and T_{DM} (Sm/Nd and Lu/Hf) model ages for meta-gabbro (ZM-10-21 and ZM-10-47) and meta-diorite (ZM-10-45) intrusives within the Katanga cover. Abbreviations: CHUR = CHondritic Uniform Reservoir; DM = Depleted Mantle.

Transition from divergent to convergent tectonic regime is recorded by Eclogite facies metamorphism, dated between 638 ± 61 and 595 ± 10 Ma by whole-rock and garnet Sm-Nd isochron on mafic boudins in the Zambezi belt (John et al., 2003; Figure 46c, d). Peak P - T conditions have been estimated at 630-690 °C and 26-28 kbars and are compatible with burial of these rocks in a subduction zone (John and Schenk, 2003; John et al., 2003). This Neoproterozoic ocean (Zambezi ocean) between the Kalahari and the Congo-Tanzania-Bangweulu cratons was relatively large (> 1000 km; John et al., 2003).

6.2. Syn-collisional convergence

The geodynamic model proposed in the literature to explain the orientation of regional structures in the Lufilian and Zambezi belts involves, respectively, thin-skinned and thick-skinned thrust tectonic (Porada and Berhorst, 2000). In the Lufilian and Zambezi belts, regional peak metamorphism reached Amphibolite facies, up to Upper Amphibolite facies characterized by kyanite-talc assemblage (Johnson and Olivier, 1998, 2002; John et al., 2004). P - T conditions recorded by kyanite-talc micaschist (whiteschists) peaked at $ca. 750 \pm 25$ °C at 13 ± 1 kbar and 600-900 °C at 8-15 kbar in the Lufilian and Zambezi belts, respectively, along a clockwise P - T path (Johnson and Oliver, 1998, 2002, 2004; John et al., 2004).

Our P - T investigations in the internal orogenic Lufilian belt give similar range of pressure and temperature, just slightly lower temperature estimates than the ones obtained by John et al. (2004) using the garnet-biotite geothermometer applied on mineral assemblages of kyanite-talc micaschists from Kabompo, Mwombezhi and Solwezi domes. The P - T conditions predicted by the pseudosection from the Neoproterozoic kyanite micaschist from the Katanga cover, outcropping around the Solwezi core, are 610 ± 30 °C and 9 ± 3 kbar, resulting in lower P - T conditions than P - T estimates calculated by John et al. (2004) on the kyanite-talc paragenesis. Pseudosection calculated for kyanite micaschists in this study shows that the kyanite-talc assemblage is a function of the fO_2 (relative to the Fe^{3+} content). We conclude that the kyanite-phlogopite-chlorite-quartz-hematite assemblage presented in this study reflects the metamorphic peak assemblage, the same as John et al. (2004), but reaching lower P - T conditions. Similar P - T conditions are estimated for the garnet amphibolite from the Mwombezhi basement, at 630 ± 10 °C and 9.3 ± 0.4 kbar.

The geochronological data presented in this paper are also discussed in relation with previously published data in order to reconstruct the tectonic context. Two ^{232}Th - ^{208}Pb age clusters were obtained on monazite grains from the kyanite micaschist cover (samples *ZM-10-07* and *ZM-10-24*) in the north of the Solwezi dome. The first cluster is characterized by ^{232}Th - ^{208}Pb dating ranging from 554 ± 13 to 539 ± 11 Ma. These ages are marginally older than the previously published U-Pb concordant ages of 525 ± 2 Ma, 532 ± 2 Ma and 529 ± 2 Ma obtained on monazite hosted by the kyanite-talc micaschists respectively from the Kabompo, Mwombezhi and Solwezi domes in the internal zone of the Lufilian belt (John, 2001; John et al., 2004). Moreover, Eglinger et al. (submitted) published a U-Pb age of 532 ± 8 Ma on synmetamorphic uraninite. These uraninite grains are hosted by the same kyanite micaschists and are synchronous to the kyanite-phlogopite-clinocllore paragenesis development. The new Lu-Hf isochron ages of 530.1 ± 1.4 and 532.8 ± 2.1 Ma obtained from the garnet amphibolite within the Mwombezhi basement are consistent with previously determined ages on monazite and uraninite. Ages obtained in this study, ranging between ca. 555-530 Ma, are interpreted to record the peak of Pan-African P - T metamorphic conditions during the continental collision between the Congo-Tanzania-Bangweulu and Kalahari cratons, as proposed by John et al. (2004).

Eglinger et al. (submitted) proposed that the second ^{232}Th - ^{208}Pb ages cluster obtained on monazite grains from the kyanite micaschists (samples *ZM-10-07* and *ZM-10-24*), ranging from 516 ± 11 Ma to 451 ± 10 Ma, record the low-grade retrogression of higher-grade metamorphic rocks (Figure 46e). These monazite grains are hosted by phlogopite marking a top to the north sense of shear. We interpret this extensional shear zone as a structure which contributed to the exhumation of metamorphic rocks of the core of the Solwezi dome in the internal orogenic Lufilian belt, between ca. 515-450 Ma, leading to isothermal decompression and transition from a MP/MT to a LP/HT metamorphic gradient (Figure 46f). These ages are synchronous to Rb-Sr isochrons obtained in the domes region (John, 2001). Indeed, the gneisses exposed in the core of the Solwezi dome yield a Rb-Sr muscovite-plagioclase isochron at 490 ± 5 Ma and a Rb-Sr biotite-plagioclase isochron at 476 ± 5 Ma. The kyanite-garnet micaschist rimming the core of Solwezi dome yields a biotite-plagioclase Rb-Sr isochron at 469 ± 5 Ma (John, 2001). Considering a closure temperature of muscovite for Rb-Sr at ca. 500 ± 50 °C, and for biotite at ca. 350 °C (Hanson and Gast, 1967; Dodson, 1979), these results indicate that rocks from the cover and basement of the Solwezi dome experienced a similar cooling history below about 350 °C after the peak of metamorphism.

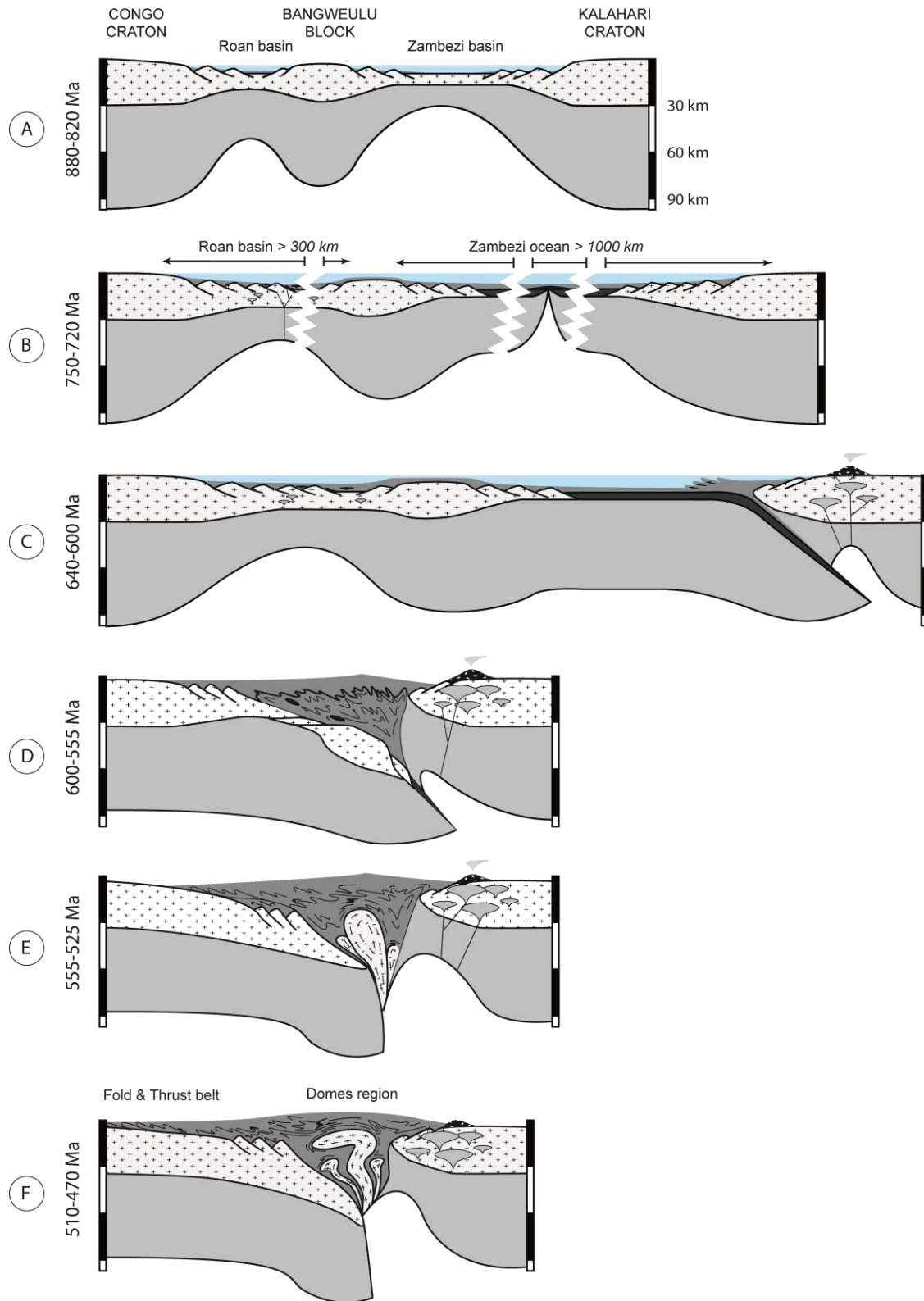


Figure 46: Schematic diagrams showing the Pan-African Wilson cycle of the Lufilian belt. a, b: Rodinia dislocation during two successive rifting stages. c, d: Oceanic followed by continental subduction. e, f: Continental tectonic accretion and high grade rocks exhumation.

6.3. *Pre- to syn-collisional geodynamic evolution of the Lufilian belt*

Detrital zircon from kyanite micaschists are shown to be derived from, mainly, a Paleoproterozoic and, minimally, Mesoproterozoic basement sources, without an Archean inheritance. Paleoproterozoic crystallization ages are known in the Bangweulu block (De Waele et al., 2006; De Waele and Fitzsimons, 2007), in the Irumide belt (De Waele et al., 2006), and also in the Domes region of the Lufilian belt (John, 2001; Rainaud et al., 2005; Eglinger et al., to be submitted). Mesoproterozoic crystallization ages are mostly described in the Irumide belt (De Waele et al., 2006) and in the western part of the Domes region, within the Mwombezhi and Solwezi basement inliers (Eglinger et al., to be submitted). Using coupled U-Pb and Lu-Hf isotopes, Eglinger et al. (to be submitted) proposed that the basement inliers exposed in the internal orogenic Lufilian belt, referred as the Domes region, represent the southwestern metacratonic boundary of the Bangweulu block. On the basis of the detrital ages from the Lower Roan kyanite micaschists collected in the Solwezi area, we propose that during the Neoproterozoic at ca. 880-820 Ma, the south margin of the Bangweulu block, which is part of the Congo-Tanzania craton, was affected by extension,. This continental margin was also characterized by a second extensional stage, at ca. 760-720 Ma (Key et al., 2001; this study), characterized by the emplacement of continental tholeiites (Tembo et al., 1999) with mafic to intermediate intrusions (Barron, 2003; this study). According to the geochemical signatures of its sedimentary deposits, the Mwashia-Kundelungu basin did not evolve into a true ocean basin.

In summary, we distinguish from north to south (present coordinates): (i) the southern margin of the Congo-Tanzania-Banweulu craton (ii) a continental rifting basin filled with the Roan Group and then the Mwashia-Kundelungu Groups sediments; (iii) a micro-continental block representing the southern margin of the Bangweulu block; (iv) a large basin which will evolve as a true oceanic basin, called the Zambezi ocean (Johnson et al., 2005; Figure 46). The closure of the Zambezi ocean occurred at ca. 600 Ma by subduction leading to the formation of the Zambezi belt, driving the Congo-Tanzania-Bangweulu lithospheric plate. The development of Upper Amphibolite assemblages in both the Paleoproterozoic-Mesoproterozoic reworked basement and the Neoproterozoic cover sequence in the Domes region implies that they originated by aborted subduction of the micro-continental block during the Lufilian orogeny. Continental collision leading to the Gondwana formation is dated at ca. 555-525 Ma (John et al., 2004; this study).

Similar ages are known in the Zambezi belt, at ca. 550-520 Ma (Johnson et al., 2005), and in the Damara belt, at ca. 540-510 Ma (Jung et al., 2001; Jung and Mezger, 2003), suggesting the closure of a single ocean basin, the Adamastor-Zambezi oceans (Johnson et al., 2005).

This new geodynamic model implies that the Gondwana amalgamation is not a single collision between two large cratons, as it is was suggested by some authors (e.g. John et al., 2004).

Acknowledgments

We would like to thank CNRS (NEEDS) and AREVA for financial support. Barrick Limited is thanked for providing the samples and their technical support in the field. The authors are grateful to Olivier Rouer (GeoRessources, Nancy) for their technical support in providing analytical data on EMP.

Table 27: Sampling details. Abbreviations: Am = Amphibole, Ap = Apatite, Bt = Biotite, Chl = Chlorite, Ep = Epidote, Fsp = Feldspar, Grt = Garnet, Hem = Hematite, Ilm = Ilmenite, Ky = Kyanite, Mag = Magnetite, Mnz = Monazite, Ms = Muscovite, Phl = Phlogopite, Pl = Plagioclase, Qtz = Quartz, Rt = Rutile, Ttn = Titanite, Zrn = Zircon.

Number	Label	Sampling	Coordinates		Lithology	Mineralogy	
			North	East		Primary	Accessory
1	ZM-10-07	Outcrop	8647897	432804	Ky micaschist	Qtz, Ky, Phl, Chl, Hem, Rt	Ms, Mnz, Zrn
1	ZM-10-08	Outcrop	8648445	434800	Ky micaschist	Qtz, Ky, Phl, Chl, Hem, Rt	Ms, Mnz, Zrn
1	ZM-10-24	Outcrop	8646101	446153	Ky micaschist	Qtz, Ky, Phl, Chl, Hem, Rt	Ms, Mnz, Zrn
1	ZM-10-41	Outcrop	8647790	430690	Ky micaschist	Qtz, Ky, Phl, Chl, Hem, Rt	Ms, Mnz, Zrn
2	ZM-10-21	Outcrop	8649847	444491	Metagabbro	Am, Pl, Mag, Rt	Ttn, Ep
3	ZM-10-47	Outcrop	8631253	428480	Metagabbro	Am, Pl, Mag, Rt	Ttn, Ep
4	ZM-10-45	Outcrop	8632313	428214	Metadiorite	Pl, Fsp, Qtz, Mag	Ttn, Ap, Chl, Ep
4	ZM-12-18	Outcrop	8629989	429138	Metadiorite	Pl, Fsp, Qtz, Mag	Ttn, Ap, Chl, Ep
5	ZM-82-14	Drill core	Chimiwungo	Chimiwungo	Ky-Gt amphibolite	Ky, Gt, Qtz, Pl, Fsp	
6	ZM-12-13	Open pit	Malundwe	Malundwe	Gt amphibolite	Gt, Am, Bt, Pl	Qtz, Rt, Ilm
6	ZM-12-16	Open pit	Malundwe	Malundwe	Gt amphibolite	Gt, Am, Bt, Pl	Qtz, Rt, Ilm

Table 28: Major element composition of whole-rock samples from the Solwezi area analyzed by ICP-OES

Location	Solwezi area (cover and intrusive rocks)							
Lithology	Kyanite, micaschist				Metagabbro		Metadiorite	
Sample	ZM-10-24	ZM-10-07	ZM-10-08	ZM-10-41	ZM-10-21	ZM-10-47	ZM-10-45	ZM-12-18
<i>Oxides / wt. %</i>								
SiO₂	57.71	75.50	74.63	65.46	45.60	47.16	60.93	60.95
TiO₂	0.74	0.21	0.19	0.60	2.76	2.02	0.93	0.94
Al₂O₃	17.12	16.01	17.63	18.78	15.66	15.17	15.33	17.38
Fe₂O₃	5.47	1.70	1.84	2.44	13.19	12.74	9.06	8.07
MnO	0.01	0.00	0.00	0.01	0.09	0.17	0.02	0.02
MgO	11.37	4.26	3.00	7.46	4.40	6.73	0.75	1.17
CaO	0.00	0.04	0.00	0.00	9.93	10.49	2.21	3.53
Na₂O	0.21	0.11	0.09	0.24	3.88	3.07	8.29	7.01
K₂O	4.13	1.59	1.08	3.24	1.02	0.72	0.60	0.88
P₂O₅	0.00	0.00	0.00	0.00	0.25	0.25	0.22	0.28
LOI	3.34	1.43	1.33	1.99	2.08	1.53	1.19	1.22
Total	100.10	100.85	99.79	100.22	98.85	100.04	99.51	101.55
<i>Trace / ppm</i>								
Cr	138.70	35.78	30.20	49.40	27.01	215.90	7.87	9.59
Co	46.04	3.24	5.34	8.64	40.25	44.46	9.48	11.54
Ni	111.70	55.11	26.80	78.30	39.27	94.87	10.87	12.51
Rb	146.30	39.25	23.30	71.10	7.24	24.96	3.68	7.56
Sr	4.31	4.75	2.04	12.30	411.30	306.60	113.60	108.10
Cs	0.77	0.26	0.00	0.44	0.00	0.22	0.00	0.00
Ba	165.50	99.04	147.00	273.00	106.00	114.40	62.34	108.90
Sc	-	-	-	-	32.98	32.16	17.38	15.40
V	117.70	39.66	26.40	89.70	417.90	266.10	3.35	6.98
Ta	0.51	1.05	0.23	0.86	0.96	0.95	5.20	4.92
Nb	5.79	19.37	1.98	11.4	11.49	13.41	85.54	75.93
Zr	86.62	92.59	2.58	121.00	98.35	120.50	1312.00	1265.00
Hf	2.32	3.38	0.16	3.30	2.74	3.15	27.79	23.87
Th	1.33	3.22	1.14	2.30	1.97	4.69	9.73	8.47
U	1.36	0.48	0.30	0.40	0.49	1.95	1.54	1.97
Y	13.47	52.29	0.97	46.80	19.92	24.71	106.90	116.70
La	11.15	16.33	1.32	2.03	15.81	14.78	99.86	88.47
Ce	22.83	28.49	3.97	4.87	34.33	34.00	197.40	191.40
Pr	2.85	3.81	0.40	0.63	4.06	4.42	32.51	29.67
Nd	10.95	13.43	1.56	2.53	19.10	19.30	134.70	115.90
Sm	2.24	2.56	0.33	1.02	4.33	4.77	28.41	23.85
Eu	0.82	1.00	0.11	0.65	1.68	1.55	9.37	7.40
Gd	3.09	4.27	0.31	4.33	4.28	4.74	24.30	21.40
Tb	0.57	1.04	0.04	1.07	0.65	0.74	3.80	3.32
Dy	2.95	8.01	0.18	7.42	3.76	4.47	21.29	19.44
Ho	0.51	1.87	0.04	1.64	0.72	0.88	4.02	3.78
Er	1.36	5.86	0.10	4.81	1.90	2.38	10.69	10.53
Tm	0.19	0.98	0.02	0.71	0.28	0.34	1.58	1.46
Yb	1.28	7.09	0.13	4.78	1.77	2.29	10.35	9.90
Lu	0.19	1.09	0.02	0.72	0.26	0.35	1.60	1.50
Cu	12.58	0.00	8.17	0.00	39.13	63.35	0.00	5.16
Zn	0.00	0.00	0.00	0.00	55.36	95.02	19.51	22.36
Pb	0.00	0.00	0.00	0.00	2.41	2.71	1.57	2.53

Table 29: Major element composition of whole-rock samples from Mwombezi area analyzed by ICP-OES

Location	Mwombezi area			
Lithology	Garnet amphibolite		Gt-Ky amphibolite	Metabasalt
Sample	ZM-12-13	ZM-12-16	ZM-82-14	ZM-12-27
<i>Oxides / wt.%</i>				
SiO₂	54.96	54.28	47.56	45.78
TiO₂	1.60	1.54	1.01	2.85
Al₂O₃	14.01	14.87	14.41	14.82
Fe₂O₃	14.33	11.68	11.58	9.38
MnO	0.27	0.19	0.14	0.07
MgO	6.04	7.17	7.77	6.31
CaO	6.30	4.88	7.18	12.87
Na₂O	1.01	1.73	3.32	4.00
K₂O	0.78	1.68	0.56	0.97
P₂O₅	0.23	0.05	0.04	0.46
LOI	1.03	2.28	1.30	2.21
Total	100.56	100.35	98.87	99.71
<i>Trace / ppm</i>				
Cr	195.90	163.80	364.00	113.00
Co	100.40	91.54	55.72	23.64
Ni	46.80	81.66	176.90	73.26
Rb	35.12	44.80	13.93	19.85
Sr	18.59	53.50	303.10	325.40
Cs	0.55	1.05	0.54	0.17
Ba	52.37	157.00	134.20	106.30
Sc	35.05	44.80	28.27	28.35
V	214.70	262.20	264.60	272.80
Ta	1.21	0.74	0.43	1.60
Nb	16.15	10.30	5.09	21.57
Zr	200.50	120.10	38.55	173.80
Hf	5.28	3.28	1.31	4.31
Th	17.99	3.82	1.37	6.34
U	17.31	4.70	0.54	1.85
Y	50.37	57.93	7.55	29.32
La	28.72	13.10	12.13	20.13
Ce	63.28	27.93	21.81	47.84
Pr	7.55	3.85	2.41	6.30
Nd	29.57	16.69	10.14	27.14
Sm	6.85	4.60	1.90	6.18
Eu	1.92	1.78	1.01	1.68
Gd	7.20	5.60	1.60	5.89
Tb	1.32	1.07	0.23	0.91
Dy	8.50	7.85	1.31	5.35
Ho	1.74	1.87	0.25	1.04
Er	4.88	6.26	0.74	2.82
Tm	0.74	1.13	0.11	0.42
Yb	5.00	8.86	0.81	2.67
Lu	0.76	1.52	0.14	0.41
Cu	392.30	22.85	14.17	7.01
Zn	27.70	28.09	122.30	33.34
Pb	12.59	6.17	4.88	2.12

Table 30: Average mineral compositions with confidence interval of 95% in brackets (n = number of samples) from samples ZM-10-07 and ZM-10-24

Mineral Sample Location	Phlogopite		Chlorite		Muscovite		
	ZM-10-07 Solwezi	ZM-10-24 Solwezi	ZM-10-07 Solwezi	ZM-10-24 Solwezi	ZM-10-07 Solwezi	ZM-10-24 Solwezi	
<i>Oxides / wt. %</i>	SiO₂	40.67 (0.18)	40.16 (0.40)	28.81	27.96 (0.24)	45.05	47.77
	TiO₂	0.66 (0.03)	0.69 (0.01)	0.05	0.04 (0.01)	0.39	0.53
	Al₂O₃	17.93 (0.22)	17.58 (0.13)	23.89	23.3 (0.14)	32.51	32.77
	FeO	1.88 (0.07)	2.37 (0.06)	1.45	1.88 (0.04)	3.80	2.80
	MnO	0.03 (0.02)	0.01 (0.01)	0.00	0.03 (0.01)	0.02	0.00
	MgO	23.85 (0.18)	22.83 (0.20)	32.85	31.36 (0.42)	1.39	1.26
	CaO	0.04 (0.04)	0.01 (0.01)	0.00	0.00 (0.01)	0.02	0.00
	Na₂O	0.48 (0.03)	0.48 (0.03)	0.00	0.02 (0.01)	1.08	1.04
	K₂O	8.68 (0.19)	9.70 (0.30)	0.08	0.02 (0.02)	9.32	9.53
	Total	94.24 (0.45)	93.86 (0.50)	87.13	86.62 (0.53)	93.58	95.70
<i>Oxygens</i>	11	11	14	14	11	11	
<i>Cations</i>	Si	2.845 (0.013)	2.847 (0.015)	2.686	2.689 (0.012)	3.088	3.173
	Al^{IV}	1.155 (0.013)	1.153 (0.015)	1.314	1.311 (0.012)	0.912	0.827
	Al^{VI}	0.323 (0.010)	0.315 (0.014)	1.312	1.329 (0.027)	1.716	1.740
	Ti	0.035 (0.002)	0.037 (0.001)	0.004	0.003 (0.001)	0.020	0.026
	Fe^{tot}	0.110 (0.005)	0.140 (0.003)	0.113	0.151 (0.003)	0.218	0.156
	Mn	0.002 (0.001)	0.001 (0.001)	0.000	0.002 (0.000)	0.001	0.000
	Mg	2.488 (0.013)	2.413 (0.019)	4.564	4.496 (0.047)	0.142	0.125
	Ca	0.003 (0.003)	0.000 (0.001)	0.000	0.001 (0.001)	0.001	0.000
	Na	0.065 (0.004)	0.067 (0.003)	0.000	0.004 (0.002)	0.144	0.134
	K	0.775 (0.015)	0.877 (0.028)	0.010	0.002 (0.002)	0.815	0.808
	X_{Mg}	0.958 (0.002)	0.945 (0.001)	0.976	0.968 (0.000)	-	-
	n	7	13	1	5	1	1

Table 31: Representative mineral analyses by electronic microprobe

Sample		ZM-12-13	ZM-12-13	ZM-12-13	ZM-12-13	ZM-12-13	ZM-12-13
Mineral		Am	Am	Grt (rim)	Grt (rim)	Grt (core)	Grt (core)
Location		Mwombezi	Mwombezi	Mwombezi	Mwombezi	Mwombezi	Mwombezi
Oxides (wt.%)	SiO₂	41.53	39.24	37.66	37.39	37.63	37.48
	TiO₂	0.61	0.34	0.06	0.08	0.10	0.12
	Al₂O₃	17.34	18.74	21.89	21.59	21.71	21.36
	FeO	14.98	18.79	28.51	29.35	28.71	29.39
	MnO	0.00	0.16	0.67	0.53	1.38	1.72
	MgO	9.86	6.60	4.47	4.34	4.48	4.47
	CaO	11.16	11.63	7.05	7.15	6.43	6.16
	Na₂O	1.46	1.44	0.03	0.00	0.01	0.03
	K₂O	0.66	0.56	0.01	0.01	0.02	0.00
Total	97.60		100.35	100.46	100.47	100.73	
Oxygens		23	23	12	12	12	12
Cations	Si	6.136	5.936	2.958	2.947	2.960	2.954
	Al^{IV}	1.864	2.064	0.042	0.053	0.040	0.046
	Al^{VI}	1.157	1.279	1.985	1.954	1.973	1.939
	Ti	0.068	0.039	0.004	0.005	0.006	0.007
	Fe^{tot}	1.851	2.377	1.873	1.935	1.889	1.937
	Mn	0.000	0.021	0.045	0.035	0.092	0.115
	Mg	2.171	1.488	0.523	0.510	0.525	0.525
	Ca	1.767	1.885	0.593	0.606	0.542	0.520
	Na	0.418	0.422	0.005	0.000	0.002	0.005
	K	0.124	0.108	0.001	0.001	0.002	0.000
	X_{Mg}	-	-	0.175	0.167	0.178	0.176
	X_{Fe}	-	-	0.627	0.634	0.639	0.650
	X_{Ca}	-	-	0.198	0.199	0.183	0.174

Table 32: Representative mineral analyses by electronic microprobe

Sample		ZM-12-13	ZM-12-13	ZM-12-13	ZM-12-13	ZM-12-13	ZM-12-13	ZM-12-13
Mineral		Bt (core)	Bt (core)	Bt (rim)	Bt (rim)	Pl	Pl	Chl
Location		Mwombezi	Mwombezi	Mwombezi	Mwombezi	Mwombezi	Mwombezi	Mwombezi
Oxides wt.%	SiO₂	35.94	36.19	35.92	35.52	56.92	57.05	25.12
	TiO₂	1.55	1.58	1.52	1.56	0.01	0.00	0.05
	Al₂O₃	17.39	17.75	17.88	17.34	27.55	27.15	22.99
	FeO	18.73	19.48	20.57	19.45	0.11	0.00	21.55
	MnO	0.13	0.02	0.16	0.00	0.03	0.06	0.00
	MgO	11.38	10.96	10.51	11.26	0.00	0.00	18.38
	CaO	0.00	0.00	0.01	0.02	9.62	9.30	0.02
	Na₂O	0.18	0.12	0.06	0.10	6.12	6.36	0.00
	K₂O	9.41	9.28	9.43	9.32	0.06	0.04	0.00
	Total	94.71	95.38	96.06	94.57	100.42	99.96	88.11
	Oxygens		11	11	11	11	8	8
Cations	Si	2.748	2.749	2.728	2.729	2.544	2.559	2.578
	Al^{IV}	1.252	1.251	1.272	1.271	0.000	0.000	1.422
	Al^{VI}	0.315	0.338	0.329	0.300	1.452	1.436	1.360
	Ti	0.089	0.090	0.087	0.090	0.000	0.000	0.004
	Fe^{tot}	1.198	1.237	1.307	1.250	0.004	0.000	1.850
	Mn	0.008	0.001	0.010	0.000	0.001	0.002	0.000
	Mg	1.297	1.241	1.190	1.289	0.000	0.000	2.811
	Ca	0.000	0.000	0.001	0.002	0.461	0.447	0.002
	Na	0.027	0.018	0.009	0.015	0.530	0.553	0.000
	K	0.918	0.899	0.914	0.914	0.003	0.002	0.000
	X_{Mg}	0.520	0.501	0.477	0.508	-	-	0.603
	An	-	-	-	-	0.465	0.447	-

Table 33: Representative mineral analyses by electronic microprobe

Sample		ZM-82-14	ZM-82-14	ZM-82-14	ZM-82-14	ZM-82-14	ZM-82-14
Mineral		Am1	Am2	Grt (rim)	Grt (rim)	Grt (core)	Grt (core)
Location		Mwombezi	Mwombezi	Mwombezi	Mwombezi	Mwombezi	Mwombezi
Oxides / wt. %	SiO ₂	42.20	48.26	38.33	38.60	37.60	38.31
	TiO ₂	0.45	0.11	0.05	0.06	0.08	0.10
	Al ₂ O ₃	15.98	10.31	21.90	21.98	21.69	21.55
	FeO	15.34	19.43	27.38	26.60	27.11	26.93
	MnO	0.13	0.44	1.39	1.86	2.86	2.96
	MgO	11.20	18.21	6.68	6.03	5.75	5.85
	CaO	9.67	0.47	5.00	5.48	5.41	5.38
	Na ₂ O	1.76	1.06	0.03	0.01	0.04	0.03
	K ₂ O	0.31	0.01	0.01	0.01	0.00	0.00
	Total	97.04	98.30	100.77	100.63	100.54	101.11
Oxygens		23	23	12	12	12	12
Cations	Si	6.253	6.928	2.970	2.991	2.946	2.977
	Al ^{IV}	1.747	1.072	0.030	0.009	0.054	0.023
	Al ^{VI}	1.044	0.673	1.970	1.999	1.949	1.951
	Ti	0.050	0.012	0.003	0.003	0.005	0.006
	Fe ^{tot}	1.901	2.333	1.774	1.724	1.776	1.750
	Mn	0.016	0.054	0.091	0.122	0.190	0.195
	Mg	2.473	3.896	0.771	0.696	0.671	0.678
	Ca	1.535	0.072	0.415	0.455	0.454	0.448
	Na	0.506	0.295	0.005	0.002	0.006	0.005
	K	0.059	0.002	0.001	0.001	0.000	0.000
	X _{Mg}	-	-	0.260	0.242	0.231	0.235
	X _{Fe}	-	-	0.599	0.600	0.612	0.609
	X _{Ca}	-	-	0.141	0.158	0.157	0.156

Table 34: Representative mineral analyses by electronic microprobe

Sample		ZM-82-14	ZM-82-14	ZM-82-14	ZM-82-14	ZM-82-14	ZM-82-14	ZM-82-14
Mineral		Bt (core)	Bt (core)	Bt (rim)	Bt (rim)	Pl	Pl	Pl
Location		Mwombezi	Mwombezi	Mwombezi	Mwombezi	Mwombezi	Mwombezi	Mwombezi
Oxides wt. %	SiO ₂	37.86	37.74	37.60	38.46	61.37	58.81	57.28
	TiO ₂	1.52	1.48	1.27	1.34	0.01	0.00	0.00
	Al ₂ O ₃	17.26	17.28	17.53	17.89	24.33	26.02	26.63
	FeO	13.49	13.19	12.92	12.68	0.08	0.00	0.06
	MnO	0.06	0.00	0.02	0.04	0.00	0.05	0.00
	MgO	16.77	17.03	16.69	16.11	0.01	0.00	0.03
	CaO	0.00	0.03	0.05	0.16	5.50	7.65	8.78
	Na ₂ O	0.36	0.42	0.37	0.38	8.37	7.19	6.62
	K ₂ O	8.48	8.30	8.41	8.28	0.04	0.05	0.02
	Total	95.80	95.47	94.86	95.34	99.71	99.77	99.43
Oxygens		11	11	11	11	8	8	8
Cations	Si	2.765	2.760	2.765	2.801	2.729	2.630	2.580
	Al ^{IV}	1.235	1.240	1.235	1.199	-	-	-
	Al ^{VI}	0.251	0.250	0.285	0.337	1.276	1.372	1.414
	Ti	0.083	0.081	0.070	0.073	0.000	0.000	0.000
	Fe ^{tot}	0.824	0.807	0.795	0.772	0.003	0.000	0.002
	Mn	0.004	0.000	0.001	0.002	0.000	0.002	0.000
	Mg	1.825	1.856	1.829	1.749	0.001	0.000	0.002
	Ca	0.000	0.002	0.004	0.012	0.262	0.367	0.424
	Na	0.051	0.060	0.053	0.054	0.722	0.623	0.578
	K	0.790	0.774	0.789	0.769	0.002	0.003	0.001
	X _{Mg}	0.689	0.697	0.697	0.694	-	-	-
	An	-	-	-	-	0.266	0.370	0.423

Table 35: Whole rock Nd and Sr isotopic data for samples from Solwezi and Mwombezhi areas (Abbreviations: Metagab. = metagabbro; Amphib. = amphibolite)

Sample	Unit	Lithology	Age	$^{147}\text{Sm}/^{144}\text{Nd}$	$^{143}\text{Nd}/^{144}\text{Nd}$	Err.	$^{143}\text{Nd}/^{144}\text{Nd}_i$	$\epsilon\text{Nd}(t)$	T_{DM}	$^{87}\text{Sr}/^{86}\text{Sr}$	$^{87}\text{Sr}/^{86}\text{Sr}(i)$
ZM-10-47	Katanga	Metagab.	750	0.140735	0.512294	5×10^{-6}	0.511602	-1.4	1.54	0.709110	0.706620
ZM-10-21	Katanga	Metagab.	750	0.133176	0.512310	5×10^{-6}	0.511655	-0.3	1.38	0.708961	0.708408
ZM-12-27	Katanga	Metabasalt	750	0.130851	0.512208	5×10^{-6}	0.511565	-2.1	1.51	0.709975	0.708056
ZM-12-18	Katanga	Metadiorite	720	0.119803	0.512347	5×10^{-6}	0.511782	1.4	1.14	0.707507	0.705449
ZM-12-13	Pre-Kat.	Amphib.	-	0.134930	0.511917	5×10^{-6}	-	-	2.09	-	-
ZM-12-16	Pre-Kat.	Amphib.	-	0.160221	0.512116	5×10^{-6}	-	-	2.45	-	-
ZM-21-04	Pre-Kat.	Amphib.	-	0.134031	0.511932	5×10^{-6}	-	-	2.04	-	-

Table 36: U-Pb isotope analyses of detrital zircon from kyanite micaschist (ZM-10-24)

Grain	$^{207}\text{Pb}^a$	U^b	Pb^b	$\frac{\text{Th}^b}{\text{U}}$	$^{206}\text{Pbc}^c$	$\frac{^{206}\text{Pbd}}{^{238}\text{U}}$	$\pm 2s$	$\frac{^{207}\text{Pbd}}{^{235}\text{U}}$	$\pm 2s$	$\frac{^{207}\text{Pbd}}{^{206}\text{Pb}}$	$\pm 2s$	ρ^c	$\frac{^{206}\text{Pb}}{^{238}\text{U}}$	$\pm 2s$	$\frac{^{207}\text{Pb}}{^{235}\text{U}}$	$\pm 2s$	$\frac{^{207}\text{Pb}}{^{206}\text{Pb}}$	$\pm 2s$	conc. ^f
	(cps)	(ppm)	(ppm)	U	(%)		(%)		(%)		(%)		(Ma)	(Ma)	(Ma)	(Ma)	(%)	(%)	
164	150247	1984	540	0.19	0.00	0.2726	2.1	4.1070	2.1	0.1093	0.3	0.99	1554	29	1656	17	1787	6	87
165	76200	3482	430	0.14	0.00	0.1250	2.3	1.8240	2.3	0.1058	0.5	0.98	759	16	1054	15	1728	9	44
166	20353	294	91	0.99	b.d.	0.2571	1.4	3.6140	1.7	0.1019	0.8	0.86	1475	19	1553	13	1660	16	89
167	26982	330	110	0.98	b.d.	0.2758	1.6	4.1640	1.7	0.1095	0.8	0.90	1570	22	1667	14	1791	14	88
168	11574	112	45	1.02	0.00	0.3399	1.6	5.4260	1.8	0.1158	0.9	0.88	1886	26	1889	16	1892	16	100
169	18880	186	78	1.40	0.00	0.3298	1.5	5.1720	1.7	0.1137	0.9	0.84	1837	24	1848	15	1860	17	99
170	17346	182	64	0.78	0.00	0.3084	1.6	4.7910	1.9	0.1127	1.0	0.84	1733	24	1783	16	1843	18	94
171	31212	353	120	0.65	0.00	0.2999	1.5	4.5460	1.6	0.1099	0.7	0.90	1691	22	1739	14	1798	13	94
172	73401	1508	210	0.27	b.d.	0.1338	3.7	1.9290	3.8	0.1045	0.5	0.99	810	29	1091	26	1706	8	47
173	57618	688	190	0.19	0.00	0.2750	1.5	4.2070	1.6	0.1109	0.5	0.96	1566	21	1675	13	1815	9	86
174	38599	372	150	1.22	0.00	0.3198	1.5	5.0960	1.6	0.1156	0.7	0.90	1789	23	1835	14	1889	13	95
175	42421	400	170	1.23	0.00	0.3381	1.5	5.3590	1.6	0.1150	0.6	0.92	1877	24	1878	14	1879	11	100
176	27573	432	77	0.61	b.d.	0.1416	3.9	2.2190	4.0	0.1137	0.7	0.98	854	31	1187	28	1859	13	46
177	133097	3209	510	0.18	0.34	0.1520	2.5	2.3700	2.6	0.1131	0.5	0.98	912	22	1234	19	1849	10	49
178	49664	573	170	0.41	b.d.	0.2760	1.5	4.1350	1.6	0.1087	0.6	0.93	1571	20	1661	13	1777	11	88
179	36326	368	120	0.51	b.d.	0.3108	1.5	4.8040	1.8	0.1121	0.9	0.87	1744	24	1786	15	1834	16	95
180	71156	340	120	0.99	b.d.	0.3151	2.0	4.8840	2.1	0.1124	0.7	0.95	1766	31	1799	18	1839	12	96
181	20018	179	44	1.96	0.15	0.2040	3.2	3.1380	3.3	0.1116	0.9	0.96	1197	35	1442	26	1825	16	66
182	14513	137	57	1.16	0.00	0.3400	1.5	5.4040	1.7	0.1153	0.9	0.86	1887	24	1886	15	1884	16	100
183	108108	2431	77	0.11	b.d.	0.0262	7.3	0.4102	7.3	0.1135	0.4	1.00	167	12	349	22	1855	7	9
184	31181	400	140	1.28	0.00	0.2739	1.5	3.9890	1.6	0.1056	0.6	0.92	1561	21	1632	13	1725	12	90
185	82695	1006	310	0.22	0.00	0.3058	1.9	4.6480	1.9	0.1102	0.5	0.96	1720	28	1758	16	1803	9	95
186	88799	989	260	0.29	b.d.	0.2579	1.6	3.8480	1.8	0.1082	0.9	0.87	1479	21	1603	15	1769	17	84
187	18484	227	70	0.68	b.d.	0.2755	1.5	4.0440	1.7	0.1064	0.9	0.86	1569	21	1643	14	1739	16	90
188	14473	158	50	0.75	b.d.	0.2751	1.7	4.1940	1.9	0.1106	0.9	0.87	1567	23	1673	16	1809	17	87
189	48560	668	220	0.32	0.02	0.3166	3.5	4.8540	3.6	0.1112	0.7	0.98	1773	54	1794	30	1819	13	97
190	6251	77	17	0.79	0.97	0.1811	2.3	2.3410	3.2	0.0938	2.2	0.73	1073	23	1225	23	1503	42	71
191	75264	1111	270	0.20	0.00	0.2425	2.1	3.5810	2.1	0.1071	0.4	0.98	1400	26	1545	17	1751	8	80
192	36088	435	150	1.14	0.00	0.2718	1.5	3.9880	1.7	0.1064	0.8	0.89	1550	20	1632	14	1739	14	89
193	27087	266	110	1.35	0.00	0.3289	1.4	5.1360	1.7	0.1132	0.8	0.87	1833	23	1842	14	1852	15	99
199	39906	412	150	0.69	0.03	0.3204	1.5	5.0060	1.7	0.1133	0.8	0.88	1792	23	1820	14	1853	14	97
200	30994	692	130	0.19	0.00	0.1833	1.7	2.0630	1.8	0.0816	0.7	0.92	1085	17	1137	12	1237	14	88
201	33803	341	130	1.29	0.00	0.3046	1.5	4.8120	1.6	0.1146	0.6	0.92	1714	22	1787	14	1873	12	92
202	27805	336	110	1.04	b.d.	0.2732	1.6	4.2040	1.7	0.1116	0.8	0.89	1557	21	1675	14	1826	14	85
203	25848	210	88	1.30	b.d.	0.3319	1.6	5.1800	1.9	0.1132	1.0	0.85	1848	26	1849	16	1851	18	100

204	26638	245	100	1.12	0.00	0.3398	1.5	5.4320	1.7	0.1159	0.8	0.90	1886	25	1890	15	1895	14	100
205	24441	227	94	1.36	b.d.	0.3233	1.4	5.1700	1.6	0.1160	0.7	0.90	1806	23	1848	14	1895	12	95
206	6228	59	23	0.97	0.00	0.3260	1.7	5.1710	2.3	0.1150	1.5	0.74	1819	27	1848	20	1881	28	97
207	16224	294	75	1.10	b.d.	0.2055	1.5	2.5520	1.9	0.0901	1.1	0.82	1205	17	1287	14	1427	21	84
208	34399	337	130	1.21	0.00	0.3166	1.5	5.0010	1.7	0.1146	0.7	0.90	1773	24	1820	14	1873	13	95
209	32336	352	130	1.14	0.00	0.2964	1.5	4.4640	1.6	0.1093	0.7	0.90	1673	22	1724	14	1787	13	94
210	21844	208	87	1.64	0.01	0.3197	1.6	4.9070	1.7	0.1113	0.8	0.90	1788	24	1803	15	1821	14	98
211	27081	286	100	0.88	0.00	0.3151	1.4	4.8450	1.6	0.1115	0.7	0.90	1766	22	1793	14	1824	13	97
212	19427	215	73	0.86	b.d.	0.2922	1.5	4.4240	1.8	0.1098	1.0	0.85	1652	22	1717	15	1796	17	92
213	46535	980	240	0.14	0.45	0.2511	1.5	3.6690	1.7	0.1060	0.9	0.84	1444	19	1565	14	1731	17	83
214	60170	1029	260	0.16	0.13	0.2517	2.6	3.7890	2.7	0.1092	0.6	0.98	1447	34	1590	22	1786	10	81
215	69645	1079	310	0.31	0.00	0.2861	4.5	4.1460	4.5	0.1051	0.8	0.98	1622	64	1663	38	1716	15	95
216	32008	279	82	0.41	0.01	0.2691	1.6	4.3000	2.1	0.1159	1.3	0.78	1536	22	1693	17	1894	23	81
217	90169	929	260	0.25	0.00	0.2676	1.5	4.2510	1.6	0.1152	0.5	0.96	1528	21	1684	13	1883	8	81
218	153638	1992	530	0.21	0.00	0.2611	1.5	3.8680	1.6	0.1075	0.4	0.97	1495	21	1607	13	1757	8	85
219	70069	703	260	0.65	b.d.	0.3346	1.5	5.2590	1.6	0.1140	0.5	0.94	1861	24	1862	14	1864	9	100
220	98043	1594	280	0.27	0.00	0.1688	1.6	2.6250	1.6	0.1128	0.4	0.98	1006	15	1308	12	1844	6	55
221	62392	749	230	0.34	0.00	0.3040	1.6	4.7230	1.7	0.1127	0.6	0.93	1711	24	1771	15	1843	11	93
222	56910	569	180	0.34	0.00	0.2956	1.5	4.7410	1.6	0.1163	0.5	0.95	1670	23	1775	14	1900	9	88
223	53758	648	180	0.23	0.00	0.2697	1.8	4.2260	1.9	0.1137	0.7	0.93	1539	25	1679	16	1859	12	83
224	17050	178	59	0.52	0.00	0.3065	1.5	4.8530	1.7	0.1148	0.7	0.90	1723	23	1794	14	1877	13	92
225	21885	203	89	1.52	b.d.	0.3382	1.5	5.3770	1.6	0.1153	0.7	0.89	1878	24	1881	14	1885	13	100
226	47004	583	160	0.47	b.d.	0.2452	1.7	3.7050	1.8	0.1096	0.6	0.94	1414	21	1572	14	1792	11	79
227	68369	3107	96	0.16	0.00	0.0268	8.1	0.4014	8.1	0.1088	0.7	1.00	170	14	343	24	1780	13	10
228	35269	431	98	0.27	0.00	0.2218	1.7	3.2200	1.9	0.1053	0.8	0.90	1291	20	1462	15	1720	15	75
229	26309	287	110	1.26	0.00	0.3073	1.7	4.6550	1.9	0.1099	0.9	0.89	1727	26	1759	16	1797	16	96
230	76798	2313	290	0.16	0.00	0.1245	1.8	1.9420	1.9	0.1131	0.5	0.96	757	13	1096	13	1850	9	41
231	45172	647	110	0.38	0.00	0.1554	3.2	2.3930	3.3	0.1117	0.8	0.97	931	28	1240	24	1827	15	51
232	59350	647	200	0.25	0.00	0.3060	1.5	4.6470	1.7	0.1102	0.8	0.88	1721	23	1758	15	1802	15	95
233	25030	237	88	0.63	0.00	0.3364	1.5	5.3140	1.6	0.1146	0.7	0.90	1869	24	1871	14	1873	13	100
234	51310	697	140	0.73	b.d.	0.1754	2.9	2.7060	3.0	0.1119	0.6	0.98	1042	28	1330	22	1830	12	57
235	151346	2052	670	0.20	0.01	0.3266	1.6	4.9970	1.7	0.1110	0.5	0.96	1822	26	1819	14	1815	8	100
236	24101	286	100	1.12	0.00	0.2958	1.5	4.3040	1.8	0.1055	0.9	0.87	1670	23	1694	15	1724	16	97
237	7245	146	34	0.74	0.00	0.2075	1.6	2.4150	2.2	0.0844	1.5	0.72	1216	18	1247	16	1301	29	93
243	60222	4054	170	0.10	0.00	0.0402	10.4	0.6143	10.5	0.1108	0.7	1.00	254	26	486	41	1813	14	14
244	40081	1368	290	0.15	0.13	0.2126	3.0	3.3150	3.0	0.1131	0.5	0.98	1243	34	1485	24	1849	10	67
245	11767	147	45	0.69	b.d.	0.2766	1.7	4.0330	2.0	0.1058	1.1	0.85	1574	24	1641	17	1727	20	91
246	13801	128	49	0.81	b.d.	0.3355	1.4	5.3080	1.9	0.1147	1.3	0.74	1865	23	1870	17	1876	23	99
247	14315	140	53	0.71	0.00	0.3391	1.8	5.3910	2.1	0.1153	1.1	0.84	1882	29	1883	18	1885	20	100

248	32754	443	140	0.58	0.00	0.2806	1.6	4.0990	1.9	0.1060	0.9	0.87	1594	23	1654	15	1731	17	92
249	24078	335	100	0.78	0.00	0.2735	1.5	3.8650	1.8	0.1025	1.0	0.82	1559	20	1606	15	1670	19	93
250	59943	5065	170	0.10	0.00	0.0319	4.2	0.4952	4.2	0.1125	0.7	0.99	203	8	408	14	1840	13	11
251	12373	233	59	1.04	b.d.	0.2166	1.5	2.4950	1.8	0.0835	1.1	0.81	1264	17	1270	13	1282	21	99
252	43490	389	130	0.59	0.19	0.2889	1.7	4.7270	1.9	0.1187	0.9	0.89	1636	25	1772	16	1936	16	84
253	11395	118	36	0.64	b.d.	0.2741	1.7	4.1160	2.2	0.1089	1.4	0.77	1561	23	1657	18	1781	25	88
254	12134	145	52	1.39	0.01	0.2770	1.5	4.1220	1.8	0.1079	1.1	0.81	1576	21	1659	15	1764	20	89
255	10018	117	35	0.95	0.00	0.2439	1.6	3.7250	2.0	0.1108	1.1	0.82	1407	21	1577	16	1812	20	78
256	74138	2178	160	0.22	0.00	0.0642	5.1	0.9703	5.2	0.1096	0.6	0.99	401	20	689	26	1793	10	22
257	168708	1880	560	0.19	0.00	0.2946	1.6	4.6540	1.7	0.1146	0.4	0.96	1664	24	1759	14	1873	8	89
258	34573	5796	99	0.03	0.00	0.0155	2.7	0.2304	3.0	0.1075	1.2	0.92	99	3	211	6	1758	22	6
259	21001	390	100	0.32	0.98	0.2479	1.7	3.2510	2.4	0.0951	1.7	0.69	1428	21	1469	19	1530	33	93

Table 37: Lu-Yb-Hf isotope analyses of detrital zircon grains from the kyanite micaschist (ZM-10-24)

Grain	$^{176}\text{Yb}/^{177}\text{Hf}^a$	$\pm 2s$	$^{176}\text{Lu}/^{177}\text{Hf}^a$	$\pm 2s$	$^{178}\text{Hf}/^{177}\text{Hf}$	$^{180}\text{Hf}/^{177}\text{Hf}$	Sig_{Hf}^b (V)	$^{176}\text{Hf}/^{177}\text{Hf}$	$\pm 2s^c$	$^{176}\text{Hf}/^{177}\text{Hf}_{(0)}^d$	$\text{eHf}_{(0)}^d$	$\pm 2s^c$	T_{DM2}^e (Ga)	age^f (Ma)	$\pm 2s^c$
164	0.0410	41	0.00162	16	1.46717	1.88662	11	0.281532	27	0.281477	-6.0	1.0	2.73	1787	6
165	0.0217	13	0.00079	4	1.46712	1.88656	10	0.281524	25	0.281498	-6.6	0.9	2.72	1728	9
167	0.0309	9	0.00114	3	1.46714	1.88651	11	0.281535	25	0.281496	-5.2	0.9	2.69	1791	14
168	0.0353	32	0.00129	13	1.46714	1.88655	10	0.281528	25	0.281481	-3.4	0.9	2.67	1892	16
169	0.0407	39	0.00147	16	1.46716	1.88658	11	0.281533	25	0.281481	-4.1	0.9	2.69	1860	17
171	0.0197	9	0.00076	3	1.46718	1.88658	13	0.281524	23	0.281498	-5.0	0.8	2.69	1798	13
172	0.0505	39	0.00170	12	1.46712	1.88642	12	0.281557	25	0.281502	-6.9	0.9	2.72	1706	8
173	0.0167	23	0.00064	8	1.46715	1.88658	12	0.281512	28	0.281490	-4.9	1.0	2.69	1815	9
174	0.0355	6	0.00131	3	1.46717	1.88651	10	0.281535	23	0.281488	-3.2	0.8	2.66	1889	13
175	0.0380	5	0.00134	3	1.46715	1.88662	10	0.281526	25	0.281478	-3.8	0.9	2.69	1879	11
176	0.0186	11	0.00067	4	1.46720	1.88672	11	0.281579	26	0.281555	-1.5	0.9	2.55	1859	13
177	0.0519	23	0.00175	7	1.46721	1.88670	11	0.281569	27	0.281507	-3.5	1.0	2.64	1849	10
178	0.0190	4	0.00075	1	1.46718	1.88667	10	0.281492	28	0.281467	-6.6	1.0	2.76	1777	11
179	0.0143	2	0.00052	1	1.46714	1.88654	14	0.281535	24	0.281516	-3.5	0.8	2.63	1834	16
180	0.0179	9	0.00061	3	1.46712	1.88649	11	0.281413	24	0.281391	-7.8	0.8	2.87	1839	12
181	0.0669	108	0.00210	32	1.46712	1.88654	14	0.281574	33	0.281501	-4.2	1.2	2.67	1825	16
182	0.0268	6	0.00095	2	1.46710	1.88653	10	0.281508	24	0.281474	-3.8	0.9	2.69	1884	16
183	0.0434	10	0.00143	4	1.46714	1.88665	16	0.281524	26	0.281474	-4.5	0.9	2.71	1855	7
184	0.0338	21	0.00125	8	1.46720	1.88678	13	0.281539	27	0.281498	-6.6	0.9	2.72	1725	12
185	0.0535	17	0.00182	6	1.46713	1.88664	13	0.281513	26	0.281450	-6.5	0.9	2.78	1803	9
186	0.0476	36	0.00153	9	1.46717	1.88667	13	0.281522	23	0.281471	-6.6	0.8	2.75	1769	17
187	0.0198	6	0.00074	3	1.46715	1.88650	12	0.281494	26	0.281470	-7.3	0.9	2.77	1739	16
188	0.0189	7	0.00069	2	1.46715	1.88652	13	0.281505	23	0.281481	-5.3	0.8	2.71	1809	17
189	0.0706	33	0.00251	10	1.46716	1.88665	13	0.281575	25	0.281489	-4.8	0.9	2.69	1819	13
191	0.0691	91	0.00244	32	1.46717	1.88661	10	0.281563	25	0.281482	-6.6	0.9	2.74	1751	8
192	0.0421	15	0.00161	6	1.46720	1.88658	10	0.281575	30	0.281522	-5.5	1.1	2.67	1739	14
193	0.0323	4	0.00122	2	1.46715	1.88670	9	0.281517	25	0.281474	-4.6	0.9	2.71	1852	15
200	0.0212	32	0.00086	13	1.46713	1.88654	11	0.281404	25	0.281384	-21.8	0.9	3.16	1237	14
199	0.0266	19	0.00097	6	1.46714	1.88664	13	0.281506	25	0.281471	-4.6	0.9	2.71	1853	14
201	0.0363	10	0.00138	4	1.46711	1.88652	9	0.281534	25	0.281485	-3.7	0.9	2.68	1873	12
202	0.0339	16	0.00128	7	1.46707	1.88656	9	0.281562	30	0.281517	-3.6	1.1	2.64	1826	14
203	0.0275	16	0.00102	7	1.46715	1.88650	10	0.281542	24	0.281506	-3.5	0.8	2.65	1851	18
204	0.0353	5	0.00127	2	1.46713	1.88647	10	0.281536	26	0.281491	-3.0	0.9	2.65	1895	14
205	0.0303	6	0.00106	1	1.46717	1.88658	10	0.281511	27	0.281473	-3.6	1.0	2.69	1895	12

206	0.0254	9	0.00089	3	1.46714	1.88663	9	0.281512	23	0.281480	-3.7	0.8	2.68	1881	28
207	0.0444	12	0.00167	5	1.46711	1.88652	9	0.281586	29	0.281541	-11.9	1.0	2.78	1427	21
209	0.0429	26	0.00162	10	1.46714	1.88662	9	0.281535	26	0.281480	-5.9	0.9	2.73	1787	13
208	0.0247	20	0.00093	8	1.46716	1.88649	10	0.281539	23	0.281506	-3.0	0.8	2.64	1873	13
210	0.0227	11	0.00085	4	1.46713	1.88648	9	0.281499	24	0.281470	-5.4	0.9	2.73	1821	14
211	0.0151	3	0.00056	1	1.46713	1.88668	11	0.281524	25	0.281505	-4.1	0.9	2.66	1824	13
212	0.0207	9	0.00079	3	1.46713	1.88649	13	0.281508	23	0.281481	-5.6	0.8	2.72	1796	17
213	0.0291	7	0.00111	4	1.46716	1.88645	12	0.281517	27	0.281480	-7.1	0.9	2.75	1731	17
214	0.0226	9	0.00087	4	1.46717	1.88661	13	0.281522	25	0.281493	-5.4	0.9	2.70	1786	10
215	0.0260	15	0.00089	5	1.46698	1.88580	14	0.281543	31	0.281514	-6.3	1.1	2.69	1716	15
216	0.0242	14	0.00094	6	1.46718	1.88650	12	0.281478	25	0.281444	-4.7	0.9	2.75	1894	23
217	0.0278	13	0.00098	4	1.46720	1.88673	11	0.281512	28	0.281477	-3.8	1.0	2.69	1883	8
218	0.0514	23	0.00189	8	1.46710	1.88643	12	0.281536	28	0.281473	-6.8	1.0	2.75	1757	8
219	0.0197	25	0.00075	10	1.46716	1.88654	12	0.281539	26	0.281512	-2.9	0.9	2.63	1864	9
220	0.0407	29	0.00143	10	1.46715	1.88660	12	0.281515	29	0.281465	-5.1	1.0	2.73	1844	6
221	0.0740	56	0.00239	12	1.46716	1.88663	12	0.281568	24	0.281484	-4.4	0.8	2.69	1843	11
222	0.0480	46	0.00163	13	1.46712	1.88668	12	0.281593	31	0.281534	-1.3	1.1	2.57	1900	9
223	0.0226	8	0.00086	3	1.46711	1.88655	12	0.281479	25	0.281448	-5.3	0.9	2.75	1859	12
224	0.0197	19	0.00072	7	1.46709	1.88647	10	0.281521	24	0.281496	-3.2	0.8	2.65	1877	13
225	0.0292	10	0.00104	3	1.46712	1.88649	10	0.281511	22	0.281474	-3.8	0.8	2.69	1885	13
226	0.0245	34	0.00093	13	1.46721	1.88681	12	0.281506	36	0.281474	-5.9	1.3	2.74	1792	11
227	0.0460	66	0.00160	23	1.46712	1.88649	14	0.281506	29	0.281452	-7.0	1.0	2.78	1780	13
228	0.0262	57	0.00092	19	1.46714	1.88653	13	0.281541	31	0.281511	-6.3	1.1	2.70	1720	15
229	0.0166	13	0.00064	4	1.46713	1.88674	11	0.281480	24	0.281458	-6.4	0.9	2.77	1797	16
230	0.0527	33	0.00169	10	1.46713	1.88643	14	0.281558	27	0.281499	-3.7	1.0	2.66	1850	9
231	0.0342	12	0.00124	3	1.46714	1.88653	12	0.281499	28	0.281456	-5.8	1.0	2.75	1827	15
232	0.0146	15	0.00057	6	1.46711	1.88651	11	0.281465	30	0.281446	-6.7	1.1	2.79	1802	15
233	0.0172	3	0.00065	1	1.46713	1.88665	13	0.281522	22	0.281498	-3.2	0.8	2.65	1873	13
234	0.0251	19	0.00096	7	1.46714	1.88657	14	0.281495	33	0.281461	-5.5	1.2	2.74	1830	12
235	0.0672	26	0.00254	5	1.46717	1.88656	12	0.281596	24	0.281508	-4.2	0.9	2.66	1815	8
236	0.0224	4	0.00082	0	1.46715	1.88666	12	0.281504	25	0.281477	-7.4	0.9	2.76	1724	16
237	0.0077	4	0.00028	1	1.46712	1.88640	10	0.281483	28	0.281477	-17.1	1.0	2.96	1301	29
243	0.0683	27	0.00213	11	1.46715	1.88644	16	0.281537	45	0.281464	-5.8	1.6	2.75	1813	14
245	0.0163	6	0.00061	3	1.46712	1.88652	9	0.281468	28	0.281448	-8.4	1.0	2.82	1727	20
246	0.0273	11	0.00101	5	1.46714	1.88646	9	0.281534	28	0.281498	-3.2	1.0	2.65	1876	23
247	0.0281	15	0.00102	6	1.46714	1.88660	10	0.281500	27	0.281464	-4.2	0.9	2.71	1885	20
248	0.0116	8	0.00042	2	1.46713	1.88655	9	0.281490	38	0.281476	-7.3	1.3	2.76	1731	17
250	0.0519	61	0.00172	20	1.46706	1.88622	12	0.281547	27	0.281487	-4.4	0.9	2.69	1840	13
251	0.0215	8	0.00085	3	1.46717	1.88662	9	0.281522	30	0.281502	-16.7	1.1	2.92	1282	21

252	0.0294	16	0.00115	7	1.46710	1.88648	10	0.281527	23	0.281484	-2.3	0.8	2.65	1936	16
253	0.0205	11	0.00078	4	1.46715	1.88655	14	0.281533	26	0.281506	-5.1	0.9	2.68	1781	25
254	0.0184	13	0.00066	4	1.46718	1.88665	10	0.281488	25	0.281466	-6.9	0.9	2.76	1764	20
255	0.0229	5	0.00082	2	1.46714	1.88672	10	0.281496	24	0.281468	-5.7	0.8	2.74	1812	20
256	0.0396	17	0.00139	6	1.46717	1.88639	15	0.281529	33	0.281481	-5.7	1.2	2.72	1793	10
257	0.0537	26	0.00188	10	1.46716	1.88654	13	0.281516	31	0.281449	-5.0	1.1	2.75	1873	8
259	0.0277	10	0.00104	5	1.46712	1.88623	13	0.281508	39	0.281477	-11.9	1.4	2.85	1530	33

Table 38: U-Pb isotope analyses of magmatic zircon grains from the metadiorite (*ZM-10-45*)

Grain	$^{207}\text{Pb}^{\text{a}}$	U^{b}	Pb^{b}	$\frac{\text{Th}^{\text{b}}}{\text{U}}$	$^{206}\text{Pb}^{\text{c}}$	$\frac{^{206}\text{Pb}^{\text{d}}}{^{238}\text{U}}$	$\pm 2\text{s}$	$\frac{^{207}\text{Pb}^{\text{d}}}{^{235}\text{U}}$	$\pm 2\text{s}$	$\frac{^{207}\text{Pb}^{\text{d}}}{^{206}\text{Pb}}$	$\pm 2\text{s}$	rho^{e}	$\frac{^{206}\text{Pb}}{^{238}\text{U}}$	$\pm 2\text{s}$	$\frac{^{207}\text{Pb}}{^{235}\text{U}}$	$\pm 2\text{s}$	$\frac{^{207}\text{Pb}}{^{206}\text{Pb}}$	$\pm 2\text{s}$	conc.^{f}
	(cps)	(ppm)	(ppm)	U	(%)	^{238}U	(%)	^{235}U	(%)	^{206}Pb	(%)		^{238}U	(Ma)	^{235}U	(Ma)	^{206}Pb	(Ma)	(%)
08	1510	76	9.9	0.82	0.08	0.1153	1.7	1.0010	3.3	0.0630	2.8	0.52	703	11	704	17	707	60	100
09	1811	85	11	0.81	0.02	0.1151	1.8	1.0080	3.1	0.0635	2.5	0.58	702	12	708	16	725	53	97
10	2288	114	14	0.80	0.00	0.1118	1.8	0.9904	4.0	0.0642	3.6	0.44	683	11	699	20	749	75	91
11	1721	84	11	0.90	0.05	0.1168	1.6	1.0160	3.1	0.0631	2.7	0.51	712	11	712	16	711	57	100
12	1714	83	11	0.83	0.02	0.1168	1.6	1.0330	2.9	0.0641	2.4	0.57	712	11	720	15	745	50	96
13	1790	87	11	0.59	0.14	0.1153	1.6	0.9988	2.9	0.0628	2.5	0.55	704	11	703	15	702	52	100
14	4596	99	13	0.74	0.36	0.1170	1.6	1.0160	2.9	0.0630	2.3	0.57	713	11	712	15	708	50	101
15	2672	54	7	0.70	b.d.	0.1190	1.6	1.0460	2.7	0.0638	2.1	0.61	725	11	727	14	733	44	99
16	4598	95	13	0.92	0.01	0.1171	1.8	1.0210	2.5	0.0632	1.7	0.74	714	12	714	13	715	36	100
17	4955	72	11	1.24	0.00	0.1201	1.7	1.0600	2.3	0.0640	1.5	0.73	731	11	734	12	742	33	99
18	3334	70	9.2	0.78	0.17	0.1189	1.5	1.0720	4.0	0.0654	3.6	0.39	724	11	740	21	787	77	92
19	2472	53	6.5	0.54	0.01	0.1165	1.5	1.0200	2.8	0.0635	2.4	0.53	710	10	714	15	725	51	98
20	2621	55	6.7	0.49	0.03	0.1182	1.6	1.0290	2.5	0.0632	1.9	0.65	720	11	719	13	714	41	101
21	2230	45	5.7	0.53	0.02	0.1188	1.8	1.0410	3.0	0.0635	2.3	0.62	724	13	724	15	725	49	100
22	4215	82	11	0.90	0.02	0.1157	1.5	1.0220	2.3	0.0640	1.7	0.65	706	10	715	12	742	37	95
23	4526	95	12	0.90	0.00	0.1088	2.4	0.9617	2.9	0.0641	1.8	0.80	666	15	684	15	745	37	89
24	3779	79	10	0.80	0.10	0.1148	1.4	1.0070	2.5	0.0636	2.1	0.57	700	10	707	13	730	44	96
25	3302	76	9.9	0.73	0.05	0.1186	1.7	1.0450	2.5	0.0639	1.9	0.67	722	11	727	13	739	39	98
26	3312	74	9.3	0.77	0.00	0.1131	1.5	0.9807	2.5	0.0629	1.9	0.63	691	10	694	12	704	41	98
27	3076	65	8.2	0.76	0.03	0.1158	1.5	1.0110	2.4	0.0633	1.9	0.62	707	10	709	12	718	40	98
28	3970	86	11	0.84	b.d.	0.1171	1.4	1.0240	2.5	0.0634	2.0	0.58	714	10	716	13	722	43	99
29	4058	91	12	0.85	0.00	0.1127	1.5	0.9737	2.5	0.0627	1.9	0.63	688	10	690	12	698	41	99
30	5379	99	13	1.02	0.07	0.1165	1.6	1.0690	2.2	0.0666	1.6	0.70	710	11	738	12	825	33	86
31	2462	53	6.2	0.63	0.01	0.1109	1.6	0.9975	2.4	0.0653	1.8	0.67	678	10	703	12	783	37	87
32	3621	82	10	0.69	0.42	0.1130	1.5	0.9850	2.7	0.0632	2.2	0.54	690	10	696	14	716	48	96
38	2643	59	7.5	0.73	0.02	0.1153	1.6	1.0050	3.0	0.0632	2.5	0.55	704	11	706	15	715	53	98
39	5412	84	12	0.70	2.80	0.1165	2.1	1.1910	4.4	0.0742	3.9	0.47	710	14	796	25	1046	79	68
40	2990	66	8.5	0.81	0.00	0.1154	1.6	1.0040	2.7	0.0631	2.3	0.57	704	10	706	14	713	48	99
41	3898	81	11	0.81	0.01	0.1164	1.7	1.0430	2.4	0.0650	1.6	0.74	710	12	726	12	774	34	92
42	2072	44	5.8	0.86	0.01	0.1172	1.8	1.0250	2.7	0.0635	1.9	0.69	714	12	716	14	723	41	99
43	2328	46	5.9	0.87	b.d.	0.1132	1.5	0.9819	2.7	0.0629	2.2	0.57	692	10	695	13	704	47	98
44	4559	94	12	0.71	0.01	0.1131	1.5	1.0020	2.5	0.0642	2.0	0.62	691	10	705	13	749	41	92
45	3252	73	9.4	0.73	0.00	0.1175	1.5	1.0250	2.5	0.0633	1.9	0.63	716	10	716	13	717	41	100

46	3621	74	9.8	0.90	b.d.	0.1172	1.6	1.0190	2.3	0.0631	1.6	0.71	715	11	714	12	710	35	101
47	4776	100	13	0.95	0.04	0.1174	2.2	1.0230	2.7	0.0632	1.6	0.82	716	15	716	14	716	33	100
48	5993	128	17	0.96	0.01	0.1177	1.6	1.0270	2.0	0.0633	1.3	0.76	717	11	717	11	717	28	100
49	2280	47	5.9	0.56	0.01	0.1190	1.9	1.0380	2.9	0.0633	2.2	0.65	725	13	723	15	718	47	101
50	3936	67	9.3	1.13	0.06	0.1162	1.6	1.0090	2.2	0.0630	1.5	0.73	709	11	708	11	707	32	100

Table 39: Lu-Yb-Hf isotope analyses of magmatic zircon grains from the metadiorite (*ZM-10-45*)

Grain	$^{176}\text{Yb}/^{177}\text{Hf}^a$	$\pm 2s$	$^{176}\text{Lu}/^{177}\text{Hf}^a$	$\pm 2s$	$^{178}\text{Hf}/^{177}\text{Hf}$	$^{180}\text{Hf}/^{177}\text{Hf}$	Sig_{Hf}^b (V)	$^{176}\text{Hf}/^{177}\text{Hf}$	$\pm 2s^c$	$^{176}\text{Hf}/^{177}\text{Hf}_{(0)}^d$	$e\text{Hf}_{(0)}^d$	$\pm 2s^c$	T_{DM2}^e (Ga)	age ^f (Ma)	$\pm 2s^c$
10	0.0380	25	0.00127	8	1.46718	1.88791	11	0.282408	28	0.282391	1.3	1.0	1.46	683	11
11	0.0387	26	0.00131	7	1.46718	1.88838	10	0.282406	23	0.282389	1.9	0.8	1.46	712	11
12	0.0383	20	0.00129	8	1.46719	1.88835	12	0.282394	27	0.282377	1.5	1.0	1.48	712	11
13	0.0362	10	0.00124	4	1.46721	1.88784	11	0.282417	27	0.282401	2.1	1.0	1.44	704	11
14	0.0217	10	0.00077	3	1.46720	1.88844	11	0.282376	26	0.282365	1.1	0.9	1.50	713	11
15	0.0289	8	0.00095	2	1.46723	1.88782	12	0.282407	23	0.282394	2.4	0.8	1.44	725	11
16	0.0328	26	0.00112	7	1.46724	1.88804	10	0.282392	25	0.282376	1.5	0.9	1.48	714	12
18	0.0412	18	0.00141	6	1.46718	1.88654	9	0.282418	25	0.282399	2.5	0.9	1.43	724	11
19	0.0211	11	0.00073	3	1.46721	1.88677	10	0.282403	30	0.282393	2.0	1.1	1.45	710	10
20	0.0292	8	0.00105	3	1.46719	1.88659	9	0.282415	23	0.282401	2.5	0.8	1.43	720	11
21	0.0209	3	0.00073	1	1.46723	1.88670	10	0.282427	25	0.282417	3.1	0.9	1.40	724	13
22	0.0373	50	0.00123	15	1.46717	1.88657	10	0.282411	29	0.282394	1.9	1.0	1.45	706	10
23	0.0269	18	0.00094	5	1.46720	1.88659	9	0.282430	24	0.282418	1.9	0.9	1.42	666	15
24	0.0553	44	0.00186	15	1.46721	1.88663	9	0.282415	26	0.282391	1.7	0.9	1.46	700	10
25	0.0272	30	0.00099	9	1.46715	1.88655	10	0.282424	27	0.282410	2.9	0.9	1.41	722	11
26	0.0555	60	0.00186	20	1.46717	1.88658	9	0.282448	24	0.282424	2.7	0.9	1.40	691	10
27	0.0162	16	0.00055	4	1.46718	1.88660	10	0.282388	24	0.282381	1.5	0.8	1.47	707	10
28	0.0454	28	0.00156	11	1.46717	1.88643	10	0.282422	27	0.282401	2.4	1.0	1.43	714	10
29	0.0493	17	0.00165	6	1.46715	1.88661	9	0.282435	28	0.282414	2.2	1.0	1.42	688	10
30	0.0340	9	0.00112	3	1.46721	1.88662	10	0.282427	27	0.282412	2.7	1.0	1.41	710	11
31	0.0539	26	0.00173	7	1.46717	1.88661	10	0.282425	24	0.282403	1.6	0.9	1.44	678	10
32	0.0334	23	0.00116	7	1.46721	1.88672	9	0.282413	24	0.282398	1.7	0.8	1.45	690	10
38	0.0203	18	0.00070	5	1.46719	1.88670	10	0.282412	28	0.282402	2.2	1.0	1.43	704	11
39	0.0399	12	0.00138	3	1.46713	1.88655	9	0.282418	25	0.282399	2.2	0.9	1.44	710	14
40	0.0353	5	0.00121	2	1.46718	1.88666	9	0.282432	25	0.282416	2.7	0.9	1.41	704	10
41	0.0274	15	0.00103	4	1.46722	1.88662	8	0.282413	30	0.282400	2.2	1.1	1.44	710	12
42	0.0200	8	0.00074	3	1.46717	1.88648	10	0.282397	26	0.282387	1.9	0.9	1.46	714	12
43	0.0311	7	0.00103	2	1.46715	1.88678	10	0.282396	26	0.282383	1.2	0.9	1.48	692	10
45	0.0420	41	0.00150	14	1.46716	1.88660	11	0.282426	35	0.282405	2.6	1.3	1.42	716	10
46	0.0413	31	0.00138	10	1.46716	1.88660	10	0.282428	26	0.282410	2.7	0.9	1.41	715	11
47	0.0483	17	0.00163	6	1.46714	1.88648	9	0.282390	26	0.282368	1.2	0.9	1.49	716	15
48	0.0395	27	0.00131	8	1.46713	1.88657	10	0.282391	32	0.282374	1.5	1.1	1.48	717	11
50	0.0454	26	0.00149	9	1.46721	1.88669	9	0.282433	27	0.282414	2.7	1.0	1.41	709	11

PARTIE III:

IMPLICATIONS

METALLOGENIQUES:

SOURCE, TRANSPORT,

DEPOT DE L'URANIUM

CHAPITRE 5: Geochemical signatures of uranium oxides in the Lufilian belt: from unconformity-related to syn-metamorphic uranium deposits during the Pan-African orogenic cycle

Aurélien Eglinger¹, Anne-Sylvie André-Mayer¹, Olivier Vanderhaeghe¹, Julien Mercadier¹,
Michel Cuney¹, Sophie Decrée², Jean-Louis Feybesse³ ; Jean-Pierre Milesi³

Article publié dans *Ore Geology Reviews* (54, 197-213)

¹GeoRessources, CNRS-CREGU, Université de Lorraine, France

²Royal Museum of Central Africa, Tervuren, Belgium

³AREVA, BU Mines Paris, France

Abstract

The Pan-African Lufilian belt (Zambia and Democratic Republic of Congo) is known for its world-class copper and cobalt deposits. In addition, the Lufilian Copperbelt hosts several uranium occurrences concentrated within deformed siliciclastic rocks of the basal Neoproterozoic Katanga supergroup. We report LA-ICPMS and EMP analysis of the rare earth element (REE) and yttrium (Y) abundances (designated as the REY signatures) of uranium oxides from two uranium mineralizing events of the Lufilian belt previously dated at 652 ± 8 Ma and 530 ± 6 Ma by the U-Pb method on uraninite. Uranium oxides dated at ca. 650 Ma from the External fold-and-thrust belt are characterized by (i) bell shape REE patterns centered on middle REE (MREE), (ii) positive europium (Eu) anomalies and (iii) relatively low Y contents. In contrast, uranium oxides dated at ca. 530 Ma from the Domes region are characterized by (i) REE patterns with a less pronounced light REE (LREE) fractionation, (ii) negative Eu anomalies and (iii) higher Y contents. Moreover, the External fold-and-thrust belt also contains uranium mineralization dated at ca. 530 Ma having the same characteristics as the ca. 530 Ma uranium oxides from the Domes region (a moderately fractionated REE pattern and a negative Eu anomaly). As REY signatures are known to reflect mineralizing processes, the distinct geochemical signatures of the two uranium oxides generations (ca. 650 Ma and ca. 530 Ma) provide meaningful information about the uranium cycle during the Pan-African orogeny. Compared to the REY signatures of the known worldwide uranium deposit types, the REY signature of uranium oxides dated at ca. 650 Ma of the External fold-and-thrust belt is similar to the REE patterns from unconformity-related U deposits (Athabasca in Canada and Kombolgie in Australia). Uranium oxides of the Domes region and some of the External fold-and-thrust belt display similar characteristics to syn-metamorphic U deposit (Mistamisk in Canada). Accordingly, we propose that the two stages of uranium oxide crystallizations within the Lufilian belt, at ca. 650 and ca. 530 Ma, occurred under distinct physico-chemical conditions. The first stage, at ca. 650 Ma, may be related to late diagenesis hydrothermal processes, at the basement/cover interface, with the circulation of highly saline basinal brines linked to evaporites of the Roan group. This Pan-African unconformity-related uranium deposit is the youngest of this type described to date. The second stage may be connected to metamorphic fluid circulations, at about 530 Ma, during the Lufilian orogeny in the Domes region and also in the External fold-and-thrust belt.

Keywords: Lufilian belt; Uranium oxide; Rare Earth Elements; Yttrium; Unconformity-related deposit; Syn-metamorphic deposit

1. Introduction

The Pan-African Lufilian belt is known for its world-class sediment-hosted Cu-Co ore deposits with a proposed multiphase origin (Key et al., 2001; Cailteux et al., 2005; De Waele et al., 2006; Muchez et al., 2008; El Desouky et al., 2009; Hitzman et al., 2010; Figure 47). This belt also hosts some Pb-Zn-Cu ore deposits and significant uranium mineralization (Mendelsohn, 1961; Meneghel, 1981; Cosi et al., 1992; Kampunzu et al., 2009). In totality, about 42 uranium occurrences (mines and showings) have been discovered in the Lufilian belt and are distributed within the External fold-and-thrust belt in Democratic Republic of Congo (DRC) and within the Domes region in Zambia (Figure 47). Uranium occurrences were first discovered in the External fold-and-thrust belt in 1915 by UMHK (*Union Minière du Haut Katanga*; Derriks and Vaes, 1956) and much later in the northwestern part of the Domes region in 1972 by AGIP (Meneghel, 1981). The first uranium mining in the Katanga Copperbelt, the Shinkolobwe deposit exploited from 1921 to 1960 and, in 1939, yielded a large part of the ore used for production of the first nuclear bombs deployed at the end of the Second World War (Derriks and Vaes, 1956; Ngongo, 1975). Mineralization occurs mainly as uranium oxides within a basal sedimentary sequence, known as the Roan group and attributed to the Neoproterozoic (Cailteux, 1983, 1994; Porada and Berhorst, 2000). The host rocks are dolomitic shale in the External fold-and-thrust belt, and carbonaceous quartzite/quartz micaschist in the Domes region (Meneghel, 1981; Cosi et al., 1992).

The Shinkolobwe uranium deposit, in the External fold-and-thrust belt, was initially assigned to a magmatic origin, although no magmatic rocks were described in this area (Derriks and Oosterbosch, 1958). More recently, uranium mineralization in the External fold-and-thrust belt has been interpreted as being of syngenetic/early diagenetic origin because of the strong lithostratigraphic control, such as identified for copper and cobalt ore deposits (François, 1974; Ngongo, 1975; Meneghel, 1981; Cailteux, 1983, 1997; Loris, 1996). Recent work suggests that uranium has been re-concentrated during the Lufilian orogeny leading to epigenetic deposits (Loris et al., 2002). U-Pb ages on uranium oxides from the Lufilian belt yield a wide range of ages from 706 to 235 Ma based on concordant $^{207}\text{Pb}/^{206}\text{Pb}$, $^{206}\text{Pb}/^{238}\text{U}$ and $^{207}\text{Pb}/^{235}\text{U}$ ages or on upper intercept of discordia lines (Begemann et al., 1952, 1953; Ledent, 1958; Cahen et al., 1961; Meneghel, 1981; Cahen and Snelling, 1984; Richards et al., 1988; Loris, 1996). These

geochronological data have been recently reassessed based on new U-Pb dating by SIMS (Decrée et al., 2011), yielding a discordia with an upper intercept at 652.3 ± 7.3 Ma for uranium oxide from the External fold-and-thrust belt (Shinkolobwe, Swambo and Kalongwe; Figure 49) and a discordia with an upper intercept at 530.1 ± 5.9 Ma for uranium oxide from the Domes region (Musoshi and Nkana, Figure 49) and from the External fold-and-thrust belt (Kolwezi and Luiswishi, Figure 48). Other uranium oxides from the Kawanga occurrence in the Domes region yielded 542 ± 12 Ma by U-Pb geochronology by SIMS (Cathelineau et al., 1990).

Accordingly, the Lufilian belt is characterized by two stages of uranium oxide crystallization. The first mineralization event at ca. 650 Ma took place during proto-oceanic rift basin whereas the second event at ca. 530 Ma is associated with the final collision stage of the Pan-African orogeny in the Lufilian belt (Decrée, et al., 2011). In order to better understand and constrain this uranium mineral system in the Lufilian belt, we use trace elements of uranium oxides as geochemical tracer of ore genesis. Indeed, the uraninite mineral is a non-stoichiometric compound with a fluorite-type structure, which can incorporate a large amount of impurities, trivalent (Y and REE) and divalent (Pb, Ca) cations. The structural formula, emphasizing the role of these cationic substitutions, is $(U^{4+}_{1-x-y-z} U^{6+}_x REE^{3+}_y M^{2+}_z)O_{2+x-(0.5y)-z}$ (Janeczek and Ewing, 1992). Previous studies have demonstrated that the REE content within uranium oxides is a function of the physico-chemical conditions (temperature, redox conditions, fluid composition...) during uranium oxide formation (Fryer and Taylor, 1987; Pagel et al., 1987; Bonhoure et al., 2007; Mercadier et al., 2011). In this paper, we present new LA-ICPMS rare earth elements (REE) and yttrium (Y) contents (designated as the REY signature) of uranium oxides from five occurrences in the External fold-and-thrust belt (Kolwezi, Kalongwe, Swambo, Shinkolobwe and Luiswishi) and four occurrences in the Domes region (Malundwe, Mitukuluku, Musoshi and Nkana). These REY signatures confirm the distinction between the two stages of uranium oxide crystallization within the Lufilian belt and provide evidence for distinct physico-chemical conditions associated with these mineralization events. Based on these data, we propose a new model for the genesis of the uranium mineralization at the orogenic scale, both in space and time, distinguishing processes involved in the External fold-and-thrust belt and in the Domes region of the Lufilian belt.

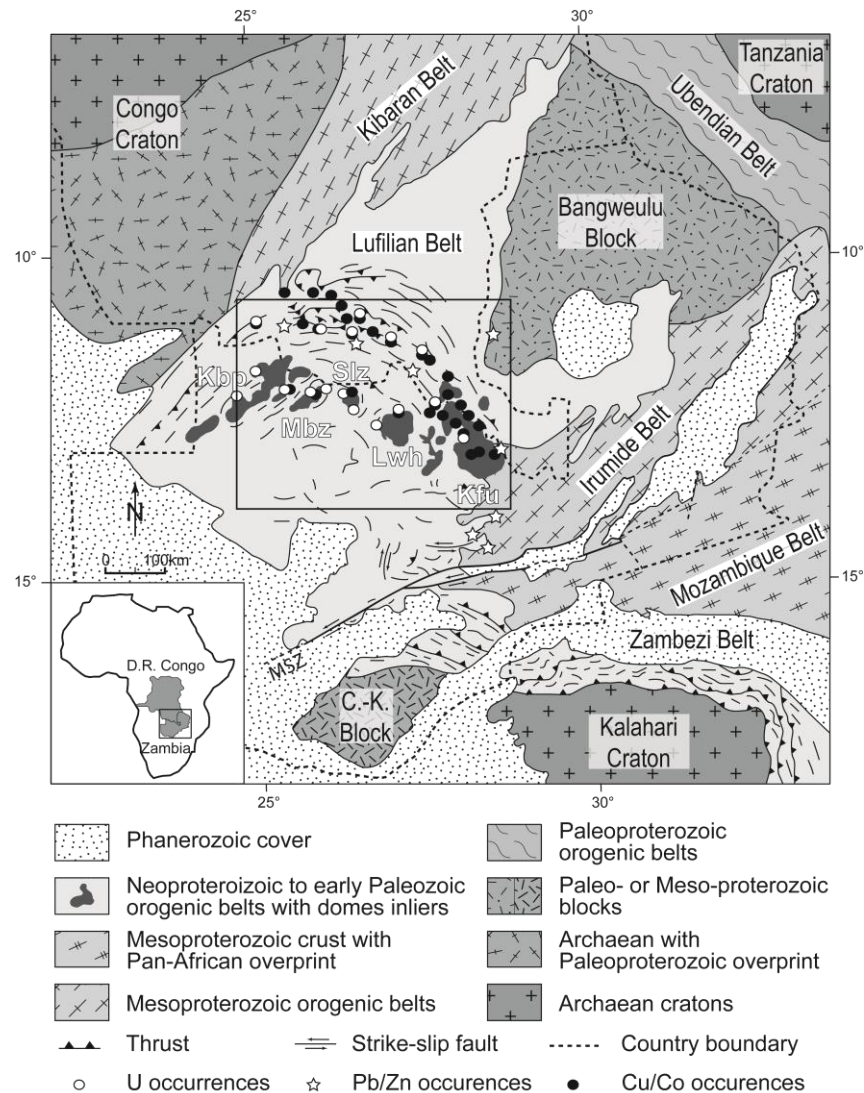


Figure 47: Geological map of the Pan-African Lufilian belt indicating the main structural trends and mineral occurrences (modified after De Waele et al., 2008). Abbreviations: Kbp = Kabompo Dome; Mbz = Mwombezhi Dome; Slz = Solwezi Dome; Lwh = Luswishi Dome; Kfu = Kafue Anticline; C.-K. = Choma Kalomo block; MSZ = Mwembezhi Shear Zone. (Black rectangle: study area enlarged in Figure 49).

2. Geological setting

The Lufilian belt formed between the Congo and Kalahari cratons as a result of the amalgamation of the west Gondwana supercontinent during the Pan-African orogeny (Unrug, 1983). It comprises (i) an External zone characterized by a Neoproterozoic metasedimentary sequence, the Katanga supergroup composed of the Roan, Nguba and Kundelungu groups (Figure 48), affected by folds and thrusts and low grade metamorphism reaching the lower Greenschist facies (here referenced as External fold-and-thrust belt) and (ii) an Internal zone comprising the

Domes region marked by higher grade metamorphism ranging from upper Greenschist to upper Amphibolite facies affecting a complexly folded nappe pile made up of metasedimentary rocks overlying migmatitic gneisses exhumed in the core of low-amplitude dome-shaped structures (Mendelsohn, 1961; Cosi et al., 1992; Porada and Berhorst, 2000; John et al., 2004).

2.1. Lithostratigraphy of the Katanga sequence

The Katanga supergroup sits unconformably on a pre-Katanga crystalline basement and comprises at its base the Roan sedimentary sequence. In the External fold-and-thrust belt, the Lower Roan subgroup includes coarse to fine siliciclastic sediments ranging from conglomerates to siltstones (Porada and Berhorst, 2000). The Upper Roan subgroup is characterized by a dolomitic marble sequence including mafic and ultramafic boudins (Tembo et al., 1999; John et al., 2003). In the eastern part of Domes region (known as the Zambian Copperbelt), the Roan group is composed, from bottom to top, by a basal siliciclastic unit, a middle carbonate and siliciclastic unit and an uppermost carbonate unit (Selley et al., 2005; Bull et al., 2011). In the western part of the Domes area, deformation and metamorphism have been much more intense and reconstruction of the stratigraphy is more speculative but is thought to be generally similar to the eastern part of the Domes region (Cosi et al., 1992). The stratigraphic correlations of the Roan group between the External fold-and-thrust belt and the Domes region were established by Cailteux (1994) and Cailteux and Kampunzu, (1995). They proposed that the sedimentary units of the Domes region described above are correlated to the R.A.T. (“Roches Argilo-Talqueuses”), Mines and Dipeta subgroups, respectively, in the External fold-and-thrust belt. The Roan group is moreover characterized by many evaporitic levels showing sedimentary features typical of sabkhas, such as pseudomorphs after gypsum, anhydrite (Porada and Berhorst, 2000; Muchez et al., 2008) and, locally, albitic lenses and desiccation cracks (Garlick and Fleischer, 1972).

Hanson et al. (1994) and Johnson et al. (2007) proposed that the onset of rifting is associated with the emplacement of the Kafue rhyolite dated at 879 ± 16 Ma and with the deposition of the Zambezi supracrustal sequence (ZSC) in the Zambezi belt. In the Lufilian belt, the Nchanga granite, dated at 877 ± 11 Ma by U-Pb on zircon, which is unconformably overlain by conglomerates of the Lower Roan group, provides a maximum age of deposition of these sediments (Armstrong et al., 1999). Detrital zircon grains, found within cross-bedded Lower

Roan quartzite, dated at around 880 Ma by U-Pb (Armstrong et al., 2005) are interpreted to originate from the Nchanga granite and corroborate that the emplacement of the Roan detrital sediments is younger than ca. 880 Ma. The Nchanga granite and the Kafue rhyolite share geochemical signatures with “within plate granitoids” (Katongo et al., 2004; Johnson et al., 2007). The emplacement of these granitoids and associated felsic metavolcanic rocks is proposed to mark the onset of continental rifting in the Lufilian-Zambezi belts (Katongo et al., 2004). In this context, the Roan group has been interpreted to represent sedimentation of detritals, carbonates and evaporates in a continental lagoon environment developed in a continental rift (Cailteux, 1983; Porada and Berhorst, 2000; Selley et al., 2005). Lateral facies transitions suggest that rifting was first characterized by the formation of several relatively small, isolated continental sub-basins bounded by a complex set of discontinuous faults (Selley et al., 2005). The mafic and ultramafic boudins in the Upper Roan subgroup have geochemical signatures of within-plate tholeiites and have been interpreted as deformed dykes or sills intruded during the initial stages of continental rifting in Lufilian belt (Tembo et al., 1999) whereas the mafic and ultramafic rocks of the Zambezi supracrustal sequence have N-MORB and depleted mantle-like geochemical and isotopic signatures and are interpreted as vestiges of an oceanic crust in the Zambezi belt (John et al., 2003).

The Mwashya group shows lateral facies transitions. In the northern part of the Lufilian belt, in DRC, it is mainly composed by dolomitic and volcanic sequences, whereas in the southern part of the Lufilian belt in Zambia, it is dominated by shales in Zambia (Cailteux, 1994). The black shale sequence of Lower Mwashya group comprises the Luakela volcanics dated at 765 ± 5 Ma (Kampunzu et al., 2000; Porada and Berhorst, 2000; Key et al., 2001; Figure 48). The Mwashya group is directly overlain by a diamictite horizon known as the *Grand Conglomérat* which marks the base of the Nguba group (Binda and Van Eden, 1972). This diamictite, correlated to the Sturtian glaciation, is located between the Mwashya volcanics dated at ca. 765 Ma and the Kundelungu volcanic dated at ca. 735 Ma (Key et al., 2001; Figure 48). The Nguba group is dominated by a mixed carbonate-siliciclastic sequence (Kampunzu et al., 1991). The top of the Katanga sedimentary sequence is marked by the Kundelungu group. The base of the Kundelungu group is also formed by a basal diamictite, the *Petit Conglomérat*, correlated to the Marinoan glaciation at around 635 Ma (Robb et al., 2002; Condon et al., 2005; Figure 48). The Kundelungu

group consists mainly of siltstones-shales-carbonates alternations for the lower part, a sequence of pelites, siltstones and sandstones for the middle part, and an arenaceous unit in the upper part (Figure 48). Rocks of the Bianco subgroup, forming the upper part of the Kundelungu group, are not metamorphosed and represent the youngest unit of the Katanga supergroup with a maximum age of 573 ± 5 Ma, obtained by $^{40}\text{Ar}-^{39}\text{Ar}$ on detrital muscovite grains (Master et al., 2005; Figure 48). These sedimentary sequences record the transition from a continental rift stage evolving to a carbonate platform as attested to by deposition of the Lower Mwashya group grading vertically to an open marine basin as evidenced with deposition of the Upper Mwashya group. The emplacement of gabbros and coeval mafic extrusive rocks in the Upper Mwashya and Lower Nguba groups are interpreted to reflect a proto-oceanic rift (Kampunzu et al., 1991). Finally, the upper part of the Kundelungu group corresponds to the deposition of post-rift sediments (Kampunzu et al., 2009).

	Age (Ma)	External fold-and-thrust belt		Domes region			
		Group	Subgroup	Lithology			
SUPERGROUP	$< 573 \pm 5^3$ Detrital muscovite	Kundelungu	Biano	Arkoses, conglomerates, sandstones, shales			
			Ngule	Sandstones, carbonated silstones, shales, limestones			
			Gombela	Carbonated silstones, shales, limestones, dolomites « <i>Petit Conglomérat</i> »: glacial diamictite			
	(± 635)	Nguba	Bunkeya	Dolomitic sandstones, silstones, shales			
			Muombe	Carbonated silstones, shales, dolomites, limestones, lavas « <i>Grand Conglomérat</i> »: glacial diamictite			
	735 ± 5^2 Magmatic zircon						
KATANGA	765 ± 5^2 Magmatic zircon	Group	Subgroup	Lithology	Group	Subgroup	Lithology
			Mwashya	Shales, carbonaceous shales or sandstones	Mwashya		Black shales, lavas
		Roan	Dipeta	Dolomites, dolomitic silstones	Upper Roan	Bancroft	Dolomites, dolomitic shales, gabbroic bodies
			☆ Mines	Shales, dolomitic shales, silstones	Lower Roan	☆ Kitwe	Shales, dolomites, arenites, evaporites
			R.A.T.	Hematitic, chloritic, dolomitic silstones, conglomerates		☆ Mindola	Quartzites, quartz micaschists, conglomerates

Figure 48: Lithostratigraphic correlations for the Katanga supergroup between the External fold-and-thrust belt and the Domes region (modified after Kampunzu and Cailteux, 1999; Porada and Berhorst, 2000; Kampunzu et al., 2009) and uranium occurrences (grey stars). Age constraints are provided by U-Pb geochronology on magmatic zircon grains of volcanic rocks (¹ Hanson et al., 1994; ² Key et al., 2001) and by argon thermochronology on detrital muscovite grains (³ Master et al., 2005).

In summary, the Katanga supergroup in the Lufilian belt records approximately 300 Ma of sedimentary deposition into extensional basins developed along the margins of the Congo, Tanzania, and Zimbabwe cratons. This history marked by the development of the Roan basin which evolved progressively from (i) a continental rift basin starting at around 880 Ma, as evidenced by the coarse clastic sediments of the Lower Roan group, to (ii) a deeper marine basin as recorded by the deposition of the black shales of the Upper Mwashya subgroup. The metasedimentary sequences exposed in the Lufilian belt are interpreted to represent a lagoonal basin bordered to the North by the margins of the Congo and Tanzanian cratons dominated by clastic deposits, and to the South, by a carbonate platform deposited on the margin of the Zimbabwe craton (Porada and Berhorst, 2000). Opening of the Kundelungu marine basin was accompanied by mafic volcanism between 760-740 Ma (Porada and Berhorst, 2000). Subsidence of the barrier platform allowed transgression attested to by deposition of the Upper Mwashya and Nguba groups. Deposition of the Kundelungu group reflects post-rift infilling of this basin (Porada and Berhorst, 2000; Kampunzu et al., 2009).

2.2. Tectonic evolution of the Lufilian belt

Rift basin opening (from 880 Ma to 600 Ma) was followed by convergence (from 600 Ma to 530 Ma) of the Congo and Kalahari cratons. Transition from divergent to convergent context is underlined by eclogitic rocks formation, dated at ca. 595 Ma by Sm-Nd whole-rock and garnet isochron, in the Zambezi belt (John et al., 2003). The Lufilian belt displays all the structural and metamorphic features typical of the thermal-mechanical evolution of Phanerozoic orogenic belts (Vanderhaeghe, 2012). Subduction and exhumation of crustal units under a low geothermal gradient is depicted by *P-T* estimates of kyanite-bearing eclogites with temperatures of 590-750 °C at a minimum pressure of 20 kbar. Phengite-bearing eclogites equilibrated at temperatures between 720 and 755 °C and at pressures between 26 and 28 kbar (John et al., 2003). Continent-continent collision is marked by the development of the Lufilian orogenic belt characterized by formation of a fold-and-thrust belt in the external zone and by the emplacement of a nappe pile affected by high-grade high-pressure/low-temperature metamorphism (talc-kyanite whiteschists) in the Domes region (Cosi et al., 1992; Porada and Berhorst, 2000; John et al., 2004). Crustal thickening is followed by an increase in the geothermal gradient marked and recorded by intermediate-pressure/high-temperature *P-T* conditions with a pressure around 13 ± 1 kbar and a

temperature of 750 ± 25 °C dated at 529 ± 2 Ma, by U-Pb on monazite grains from whiteschists in three localities: the Kabompo, Mwombezhi and Solwezi domes (John et al., 2004; Figure 47). Metamorphic grade increased from Prehnite-Pumpellyite facies in the External fold-and-thrust belt to upper Amphibolite facies in the Domes region. ^{40}Ar - ^{39}Ar analyses thermochronology on biotite and Rb-Sr dating on muscovite and biotite yield ages ranging from 510 to 463 Ma that are interpreted to represent post-orogenic cooling of the metamorphic rocks in the Lufilian belt (Cosi et al., 1992; John et al., 2004; Rainaud et al., 2005).

3. Uranium mineralization

The Lufilian belt hosts several uranium deposits and occurrences within metasedimentary rocks of the so-called Katanga supergroup (Mendelsohn, 1961; Figure 49; Table 40).

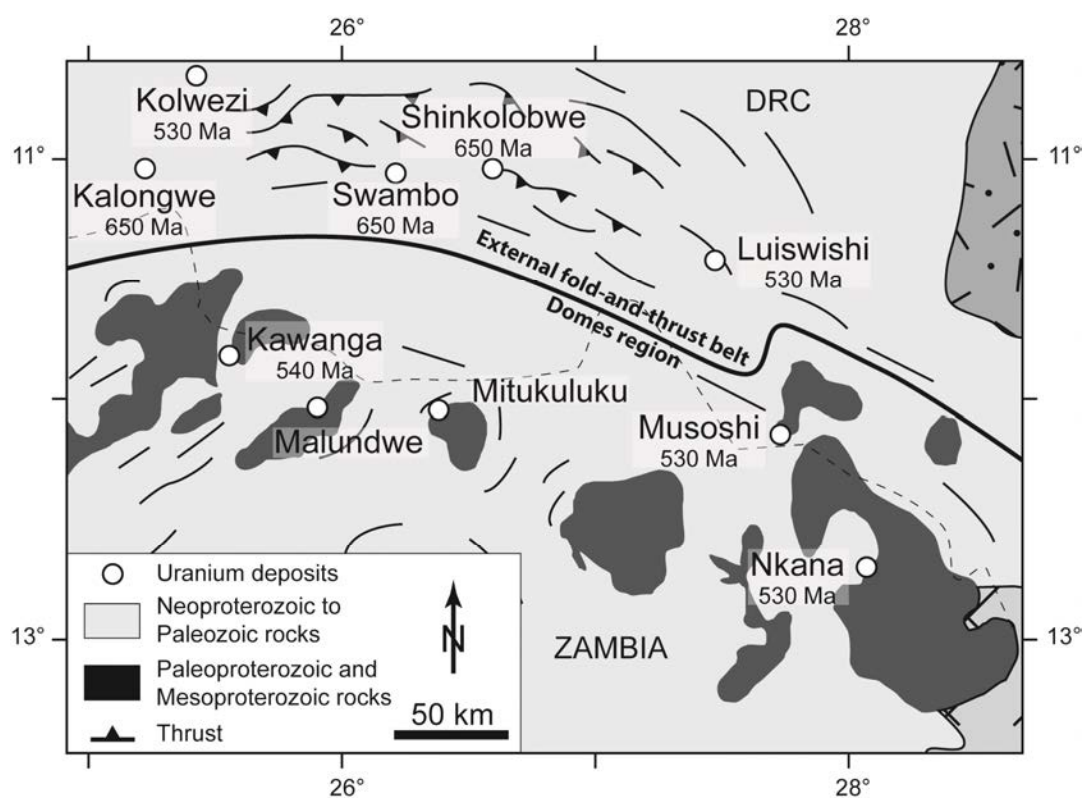


Figure 49: Study area and location of studied uranium occurrences with their ages (from Decrée et al., 2011): Kalongwe, Kolwezi, Swambo, Shinkolobwe and Luiswishi in the External fold-and-thrust belt and Kawanga, Malundwe, Mitukuluku, Musoshi and Nkana in the Domes region. The dashed black line represents the international boundary between Democratic Republic of Congo (DRC) and Zambia. The thick black line is the approximate limit between the External fold-and-thrust belt and the Domes region.

3.1. External fold-and-thrust belt uranium occurrences

Uranium deposits and occurrences in the External fold-and-thrust belt are distributed along an arcuate structural belt, approximately 300 km long, from Kalongwe to Luswishi (Cailteux et al., 2005; Figure 49). Uranium mineralization is mainly represented by uraninite [UO₂] and hosted by chloritic-dolomitic shales, known as the grey R.A.T., *Roches Argilo-Talqueuses*, at the base of the Mines subgroup (Cahen et al., 1971; François, 1974; Ngongo, 1975; Loris, 1996; Cailteux, 1997; Loris et al., 1997, 2002; Kampunzu and Cailteux, 1999; Figure 48). Uraninite occurs mainly as scattered grains, sometimes concentrated in lenses (up to 2000 ppm of U) or in tectonic breccias affecting chloritic-dolomitic shales (Table 40). Secondary hexavalent uranium minerals are kasolite [Pb(UO₂)SiO₄.H₂O], sklodowskite [Mg(UO₂)₂(SiO₃OH)₂.6H₂O], uranophane [Ca(UO₂)₂(SiO₃OH)₂.5H₂O], soddyite [(UO₂)₂SiO₄.2(H₂O)], coffinite [U(SiO₄.OH)₄], vandenbrandeite [CuUO₂(OH)₄] and schoepite [(UO₂)₈O₂(OH)₁₂.12H₂O] (Decrée et al., 2011). The host rock mineralogy is dominated by dolomite, quartz, magnesite, sericite and chlorite with apatite, tourmaline and monazite as accessory minerals (Derriks and Vaes, 1956; Ngongo, 1975; Meneghel, 1981; Table 40). These sediments were metamorphosed during the Pan-African orogeny from Prehnite-Pumpellyite to lower Greenschist facies (< 300-350 °C; Table 40) with the crystallization of authigenic sericite and chlorite (François, 1974). Locally, uranium oxides are in association with Cu-Co-Ni-(Mo-, Se-) sulfides (Cailteux, 1997; Loris et al., 2002) and/or with Au and PGE, notably palladium (Derriks and Oosterbosch, 1958; Jedwab, 1994). U-Pb geochronology on uranium oxide yields an age of ca. 650 Ma for Shinkolobwe deposit and for the Kalongwe and Swambo occurrences (Derriks and Oosterbosch, 1958). In the External fold-and-thrust belt, the Kolwezi and Luiswishi occurrences yield a second age for uranium mineralization at ca. 530 Ma (Decrée et al., 2011). The Kolwezi deposit is part of a klippe located to the north of the Luiswishi-Kalongwe tectonic lineament but is probably rooted 150 km to the south of its present-day location in a more internal position with regard to the orogenic belt (François, 1974).

3.2. Domes region uranium occurrences

The Domes region is characterized by complexly folded metasediments of the Katanga supergroup overlying a gneissic and migmatitic unit interpreted as representing the basement of

the Katanga supergroup and exposed in the core of dome-shaped structures (Mendelsohn, 1961; De Swardt and Drysdall, 1964; Cosi et al., 1992; Porada and Berhorst, 2000; Figure 49). Uranium mineralization occurs mainly in the Lower Roan group, which crops out for 600 km along the contact between the metasedimentary cover and the gneissic-migmatitic basement (Meneghel, 1981; Figure 49). The uranium occurrences are distributed over about 300 km from west to east and include Kawanga, Malundwe, Mitukuluku, Musoshi and Nkana. Within the Domes region, the metamorphic grade increases from east to west. In the eastern part, the Nkana mine uranium-bearing rocks are characterized by an upper Greenschist facies mineral paragenesis (> 300-350 °C) with chlorite and biotite (Meneghel, 1981; Brems et al., 2009; Table 40). In the western part (Kabompo, Mwombezi and Solwezi domes), uranium mineralization is hosted in quartz-rich micaschists at upper Amphibolite facies (> 500-550 °C) characterized by porphyroblasts of kyanite associated with phlogopite, garnet, white mica, Mg-chlorite and talc (Meneghel, 1981; Cosi et al., 1992; Table 40).

Ore mineralogy is characterized by uraninite [UO₂] and brannerite [(U, Ca)(Ti, Fe)₂O₆] hosted by the siliciclastic and carbonaceous quartzite of the Lower Roan group (Meneghel, 1981; Cosi et al., 1992). Some uranium occurrences were described in quartz-carbonate veins within the Nguba subgroup in the Kansanshi open pit (Meneghel, 1981). Secondary hexavalent uranium minerals are autunite [Ca(UO₂)₂(PO₄)₂·10-12H₂O], torbernite [Cu(UO₂)₂(PO₄)₂·8-12H₂O], sabugalite [HAl(UO₂)₄(PO₄)₄·16H₂O] and gummite [UO₃·nH₂O]. The highest grade/thickness intersections that have been obtained in drill holes occurs at the Mitukuluku showing, with 1.4 wt.% U₃O₈ over a thickness of 9 m (Arthurs, 1974). In the Kawanga showing, discontinuous uranium mineralization has been intersected by drilling over several meters (with a maximum of 25 m) with U₃O₈ content of up to 1 wt.% (Meneghel, 1981). Minerals associated with uranium oxides include iron oxides, apatite, monazite, zircon, rutile, titano-magnetite and locally scapolite (Table 40). The mineralization is located in a shear zone marking the contact between the isoclinally folded metasedimentary rocks of the Lower Roan and the gneissic-migmatitic basement for the Kawanga and Mitukuluku occurrences (Meneghel, 1981; Cosi et al., 1992) or within a sheared tectonic slice of gneissic-migmatitic basement intercalated on the Lower Roan metasedimentary sequences, as for Malundwe deposit (Bernau, 2007). U-Pb geochronology on

uranium oxides yielded an age of ca. 530 for Musoshi and Nkana (Decrée et al., 2011) and of ca. 542 Ma for Kawanga (Cathelineau et al., 1990).

4. Materials and methods

For this study, sixteen uranium oxide-bearing mineralized samples were selected from the mineral collection of the Royal Museum for Central Africa (RMCA) and from the drill cores extracted during the exploration campaign by AGIP-COGEMA between 1980 and 1986. These samples come from seven deposits, covering the External fold-and-thrust belt (Kalongwe, Kolwezi, Swambo, Shinkolobwe and Luiswishi) and the intermediate metamorphic grade eastern part of the Domes region (Musoshi and Nkana), and from two occurrences intersected by drill cores covering the high metamorphic grade western part of the Domes region (Malundwe and Mitukuluku; Figure 48; Figure 49; Table 40). Most of the selected samples correspond to the ones that have been previously dated, using the U-Pb method by Decrée et al., (2011), at ca. 650 Ma for Kalongwe, Swambo and Shinkolobwe, at ca. 530 Ma for Kolwezi and Luiswishi in the External fold-and-thrust belt and at ca. 530 Ma for Musoshi and Nkana in the intermediate metamorphic grade eastern part of the Domes region. In this paper, we present REE and Y signatures of uranium oxides from nine uranium deposits and occurrences described above. The petrography and metallography were carried out at the GeoRessources laboratory (Nancy, France). We selected appropriate unaltered mineral areas suitable for laser ablation analysis using (i) a JEOL J7600F scanning electron microscopy (SEM) and (ii) a CAMECA SX100 electron microprobe (EMP), both at the interdepartmental microanalysis facility of the GeoRessources laboratory (Nancy, France). Major and trace (U, Pb, Th, Ca, Si and Y) elements were obtained by the EMP method and are expressed in weight percent oxides (Table 41; Table 42; Table 43).

Rare Earth Element (REE) contents of uranium oxides were determined using laser ablation inductively coupled plasma mass spectrometry (LA-ICPMS) at the GeoRessources laboratory. For each experiment, fourteen REE (La, Ce, Pr, Nd, Sm, Eu, Gd, Tb, Dy, Ho, Er, Tm, Yb and Lu), ^{238}U and Pb_{tot} were analyzed. Pb_{tot} is the sum of ^{206}Pb , ^{207}Pb and ^{208}Pb . ^{204}Pb was not detected during the first analytical tests and thus was not measured during later analyses. All data were acquired as raw counts (cps) using the time resolved mode. For each individual analysis

(external standard and unknown sample), the background was measured before ablation during 20s and its return to its initial value was checked before ablating a new zone. Signal intensity integration of ^{238}U and 14 REE masses was carried out during the plateau regime. Signal acquisition of the sample was stopped after 150 pulses (30s at 5 Hz). A spot size between 24 and 60 μm was selected depending on the size of the uranium oxides. For each individual analysis, the signal acquisition was recorded during 80s (including 20s of background acquisition and 30s of ablation). The certified glass standards NIST610, NIST612 and NIST614 were used as reference materials (Pearce et al., 1997). Lach et al. (2012) analyzed and calculated REE concentrations in several natural uranium oxides from worldwide uranium deposits. They used both matrix-matched (uranium oxide) and non-matrix-matched (NIST 610 SRM certified silicate glass) standards. REE quantification performed using both of these standards yield similar results, demonstrating the limited matrix effect for REE analysis by LA-ICP-MS. The methodology is described in details in Lach et al. (2013).

5. Results

Following the procedure described by Mercadier et al. (2011), only the unaltered areas in uranium oxides were used to determine the primary REE content by LA-ICPMS and Y content by EMP (Figure 50; Table 41; Table 42; Table 43).

5.1. Description of the samples investigated and chemical composition for the major elements determined by EMP

5.1.1. Uranium oxides dated at ca. 650 Ma in the External fold-and-thrust belt

In the Shinkolobwe deposit, uranium oxides can contain gold and secondary uranium minerals such as kasolite and sklodowskite occurring as isolated minerals or as vein fillings (Decrée et al., 2011). Uranium oxides from Shinkolobwe do not present alteration texture on SEM images; this observation is confirmed by their homogeneous composition obtained by EMP (Figure 50a; Table 41). These uranium oxides have homogeneous contents of UO_2 and PbO , ranging from 88.18 to 89.09 and from 7.30 to 7.69 wt.%, respectively. CaO content is between 0.63 and 1.37 wt.%; ThO_2 , SiO_2 and Y_2O_3 are present in concentrations below 0.08 in wt.%,

(detection limit). In Kalongwe and Swambo deposits, uranium oxides are replaced by uranophane, associated with galena, soddyite, coffinite and/or secondary rich calcium and uranium minerals (Decrée et al., 2011). Under the SEM, these uranium oxides present a patchy zoning, a texture typical of alteration. This patchy texture is confirmed by the heterogeneous composition obtained by EMP (Figure 50b, c; Table 41). These grains contain variable contents of UO_2 and PbO , ranging from 75.35 to 84.24 wt.% and from 3.95 to 17.46 wt.%, respectively. They also contain variable SiO_2 (0.00-3.84 wt.%) and CaO (0.08-2.52 wt.%) contents.

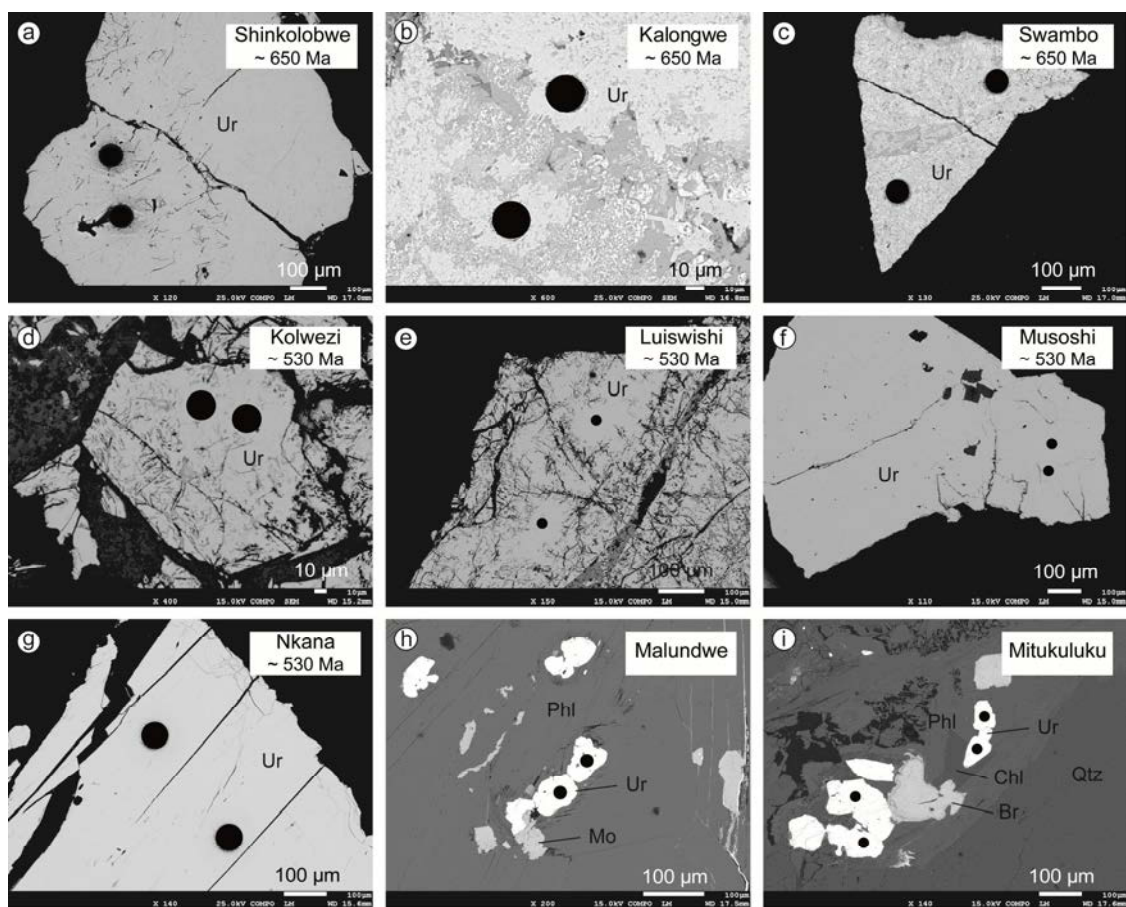


Figure 50: SEM images (backscattered electron mode) of all uranium oxides analyzed by LA-ICPMS in this study. a: Altered uranium oxide from the Kalongwe deposit. b: Altered uranium oxide from the Swambo deposit. c: Unaltered uranium oxide from the Shinkolobwe deposit. d: Unaltered uranium oxide from the Kolwezi deposit. e: Unaltered uranium oxide from the Luiswishi deposit. f: Unaltered uranium oxide from the Musoshi deposit. g: Unaltered uranium oxide from the Nkana deposit. h: Cogenetic unaltered uranium oxide and molybdenite from Malundwe showing. I: Cogenetic unaltered uranium oxide and brannerite from the Mitukuluku showing. Abbreviations: Br = Brannerite; Chl = Chlorite; Mo = Molybdenite; Phl = Phlogopite; Qtz = Quartz; Ur = Uranium oxide. Black dots represent LA-ICPMS spots with a size ranging from 24 to 60 µm.

5.1.2. Uranium oxides dated at ca. 530 Ma in the External fold-and-thrust belt

In the Kolwezi and Luiswishi occurrences, uranium oxides are associated with various types of Co-Fe-Mo-Pb sulfides. Uranium oxides are highly fractured but their composition is homogeneous (Figure 50d, e; Table 42). UO₂ and PbO contents range from 88.32 to 90.69 wt.% and from 6.15 to 7.39 wt.%, respectively. ThO₂ and CaO contents vary, respectively, from below the microprobe detection to 1.23 wt.% and from 0.70 to 1.1 wt.%. Si and Y contents are very low or below the detection limit (< 0.08 wt.%) of the electron microprobe.

5.1.3. Uranium oxides dated at ca. 530 Ma in the Domes region

In the Musoshi and Nkana deposits, uranium oxides are associated with brannerite, Cu-(Co) sulfides and molybdenite. Uranium oxides present a homogeneous texture with UO₂ and PbO contents ranging from 86.45 to 90.95 wt.% and from 6.10 to 6.88 wt.%, respectively (Figure 50f, g; Tabs. 3 and 4). ThO₂, CaO and SiO₂ are lower than 1.65 wt.%. Yttrium content varies from 0.18 to 0.74 wt.%. In the Malundwe and Mitukuluku occurrences, uranium oxides hosted by metamorphic phlogopites are also associated with brannerite, molybdenite and Cu sulfides (Figure 50h, i). These grains contain homogeneous contents of UO₂ and PbO, ranging from 85.83 to 90.04 wt.% and from 6.25 to 7.02 wt.%, respectively (Table 43). Uranium oxides from the Mitukuluku showing are characterized by high CaO content ranging from 4.35 to 5.09 wt.%. Yttrium content is higher than uranium oxides from Musoshi and Nkana with a range from 0.60 to 1.05 wt.%.

5.2. Rare Earth Element (REE) analyses by LA-ICPMS

The REE signatures of uranium oxides of the Lufilian belt display a variety of patterns that are a function of their age and structural position within the belt (Figure 51). For each structural zone (Figure 51a), at least two samples have been analyzed and the uranium oxide REE signatures show a very consistent pattern. The REE patterns of uranium oxides from the External fold-and-thrust belt dated at ca. 650 Ma (Kalongwe, Swambo and Shinkolobwe deposits) delineate a “bell shape” with the enrichment of MREE (Sm, Eu, Gd, Tb, Dy, Ho; Figure 51b). Their chondrite-normalized REE patterns display a positive slope from La to Sm with a (La/Sm)_N

ratio ($N = \text{chondrite-normalization}$) ranging from 0.01 to 0.08 and show a negative slope from Tb to Lu with a $(\text{Tb}/\text{Lu})_N$ ranging from 5.71 to 21.44 (Table 41). The maximum enrichment is in Sm for uranium oxides from Kalongwe, Eu for Swambo and Tb for Shinkolobwe (Figure 51b).

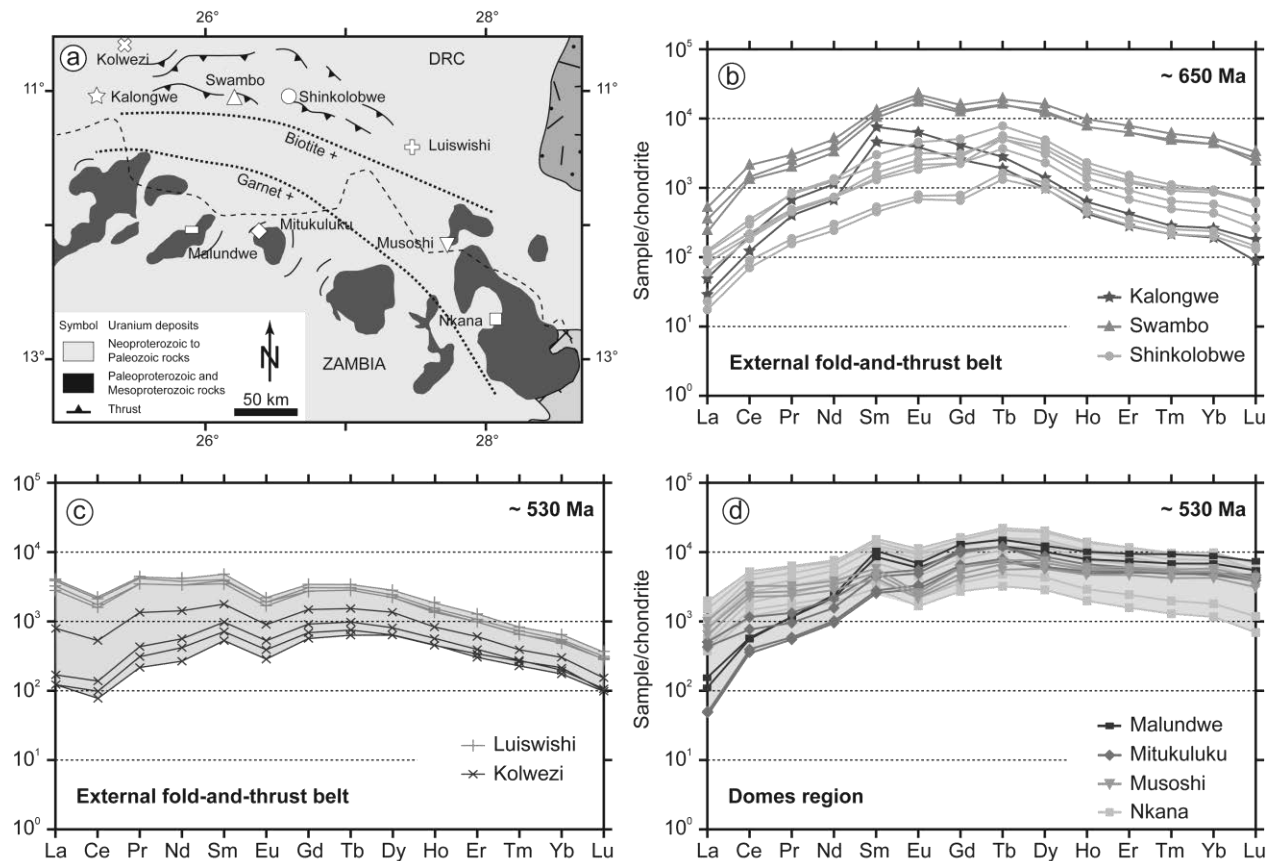


Figure 51: a: Location of uranium oxide samples from nine occurrences and symbol equivalence. Thick dashed black line represents garnet and biotite isograds (after François and Cailteux, 1981). b: Chondrite-normalized REE patterns for uranium oxides from three deposits in the External fold-and-thrust belt dated at ca. 650 Ma. c: Chondrite-normalized REE patterns for uranium oxides from two deposits in the External fold-and-thrust belt dated at ca. 530 Ma. d: Chondrite-normalized REE patterns for uranium oxides from five deposits/showings in the Domes region dated at ca. 530 Ma. See Table 41; Table 42; Table 43 for analytical data. Chondrite values are from McDonough and Sun (1995).

The REE patterns of uranium oxides from the External fold-and-thrust belt dated at ca. 530 Ma (Kolwezi and Luiswishi deposits) display a flatter shape, without strong fractionation between LREE (La, Ce, Pr, Nd) and HREE (Er, Tm, Yb, Lu). Uranium oxides from the Luiswishi deposit display a particularly flat pattern from La to Sm with a $(\text{La}/\text{Sm})_N$ ratio ranging from 0.80 to 0.89. Uranium oxides from the Kolwezi deposit show a slightly positive slope from La to Sm with a $(\text{La}/\text{Sm})_N$ ratio ranging from 0.14 to 0.24 (Table 42). Uranium oxides from both

of these deposits have a specific negative Eu and Ce anomalies and a depletion of HREE, from Tb to Lu, with a $(\text{Tb/Lu})_N$ ranging from 6.72 to 10.08 (Figure 51c).

Uranium oxides from the Domes region dated at ca. 530 Ma (Musoshi and Nkana deposits, Malundwe and Mitukuluku showings) also display flat REE patterns with a specific negative Eu anomaly. The main difference between these uranium oxides and those of the External fold-and-thrust belt is their MREE and HREE enrichments (Figure 51d). Their chondrite-normalized REE patterns show a slightly positive slope from La to Sm with a $(\text{La/Sm})_N$ ratio ranging from 0.01 to 0.18 and are relatively flat from Tb to Yb with a $(\text{Tb/Yb})_N$ ranging from 1.20 to 2.43 (Tabs. 3 and 4). Uranium oxides from Malundwe and Mitukuluku occurrences (high-grade western part of the Domes region) have not been dated but their REE patterns display exactly the same shape as the ones of uranium oxides from Musoshi and Nkana (intermediate-grade eastern part of the Domes region) dated at ca. 530 Ma by Decrée et al. (2011) and also as the ones of uranium oxides from Kawanga occurrence (high metamorphic grade western part of the Domes region), dated at ca. 542 Ma by Cathelineau et al. (1990) and analyzed in REE content by Mercadier et al. (2011).

Figure 52 presents the REE patterns of uranium oxides dated at ca. 650 Ma and at ca. 530 Ma normalized to the uranium oxide from the Shinkolobwe deposit (sample 12048-1'; Table 41). We chose the Shinkolobwe uraninite for normalization because its texture and composition suggest that it is homogeneous and not altered.

Uraninite crystals from the Kolwezi and Luiswishi deposits, in the External fold-and-thrust belt, display similar uraninite-normalized patterns with a flat pattern in MREE and HREE, from Tb to Lu, and a negative slope from La to Eu (Figure 52). Uraninite crystals from the Musoshi and Nkana deposits, in the intermediate metamorphic grade eastern part of the Domes region, have identical abundances and REE distribution. Their uraninite-normalized patterns are enriched in LREE and HREE with a negative slope from Ce to Eu and a positive slope from Tb to Lu. Uraninite crystals from the Malundwe and Mitukuluku deposits, in the high metamorphic grade western part of the Domes region, also show similarities in their REE abundances and distribution. Their uraninite-normalized patterns display a stronger enrichment in HREE, with an increase from Tb to Lu compared to the Musoshi and Nkana deposits of uraninite REE patterns. In summary, uraninite-normalized patterns highlight two important points: (i) REE patterns of

uraninite dated at ca. 650 Ma and at ca. 530 Ma show distinct LREE and HREE enrichments, (ii) REE uraninite-normalized patterns of uranium oxides dated at ca. 530 Ma are directly correlated with the metamorphic conditions under which the deposits formed.

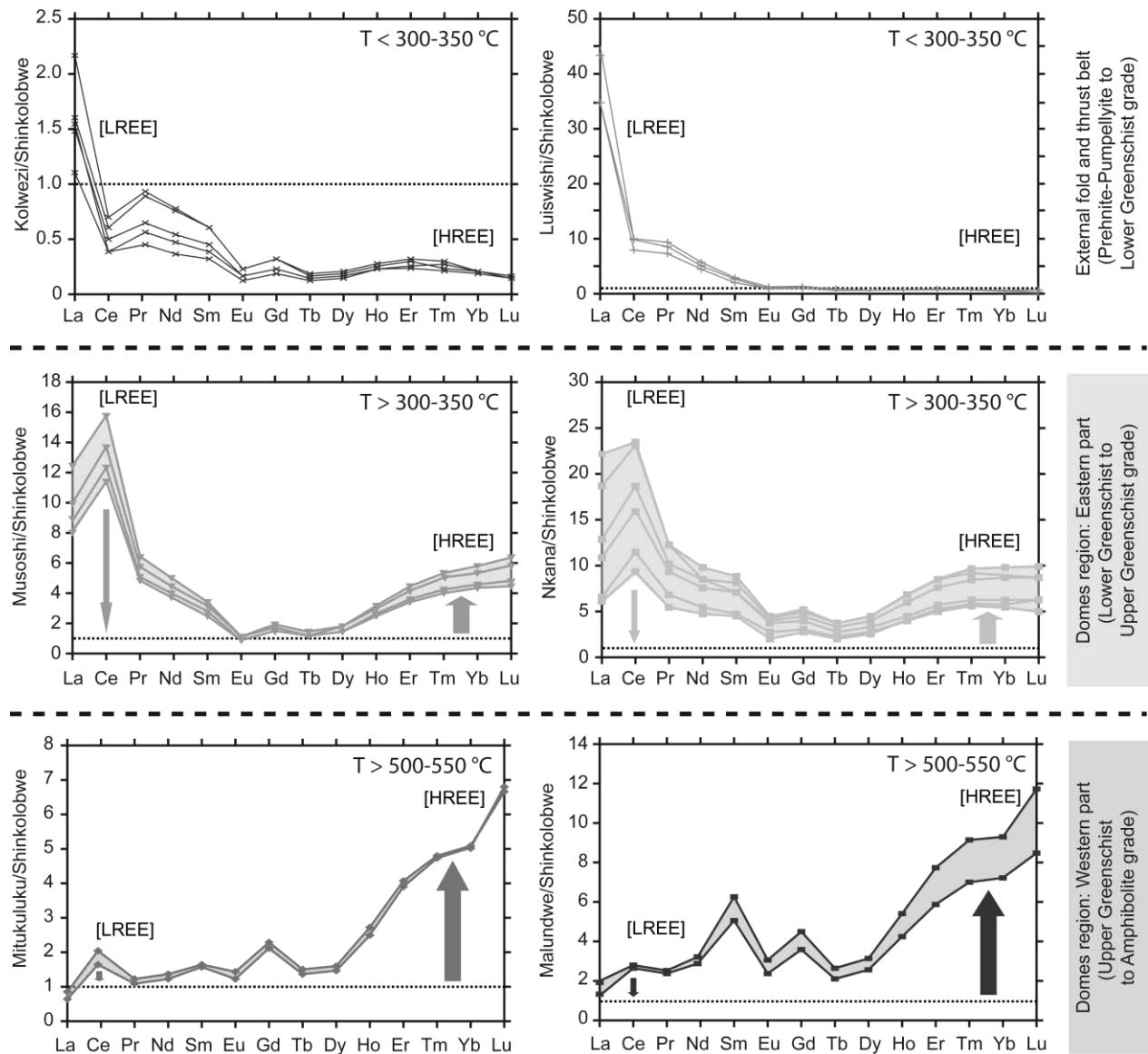


Figure 52: Uraninite-normalized REE patterns for uranium oxides dated at ca. 530 Ma from Kolwezi and Luiswishi (upper part), Musoshi and Nkana (middle part), Mitukuluku and Malundwe (lower part) deposits. Values used for normalization are from the Shinkolobwe deposit uraninite dated at ca. 650 Ma (sample: 12048-1', Table 41).

5.3. Yttrium (Y) content measured by EMP and LA-ICPMS

The contrast in signatures between uranium oxides of the Lufilian belt dated at ca. 650 Ma and ca. 530 Ma is best illustrated in a diagram representing the europium anomaly Eu^*

($\text{Eu}_N/[\text{Sm}_N.\text{Gd}_N]^{1/2}$, McLennan, 1989) versus the yttrium oxide content (Y_2O_3 ; Figure 53; Tabs. 2, 3 and 4). Uranium oxides dated at ca. 650 Ma in the External fold-and-thrust belt are characterized by low Y content and specific positive Eu anomaly (Figure 53). For non-altered uranium oxides from the Shinkolobwe deposit, the Y content ranges from 154 to 803 ppm (Table 41). In contrast, uranium oxides dated at ca. 530 Ma show a strong dispersion in yttrium contents and are characterized by a specific negative Eu anomaly (Figure 53). Uranium oxides, which crystallized in the External fold-and-thrust belt (Kolwezi and Luiswishi deposits), have a low Y content ranging from 290 to 1146 ppm (Figure 53; Table 42). In contrast, uranium oxides, which crystallized in the high metamorphic grade western part of the Domes region (Mitukuluku and Malundwe deposits), have a higher Y content ranging from 11204 to 23476 ppm (Figure 53; Table 43).

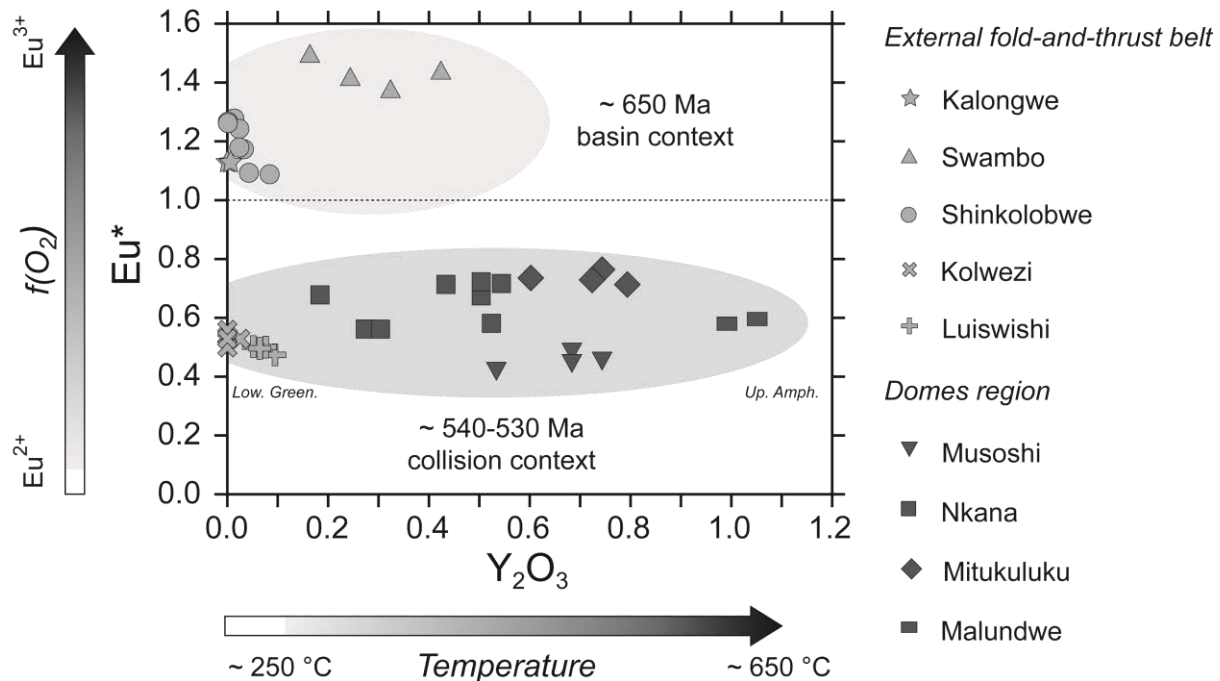


Figure 53: Eu^* versus Y_2O_3 contents diagram for uranium oxides, dated at ca. 650 Ma and ca. 530 Ma, from the External fold-and-thrust belt (light grey symbols) and for uranium oxides, dated at ca. 530 Ma, from the Domes region (dark grey symbols). Yttrium content increases with the increasing crystallization temperature of uranium oxides. Abbreviations: Low. Green. = Lower Greenschist metamorphic conditions; Up. Amph. = Upper Amphibolite metamorphic conditions.

6. Discussion

6.1. Interpretation of the geochemical uranium oxide signatures from the U occurrences in the Lufilian belt

Significant textural and chemical variations among the various uranium oxides dated at ca. 650 Ma from the External fold-and-thrust belt are identified by SEM imaging and EMP analyses. Indeed, EMP analyses of uraninites from the Swambo and the Kalongwe deposits indicate heterogeneous major element compositions. Patchy zoning and heterogeneous compositions reflect that these uranium oxides readily exchanged elements with the later fluids during post-crystallization alteration (Alexandre and Kyser, 2005b). Some uranium oxides from these two deposits have a negative correlation between the PbO content and both the CaO and SiO₂ content. The incorporation of Si and Ca into the crystalline structure of uranium oxides is presumably counterbalanced by Pb loss (Alexandre and Kyser, 2005b). Moreover, owing to the similar ionic radii of calcium and uranium, respectively 106 and 105 picometers (pm), U is commonly replaced by Ca in the structure of uraninite. Significant Ca \Leftrightarrow U substitution leads to the conversion of uraninite into secondary calcium-rich and uranium-rich minerals (CaO up to 25.37 wt.% for sample from Swambo; Table 42). De facto, the REE content of uranium oxides from Kalongwe and Swambo reflects the late uraninite-fluid interactions, providing an explanation for the slight differences of their REE patterns (Figure 51b).

The behavior of a trace element in geochemical systems is a function of its ionic charge and ionic radius; REE's constitute a coherent group of elements with equal ionic charges (3+) and similar ionic radii (Henderson, 1984). The incorporation of REE into the crystallographic structure of uranium oxide is a function of both their atomic radius and temperature (Cuney, 2010; Mercadier et al., 2011). However, REE has a charge of 3+ (except for Eu which has a charge 2+ under reducing conditions) and thus their substitution with U⁴⁺ requires a coupled substitution in order to balance the charges. This is particularly the case at a relatively low crystallization temperature. However, the uranium oxide crystallographic structure tends to dilate with increasing temperature. As a consequence, fractionation of REE as a function of their atomic radius is less pronounced as the crystallization temperature increases. Moreover, Sm, Eu, Tb and

neighbors middle REE have their ionic radius similar to uranium (IV) and are thus highly prone to substitute to U(IV). Owing to these particularities, the REE patterns of uranium oxides are very specific to each uranium deposit type and directly reflect the conditions of their genesis: temperature, redox conditions (for Eu) and fluid composition (Mercadier et al., 2011). Y and REE are physicochemically similar, all being trivalent with similar ionic radii and electronegativities. Thus, the yttrium content in uranium oxides is also a good indicator of ore genesis physical-chemical conditions and associated crystallization-recrystallization processes. This study of the Lufilian belt mineralizations shows that the yttrium content of uranium oxides seems to be controlled by the uraninite crystallization temperature. Moreover, in natural systems, Eu^{3+} can be reduced to Eu^{2+} as a function of temperature and, to a minor extent, of pressure and pH (Sverjensky, 1984; Bau, 1991; Bau and Möller, 1992). In turn, the behavior of the Eu ion is dominantly a function of the redox conditions (Eu^{2+} or Eu^{3+}). Consequently, the presence and the sign of the Eu anomaly are a good proxy for oxygen fugacity and temperature of the uranium-bearing hydrothermal fluids (Henderson, 1984; Fryer and Taylor, 1987). For uranium oxides, the ionic radius of trivalent europium in octahedral coordination is 107 pm, very close to the one of uranium (IV) (Shannon, 1976). Divalent europium in octahedral coordination has a much larger ionic radius than Eu^{3+} and cannot substitute for uranium (IV).

Consequently, REE patterns, Y content and Eu anomaly (the REY signature) of uranium occurrences are powerful indicators of the physico-chemical conditions under which the uranium oxides crystallized. Uranium oxides from Kalongwe, Swambo and Shinkolobwe deposits, dated at ca. 650 Ma, are characterized by a “bell-shape” pattern respectively centered on Sm, Eu and Tb elements and a low Y content (Figure 51b; Table 41). These slight differences of elemental maximum enrichment may reflect alteration of uranium oxides from Kalongwe and Swambo as evidenced by their patchy textures (Figure 50b, c) and by their heterogeneous major element composition (Table 41). This REY signature probably indicates that they crystallized at low temperature. In contrast, uranium oxides dated at ca. 530 Ma from the Domes region (Malundwe, Mitukuluku, Musoshi and Nkana), with high HREE and Y contents, probably crystallized at a higher temperature than the uranium oxides in the External fold-and-thrust belt (Tabs. 3 and 4). This interpretation is in good agreement with the paragenesis of the host rocks in the Domes region reflecting metamorphism from upper Greenschist (> 350 °C) to upper Amphibolite (> 550

°C) metamorphic facies (Meneghel, 1981; Cosi et al., 1992; Brems et al., 2009; Figure 53). Moreover, the REE patterns of uranium oxide from the External fold-and-thrust belt are characterized by a positive Eu anomaly (Eu^* from 1.09 to 1.50), which would demonstrate that Eu is present as Eu^{3+} in the ore fluids (Figure 53). In contrast, REE patterns in uranium oxides from the Domes region which exhibit a negative Eu anomaly (Eu^* from 0.56 to 0.77) would indicate that Eu is present as Eu^{2+} in the hydrothermal fluids. Based on these characteristics, we propose that the hydrothermal fluids associated with uranium mineralization dated at ca. 650 Ma, in the External fold-and-thrust belt, had an initially higher oxidation state than the ore fluids associated with uranium mineralization dated at ca. 530 Ma, both in the External fold-and-thrust belt and in the Domes region. Alternatively, the Eu anomaly might be partly controlled by the signature of the leached source-rock.

Syn-metamorphic uranium oxides from the Lufilian belt present a positive correlation between the HREE and Y contents (Figure 54). This positive correlation has also been described by Förster (1999) in magmatic uraninites. Figure 54 also shows the positive correlation between the crystallization temperature of uraninite oxides and their HREE and Y content. HREE and Y contents of uraninite oxides are (i) low for the Shinkolobwe deposit crystallized at low temperature (< 250 °C; Audeoud, 1982; Table 40), (ii) intermediate for uranium oxides from the Kolwezi and the Luiswishi deposits, crystallized under low-grade greenschist facies metamorphism (< 300-350 °C; Figure 54; Table 40), and (iii) high for uranium oxides from the Musoshi, the Nkana, the Mitukuluku and the Malundwe deposits, crystallized under higher metamorphic grade (> 300-350 °C; Tabs. 3 and 4). Data available in literature for magmatic uraninites, which crystallized at a temperature between 700 and 750 °C, show that the Y content is much higher, up to 57000 ppm, in the absence of crystallization of co-genetic rich Y minerals such as xenotime (Förster, 1999; Toé, 2012). Based on these data, we propose that the incorporation of Y and HREE in the crystalline structure of syn-metamorphic uraninite oxides is a function of the crystallization-recrystallization temperature. Considering this correlation, we propose that HREEs and Y contents of uranium oxides could represent thermometers for uraninite crystallization during magmatic, metamorphic and/or hydrothermal events.

To summarize, uranium oxides from the occurrences at ca. 650 Ma and at ca. 530 Ma display clearly distinct geochemical signatures (REE pattern, Y content and Eu anomaly), which demonstrates different crystallization conditions. To better understand these conditions and to provide new insights for the understanding of Lufilian uranium occurrences, the geochemical signatures of the uranium oxides from the Lufilian belt are compared to the ones obtained for other uranium deposits worldwide.

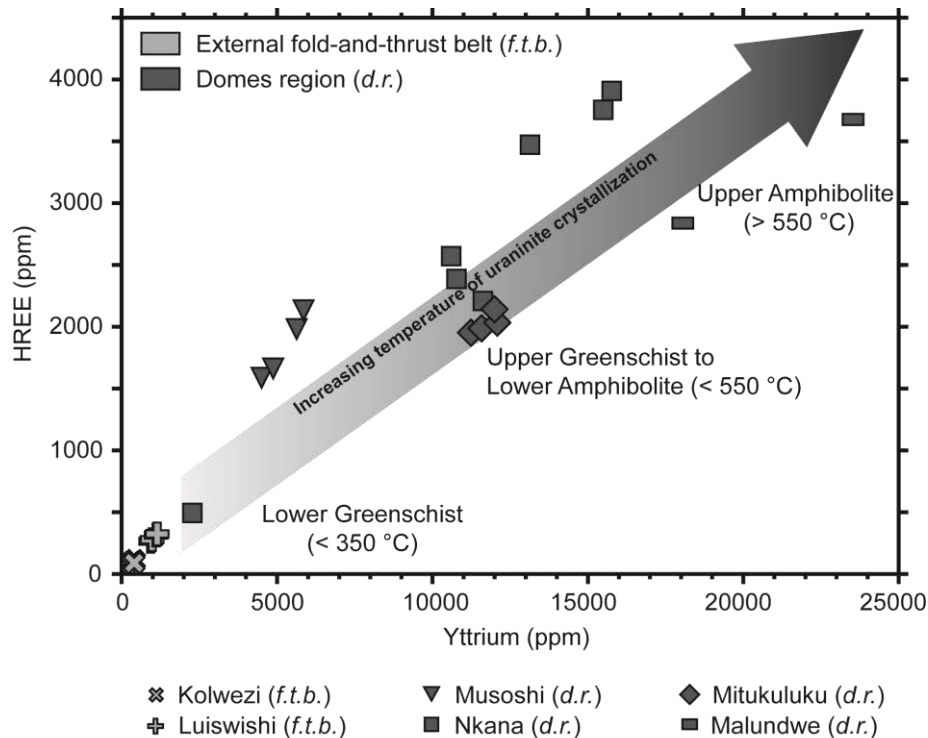


Figure 54: HREE (Er + Tm + Yb + Lu) versus Yttrium contents diagram for uranium mineralization dated at ca. 530 Ma in the External fold-and-thrust belt (light grey symbols) and in the Domes region (dark grey symbols). The arrow shows the correlation between the increasing HREE and Y contents of uranium oxides and the increasing temperature of uranium oxide crystallization in relation with the metamorphic grade of the host rock. Abbreviations: *f.t.b.* = Fold-and-thrust belt; *d.r.* Domes region.

6.2. Comparison between uranium occurrences of the Pan-African Lufilian belt and worldwide uranium deposits

The chondrite-normalized REE patterns displayed by the uranium oxides of the Lufilian belt are compared to the chondrite-normalized REE patterns referenced for a selection of

representative worldwide uranium occurrences (Mercadier et al., 2011). The “bell-shape” REE pattern displayed by uranium oxides dated at ca. 650 Ma from the External fold-and-thrust belt is similar to the REE patterns of uranium oxides from the world-class unconformity-related uranium deposits (Jefferson et al., 2007; Kyser and Cuney, 2008) of the Kombolgie Basin (Koongarra, Nabarlek; Figure 55a) and the Athabasca Basin (Shea Creek, Eagle Point, Mc Arthur River; Figure 55a). For example, the uraninite-normalized REE pattern displayed by the uranium oxides from the Shinkolobwe deposit is identical to the REE pattern from the Shea Creek deposit (unconformity-related uranium deposit in Athabasca Basin; Figure 55b). Moreover, these two deposits (Shinkolobwe and Shea Creek) present similar ore paragenesis. The polymetallic uranium deposits, dated at ca. 650 Ma, of the External fold-and-thrust belt with Cu-Co-Ni-Fe-(Mo)-(Pb)-(Se)-(Au) sulfides assemblage is comparable to the polymetallic assemblage from unconformity-related deposit hosted by sandstone in the Athabasca Basin (Fayek and Kyser, 1997; Jefferson et al., 2007).

Based on this equivalent geochemical signature, we propose that the first U mineralizing event in the External fold-and-thrust zone, at ca. 650 Ma, is related to late-diagenesis hydrothermal processes predating temperature peak of the Pan-African metamorphism in the Lufilian belt, in the similar conditions prevailing during the Paleoproterozoic for the formation of Canadian and Australian unconformity-related U deposits (Kyser and Cuney, 2008). They were formed through large-scale circulations of brines (25-35 wt.% eq. NaCl) at temperatures around 120-200 °C that percolated between sedimentary basins and underlying crystalline basement rocks. The mineralizing fluids were acidic (Richard et al., 2012) and oxidizing evaporated seawater-derived brines (Richard et al., 2011; Mercadier et al., 2012). They acquired their exceptional metal enrichment, especially for U, through mainly brines-basement rock interaction (Richard et al., 2010, 2012) during reopening of ancient fractures and microfractures (Mercadier et al., 2010).

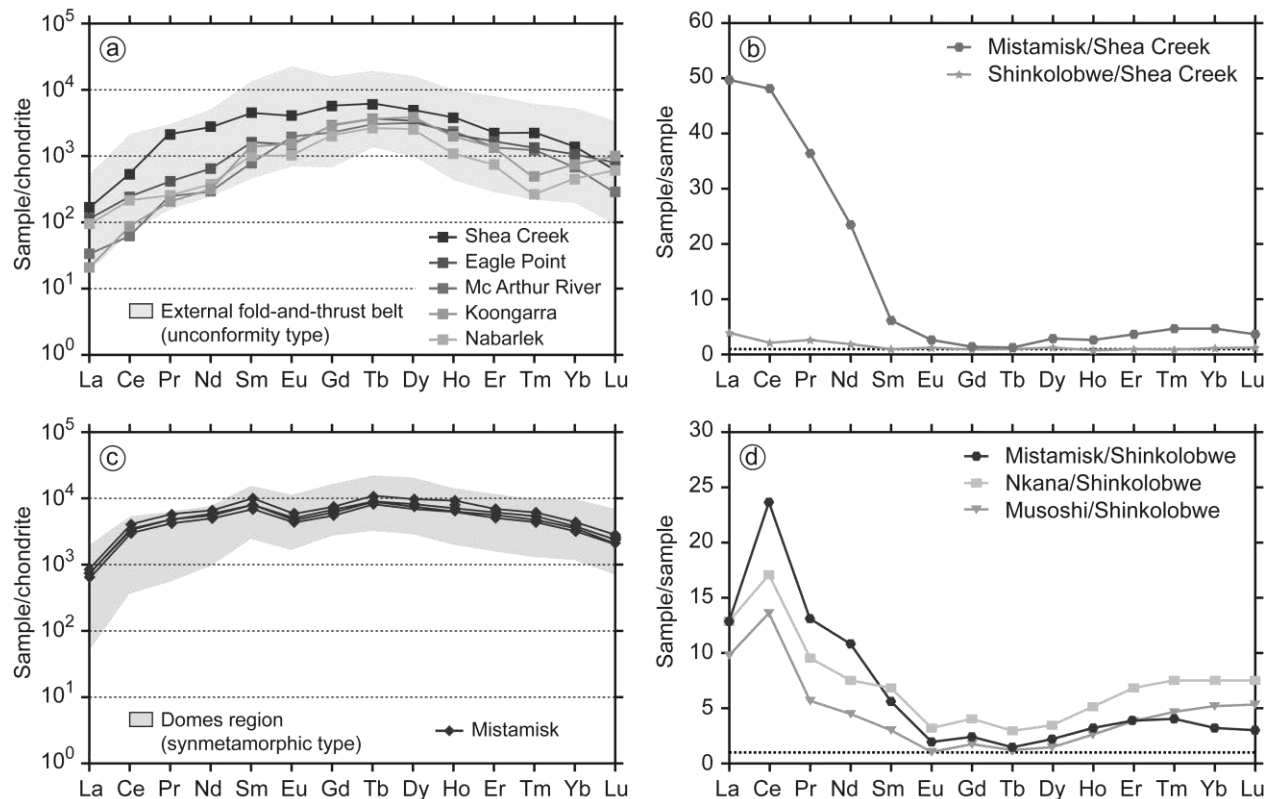


Figure 55: REE patterns of uranium oxides from the Lufilian belt compared to ones from known uranium deposits. a: Chondrite-normalized REE patterns for uranium oxides dated at ca. 650 Ma from the External fold-and-thrust belt of the Lufilian belt compared with chondrite-normalized REE patterns for uranium oxides from unconformity-related uranium deposits of the Athabasca Basin (Shea Creek, Eagle Point, Mc Arthur River; data from Bonhoure, 2007; Mercadier et al., 2011) and the Kombolgie Basin (Koongarra, Nabarlek; data from Mercadier et al., 2011). b: Uraninite-normalized REE patterns for uranium oxides from Mistamisk (syn-metamorphic uranium mineralization; Kish and Cuney, 1981) and Shinkolobwe deposits. The uraninite values using for normalization are from Shea Creek deposit (data from Mercadier et al., 2011). c: Chondrite-normalized REE patterns for uranium oxides dated at ca. 530 Ma from the Domes region of the Lufilian belt compared with REE patterns for uranium oxides from the Mistamisk syn-metamorphic uranium deposit (data from Bonhoure, 2007). Chondrite values are from McDonough and Sun, (1995). d: Uraninite-normalized REE patterns for uranium oxides from Mistamisk, Musoshi and Nkana deposits. The uraninite values using for normalization are from Shinkolobwe deposit in External fold-and-thrust belt (sample: 12048-1').

Uranium deposits, dated at ca. 650 Ma in the External fold-and-thrust-belt of the Lufilian belt, are proposed to also represent an unconformity-type deposit. Evaporitic layers that were deposited in the upper part of the basin (Kundelungu group) and in the lower part of the basin (Roan group) constitute the potential sources for the formation of highly saline fluids, containing

MgCl₂-CaCl₂-NaCl-KCl. The analysis of fluid inclusions indicates that such highly saline fluids have been trapped at a pressure between 1.00 and 1.25 kbar and a temperature ranging from 200 to 350 °C in the Shinkolobwe deposit (Audeoud, 1982). The nature and composition of the U-mineralizing brines are further constrained on the basis of published descriptions of Cu-mineralizing fluids within the Lufilian belt. In the Domes region, at the Chambishi deposit, Annels (1989) described a fluid phase linked to the diagenetic Cu-Co mineralization. This fluid is characterized by a minimum trapping temperature between 100 and 180 °C and a salinity ranging from 9 to 22 wt.% eq. NaCl (Annels, 1989). Greyling et al. (2005) and Greyling (2009) analyzed fluid inclusions in various deposits of the Lufilian belt. They subdivided the fluid types into basinal, early orogenic and late orogenic fluid circulations.

The earliest fluids, namely basinal brines, identified in quartz veins sampled at the Chambishi, Nchanga and Konkola Cu deposits are characterized by aqueous solutions containing chloride complexes. Basinal fluids of the Chambishi deposit comprise NaCl-MgCl₂±CaCl₂ solutions with salinity between 11.9 and 23.1 wt.% eq. NaCl. At the Nchanga deposit, fluids are represented by NaCl_{saturated}-CaCl₂-H₂O and MgCl₂-KCl-NaCl-H₂O systems. Finally, at the Konkola deposit, fluids are composed of MgCl₂-KCl-H₂O±NaCl. These basinal fluids from the Chambishi, Nchanga and Konkola Cu deposits were trapped at a minimum temperature ranging from 120 to 190 °C and at a minimum pressure between 0.35 and 0.60 kbar (Greyling, 2009). On the other hand, El Desouky et al. (2009) proposed to distinguish two contrasting fluid systems associated with two Cu-Co sulfide phases in the Katanga Copperbelt. The first phase is related to a hydrothermal fluid with a moderate trapping temperature, 115 to 220 °C, and a salinity ranging from 11.3 to 20.9 wt.% eq. NaCl, similar to the basinal brines described by Greyling (2009). This fluid probably corresponds to a seawater-derived fluid enriched in salt after some evaporation which increased in temperature owing to thermal exchange with host rocks during circulations at depth and possibly even into the basement (El Desouky et al., 2009). The second fluid and Cu-Co mineralizing event described by El Desouky et al. (2009) is related to the Lufilian orogeny. Fluid inclusion characteristics, mostly from Cu deposits of the Lufilian belt, point to a derivation from evaporites of the Lower Roan subgroup (> 765 Ma; Key et al., 2001; El Desouky et al., 2009). Primary and pseudosecondary fluid inclusions in dolomite and quartz crystals from the Kipushi and Luiswishi Zn-Cu deposits, characterized by the presence of halite cubes (ca. 30-43 wt.% eq.

NaCl) and trapped solids, present an elevated molar Cl/Br ratio (> 1000) indicating that the mineralizing brines derived from evaporite dissolution by a dominantly seawater-derived fluid (Heijlen et al., 2008; El Desouky et al., 2012). This early fluid phase presents the same chemical characteristics as the brines described in the quartz veins of Australian and Canadian unconformity-related U deposits (Derome et al., 2005, 2007). These fluids were trapped at a pressure between 0.48 and 0.80 kbars and a temperature ranging from 130 to 270 °C. The only major difference is the origin of the high salinity of the fluid. The high salinity fluid is proposed to correspond to primary brines expelled from evaporite layers for Australian and Canadian deposits (Derome et al., 2007; Richard et al., 2011), whereas for the deposits in the Lufilian belt they are proposed to correspond to secondary brines formed by late dissolution of evaporites (Heijlen et al., 2008; El Desouky et al., 2012).

Irrespective of the origin of the brines (primary or secondary), the high salinity of these fluids is a key parameter to achieve transportation of a number of metals. In the Lufilian belt, uranium was potentially transported by these Cl-rich basinal brines rich in Ca-Mg-NaCl within the dolomitic sandstones of the R.A.T. subgroup (red R.A.T.). Fluid circulation through the sedimentary sequence was likely facilitated by the primary porosity of the sediments during the early diagenesis and circulation through the basement rocks by high density of the previous structural architecture (Koziy et al., 2009). High hydrothermal alteration evidenced by the secondary crystallization of Mg-chlorite, tourmaline and hematite, described by Audeoud (1982), Okitaudji (1989) and Cailteux (1994), in the dolomitic siltstones of the R.A.T. subgroup (Roan group; Figure 48), is potentially associated with this circulation of oxidized fluids. Microprobe analyses indicate that diagenetic chlorites are exceptionally rich in MgO, 26-33 wt.%, with ca. 7 wt.% total FeO (Audeoud, 1982). Tourmaline grains show a Fe-rich detrital core overgrown by a Mg-rich diagenetic rim (Audeoud, 1982; Okitaudji, 1989; Cailteux, 1994). The alteration is Mg-dominant as observed for the alteration halo surrounding Paleoproterozoic unconformity-related U deposits (Alexandre et al., 2005a; Mercadier et al., 2012). Hematite crystallized as a rim overgrowing tourmaline and quartz crystals (Cailteux et al., 2005). As a consequence, the oxygen fugacity (fO_2) in the system had to be above the hematite–magnetite buffer and the U had to be dissolved in the form of U(VI), as described for unconformity-related U deposits (Komninou and Sverjensky, 1995; Derome et al., 2005; Richard et al., 2012). Above this oxidized R.A.T.

subgroup (red R.A.T.), the reduced R.A.T. subgroup (gray R.A.T.) is in conformable sedimentary contact and formed the base of the Mines subgroup (Cailteux et al., 2005). The gray R.A.T. subgroup which contains organic matter, pyrite and Cu-Co sulfides could have played the role of a reducing barrier. The reduction of U(VI) to U(IV) and subsequent uranium oxide precipitation was spatially associated with the intersection of organic matter and sulfide-rich units, which may have acted as a redox interface. The source of uranium could be the basement rocks, in addition to the Katanga supergroup rocks. This model is in good agreement with the one of Koziy et al. (2009) who proposed the basement rocks as a source of copper, transported by basinal brines, for stratiform sediment-hosted copper deposits in the Zambian Copperbelt (here designated as the intermediate metamorphic grade eastern part of the Domes region).

The second mineralization event, recorded at ca. 530 Ma, is synchronous to deformation and metamorphism marking the formation of the Lufilian orogenic belt (Figure 56). This tectonic evolution is presumably associated with hydrothermal fluid circulation. The REE patterns of uranium oxides from the Domes region are similar to the Mistamisk syn-metamorphic uranium deposit, in Canada, characterized by a negative Eu anomaly and high REYs content controlled by the dilatation uranium oxide structure (Kish and Cuney, 1981; Mercadier et al., 2011; Figure 55c). The closest match to the Mistamisk deposits is depicted in the uraninite-normalized REE patterns (normalization on Shinkolobwe values) for uranium oxides from the intermediate metamorphic grade eastern part of the Domes region (Musoshi and Nkana deposits; Figure 55d). Albitic alteration and *P-T* conditions reaching the lower Greenschist grade in the Musoshi and Nkana deposits are very similar to the Mistamisk deposit. Kish and Cuney (1981) described uraninite-albite veins deposited in fractures by metamorphic-hydrothermal fluids during the Hudsonian orogeny. Temperature and pressure of vein formation, estimated from fluid inclusion data, were 300-350 °C and 2.5 kbars, respectively. In the intermediate metamorphic grade eastern part of the Domes region, uranium mineralization, uraninite and brannerite, is also controlled by deformation, under Greenschist metamorphic grade (300-400 °C), and occurs as sigmoidal porphyroblasts, as simple grains scattered within the foliation or as deformed veins (Cosi et al., 1992; Figure 56) associated with albite minerals.

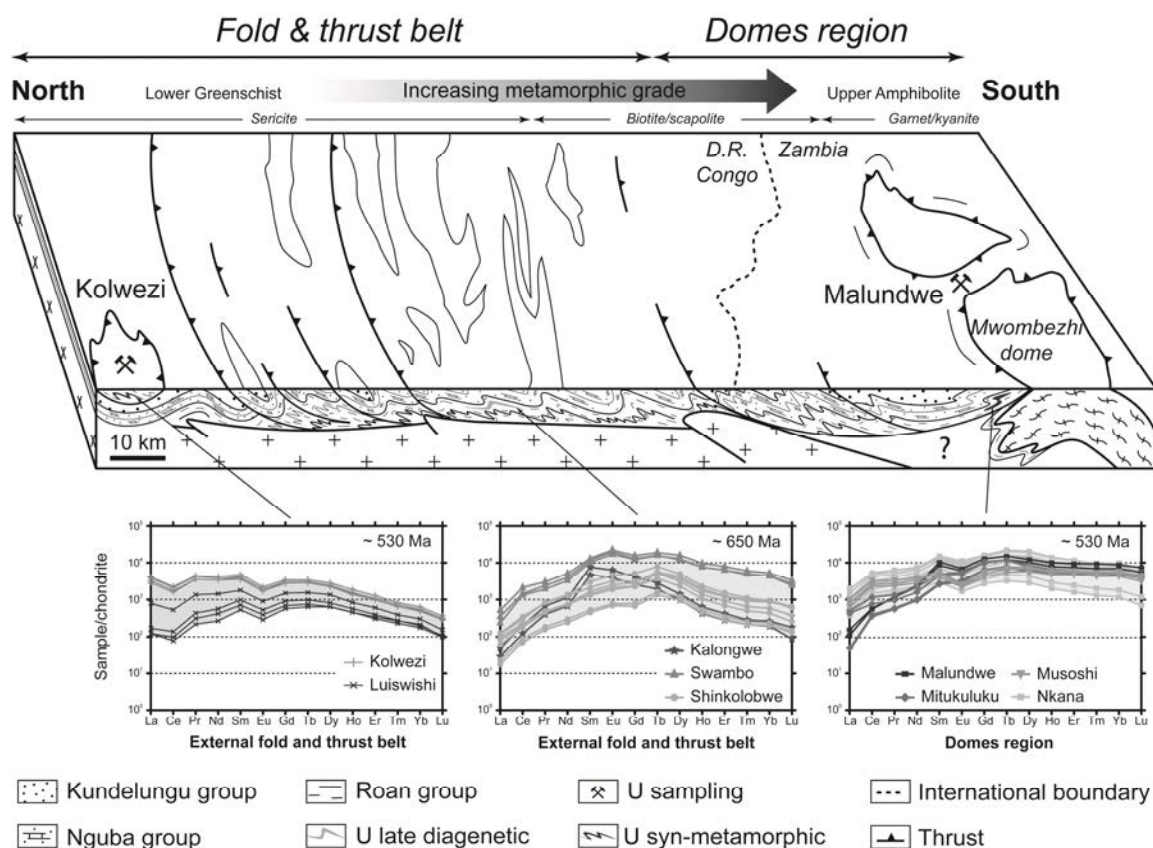


Figure 56: North-South cross section from the External fold-and-thrust belt to the Domes region with uranium mineralization location, their REE patterns and ages, metamorphic grades and their metamorphic index minerals.

7. Conclusion

The REY signatures (REE patterns, Y content and Eu anomaly) of uranium oxides from uranium occurrences dated at ca. 650 Ma and at ca. 530 Ma of the Pan-African Lufilian belt are significantly different. Uranium oxides dated at ca. 650 Ma display a “bell shape” chondrite-normalized REE pattern, centered on Tb, and a positive europium anomaly contrasting with the relatively “flat-shape” chondrite-normalized REE pattern and the negative Eu anomaly of uranium oxide dated at ca. 530 Ma. These geochemical signatures are directly related (i) to the physical-chemical behavior of these elements at the time of uranium oxide crystallization and (ii) to the crystallographic structure of uranium oxide mainly related to temperature and redox conditions. Combined with the U-Pb dating of uranium oxide, these data pinpoint the timing and physico-chemical conditions of uranium ore crystallization during the Pan-African orogenic cycle.

REY signatures of uranium oxides from the Kalongwe, Swambo and Shinkolobwe occurrences in the External fold-and-thrust belt are characterized by a “bell-shape” chondrite-normalized REE pattern and a positive Eu anomaly indicating that the ca. 650 Ma mineralizing event occurs in an oxidizing environment with a low crystallization temperature (below 250 °C). Uranium was probably mobilized and transported by highly saline oxidized brines through the sedimentary sequence and/or basement rocks. We propose that these brines have a similar origin as those described for the surrounding Cu deposits, by dissolution of evaporitic layers from the Roan group during the late diagenetic or early compressional tectonic events with a time gap between sedimentation and fluid movement ranging from ca. 100 to 200 Ma. Uranium precipitated within the fined-grained siliciclastic Lower Roan group as scattered uranium oxides in the vicinity of the reduced gray R.A.T. subgroup or as more massive uraninite accumulation within brecciated structures as at the Shinkolobwe deposit. This mineralizing event is considered as a Neoproterozoic equivalent to the world-class Canadian and Australian unconformity-related U deposits. Accordingly, the Kalongwe, Swambo and Shinkolobwe uranium deposits of the External fold-and-thrust belt of the Lufilian belt are the youngest unconformity-type described to date. Moreover, this pre-orogenic mineralization shares the same general characteristics (age, type of fluids, geodynamic context) of the world-class Lufilian Cu and Co deposits and could indicate a regional polymetallic event related to brine circulations.

REY signatures of uranium oxides from Kolwezi and Luiswishi in the External fold-and-thrust belt and from Musoshi, Nkana, Malundwe and Mitukuluku in the Domes region are characterized by a relatively “flat-shape” chondrite-normalized REE patterns and a negative Eu anomaly indicative of a less oxidizing environment and a higher temperature during the precipitation of uranium oxides at ca. 530 Ma. The high Y content for uranium oxides from the Domes region corroborates the high crystallization temperature, above 300-350 °C (from upper Greenschist to upper Amphibolite facies), which is also consistent with the metamorphic paragenesis of the host rocks. The low Y content for uranium oxides, dated at ca. 530 Ma, from the External fold-and-thrust belt gives a temperature of crystallization lower than 350 °C (from Prehnite-pumpellyite to lower Greenschist facies), as corroborated by the metamorphic paragenesis of the host rocks. This uranium mineralizing event at ca. 530 Ma is temporally associated with the collision stage of the

Pan-African orogeny in the Lufilian belt (John et al., 2004). We propose that uranium mobilization was assured by metamorphic fluids expelled during the metamorphism of epicontinental platform sediments and that the ore mineral location was controlled by major tectonic structures: schistosity, shear zone and fault/thrust. A precise characterization of these different fluid types and of the regional structural and metamorphic evolution is envisioned in order to further constrain this model.

To conclude, this study clearly demonstrates the crucial importance of the combination of *in-situ* geochemical and U-Pb dating methods to better understand the evolution through time of metal systems during an orogenic cycle.

Acknowledgments

We would like to thank the CNRS (NEEDS) and AREVA for financial support, the Royal Museum of Central Africa and AREVA for providing the samples. The authors are grateful to Sandrine Mathieu, Olivier Rouer (GeoRessources, Nancy) and Philippe Lach (GeoRessources, Nancy) for technical support in providing analytical data on SEM, EMP and LA-ICPMS, respectively. We would also like to acknowledge the stimulating discussions with Philippe Goncalves, Cyril Durand and to thank Antonin Richard for text improvements. The authors thank Franco Pirajno for editorial handling and two anonymous reviewers for their constructive comments. All co-authors would like to dedicate this work to Jean-Louis Feybesse. In particular, he gave the taste for field geology in Perros-Guirec (France) in 2007 to the first author (Aurélien Eglinger) who will remain grateful to Jean-Louis for the opportunity to work with him.

Table 40: Overview of the different uranium occurrences in the Lufilian belt: External fold-and-thrust belt (Abbreviation: Ext. f. & t.) and Domes region (Abbreviation: Domes r.; Derricks and Vaes, 1956; Derricks and Oosterbosch, 1958; Ngongo, 1975; Meneghel, 1981; Cosi et al., 1992; Bernau, 2007). Temperature estimates based on fluid inclusion analysis and/or on metamorphic paragenesis (François, 1974; Audeoud, 1982; Meneghel, 1981; Cosi et al., 1992). Abbreviations: Ab = Albite ; Ap = Apatite; Br = Brannerite ; Bt = Biotite; Cal = Calcite ; Chl = Chlorite; Cof = Coffinite; Dol = Dolomite; Gt = Garnet; Qtz = Quartz; Ky = Kyanite ; Mns = Magnesite; Mnz = Monazite ; Mo = Molybdenite ; Msc = Muscovite; Ox = Oxides; Py = Pyrite ; Rt = Rutile ; Ser = Sericite; Tlc = Talc; Tur = Tourmaline ; Zr = Zircon.

Deposit	Location	Units	Distribution	Host rock	Mineralogy	Acc. minerals	Temperature
Shinkolobwe	Ext. f. & t.	Lower Roan	Massive aggregates, veins	Siliceous dolomite	Chl, Mns, Dol, Qtz, Ser, Mnz, Cal	Py, Ni-Co selenio-sulfides, Tur, Rt, Mo and V, Se, Au, Pt, Pd, Te, Cu elmts	~ 150-250 °C
Swambo	Ext. f. & t.	Lower Roan	Massive aggregates, veins	Siliceous dolomite	Dol, Qtz, Ser, Chl, Mnz	Py, Cu-Co sulfides,	~ 150-250 °C
Kalongwe	Ext. f. & t.	Lower Roan	Massive aggregates, veins	Siliceous dolomite	Dol, Qtz, Ser, Chl	Py, Cu-Co sulfides	~ 150-250 °C
Kolwezi	Ext. f. & t.	Lower Roan (allochton)	Disseminated, veinlets	Dolomite	Dol, Mns, Qtz, Ser, Chl	Cu-Co sulfides	< 300-350 °C
Luiswishi	Ext. f. & t.	Lower Roan	Disseminated, veinlets	Siliceous dolomite	Dol, Mns, Qtz, Ser, Chl	Cu-Co-(Ni) sulfides	< 300-350 °C
Musoshi	Domes r.	Lower Roan	Veins	Arkose	Cal, Qtz, Ab, Bt	Py, Mo	> 300-350 °C
Nkana	Domes r.	Lower Roan	Disseminated, veins	Argillite, sandy and argillaceous dolomites	Cal, Qtz, Bt, Ab, Chl	Rt, Mo, Ap, Zr, Mnz, Py, Cu-Co sulfides, Br, Cof	> 300-350 °C
Mitukuluku	Domes r.	Lower Roan	Disseminated, veins	Micaschist	Qtz, Phl, Msc, Ky, Chl, Tlc	Rt, Ox, Gr, Mo, Cu sulfides, Zr, Br	> 500-550 °C
Malundwe	Domes r.	Basement	Disseminated, veins, aggregates	Schist	Qtz, Bt, Msc, Ky, Gt, Chl	Rt, Ox, Cu sulfides, Zr, Br	> 500-550 °C

Table 41: Electron microprobe data expressed in weight percent oxides and LA-ICPMS data expressed in ppm (with a 1σ uncertainty of 15-35 %) for uranium oxides from the External fold-and-thrust belt. Abbreviations: Loc. = location; Occ. = Occurrences; N° = Measurement label; N = normalized. Ages are from Decrée et al., (2011).

Loc. Occ. Age	External fold-and-thrust belt												
	Shinkolobwe 650 Ma					Kalongwe 650 Ma				Swambo 650 Ma			
N°	2233-1	2233-1'	2237-1'	2237-2'	2237-2''	12048-1	12048-1'	3080-1	3080-1'	6425-1'	6425-1''	6425-2	6425-2'
UO ₂	88.18	88.83	88.85	88.54	88.70	88.24	89.09	84.24	75.35	45.76	58.86	79.53	82.05
PbO	7.47	7.69	7.34	7.42	7.38	7.30	7.30	3.95	17.46	8.70	8.78	10.05	5.28
ThO ₂	0.01	0.02	0.08	0.13	0.03	0.00	0.02	0.01	0.00	0.00	0.00	0.00	0.21
CaO	0.79	0.63	0.74	0.71	0.99	1.15	1.37	0.20	0.08	25.37	19.51	2.03	2.52
SiO ₂	0.00	0.00	0.01	0.00	0.00	0.00	0.00	3.51	0.00	0.58	0.71	3.05	3.84
Y ₂ O ₃	0.02	0.00	0.03	0.00	0.01	0.04	0.08	0.01	0.00	0.16	0.24	0.32	0.42
Total	96.47	97.17	97.05	96.80	97.11	96.73	97.86	91.92	92.89	80.57	88.10	94.98	94.32
La	4	5	28	25	29	24	20	7	12	89	86	125	57
Ce	45	53	184	178	205	137	125	76	115	930	890	1295	826
Pr	15	17	82	69	76	48	46	39	62	221	232	290	182
Nd	115	130	633	518	567	347	359	324	549	1857	1916	2251	1514
Sm	66	75	463	290	314	206	264	723	1197	1991	1921	2126	1663
Eu	38	45	266	170	186	113	143	230	379	1096	1101	1217	1013
Gd	132	157	1036	586	631	484	607	531	872	2781	2712	3091	2553
Tb	50	60	296	181	191	195	217	73	108	630	597	700	586
Dy	247	291	1299	775	823	986	1080	256	365	3337	3258	3910	3299
Ho	25	30	134	78	82	103	114	24	36	447	441	534	445
Er	48	56	253	146	153	207	224	47	69	1044	1040	1272	1055
Tm	5	6	28	16	17	24	26	6	6	126	124	152	127
Yb	33	39	166	99	102	161	168	34	46	753	736	897	756
Lu	3	4	15	9	10	16	17	2	5	67	66	83	69
ΣREE	827	967	4886	3140	3387	3054	3409	2372	3821	15368	15119	17944	14144
Y	154	176	858	476	482	743	803	217	394	4880	5118	6175	4867
Eu*	1.24	1.27	1.18	1.26	1.28	1.10	1.09	1.13	1.14	1.42	1.47	1.45	1.50
Ce*	1.38	1.36	0.94	1.06	1.07	0.99	1.02	1.12	1.04	1.62	1.55	1.67	2.00
(Tb/Lu) _N	10.66	11.13	13.02	13.11	13.13	8.13	8.85	21.44	15.91	6.39	6.10	5.71	5.78
(La/Sm) _N	0.04	0.05	0.04	0.05	0.06	0.08	0.05	0.01	0.01	0.03	0.03	0.04	0.02
(Tb/Yb) _N	6.96	7.07	8.12	8.34	8.52	5.51	5.86	9.86	10.73	3.80	3.69	3.55	3.52

Table 42: Electron microprobe data expressed in weight percent oxides and LA-ICPMS data expressed in ppm (with a 1σ uncertainty of 15-35 %) for uranium oxides from the External fold-and-thrust belt. Abbreviations: Loc. = location; Occ. = Occurrences; N° = Measurement label; N = normalized. Ages are from Decrée et al., (2011).

Loc. Occ. Age N°	External fold-and-thrust belt								Domes region (eastern part)			
	Kolwezi 530 Ma				Luiswishi 530 Ma				Musoshi 530 Ma			
	13156-1	13156-1'	13156-3	13156-3'	13320-1	13320-1'	13320-2	13320-2'	6420-1	6420-1'	6420-2	6420-2'
UO ₂	90.69	90.69	90.12	90.42	88.32	89.01	88.95	88.95	88.39	88.39	90.32	90.16
PbO	6.54	6.36	7.39	6.67	6.15	6.53	6.62	6.62	6.10	6.10	6.20	6.30
ThO ₂	0.24	0.21	0.21	0.26	1.17	1.09	1.23	1.23	0.00	0.00	0.01	0.02
CaO	0.70	0.93	0.59	0.75	1.10	0.72	0.76	0.76	1.58	1.58	1.48	1.65
SiO ₂	0.06	0.00	0.00	0.04	0.00	0.00	0.00	0.00	0.00	0.00	0.01	0.02
Y ₂ O ₃	0.00	0.00	0.00	0.00	0.05	0.07	0.06	0.05	0.68	0.68	0.74	0.53
Total	98.23	98.19	98.31	98.14	96.79	97.42	97.62	97.61	96.75	96.75	98.76	98.68
La	21	29	43	30	880	687	879	847	173	157	194	243
Ce	48	60	87	46	1234	978	1211	1172	1575	1463	1741	2002
Pr	26	30	44	21	412	334	398	385	237	219	264	301
Nd	164	193	273	123	1826	1485	1823	1670	1410	1321	1593	1751
Sm	100	114	152	80	691	556	675	614	701	659	806	858
Eu	21	22	32	16	113	91	110	101	120	124	140	139
Gd	129	135	191	113	694	557	675	607	949	891	1087	1151
Tb	26	28	37	24	126	104	121	111	219	209	257	269
Dy	163	169	216	161	682	560	667	602	1508	1447	1755	1827
Ho	25	26	32	26	94	76	92	81	272	262	322	336
Er	54	56	70	59	198	164	193	171	775	744	916	968
Tm	5	6	7	7	21	17	20	18	108	104	129	138
Yb	29	30	35	34	115	86	105	93	756	718	893	976
Lu	2	3	3	2	9	7	8	8	79	74	95	105
ΣREE	813	899	1221	741	7096	5701	6977	6481	8881	8391	10193	11064
Y	290	297	390	290	1146	900	1107	990	4856	4484	5618	5835
Eu*	0.56	0.54	0.57	0.50	0.50	0.50	0.50	0.51	0.45	0.49	0.46	0.43
Ce*	0.50	0.50	0.49	0.46	0.50	0.50	0.50	0.50	1.91	1.94	1.89	1.82
(Tb/Lu) _N	8.26	7.53	8.89	6.72	10.08	10.06	9.79	9.75	1.89	1.91	1.83	1.74
(La/Sm) _N	0.14	0.17	0.18	0.24	0.82	0.80	0.84	0.89	0.16	0.15	0.16	0.18
(Tb/Yb) _N	4.11	4.25	4.84	3.18	4.99	5.49	5.24	5.41	1.32	1.32	1.31	1.25

Table 43: Electron microprobe data expressed in weight percent oxides and LA-ICPMS data expressed in ppm (with a 1 σ uncertainty of 15-35 %) for uranium oxides from the Domes region. Abbreviations: Loc. = location; Occ. = Occurrences; N° = Measurement label; N = normalized. Ages are from Decrée et al., (2011).

Loc. Occ. Age N°	Domes region (eastern part)							Domes region (western part)					
	Nkana 530 Ma							Malundwe Unknown		Mitukuluku Unknown			
	3632-1	3632-1''	3632-2'	3636a-2	3636a-2'	3636b-1	3636b-1'	02-1	02-1'	29-1	29-1'	29-2	29-2'
UO ₂	89.97	89.74	90.95	90.13	88.98	86.45	87.70	88.00	90.04	87.13	85.83	87.32	87.03
PbO	6.44	6.34	6.63	6.41	6.38	6.88	6.40	6.38	6.69	6.34	6.67	6.25	7.02
ThO ₂	0.07	0.10	0.65	0.12	0.09	0.37	0.19	0.57	0.08	0.12	0.22	0.09	0.15
CaO	0.78	1.16	0.59	0.80	0.99	0.84	1.22	0.33	0.11	4.63	5.09	4.57	4.35
SiO ₂	0.05	0.12	0.03	0.07	0.00	1.04	0.02	0.00	0.00	0.11	0.09	0.09	0.04
Y ₂ O ₃	0.54	0.52	0.27	0.18	0.50	0.43	0.50	1.05	0.99	0.79	0.74	0.72	0.60
Total	97.85	97.98	99.12	97.71	96.94	96.01	96.03	96.33	97.91	99.12	98.64	99.04	99.19
La	122	117	76	211	252	435	367	27	37	10	13	115	97
Ce	1451	1186	679	2021	2382	2978	2949	352	367	216	263	691	468
Pr	299	244	133	423	468	545	565	112	116	53	59	126	90
Nd	1892	1627	799	2681	3014	3120	3443	1049	1185	445	500	966	701
Sm	1223	1125	434	1893	2122	1867	2301	1393	1717	423	453	752	651
Eu	352	260	88	505	558	499	635	349	423	176	203	305	278
Gd	1834	1635	528	2723	3012	2428	3112	2258	2813	1336	1441	2155	2026
Tb	428	407	119	650	761	568	772	471	581	303	333	437	434
Dy	2809	2664	711	4166	4764	3397	4821	2765	3380	1633	1731	2103	2146
Ho	435	439	108	664	756	498	736	464	585	299	322	348	364
Er	1098	1173	258	1708	1897	1261	1879	1296	1674	895	938	958	1056
Tm	144	150	32	216	236	162	249	182	239	126	127	121	136
Yb	900	979	195	1423	1496	1061	1633	1234	1584	864	869	790	851
Lu	83	102	18	144	143	103	164	142	197	118	116	98	114
Σ REE	13071	12108	4178	19427	21861	18923	23626	12093	14899	6898	7368	9967	9412
Y	11615	10744	2263	13102	15456	10554	15727	18010	23476	11549	12053	11204	11963
Eu*	0.72	0.59	0.56	0.68	0.68	0.72	0.72	0.60	0.59	0.72	0.77	0.73	0.74
Ce*	1.86	1.72	1.66	1.66	1.70	1.50	1.59	1.58	1.37	2.27	2.34	1.41	1.23
(Tb/Lu) _N	3.51	2.72	4.52	3.07	3.61	3.73	3.20	2.25	2.01	1.74	1.95	3.02	2.59
(La/Sm) _N	0.06	0.07	0.11	0.07	0.08	0.15	0.10	0.01	0.01	0.02	0.02	0.10	0.10
(Tb/Yb) _N	2.16	1.89	2.78	2.08	2.31	2.43	2.15	1.74	1.67	1.59	1.74	2.51	2.32

CHAPITRE 6: Hypersaline fluids generated by high-grade metamorphism of evaporites: fluid inclusion study of uranium occurrences in the Western Zambian Copperbelt

Aurélien Eglinger¹ ; Clément Ferraina¹ ; Alexandre Tarantola¹ ; Anne-Sylvie André-Mayer¹ ;
Olivier Vanderhaeghe¹ ; Marie-Christine Boiron¹ ; Jean Dubessy¹ ; Antonin Richard¹ ;
Marc Brouand²

Article publié dans *Contributions to Mineralogy and Petrology*

¹ GéoRessources, CNRS-CREGU, Université de Lorraine, France

² AREVA, BU Mines Paris, France

Abstract

In the Pan-African Lufilian belt (Western Zambian Copperbelt), uranium mineralizations, preferentially scattered in kyanite±talc micaschists (metamorphosed evaporitic sediments) or concentrated along transposed quartz veins provide an opportunity to (i) understand the time/space relationship between the ore minerals and the deformation of the host rocks, (ii) identify the different fluid events associated with specific stages of quartz deformation and (iii) characterize the ore fluid geochemistry in terms of fluid origin and fluid/rock interactions.

In the U occurrences studied in Lolwa and Mitukuluku (Domes region, Western Zambian Copperbelt), two mineralizing stages are described. The first generation of ore fluids (53-59 wt.% CaCl₂, 13-15 wt.% NaCl; N₂-H₂ in the gas phase of fluid inclusions) circulated during the high-temperature quartz recrystallization, at 500-700 °C. This temperature is in agreement with the *P-T* conditions recorded during the crustal thickening related to continental collision at ca. 530 Ma. LA-ICPMS analyses show the presence of uranium within this fluid, with a concentration mode around 20 ppm. The second generation of ore fluid (21-32 wt.% NaCl, 19-21 wt.% CaCl₂; CO₂-CO in the gas phase of fluid inclusions) percolated at lower temperature conditions, at the brittle-ductile transition, between 200 and 300 °C. This temperature could be related to the exhumation of the high-grade metamorphic rocks at ca. 500 Ma. The formation of H₂ and CO is interpreted as the result of radiolysis in presence of dissolved uranium in the aqueous phase of these fluid inclusions. Finally, a late fluid (14-16 wt.% NaCl_{equiv}), circulating in the brittle domain, is also described but seems unrelated to U (re-)mobilization event.

Keywords: Uranium, Gondwana, Pan-African, Evaporite, Metamorphic brines, Sinjarite

1. Introduction

The generation of highly saline metamorphic fluids (metamorphic brines) has been proposed to be related to leaching of evaporites in metamorphosed continental platform sediments (Yardley and Graham, 2002; Yardley, 2012; Touret and Nijland, 2013). The salinity of the resulting fluids is in first approximation controlled by the solubility of halite. Accordingly, the salinity of metamorphic brines can reach up to 60 wt.% NaCl_{equiv} at 700-750 °C under Eclogite facies conditions (Yardley and Graham, 2002; Yardley, 2012). Owing to their high chlorinity, metamorphic brines have the potential to transport significant amounts of metals as chloride complexes (Yardley, 2005) that may, under specific conditions, be deposited to form an economic ore body (Pohl, 1992; Bakker and Foster, 1993; Spry et al., 2000). In this study, we test this scenario for U mineralizations in the Lufilian Belt (Zambia) renowned for its Cu mineralizations associated with metamorphosed evaporites (Key et al., 2001; Cailteux et al., 2005; Dewaele et al., 2006; Muchez et al., 2008; El Desouky et al., 2009, 2012; Hitzman et al., 2010). The Lufilian belt formed during the Pan-African orogeny as a result of the collision between the Congo and Kalahari cratons that led to the formation of the West Gondwana supercontinent (Unrug, 1983; Figure 57). The Lufilian belt consists, from north to south, of four distinct litho-tectonic zones: (i) the External fold-and-thrust belt; (ii) the Domes region; (iii) the Synclinorial belt and (iv) the Katanga high. According to the metamorphic isogrades described by François and Cailteux (1981), the metamorphic grade increases from north to south. In the External fold-and-thrust belt, the sedimentary and metasedimentary sequences are affected by folds and thrusts with low grade metamorphism reaching the Lower Greenschist facies. In contrast, the Domes region displays a higher grade metamorphism ranging from Upper Greenschist to Upper Amphibolite. This orogenic belt hosts (i) world-class syn- to epigenetic Cu-Co deposits within evaporitic sedimentary rocks of the External fold-and-thrust belt, designated as the Katanga Copperbelt (Key et al., 2001; Cailteux et al., 2005; Dewaele et al., 2006; Muchez et al., 2008; El Desouky et al., 2009; Hitzman et al., 2010); (ii) stratabound epigenetic Pb-Zn-Cu deposits within deformed marine platform carbonates in the External fold-and-thrust belt (Kampunzu et al., 2009) and (iii) epigenetic U mineralizations within siliciclastic metasedimentary rocks in the External fold-and-thrust belt and in the Domes region (Cahen et al., 1961, 1971; Meneghel, 1981; Cosi et al., 1992; Decrée et al., 2011; Eglinger et al., 2013). The

Domes region is subdivided into (i) the Eastern Zambian Copperbelt which comprises deposits around the Kafue Anticline and (ii) the Western Zambian Copperbelt which includes deposits surrounding the Domes inliers (i.e. Mwombezhi to Luiswishi dome; Hitzman et al., 2012).

Evidences for fluid circulations associated with Cu deposits, in the External fold-and-thrust belt (Katanga Copperbelt) and in the eastern part of the Domes region (Eastern Zambian Copperbelt), have been extensively studied in the Musoshi, Konkola, Chambishi, Mufulira, Nkana and Nchanga occurrences in Zambia, and in the Kamoto and Luiswishi occurrences in the Democratic Republic of Congo. Several generations of fluids were trapped during the multiple mineralizing stages (Cailteux et al., 2005; Selley et al., 2005; Dewaele et al., 2006; El Desouky et al., 2009) and described as early to late diagenetic, early and late orogenic, and post-orogenic, successively (Richards et al., 1988; Greyling et al., 2005; El Desouky et al., 2008, 2009; Greyling, 2009; Muchez et al., 2010). Diagenetic hydrothermal Cu mineralizations have been attributed to the downward migration of brines originating from seawater evaporation (salinity = 11.3 to 20.9 wt.% NaCl_{equiv}; temperature = 115 to \leq 220 °C) of Neoproterozoic age through the basement (Selley et al., 2005; El Desouky et al., 2009, 2010). Orogenic hydrothermal Cu mineralizations have been interpreted as being related to a deep-seated highly saline fluid (salinity = 35.0 to 45.5 wt.% NaCl_{equiv}; temperature > 270 °C) generated by the dissolution of the Roan evaporites (El Desouky et al., 2009, 2010, 2012).

Three successive uranium mineralizing events in the Lufilian belt, described as diagenetic, syn-orogenic and late-orogenic, have been dated at ca. 652.3 ± 7.8 Ma, at ca. 530.1 ± 5.9 Ma, by *in-situ* SIMS U-Pb analyses on uraninite (Decrée et al., 2011) and at ca. 503 ± 15 Ma by dissolution TIMS U-Pb analyses on brannerite (Darnley et al., 1961). The oldest uranium event is only described in the External fold-and-thrust belt (Katanga Copperbelt). The analysis of fluid inclusions in the Shinkolobwe U deposit indicates that highly saline fluids have been trapped at a pressure between 1.00 and 1.25 kbar and at a temperature ranging from 200 to 350 °C (Audeoud, 1982). Based on uraninite REE content, this event is considered as a Neoproterozoic equivalent of the world-class Mesoproterozoic Canadian and Australian diagenetic-hydrothermal uranium deposits and occurred during the late diagenetic or early compressive tectonic events (Eglinger et al., 2013). Based on U-Pb ages coupled with REE content in uraninite, the second event appears

to be synchronous to the Pan-African MP/MT metamorphism, in relation with metamorphic hydrothermal processes during the Lufilian orogeny (Meneghel, 1981; Cosi et al., 1992; Decrée et al., 2011; Bernau et al., 2013; Eglinger et al., 2013). Based on structural observations and U-Pb ages, the third event is interpreted as a late-orogenic uranium mineralization. However, in contrast to Cu mineralizations, the fluids involved in the syn- and late-orogenic uranium mineralizations and their potential link with the Roan evaporitic metasediments have not been investigated in details so far. More generally, at the worldwide scale, only a few uranium deposits are thought to be related to metamorphosed evaporite-bearing sequences and to the circulation of metamorphic brines, in place involving regional metasomatism. For example, uranium deposits are described in the Mary Kathleen Fold Belt of Queensland (Australia) in metasedimentary sequence overprinted by large-scale sodic metasomatism involving scapolitization and albitization (Ramsay and Davidson, 1970; Oliver et al., 1992). The generation of these highly saline metamorphic brines has been attributed to regional metamorphism of marine carbonates including evaporites, up to the Amphibolite grade (Oliver and Wall, 1987). In the Mistamisk Valley of the Labrador Trough (Canada), the occurrence of uraninite-albite veins within metamorphosed argillite is explained by the circulation of highly saline metamorphic fluids (Kish and Cuney, 1981). The generation of the fluids, containing halite and Ca^{2+} - Mg^{2+} cations, has been related to metamorphism of sodic schists of a presumably evaporitic origin during the Hudsonian Orogeny (Kish and Cuney, 1981).

In order to (i) identify the uranium ore fluids associated to the tectono-metamorphic events in the Domes region, (ii) evaluate their potential genetic link with the Roan evaporites and (iii) integrate these fluid circulations within the structural, metamorphic, metasomatic and metallogenic framework of the Lufilian belt, quartz veins and their host rocks from the Lolwa and the Mitukuluku U occurrences, located respectively along the edge of the Kabompo and the Solwezi domes, have been sampled (Figure 57). These uranium mineralizations are hosted by sheared kyanite-talc micaschists attributed to the Lower Roan Group (Figure 58; Figure 59) and interpreted as metamorphosed evaporitic sediments. The analytical strategy is the following: (i) establish the structural position of uranium oxides relatively to the rock schistosity; (ii) provide the relationships between quartz deformation and the relative timing of fluid circulations within sheared veins and (iii) determine the chemistry of paleofluids and discuss their potential sources

by using microthermometry, Raman spectroscopy and laser ablation-inductively coupled plasma-mass spectrometry (LA-ICPMS) analysis.

2. Regional geology

The External fold-and-thrust belt is characterized by a Neoproterozoic sedimentary and metasedimentary sequence, the Katanga Supergroup, composed from bottom to top of the Roan, Nguba and Kundelungu Groups presumably overlying a pre-Katanga basement (Figure 58). This sedimentary sequence of the External fold-and-thrust belt is affected by folds and thrusts and low grade metamorphism reaching Lower Greenschist facies.

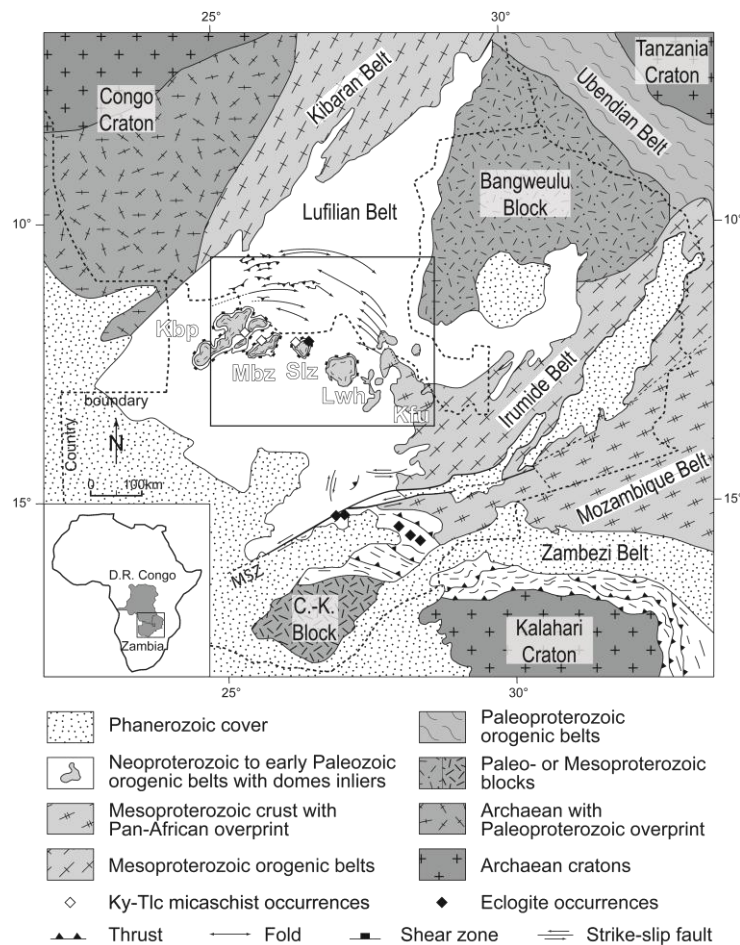


Figure 57: Geological map of the Pan-African Lufilian belt indicating the main structural trends and HP-HT metamorphic rocks occurrences (modified after De Waele et al., 2008; Eglinger et al., 2013). Abbreviations: Kbp = Kabompo dome; Mbz = Mwombeshi dome; Slz = Solwezi dome; Lwh = Luswishi dome; Kfu = Kafue Anticline; C.-K. = Choma Kalomo block; MSZ = Mwembeshi Shear Zone; Ky = Kyanite; Tlc = Talc. (Black rectangle: study area enlarged in Figure 59).

2.1. Lithostratigraphy of the Katanga sequence

The Lower Roan Group represents the basal unit of the Neoproterozoic to early Paleozoic Katanga Supergroup. In the External fold-and-thrust belt (Katanga Copperbelt), the Roan Group is composed, from bottom to top, by a siliciclastic unit, a carbonate/siliciclastic unit and a carbonate unit (Cailteux, 1983, 1994; Selley et al., 2005; Bull et al., 2011; Figure 58). In the western part of the Domes region (Western Zambian Copperbelt), deformation and metamorphism have been much more intense and the reconstruction of the stratigraphy is thus more speculative, but is thought to be generally similar to this western part of the Domes region (Cosi et al., 1992). The Roan Group is moreover characterized by many evaporitic levels showing sedimentary features typical of sabkhas, such as pseudomorphs after gypsum and anhydrite (Porada and Berhorst, 2000; Muchez et al., 2008).

	Age (Ma)	Domes region		
		Group	Subgroup	Lithology
KATANGA SUPERGROUP	$< 573 \pm 5$ ⁵ Detrital muscovite	Kundelungu	Biano	Arkoses, sandstones, shales, conglomerates
	± 635 ^{3,4}		Ngule	Sandstones, shales, carbonated siltstones
			Gombela	Carbonated siltstones, limestones, dolomites « <i>Petit Conglomérat</i> »: glacial diamictite
		Nguba	Bunkeya	Dolomitic sandstones, siltstones, shales
	Muombe		Carbonated siltstones, shales, dolomites, limestones, lavas « <i>Grand Conglomérat</i> »: glacial diamictite	
	735 ± 5 ² Magmatic zircon	Upper Roan	Mwashya	Black shales, lavas
	765 ± 5 ² Magmatic zircon		Bancroft	Dolomites, dolomitic shales, gabbros
	879 ± 16 ¹ Magmatic zircon	Lower Roan	☆ Kitwe	Shales, dolomites, arenites, evaporites
			☆ Mindola	Quartzites, arenites, conglomerates

Figure 58: Lithostratigraphy of the Katanga Supergroup in the Domes region in Zambia (modified after Porada and Berhorst, 2000; Kampanzu et al., 2009). Uranium occurrences of Lolwa and Mitukuluku are represented by gray stars within the Lower Roan Group (modified after Meneghel, 1981; Cosi et al., 1992). Age constraints are provided by U-Pb geochronology on magmatic zircon grains of volcanic rocks (¹ Hanson et al., 1994; ² Key et al., 2001), by stratigraphical correlations (³ Robb et al., 2002; ⁴ Condon et al., 2005) and by argon thermochronology on detrital grains (⁵ Master et al., 2005).

Hanson et al. (1994) and Johnson et al. (2007) proposed that the onset of rifting is associated with the emplacement of the Kafue rhyolite (879 ± 16 Ma by U-Pb on zircon). Detrital zircon grains, found within cross-bedded Lower Roan quartzite, dated at around 880 Ma by U-Pb (Armstrong et al., 2005) confirm the emplacement of the Roan detrital sediments just after the uplift and erosion of these magmatic rocks. At the top of the Upper Roan Group, the Mwashya Subgroup, in the Domes region, is dominated by shales (Mendelsohn, 1961; Cailteux, 1994; Marjonen, 2000; Cailteux et al., 2005; Hitzman et al., 2012) and comprises the Luakela volcanics dated at 765 ± 5 Ma by U-Pb on zircon (Kampunzu et al., 2000; Porada and Berhorst, 2000; Key et al., 2001; Figure 58). The Mwashya Subgroup is directly overlain by a diamictite horizon known as the Grand Conglomérat which marks the base of the Nguba Group (Binda and Van Eden, 1972). This diamictite, correlated to the Sturtian glaciations, is located between the Mwashya volcanics dated at ca. 765 Ma and the Kundelungu volcanics dated at ca. 735 Ma (Kampunzu et al., 2000; Porada and Berhorst, 2000; Key et al., 2001; Figure 58). The top of the Katanga sedimentary sequence is marked by the Kundelungu Group. The base of this group is also formed by a basal diamictite, the Petit Conglomérat, correlated to the Marinoan glaciations at around 635 Ma (Robb et al., 2002; Condon et al., 2005). The Kundelungu Group is poorly known in the Domes region but generally consists of carbonates and sandstones-siltstones-mudstones (Figure 58). Rocks of the Bianco Subgroup, forming the upper part of the Kundelungu Group, are not metamorphosed and represent the youngest unit of the Katanga Supergroup with a maximum age of 573 ± 5 Ma, constrained by ^{40}Ar - ^{39}Ar on detrital muscovite grains (Master et al., 2005; Figure 58).

2.2. Tectonic evolution of the Lufilian belt

Rift basin opening (from 880 to 600 Ma) was followed by convergence (from 600 to 530 Ma) of the Congo and Kalahari cratons. Transition from divergent to convergent tectonic regime is underlined by eclogitic metamorphism, dated at ca. 595 Ma by Sm-Nd whole-rock and garnet isochron on mafic boudins in the Zambezi belt (John et al., 2003). Subduction and exhumation of crustal units under a low geothermal gradient is depicted by *P-T* estimates of kyanite-bearing eclogites with temperatures of 590-750 °C at a minimum pressure of 20 kbar (John et al., 2003). Phengite-bearing eclogites equilibrated at a temperature between 720 and 755 °C and a pressure

between 20 and 28 kbar (John et al., 2003). Continent-continent collision is marked by the development of the Lufilian orogenic belt characterized by the formation of an external fold-and-thrust belt and by the emplacement of a nappe-pile affected by intermediate-pressure/intermediate-temperature metamorphism (Barrovian metamorphism), characterized by kyanite-talc paragenesis in the western part of the domes region (Western Zambian Copperbelt) (Cosi et al., 1992; Porada and Berhorst, 2000; John et al., 2004; Figure 57). Nappe-pile is composed of both gneissic-migmatitic basement and Neoproterozoic metasediments cover (Cosi et al., 1992). The evaporitic sediments of the Lower Roan Group are metamorphosed into kyanite-talc micaschist during crustal thickening. These rocks are characterized by a S_{n+1} foliation developed during regional-scale isoclinal folds. The S_{n+1} schistosity wraps kyanite porphyroblasts that display an inherited schistosity, S_n . Despite the intensity of deformation, these rocks have locally preserved relics of sedimentary structures such as channels, cross bedding and rare conglomerates. These Mg-rich metasediments are interpreted as continental to lagoonal-evaporitic deposits (Cosi et al., 1992). Crustal thickening is followed by an increase of the geothermal gradient recorded by intermediate-pressure/intermediate-temperature conditions with a pressure around 13 ± 1 kbar and a temperature of 750 ± 25 °C dated at 529 ± 2 Ma, by U-Pb on monazite grains from kyanite-talc micaschist in three localities: the Kabompo, Mwombezi and Solwezi domes (John et al., 2004; Figure 57). ^{40}Ar - ^{39}Ar analyses thermochronology on biotite and Rb-Sr dating on muscovite and biotite yield ages ranging from 510 to 463 Ma that are interpreted to represent post-orogenic cooling of the metamorphic rocks in the Lufilian belt (Cosi et al., 1992; John et al., 2004; Rainaud et al., 2005).

2.3. Synmetamorphic U mineralizations

In the Domes region (Western and Eastern Zambian Copperbelt), uranium occurrences within the Lower Roan Group are distributed over about 300 km from west to east. They include the Lolwa, Kawanga, Malundwe, Mitukuluku, Dumbwa, Kimale, Musoshi and Nkana occurrences (Meneghel, 1981; Figure 59). Uranium mineralizations are (i) mainly located in shear zones marking the contact between the isoclinally folded metasedimentary rocks, equivalent of the Lower Roan Group, and the gneissic-migmatitic basement, as for the Lolwa, Kawanga, Mitukuluku, Musoshi and Nkana occurrences (Meneghel, 1981; Cosi et al., 1992), and (ii)

locally, within a sheared tectonic slice of gneissic-migmatitic basement intercalated within the Lower Roan metasedimentary sequences, as for the Malundwe deposit (Bernau et al., 2013). The metamorphic grade increases from east (Kafue Anticline) to west (Kabompo dome). In the Nkana mine uranium-bearing rocks are characterized by an Upper Greenschist facies mineral paragenesis with chlorite and biotite coeval with the crystallization of uranium oxides (Meneghel, 1981; Brems et al., 2009; Eglinger et al., 2013; Figure 59). In the western part of the Lufilian belt, uranium mineralization is hosted by quartz-rich micaschists of Upper Amphibolite facies characterized by the presence of kyanite, talc and phlogopite and designated as whiteschist by Meneghel (1981), Cosi et al. (1992) and John et al. (2004). Some uranium occurrences were described in quartz-carbonate-Cu sulfide undeformed veins crosscutting the Mwashya Subgroup in the Kansanshi open pit (Meneghel 1981; Figure 59). U-Pb geochronology on uranium oxides yielded an age of 530 ± 6 Ma for Musoshi and Nkana (Decrée et al., 2011), of 542 ± 12 Ma for Kawanga (Cathelineau et al., 1990) and of 536 ± 12 Ma for Kawanga and Dumbwa occurrences (Meneghel 1981).

During an extensive exploration campaign for uranium in the period 1980-1986, carried out by Agip-Cogema, several uranium mineralizations were intersected by drilling in the western part of the Domes region (Western Zambian Copperbelt). As a result of the program, three uranium occurrences of economic interest were discovered in the Kabompo (Kawanga occurrence), Mwombezi (Malundwe occurrence) and Solwezi (Mitukuluku occurrence) domes (Cosi et al., 1992). The highest ore grade obtained in drill holes occur at the Mitukuluku occurrence, with 1.4 wt. % U_3O_8 over a thickness of 9 m (Arthurs and Legg, 1974). For this study, we have selected two quartz veins and their mineralized host rocks from the Lolwa (Kabompo dome) and Mitukuluku (Solwezi dome). Uranium mineralizations at Lolwa and Mitukuluku occurrences are mainly hosted by siliciclastic-evaporitic rocks metamorphosed within the Amphibolite facies (Meneghel, 1981; Cosi et al., 1992). At Lolwa occurrence, uranium oxides are directly found at the vicinity of the quartz vein whereas at Mitukuluku occurrence, uranium oxides are disseminated within the schistosity. Ore mineralogy is characterized by uraninite [UO_2] and brannerite [UTi_2O_6] (Meneghel, 1981; Cosi et al., 1992; Figure 60). Secondary hexavalent uranium minerals are autunite [$Ca(UO_2)_2(PO_4)_2 \cdot 10-12H_2O$], torbernite [$Cu(UO_2)_2(PO_4)_2 \cdot 8-12H_2O$], sabugalite [$HAl(UO_2)_4(PO_4)_4 \cdot 16H_2O$] and gummite [$UO_3 \cdot nH_2O$] (Meneghel, 1981).

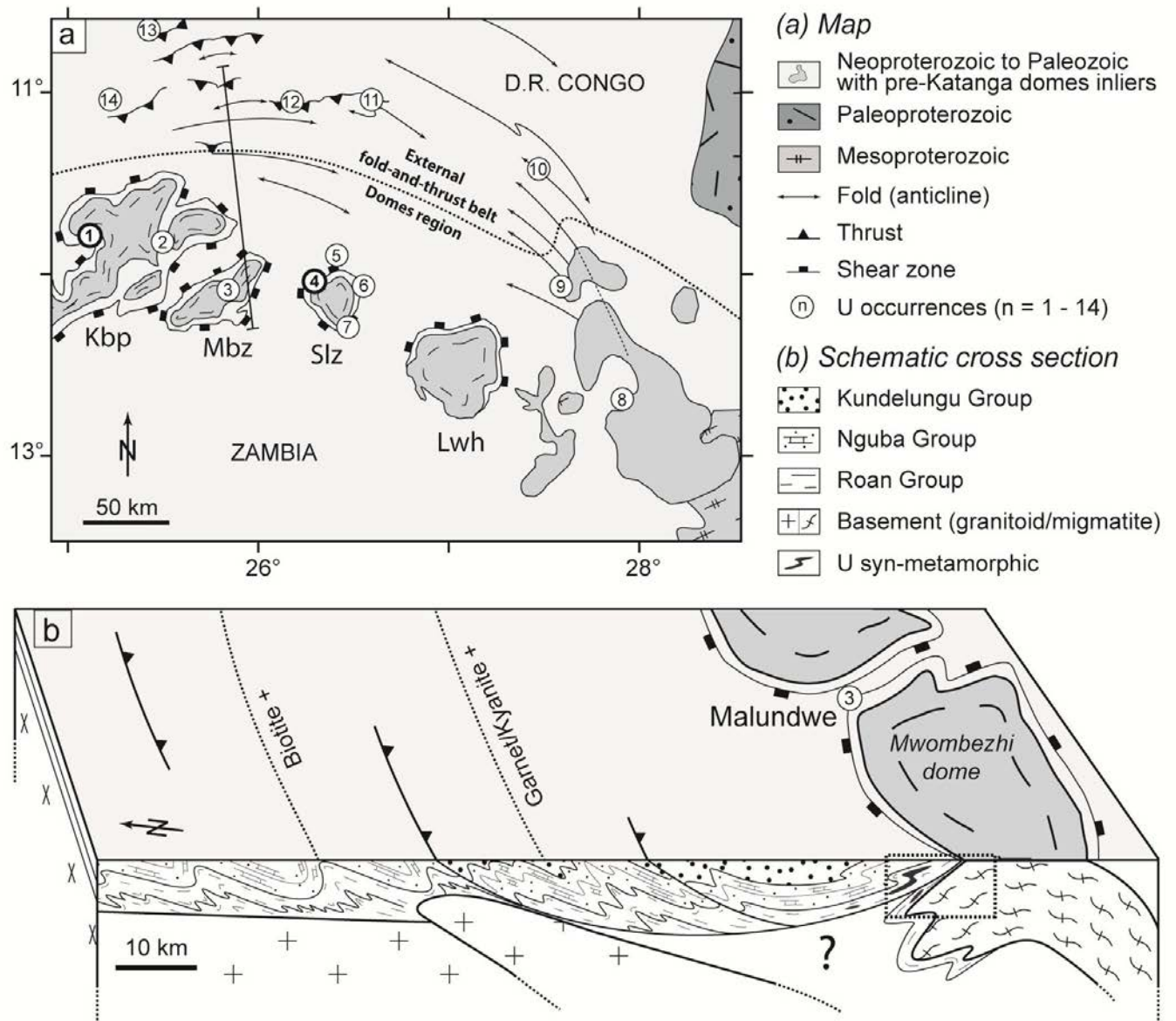


Figure 59: a: Regional geological map of the Lufilian belt with uranium occurrences and metamorphic index minerals (modified after Eglinger et al., 2013). Abbreviations: Kbp = Kabompo domes; Mbz = Mwombezi dome; Slz = Solwezi dome; Lwh = Luswishi dome. Numbers represent uranium occurrences in the high metamorphic grade western part of the Domes region: 1 = Lolwa; 2 = Kawanga; 3 = Malundwe; 4 = Mitukuluku; 5 = Kansansi; 6 = Kimale; 7 = Dumbwa; 8 = Nkana; 9 = Musoshi; 10 = Luiswishi; 11 = Shinkolobwe; 12 = Swambo; 13 = Kolwezi; 14 = Kalongwe. b: Schematic cross section along the line of Figure 59a showing the spatial and structural location of synmetamorphic uranium mineralizations (black dashed rectangle).

3. Analytical methods

All analyses were performed at the GeoRessources laboratory (Université de Lorraine, Nancy, France).

3.1. Petrography and mineral chemistry

The mineralogy, texture and composition of the uranium oxides and their host rock minerals were investigated using: (i) an Olympus BX51 microscope; (ii) a Jeol J7600F scanning electron microscope (SEM) and (iii) a Cameca SX100 electron microprobe (EMP). Major and minor elements on minerals were obtained by EMP method and are expressed in weight percent oxides (Table 44 to Table 49). Fluid inclusions were studied using doubly polished 200 μm -thick sections. Because of the small size of the inclusions, the use of a spindle-stage to measure the volume fraction φ of the non-aqueous phase was not possible (Bakker and Diamond, 2006). The area fraction (a_{vap} (fluid types 1 and 3) and a_{car} (fluid type 2)) of the non-aqueous phase, was obtained on two dimension sections by measurement using ImageJ (freeware obtainable at <http://rsb.info.nih.gov/>).

3.2. Microthermometry

Measurements were performed on a Linkam THMS600 heating-cooling stage connected to an Olympus BX51 microscope. The stage was calibrated using fluid inclusion standards (M11, H11 and E11) synthesized at the University of Leoben (Austria) with the following phase transitions: the melting temperature of a CO_2 -Ar mixture at $-56.9\text{ }^\circ\text{C}$, the eutectic point of H_2O -NaCl at $-21.2\text{ }^\circ\text{C}$, the ice melting and the critical homogenization temperatures of pure H_2O respectively at 0.0 and $374.0\text{ }^\circ\text{C}$. The composition of fluid inclusions in the H_2O -NaCl- CaCl_2 system was calculated using the Microsoft Excel-based calculation sheet of Steele-MacInnis et al. (2011). With this model, we used the combination of the measured temperatures of the final dissolution of halite and dissociation of hydrates, hydrohalite ($\text{NaCl}\cdot 2\text{H}_2\text{O}$) or sinjarite ($\text{CaCl}_2\cdot 2\text{H}_2\text{O}$), as input parameters. The following phase transition temperatures were checked for all types of fluid inclusions: first visible melting (T_{fm} ; as the eutectic transition could not be observed with a high

degree of confidence, we measured the temperature at which the first liquid was optically visible, the eutectic point being likely at a lower temperature), final melting of the carbonic phase ($T_{m\text{car}}$), final melting of ice ($T_{m\text{ice}}$), final dissociation of hydrohalite ($T_{m\text{HH}}$), carbonic phase homogenization ($T_{h\text{car}}$), final dissociation of antarcticite ($T_{m\text{ant}}$), final dissociation of sinjarite ($T_{m\text{sin}}$), final dissolution of halite ($T_{m\text{H}}$), disappearance of the vapor phase in type-I and-III inclusions ($T_{L+V\rightarrow L}$), disappearance of the carbonic phase in type-II inclusions ($T_{L+\text{car}\rightarrow L}$), disappearance of the liquid phase in type-II inclusions ($T_{L+\text{car}\rightarrow \text{car}}$).

3.3. Raman spectroscopy

A Horiba Jobin-Yvon LabRAM HR laser-Raman spectrometer (exciting radiation at 514.532 nm; focal length 800 mm; 1 grating with 1800 grooves per mm; 100 μm slit width; spectral resolution of 1.5 cm^{-1} ; liquid N_2 cooled CCD) coupled with a Linkam THMS600 heating-cooling stage and an Olympus BX40 microscope was used for solid, liquid and gas phase investigations (Dubessy et al., 1989). The gas phases were analyzed at a temperature just above the critical point of pure CO_2 at 31.1 $^\circ\text{C}$ in order to avoid any fractionation between liquid and vapor. The spectra obtained after quartz subtraction were compared for identification with the database of Burke (2001) and Frezzotti et al. (2012). The quantitative analysis of the gas phase was determined using in-house calibration. The results are expressed in mol%.

3.4. LA-ICPMS

The laser ablation inductively coupled plasma mass spectrometry (LA-ICPMS) system is composed of: (i) a GeoLas excimer laser (ArF, 193nm, Microlas, Göttingen, Germany); (ii) a microscope for sample observation and laser beam focusing onto the sample and (iii) an Agilent 7500c quadrupole ICPMS, equipped with a collision-reaction cell which decreases strongly mass interferences. The sample is located inside a 24.5 cm^3 cylindrical ablation cell, attached to a motorized X-Y stage of an optical microscope (Olympus BX41). The laser beam is focused onto the sample with a Schwarzschild reflective objective (magnification $\times 25$; numerical aperture = 0.4). Samples are observed using the microscope equipped with a glass objective ($\times 10$, $\times 15$) or the Schwarzschild objective ($\times 25$) and a CCD camera attached to the microscope. Sample

observation is possible during the ablation. In order to reduce elemental fractionation (Günther and Heinrich 1999), the ablated material is carried in helium gas ($0.5 \text{ L}\cdot\text{min}^{-1}$) mixed with argon via a cyclone mixer (volume of 9.5 cm^3) prior to entering the ICP torch. Data are collected with an integration time of 0.01 s per channel for most isotopes ($> 100 \mu\text{g}\cdot\text{g}^{-1}$) and 0.02 to 0.05 s ($< 100 \mu\text{g}\cdot\text{g}^{-1}$) to enhance the number of counts. Because it takes typically between 5 and 10 s to extract the whole content of the fluid inclusions using a laser operating at a frequency of 5 Hz, each analytical series is limited to a maximum of 20 elements and the counting time per channel did not exceed 0.30 s.

The recorded elements were ^{23}Na , ^{24}Mg , ^{39}K , ^{43}Ca , ^{47}Ti , ^{63}Cu , ^{88}Sr , ^{137}Ba , ^{95}Mo and ^{238}U . The quantification of Ca by LA-ICPMS is imprecise in reason of the high background on mass ^{40}Ca and ^{42}Ca caused by the Argon plasma, limiting signal/noise ratio (Schlegel et al., 2012). The alternative isotope ^{44}Ca overlaps $^{28}\text{Si}^{16}\text{O}$, possibly inducing systematic errors (Schlegel et al., 2012). In reason of the high calcium contents of the fluid inclusions, ^{43}Ca was used as internal reference element for these calcic-sodic fluids to avoid systematic errors.

During data reduction, the transient time-resolved signals of each isotope were carefully examined and considered only if the peak is synchronous with the major elements signal (Ca and Na). Calibration and signal integration were achieved using the NIST SRM 610, 612, 614 synthetic glasses as reference material (Pearce et al., 1997) and the LASP software (Leisen, 2012). Absolute element concentrations were calculated using the charge-balance technique (Allan et al., 2005), based on microthermometric measurements, A chlorinity of $12.8 \text{ mol}\cdot\text{kg}^{-1}$ solution (as reported in the $\text{H}_2\text{O}-\text{NaCl}-\text{CaCl}_2$ system), corresponding to the mode of all measured inclusions (range from 12.2 to $13.0 \text{ mol}\cdot\text{kg}^{-1}_{\text{solution}}$) was applied.

For the other elements, the limits of detection were calculated using the 3σ criterion (Longerich et al. 1996). The signal of the matrix near the fluid inclusions is used to quantify the background and to correct the signal intensity for each element (Leisen, 2011; Leisen et al., 2012). Absolute element concentrations are given in $\mu\text{g}\cdot\text{g}^{-1}$ (equivalent to ppm) and uncertainties for major elements (Na, Ca, K and Mg) range from 10 to 30% and for trace elements (Ba, Sr, Cu, Ti, U and Mo) range from 30 to 50%.

4. Results

4.1. Mineral paragenesis

4.1.1. Lolwa occurrence

Uranium oxides are hosted within a micaschist showing a lepidoblastic fabric underlined by a shape preferred orientation of talc, biotite and chlorite crystals (Figure 60a, b). Biotite grains are typically phlogopite with X_{Mg} ranging from 0.89 to 0.92 (Table 44). They present a TiO_2 content ranging from 0.68 to 0.83 wt.% (Table 44). Chlorite grains are clinochlore with X_{Mg} ranging from 0.94 to 0.95 (Table 45). Sigmoid lenses of quartz and calcite grains are transposed in the schistosity. Calcite and quartz crystals are partially re-crystallized during ductile deformation. Kyanite appears either (i) as small and rounded crystals transposed and recrystallized within the sigmoid quartz lenses or (ii) as elongated sub-automorphous porphyroblasts oriented with their long axes parallel to the talc-biotite-chlorite schistosity S_{n+1} (Figure 60a, b). Hematite and elongated chloro-apatite are also oriented parallel to the schistosity and are interpreted as syn-tectonic porphyroblasts (Figure 61). Plagioclase crystals of andesine composition (An_{31} to An_{38}) contain elongate inclusions of quartz, biotite, talc, chlorite and apatite. Internal schistosity, underlined by inclusions of phlogopite within plagioclase grains, is parallel and continuous with the external schistosity. These plagioclase crystals have grown after the development of the talc-biotite-chlorite schistosity and are interpreted as post-tectonic porphyroblasts (Figure 60a, b, Figure 61). Uranium-titanium oxides are the most abundant uranium minerals (Figure 62a, b, c; Table 48). The schistosity is deflected around some uranium-titanium oxides that contain inclusions delineating an internal schistosity, symmetrically arranged with respect to the external schistosity (Figure 62a). These uranium oxides are interpreted as syn-tectonic porphyroblasts, synchronous to the development of the schistosity marked by kyanite-talc-phlogopite-clinochlore-hematite-apatite, S_{n+1} (Figure 61). These oxides are characterized by UO_2 content ranging between 52.42 and 53.52 wt.% and TiO_2 content between 25.56 and 28.74 wt.%. Uranium and titanium oxides described in the literature are designated as brannerite. The chemical composition of brannerite is UTi_2O_6 . However, it is commonly reported as $(U, Ca, Th, Y, REE)(Ti, Si, Fe, Al)_2O_{6-8}(OH)_x$ because U may be replaced by Ca, Th, Y and REE whereas Si,

Al and Fe replace Ti as a result of oxidation and partial hydration (Smith, 1984). We have calculated the structural formula of these uranium-titanium oxides, $(U_{0.9}Ca_{0.2})(Ti_{1.5-1.7}Si_{0.2-0.5})O_6$, close to the idealized structural formula of brannerite. Other brannerite grains do not present strain shadows and are not wrapped into the schistosity (Figure 62b, c). These uranium oxides represent a second generation of brannerite interpreted as post-tectonic porphyroblasts. All brannerite grains present small radiogenic galena inclusions (Figure 62e).

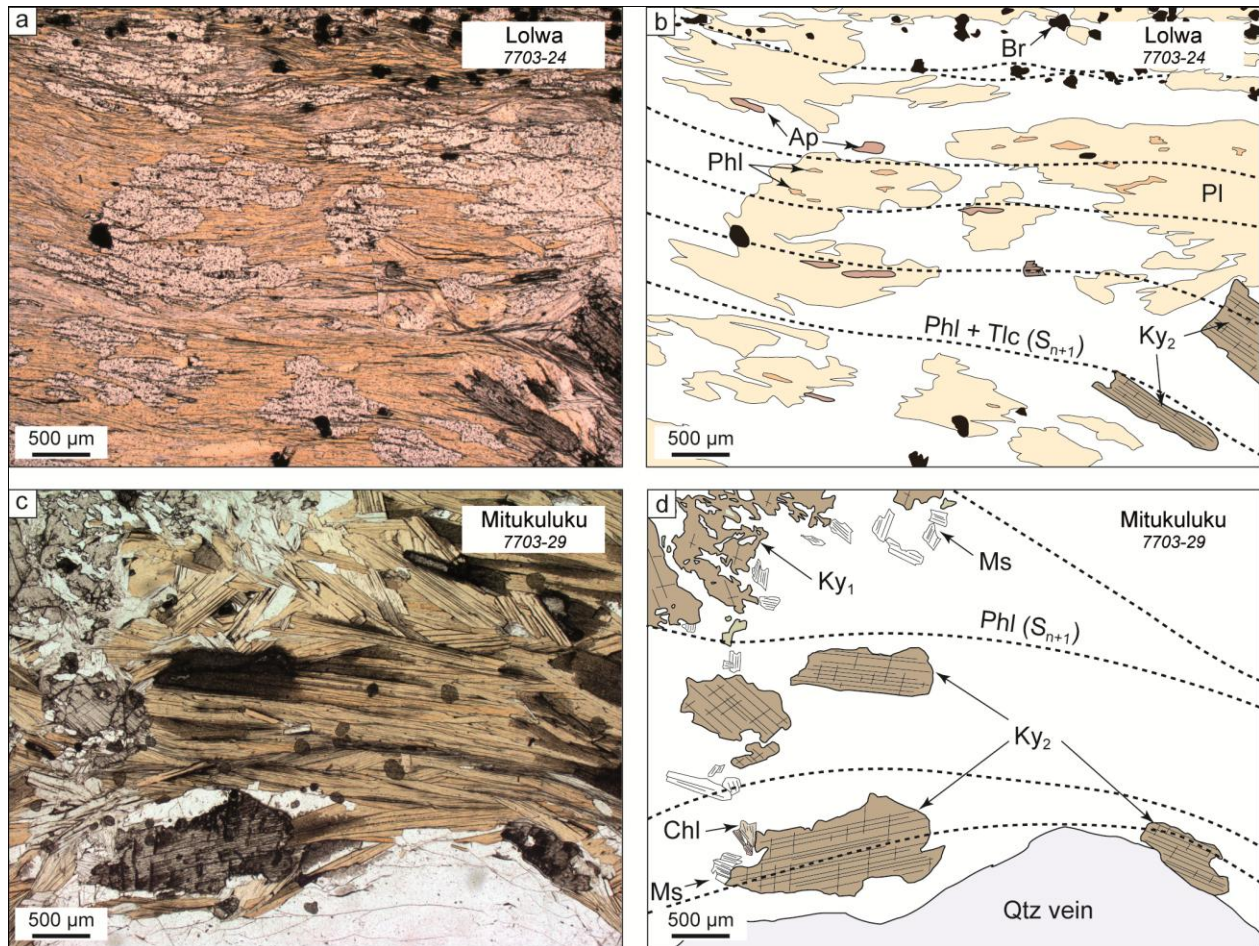


Figure 60: Microphotographs of thick sections showing the relationships between metamorphic minerals. a: LPNA optical microscopic image of the kyanite-talc micaschist with brannerite mineralization. Schistosity (S_{n+1}) is underlined by phlogopite and talc minerals. b: Schematic sketch showing the relationships between metamorphic minerals of the kyanite-talc micaschist. c: LPNA optical microscopic image of the kyanite micaschist with uraninite and brannerite mineralization. Schistosity (S_{n+1}) is underlined by phlogopite minerals. Two generations of kyanite are observed (Ky_1 and Ky_2). d: Schematic sketch showing the relationship between metamorphic minerals of the kyanite micaschist. Abbreviations: Ap = Apatite; Br = Brannerite; Chl = Chlorite; Ky = Kyanite; Ms = Muscovite; Phl = Phlogopite; Qtz = Quartz; Tlc = Talc.

	HP-HT ~600 Ma	MP-MT Up. Amp. ~530 Ma	LP-MT Amp. => G.S. ~500 Ma
Quartz	—————	————— <i>GBM recrystallization</i>	- - - - -
Calcite	—————	- - - - -	
Kyanite I	—————	- - -	
Kyanite II		—————	- - -
Phlogopite	- - - - -	—————	—————
Clinochlore		—————	—————
Talc		—————	—————
Cl-apatite		—————	- - -
Hematite		—————	- - -
Andesine		- - - - -	—————
Uraninite	- - -	—————	- - -
Brannerite	- - -	—————	—————

Figure 61: General paragenetic sequence of the kyanite±talc micaschist from Lolwa (Kabompo dome) and Mitukuluku (Solwezi dome) occurrences in the internal zone. Abbreviations: Up. Amp. = Upper Amphibolite; G.S. = Greenschist; GBM = Grain boundary migration.

4.1.2. Mitukuluku occurrence

Uranium oxides are hosted within a quartz micaschist showing a grano-lepidoblastic texture. The matrix is dominated by plagioclase and quartz grains alternating with biotite and chloro-apatite layers that define the schistosity (Figure 60c, d). Biotite grains are typically phlogopite with X_{Mg} ranging from 0.889 to 0.909 (Table 46). They present a TiO_2 content ranging from 0.71 to 0.81 wt.% (Table 46). Syn- to post-tectonic chlorite porphyroblasts are also observed. Chlorite grains are clinochlore with X_{Mg} ranging from 0.93 to 0.95 (Table 47). Two generations of kyanite are observed. The first generation is represented by kyanite poikiloblasts wrapped into the schistosity (S_{n+1}) and containing inclusions of quartz, defining an inherited schistosity (S_n). These kyanite grains are interpreted as pre-tectonic porphyroblasts (Figure 60c, d; Figure 61). The other generation is represented by sub-euhedral grains, oriented parallel to the schistosity S_{n+1} and do not present any minerals as inclusions. They are interpreted as syn-tectonic porphyroblasts

(Figure 60c, d; Figure 61). Kyanite crystals present an incipient destabilization into muscovite during the retrograde path (Table 47).

Uranium oxides are represented by uraninite and brannerite (Figure 62d, f; Table 49). Uraninite and some brannerite are wrapped into the phlogopite-kyanite schistosity (Figure 62d). These uranium oxides are considered as syn-tectonic porphyroblasts, synchronous to chlorapatite growth (Figure 61). Uraninite grains have homogeneous contents of UO_2 and PbO , ranging from 85.83 to 87.32 wt.% and from 6.25 to 7.02 wt.% respectively (Figure 62d; Table 49). These uraninite grains are characterized by high CaO content ranging from 4.35 to 5.09 wt.% (Table 3). Some brannerite within the schistosity (S_{n+1}) marked by phlogopite are surrounded by coffinite $[\text{U}(\text{SiO}_4)_{1-x}(\text{OH})_{4x}]$ (Figure 62f). Some brannerite grains without strain shadows and not wrapped by the schistosity are interpreted as post-tectonic porphyroblasts. Other rare brannerite grains were found within the first generation of kyanite crystals and interpreted as pre-tectonic porphyroblasts. All brannerite grains are partially or totally metamict due to alpha-radiation decay of the mineral structure (Smith, 1984; Lumpkin et al., 2000). The metamictization state is well illustrated on the BSE image (Figure 62b, c) where an iron oxide halo is formed surrounding brannerite grain. The total oxide content measured for brannerite ranges from 85.49 to 94.38 wt.% (Table 48; Table 49). This low total content could highlight the hydration, the amorphous and/or metamict state of brannerite grains as described by Lumpkin et al. (2000).

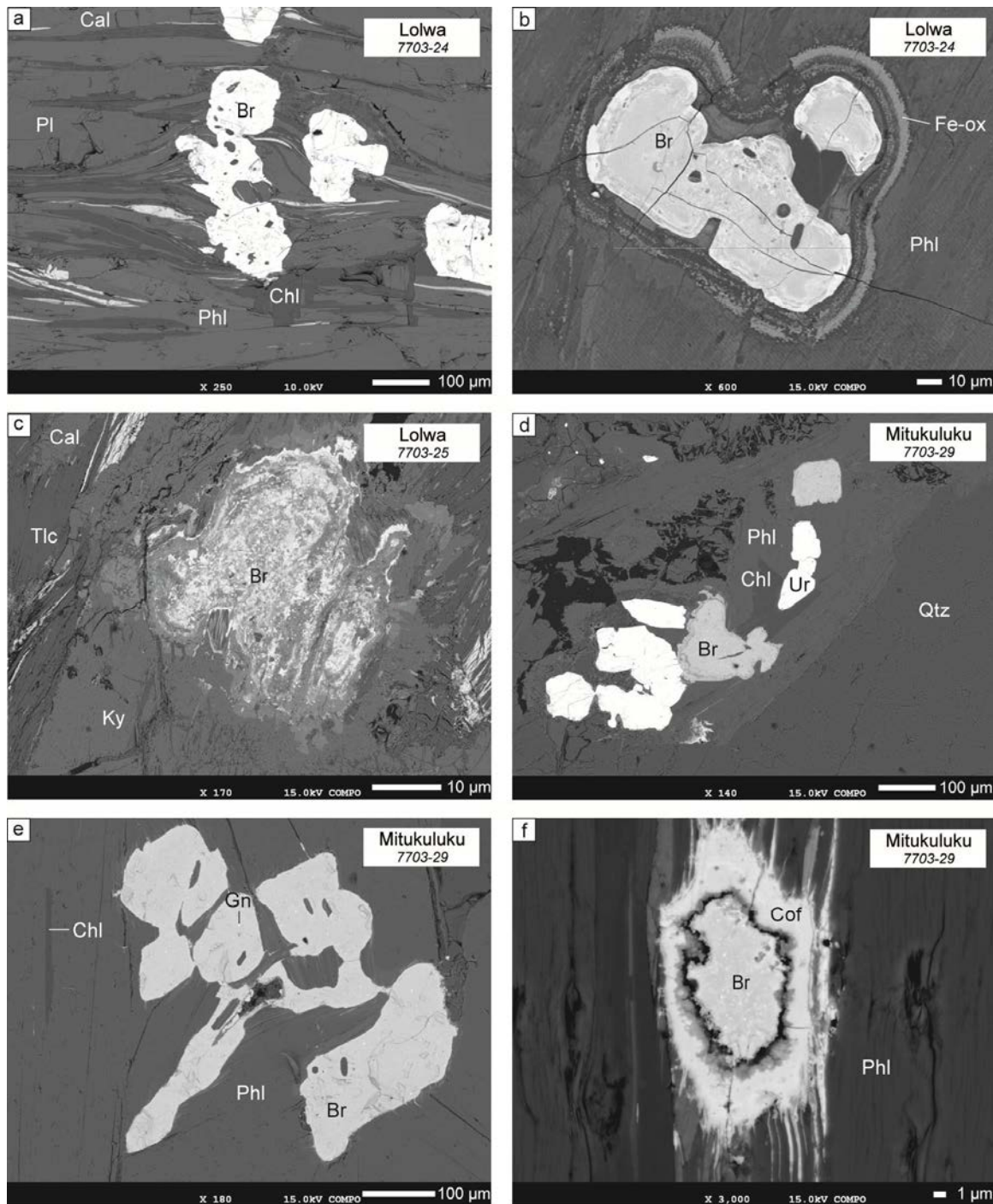


Figure 62: SEM images (backscattered electron mode) of all types of uranium minerals analyzed by EMP. a: Syn-tectonic porphyroblast of brannerite. b: Iron oxide halo surrounding metamict brannerite grain. c: Totally metamict brannerite grain. d: Uraninite porphyroblasts with co-genetic brannerite grains within phlogopite-chlorite minerals. e: Brannerite porphyroblast within phlogopite. f: Secondary coffinite around brannerite grain. Abbreviations: Ap = Apatite; Br = Brannerite; Cal = Calcite; Chl = Chlorite; Cof = Coffinite; Fe-ox = Iron oxide; Gn = Galena; Ky = Kyanite; Ms = Muscovite; Phl = Phlogopite; Pl = Plagioclase; Qtz = Quartz; Tlc = Talc; Ur = Uraninite.

4.2. Quartz vein microstructures and fluid inclusion petrography

4.2.1. Quartz vein microstructures

Quartz veins at the Lolwa and Mitukuluku occurrences display similar petrographic, structural and microstructural features. Quartz veins, composed exclusively of smoky-quartz, are parallel to the main schistosity of the kyanite±talc micaschist and are boudinaged. Quartz grains have variable sizes ranging from 250 μm to 3 cm. They present irregular and interlobate boundaries which suggest grain boundary migration (GBM, Jessell, 1987; Stipp et al., 2002; Figure 63). Some isolated smaller grains with more regular shapes and without subgrain boundary or undulatory extinction are interpreted as dislocation-free grains after subgrain rotation recrystallization (e.g. Passchier and Trouw, 2005). Most of the grains show deformation bands and elongated subgrains (Figure 63). Finally, at both localities, hematite crystals are found along quartz grain boundaries (Figure 63).

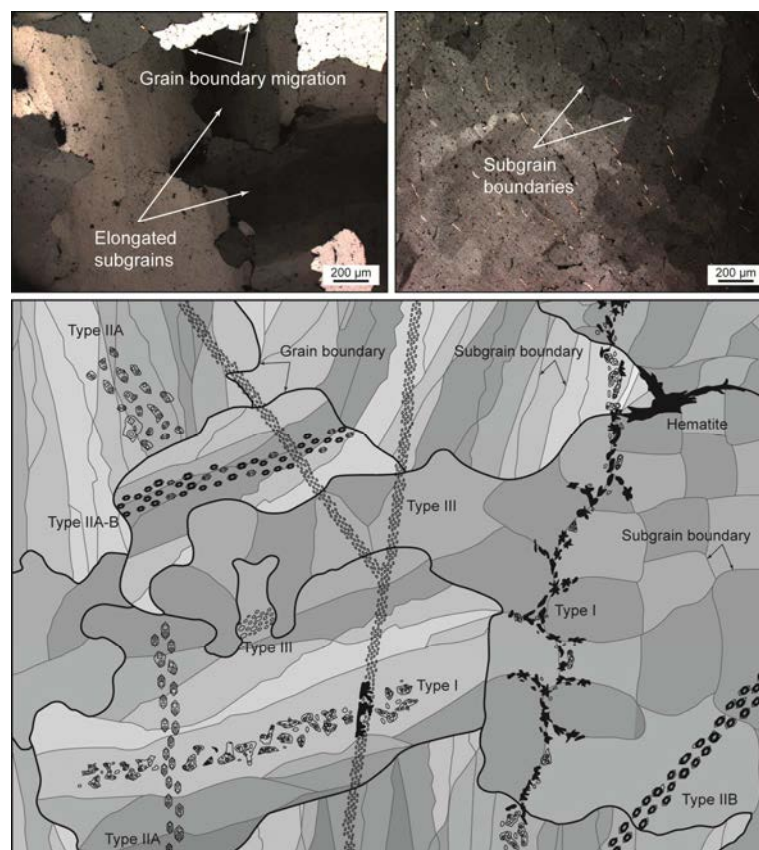


Figure 63: Schematic sketch of quartz veins showing the different quartz grain typologies, fluid inclusion types and the relationship between quartz-scale deformation and chronology of fluid circulations.

4.2.2. Fluid inclusion petrography

- *Lolwa occurrence*

The first type (Type-I) is composed of irregularly shaped fluid inclusions containing numerous solids. These inclusions have a size ranging from 10 to 100 μm (Figure 64a, b). A vapor bubble is always present with an a_{vap} ranging from 3 to 15 %. These inclusions are disposed along transgranular trails (Figure 63; Figure 64). The transgranular trails might be cut and isolated during quartz recrystallization and migrating grain boundary. More generally, the trails are slightly deviated by subgrain boundaries. Within quartz grains showing more intense dynamic recrystallization, fluid inclusions might decorate subgrain boundaries. These fluid inclusions have elongated and irregular shapes resulting from plastic deformation (Figure 64b). Microthermometric and Raman spectroscopy investigations were restricted to the less-deformed domains where inclusions have more regular shapes. The second type is subdivided into two categories (types-IIA and IIB), locally found within the same trails. Inclusions occur within intragranular border to interior trails or in border to border trails (Van den Kerkhof and Hein, 2001; Figure 63). These fluid inclusions trails crosscut the subgrain boundaries, and are considered as unaffected by the quartz plastic deformation. Type-IIA fluid inclusions are equant to round (up to 40 μm in size) and contain four phases ($L_{\text{aq}}L_{\text{car}}V_{\text{car}}H$; see Figure 64 for abbreviations) at room temperature with an a_{car} in the range 10 to 30% (Figure 64c, d). Inclusions of type-IIB have crystal-negative (euhedral) shapes and their mean size is around 5-15 μm . Type-IIB inclusions are two-phase ($L_{\text{aq}}L_{\text{car}}$) at room temperature with a a_{car} higher than 70% (Figure 64e, f). These two types of inclusions (type-IIA and IIB) locally present some unidentified solids. Type-III fluid inclusions consist mainly of one-phase (L_{aq}) and display various shapes and small sizes (< 10 μm). Most of them present a negative crystal shape (Figure 64g, h) but a few ones are irregular, probably as the result of necking-down processes (Roedder, 1984). They are distributed along straight transgranular trails, unaffected by quartz plastic recrystallization, cross-cutting all of the other populations (Figure 63). A few inclusions present a vapor phase with an a_{vap} up to 20%.

- *Mitukuluku occurrence*

The first type (type-I) of fluid inclusions encountered in the Mitukuluku samples is similar to the type-I in Lolwa occurrence. They have irregular shapes (Figure 64a, b), contain numerous solids and are distributed as transgranular trails deviated by quartz recovery and grain boundary migration (Figure 63). The second type is composed by equant to round fluid inclusions with an a_{car} higher than 80%, located along intragranular trails, unaffected by the quartz plastic deformation (Figure 63). These inclusions are similar to the type-IIB of Lolwa samples (Figure 64e, f). Finally, the third type of fluid inclusion (type-III) is equivalent to the type-III found in Lolwa locality. It is composed by one-phase (Laq) fluid inclusions which could rarely present a vapor phase up to 10% (Figure 64g, h).

4.3. *Fluid inclusion geochemistry*

In both quartz veins from Lolwa and Mitukuluku uranium occurrences, three main types of fluid inclusions are distinguished based on textural and physical-chemical characteristics identified by microthermometric and Raman spectroscopy data (Figure 63; Figure 64; Figure 65):

- Type I: $\text{H}_2\text{O}-\text{CaCl}_2-\text{NaCl}-(\text{N}_2-\text{H}_2) + \text{calcium hydrates} + \text{halite} \pm \text{hematite} \pm \text{calcite}$,
- Type II: $\text{H}_2\text{O}-\text{NaCl}-\text{CaCl}_2-\text{CO}_2-(\text{CO}) + \text{halite} \pm \text{unidentified solid}$,
- Type III: $\text{H}_2\text{O}-\text{NaCl}-\text{CaCl}_2-(\text{O}_2 \pm \text{N}_2 \pm \text{H}_2)$.

4.3.1. *Lolwa occurrence*

- *Microthermometry*

Type-I inclusions: During cooling, inclusions of type-I showed a contraction of the gas phase associated with the disappearance of the outline of the inclusion between -20 and -30 °C. During heating, no phase transitions were observed until -10 °C, the temperature at which a liquid phase appeared (first visible melting). Further heating showed melting of antarcticite ($\text{CaCl}_2 \cdot 6\text{H}_2\text{O}$) between 14.4 and 27.9 °C and sinjarite ($\text{CaCl}_2 \cdot 2\text{H}_2\text{O}$) between 121 and 165 °C (Table 50), both identified by Raman spectroscopy (cfr. Baumgartner and Bakker, 2010). With exception of the first visible melting, these phase transitions point to a composition compatible with the H_2O -

NaCl-CaCl₂ system described by Schiffries (1990). Bulk homogenization occurred either by disappearance of the halite crystal or by disappearance of the gas bubble. T_{mH} was observed between 148 and 345 °C (Table 50). $T_{L+V \rightarrow L}$ occurred between 100 and more than 350 °C.

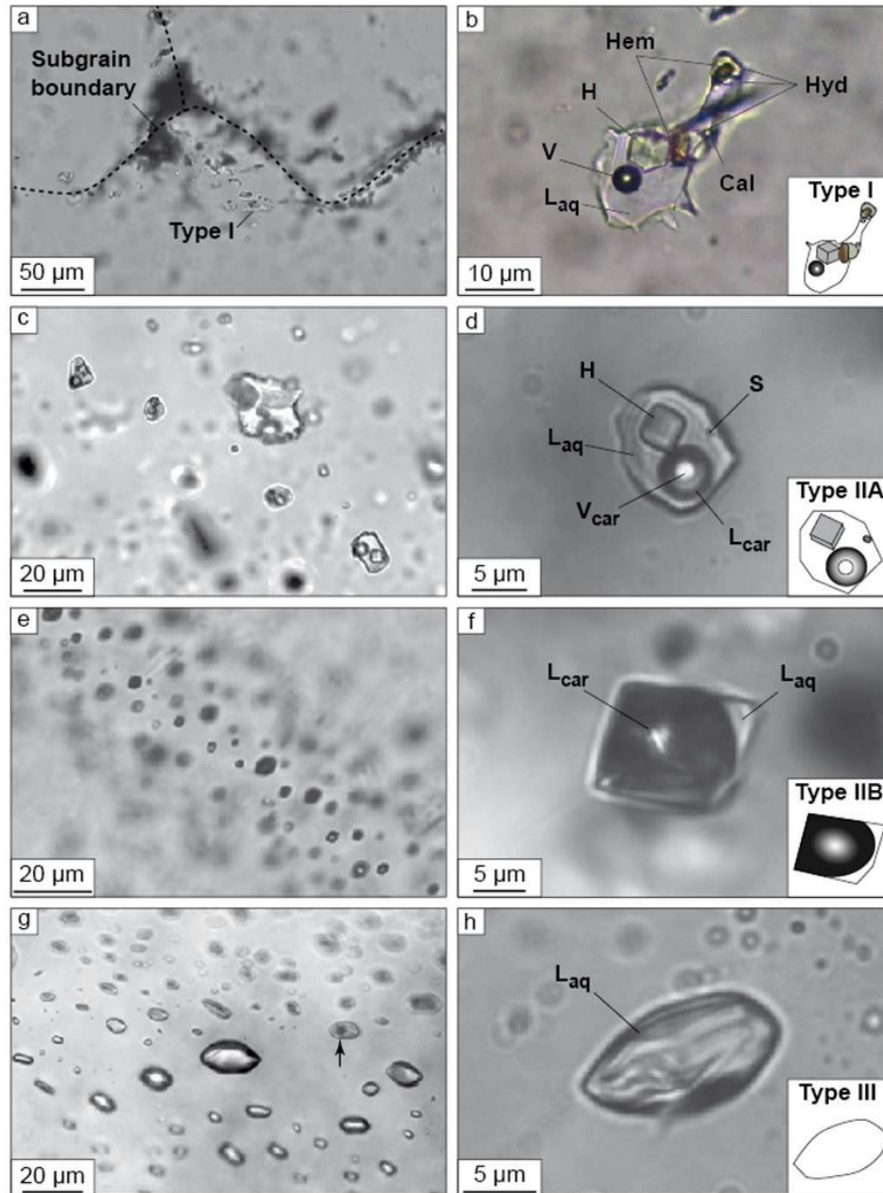


Figure 64: Microphotographs showing the different generations of fluids inclusions. Detailed description of each fluid inclusion generation is given in the text. a: trails of fluid inclusions type-I, deviated by subgrains boundaries. b: multiphase fluid inclusion of type-I. c: trails of fluid inclusions type-IIA. d: multiphase fluid inclusion of type-IIA. e: trails of fluid inclusions type-IIB. f: CO₂-rich fluid inclusion of type-IIB. g: trails of fluid inclusions of type-III. The arrows point to a two-phase inclusion. h: one-phase type-III fluid inclusion. Abbreviations: Cal = Calcite; H = Halite; Hem = Hematite; Hyd = Hydrate; L_{aq} = Aqueous Liquid; V = N₂-H₂ Vapor; L_{car} = Carbonic Liquid; V_{car} = Carbonic Vapor; S = Unidentified Solid.

Type-II inclusions are characterized by the following phase transitions. T_{fm} of the aqueous part was measured between -68.5 and -62.9 °C (Table 51). T_{mcar} in presence of a vapor phase occurred at -57.1 ± 0.5 °C. T_{mHH} occurred between -18.7 and -13.5 °C (Table 51). T_{hcar} occurred between 28.3 and 31.1 °C always by disappearance of V_{car} (Table 51). T_{mH} was measured at temperatures above 200 °C (Table 51). At temperatures above 350 °C, the fluid inclusions decrepitate. Bulk homogenization of the inclusions always took place by disappearance of the liquid carbonic phase ($L_{aq} + L_{car} \rightarrow L_{aq}$) at a temperature higher than 230 °C, always above T_{mH} (Table 51). Type-IIB inclusions showed the following phase transitions: T_{mcar} in presence of a vapor phase was observed at -56.2 ± 0.2 °C (Table 52), slightly above the triple point of pure CO₂. This incoherent temperature was interpreted as a delay in the melting of the carbonic solid possibly related to the high density of the carbonic phase (cfr. Van den Kerkhof and Olsen, 1990). T_{hcar} occurred between -10.1 and +0.2 °C ($L_{car} + V_{car} \rightarrow L_{car}$). Due to the high volumetric proportion of the carbonic phase, no clathrate could be observed within the inclusions. Finally, bulk homogenization ranged between 172 and 254 °C by expansion of the liquid carbonic phase ($L_{car} + L_{aq} \rightarrow L_{car}$; Table 52).

Types-IIA and IIB inclusions are locally observed within the same single trail. In total, over all our sections, three of these trails were found. The euhedral shapes of the inclusions hindered a correct observation of bulk homogenization of CO₂-rich inclusions (type-IIB). Therefore, in such trails, only the high-temperature phase transitions of type-IIA inclusions are reliable with, in any case, melting of halite (T_{mH} from 203 to > 350 °C) at temperature lower than disappearance of the carbonic liquid phase. Bulk homogenization temperatures ($T_{L+car \rightarrow L}$) are rather scattered from 233 to > 350 °C. Most of the inclusions decrepitated before bulk homogenization at a temperature of about 350 °C.

Type-III inclusions: T_{fm} of the aqueous part of type-III inclusions ranged between -59.0 and -51.7 °C (Table 53). T_{mice} occurred at -13.3 to -6.7 °C. The few inclusions with a vapor phase at room temperature showed bulk homogenization at temperatures between 68 and 188 °C (Table 53).

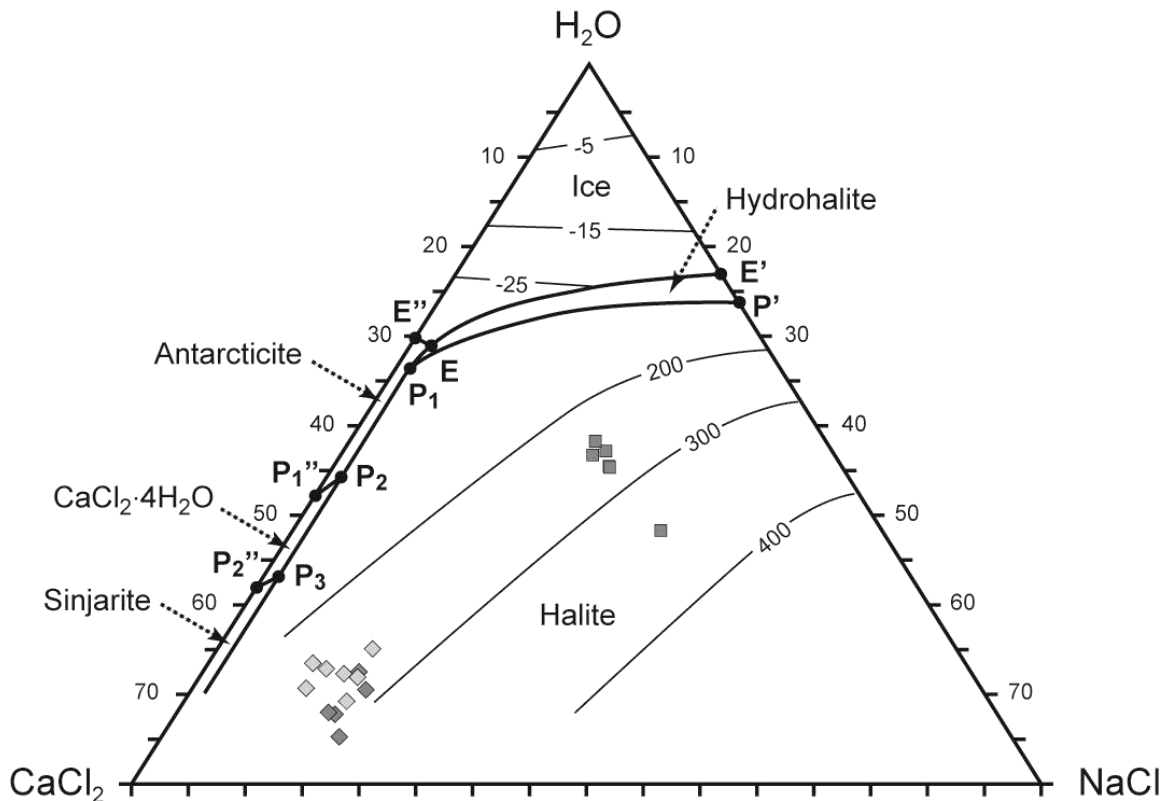


Figure 65: Vapor-saturated phase equilibria in the $\text{H}_2\text{O-NaCl-CaCl}_2$ system showing isotherms (in degrees Celsius) of halite solubility and ice-melting (modified after Steele-MacInnis et al., 2011). Diamond symbols represent data for type-I fluid inclusions (dark grey diamond => Lolwa occurrence; light grey diamond => Mitukuluku occurrence) and square symbols for type-IIA fluid inclusions (dark grey square => Lolwa occurrence; no type-IIA fluid inclusions were found in Mitukuluku occurrence). Abbreviations: E = $\text{H}_2\text{O-CaCl}_2\text{-NaCl}$ eutectic (-52.0°C); E' = $\text{H}_2\text{O-NaCl}$ eutectic (-21.2°C); E'' = $\text{H}_2\text{O-CaCl}_2$ eutectic (-49.9°C); P1 = $\text{H}_2\text{O-CaCl}_2\text{-NaCl}$ first peritectic (-22.4°C); P2 = $\text{H}_2\text{O-CaCl}_2\text{-NaCl}$ second peritectic (29.0°C); P3 = $\text{H}_2\text{O-CaCl}_2\text{-NaCl}$ third peritectic (45.0°C); P' = $\text{H}_2\text{O-NaCl}$ peritectic (0.1°C); P1'' = $\text{H}_2\text{O-CaCl}_2$ first peritectic (30.1°C); P2'' = $\text{H}_2\text{O-CaCl}_2$ second peritectic (45.1°C).

- Raman spectroscopy

The gas phase of fluid inclusions of type-I contains a mixture of N_2 (58-100 mol%) and H_2 (0-42 mol%) in variable proportions (Table 54). Calcium chloride hydrates were observed at room temperature. Hematite and calcite are trapped in most of the type-I inclusions. The gas phase of fluid inclusions of type-II contains a mixture of CO_2 and CO (Table 54). The proportion of CO within type-IIA can be as high as 10 mol% (Table 54). Type-IIB inclusions also contain a gas mixture of $\text{CO}_2\text{-CO}$, but the CO proportion is lower than 1.5 mol% (Table 54). The gas phase of type-III is essentially composed of O_2 with a $\text{N}_2\text{-H}_2$ content of maximum 6.3 mol% (Table 54). It is noteworthy that the estimation of these proportions yield uncertainties due to the movement of

the bubble during the analysis. Deformation of the stretching band of H₂O at quartz extinction was used on the liquid phase of type-III in order to determine the salinity of the fluid (cfr. Mernagh and Wilde, 1989; Dubessy et al., 2002; Baumgartner and Bakker, 2010; Caumon et al., 2013). This fluid has a salinity of 14-16 mass% NaCl_{equiv}, in agreement with microthermometric analyses (T_{mice}).

- LA-ICPMS

Only the type-I fluid inclusions were analyzed by LA-ICPMS; types-II and -III were too small to obtain a good signal. Results of LA-ICPMS analyses are summarized in Table 55 showing compositions of individual type-I fluid inclusion expressed as element concentrations in $\mu\text{g.g}^{-1}$ and as molar ratios relative to Na. In general, all inclusions contained Ca and Na as the dominant cations, in agreement with microthermometric observations. However, the K concentrations are close to the measured Na contents. Thus, the three main cations are Ca, Na and K and range from 100 000 and 160 000 $\mu\text{g.g}^{-1}$, from 23 000 to 100 000 $\mu\text{g.g}^{-1}$ and from 19 000 to 130 000 $\mu\text{g.g}^{-1}$, respectively (Figure 66; Table 55). All these inclusions contain also lower amounts of Mg, Ba and Sr. Concentrations of these elements range from 1 300 to 51 000 $\mu\text{g.g}^{-1}$, from 1 800 to 37 000 $\mu\text{g.g}^{-1}$ and from 5 100 to 35 000 $\mu\text{g.g}^{-1}$, respectively (Figure 66; Table 55). The molar abundance of the analyzed metals in most fluid inclusions from Lolwa occurrences is: Cu>Ti>U>Mo. These metals present a large range of concentrations: from 1 300 to 22 000 $\mu\text{g.g}^{-1}$ for Cu, from 60 to 1 700 $\mu\text{g.g}^{-1}$ for Ti, from 1 to 570 $\mu\text{g.g}^{-1}$ for U and from 1 to 25 $\mu\text{g.g}^{-1}$ for Mo (Figure 66).

4.3.2. Mitukuluku occurrence

The same three main types of fluid inclusions were recognized in the Mitukuluku samples with the exception of type IIA (Figure 64).

- Microthermometry

Type-I inclusions showed the same phase transitions as in Lolwa. Indeed, no eutectic point was visible until T_{mant} between 19.2 and 26.6 °C. Sinjarite was also present in these inclusions with T_{msin} between 98 and 142 °C (Table 50). The disappearance of the vapor phase occurred between 127 and 198 °C (Table 50). Bulk homogenization of the inclusions occurred by halite melting (L + H → L) at temperatures between 249 and 299 °C (Table 50).

Type-II inclusions: In this quartz vein, type-IIA fluid inclusions were not observed. Type-IIB fluid inclusions displayed the same transitions as type-IIB as at Lolwa. T_{mcar} in presence of a vapor phase occurred between -56.7 and -56.1 °C. As for Lolwa, some of these temperatures are above the triple point of CO₂, a delay possibly attributed to a high CO₂ density (Van den Kerkhof and Olsen 1990). T_{hcar} (L_{car} + V_{car} → L_{car}) ranged from 0.4 to 19.6 °C (Table 52). Bulk homogenization by expansion of the carbonic liquid phase occurred between 278 and 307 °C (L_{aq} + L_{car} → L_{car}; Table 52).

Type-III inclusions: T_{fm} occurred between -55.5 and -52.6 °C (Table 53). T_{mice} was observed between -8.7 and -4.4 °C (Table 10). Bulk homogenization ranged between 139 and 176 °C, by homogenization into the liquid phase (L + V → L; Table 53).

- Raman spectroscopy

Fluid inclusions of type-I have a vapor phase composed by a N₂-H₂ mixture similar as type-I inclusions of Lolwa but with H₂ in slightly higher amounts (39 to 54 mol%, Table 54). Solids were not analyzed by Raman spectroscopy but petrographic and microthermometric observations are strictly similar with the ones described in Lolwa. Type-IIB fluid had a vapor phase composed by a CO₂-CO mixture similar to Lolwa (Table 54). The difference lies in the presence of small amounts of N₂. The proportion of CO₂ ranged from 98.2 to 99.8 mol%, CO from 0.0 to 1.3 mol% and N₂ from 0.1 to 0.8 mol% (Table 54). Finally, the vapor phase of type-III inclusions contains a mixture of O₂-N₂-H₂ with proportions of 79-99.9 mol% for O₂, 0-7 mol% for N₂ and 0-21 mol% for H₂ (Table 54).

- LA-ICPMS

LA-ICPMS were also carried out only on the type-I fluid inclusions. The results, expressed as element concentration in µg.g⁻¹ and as molar ratios relative to Na, are presented in Table 55. Major cations are also represented by Ca, Na and K and range from 110 000 and 170 000 µg.g⁻¹, from 20 000 to 100 000 µg.g⁻¹ and from 16 000 to 87 000 µg.g⁻¹, respectively (Figure 66; Table 55). All these inclusions contain also lower amounts of Mg, Ba and Sr. Concentrations of these elements range from 6 600 to 29 000 µg.g⁻¹, from 1 700 to 16 000 µg.g⁻¹ and from 6 000 to 16 000 µg.g⁻¹, respectively (Figure 66; Table 55). The molar abundance of the analyzed metals in

most fluid inclusions from Mitukuluku occurrence is similar as the Lolwa occurrence, except for Cu which is much lower: $\text{Cu} > \text{Ti} > \text{U} > \text{Mo}$. Metals concentrations range: from 480 to 2 300 $\mu\text{g}\cdot\text{g}^{-1}$ for Cu, from 140 to 1 300 $\mu\text{g}\cdot\text{g}^{-1}$ for Ti, from 5 to 150 $\mu\text{g}\cdot\text{g}^{-1}$ for U and from 5 to 60 $\mu\text{g}\cdot\text{g}^{-1}$ for Mo (Figure 66; Table 55).

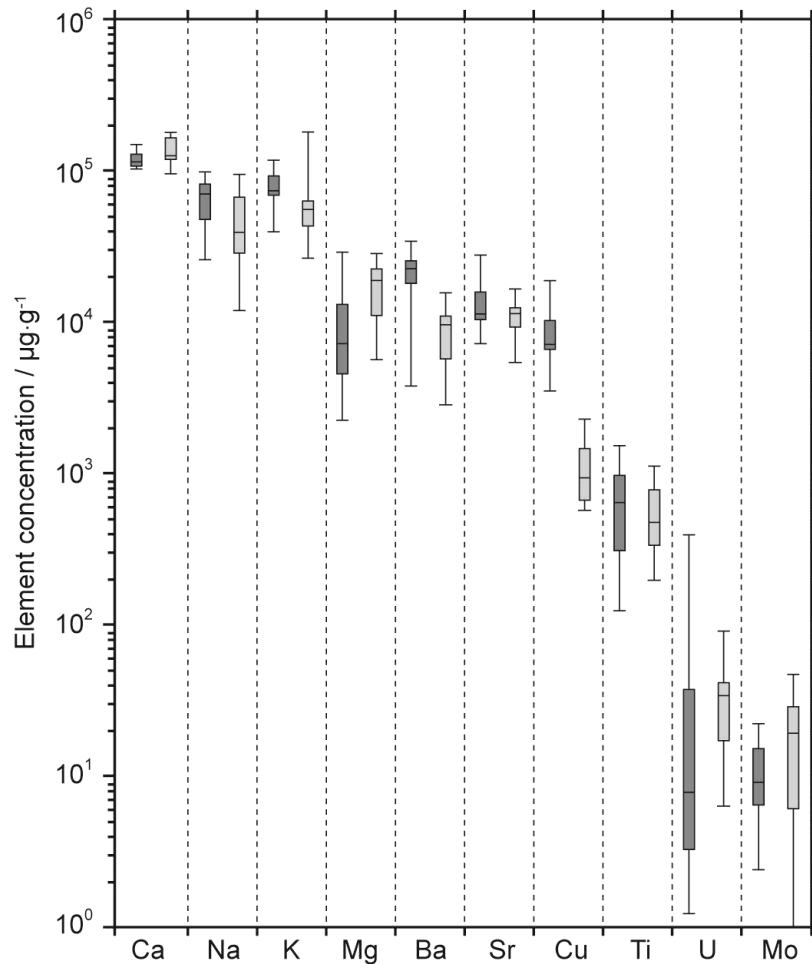


Figure 66: Box diagram of Ca, Na, K, Mg, Ba, Sr, Cu, Ti, U and Mo element concentrations in Lolwa (dark grey) and Mitukuluku (light grey) fluid inclusions. Lower whiskers, bottoms of boxes, central lines, tops of boxes and upper whiskers represent 5th, 25th, 50th, 75th and 95th percentiles, respectively.

5. Discussion

5.1. Deformation and fluid circulation

The kyanite±talc micaschist from Lolwa and Mitukuluku, hosting the quartz veins, is located in the hangingwall of a low-angle detachment with a top to the north sense of shear. It displays a pervasive schistosity with C-S fabric development and marks the transition between a lower unit made of migmatites and gneissic rocks, considered as the Archean to Mesoproterozoic basement, and an upper unit composed of alternating schists and marbles, representing the Neoproterozoic metasedimentary cover (Mendelsohn 1961; Cosi et al., 1992). These Mg-rich micaschists characterized by relics of sedimentary structures such as channels, cross bedding and locally rare conglomerates, are considered as the Lower Roan equivalent rocks (Cosi et al., 1992). John et al. (2004) obtained *P-T* conditions of 13 ± 1 kbar and 750 ± 25 °C using the garnet-aluminosilicate-quartz-plagioclase (GASP) and the garnet-biotite geothermobarometers applied on mineral assemblages of kyanite-talc micaschists (whiteschists) from Kabompo, Mwombezi and Solwezi domes. U-Pb geochronology on monazite yields concordant ages of 525 ± 2 Ma and 532 ± 2 Ma on kyanite-talc micaschists from the Lower Roan group exposed respectively in the Kabompo and Mwombezi domes (John et al., 2004). These *P-T* conditions are interpreted as the peak of high-temperature metamorphism related to crustal thickening at the end of continental collision between the Congo and Kalahari cratons at ca. 530 Ma (John et al., 2004). Our petrographic and microstructural observations for both Lolwa and Mitukuluku occurrences show that uraninite and brannerite mineralization is synchronous to the kyanite±talc±phlogopite paragenesis (S_{n+1}).

The quartz veins from Lolwa and Mitukuluku occurrences are boudinaged and totally transposed during this plastic shearing deformation event indicating that they formed before or during this high-temperature event. Thus, these veins must have recorded syn- to post- high-temperature deformation fluid circulation events. Microstructures of quartz grains from Lolwa and Mitukuluku veins imply dynamic recrystallization dominated by grain boundary migration and subgrain formation (Urai et al., 1986; Jessell, 1987; Drury and Urai, 1990; Stipp et al., 2002). These two microstructural features are synchronous and indicate a deformation at high temperature (> 500 - 700 °C for grain boundary migration), in agreement with temperature

conditions of the Amphibolite facies obtained by garnet-biotite thermometer on host rocks by John et al. (2004).

Irregularly-shaped fluid inclusions of type-I are found as intra- to intergranular planes deviated in the vicinity of subgrain boundaries. The deviated fluid inclusion trails suggest that they were deflected by ductile intracrystalline deformation during quartz recrystallization by grain boundary migration (GBM). According to these features, we propose that these type-I aqueous fluid inclusions were trapped during the high-temperature deformation and that their composition evolved during dynamic recrystallization. Some inclusions decorate the quartz grain boundaries, some are dismembered at the vicinity of the grain/subgrain boundaries. The large range of shape and bulk homogenization temperatures of the type-I inclusions is interpreted to result from such successive deformation-driven modifications affecting quartz grains (Kerrick, 1976; Johnson and Hollister, 1995; Diamond et al., 2010; Tarantola et al., 2010, 2012). Moreover the external shape of the inclusions varies according to the distance to the closest subgrain boundary. In order to improve the estimation of the original homogenization temperature of type-I fluid inclusions, we plotted a factor measuring the irregularity of the external shape of a given inclusion ($P^2/4\pi A$; Bakker and Diamond, 2006) versus the measured distance to the closest grain/subgrain boundary (Figure 67). When the inclusions have a regular shape and are located at a significant distance of grain/subgrain boundary, bulk homogenization temperature is generally comprised between 250 and 300 °C by dissolution of halite, either for Lolwa or Mitukuluku occurrences.

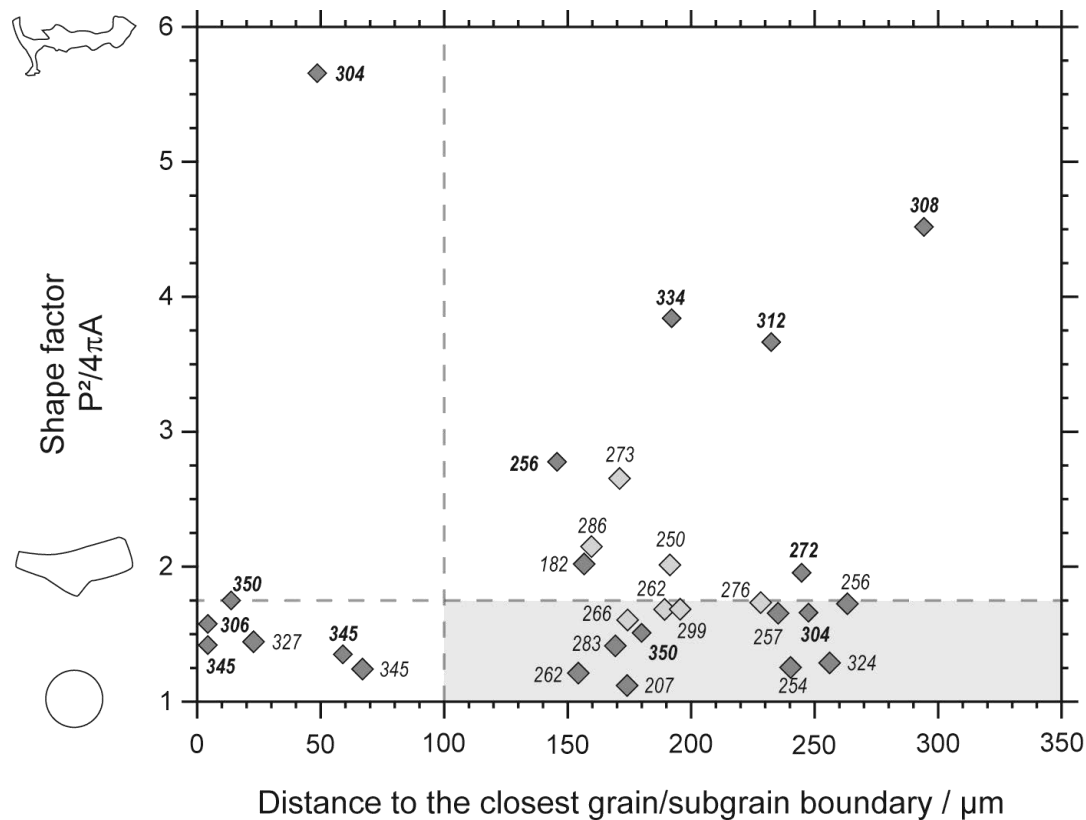


Figure 67: Shape factor ($P^2/4\pi A$; P = Perimeter; A = Area; Bakker and Diamond, 2006) of type-I fluid inclusions versus the distance to the closest grain or subgrain boundary. The external shape of fluid inclusions with various shapes (1, perfect circle, 2 and 6) are schematized on the vertical axes. Symbols in dark grey represent data of fluid inclusions from Lolwa and in light grey from Mitukuluku occurrences. Data in italic represent bulk homogenization temperature by halite melting and, data in bold italic, by vapor disappearance. The horizontal dashed line at 1.75 delimits the inclusions with regular or irregular shapes (Bakker and Diamond, 2006). The vertical dashed line is shown at 100 μm , arbitrary distance to the closest grain/subgrain boundary to which the inclusions are less deformed. The resulting light grey field is the domain where inclusions are less affected by dynamic recrystallization.

Fluid inclusions of type-IIA are localized within intra- to intergranular planes crosscutting grain/subgrain boundaries and type-I trails. Thus, this carbonic fluid event postdates the high temperature deformation and also the fluid circulation of type-I fluid. Only three trails among our sections bear types IIA and IIB inclusions within the same single plane. Unfortunately the inclusions had decrepitated during microthermometric experiments. Still, because all inclusions are approximately of the same size, this information indicates that they had reached the same pressure of about 1.6 to 2.2 kbar on heating at 350 °C, on account of their size (Leroy, 1979; Bodnar, 2003). This observation added to the variable homogenization temperatures found within the same planes of both types-IIA and -B inclusions could be interpreted by fluid immiscibility

between a CO₂-rich end-member and a H₂O-salt-rich end-member. In such a case, the lower temperatures of homogenization of both types of inclusions should be in the same range and correspond to the actual temperatures of entrapment, in our case in the range 200-300 °C. Immiscibility of fluids is generally observed in veins having formed during exhumation and low-grade retrogression of higher-grade metamorphic rocks (Diamond, 1990, 2001; Boullier et al., 1991; Craw and Norris, 1993). Fluid inclusions of type-III are distributed in transgranular planes cross-cutting all quartz grains and subgrains and trails of type I and type II fluid inclusions. Accordingly, we propose that they were the last fluids trapped in these veins during brittle deformation.

5.2. Chemistry and source of fluids

In the H₂O-NaCl-CaCl₂ system, recrystallization processes of ice or hydrates occur frequently and may be misinterpreted as eutectic reactions (Baumgartner and Bakker, 2009). Here, we probably did not observe eutectic melting in the H₂O-NaCl-CaCl₂ system (-52.0 °C), due to the metastable phase assemblage, but we measured the temperature at which the first liquid was optically visible (Table 51). A first transition at 14.4 to 27.9 °C is observed a few degrees below the H₂O-CaCl₂-NaCl second peritectic (P₂ at 29.0 °C). This transition could be compatible with a metastable eutectic transition between antarcticite and sinjarite around 25 °C (Baumgartner and Bakker 2009). This is consistent with the fact that peritectic transitions were never observed in our type-I fluid inclusions. The formation of CaCl₂·4H₂O could not be ascertained during a peritectic transition, nor phase transition at around 45.0 °C (P₃) and final dissociation only of antarcticite and sinjarite could be observed. Moreover, a liquid phase was present before dissociation of antarcticite which reflects a multi-component fluid inclusion. This could be a consequence of the high KCl content determined by LA-ICPMS, the complexity of the system and the metastable behavior of salt-hydrates (Figure 66). NaCl and CaCl₂ are the dominant salts as shown by LA-ICPMS, although Mg, Ba, Sr and Cu are present in significant amounts. However, as the thermodynamic properties of Mg, Ba, Sr, Cu and halite-saturated fluids are not available, the chlorinity is estimated using the H₂O-NaCl-CaCl₂ reference system. Several authors have demonstrated that the last and second-to-last solid phase melting temperatures can be used to determine the bulk composition of the NaCl-CaCl₂ brine (Haynes, 1985; Sterner et al., 1988; Schiffries, 1990; Vanko et al., 1992; Steele-MacInnis et al., 2011). The salinity of type-I

fluid inclusions is calculated from the sinjarite dissociation (Steele-MacInnis et al., 2011) and halite (Sternner et al., 1988) dissolution temperatures and is in the range 53-59 wt.% CaCl_2 and 13-15 wt.% NaCl (Figure 65). The salinity of type-II fluid inclusions is calculated from halite dissolution and hydrohalite dissociation temperatures and is between 19-21 wt.% CaCl_2 and 21-32 wt.% NaCl wt.%.

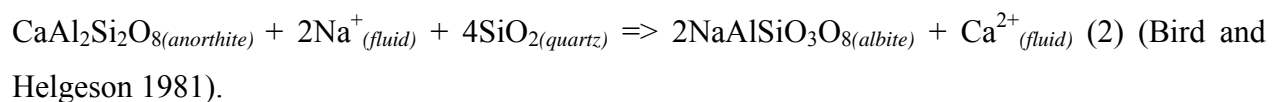
The high Mg-content of the host rock of the veins, as shown by the presence of Mg-silicate points to an evaporitic protolith. The dissolution of evaporitic sediments during peak and retrograde metamorphism leads to the production of Mg-rich fluids (e.g. Touret, 1979; Nijland et al., 1993) and to crystallization of Mg-rich minerals as expressed by the phlogopite-clinocllore-talc paragenesis. Hence, the high salinity of types-I and -II fluids might be related to the dissolution of evaporitic minerals of the evaporitic sequence of the Lower Roan Group. Thick NaCl sequences were most likely present and resulted after dissolution in the formation of collapse breccias described in the External fold-and-thrust belt (Jackson et al., 2003; Hitzman et al., 2012). High salinity fluids were described in several syn-orogenic and post-orogenic copper deposits in the Copperbelt (El Desouky et al., 2009; Greyling, 2009). The high molar Cl:Br ratios (> 1000) indicate that these mineralizing brines acquired their salinities by halite dissolution (Heijlen et al., 2008; El Desouky et al., 2012). On the contrary to halogens, cations do not behave conservatively and are therefore useful tracers of water-rock interactions processes (Fontes and Matray, 1993). Two parameters can control the Na and Ca content of the analyzed fluids: (i) the nature and relative amounts of evaporitic minerals that have been dissolved (halite, gypsum, anhydrite...) and (ii) metasomatic reactions such as albitization and scapolitization. Pseudomorphs of anhydrite nodules and lenses have been described in the stratiform Cu-Co ore deposits hosted by the Roan Group in the External fold-and-thrust belt, where metamorphic grade reached the Lower Greenschist facies (Muechez et al., 2008). Accordingly, anhydrite dissolution during Pan-African high grade metamorphism possibly explains the high CaCl_2 content of these fluids. Newton and Manning (2005) demonstrated that CaSO_4 solubility increases with NaCl activity at 800 °C and 10 kbar and that CaSO_4 molality is 200 times higher than with pure water. The *P-T* conditions (13 ± 1 kbar and 750 ± 25 °C; John et al., 2004) recorded in the western part of the Domes region (Western Zambian Copperbelt) by the metamorphosed evaporitic sequence of the Lower Roan Group are comparable to the experimental conditions of Newton and Manning

(2005). Ca-enrichment of type-I and -II fluids could be related to the dissolution of anhydrite crystals from evaporitic sequence during the Pan-African metamorphism reaching Upper Amphibolite facies in the western part of the Domes region. However, despite intensive investigation of the fluid inclusions' composition by Raman spectroscopy no sulfate ions have been identified. This absence of dissolved sulfate, could reflect thermochemical sulfate reduction (TSR) induced by organic carbon materials or methane. This hypothesis would imply H₂S production and subsequent metal-sulfide precipitation, as evidenced by the occurrence of copper sulfides in the Mitukuluku area. Metal sulfide precipitation induced by TSR is also proposed by McGowan et al. (2003) and Bernau et al. (2013) for copper mineralizations in the Domes region (Zambian Copperbelt), respectively, at the Nchanga (Eastern Zambian Copperbelt) and the Lumwana (Western Zambian Copperbelt) mines. In this case, copper mineralizations are related to the migration of metal-rich brines through methane-rich arenites during the Pan-African deformation (McGowan et al., 2003; Reaction 1).



If sulfate reduction occurred, implicitly U(VI) transported by hydrothermal fluid will also be reduced into uranium oxides (Hua et al. 2006).

In another way, Na-Ca-Cl brines are frequently associated to albitization and/or scapolitization processes (Yardley, 2012). Intense metasomatic scapolitization has been described at the regional scale by Cosi et al. (1992). Brine-rock interaction processes, in particular albitization, could be explained by the Ca-enrichment of these brines following the reaction (2):

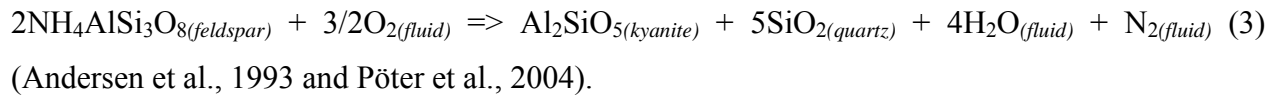


Ba and Sr can enter the M position of plagioclase to balance the charge deficiency caused by the substitution of Al for Si (Ren et al., 2003). Therefore, plagioclase alteration by albitization process is a possible explanation of the Sr and Ba enrichment of type-I fluid inclusions (Figure 66).

Once the fluids acquired their salinity, they were able to transport significant amounts of metals especially as chloride complexes (Yardley, 2005). The quantification of the concentrations of copper, titanium, uranium and molybdenum was performed in the type-I fluid inclusions and allow discussing the possible correlation between uranium and copper, and other metals, within the ore mineralizing fluids of the Domes region. Uranium content in this fluid, with a concentration mode around $20 \mu\text{g.g}^{-1}$, is in the order of uranium concentration measured in the brines which formed the giant unconformity-related U deposits in the Athabasca (Richard et al., 2011, 2013) and which are considered as the richest U-bearing fluids reported so far. Copper content within type-I fluid inclusions is comparable to that of the syn-orogenic fluids in the External fold-and-thrust belt (Katanga Copperbelt) described by El Desouky et al. (2012). This syn-orogenic mineralizing fluid at Luiswishi mine, with a copper average around $1\,870 \mu\text{g.g}^{-1}$, has acquired its Cu content by (i) remobilization of the diagenetic sulfides and/or (ii) during fluid/rock interaction as albitization (El Desouky et al., 2012). In type-I fluid inclusions, Cu content is in the same range, with a concentration mode around $7\,000 \mu\text{g.g}^{-1}$ at Lolwa and $1\,000 \mu\text{g.g}^{-1}$ at Mitukuluku occurrences. Therefore, the same origins for copper as those proposed by El Desouky et al. (2012) can be inferred. The difference in Cu content between Lolwa and Mitukuluku occurrences is likely related to the initial Cu content of the source and thus to the initial diagenetic stock remobilized. The high chloride content in type-I fluid inclusions may explain the high Ti concentrations, which is usually considered as an immobile element, by the formation of Ti-Cl complexes (Rapp et al., 2010). Rapp et al. (2010) demonstrated that rutile solubility in metamorphic chloride brines is 2 to 4 times higher than in pure water. Moreover, they proposed a possible mechanism for rutile precipitation in metamorphic environment due to a change in fluid chemistry, following the precipitation of halogen-rich minerals. In our case, we propose that brannerite (UTi_2O_6) precipitation follows the same mechanism, after apatite precipitation. Due to the presence of potential fluorinated minerals as talc or mica associated with uranium oxides, fluoride could be also played the role of ligand in the uranium transport.

Multiphase fluid inclusions of type-I are characterized by a N_2 -dominated vapor phase. Moreover, some of these inclusions might contain hematite and calcite such as accidentally-trapped minerals. Hematite is also observed within the kyanite-phlogopite schistosity and crystallized from the oxidizing metamorphic fluid, above the hematite-magnetite buffer. The

source of N₂-rich fluids can be related to the breakdown of NH₄⁺-bearing K-minerals as mica or feldspar, liberating nitrogen during prograde metamorphism (Dubessy and Ramboz, 1996). A possible reaction (3) involving destabilization of NH₄-bearing minerals and producing aluminum silicate is:



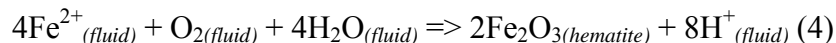
The principal source of nitrogen in metasediments is related to organic matter deposited in sediments (Krohn et al., 1993; Ramseyer et al., 1993; Holloway and Dahlgren, 1999). Organic matter present in the host sedimentary rock evolves into carbonaceous material during diagenesis and is then transformed into graphite during regional metamorphism. During a fast burial, amino acids decompose under anoxic conditions, and NH₄⁺ is released as a fluid component. NH₄⁺-bearing fluids may precipitate (K-NH₄⁺)-minerals or react with K-bearing silicates via cation exchange (Pöter et al., 2004). The Roan Group characterized by the presence of graphite and sulfide (Cosi et al., 1992) could represent a potential source of nitrogen. Three-phase fluid inclusions of type-II are characterized by a CO₂-dominant gas phase. Several models can be proposed for the source of aqueous CO₂-rich fluids in the Lolwa occurrence. A first model involves the production of a primary CO₂-rich fluid during regional metamorphism by decarbonation reactions of the Lower Roan Group metasedimentary rocks which are mainly composed of dolomites, carbonaceous siliciclastics rocks and evaporites (Cosi et al., 1992). A second model implies the oxidation of graphite into CO₂ (Connolly and Cesare, 1993; Pattison, 2006).

Oxidation of graphite was described by Kribek et al. (2005) in the Kansanshi Cu deposit, located in the north of the Solwezi dome. In this deposit, copper-uranium mineralization occurs as veins crosscutting metamorphic rocks of the Pan-African orogen (Torrealdy et al., 2000). Fluid inclusion studies indicate that the mineralizing fluids were saline (> 30 wt.% NaCl_{equiv}) and CO₂-rich (Torrealdy et al., 2000). A third model to explain the origin of the aqueous-carbonic fluids implies a dehydration/decarbonation of crustal rocks by partial melting of the middle to

lower crust (Siebenaller et al., 2012). In our case, in the absence of any isotopic data, the origin of CO₂-rich fluids in the Lolwa occurrence remains uncertain.

The three fluids present metastable assemblages (H₂O-H₂-hematite for type-I, H₂O-CO₂-CO for type-II and H₂O-O₂-H₂, in rare cases, for type-III). These compositions suggest that the molecules of these fluids were affected by radiolysis (Dubessy et al., 1988). Uranium α -radiation is susceptible to break chemical bonds of H₂O and CO₂ molecules and may induce the formation of H₂, O₂ (Maozhong et al., 1994) and CO (Willis et al., 1970), respectively.

Three scenarios regarding the relationships between uranium and the different fluids are discussed to interpret radiolysis by α -radiation: (i) free aqueous fluid circulating within the porosity of a uranium ore (external radiolysis), (ii) trapping of a uranium-bearing solution within the inclusions (internal radiolysis) and, (iii) heterogeneous trapping of a uranium oxide inside fluid inclusions at the time of fluid entrapment (internal radiolysis) (Dubessy et al., 1988). In type-I fluid inclusions, uranium was quantified by LA-ICPMS with a mode concentration around 20 $\mu\text{g.g}^{-1}$ (Table 55). This is compatible with internal radiolysis. Furthermore, as no uranium minerals were observed by microscopy or detected by Raman spectroscopy, we conclude that the internal radiolysis is related to the entrapment of a uranium-bearing solution. The incompatible presence of H₂ within this oxidizing fluid is attributed to chemical modification by radiolysis of water after fluid entrapment. The fact that no O₂ was detected by Raman spectroscopy in type-I fluid inclusions could be related to the presence of hematite. Indeed, Fe²⁺ ions, mostly dominant in fluid inclusions, are oxidized to Fe³⁺ with O₂ as oxidizing agent, following reaction (4):



Accordingly, all O₂ produced by radiolysis is likely consumed by hematite precipitation.

For type-II fluid inclusions, the key point is the heterogeneous content in CO gas between type-IIA and -IIB. In type-IIA (water-rich), CO content ranges from 0.1 to 10 mol% whereas in type-IIB (water-poor) CO content is lower than 1.5 mol%. This observation shows that when there is more water within the inclusion, the ratio CO/CO₂ is larger and the effect of the

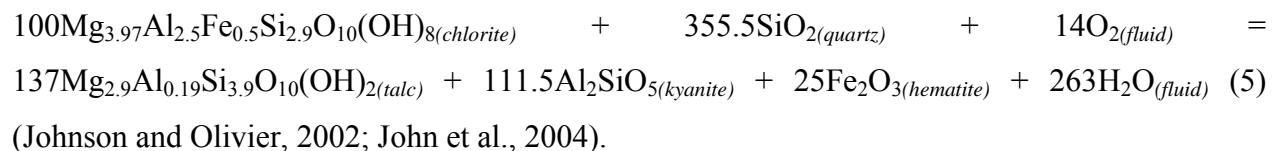
radiolysis is more pronounced. Accordingly, this feature is consistent with the presence of dissolved uranium in water trapped in these fluid inclusions. Moreover, as no uranium crystals were identified within the inclusions by petrography and Raman spectroscopy, uranium is likely dissolved in these uranium-bearing fluids (Dubessy et al., 1988). As a result, α -particles ejected by dissolved uranium are responsible of internal radiolysis after entrapment of fluid inclusions.

Only a few inclusions of late type-III were two-phase L+V at room temperature (Figure 64g). Raman spectroscopy showed a heterogeneous composition of the gas phase from O₂-N₂ to 21 mol% H₂ in a O₂-H₂-N₂ mixture. No crystals were found within these inclusions. These observations are not coherent with internal radiolysis, but with a radiolyzed fluid circulating within uranium ore trapped with a heterogeneous O₂-H₂ composition. In comparison to type-I hematite-bearing fluid, no iron oxidation allows O₂ consumption.

5.3. Geodynamic context, fluid circulations and uranium mineralization

Fluid records from transposed quartz veins of both the Lolwa and the Mitukuluku occurrences and U-Pb dating on uranium oxides in the literature serve as a basis to propose a model linking the fluid circulation, uranium mineralization and the geodynamic context in the Domes region.

The first stage corresponds to trapping of high-salinity aqueous fluids, represented by type-I, probably derived from metamorphic reactions and dissolution of evaporites. Kyanite-talc micaschist (whiteschists) formation at about 13 ± 1 kbar and 750 ± 25 °C is related to oxidizing fluids expelled during the metamorphism of shallow water sediments following the reaction (5):



The presence of hematite within (i) the schistosity of the kyanite±talc micaschist, hosting the mineralizations along quartz grains boundaries, (ii) the quartz veins and (iii) the fluid inclusions

of type-I demonstrate the circulation of an oxidizing fluid. Moreover, this fluid circulation is synchronous to high temperature deformation of quartz grains characterized by grain boundary migration recrystallization above 500-700 °C (Jessel, 1987; Stipp et al., 2002). High temperature metamorphism in the internal zone is recorded by kyanite-talc micaschist at ca. 530 Ma by U-Pb dating on monazite. Uraninite and brannerite mineralization, synchronous to the kyanite±talc±phlogopite schistosity, is attributed to this high temperature tectono-metamorphic event related to type-I fluid circulation. The U-Pb ages on uraninite at 542 ± 12 Ma for Kawanga (Cathelineau et al., 1990) and of 536 ± 12 Ma for the Kawanga and Dumbwa occurrences (Meneghel 1981) are consistent with the U-Pb monazite age. We propose that these uranium-bearing fluids (type-I) were trapped during the temperature peak of the Pan-African metamorphism following continental collision and thickening of the orogenic crust. Several hypotheses can be considered regarding the source of uranium. In the external zone of the Lufilian belt, a first uranium mineralization, at ca. 650 Ma (Decrée et al., 2011), is described and related to late diagenetic hydrothermal processes preceding the Pan-African orogeny (Eglinger et al., 2013). This uranium mineralization hosted by the low metamorphic grade Lower Roan Group rocks could be a first metal stock which could be (re-)mobilized during the Lufilian tectono-metamorphic events at ca. 530 Ma. The high metamorphic grade reaching the Upper Amphibolite facies in the internal zone, recorded by uranium-bearing rocks of the Lower Roan Group, could have erased any traces of this original uranium stock. A second uranium source could be the felsic gneissic-migmatitic basement overprinted by an intense metasomatism expressed by albitisation and scapolitisation. Uranium could be leached from U-bearing minerals such as monazite and allanite and transported by these highly saline oxidized metamorphic brines through the metasedimentary sequence and basement rocks during the Pan-African deformation at ca. 530 Ma. Uraninite grains from Mitukuluku occurrence, which crystallized from these Ca-rich brines, incorporate calcium up to 5.09 wt.% in CaO (Table 49). The presence of chlorapatite, synchronous to the kyanite±talc±phlogopite schistosity, corroborates the link between these Ca-rich brines and the uranium mineralizing event at ca. 530 Ma.

The second stage corresponds to trapping of high-salinity carbonic fluids (represented by type-II fluid inclusions), probably derived from dehydration/decarbonation reactions and/or from oxidation reactions of graphitized organic matter (Reaction 3). In the Kansanshi mine, brannerite

grains hosted by discordant vein were dated at 503 ± 15 Ma by U-Pb method (Darnley et al. 1961). These uraninite-brannerite-sulfides veins crosscutting the metasedimentary sequence of the Upper Roan Group represented by marbles, carbonaceous phyllites and biotite-garnet schists also host molybdenite. The previous U-Pb age of 503 ± 15 Ma on brannerite from late veins at the Kansanshi deposit broadly overlaps the 502 ± 1 Ma Re-Os age for molybdenite (Torrealdy et al., 2000). Fluid inclusion studies have shown the presence of carbonic saline fluids, higher than 30 mass% $\text{NaCl}_{\text{equiv}}$, related to the mineralization (Torrealdy et al., 2000). Our study demonstrates that carbonic saline fluids are also uranium-bearing and we propose that these fluids have been trapped during ductile deformation. Ductile-brittle transition could be underlined by fluid immiscibility between highly saline aqueous and CO_2 -rich fluids at temperatures ranging from 170 to more than 350 °C. This fluid event could be associated to the CO_2 -rich fluid event described by Torrealdy et al. (2000) at ca. 500 Ma. This age is in good agreement with ^{40}Ar - ^{39}Ar thermochronology analyses on biotite and Rb-Sr dating on muscovite and biotite yielding ages between 510 and 463 Ma (John, 2001). These ages are interpreted to represent post-orogenic cooling of the metamorphic rocks in the Lufilian belt (Cosi et al., 1992; John et al., 2004; Rainaud et al., 2005). We suggest that the CO_2 -rich fluid circulated during exhumation of metamorphic rocks and their tectonic accretion in the Domes region of the Lufilian belt.

The last event corresponds to trapping of low-salinity aqueous fluids, represented by type-III inclusions, whose origin is uncertain. This fluid circulated at temperatures ranging from 70 to 190 °C, during brittle deformation.

6. Conclusion

The detailed microstructural and chemical analysis of fluid inclusions of two quartz veins sampled in the Lolwa and Mitukuluku uranium occurrences in the Western Zambian Copperbelt of the Lufilian belt, allows to identify two uranium-bearing Ca-Na-Cl fluids. The microstructural position of these fluids indicates that they have circulated during the Pan-African metamorphism from burial to exhumation of the metamorphic host rocks.

- (1) The first uranium (re-)mobilization was assured by CaCl₂-NaCl-KCl-(MgCl₂) aqueous fluid (type-I), with salinities of 53-59 wt.% CaCl₂ and 13-15 wt.% NaCl. According to their microstructural position, these fluid inclusions have been trapped synchronous to high-temperature quartz deformation, around 500-700 °C, at ca. 530 Ma. We propose that this hypersaline metamorphic fluid is related to the dissolution of Neoproterozoic evaporite units, known in the Roan Group and that they have been enriched in cations (Ca²⁺, Sr²⁺, Ba²⁺) during water-rock interaction leading to albitization and/or scapolitization of the crystalline rocks. Uranium concentrations are in the order of tens of µg.g⁻¹ and copper concentrations are in the order of thousand of µg.g⁻¹. Copper and uranium mineralizations are known in the Western Zambian Copperbelt, and could be related to the circulation of these metamorphic brines at ca. 530 Ma.
- (2) The second uranium (re-)mobilization is related to the circulation of aquo-carbonic metamorphic fluids postdating the circulation of type-I aqueous fluids and characterized by a salinity of 21-32 wt.% NaCl and 19-21 wt.% CaCl₂. The metastable composition (CO₂-CO) of these fluids is explained by radiolysis induced by the presence of dissolved uranium within water-rich inclusions. According to the distribution of type-II fluid inclusions in planes cross-cutting quartz grain boundaries, this aquo-carbonic fluid circulated during the exhumation of the high-grade metamorphic rocks through the brittle-ductile transition dated at ca. 500 Ma.

Acknowledgments

We would like to thank CNRS (NEEDS) and AREVA for financial support. AREVA is also thanked for providing the samples. The authors are grateful to Sandrine Mathieu, Olivier Rouer, Marie-Camille Caumon (GeoRessources, Nancy) and Romain Dalleu (Ecole Nationale Supérieure de Géologie, Nancy) for technical support in providing analytical data on SEM, EMP, Raman spectroscopy and microthermometry, respectively. We would also like to acknowledge the stimulating discussions with Matthew Steele-MacInnis and Michel Cuney. The authors are grateful to Maurice Pagel and two anonymous journal reviewers for their helpful comments and to Jacques Touret for editorial advice.

Table 44: Chemical composition of phlogopite from the Lolwa occurrence analyzed by electron microprobe

Sample		7703-24	7703-24	7703-24	7703-24	7703-25	7703-25	7703-25	7703-25
Analysis n°		A-p7	B-p6	D-p7	G-p6	A-p1	B-p5	F-p1	F-p3
Mineral		Phl	Phl	Phl	Phl	Phl	Phl	Phl	Phl
Location		Lolwa	Lolwa	Lolwa	Lolwa	Lolwa	Lolwa	Lolwa	Lolwa
Oxides / wt. %	SiO ₂	39.75	40.05	39.38	40.11	39.24	39.93	39.08	39.61
	TiO ₂	0.78	0.71	0.79	0.68	0.83	0.82	0.82	0.75
	Al ₂ O ₃	17.60	17.40	17.67	17.62	17.30	17.79	17.40	17.67
	FeO	3.69	3.69	3.54	3.64	4.81	4.76	4.95	4.75
	MnO	0.00	0.08	0.10	0.00	0.07	0.02	0.04	0.00
	MgO	23.10	22.81	23.04	23.70	22.00	21.83	22.05	21.78
	CaO	0.04	0.11	0.07	0.00	0.07	0.00	0.00	0.00
	Na ₂ O	0.35	0.31	0.36	0.40	0.29	0.34	0.33	0.07
	K ₂ O	9.09	9.31	9.51	9.65	9.52	9.57	9.55	10.23
	Total	94.40	94.52	94.46	95.80	94.13	95.06	94.22	94.86
Oxygens		22	22	22	22	22	22	22	22
Cations	Si	5.624	5.668	5.587	5.609	5.620	5.649	5.597	5.636
	Al ^{IV}	2.376	2.332	2.413	2.391	2.380	2.351	2.403	2.364
	Al ^{VI}	0.560	0.572	0.542	0.515	0.540	0.615	0.535	0.600
	Ti	0.083	0.076	0.084	0.072	0.089	0.087	0.088	0.080
	Fe ^{tot}	0.437	0.437	0.420	0.426	0.576	0.563	0.593	0.565
	Mn	0.000	0.010	0.012	0.000	0.008	0.002	0.005	0.000
	Mg	4.871	4.811	4.872	4.940	4.695	4.602	4.706	4.618
	Ca	0.006	0.017	0.011	0.000	0.011	0.000	0.000	0.000
	Na	0.096	0.085	0.099	0.108	0.081	0.093	0.092	0.019
	K	1.641	1.681	1.721	1.722	1.739	1.727	1.745	1.857
	X _{Mg}	0.918	0.917	0.921	0.921	0.891	0.891	0.888	0.891
	X _{Fe}	0.082	0.083	0.079	0.079	0.109	0.109	0.112	0.109

Table 45: Chemical composition of talc and chlorite from the Lolwa occurrence analyzed by electron microprobe

Sample		7703-24	7703-24	7703-25	7703-25	7703-24	7703-24	7703-24	7703-24
Analysis n°		A-m3	B-m4	C-m1	D-m2	E-c1	E-c3	F-c1	F-c4
Mineral		Tlc	Tlc	Tlc	Tlc	Chl	Chl	Chl	Chl
Location		Lolwa	Lolwa	Lolwa	Lolwa	Lolwa	Lolwa	Lolwa	Lolwa
Oxides / wt. %	SiO ₂	60.65	61.47	60.31	60.17	28.50	27.59	28.41	28.55
	TiO ₂	0.04	0.05	0.05	0.03	0.00	0.02	0.02	0.04
	Al ₂ O ₃	2.16	1.77	1.97	2.26	23.44	22.49	23.16	23.17
	FeO	1.09	1.21	1.56	1.57	3.28	3.31	3.23	3.35
	MnO	0.00	0.05	0.00	0.00	0.09	0.03	0.00	0.10
	MgO	30.64	31.73	30.32	30.29	32.32	30.50	31.89	31.66
	CaO	0.07	0.04	0.04	0.00	0.00	0.11	0.00	0.00
	Na ₂ O	0.26	0.23	0.21	0.24	0.01	0.05	0.01	0.06
	K ₂ O	0.02	0.01	0.01	0.02	0.00	0.03	0.02	0.00
	Total	94.93	95.56	94.47	94.58	86.64	84.13	86.74	86.93
Oxygens		22	22	22	22	28	28	28	28
Cations	Si	7.753	7.738	7.763	7.737	5.393	5.387	5.373	5.392
	Al ^{IV}	0.247	0.262	0.237	0.263	2.607	2.613	2.627	2.608
	Al ^{VI}	0.079	0.001	0.062	0.080	2.623	2.563	2.536	2.551
	Ti	0.004	0.005	0.005	0.003	0.000	0.003	0.003	0.006
	Fe ^{tot}	0.117	0.127	0.168	0.343	0.519	0.540	0.511	0.529
	Mn	0.000	0.005	0.000	0.000	0.014	0.005	0.000	0.016
	Mg	5.837	5.953	5.816	5.805	8.833	8.875	8.988	8.911
	Ca	0.010	0.005	0.006	0.000	0.000	0.023	0.000	0.000
	Na	0.064	0.056	0.052	0.060	0.002	0.019	0.004	0.022
	K	0.003	0.002	0.002	0.003	0.000	0.007	0.005	0.000
	X _{Mg}	-	-	-	-	0.944	0.943	0.946	0.944
	X _{Fe}	-	-	-	-	0.056	0.057	0.054	0.056

Table 46: Chemical composition of phlogopite from the Mitukuluku occurrence analyzed by electron microprobe

Sample		7703-29	7703-29	7703-29	7703-29	7703-30	7703-30	7703-30	7703-30
Analysis n°		A-p1	A-p3	B-p3	C-p4	C-p1	D-p1	E-p1	E-p3
Mineral		Phl	Phl	Phl	Phl	Phl	Phl	Phl	Phl
Location		Mitukuluku	Mitukuluku	Mitukuluku	Mitukuluku	Mitukuluku	Mitukuluku	Mitukuluku	Mitukuluku
Oxides / wt. %	SiO₂	40.09	38.79	40.30	39.96	38.69	39.99	39.25	39.93
	TiO₂	0.76	0.76	0.73	0.71	0.75	0.81	0.78	0.80
	Al₂O₃	17.82	18.11	17.46	18.12	17.96	18.30	18.02	17.58
	FeO	4.00	4.66	4.71	4.04	4.14	4.45	4.16	4.12
	MnO	0.07	0.00	0.03	0.00	0.10	0.01	0.16	0.08
	MgO	22.41	20.94	21.83	21.98	22.53	21.42	21.71	22.20
	CaO	0.06	0.09	0.01	0.00	0.00	0.00	0.01	0.00
	Na₂O	0.44	0.48	0.38	0.38	0.36	0.40	0.45	0.42
	K₂O	9.07	9.25	9.38	9.44	8.73	9.58	9.41	9.43
	Total	94.72	93.08	94.83	94.63	93.26	94.96	93.95	94.56
Oxygens		22	22	22	22	22	22	22	22
Cations	Si	5.657	5.603	5.704	5.651	5.552	5.650	5.609	5.661
	Al^{IV}	2.343	2.397	2.296	2.349	2.448	2.350	2.391	2.339
	Al^{VI}	0.621	0.686	0.617	0.673	0.590	0.698	0.644	0.600
	Ti	0.081	0.083	0.078	0.076	0.081	0.086	0.084	0.085
	Fe^{tot}	0.472	0.563	0.558	0.478	0.497	0.526	0.497	0.489
	Mn	0.008	0.000	0.004	0.000	0.012	0.001	0.019	0.010
	Mg	4.713	4.508	4.605	0.104	4.818	4.510	4.623	4.691
	Ca	0.009	0.014	0.002	1.703	0.000	0.000	0.002	0.000
	Na	0.120	0.134	0.104	0.000	0.100	0.110	0.125	0.115
	K	1.633	1.705	1.694	1.703	1.598	1.727	1.715	1.706
	X_{Mg}	0.909	0.889	0.892	0.906	0.907	0.896	0.903	0.906
	X_{Fe}	0.091	0.111	0.108	0.094	0.093	0.104	0.097	0.094

Table 47: Chemical composition of chlorite and muscovite from the Mitukuluku occurrence analyzed by electron microprobe

Sample		7703-29	7703-29	7703-29	7703-29	7703-29	7703-29	7703-29	7703-29
Analysis n°		B-c5	B-c6	C-c1	C-c6	A-c1	B-c10	C-c20	C-c21
Mineral		Chl	Chl	Chl	Chl	Ms	Ms	Ms	Ms
Location		Mitukuluku	Mitukuluku	Mitukuluku	Mitukuluku	Mitukuluku	Mitukuluku	Mitukuluku	Mitukuluku
Oxides / wt. %	SiO₂	28.34	27.78	28.37	30.71	45.05	46.45	46.01	45.87
	TiO₂	0.00	0.03	0.06	0.02	0.38	0.28	0.52	0.40
	Al₂O₃	23.15	23.32	23.00	20.43	33.95	34.61	33.48	33.11
	FeO	4.22	4.26	4.15	3.10	2.54	2.32	3.02	2.91
	MnO	0.00	0.19	0.10	0.21	0.07	0.00	0.03	0.02
	MgO	30.91	31.04	31.32	33.17	1.16	1.16	1.18	1.26
	CaO	0.00	0.03	0.01	0.07	0.00	0.00	0.00	0.00
	Na₂O	0.01	0.04	0.00	0.00	1.34	1.05	1.04	0.99
	K₂O	0.01	0.00	0.00	0.02	9.76	9.90	10.02	9.96
	Total	86.64	86.69	87.01	87.73	94.24	95.52	95.31	94.53
Oxygens		28	28	28	28	22	22	22	22
Cations	Si	5.390	5.295	5.377	5.737	6.112	6.188	6.183	6.209
	Al^{IV}	2.610	2.705	2.623	2.263	1.888	1.812	1.817	1.791
	Al^{VI}	2.580	2.535	2.515	2.237	3.543	3.623	3.487	3.492
	Ti	0.000	0.004	0.009	0.003	0.039	0.028	0.053	0.041
	Fe^{tot}	0.671	0.679	0.658	0.484	0.288	0.258	0.339	0.329
	Mn	0.000	0.031	0.016	0.033	0.008	0.000	0.003	0.002
	Mg	8.761	8.817	8.846	9.236	0.235	0.181	0.236	0.254
	Ca	0.000	0.006	0.002	0.014	0.000	0.000	0.000	0.000
	Na	0.004	0.015	0.000	0.000	0.353	0.271	0.271	0.260
	K	0.002	0.000	0.000	0.000	1.689	1.682	1.718	1.720
	X_{Mg}	0.929	0.928	0.931	0.950	-	-	-	-
	X_{Fe}	0.071	0.072	0.069	0.050	-	-	-	-

Table 48: Chemical composition of brannerite from the Lolwa occurrence analyzed by electron microprobe

Sample	7703-25	7703-25	7703-25	7703-25	7703-25	7703-25	7703-25	7703-25
Analysis n°	c1-p1	c1-p2	c1-p3	c1-p4	c1-p5	c1-p6	c1-p7	c1-p8
Mineral	Br	Br	Br	Br	Br	Br	Br	Br
Location	Lolwa	Lolwa	Lolwa	Lolwa	Lolwa	Lolwa	Lolwa	Lolwa
Oxides / wt. %								
UO ₂	61.73	42.31	41.12	53.13	47.59	51.05	58.26	24.58
PbO	0.00	0.00	0.00	0.00	0.00	0.00	0.00	0.00
ThO ₂	0.00	0.03	0.00	0.00	0.00	0.17	0.00	0.00
CaO	5.26	3.57	3.61	4.16	3.90	3.88	4.71	2.46
TiO ₂	14.07	37.92	23.50	25.68	30.20	27.47	18.70	56.45
FeO	0.90	4.89	13.42	2.95	4.59	3.31	3.09	7.72
Al ₂ O ₃	0.00	0.00	0.00	0.00	0.03	0.00	0.14	0.10
SiO ₂	6.16	3.91	3.84	4.21	4.14	4.25	4.46	2.97
Y ₂ O ₃	-	-	-	-	-	-	-	-
Ce ₂ O ₃	0.02	0.00	0.00	0.00	0.00	0.00	0.00	0.01
Total	88.14	92.63	85.49	90.13	90.45	90.13	89.36	94.38

Table 49: Chemical composition of uraninite and brannerite from the Mitukuluku occurrence analyzed by electron microprobe

Sample	7703-29	7703-29	7703-29	7703-29	7703-29	7703-29	7703-29	7703-29
Analysis n°	1	1'	2	2'	c1-3	c1-1	c5-1	c7-1
Mineral	Ur	Ur	Ur	Ur	Br	Br	Br	Br
Location	Mitukuluku	Mitukuluku	Mitukuluku	Mitukuluku	Mitukuluku	Mitukuluku	Mitukuluku	Mitukuluku
Oxides / wt. %								
UO ₂	87.13	85.83	87.32	87.03	53.52	52.42	52.89	52.97
PbO	6.34	6.67	6.25	7.02	0.00	0.00	0.00	0.00
ThO ₂	0.12	0.22	0.09	0.15	0.39	0.34	0.35	0.00
CaO	4.63	5.09	4.57	4.35	2.25	2.06	2.94	2.44
TiO ₂	-	-	-	-	25.56	27.53	26.33	28.74
FeO	0.00	0.12	0.00	0.10	0.72	1.05	1.20	0.65
Al ₂ O ₃	0.00	0.00	0.00	0.00	0.44	0.56	1.62	0.47
SiO ₂	0.11	0.09	0.09	0.04	6.58	4.11	2.94	3.55
Y ₂ O ₃	0.68	0.67	0.66	0.60	-	-	-	-
Ce ₂ O ₃	-	-	-	-	0.01	0.00	0.00	0.02
Total	99.01	98.69	98.98	99.29	89.47	88.07	88.27	88.84

Table 50: Results of microthermometry for type-I fluid inclusions of the Lolwa and Mitukuluku occurrences

Type I	a_{vap} (25 °C)	Microthermometry / °C				
		$T_{\text{m,ant}}$	$T_{\text{m,sin}}$	$T_{\text{m,H}}$	$T_{\text{L+V} \rightarrow \text{L}}$	Phase transition
<i>Lolwa</i>	3 to 15	14.4 to 27.9	121 to 165	148 to 345	100 to >350	L+V→L or L+H→L
Mode	7	26.5	151	325	>350	
n	59	29	29	7	31	
<i>Mitukuluku</i>	4 to 9	19.2 to 26.6	98 to 142	249 to 299	127 to 198	L+H→L
Mode	7	25.5	125	270	155	
n	10	10	8	7	8	

Table 51: Results of microthermometry for type-IIA fluid inclusions of the Lolwa occurrence

Type IIA	a_{vap} (25 °C)	Microthermometry / °C						
		T_{in}	$T_{\text{m,HH}}$	$T_{\text{m,car}}$	$T_{\text{L,car}}$	Phase transition	$T_{\text{m,H}}$	$T_{\text{L+car} \rightarrow \text{L}}$
<i>Lolwa</i>	11 to 33	-68.5 to -62.9	-18.7 to -13.5	-57.6 to -56.6	28.3 to 31.1	$\text{L}_{\text{car}} + \text{V}_{\text{car}} \rightarrow \text{L}_{\text{car}}$	200 to >350	>233
Mode	24	-65.4	-16.5	-56.7	31.1		>350	>350
n	49	18	13	15	43		22	25

Table 52: Results of microthermometry for type-IIB fluid inclusions of the Lolwa and Mitukuluku occurrences

Type IIB	a_{vap} (25°C)	Microthermometry /°C			
		T_{mcar}	T_{icar}	Phase transition	$T_{\text{L+car} \rightarrow \text{car}}$
<i>Lolwa</i>	73 to 100	-56.4 to -55.9	-10.1 to +0.2	$L_{\text{car}}+V_{\text{car}} \rightarrow L_{\text{car}}$	172 to 254
Mode	100	-56.0	-9.5		254
n	37	26	26		8
<i>Mitukuluku</i>	84 to 100	-56.7 to -56.1	0.4 to 19.6	$L_{\text{car}}+V_{\text{car}} \rightarrow L_{\text{car}}$	278 to 307
Mode	100	-56.2	19.5		Undefined
n	16	16	16		3

Table 53: Results of microthermometry for type-III fluid inclusions of the Lolwa and Mitukuluku occurrences

Type III	a_{vap} (25°C)	Microthermometry /°C		
		T_{fm}	T_{mice}	$T_{\text{L+V} \rightarrow \text{L}}$
<i>Lolwa</i>	0 or 6 to 19	-59.0 to -51.7	-13.3 to -6.7	68 to 188
Mode	9	-55.2	-11.0	110
n	40	17	30	14
<i>Mitukuluku</i>	0 or 4 to 7	-55.5 to -52.6	-8.7 to -4.4	139 to 176
Mode	4	-53.5	-7.0	Undefined
n	3	5	10	3

Table 54: Results of Raman spectroscopy for all fluid inclusions of the Lolwa and Mitukuluku occurrences

Type I	CO ₂	CO	N ₂	H ₂	O ₂
<i>Lolwa</i>	0.0	0.0	58.5 to 100	0.0 to 41.5	0.0
Mode	0.0	0.0	100	0.0	0.0
n	27	27	27	27	27
<i>Mitukuluku</i>	0.0	0.0	45.8 to 60.8	39.2 to 54.2	0.0
Mode	0.0	0.0	55	45	0.0
n	5	5	5	5	5
Type IIA					
<i>Lolwa</i>	89.7 to 100	0.0 to 10.3	0.0	0.0	0.0
Mode	100	0.0	0.0	0.0	0.0
n	17	17	17	17	17
Type IIB					
<i>Lolwa</i>	98.5 to 100	0.0 to 1.5	0.0	0.0	0.0
Mode	100	0.0	0.0	0.0	0.0
n	12	12	12	12	12
<i>Mitukuluku</i>	98.2 to 99.8	0.0 to 1.3	0.1 to 0.8	0.0	0.0
Mode	98.8	0.5	0.7	0.0	0.0
n	7	7	7	7	7
Type III					
<i>Lolwa</i>	0.0	0.0	0.0 to 5.5	0.0 to 4.0	93.7 to 100
Mode	0.0	0.0	0.0	1.0	99.0
n	10	10	10	10	10
<i>Mitukuluku</i>	0.0	0.0	0.0 to 7.1	0.0 to 21.3	78.7 to 99.9
Mode	0.0	0.0	Undefined	Undefined	Undefined
n	3	3	3	3	3

Table 55: Chemical compositions obtained by LA-ICPMS of 20 fluid inclusions from the Lolwa and Mitukuluku occurrences. The element concentration for each fluid inclusion is expressed in $\mu\text{g.g}^{-1}$ and as molar ratios

N°FI	Ca	Na	K	Mg	Ba	Sr	Cu	Ti	U	Mo	Na/Ca	Na/K
<i>Lolwa</i>												
3.25	110 000	80 000	73 000	6 800	1 800	5 100	22 000	1 700	570	10	0.74	1.10
3.22(1)	130 000	73 000	70 000	14 000	6 500	10 000	6 700	210	1	5	0.56	1.04
3.22(2)	140 000	43 000	95 000	6 900	23 000	16 000	11 000	840	50	25	0.30	0.45
3.21	130 000	65 000	74 000	11 000	37 000	15 000	6 300	680	10	15	0.51	0.87
3.19	160 000	23 000	130 000	1 300	23 000	21 000	7 600	60	1	1	0.14	0.17
3.18	100 000	70 000	110 000	7 800	17 000	12 000	15 000	390	10	10	0.68	0.65
3.11	110 000	91 000	76 000	3 600	32 000	11 000	6 700	1 100	5	15	0.85	1.20
3.8	120 000	84 000	86 000	3 900	25 000	10 000	6 900	290	5	5	0.68	0.97
3.7	110 000	100 000	19 000	15 000	22 000	11 000	8 100	1 400	10	20	0.97	5.59
3.31.2	110 000	31 000	66 000	51 000	26 000	35 000	1 300	640	200	10	0.29	0.47
<i>Mitukuluku</i>												
3.4	160 000	36 000	63 000	20 000	16 000	15 000	680	260	10	5	0.23	0.57
1.1	170 000	39 000	66 000	6 600	9 500	12 000	2 300	980	40	15	0.22	0.59
1.1(2)	120 000	52 000	16 000	22 000	1 700	6 000	480	380	30	35	0.43	3.15
1.2	110 000	61 000	87 000	22 000	16 000	12 000	1 400	1 300	40	20	0.55	0.70
1.4	130 000	90 000	52 000	6 600	13 000	16 000	970	140	10	30	0.67	1.75
1.4(2)	120 000	88 000	55 000	13 000	10 000	11 000	940	710	5	20	0.73	1.62
6.1	120 000	42 000	59 000	29 000	9 200	8 900	2 300	490	50	30	0.34	0.71
6.1(1)	170 000	20 000	47 000	28 000	11 000	12 000	1 700	300	150	20	0.12	0.43
6.2	120 000	100 000	36 000	14 000	6 400	9 600	1 000	480	20	-	0.84	2.88
6.3	170 000	32 000	58 000	18 000	10 000	12 000	680	1 000	40	60	0.19	0.55
Average	130 000	61 000	67 000	15 000	16 000	13 000	5 200	670	65	20	-	-
S.D.	22 000	26 000	27 000	11 000	9 500	6 100	5 500	450	130	15	-	-
Mode	130 000	40 000	70 000	10 000	10 000	15 000	1 000	300	20	25	-	-

CHAPITRE 7: Uranium mobilization by fluids associated with Ca-Na metasomatism: a P-T-t record of fluid-rock interactions during Pan-African metamorphism (Western Zambian Copperbelt)

Aurélien Eglinger¹ ; Alexandre Tarantola¹ ; Cyril Durand² ; Clément Ferraina¹ ; Olivier Vanderhaeghe¹ ; Anne-Sylvie André-Mayer¹ ; Jean-Louis Paquette³ ; Etienne Deloule⁴

Article soumis à Chemical Geology

¹GeoRessources, UMR 7359, CNRS-CREGU-Université de Lorraine, Nancy, France;

²Géosystèmes, UMR 8217, Université de Lille 1, Lille, France;

³Laboratoire Magmas et Volcans, UMR 6524, Université Blaise Pascal, Clermont-Ferrand, France;

⁴CRPG, UMR 7358 CNRS-Université de Lorraine, Nancy, France

Abstract

Several uranium occurrences, hosted by Neoproterozoic kyanite±talc micaschists, interpreted as metamorphosed evaporites, are known in the Western Zambian Copperbelt (Domes region, Zambia). These evaporitic rocks are considered as part of an epicontinental sequence, known as the Katanga Supergroup, deposited during the Rodinia dislocation between 880 and 820 Ma. During the Pan-African orogeny at ca. 550-530 Ma, the Katanga sequence has been metamorphosed in the Upper Amphibolite facies. Owing to their high chlorinity, metamorphic fluids derived from these evaporitic units have the potential to transport significant amounts of metals including uranium. This study is focused on the Solwezi dome in the Western Zambian Copperbelt, where two distinct uranium mineralizing stages are described from continental tectonic accretion to exhumation of the metamorphic host rocks.

We identify a first mineralizing event (uraninite+brannerite) dated between ca. 555 and ca. 525 Ma, contemporaneous to continental collision and related to $\text{CaCl}_2\text{-NaCl-KCl-(MgCl}_2\text{)-H}_2\text{O}$ metamorphic brines. These fluids were trapped at minimal P - T conditions of 460 MPa and 500 °C, in the ductile domain. The epidote-apatite assemblage observed at the regional scale reflects fluid-rock interactions related to these fluid circulations. The second mineralizing event (brannerite) dated between ca. 515 and ca. 450 Ma occurred during the high grade metamorphic rocks exhumation and is related to $\text{NaCl-CaCl}_2\text{-H}_2\text{O-CO}_2$ metamorphic fluids. These fluids were trapped at the ductile/brittle transition at 150 to 260 MPa and 200 to 300 °C. The regional scapolitisation is attributed to these late fluid circulations. These fluid-rock interactions, described at the regional scale, are also characterized at the mineral scale. Mass balance calculation indicates that monazite and allanite alteration, assisted by CaCl_2 -rich fluids, may liberate respectively ca. 1400 and ca. 2000 t U.km^{-3} of migmatitic gneiss, a non-negligible uranium source for these Pan-African synmetamorphic uranium mineralizations.

Keywords: Uranium, Monazite, Scapolite, Lufilian belt, Gondwana

1. Introduction

In metamorphic terrains, fluid circulations and associated fluid-rock interactions may be recorded by mineral assemblages and fluid inclusions (Ague, 1994a, b, 1997). The involved geological processes, metamorphism and/or metasomatism, are both expressed by fluid inclusions and the re-equilibration of mineral assemblages as a response to the evolution of pressure, temperature and/or chemical environment (Wood and Walther, 1983; Walther and Wood, 1984; Putnis, 2009; Putnis and Austrheim, 2010). Fluid flow and mass transport play fundamental roles in both metamorphism and metasomatism (Etheridge et al., 1983; Philpotts and Ague, 2009) which are defined as mass transfer processes occurring in chemically closed or open system, respectively (Carmichael, 1969; Putnis and Austrheim, 2010). Both processes involve dissolution-precipitation along mineral grain boundaries that correspond to the reaction interface (Putnis and Austrheim, 2010). During prograde *P-T* paths, metamorphic fluids are produced by devolatilization reactions such as dehydration and/or decarbonation and these fluids are then possibly agents of metasomatism at the mineral to rock scale (Chinner, 1967; Yardley and Baltatzis, 1985; Ferry, 1992; Ague, 1994a, b, 1997; Oliver et al., 1998). It has been proposed that there is a correlation between the nature of the protolith and the salinity of metamorphic fluids in metasediments (Yardley and Graham, 2002). For example, Yardley (2012) suggests that the presence of very saline metamorphic fluids (metamorphic brines) is to be related to the original presence of evaporites in the continental platform sediment sequences. In these environments, the observed high content of salt is explained by (i) the increase of salt content in the fluid phase by dissolution of evaporitic minerals (e.g. halite) at elevated temperatures, and/or (ii) the decrease of water in the fluid phase by the consumption of water to form hydrous minerals involving a passive concentration of salts (Yardley, 2012).

Metamorphic highly saline fluids are able to leach and transport significant amounts of metals (Yardley, 2005) that may, under specific conditions, be deposited to form an economic ore body (Pohl, 1992; Bakker and Foster, 1993; Spry et al., 2000). A few number of uranium deposits are related to metamorphosed evaporite-bearing sequences and to the circulation of these metamorphic brines, involving sometimes a regional metasomatism. For example, uranium deposits are described in the Mary Kathleen Fold Belt of Queensland (Australia) in a

metasedimentary sequence overprinted by large-scale sodic metasomatism involving scapolitisation and albitisation (Ramsay and Davidson, 1970; Oliver et al., 1992). The generation of these highly saline metamorphic brines has been attributed to regional metamorphism of marine carbonates, up to the Amphibolite grade (Oliver and Wall, 1987). In the Mistamisk Valley of the Labrador Trough (Canada), uraninite-albite veins within metamorphosed argillite are described and their presence is explained to be related with highly saline metamorphic fluids (Kish and Cuney, 1981). The generation of the fluids, containing halite and Ca^{2+} - Mg^{2+} cations, has been related to metamorphism of sodic schists of a presumably evaporitic origin during the Hudsonian Orogeny (Kish and Cuney, 1981). Cuney (2009) concluded that the most favorable conditions for synmetamorphic uranium mineralizations correspond to the metamorphism of epicontinental platform sediments during which highly saline and oxidized Na-Ca-rich fluids are generated. Indeed, uranium solubility (U^{6+}) is generally enhanced with increasing concentrations of chloride ions as well as phosphate, bicarbonate, sulfate and fluoride (Pearson, 1968; Langmuir, 1978; Keppler and Wylie, 1990; Cuney, 2009; Hazen et al., 2009; Skirrow, 2009). For example, in the Athabasca basin, Na-rich brines have percolated the Precambrian basement considered as a potentially important uranium source for the U unconformity-related deposits (e.g. Athabasca and Kombolgie basins; Hecht and Cuney, 2000; Derome et al., 2003, 2007; Richard et al., 2010, 2013). These large-scale circulations of brines at the basement/cover interface may result in intense alteration of U-bearing accessory minerals such as monazite, allanite or zircon hosted by felsic rocks or detrital sedimentary sequences.

The Lufilian belt formed during the Pan-African orogeny as a result of the collision between the Congo and Kalahari cratons that led to the formation of the Gondwana supercontinent (Fig. 1; Unrug, 1983). In addition to numerous Cu-Co deposits (Cailteux et al., 2005), several uranium deposits are described in this orogenic belt involving three successive uranium mineralizing events at (i) 652.3 ± 7.8 Ma (Decrée et al., 2011) related to late diagenetic hydrothermal aqueous highly saline fluid circulations (Audeoud, 1982), identified in rocks from the External fold-and-thrust belt of the Lufilian belt (Eglinger et al., 2013), (ii) 530.1 ± 5.9 Ma (Decrée et al., 2011), connected to aqueous hypersaline metamorphic fluid circulations, recognized in both the External fold-and-thrust belt and the Domes region (Eglinger et al., 2013, in press) and (iii) 503 ± 15 Ma

(Darnley et al., 1961) related to late aquo-carbonic metamorphic fluid circulations, documented only in the Domes region (Torrealdy et al., 2000; Eglinger et al., 2013, in press).

This paper focuses on the two stages of uranium mineralizations dated at ca. 530 and ca. 500 Ma and described in the Domes region of the Lufilian belt. These two last mineralizing events have been identified in the kyanite±talc micaschists, interpreted as Pan-African metamorphosed evaporites (Cosi et al., 1992). Eglinger et al. (2013, in press) further described these synmetamorphic uranium mineralizations in Lolwa (Kabompo dome) and in Mitukuluku (Solwezi dome) occurrences. The combination of petrography and geochemical signature of uranium oxides with fluid inclusion analyses yields to the distinction of (i) a first mineralization stage coeval with the development of the ductile fabric of the quartz veins and of the host kyanite±talc micaschists, and (ii) a second one postdating ductile deformation. Accordingly, this area is an ideal place to understand the links between evaporite-bearing metasediments, metamorphic brines and uranium mass transfer. With this objective, rocks from both main litho-tectonic units were sampled: kyanite micaschists (metamorphosed evaporites) mantling the dome-shaped structure and gneissic-migmatitic rocks exhumed in the core of this dome-shaped structure. Our strategy is to (i) characterize the mineralogy and re-equilibration mineral assemblages resulting from fluid-rock interactions, (ii) determine the *P-T* conditions recorded by these metamorphic fluid circulations using fluid geochemistry and mineral assemblages, (iii) provide time constraints on these ore fluid circulations by U-Pb SIMS dating of uraninite and by U-Pb-Th LA-ICPMS dating of monazite and (iv) discuss the uranium transport during this metamorphic event by mass balance calculation.

2. Regional geology

The Lufilian belt is located between the Congo and Kalahari cratons and forms an arc marking the transition from the Damara belt in Namibia and the Zambezi belt in Zimbabwe (Unrug, 1983). The external zone of the Lufilian belt is characterized by a Neoproterozoic metasedimentary sequence, the Katanga Supergroup, composed from bottom to top by the Roan, Nguba and Kundelungu Groups presumably deposited on top of a pre-Katanga basement (Porada and Berhorst, 2000). This sedimentary sequence of the external zone is affected by folds and

thrusts (Figure 68) and low grade metamorphism up to lower Greenschist facies (François, 1974). This external zone is referred to as the External fold-and-thrust belt in the literature (De Swardt and Drysdal, 1964) and this style of deformation is illustrated by the anticlinal axes in Figure 68. The internal zone of the Lufilian belt, comprising the Domes region, is marked by a higher metamorphic grade ranging from upper Greenschist to upper Amphibolite facies affecting a complexly folded nappe pile made of metasedimentary rocks interleaved with migmatitic gneisses (Mendelsohn, 1961; Cosi et al., 1992; Porada and Berhorst, 2000; John et al., 2004). In the Domes region, regional scale lithological contacts and outcrop pattern are controlled by low-amplitude dome-shaped structures.

2.1. Lithostratigraphy of the Katanga Supergroup in the internal and external zones of the Lufilian belt

The lithostratigraphy of the Katanga Supergroup has been mainly reconstructed in the External fold-and-thrust belt taking advantage of better outcrop conditions and of a large number of drilled cores and open pits. Moreover, the Katanga sequence was affected by a low metamorphic grade (Kampunzu and Cailteux, 1999), allowing a better preservation of original petrographic features. In the Domes region, in reason of the lack of outcrops and of a more intense deformation and metamorphic grade, the reconstruction of the stratigraphy is more speculative. However the Katanga sequence is thought to be generally similar to the External fold-and-thrust belt (Cailteux et al., 1983; Cosi et al., 1992). The nappe pile of the Domes region is composed of both gneissic-migmatitic layers interpreted as part of the pre-Katanga basement and of metasedimentary sheets attributed to the Katanga Supergroup (Cosi et al., 1992).

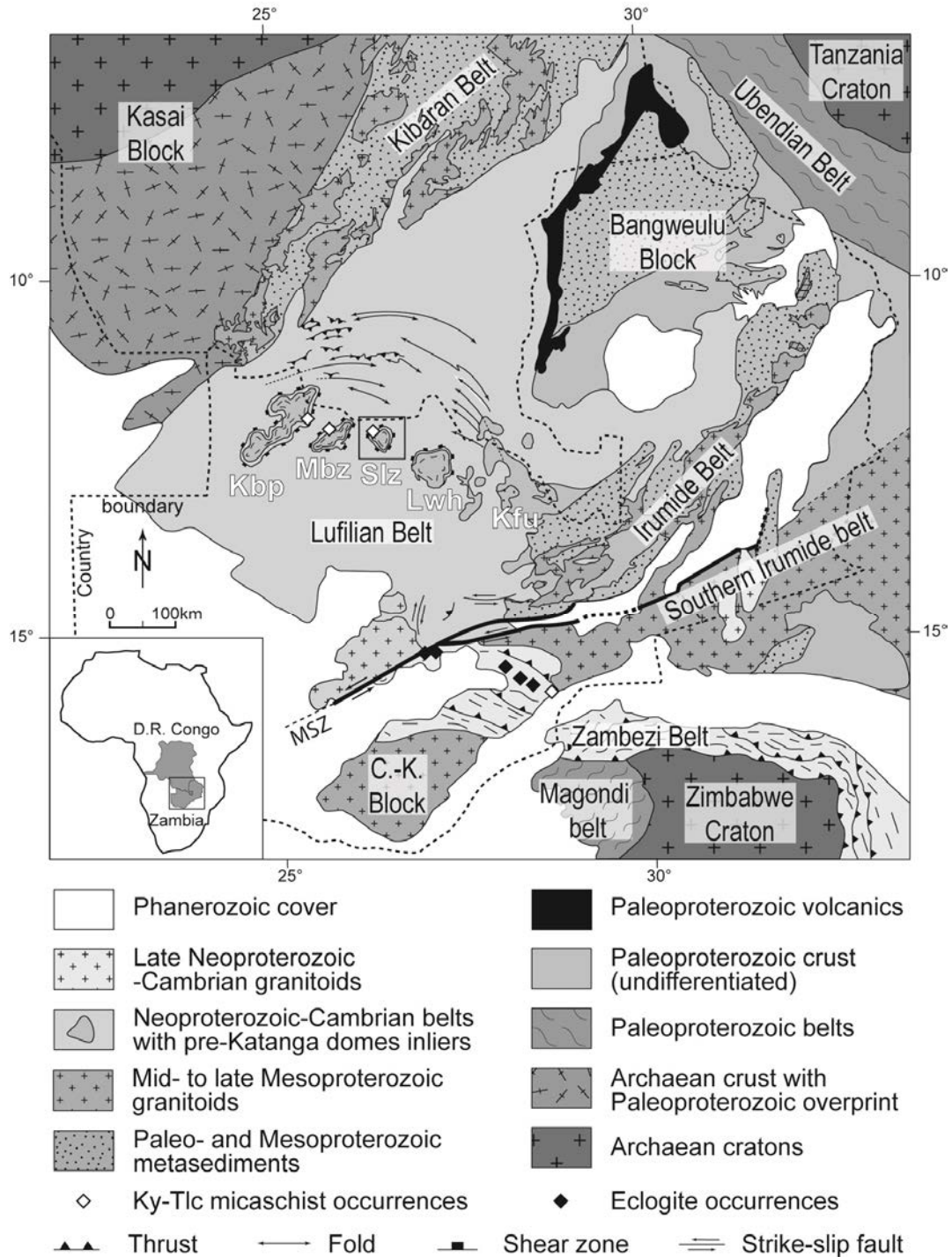


Figure 68: Geological map of the Pan-African Lufilian belt indicating the main structural trends (modified after De Waele et al., 2008; Eglinger et al., 2013). Abbreviations: Kbp = Kabompo dome; Mbz = Mwombeshi dome; Slz = Solwezi dome; Lwh = Luiswishi dome; Kfu = Kafue Anticline; C.-K. = Choma Kalomo block; MSZ = Mwembeshi Shear Zone; Ky = Kyanite; Tlc = Talc. The black rectangle represents the study area enlarged in Figure 69b.

The basal unit of the Neoproterozoic to early Paleozoic Katanga Supergroup is designed as the Roan Group. It is well-known in the External fold-and-thrust belt (Katanga Copperbelt) and is composed, from bottom to top by (i) a siliciclastic unit (Mindola Subgroup), (ii) a carbonate/siliciclastic unit (Kitwe Subgroup), (iii) a carbonate unit (Bancroft Subgroup; Cailteux, 1983, 1994; Selley et al., 2005; Bull et al., 2011) and (iv) a shale unit (Mwashya Subgroup; Hitzman et al., 2012). The Roan Group is moreover characterized by many evaporitic levels (Figure 69a) showing sedimentary features typical of sabkhas, such as pseudomorphs after gypsum and anhydrite (Porada and Berhorst, 2000; Muchez et al., 2008). In the Domes region, a unit of quartzite, marble and micaschist is attributed to the Roan Group (Cosi et al., 1992). These rocks preserved relics of sedimentary structures such as fluvial channels and cross-bedding stratification. A distinct kyanite micaschist layer marks the transition between the gneissic-migmatitic core (basement rocks) of the domes and their metasedimentary mantle (cover rocks). This particularly Mg-rich layer (as evidenced by the presence of phlogopite, talc and clinocllore) has been interpreted as a metamorphosed equivalent of the evaporites of the Roan Group (Cosi et al., 1992). Overall, the sedimentary sequence of the Roan Group is interpreted to represent a continental platform deposit associated with a passive margin (Porada and Berhorst, 2000). In this context, Mg-rich evaporites would represent continental to lagoonal-evaporitic deposits (Cosi et al. 1992). The onset of continental rifting is marked in the Lufilian belt by the emplacement of the Nchanga granite dated at 883 ± 10 Ma by U-Pb on zircon (Figure 69a; Armstrong et al., 2005). Some detrital zircon grains found within cross-bedded Lower Roan quartzite and dated at ca. 880 Ma (Armstrong et al., 2005), confirm the emplacement of the Roan detrital sediments just after the uplift and erosion of the Nchanga magmatic rocks.

At the top of the Upper Roan Group, the Mwashya Subgroup shows lateral variations of facies. It is characterized by coarse clastics in the External fold-and-thrust belt but it is dominated by black shales associated with volcanics in the Domes region (Mendelsohn, 1961; Cailteux, 1994; Marjonen, 2000). The Mwashya Subgroup is interpreted to record the opening of a Neoproterozoic oceanic basin as constrained by the age of the Luakela volcanics, in NW Zambia, dated at 765 ± 5 Ma (Figure 69a) by U-Pb on magmatic zircon (Kampunzu et al., 2000; Porada and Berhorst, 2000; Key et al., 2001). The top of the Katanga Supergroup is marked by the Nguba and Kundelungu Group dominated by carbonates and sandstone-siltstone-mudstone

alternations (Figure 69a) that are well-described in the External fold-and-thrust belt (Batumike et al., 2006) but are poorly known in the Domes region. The Bianco Subgroup, forming the upper part of the Kundelungu Group, is composed of clastic sediments that are not metamorphosed and represent the youngest unit of the Katanga Supergroup with a maximum age of 573 ± 5 Ma (Figure 69a), constrained by ^{40}Ar - ^{39}Ar on detrital muscovite grains (Master et al., 2005). It is interpreted as a foreland basin deposit (Master et al., 2005).

2.2. Tectonic evolution of the Lufilian belt

The tectonic evolution of the Lufilian belt is constrained by the evolution of sedimentary deposits and deformation into a fold and thrust belt in the external zone, and by the structural and metamorphic evolution of the nappe pile in the Domes region. Rift basin opening (from 880 to 750 Ma; Porada and Berhorst, 2000; Barron et al., 2003) was followed by convergence (from 600 to 530 Ma) of the Congo and Kalahari cratons. Transition from divergent to convergent tectonic regime is recorded by Eclogite facies metamorphism, dated at ca. 595 Ma by Sm-Nd whole-rock and garnet isochron on mafic boudins in the Zambezi belt (John et al., 2003). Subduction of crustal units under a low geothermal gradient to form the accretionary orogenic belt is depicted by P - T estimates of phengite-bearing eclogites with temperatures of 720-755 °C at pressures between 20 and 28 kbar (John et al., 2003). Crustal tectonic accretion is followed by an increase of the geothermal gradient recorded by intermediate-pressure/intermediate-temperature conditions (Barrovian metamorphism) with a pressure around 13 ± 1 kbar and a temperature of 750 ± 25 °C dated at 529 ± 2 Ma, by U-Pb on monazite grains from kyanite-talc micaschist in the Kabompo, Mwombezi and Solwezi domes (Figure 68; John et al., 2004). ^{40}Ar - ^{39}Ar analyses thermochronology on biotite and Rb-Sr dating on muscovite and biotite yield ages ranging from 510 to 463 Ma that are interpreted to represent post-orogenic cooling of the metamorphic rocks in the Domes region of the Lufilian belt (Cosi et al., 1992; John et al., 2004; Rainaud et al., 2005).

2.3. *Synmetamorphic uranium mineralizations*

In the Domes region, uranium occurrences are mainly localized within the Lower Roan Group and are distributed over about 300 km from west to east (Meneghel, 1981), including the Mitukuluku, Dumbwa and Kimale occurrences in the Solwezi dome (Figure 69b).

In the Solwezi dome, the uranium mineralizations are mainly located in the shear zones marking the contact between the isoclinally folded metasedimentary rocks, equivalent of the Lower Roan Group, and the gneissic-migmatitic basement (Meneghel, 1981; Cosi et al., 1992; Figure 69b). Two successive uranium mineralization events were described as syn- to late-deformation and identified by fluid inclusion study in quartz veins hosted by the kyanite±talc micaschists (Eglinger et al., in press).

First syn-deformation stage is related to hypersaline metamorphic brines (Type-I) characterized by the H₂O-CaCl₂-NaCl system with the presence of (N₂-H₂)+calcium hydrates+halite±hematite±calcite. Type-I inclusions are deformed and found along quartz subgrain and grain boundaries suggesting an entrapment in the ductile domain during quartz recrystallization by grain boundary migration above 500 °C (Urai et al., 1986; Drury and Urai, 1990).

Second late-deformation stage is associated with the circulation of aquo-carbonic fluids (Type-II) characterized by the H₂O-NaCl-CaCl₂-CO₂ system with the presence of (CO)+halite±unidentified solid. Type-II inclusions are found in trails crosscutting subgrain boundaries. They trapped a fluid circulating at the ductile-brittle transition. The metastable composition of both fluids was attributed to internal (types-I and -II) radiolysis. The presence of dissolved uranium was confirmed by LA-ICPMS for the type-I where uranium content ranging between 1 to 570 ppm. A late fluid event (type-III) characterized by the H₂O-NaCl-CaCl₂ system with a salinity lower than both types-I and II was also described. Type-III fluid inclusion trails crosscut types-I and -II, indicating that the last event of fluid entrapment occurred at lower temperatures in the brittle domain of deformation. This fluid event did not play a role in uranium remobilization.

Uranium oxides are hosted by quartz-rich micaschists of upper Amphibolite facies characterized by the presence of kyanite, talc and phlogopite and designated as whiteschist by Meneghel (1981), Cosi et al. (1992) and John et al. (2004). Some uranium occurrences were described in quartz-carbonate-Cu sulfide undeformed veins crosscutting the Nguba Group in the Kansanshi open pit (Meneghel, 1981). U-Pb geochronology on uranium oxides yielded “a mean value for the $^{207}\text{U}/^{206}\text{U}$ ages of $536 \pm 12 \text{ Ma}$ ” (Swainbank in Meneghel, 1981) from the Kawanga, in Kabompo dome, and Dumbwa, in Solwezi dome (Figure 69b), occurrences. Ore mineralogy is characterized by uraninite $[\text{UO}_2]$ and brannerite $[\text{UTi}_2\text{O}_6]$ (Meneghel, 1981; Cosi et al., 1992; Eglinger et al., in press). Secondary hexavalent uranium minerals are autunite $[\text{Ca}(\text{UO}_2)_2(\text{PO}_4)_2 \cdot 10\text{-}12\text{H}_2\text{O}]$, torbernite $[\text{Cu}(\text{UO}_2)_2(\text{PO}_4)_2 \cdot 8\text{-}12\text{H}_2\text{O}]$, sabugalite $[\text{HAl}(\text{UO}_2)_4(\text{PO}_4)_4 \cdot 16\text{H}_2\text{O}]$ and gummite $[\text{UO}_3 \cdot n\text{H}_2\text{O}]$ (Meneghel, 1981).

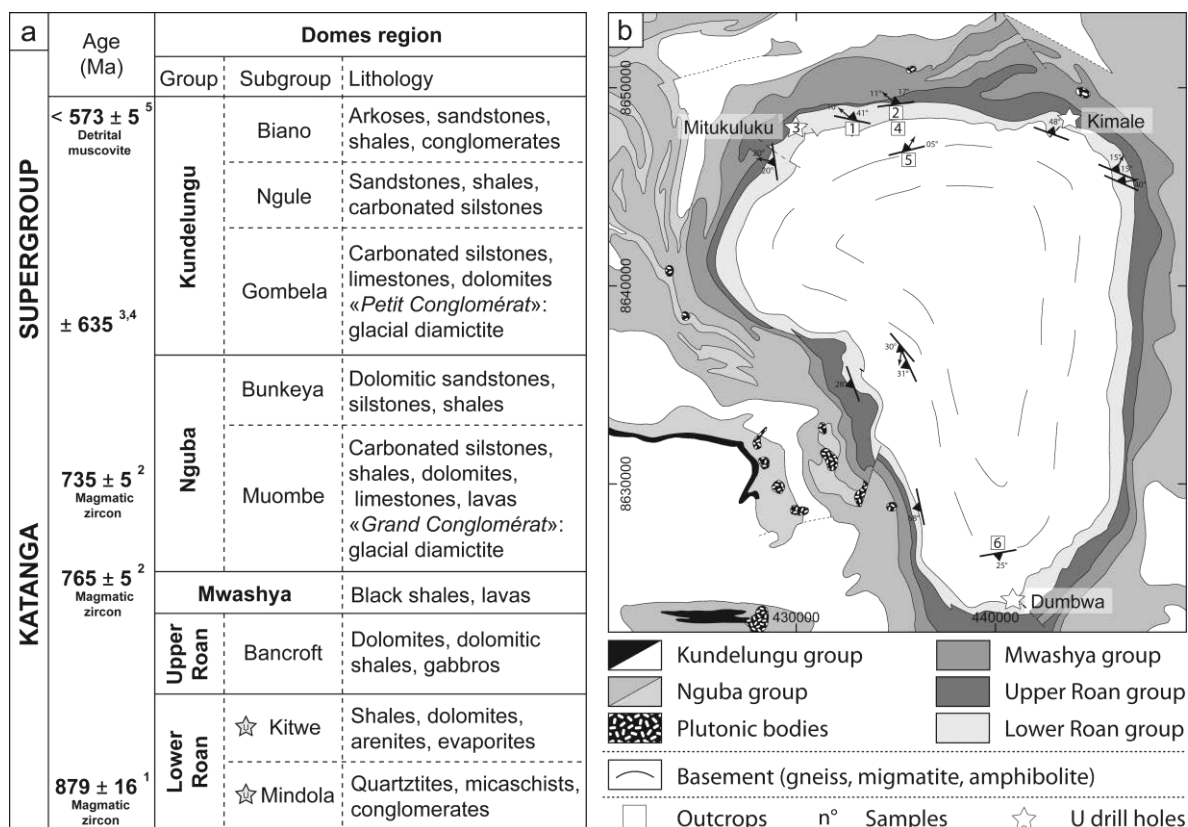


Figure 69: a: Lithostratigraphy of the Katanga Supergroup in the Domes region in Zambia (modified after Porada and Berhorst, 2000; Kampunzu et al., 2009). Uranium occurrences (stars) are found within the Lower Roan Group (modified after Meneghel, 1981; Cosi et al., 1992). Age constraints are provided by U-Pb geochronology on magmatic zircon grains of volcanic rocks (¹Hanson et al., 1994; ²Key et al., 2001), by stratigraphical correlations (³Robb et al., 2002; ⁴Condon et al., 2005) and by argon thermochronology on detrital grains (⁵Master et al., 2005). b:

Geological map of the Solwezi dome showing the sample localizations associated with the structural measurements (lineation and schistosity/foliation). Star symbols represent the uranium occurrences intersected by drilling. References to studied samples: n°1 = *ZM-10-07*; n°2 = *ZM-10-24*; n°3 = *7703-29*; n°4 = *ZM-10-09*; n°5 = *ZM-10-17*; n°6 = *ZM-10-62*. Details are found in Table 56.

3. Sampling and analytical procedures

3.1. Sampling

Five rock samples (*ZM-10-07*, *ZM-10-24*, *ZM-10-09*, *ZM-10-17* and *ZM-10-62*) were collected from outcrops during a field trip in the Solwezi area in 2011 and one sample (*7703-29*) from drill cores carried out during an exploration campaign for uranium between 1980 and 1986 by Agip-Cogema (Table 56; Cosi et al., 1992). The highest grade obtained in drill cores is observed at the Mitukuluku occurrence, with 1.4 wt. % U_3O_8 over a thickness of 9 m (Arthurs and Legg, 1974). The Solwezi dome is delineated by a kyanite=talc micaschist rim that is part of a metamorphic nappe with a protolith attributed to the Lower Roan Group (Figure 69a). Two kyanite micaschists (*ZM-10-07* and *ZM-10-24*) were sampled from outcrops in the north part of the Solwezi dome and one from the drill core (*7703-29*) from the Mitukuluku drilling occurrence, in the north-west part of the dome (Figure 69b). These kyanite micaschists comprise some conglomerates with layers of cross-bedded quartzite (Figure 70a, b). The core of the Solwezi dome is composed by gneissic and migmatitic rocks locally containing amphibolite units. Two gneissic rocks (*ZM-10-09* and *ZM-10-17*) were sampled in the northern part within the core of the Solwezi dome (Figure 69b; Figure 70c). These samples show flat-lying foliation outlined by variation in the proportions of quartz-feldspar and mica mineral phases. These rocks are characterized by the presence of centimetric feldspar clasts, transposed and recrystallized parallel to the rock foliation. These rocks present characteristics of augen gneiss and are interpreted as ortho-derived. One migmatitic sample, collected in the southern part within the core of the Solwezi dome, shows concordant leucosomes crosscut by different generations of granitic veins (*ZM-10-62*; Figure 69b; Figure 70d).

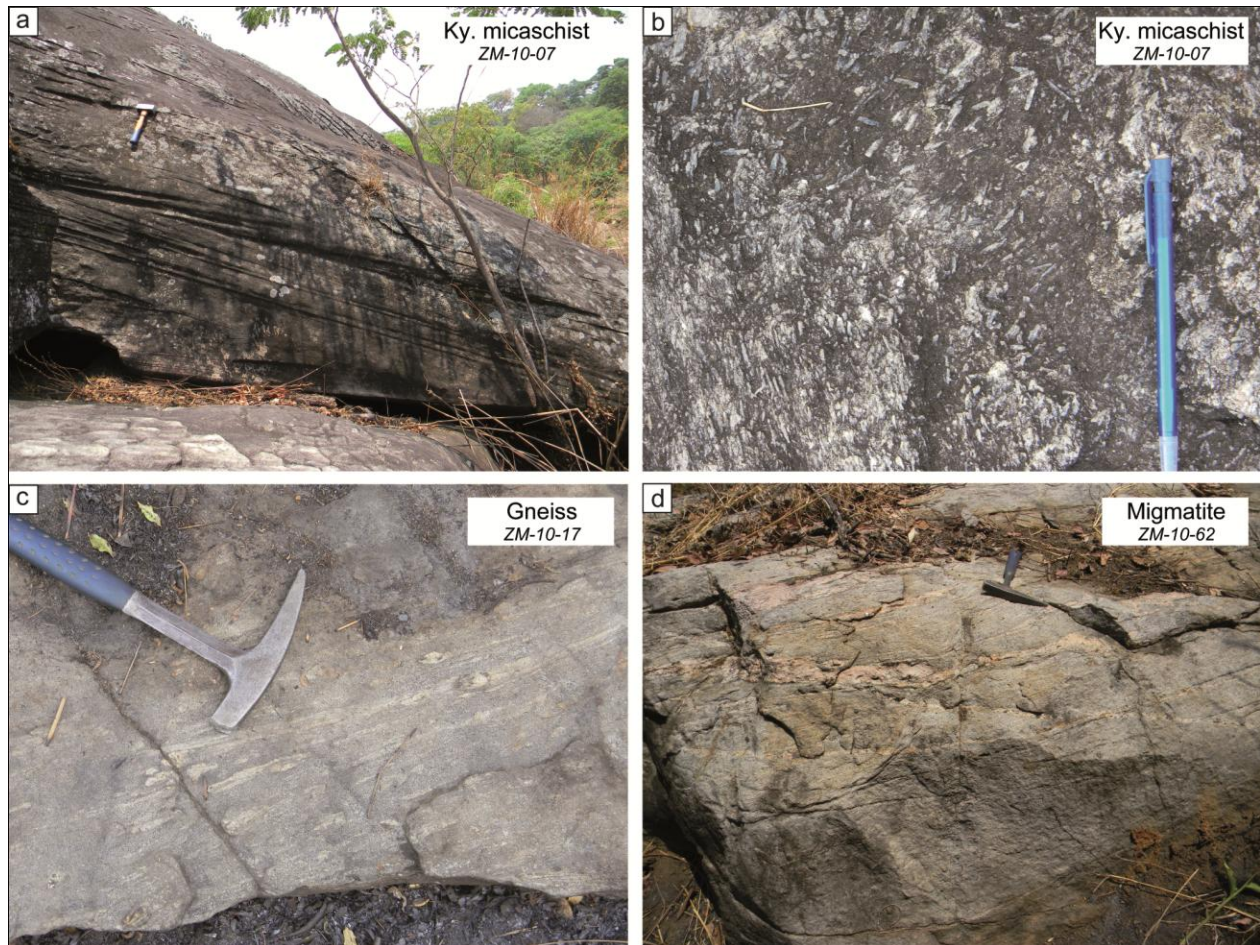


Figure 70: a: Parallel and cross-bedding structures in kyanite micaschist. b: Micaschist showing oriented kyanite porphyroblasts. c: Augen gneiss with recrystallized and transposed feldspar porphyroclasts. d: Migmatitic rock with concordant leucosome and discordant granitic veins.

3.2. *Electronic Microprobe*

Major and trace elements for silicates were obtained by the EMP method using a Cameca PC-controlled SX-100 (GeoRessources, Nancy). During analysis, an accelerating voltage of 15 kV, beam current of 12 nA and peak counting time of 10 to 20 s. Quantitative analysis and X-ray mapping of monazite were carried out using a Cameca PC-controlled SX-50 and -100 types (ENSCL, Lille and GeoRessources, Nancy). During analysis of major and trace elements, an accelerating voltage of 20 kV, beam current of 100 nA and peak counting time of 20 to 120 s. Compositional images were performed at 15 kV and 400 nA, using a stage scanning mode. The dwell time per pixel was set to 30 ms and the pixel step ranged from 0.3 to 0.9 μm . The selected X-ray lines were $\text{CaK}\alpha$, $\text{ThM}\alpha$, $\text{UM}\beta$ and $\text{YL}\alpha$.

3.3. Laser Ablation Inductively Coupled Plasma Mass Spectrometry (LA-ICPMS)

The U-Th-Pb geochronology of monazite was conducted by laser ablation inductively coupled plasma mass spectrometry (LA-ICPMS) at the Laboratoire Magmas et Volcans, Clermont-Ferrand (France). The analyses involve the ablation of minerals with a Resonetics Resolution M-50 laser system operating at a wavelength of 193 μm . Spot diameters of 11 μm associated with repetition rates of 1 Hz and laser fluency of 13 $\text{J}\cdot\text{cm}^{-2}$ were used. Detailed analytical conditions and reference material used for standardization are reported in Hurai et al. (2010, 2012) and Gasquet et al. (2010).

3.4. Ion microprobe

U-Pb isotopic composition was determined using a Cameca IMS1270 ion microprobe at the CRPG-CNRS laboratory (Nancy, France). An O_2^- primary beam with 23 kV incident energy (13 kV primary, 10 kV secondary) was used in defocused aperture illumination mode, producing a ~ 12 μm spot. In order to achieve a good reproducibility, each analysis was preceded by automated centering of the sample spot image in the field aperture (Schuhmacher et al., 2004) and of the magnetic field values by scanning the ^{206}Pb peak.

4. Petrography and geochemistry

In this section, both basal metasedimentary cover and migmatitic-gneissic basement rocks, outcropping in the Solwezi area, are described in order to characterize the different mineral assemblages and accessory minerals.

4.1. Base of the metasedimentary cover of the Solwezi dome: the Lower Roan Group

The basal unit of the Lower Roan Group is represented by a kyanite micaschist showing a grano-lepidoblastic texture with C/S fabric (Figure 71a, b, c) underlined by micas and sigmoidal-shape kyanite porphyroblasts (Table 57). The matrix is dominated by quartz, rutile and hematite alternating with biotite layers that define the schistosity (S_{n+1}). Two generations of kyanite are observed. The first one is represented by poikiloblasts grains wrapped into the schistosity (S_{n+1})

and contains oriented inclusions of quartz and iron oxide, defining an inherited schistosity. These grains are interpreted as pre-tectonic (pre- S_{n+1}) porphyroblasts. The other generation is represented by sub-automorphous grains oriented parallel to the schistosity S_{n+1} . They are interpreted as syn-tectonic porphyroblasts. Biotite grains are typically phlogopite with X_{Mg} ranging from 0.889 to 0.959 with a TiO_2 content ranging from 0.53 to 0.76 wt.% (Table 58). Locally, talc crystals are observed and oriented parallel to the schistosity S_{n+1} . Monazite grains are mainly localized within the cleavage plane of phlogopite blasts marking the C/S fabric in sample *ZM-10-24* (Figure 71d), and mainly scattered in the matrix in sample *ZM-10-07*. Monazite grains are mostly sub-automorphous and do not show any features such as a rounded shape or percussion marks that would indicate a detrital origin. Accordingly, these crystals are interpreted to have grown *in-situ* during metamorphism. Syn- to post-tectonic chlorite porphyroblasts are also observed. Chlorite grains are chlinochlore with X_{Mg} ranging from 0.928 to 0.976. Kyanite crystals are partially replaced by muscovite recording an incipient destabilization during the retrograde $P-T$ path. Uranium oxides, observed in core sample 7703-29, are represented by uraninite and brannerite (Eglinger et al., 2013, submitted). Cogenetic uraninite and brannerite grains are wrapped into the kyanite-phlogopite-chlorite schistosity (Figure 71e) and are associated with chloro-apatite grains. These uranium oxides are interpreted as syn-tectonic porphyroblasts (Eglinger et al., 2013, submitted). Some brannerite grains superimposed over the schistosity (S_{n+1}) and are not associated with strain shadows. These grains are interpreted as post-tectonic porphyroblasts. Monazite chemical compositions are reported in Table 59 and Table 60. BSE images and Ca, Y and Th mapping of monazite grains are shown in Figure 72. Monazite grains from both samples (*ZM-10-07* and *ZM-10-24*) display similar composition variations and are represented by the most common species: monazite-(Ce). P_2O_5 (29.67 to 30.44 wt.%) contents are relatively homogeneous. REE, Y, Th and Ca contents vary from one grain to another (Ce_2O_3 : 25.69 to 32.09 wt.%, La_2O_3 : 12.94 to 17.65 wt.%, Y_2O_3 : 0.32 to 1.22 wt.%; ThO_2 : 0.14 to 6.98 wt.%; CaO: 0.23 to 1.38 wt.%; Table 60; Table 61). These monazite grains are strongly depleted in UO_2 (< 0.10 wt.%). X-ray maps show complex internal zoning patterns which correspond to distinct chemical domains, as shown by the Ca, Y and Th mapping (Figure 72). Th and Ca zonings are patchy and generally present a direct correlation. Y-zoning tends to mimic the Th and Ca zonings but there is a most marked tendency for Y to increase toward the rims of the monazite grains. Positive correlation between Ca and Th

concentrations is interpreted as the consequence of cation substitutions toward the brabantite (U, Pb, Th)Ca(PO₄)₂ end-member composition (Figure 73a; Rose, 1980). This cationic substitution involves the following exchange: $2\text{REE}^{3+} \Leftrightarrow \text{Th}^{4+} + \text{Ca}^{2+}$ (Poitrasson et al., 2000), as illustrated in Figure 73.

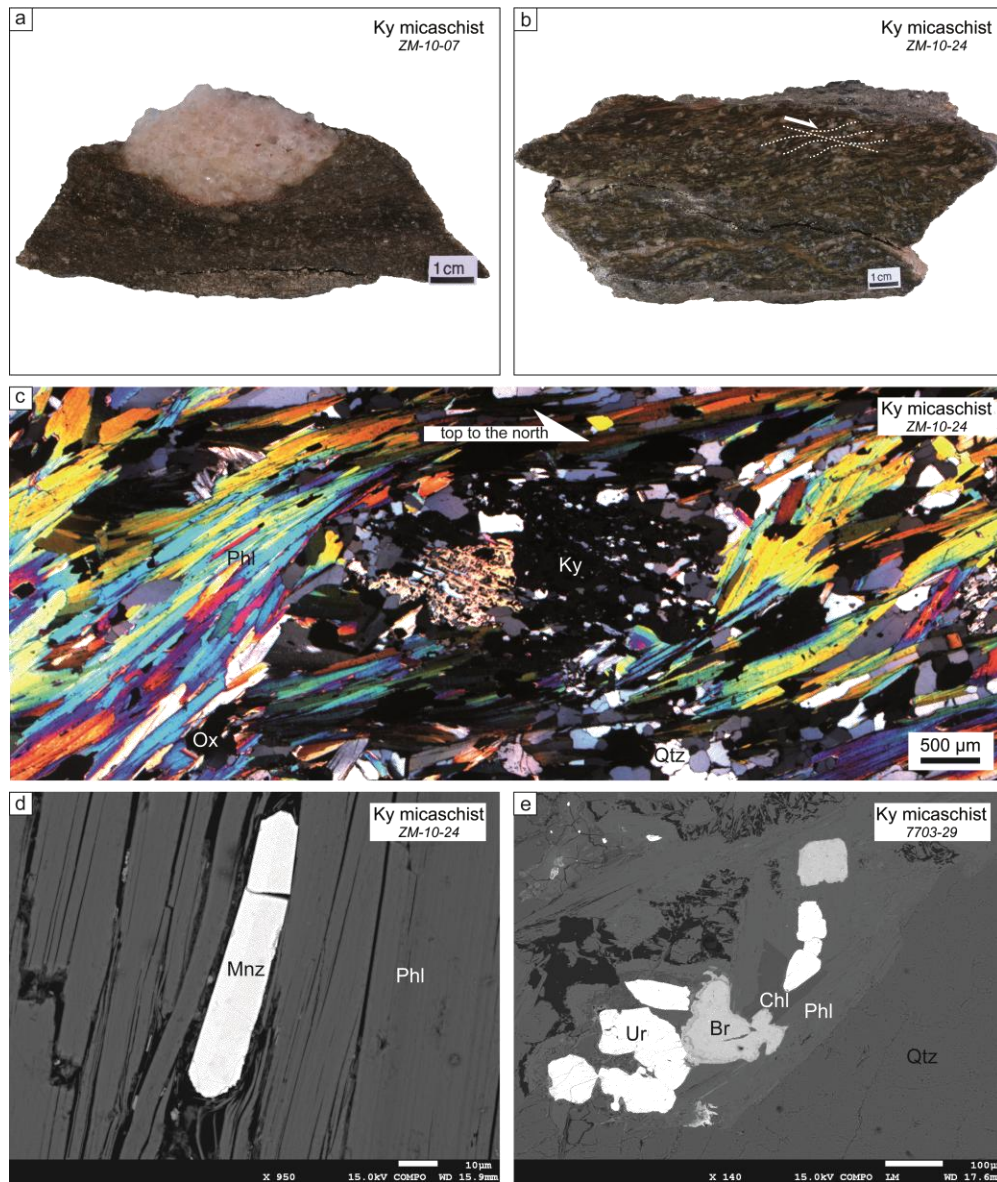


Figure 71: a: Kyanite micaschist with quartz pebble (sample *ZM-10-07*). b: Kyanite micaschist showing shear bands marked by phlogopite and sigmoidal schistosity (sample *ZM-10-24*). c: Kyanite poikiloblast grain wrapped into the schistosity and containing oriented inclusions of quartz and iron oxide, defining an inherited schistosity (sample *ZM-10-24*). d: Sub-automorphic metamorphic monazite within the cleavage plane of phlogopite blasts (sample *ZM-10-24*). e: Uraninite porphyroblasts with cogenetic brannerite grains within phlogopite-chlorite schistosity (sample 7703-29). Abbreviations: Br = Brannerite; Chl = Chlorite; Ky = Kyanite ; Mnz = Monazite; Phl = Phlogopite; Qtz = Quartz; Ur = Uraninite.

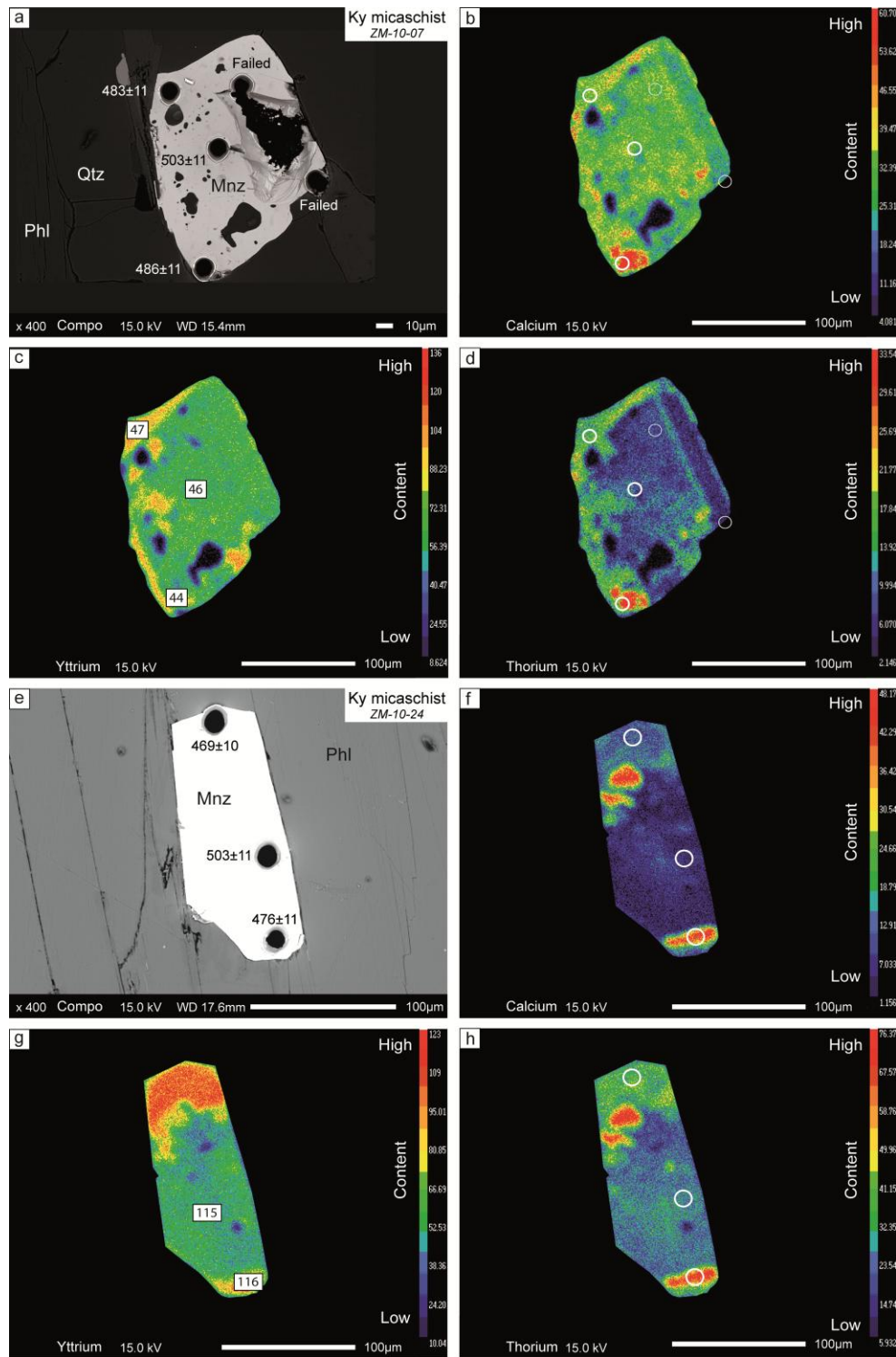


Figure 72: BSE images and X-ray maps of monazite from the Solwezi dome. Images a to d: monazite grain within Qtz-Phl matrix from sample *ZM-10-07*, and images e to h: monazite grain within phlogopite from sample *ZM-10-24*. BSE images show the location of ICPMS laser ablation pits (11 µm) and their corresponding ^{232}Th - ^{208}Pb ages (2σ level). Numbers shown on yttrium maps correspond to electronic microprobe analysis reported in Table 59 and Table 60. Abbreviations: Mnz = Monazite; Phl = Phlogopite; Qtz = Quartz.

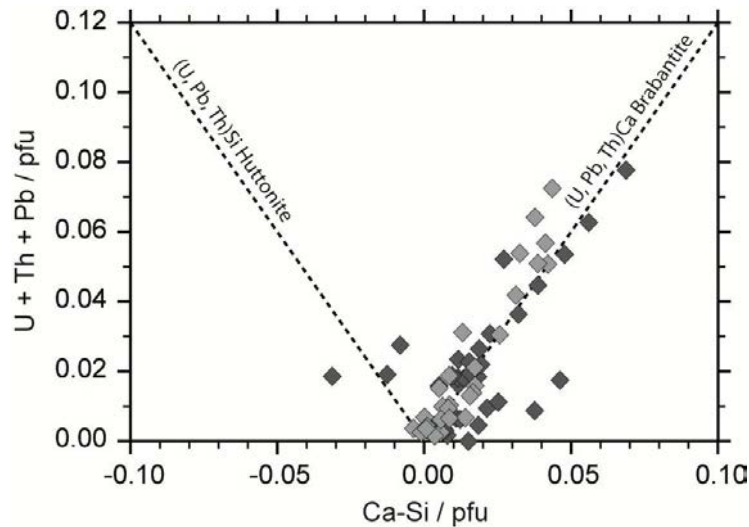


Figure 73: a: U + Th + Pb versus Ca-Si diagram (per formula for 4 oxygens) showing the relative proportions of brabantite and huttonite substitutions from the monazite end-members (dark grey diamonds => ZM-10-07 and light grey diamonds => ZM-10-24).

4.2. The pre-Katanga gneissic-migmatitic basement exposed in the core of the Solwezi dome

The core of the Solwezi dome is characterized by various lithologies comprising fine-grained gneisses (Figure 74a, b) partially migmatitic (Figure 74c, d), migmatites (Figure 70d) and amphibolites. In this section, we focus on felsic rocks represented by gneisses and migmatites. The gneiss formation (samples ZM-10-09 and ZM-10-17; Figure 69b; Figure 74a) is characterized by a primary quartz-plagioclase-biotite mineral assemblage. Locally, some quartz-feldspar leucosomes are observed. These leucosomes are boudinaged and/or folded, transposed to the syn-migmatitic-gneissic foliation (Figure 74c). These fine-grained gneisses have a granodioritic composition (Table 57). A late epidote-apatite-muscovite-scapolite assemblage is recognized. Epidote-apatite-muscovite crystals are mostly elongated and oriented parallel to the foliation and are interpreted as syn- to late-tectonic porphyroblasts. Scapolite forms large poikilitic crystals overprinting deformation microstructures (Figure 74a). Scapolite crystals contain some inclusions of epidote-apatite-muscovite and all matrix minerals (Figure 74b, d). This observation indicates that scapolite minerals formed after epidote-apatite-muscovite assemblage and are interpreted as post-tectonic porphyroblasts. Accessory minerals are represented by zircon, allanite and (Th, REE)-silicate. Alteration products of potential U-bearing

minerals are observed using BSE images on accessory minerals. The best example is the presence of metamict allanite grains which contain (REE, Th)-rich silicates (Figure 75a, b).

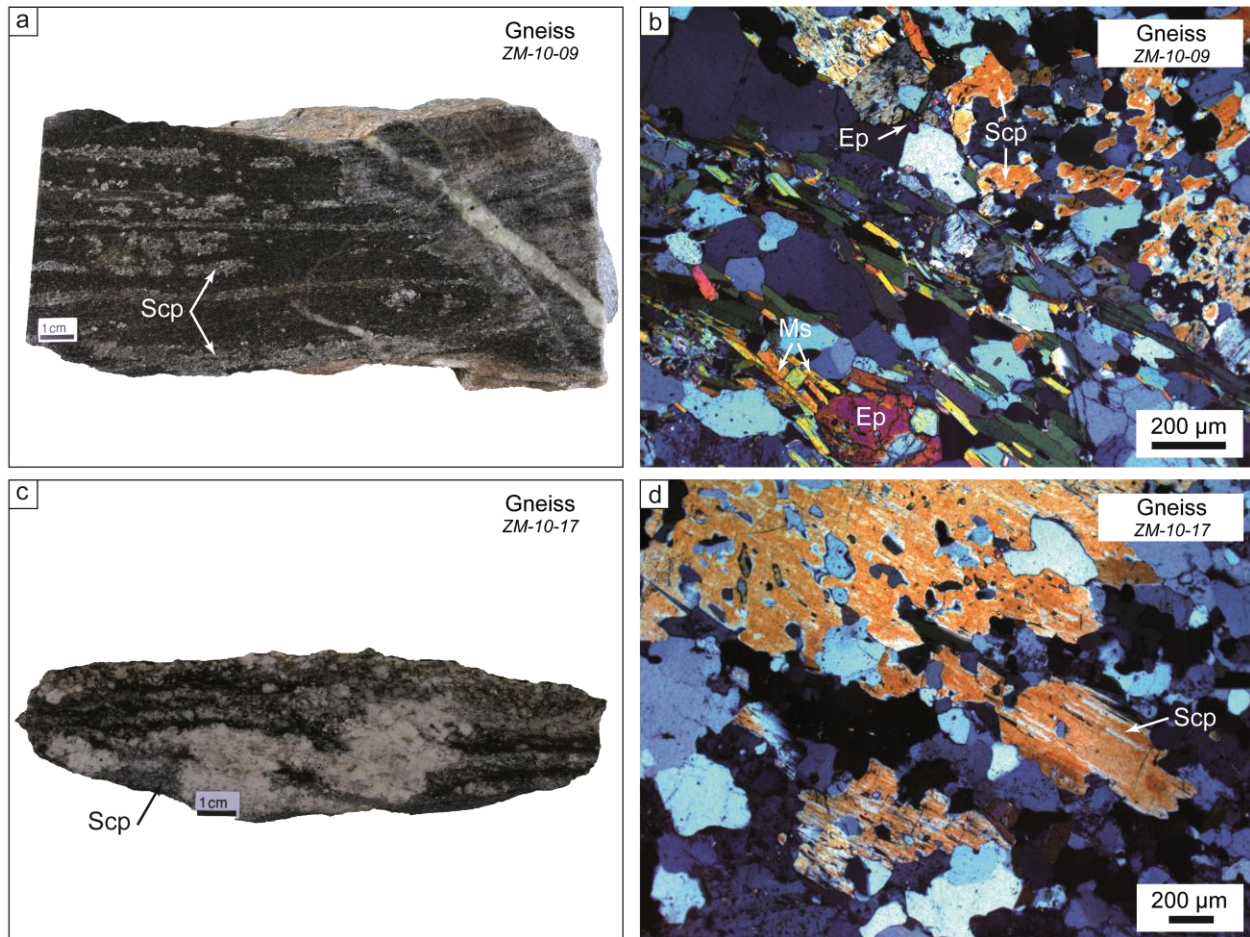


Figure 74: a: Macroscopic view of gneissic rock showing strong scapolite alteration overprinting the gneissic fabric. b: Photomicrograph of scapolite porphyroblasts with Qtz-Pl-rich matrix and epidote inclusions (sample *ZM-10-09*); epidote-muscovite assemblage is also visible in the lower part of the picture (sample *ZM-10-09*). c: Macroscopic view of gneiss showing boudinaged and folded leucosome within gneissic fabric (sample *ZM-10-17*). d: Photomicrograph of large poikilitic scapolite porphyroblasts (sample *ZM-10-17*). Abbreviations: Ep = Epidote; Pl = Plagioclase; Qtz = Quartz; Scp = Scapolite.

Migmatites (sample *ZM-10-62*; Figure 70d) are characterized by the presence of different generations of granitic veins concordant (boudinaged and transposed) and discordant to the syn-migmatitic foliation. These features indicate that ductile deformation occurred in the presence of a melt fraction (Vanderhaeghe, 1999, 2009; Vanderhaeghe and Teyssier, 2001). The granitic fraction presents a peraluminous composition (Table 57).

These rocks are characterized by quartz-microcline-garnet-muscovite-biotite assemblage. As for the granodioritic gneisses, late epidote-apatite (Figure 75c, d) and scapolite alteration is also identified. Accessory minerals are monazite, allanite, iron oxide, zircon and Th-silicate. Monazite grains present a corona texture with allanite, epidote and apatite rims (Figure 75c, d). Monazite grains are partially to totally dissolved and replaced by allanite. This replacement reaction is further supported by the positive correlation between SiO_2 and Al_2O_3 shown by monazite crystals altered to various degrees and trending toward the allanite compositional field (Figure 76). Altered monazite shows a depletion of P, U and REE compensated by strong enrichments in Ca, Si and Al (Table 61). During this process, the monazite crystalline structure is replaced by a Th-rich or REE-rich silicate as allanite.

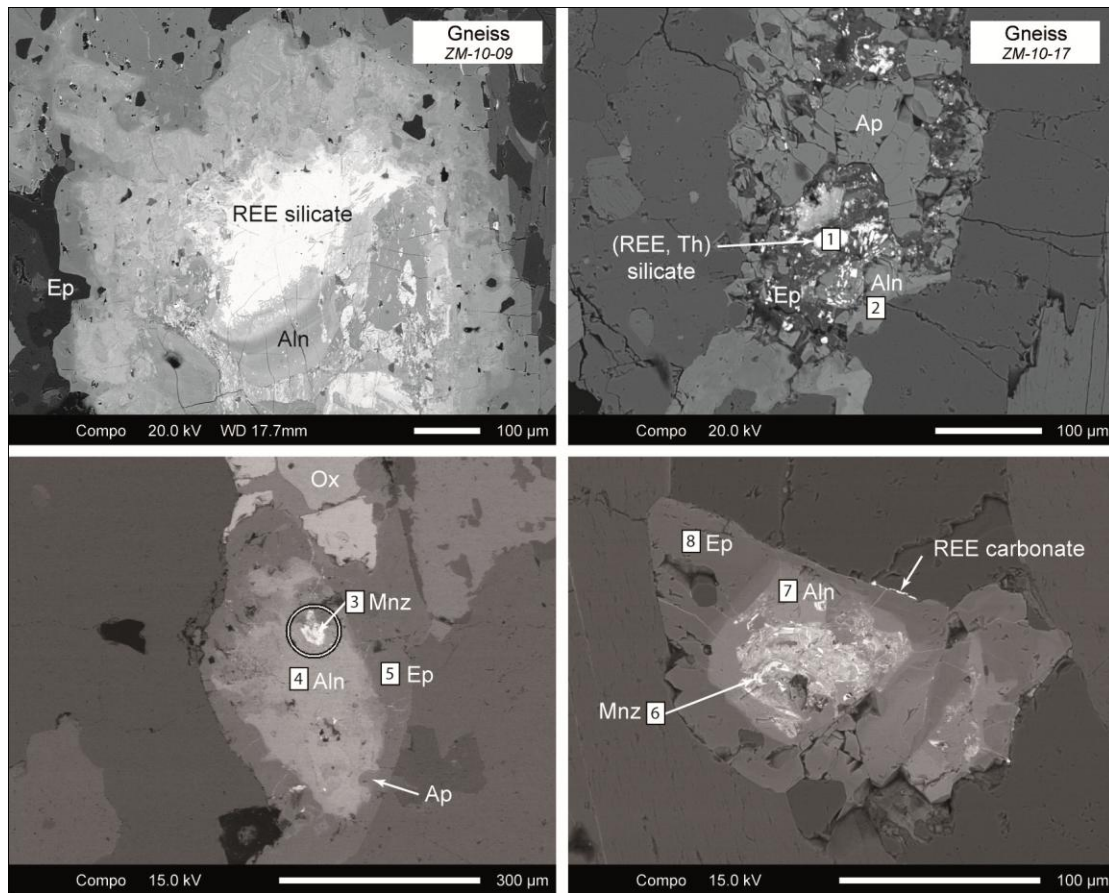


Figure 75: BSE images of accessory minerals observed in Pre-Katanga rocks from Solwezi dome. a: Metamict allanite grain surrounding by epidote. Allanite is filled by REE-rich silicate (sample ZM-10-09). b: Metamict allanite grain with newly formed apatite and (REE, Th)-rich minerals (sample ZM-10-17). c and d: Replacement of primary monazite by allanite and then by epidote-apatite. Some fractures are filled by newly REE-rich carbonates (sample ZM-10-62). Numbers shown on images b, c and d correspond to electronic microprobe analysis reported in Table 61. Abbreviations: Aln = Allanite; Ap = Apatite; Ep = Epidote; Mnz = Monazite; Ox = Iron oxide ; Zrn = Zircon.

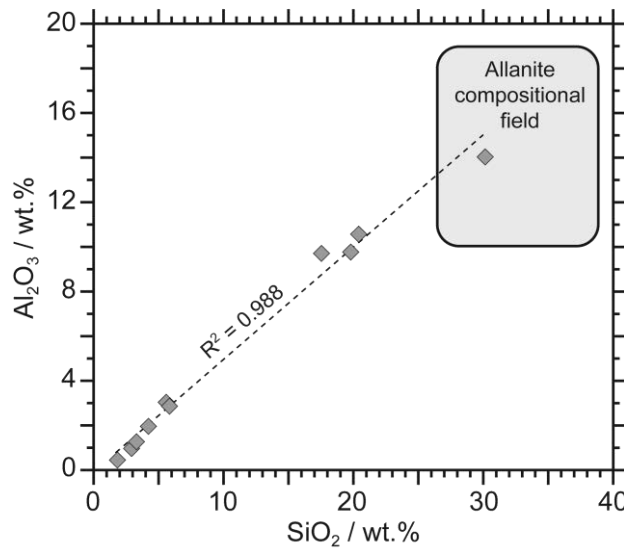


Figure 76: Al_2O_3 vs. SiO_2 diagram for electron microprobe analyses of altered monazite grains (dark grey diamonds). The linear trend toward the allanite compositional field defined after 30 analyses reported in Deer et al. (1997), suggests that the monazite alteration leads to allanite replacement.

Scapolite grains were observed in many lithologies of the Pre-Katanga rocks described above. The composition of the scapolite is commonly reported in terms of equivalent anorthite content (Table 62): $\text{Eq}_{\text{An}} = (\text{Al} - 3)/3$, where Al is expressed in a.p.f.u. (Teertstra and Sherriff, 1997) and mole fractions of $\text{XCl} = \text{Cl}$ a.p.f.u., $\text{XSO}_3 = \text{S}$ a.p.f.u. and $\text{XCO}_2 = 1 - \text{Cl} - \text{S}$ a.p.f.u. Scapolite from these Pre-Katanga rocks exhibits a homogeneous composition: Eq_{An} from 0.38 to 0.44, and XCl from 0.44 to 0.58 and are characterized by a low XSO_3 content, less than 0.12 (Table 62). All scapolite compositions fall close to the binary lines of the marialite ($\text{Na}_4\text{Al}_3\text{SiO}_24\text{Cl}$)-meionite ($\text{Ca}_4\text{Al}_6\text{Si}_6\text{O}_{24}\text{CO}_3$) and marialite ($\text{Na}_4\text{Al}_3\text{SiO}_24\text{Cl}$)-mizzonite ($\text{Ca}_3\text{Al}_5\text{Si}_7\text{O}_{24}\text{CO}_3$) (Figure 77).

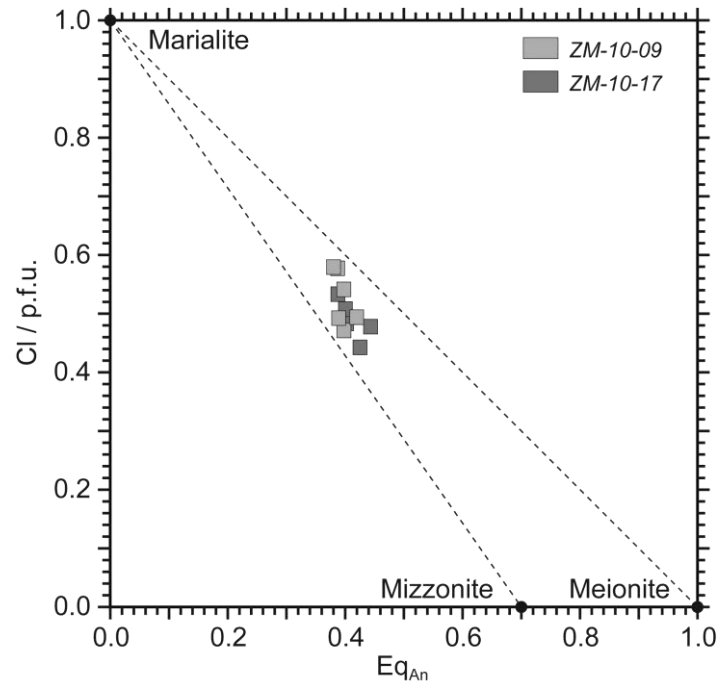
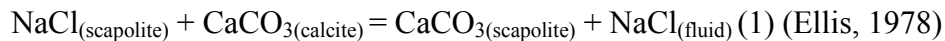


Figure 77: Cl atoms (per formula for Si + Al = 12) versus Eq_{An} (equivalent anorthite content) diagram showing the range of scapolite compositions from two samples of Solwezi dome. Dotted lines show the stoichiometry of marialite-meionite and marialite-mizzonite coupled substitutions.

Scapolite compositions were calculated by normalizing to Si + Al = 12 a.p.f.u., as recommended by Teertstra and Sheriff (1997). By neglecting the SO₃ content which is very low ($X_{SO_3} < 0.12$), the exchange of NaCl and CaCO₃ between scapolite and a fluid phase can be written:



From reaction (1), it is inferred that the variation in the scapolite composition is related to the variation in the activity ratio: $(a_{\text{Na}^+} \cdot a_{\text{Cl}^-}) / (a_{\text{Ca}^{2+}} \cdot a_{\text{CO}_3^{2-}})$ of the equilibrium grain-boundary fluid phase during scapolite growth. The $X_{\text{NaCl}(\text{fluid})}$ is calculated from the K_D formulation investigated by Ellis (1978):

$$K_D = (X_{\text{CaCO}_3}^{\text{Scp}} \cdot X_{\text{NaCl}}^{\text{Fluid}}) / (X_{\text{NaCl}}^{\text{Scp}} \cdot X_{\text{CaCO}_3}^{\text{Cc}}) \quad (2)$$

with $\ln K_D = -0.0028(X_{\text{Al}})^{-5.558}$ (3), where $X_{\text{Al}} = \text{Al}/(\text{Al}+\text{Si})$ (4)

Using this equation, the calculated NaCl content of the fluid ($X_{\text{Fluid}}^{\text{NaCl}}$) ranges from 0.41 to 0.53 for all scapolite crystals sampled in the rocks exposed in the core of the Solwezi dome (Table 62).

5. Geochronological constraints

5.1. Th-Pb on monazite from the kyanite micaschists

Nine monazite grains from *ZM-10-07* and six from sample *ZM-10-24* have been investigated for ^{232}Th - ^{208}Pb analyses based on X-Ray maps (Table 63). In *ZM-10-07* sample, the ages range from 470 ± 10 to 554 ± 13 Ma and, in *ZM-10-24* sample, from 451 ± 10 to 543 ± 12 Ma. This age scattering (Figure 78) corresponds to differences between individual grains as well as to heterogeneities within a single grain.

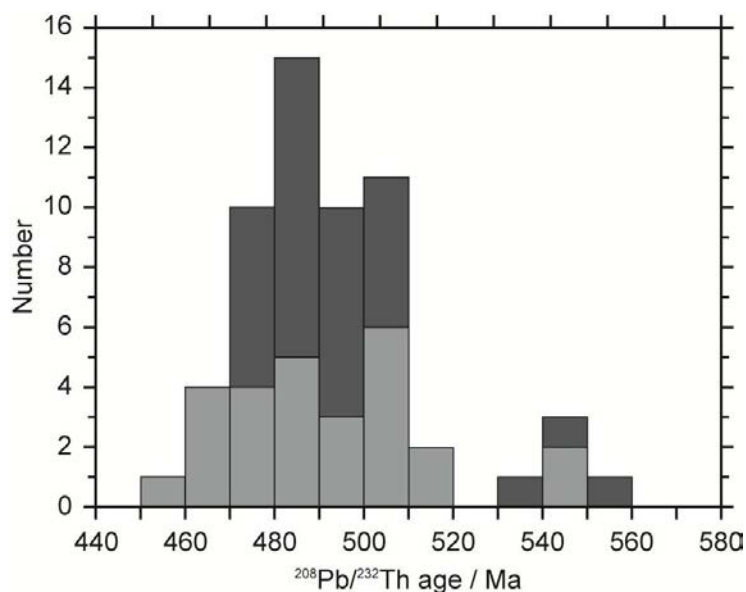


Figure 78: Histogram of Pan-African monazite ^{232}Th - ^{208}Pb ages (dark grey bars => *ZM-10-07* and light grey bars => *ZM-10-24*; Table 63).

Scattering of the ^{232}Th - ^{208}Pb are in part related to intra-grain chemical heterogeneities and age variations within single grains appear to be correlated with chemical domains (Figure 79). For example, the *ZM-10-24* monazite grain, tend to display younger ages in Th- and Ca-rich domains

(brabantite substitution; Figure 79) with distinct ThO_2 and CaO contents mapped by EMP analysis. The same relationship is observed for monazite grains from *ZM-10-07* sample.

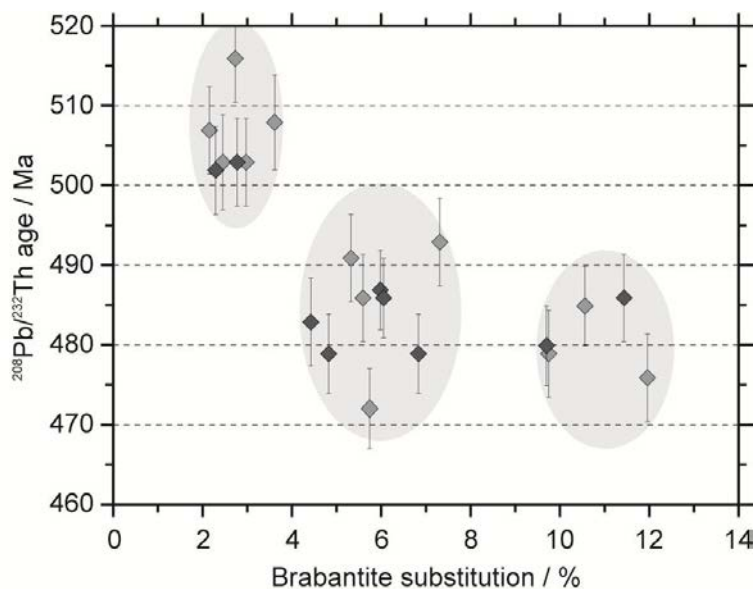


Figure 79: ^{232}Th - ^{208}Pb ages, obtained by LA-ICPMS (Table 63), versus brabantite substitution, determined by electronic microprobe analyses (Table 59; Table 60; Table 63), diagram showing different clusters interpreted as related to episodic dissolution/recrystallization events recorded during the growth of monazite grains (dark grey diamonds => *ZM-10-07* and light grey diamonds => *ZM-10-24*; vertical bars represent the age error at 2σ level).

5.2. U-Pb on uraninite from the kyanite micaschists

U-Pb isotopic ratios have been measured on six uraninite crystals hosted by the phlogopite-chlorite schistosity (S_{n+1}) from the Mitukuluku occurrence (sample 7703-29) and plotted on a Concordia diagram (Table 64, Figure 80). These data define a discordia line with an upper intercept at 515 ± 18 Ma and a lower intercept at -126 ± 180 Ma. As there is no evidence for another tectonothermal event between the Pan-African orogeny and present day, we choose to anchor the lower intercept at 0 ± 100 Ma leading to an upper intercept age at 532 ± 18 Ma which is interpreted to be the best determination of the uraninite crystallization age (Figure 80).

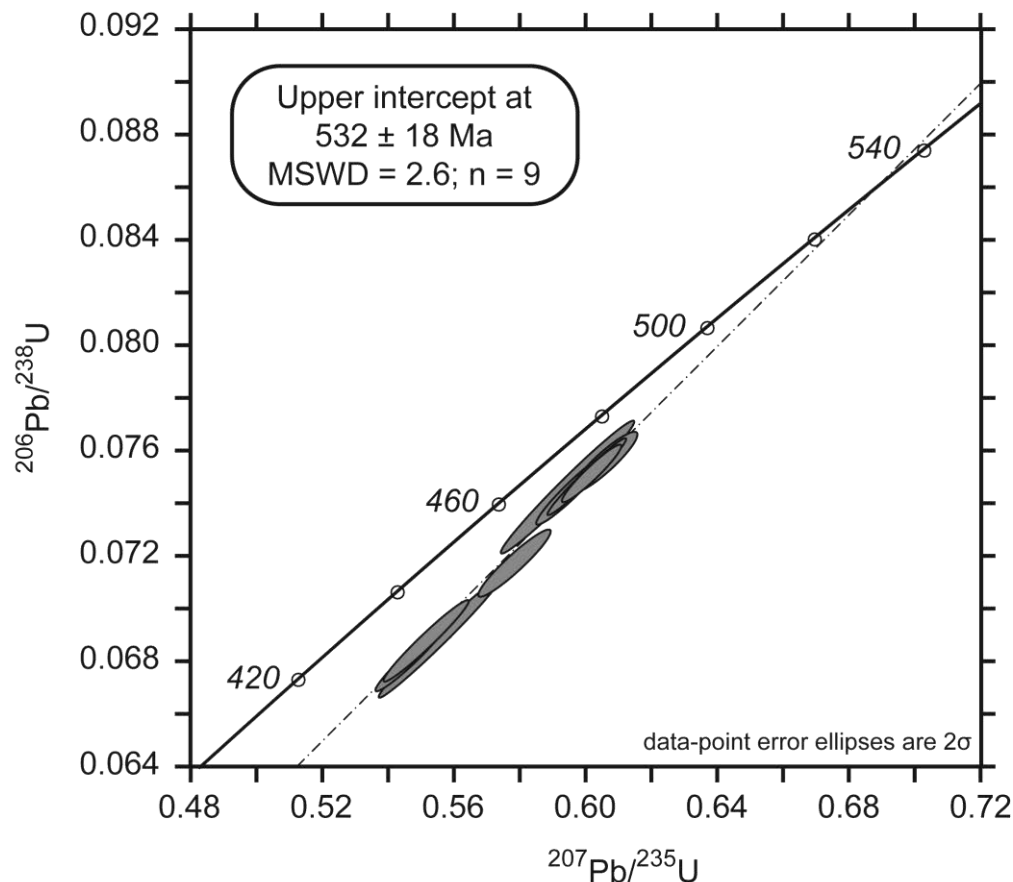


Figure 80: Concordia plots of U-Pb data (n = 9) for uraninite grains from Mitukuluku occurrence with an upper intercept at 532 ± 18 Ma associated with a lower intercept anchored at 0 ± 100 Ma.

6. *P-V-T-X* properties of the fluids

The mineralizing fluids have very uncommon compositions. As such no experimental data are available to reconstruct the corresponding trapping conditions. However these three types of fluids are very different and a rough estimate is sufficient to characterize their respective *P-T* conditions of entrapment. The simplifications of the different chemical systems made in order to make possible the calculation of the isochores for each fluid type are described in Appendix 1.

Fluid type-I:

The isochores were calculated using Lecumberri-Sanchez et al. (2012) and Steele-MacInnis et al. (2012) equations of state and are reported on Figure 81. Note that these equations of state are valid only up to 600 MPa and our calculated pressures are likely imprecise. The resulting

pressure for entrapment of type-I fluid is calculated at a minimum of 460 MPa for a minimum temperature defined at 500 °C (above the temperature of GBM recrystallization; Figure 81).

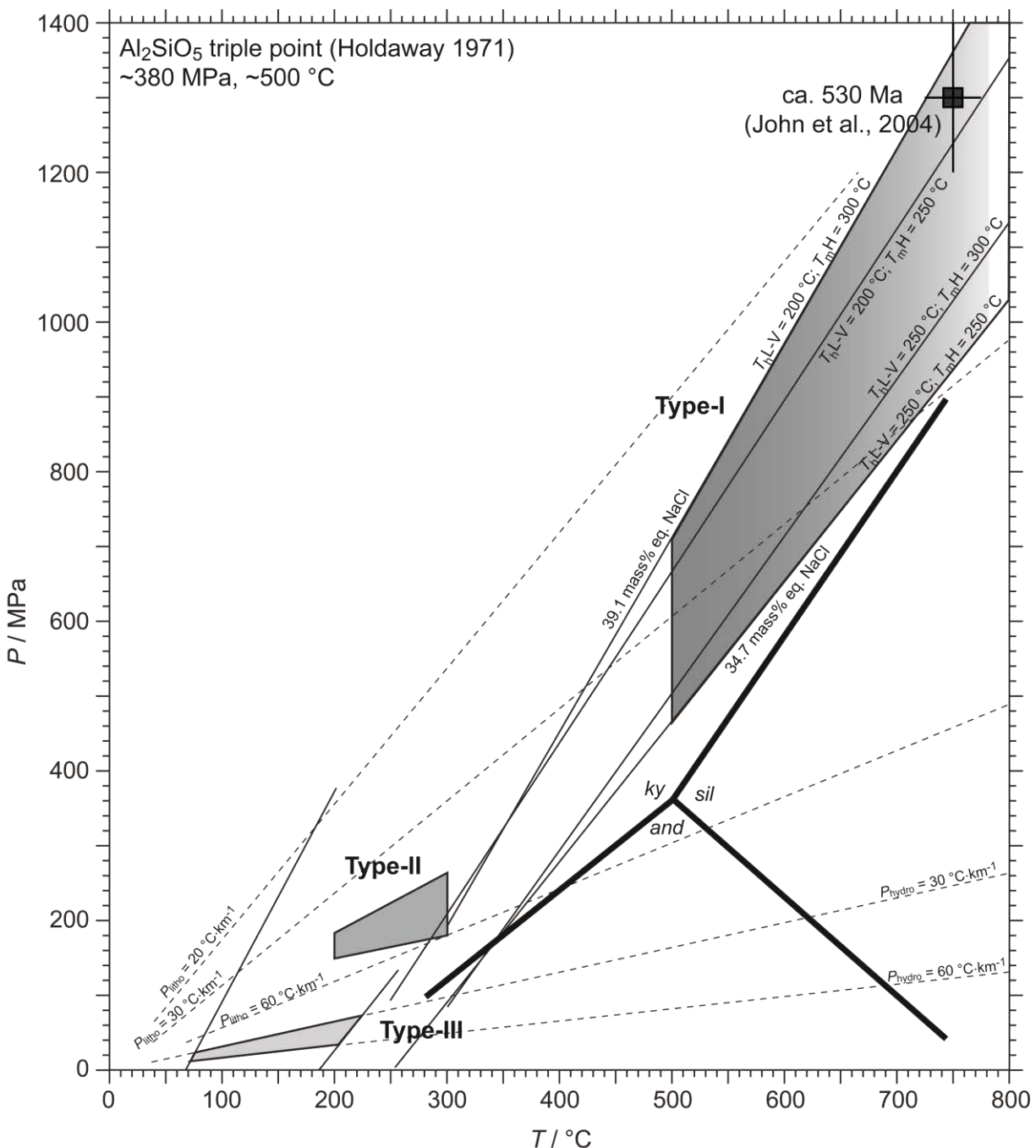


Figure 81: *P-T* trapping conditions of the three types of fluid inclusions. The age at ca.530 Ma, U-Pb on monazite, represents the *P-T* conditions at the temperature peak of metamorphism of the internal zone of the Lufilian belt, obtained by John et al. (2004) on kyanite-talc assemblage.

Fluid type-II: aquo-carbonic fluids

Petrographic and microthermometric data suggest contemporaneous entrapment of IIa and IIb inclusions representing two immiscible fluids within a 200-300 °C range. The pressure of entrapment is calculated using the equation of state of Span and Wagner (1996) for a pure CO₂ system applied to inclusions IIb in the range 200-300 °C. These data were combined with pressure obtained by simultaneous decrepitation of IIa and IIb up to 300 °C. The resulting pressures for entrapment of type-II fluid range between 150 and 260 MPa (Figure 81).

Fluid type-III: low salinity aqueous fluids

Isochores were calculated assuming a NaCl-H₂O system (15 wt.% eq. NaCl) using the experimental equation proposed by Bodnar and Vityk (1994). The estimate for the maximum trapping *P-T* conditions of this type III fluid of 70 MPa and 225 °C, entrapment being likely continuous to much lower *P-T* conditions (Figure 81).

7. Discussion

The field observations coupled to petrographic, geochemical and geochronological data presented above provide constraints on the timing of deformation, metamorphism, metasomatism and uranium mineralization in the Domes region of the Lufilian belt. In this section, these data are discussed and compared to available data for the region in order to elaborate an original metallogenic model for the mobilization, transfer and deposition of uranium during the Pan-African orogeny. In particular, mass balance quantification is provided in order to evaluate the efficiency of hydrothermal processes to mobilize and concentrate uranium in this context.

7.1. Geochronological constraints on uranium mineralizations during the tectonic evolution of the Lufilian belt

The geochronological data presented in this paper are discussed in relation with previously published structural and thermobarometric data in order to reconstruct the tectonic context favorable for uranium mineralization. Two ²³²Th-²⁰⁸Pb age clusters were obtained on monazite grains from kyanite micaschists (samples *ZM-10-07* and *ZM-10-24*) in the north of the Solwezi dome. The first cluster is characterized by ²³²Th-²⁰⁸Pb dating ranging from 554 ± 13 to 539 ± 11

Ma. The older of these ages is significantly older than the previously published U-Pb concordant ages of 525 ± 2 Ma, 532 ± 2 Ma and 529 ± 2 Ma obtained on monazite hosted by the kyanite-talc micaschists respectively from the Kabompo, Mwombezhi and Solwezi domes in the Domes region of the Lufilian belt (John, 2001; John et al., 2004). The ca. 530-525 Ma ages have been interpreted as recording the peak of Pan-African *P-T* metamorphic conditions (designated as D₂ metamorphic event; John et al., 2004) of 13 ± 1 kbar and 750 ± 25 °C at the end of continental collision between the Congo and Kalahari cratons. The new U-Pb age of 532 ± 18 Ma (Figure 80) obtained on uraninite from Mitukuluku occurrence (Solwezi dome) is consistent with previously determined ages on monazite. These data point to a first synmetamorphic uranium mineralizing event at high *P-T* conditions, during the Pan-African continental collision between ca. 555 and 525 Ma.

The second ²³²Th-²⁰⁸Pb dating cluster obtained on monazite grains from the kyanite micaschist (samples *ZM-10-07* and *ZM-10-24*) present ages ranging from 516 ± 10 Ma to 451 ± 10 Ma (Table 63; Figure 78). These ages are synchronous to Rb-Sr isochrons obtained in the Domes region (John, 2001). Indeed, the gneisses exposed in the core of the Solwezi dome yield an Rb-Sr muscovite-plagioclase isochron at 490 ± 5 Ma and an Rb-Sr biotite-plagioclase isochron at 476 ± 5 Ma. The kyanite-garnet micaschist rimming the core of Solwezi dome yields an Rb-Sr biotite-plagioclase isochron at 469 ± 5 Ma (John, 2001). Considering a closure temperature regarding the Rb-Sr thermochronometer at ca. 500 ± 50 °C for muscovite, and ca. 350 ± 50 °C for biotite (Hanson and Gast, 1967; Dodson, 1979), these results indicate that rocks from the core and rim of the Solwezi dome experienced a similar cooling history below about 350 °C after the D₂ tectonothermal event. All these ages overlap the 503 ± 15 Ma obtained by U-Pb on brannerite grains (Darnley et al., 1961) hosted by brannerite-sulfides veins crosscutting the metasedimentary sequence of the Nguba Group (marbles, carbonaceous phyllites and biotite-garnet schists) in the Kansanshi mine (Torrealdy et al., 2000). The concordance between these Rb-Sr isochron ages, the Th-Pb ages on monazite and the U-Pb ages on brannerite underlines a second uranium mineralizing event, at lower *P-T* conditions (below 350 °C), during the exhumation and low-grade retrogression of upper Amphibolite facies metamorphic rocks between ca. 515 to 450 Ma.

7.2. *P-T-t-fluid/rock interactions*

The petrographic analysis of fluid inclusions trapped in transposed quartz veins from Lolwa and Mitukuluku uranium occurrences provides further constraints on the ore fluid circulation events in the Domes region of the Lufilian belt in association with its tectonothermal evolution. These quartz veins, formed during D₂ temperature peak of metamorphism, have recorded syn- and post-D₂ fluid circulation events. Isochores and *P-T* conditions of entrapment were calculated for each generation of fluid presented in Eglinger et al. (in press) and could be related to distinct fluid events.

Type-I fluid event

The conditions of entrapment are calculated at a temperature higher than 500 °C for a minimal pressure above 460 MPa. The large *P-T* field of type-I fluid entrapment overlaps the *P-T* conditions recorded during the D₂ metamorphic event, synchronous to the Pan-African continental collision, described by John et al. (2004). These fluids are characterized by high uranium content, with a mode concentration around 20 ppm (Eglinger et al., in press). Thus, these H₂O-CaCl₂-NaCl-(N₂-H₂) fluids could have been trapped at near peak-D₂ metamorphic conditions, constituting the starting point for retrograde *P-T* path, and responsible to the uranium mineralizations dated at ca. 530 Ma (Figure 83). Epidote-apatite alteration described in various felsic rocks imply Ca- and Cl-rich fluids and, as a consequence, is correlated to these CaCl₂-rich (up to 59 wt.%) fluid circulations (Eglinger et al., in press).

Type-II fluid event

These fluids, characterized by immiscibility, could be trapped in veins having formed during exhumation and low-grade retrogression of higher-grade metamorphic rocks (Diamond, 1990, 2001; Bouiller et al., 1991; Craw and Norris, 1993). Scapolite grains described in this study present a solid-solution between marialite, meionite and mizzonite end-members which implies the presence of fluid phases with high concentrations of CO₂ and halogens. Scapolitisation at the regional scale could be related to these H₂O-CO₂-NaCl-CaCl₂ fluid circulation events during retrograde metamorphism. The estimated halogen content ($X_{\text{NaCl}}^{\text{Fluid}}$) of fluids, ranging from 0.41 to 0.53 (Table 64), is relatively constant for all analyzed scapolite grains. The homogeneous NaCl

content of scapolite suggests that crystallization of these minerals occurred before fluid immiscibility recorded by this fluid (Oliver et al., 1992). Thus, the calculated halogens content could reflect the homogeneous H₂O-CO₂ parent-fluid composition.

Monazite grains from both samples (*ZM-10-07* and *ZM-10-24*) show distinct compositions in relation to strong chemical zonations that are spatially related to distinct age domains. This is in agreement with numerous studies describing complex zoning and patchworks of age domains related to discontinuous growth or successive dissolution/recrystallization of monazite in response to changing environment (Parrish, 1990; Hawkins and Bowring, 1997; Zhu and O'Nions, 1999; Crowley and Ghent, 1999; Foster et al., 2002; Pyle and Spear, 2003; Kohn et al., 2005; McFarlane et al., 2006; Hinchey et al., 2007; Rasmussen and Muhling, 2007). The positive correlation between Ca and Th shown by X-ray maps is interpreted as brabantite substitution following the reaction: $2\text{REE}^{3+} \Leftrightarrow \text{Th}^{4+} + \text{Ca}^{2+}$ (Poitrasson et al., 2000). Because Th is poorly soluble and mobile during interaction between hydrothermal fluids and rocks (Rogers and Adams, 1969; Poitrasson et al., 1996), this element should be reincorporated into newly formed zones, as brabantite end-members, favoring the recrystallization of Th-rich and Pb-free zones (Poitrasson et al., 1996, 2000; Seydoux-Guillaume et al., 2002). These Th-rich and Pb-free zones are often younger, i.e. contain a lower Pb content than the adjacent domains (Cocherie et al., 1998; Crowley and Ghent, 1999). This fluid-rock interaction leading to U-Th-Pb isotope system perturbations is well illustrated on Figure 79 where younger ²³²Th-²⁰⁸Pb ages are correlated with high brabantite end-member substitution. This partial resetting in the U-Th-Pb isotopic system in brabantite implies a fluid enriched in calcium. Monazite grains in our study are hosted by kyanite micaschists depleted in CaO content (<0.04 wt.%). Thus, we conclude that the origin of calcium is external and probably related to a CaCl₂-fluid circulation. Experiments have shown that CaCl₂-bearing fluids are efficient in resetting the U-Th-Pb isotope system of monazite (Seydoux-Guillaume et al., 2002) and are in good agreement with our observations. This second generation of fluids, described as NaCl-CaCl₂ aqueous-carbonic fluids, percolated close to the brittle-ductile quartz transition. Therefore, the spread of younger Th-Pb ages from ca. 515 to 450 Ma probably reflects the period of aqueous carbonic fluids circulation during progressive exhumation of high grade metamorphic rocks and cooling to Greenschist facies conditions. These ages are consistent with ⁴⁰Ar-³⁹Ar thermochronology analyses on biotite and Rb-Sr dating on muscovite and biotite

yielding ages between 510 and 463 Ma and interpreted to represent post-orogenic cooling of the metamorphic rocks in the Lufilian belt (Cosi et al., 1992; John et al., 2004; Rainaud et al., 2005). These fluids are also characterized by internal radiolysis (CO₂-CO) explained by the presence of uranium dissolved within the water phase (Eglinger et al., in press). Thus, we propose that these aqueous-carbonic fluids are related to uranium remobilization with leaching processes during ductile-brittle to brittle conditions (Figure 82), as described in brittle veins from the Kansanshi mine (Torrealdy et al., 2000).

Type-III fluid event

These fluids crosscut all generations of fluid inclusion trails and have percolated in the brittle domain. The *P-T* conditions recorded by this fluid underline also a very late event, likely under hydrostatic conditions. An external radiolysis is invoked to explain the metastable composition of these fluids (Eglinger et al., in press) and so, they have not implications on uranium (re-)mobilization and precipitation in the Domes region.

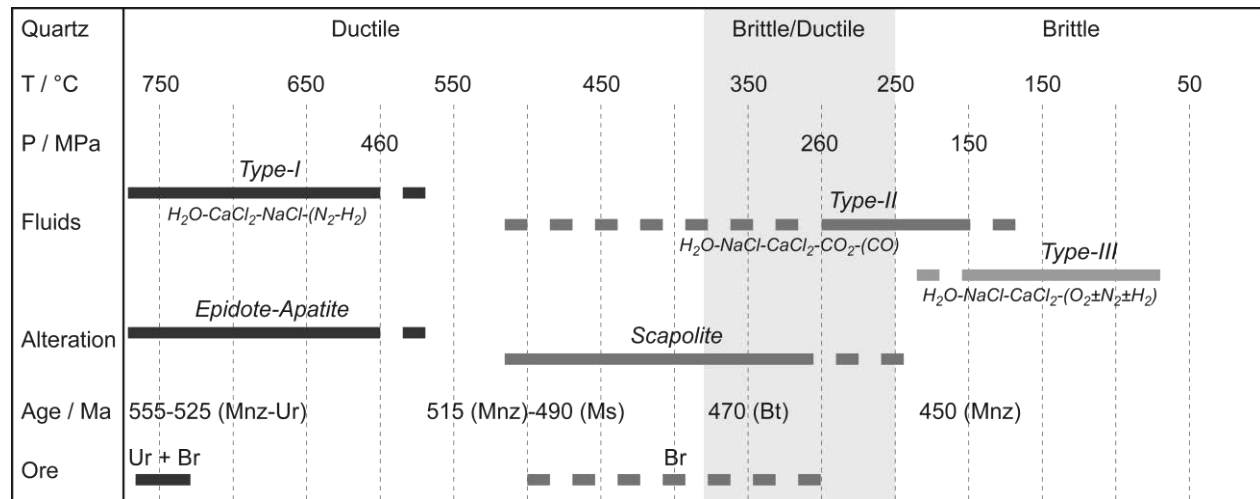


Figure 82: Fluid evolution, with respective *P-T* trapping conditions, related to fluid-rock alteration and uranium mineralization. Minerals on brackets represent the dating material and ages are from this study and from John (2001). Abbreviations: Br = Brannerite; Bt = Biotite; Mnz = Monazite; Ms = Muscovite; Ur = Uraninite.

7.3. Uranium mass balance

Evidences of uranium mobilization have been observed in different lithologies of the basement exposed in the internal zone of the Lufilian belt. The petrography of accessory minerals reveals the presence of altered monazite and allanite grains at the scale of the Solwezi dome in both gneissic and migmatitic rocks (Figure 71c, d). Monazite replacement by allanite (Figure 75c, d) implies a fluid-assisted cation transfer accompanied by a gain of Ca, Si and Al with a loss of U. The most widespread breakdown products of monazite include apatite and allanite-(Ce) to REE-rich epidote or clinozoisite which commonly form concentric corona-like textures around partly dissolved monazite core (Broska and Siman, 1998; Finger et al., 1998; Broska et al., 2005; Petrik et al., 2006; Budzyn et al., 2011). All uranium leached from monazite was not incorporated into the allanite, probably because the allanite structure can incorporate less U than the monazite crystal lattice (Poitrasson et al., 2000). The following reaction (5) from monazite to apatite/allanite could liberate dissolved uranium:



Monazite becomes unstable during fluid-activated overprinting and is replaced by secondary phases. The character of monazite alteration products strongly depends on the fluid composition and local chemistry. Replacement of monazite during a metamorphic event is a common phenomenon controlled by the release of fluids during the relaxation stage of metamorphism (Ondrejka et al., 2012).

Altered allanite is filled by (REE, Th) silicates where rare earth elements and thorium from allanite are trapped in these newly formed minerals (Figure 75a, b). High concentration of thorium within newly formed minerals is favored by the relative immobility of thorium during hydrothermal processes (Rogers and Adams, 1969). A possible alteration reaction (6) mobilizing uranium from allanite is:



These two reactions might mobilize uranium in solution during one or several hydrothermal events. Reactions (2) and (3) reflect alteration associated with Ca-rich fluid circulation leading to uranium leaching and mobilization. Epidote, apatite and scapolite minerals described in different lithologies of the Solwezi dome (section 4.1) imply halogens- and Ca-rich fluid circulations at the regional scale. A halogen-rich fluid is an oxidized saline solution and can efficiently transport large amounts of dissolved metals like uranium as chloride complexes (Yardley, 2005). A mass balance calculation is obtained based on reaction (2) describing monazite alteration observed within migmatitic rocks. This mass balance-sheet is realized using the bulk chemistry of a heterogeneous granite representative of rocks exposed in the core of the Solwezi dome (Table 57), sample *ZM-10-62*, and along an EPMA profile (Figure 75c, d). Assuming that all La content of the whole rocks (~120 ppm) is contained in monazite (~15 wt.% La), the average amount of monazite in the whole rock is ~800 ppm. The average Th and U contents in monazite being respectively 0.72 and 0.06 wt.% (Table 61), the Th and U amounts contained in monazite in whole rock are respectively 5.6 and 0.5 ppm. The comparison of average Th/U ratio in monazite (~13) and in allanite (~38) allows calculating that about 65 % of uranium from monazite is leached during its alteration. 1 km³ of migmatite containing 800 ppm of monazite with 0.06 wt.% of U may liberate $0.800 \times 0.65 = 0.520$ ppm of U, corresponding to ~1400 t.km⁻³ of U during Ca-rich fluid hydrothermal alteration of monazite. This alteration is also well expressed by the higher Th/U (~ 7) ratio of the whole rock (sample *ZM-10-62*) than the average granitic ratio (~ 3.5), which is consistent with U loss during gneissic rocks alteration (Cuney and Kyser, 2009).

The same mass balance calculation with the alteration of allanite to (Th, REE) silicate can be calculated for the gneissic rocks outcropping within the Solwezi dome. For a minimal La content at ~30 ppm (*ZM-10-17*; Figure 75b; Table 57), and a La content in allanite of ~3 wt.%, the average amount of allanite in the whole rock is ~1100 ppm. The comparison of Th/U ratio in allanite (~19) and in (REE, Th) silicate (~73) gives a similar proportion of about 70% of U leached from the allanite during fluid assisted alteration, corresponding to ~2000 t.km⁻³ of U.

8. Conclusion

This paper presents new petrologic, geochemical, geochronological and fluid inclusion data on metamorphic rocks (kyanite±talc micaschists and migmatitic gneisses) from the Domes region of the Pan-African Lufilian belt (Zambia). These results discussed in the framework of available data for the region allow the elaboration of a model for the *P-T-t* evolution of ore fluid flows and their implications in terms of uranium mobilization through fluid-rock interaction processes during the Pan-African metamorphism.

Two stages of uranium mobilization are recognized from continental tectonic accretion to exhumation of the metamorphic host rocks.

- (1) First uranium mobilization was assured by CaCl₂-NaCl-KCl-(MgCl₂)-H₂O metamorphic brines (type-I), trapped during high-temperature (> 500 °C) quartz plastic deformation and recrystallization. The *P-T* conditions and the timing of metamorphism coeval with the circulation of these fluids are constrained by geochronology of uraninite, dated at ca. 530 Ma. Uranium mineralizations are represented by uraninite and brannerite. This uranium-bearing fluid event took place near the metamorphic peak of temperature recorded during the Pan-African continental tectonic accretion. Metasomatism related to the circulation of these fluids is expressed by the presence of epidote (Ca-rich mineral) and apatite (Ca-Cl-rich mineral).
- (2) Second uranium mobilization is related to NaCl-CaCl₂-H₂O-CO₂ metamorphic fluids (type-II). These aquo-carbonic fluids have percolated close to the brittle-ductile transition, at lower *P-T* conditions. These fluid circulations are expressed by dissolution-precipitation reactions in monazite grains hosted by the kyanite±talc micaschists (metamorphosed evaporites) and dated between ca. 515 and 450 Ma, in good agreement with U-Pb age on brannerite 503 ± 15 Ma. This fluid event is interpreted to occur during the exhumation of the high grade metamorphic rocks following the thermal relaxation of the thickened orogenic crust. These crustal fluids have also generated metasomatic reactions as the regional scapolitisation (NaCl-CaCO₃-rich mineral).

All these CaCl₂-NaCl fluids partially produced by dissolution of the Lower Roan Group evaporites, during the Pan-African regional metamorphism, have percolated through the pre-Katanga felsic rocks. These high-Cl fluids have leached and transported uranium from accessory minerals such as monazite and allanite. These alteration processes may be considered as a non-negligible uranium source (1400-2000 t U.km⁻³ of gneiss-migmatite) for the synmetamorphic uranium mineralizations in high-grade Neoproterozoic (Lower Roan Group) rocks exposed in the Domes region of the Lufilian belt.

Acknowledgments

We would like to thank CNRS (NEEDS) and AREVA for financial support. AREVA is also thanked for providing the samples. We thank Marc Brouand for access to the ion microprobe. The authors are grateful to Sandrine Mathieu and Olivier Rouer (GeoRessources, Nancy) for their technical support in providing analytical data on SEM and EMP. We would also like to acknowledge the stimulating discussions with Philippe Goncalves and Michel Cuney.

Appendix 1: Simplifications of the different chemical systems for fluid inclusion isochores

Fluid type-I: highly saline aqueous fluids

In order to simplify the fluid system, the small amounts of N₂ and H₂ detected in the vapour phase are neglected in the calculation. Type-I inclusions showed antarcticite and sinjarite melting. The temperature of these transitions associated to melting temperature of halite provides a mean to calculate the bulk salinity in the CaCl₂-NaCl-H₂O system (Steele-MacInnis et al., 2012). These compositions are relatively constant for all measured inclusions (53-59 wt.% CaCl₂, 13-15 wt.% NaCl). LA-ICPMS analyses showed that the fluids are also enriched in KCl and MgCl₂ among other salts. However, no equation of states permit to describe the *PT* evolution of such fluids composed of a mixture of salts. Therefore, the salinity of type-I fluids was re-estimated by considering final melting temperature of halite only in a NaCl-H₂O binary system. Although very common in nature, and especially in ore deposits, a lack of experimental data hinders a correct *PVTX* interpretation of fluids which homogenize by disappearance of halite (Becker et al., 2008). In order to determine the salinity of fluid inclusions homogenizing by halite disappearance, two phase transition temperatures ($T_{LV \rightarrow L}$ and T_{mH}) are required (Becker et al., 2008; Lecumberri-Sanchez et al., 2012; Steele-MacInnis et al., 2012; Steele-MacInnis and Bodnar, 2013).

The temperature at which the vapour bubble disappears is scattered and type-I fluid inclusions homogenize either by halite disappearance or by vapor disappearance. However, Eglinger et al. (submitted) demonstrated that there is a link between the local intensity of host-quartz plastic deformation, bulk homogenization mode and temperature (Diamond et al 2010; Tarantola et al 2010; 2012). Non-deformed or less-deformed type-I fluid inclusions homogenize by halite melting in the range 250-300 °C. The variation in $T_{LV \rightarrow L}$ likely results from stretching of the fluid inclusions and the lowest measured $T_{LV \rightarrow L}$ closely approximates the true $T_{LV \rightarrow L}$ before stretching (Bodnar, 2003; Becker et al., 2008). For type-I inclusions, $T_{LV \rightarrow L}$ are mainly around 200-250 °C and correspond to the lower measured temperatures. The resulting salinity is comprised between 34.7 and 39.1 wt.% eq. NaCl. The isochores were calculated using Lecumberri-Sanchez et al.

(2012) and Steele-MacInnis et al. (2012) equations of state which permit to calculate the isochores for inclusions homogenizing by halite disappearance.

Fluid type-II: aquo-carbonic fluids

Type-II is characterized by two fluid inclusion subtypes, namely (i) IIa composed of H₂O-CO₂-(CO)-NaCl-CaCl₂, and (ii) IIb composed of CO₂-(CO-H₂O-NaCl-CaCl₂) (Eglinger et al., 2013, submitted). Both fluid inclusion subtypes were locally found within the same inclusion trails suggesting that they were part of the same fluid phase. This heterogeneous entrapment might be the result of immiscibility below the solvus of a homogeneous fluid. As a result, there is a large scattering of homogenization temperatures (e.g. Diamond, 2001). However, the lowest homogenization temperatures obtained for type-IIa and type-IIb are similar and range from 200 to 300 °C. They may be interpreted as the true trapping temperature (e.g. Diamond, 2001). In the case of immiscibility, the pressure of entrapment is generally obtained from inclusions with the high-carbonic content at homogenization temperatures generally easily observed in low-carbonic inclusions (e.g. Mullis 1987; Tarantola et al 2007). The pressure of entrapment was calculated using the equation of state of Span and Wagner (1996) for a pure CO₂ system applied to inclusions IIb in the range 200-300 °C. In order to cover the entire possible range of PT entrapment, simultaneous decrepitation of both types of inclusions up to around 300 °C was considered. This yields a pressure of 160-220 MPa as a function of the size of the inclusions (10 to 5 µm) (Bodnar, 2003).

Fluid type-III: low salinity aqueous fluids

The first melting temperature observed within one to two-phase type-III inclusions is low and likely indicates a fluid composition in the NaCl-CaCl₂-H₂O system. The deformation of the water band by Raman spectroscopy at quartz extinction is compatible with a 14-16 wt.% eq. NaCl (Dubessy et al., 2002; Baumgartner and Bakker, 2010; Caumon et al., in press). When present, the gas phase shows an O₂-H₂ mixture (a_{vap} lower than 20 %). Bulk homogenization ($T_{\text{LV} \rightarrow \text{L}}$) is comprised between 68 and 188 °C (Eglinger et al., 2013, submitted). These fluids were trapped in a pure brittle domain and show a wide range of homogenization temperatures reaching very-low $T_{\text{LV} \rightarrow \text{L}}$. This indicates an entrapment in a very late event, likely under hydrostatic conditions. The intersection of the isochores with hydrostatic geotherms of 30 and 60 °C.km⁻¹ provides an estimate for the maximum trapping PT conditions of this type III fluid of 70 MPa and 225 °C.

Table 56: Sample location. Abbreviations: Aln = Allanite, Ap = Apatite, Br = Brannerite, Bt = Biotite, Chl = Chlorite, Ep = Epidote, Kfs = K-Feldspar, Grt = Garnet, Hem = Hematite, Ky = Kyanite, Mc = Microcline, Mnz = Monazite, Ms = Muscovite, Phl = Phlogopite, Pl = Plagioclase, Qtz = Quartz, Rt = Rutile, Sep = Scapolite, Tlc = Talc, Ur = Uraninite, Zrn = Zircon.

Number	Label	Sampling	Coordinates		Lithology	Mineralogy	
			North	East		Primary	Secondary
1	ZM-10-07	Outcrop	8647897	432804	Kyanite micaschist	Qtz, Ky, Phl, Hem, Rt, Zrn	Ms, Chl, Mnz
2	ZM-10-24	Outcrop	8646101	446153	Kyanite micaschist	Qtz, Ky, Phl, Hem, Rt, Zrn	Ms, Chl, Mnz
3	7703-29	Drill core	8648050	429750	Kyanite micaschist	Qtz, Ky, Phl, Tlc, Hem, Rt, Zrn	Chl, Ap, Ur, Br
4	ZM-10-09	Outcrop	8648457	434886	Gneiss	Qtz, Pl, Bt, Kfs, Aln, Zrn	Ep, Ap, Ms, Sep
5	ZM-10-17	Outcrop	8647148	435744	Gneiss	Qtz, Pl, Bt, Kfs, Aln, Zrn	Ep, Ap, Ms, Sep
6	ZM-10-62	Outcrop	8627213	440243	Migmatite	Qtz, Bt, Mc, Grt, Ms, Mnz, Zrn	Aln, Ep

Table 57: Whole rock geochemistry of investigated samples

Sample	ZM-10-07	ZM-10-24	ZM-10-09	ZM-10-17	ZM-10-62
<i>Major elements / wt. %</i>					
SiO₂	75.50	57.71	67.07	67.76	72.40
Al₂O₃	16.01	17.12	14.56	15.34	12.91
Fe₂O₃	1.70	5.47	4.14	3.37	6.53
MnO	0.00	0.01	0.05	0.03	0.11
MgO	4.26	11.37	1.93	1.64	0.27
CaO	0.04	0.00	3.54	2.85	1.62
Na₂O	0.11	0.21	2.77	3.95	1.33
K₂O	1.59	4.13	2.92	2.59	3.23
TiO₂	0.21	0.74	0.36	0.39	0.60
P₂O₅	0.00	0.00	0.12	0.22	0.17
PF	1.43	3.34	2.33	1.64	0.39
Total	100.85	100.10	99.79	99.77	100.30
<i>Trace elements / ppm</i>					
Cu	0.00	12.60	305.50	14.50	7.54
Rb	39.30	146.00	115.70	113.70	91.65
Sr	4.70	4.30	227.10	367.20	120.10
Y	52.30	13.50	7.63	15.17	106.50
Zr	92.60	86.60	107.40	162.30	828.00
Nb	13.40	5.79	5.06	7.68	32.73
Ba	99.00	166.00	487.20	511.60	1342.00
Th	3.22	1.33	9.02	9.20	10.39
U	0.48	1.36	2.46	1.66	1.52
La	16.30	11.20	45.79	33.59	118.60
Ce	28.50	22.80	86.85	64.71	226.60
Pr	3.81	2.85	9.87	7.05	28.65
Nd	13.40	11.00	5.07	24.64	110.30
Sm	2.56	2.24	5.03	3.88	23.04
Eu	1.00	0.82	1.22	0.99	4.21
Gd	4.27	3.09	3.06	2.80	20.73
Tb	1.04	0.57	0.36	0.42	3.32
Dy	8.01	2.95	1.71	2.51	19.72
Ho	1.87	0.51	0.28	0.48	3.79
Er	5.86	1.36	0.74	1.45	10.51
Tm	0.98	0.19	0.10	0.21	1.54
Yb	7.09	1.28	0.80	1.31	10.12
Lu	1.09	0.19	0.14	0.19	1.54

Table 58: Average mineral compositions with confidence interval of 95% in brackets (n = number of samples) for samples ZM-10-07, ZM-10-24 and 7703-29.

Mineral Sample	Phl			Chl			Ms			
	ZM-10-07	ZM-10-24	7703-29	ZM-10-07	ZM-10-24	7703-29	ZM-10-07	ZM-10-24	7703-29	
<i>Oxides / wt. %</i>	SiO₂	40.67 (0.18)	40.16 (0.40)	39.99 (0.34)	28.81 (0.24)	27.96 (0.30)	28.59 (0.50)	45.05	47.77	45.84
	TiO₂	0.66 (0.03)	0.69 (0.01)	0.77 (0.02)	0.05 (0.01)	0.04 (0.01)	0.04 (0.01)	0.39	0.53	0.39 (0.08)
	Al₂O₃	17.93 (0.22)	17.58 (0.13)	18.16 (0.20)	23.89 (0.14)	23.3 (0.32)	23.28 (0.55)	32.51	32.77	33.78
	FeO	1.88 (0.07)	2.37 (0.06)	4.23 (0.12)	1.45 (0.04)	1.88 (0.11)	3.87 (0.28)	3.80	2.80	2.68
	MnO	0.03 (0.02)	0.01 (0.01)	0.04 (0.02)	0.00 (0.01)	0.03 (0.03)	0.08 (0.02)	0.02	0.00	0.03 (0.02)
	MgO	23.85 (0.18)	22.83 (0.20)	21.74 (0.24)	32.85 (0.42)	31.36 (0.29)	31.17 (0.04)	1.39	1.26	1.19
	CaO	0.04 (0.04)	0.01 (0.01)	0.02 (0.01)	0.00 (0.01)	0.00 (0.01)	0.03 (0.00)	0.02	0.00	0.00
	Na₂O	0.48 (0.03)	0.48 (0.03)	0.42 (0.02)	0.00 (0.01)	0.02 (0.01)	0.02 (0.13)	1.08	1.04	1.10
	K₂O	8.68 (0.19)	9.70 (0.30)	9.50 (0.08)	0.08 (0.02)	0.02 (0.13)	0.11 (0.09)	9.32	9.53	9.91
	Total	94.24 (0.45)	93.86 (0.50)	94.89 (0.70)	87.13 (0.53)	86.62 (0.38)	87.23 (0.52)	93.58	95.70	94.90
	<i>Oxygens</i>	11	11	11	14	14	14	11	11	11
	<i>Cations</i>	Si	2.845 (0.013)	2.847 (0.015)	2.824 (0.010)	2.686 (0.012)	2.689 (0.023)	2.699 (0.015)	3.088	3.173
Al^{IV}		1.155 (0.013)	1.153 (0.015)	1.175 (0.010)	1.314 (0.012)	1.311 (0.023)	1.301 (0.015)	0.912	0.827	0.919
Al^{VI}		0.323 (0.010)	0.315 (0.014)	0.336 (0.009)	1.312 (0.027)	1.329 (0.020)	1.290 (0.038)	1.716	1.740	1.758
Ti		0.035 (0.002)	0.037 (0.001)	0.041 (0.001)	0.004 (0.001)	0.003 (0.001)	0.003 (0.004)	0.020	0.026	0.020
Fe^{tot}		0.110 (0.005)	0.140 (0.003)	0.250 (0.008)	0.113 (0.003)	0.151 (0.009)	0.307 (0.016)	0.218	0.156	0.152
Mn		0.002 (0.001)	0.001 (0.001)	0.003 (0.001)	0.000 (0.000)	0.002 (0.002)	0.007 (0.001)	0.001	0.000	0.002
Mg		2.488 (0.013)	2.413 (0.019)	2.289 (0.015)	4.564 (0.047)	4.496 (0.032)	4.385 (0.013)	0.142	0.125	0.113
Ca		0.003 (0.003)	0.000 (0.001)	0.001 (0.001)	0.000 (0.001)	0.001 (0.001)	0.003 (0.000)	0.001	0.000	0.000
Na		0.065 (0.004)	0.067 (0.003)	0.057 (0.003)	0.000 (0.002)	0.004 (0.002)	0.004 (0.019)	0.144	0.134	0.144
K		0.775 (0.015)	0.877 (0.028)	0.856 (0.007)	0.010 (0.002)	0.002 (0.015)	0.013 (0.007)	0.815	0.808	0.850

X_{Mg}	0.958 (0.002)	0.945 (0.001)	0.901 (0.003)	0.976	0.968 (0.000)	0.934 (0.002)	-	-	-
n	7	13	22	1	5	23	1	1	4

Table 59: Representative monazite analyses from sample *ZM-10-07*

Sample	ZM-10-07	ZM-10-07	ZM-10-07	ZM-10-07	ZM-10-07	ZM-10-07	ZM-10-07	ZM-10-07
Analysis n°	44	46	47	57	69	72	73	79
Mineral	Mnz	Mnz	Mnz	Mnz	Mnz	Mnz	Mnz	Mnz
Oxides / wt. %								
P₂O₅	30.1	30.33	30.12	30.44	29.85	30.28	30.38	30.06
SiO₂	0.21	0.18	0.25	0.22	0.36	0.19	0.25	0.28
CaO	1.34	0.32	0.51	1.14	0.70	0.26	0.56	0.71
Y₂O₃	1.03	0.50	1.55	0.95	1.39	0.57	1.62	1.44
La₂O₃	17.27	16.19	17.00	17.65	16.79	16.15	16.75	15.80
Ce₂O₃	25.97	31.20	28.75	27.05	28.17	30.81	28.45	27.73
Pr₂O₃	3.25	4.31	3.68	3.38	3.73	4.05	3.58	3.82
Nd₂O₃	11.09	14.37	12.57	11.23	12.59	14.27	12.72	13.47
Sm₂O₃	1.66	1.86	1.69	1.63	1.73	2.03	1.73	2.05
Gd₂O₃	1.75	0.95	1.42	1.56	1.48	1.13	1.46	1.55
PbO	0.15	0.04	0.07	0.13	0.08	0.02	0.06	0.09
ThO₂	5.88	0.36	1.76	4.95	2.46	0.47	1.98	2.91
UO₂	0	0.03	0.02	0.00	0.03	0.05	0.02	0.00
Total	99.70	100.64	99.39	100.33	99.36	100.28	99.56	99.91
Oxygens	4	4	4	4	4	4	4	4
Cations								
P	0.996	0.997	0.996	0.999	0.990	0.998	1.000	0.993
Si	0.008	0.007	0.010	0.009	0.014	0.007	0.010	0.011
ΣT-site	1.004	1.004	1.006	1.007	1.004	1.005	1.010	1.004
Ca	0.056	0.013	0.021	0.047	0.029	0.011	0.023	0.030
Y	0.021	0.010	0.032	0.020	0.029	0.012	0.034	0.030
La	0.249	0.232	0.245	0.252	0.243	0.232	0.240	0.227
Ce	0.372	0.443	0.411	0.384	0.404	0.439	0.405	0.396
Pr	0.046	0.061	0.052	0.048	0.053	0.057	0.051	0.054
Nd	0.155	0.199	0.175	0.155	0.176	0.198	0.177	0.188
Sm	0.022	0.025	0.023	0.022	0.023	0.027	0.023	0.028
Gd	0.023	0.012	0.018	0.020	0.019	0.015	0.019	0.020
Pb	0.002	0.000	0.001	0.001	0.001	0.000	0.001	0.001
Th	0.052	0.003	0.016	0.044	0.022	0.004	0.018	0.026
U	0.000	0.000	0.000	0.000	0.000	0.000	0.000	0.000
Σa-site	0.998	1.000	0.995	0.993	1.000	0.996	0.989	0.999
%Hutt	0.81	0.69	0.97	0.85	1.38	0.73	0.97	1.08
%Brab	11.41	2.75	4.40	9.68	5.96	2.27	4.80	6.03
%Mnz	87.78	96.56	94.63	89.48	92.66	97.00	94.24	92.89

Table 60: Representative monazite analyses from sample *ZM-10-24*

Sample		ZM-10-24	ZM-10-24	ZM-10-24	ZM-10-24	ZM-10-24	ZM-10-24	ZM-10-24	ZM-10-24
Analysis n°		85	95	101	103	108	109	115	116
Mineral		Mnz	Mnz	Mnz	Mnz	Mnz	Mnz	Mnz	Mnz
Oxides / wt. %	P₂O₅	29.76	30.06	29.81	29.85	30.28	29.82	30.00	29.67
	SiO₂	0.47	0.19	0.34	0.21	0.41	0.28	0.22	0.52
	CaO	1.21	0.31	0.23	0.28	1.13	0.41	0.34	1.38
	Y₂O₃	1.13	0.35	0.39	0.32	1.21	1.22	0.36	1.04
	La₂O₃	13.23	14.90	15.17	14.88	12.94	14.08	14.84	13.58
	Ce₂O₃	26.29	32.09	32.07	31.66	26.46	29.40	31.38	25.69
	Pr₂O₃	3.09	3.90	3.90	3.91	3.32	3.63	3.86	3.18
	Nd₂O₃	12.09	15.05	14.46	14.63	12.49	14.02	14.16	11.58
	Sm₂O₃	2.47	1.96	1.98	2.44	2.73	2.42	2.41	2.42
	Gd₂O₃	2.82	0.69	0.70	1.33	3.18	2.49	1.11	2.73
	PbO	0.14	0.02	0.03	0.01	0.12	0.04	0.02	0.17
	ThO₂	5.83	0.23	0.31	0.14	4.57	1.04	0.66	6.98
	UO₂	0.04	0.07	0.10	0.06	0.03	0.06	0.05	0.01
	Total	98.57	99.82	99.49	99.72	98.87	98.91	99.41	98.95
Oxygens		4	4	4	4	4	4	4	4
Cations	P	0.994	0.996	0.992	0.993	1.001	0.995	0.997	0.989
	Si	0.019	0.007	0.013	0.008	0.016	0.011	0.009	0.020
	ΣT-site	1.012	1.004	1.005	1.002	1.017	1.006	1.006	1.010
	Ca	0.051	0.013	0.010	0.012	0.047	0.017	0.014	0.058
	Y	0.024	0.007	0.008	0.007	0.025	0.026	0.008	0.022
	La	1.192	0.215	0.220	0.216	0.186	0.205	0.215	0.197
	Ce	0.380	0.460	0.461	0.456	0.378	0.424	0.451	0.371
	Pr	0.044	0.056	0.056	0.056	0.047	0.052	0.055	0.046
	Nd	0.170	0.210	0.203	0.205	0.174	0.197	0.199	0.163
	Sm	0.034	0.026	0.027	0.033	0.037	0.033	0.033	0.033
	Gd	0.037	0.009	0.009	0.017	0.041	0.033	0.014	0.036
	Pb	0.001	0.000	0.000	0.000	0.001	0.000	0.000	0.002
	Th	0.052	0.002	0.003	0.001	0.041	0.009	0.006	0.063
	U	0.000	0.001	0.001	0.001	0.000	0.001	0.000	0.000
	Σa-site	0.986	1.000	0.998	1.003	0.979	0.997	0.995	0.989
	%Hutt	1.84	0.73	1.31	0.81	1.60	1.09	0.85	2.03
	%Brab	10.54	2.71	2.13	2.43	9.73	3.59	2.95	11.94
	%Mnz	87.62	96.56	96.56	96.76	88.67	95.32	96.20	86.03

Table 61: Representative monazite, allanite and epidote analyses from sample *ZM-10-62* using for uranium mass balance calculation

Sample		ZM-10-17	ZM-10-17	ZM-10-62	ZM-10-62	ZM-10-62	ZM-10-62	ZM-10-62	ZM-10-62
Analysis n°		1	2	3	4	5	6	7	8
Mineral		Aln	Th,REE-sil	Mnz	Aln	Ep	Mnz	Aln	Ep
Oxides / wt. %	P₂O₅	0.29	1.67	16.33	0.37	0.41	13.68	0.29	0.42
	SiO₂	37.96	35.29	5.43	32.87	38.21	3.14	32.05	38.43
	CaO	11.66	2.27	6.82	13.78	24.34	6.11	12.18	23.74
	FeO	9.00	11.56	1.59	12.49	12.58	1.53	13.58	13.10
	Y₂O₃	0.37	2.32	0.95	0.00	0.00	0.87	0.00	0.00
	La₂O₃	3.37	0.43	16.97	6.14	0.00	18.48	7.18	0.00
	Ce₂O₃	7.1	7.30	25.00	9.61	0.00	28.21	10.86	0.00
	Pr₂O₃	0.94	0.19	2.64	0.90	0.18	2.62	1.07	0.17
	Nd₂O₃	2.61	0.90	8.30	2.23	0.00	8.95	2.68	0.00
	Sm₂O₃	0.42	0.36	1.23	0.15	0.00	1.26	0.21	0.00
	Gd₂O₃	0.00	0.00	0.66	0.00	0.00	0.78	0.00	0.00
	PbO	0.11	0.05	0.03	0.04	0.00	0.03	0.04	0.01
	ThO₂	0.65	7.47	0.71	0.44	0.00	0.94	0.42	0.00
	UO₂	0.03	0.01	0.06	0.02	0.00	0.05	0.02	0.00
	Total		93.31	83.48	89.81	97.02	100.44	87.95	96.56
Cations / wt. %	P	0.13	0.73	7.13	0.16	0.18	5.97	0.13	0.18
	Si	17.74	16.49	2.54	15.37	17.86	1.47	14.98	17.96
	Ca	9.05	1.63	4.87	9.85	17.39	4.36	8.71	16.97
	Fe	6.99	8.99	1.23	9.71	9.78	1.19	10.55	10.19
	Y	0.29	1.83	0.75	0.00	0.00	0.68	0.00	0.00
	La	2.87	0.37	14.47	5.24	0.00	15.75	6.12	0.00
	Ce	6.07	6.23	21.35	8.21	0.00	24.09	9.27	0.00
	Pr	0.80	0.16	2.26	0.77	0.15	2.24	0.91	0.15
	Nd	2.24	0.77	7.11	1.91	0.00	7.67	2.29	0.00
	Sm	0.36	0.31	1.06	0.13	0.00	1.09	0.18	0.00
	Gd	0.00	0.00	0.57	0.00	0.00	0.68	0.00	0.00
	Pb	0.10	0.05	0.03	0.04	0.00	0.03	0.04	0.01
	Th	0.57	6.57	0.62	0.38	0.00	0.82	0.37	0.00
	U	0.03	0.09	0.06	0.01	0.00	0.05	0.01	0.00

Table 62: Representative scapolite analyses from sample *ZM-10-09* and *ZM-10-17*

Sample		ZM-10-09	ZM-10-09	ZM-10-09	ZM-10-09	ZM-10-17	ZM-10-17	ZM-10-17	ZM-10-17
Mineral		Scp	Scp	Scp	Scp	Scp	Scp	Scp	Scp
Oxides / wt. %	SiO₂	51.43	52.07	52.29	51.59	49.95	52.19	51.66	51.54
	TiO₂	0.00	0.00	0.03	0.00	0.02	0.05	0.00	0.04
	Al₂O₃	23.21	23.50	23.38	23.52	23.94	23.54	24.28	23.62
	FeO	0.02	0.02	0.04	0.01	0.00	0.05	0.00	0.08
	MnO	0.03	0.00	0.00	0.00	0.07	0.00	0.00	0.08
	MgO	0.01	0.01	0.00	0.02	0.00	0.03	0.00	0.00
	CaO	9.86	10.29	9.84	10.43	10.78	10.10	11.35	10.66
	Na₂O	8.35	7.81	8.19	7.29	7.60	7.73	7.25	7.41
	K₂O	0.73	0.71	0.81	0.64	0.60	0.69	0.60	0.62
	Cl	2.24	1.93	2.28	1.84	1.83	2.09	1.74	1.88
	SO₃	0.18	0.87	0.18	1.02	0.74	0.25	0.92	0.71
	CO₂	1.93	1.99	1.94	2.00	2.09	2.15	2.23	2.12
		Total	97.99	99.20	98.98	98.36	97.62	98.87	100.03
Si + Al		12	12	12	12	12	12	12	12
Cations	Si	7.834	7.833	7.859	7.806	7.668	7.835	7.722	7.792
	Al^{IV}	4.166	4.167	4.141	4.194	4.332	4.165	4.278	4.208
	Ti	0.002	0.002	0.005	0.001	0.000	0.007	0.000	0.010
	Fe^{tot}	0.002	0.002	0.005	0.001	0.000	0.007	0.000	0.010
	Mn	0.004	0.000	0.000	0.000	0.009	0.000	0.000	0.010
	Mg	0.002	0.002	0.000	0.005	0.000	0.007	0.000	0.000
	Ca	1.609	1.659	1.584	1.691	1.773	1.625	1.818	1.727
	Na	2.466	2.278	2.387	2.139	2.262	2.250	2.101	2.172
	K	0.142	0.136	0.155	0.124	0.118	0.132	0.114	0.120
	X_{Cl}	0.58	0.49	0.58	0.47	0.48	0.53	0.44	0.48
	X_{SO₃}	0.02	0.10	0.02	0.12	0.08	0.03	0.10	0.08
	X_{CO₂}	0.40	0.41	0.40	0.41	0.44	0.44	0.46	0.44
	Eq_{An}	0.39	0.39	0.38	0.40	0.44	0.39	0.43	0.40
	lnK_D	-1.01	-1.01	-1.04	-0.97	-0.81	-1.01	-0.87	-0.95
	X^{Fluid}_{NaCl}	0.53	0.44	0.51	0.43	0.48	0.44	0.41	0.42

Table 63: Th-Pb results on monazite grains from kyanite micaschists

Sample	Isotopic ratios		Ages / Ma	
	$^{208}\text{Pb}/^{232}\text{Th}$	2σ	$^{208}\text{Pb}/^{232}\text{Th}$	2σ
ZM-10-07				
05070212b	0.02777	0.00064	554	13
06070212b	0.02426	0.00054	484	11
07070212b	0.02433	0.00054	486	11
08070212b	0.02418	0.00054	483	11
09070212b	0.02519	0.00056	503	11
10070212b	0.02441	0.00054	488	11
11070212b	0.02524	0.00056	504	11
12070212b	0.02728	0.00060	544	12
15070212b	0.02487	0.00054	496	11
16070212b	0.02353	0.00052	470	10
17070212b	0.02408	0.00054	481	11
18070212b	0.02402	0.00052	480	10
19070212b	0.02399	0.00052	479	10
20070212b	0.02439	0.00054	487	11
21070212b	0.02507	0.00056	501	11
22070212b	0.02460	0.00054	491	11
25070212b	0.02457	0.00054	491	11
26070212b	0.02441	0.00054	487	10
27070212b	0.02396	0.00052	479	10
28070212b	0.02462	0.00054	492	11
29070212b	0.02516	0.00054	502	11
30070212b	0.02396	0.00052	479	10
31070212b	0.02405	0.00052	480	10
32070212b	0.02453	0.00054	490	11
35070212b	0.02488	0.00054	497	11
36070212b	0.02362	0.00052	472	10
37070212b	0.02385	0.00052	476	10
38070212b	0.02436	0.00052	486	10
39070212b	0.02457	0.00052	491	10
40070212b	0.02528	0.00054	505	11
41070212b	0.02704	0.00058	539	11
ZM-10-24				
05070212a	0.02349	0.00054	469	10
07070212a	0.02385	0.00054	476	11
08070212a	0.02518	0.00058	503	12
09070212a	0.02543	0.00060	508	12
10070212a	0.02554	0.00068	510	13
11070212a	0.02397	0.00054	479	11
12070212a	0.02521	0.00060	503	12
15070212a	0.02313	0.00052	462	10
16070212a	0.02254	0.00050	451	10

17070212a	0.02337	0.00072	467	14
18070212a	0.02448	0.00054	489	11
20070212a	0.02312	0.00052	462	10
21070212a	0.02428	0.00054	485	11
22070212a	0.02538	0.00058	507	11
25070212a	0.02469	0.00054	493	11
26070212a	0.02585	0.00058	516	11
27070212a	0.02461	0.00054	491	11
28070212a	0.02528	0.00056	505	11
29070212a	0.02543	0.00056	508	11
30070212a	0.02363	0.00052	472	10
31070212a	0.02435	0.00054	486	11
32070212a	0.02429	0.00054	485	10
35070212a	0.02453	0.00054	490	11
36070212a	0.02443	0.00054	488	11
37070212a	0.02714	0.00060	541	12
38070212a	0.02722	0.00060	543	12
39070212a	0.02394	0.00052	478	10

Table 64: U-Pb measurements on uraninite grains from sample 7703-29. Abbreviations: Ip = Primary intensity; nA = nanoampere; Is = Intensity (in count per second); rel. = relative; Cor. = correlation.

Sample			Corrected ratios		Calibrated ratios					Apparent ages (Ma)			
	Ip (nA)	Is ²⁰⁶ Pb (cps)	²⁰⁷ Pb/ ²⁰⁶ Pb	± rel	²⁰⁶ Pb/ ²³⁸ U	±	²⁰⁷ Pb/ ²³⁵ U	±	Cor. Err.	²⁰⁶ Pb/ ²³⁸ U	±	²⁰⁷ Pb/ ²³⁵ U	±
7703-29@0	1.58	15159	0.0577	0.0025	0.0746	0.0010	0.594	0.008	0.984	464	6	473	5
7703-29@1	1.61	16148	0.0584	0.0022	0.0689	0.0009	0.555	0.007	0.987	430	6	448	5
7703-29@2	1.64	15575	0.0581	0.0021	0.0682	0.0005	0.546	0.004	0.965	425	3	442	3
7703-29@3	1.65	17849	0.0580	0.0017	0.0750	0.0006	0.600	0.005	0.978	466	4	477	3
7703-29@4	1.65	18064	0.0579	0.0022	0.0745	0.0005	0.595	0.005	0.957	463	3	474	3
7703-29@5	1.67	16573	0.0580	0.0022	0.0688	0.0006	0.551	0.005	0.974	429	4	446	3
7703-29@6	1.60	17652	0.0580	0.0019	0.0752	0.0004	0.601	0.004	0.951	467	3	478	2
7703-29@7	1.55	18052	0.0580	0.0028	0.0756	0.0005	0.605	0.004	0.910	470	3	480	3
7703-29@8	1.57	16976	0.0584	0.0026	0.0718	0.0005	0.577	0.004	0.943	447	3	463	3

Complementary data

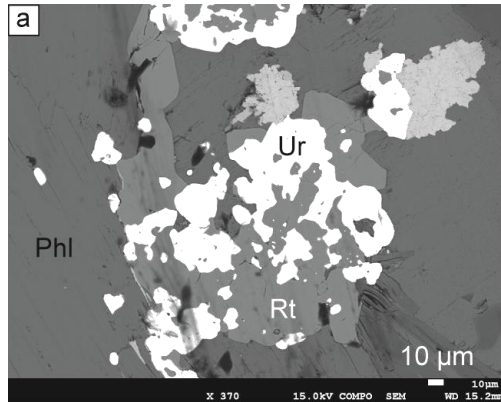
Thermometry on accessory minerals associated with uraninite

In order to determine at which temperature uranium oxides crystallized, we used conventional thermometry such as the substitution of zirconium within rutile (Zack et al., 2004) and the degree of organization of carbonaceous material (Beyssac et al., 2002). In the Malundwe deposit (Mwombezi dome), uraninite grains, scattered within the foliation defined by phlogopite and kyanite crystals, are cogenetic with rutile, molybdenite and graphite.

Zirconium content within rutile grains was obtained by LA-ICPMS, at GeoRessources laboratory (Nancy, France), using a NIST 610 SRM certified glass as external standard (Lach et al., 2013). Zirconium in rutile grain is substituted to titanium. Nine analyses were realized on different grains, core and/or rim, and yielded a Zr average of 181 ppm with a standard deviation (1σ) of 10 ppm. Using the equations of Zack et al. (2004), a temperature of 654 ± 50 °C is calculated for rutile crystallization (Figure 83a).

In addition, in the Malundwe deposit, uranium oxide is cogenetically associated with carbonaceous material. During increasing metamorphism, organic matter is progressively transformed into graphite. The degree of organisation of carbonaceous material (CM) is directly controlled by the metamorphic grade (Beyssac et al., 2002). Following the methodology of Beyssac et al. (2002) using the Raman spectroscopy at GeoRessources laboratory (Nancy, France), we characterized the degree of organization of CM by Raman spectroscopy and obtained an average temperature of 626 ± 50 °C (Figure 83b). The same temperature range is obtained with Zr-in-rutile thermometry.

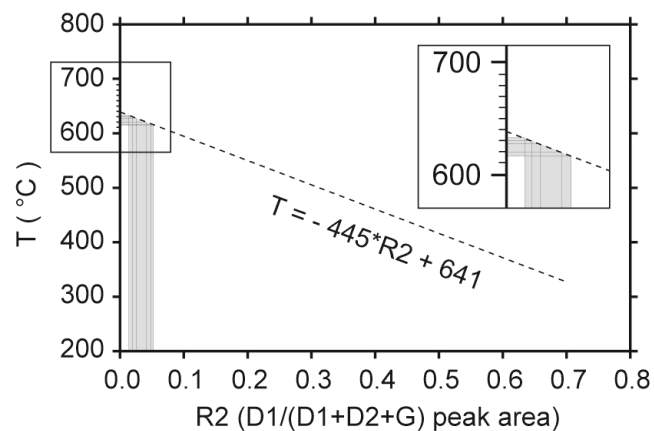
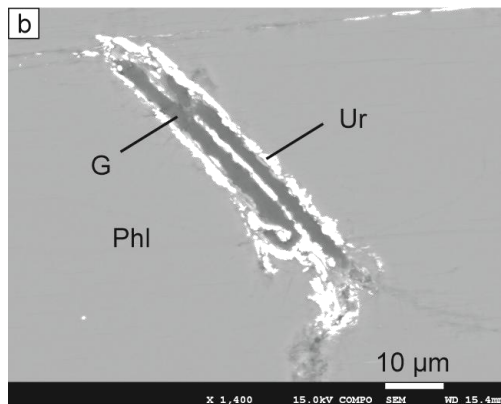
These *in-situ* crystallisation temperatures obtained on mineral, intimately associated with uranium oxides, are in good agreement (i) with *P-T* conditions obtained on whole-rocks predicted by pseudosections at 610 ± 30 °C on kyanite micaschists (Eglinger et al., to be submitted; chapter 2) and also (ii) with *P-T* conditions recorded by fluid inclusions (type-I; Eglinger et al., in press; chapter 7).



Locality (sample)	T (°C)	Zr average (ppm)	Zr maximum (ppm)	N° of analyzed grains
Malundwe (7703-2)	654	181	195	9

$$T(\text{in } ^\circ\text{C}) = 127.8 \times \ln(\text{Zr in ppm}) - 10$$

Using the Zack et al. (2004) thermometer: $T = 654 \pm 50 \text{ } ^\circ\text{C}$



Using the Beysac et al. (2002) thermometer: $T = 626 \pm 50 \text{ } ^\circ\text{C}$

Figure 83: *In-situ* thermometry on minerals using the LA-ICPMS on rutile grains (a) and the Raman spectroscopy on graphite (b).

Geochronology on uraninite grains

Several new *in-situ* U-Pb isotopic ages were obtained in this study for uraninites from the western part of the Domes region and more precisely from the Malundwe (Mwombezhi dome; Table 65; Table 66; Table 67), Kawanga (Kabompo Dome; Table 68) and Mitukuluku (Solwezi Dome; Table 64) occurrences. Uraninite grains were selected on thin section and analyzed on a SIMS CAMECA IMS1270 at the CRPG (Nancy, France). U-Pb isotopic data for uraninites from Malundwe, Kawanga and Mitukuluku occurrences plotted in Concordia diagrams give Discordia with an upper intercept at $531 \pm 5 \text{ Ma}$, $539 \pm 9 \text{ Ma}$ and $544 \pm 6 \text{ Ma}$ for Malundwe (Figure 84a, b

and c), 538 +17/-14 Ma for Kawanga (Figure 84d) and 532 ± 18 Ma for Mitukuluku (see Eglinger et al., submitted; chapter 7).

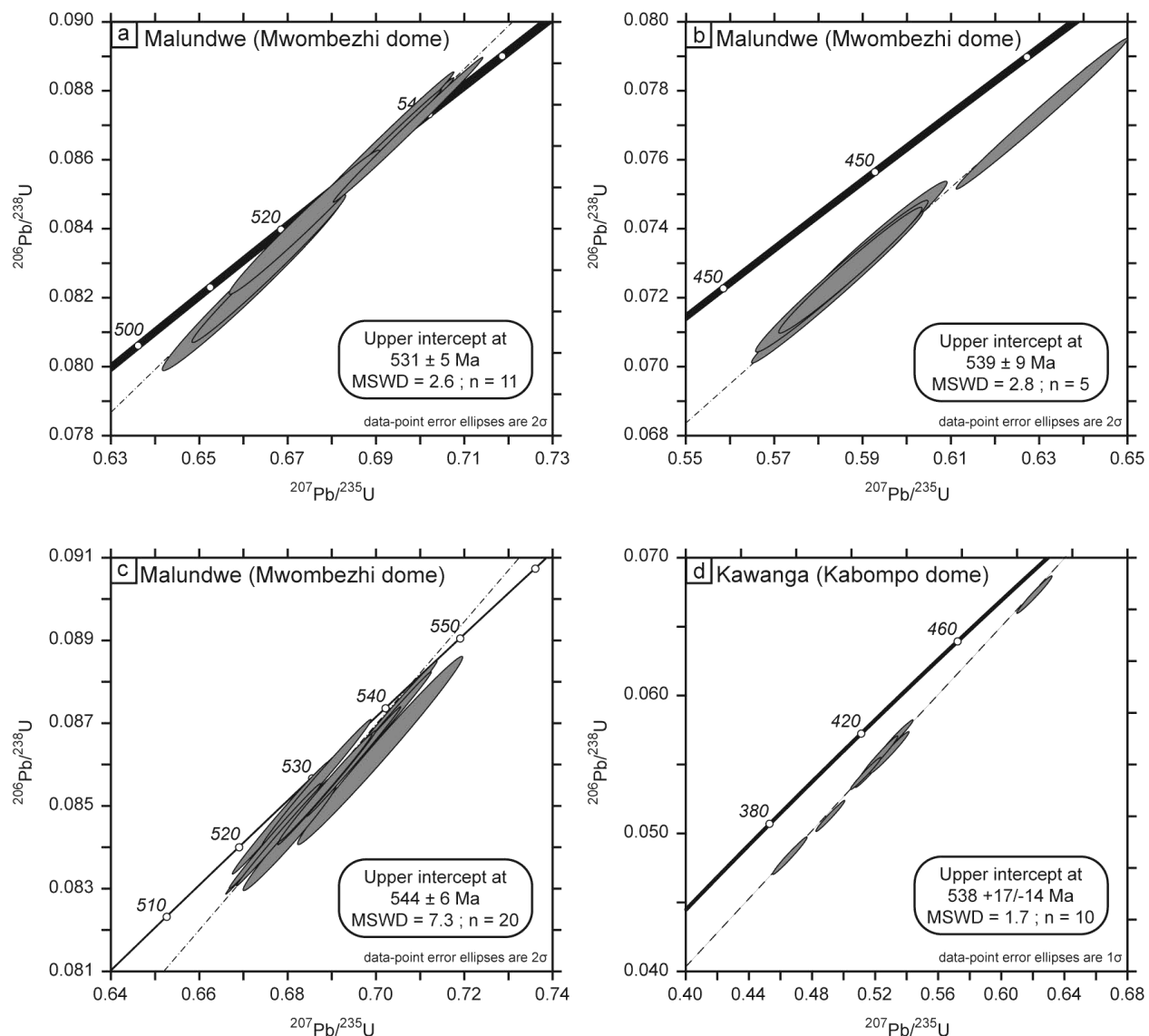


Figure 84: Concordia plots of U-Pb data for uraninite grains from Malundwe (a, b, c) and Kawanga (d) occurrences. a = sample #88-15; b = sample 7703-2; c = sample C025; d = sample 7703-21.

All these new U-Pb ages on uraninite grains confirm a main uranium mineralizing event between ca. 550 and 510 Ma, in good agreement with that of Lufilian metamorphism peak of the host rocks dated at ca. 555-525 Ma during the continental tectonic accretion.

Table 65: U-Pb measurements on uraninite grains from sample #88-15. Abbreviations: Ip = Primary intensity; nA = nanoampere; Is = Intensity (in count per second); rel. = relative; Cor. = correlation.

Sample			Corrected ratios		Calibrated ratios				Apparent ages (Ma)				
	Ip (nA)	Is ²⁰⁶ Pb (cps)	²⁰⁷ Pb/ ²⁰⁶ Pb	± rel	²⁰⁶ Pb/ ²³⁸ U	±	²⁰⁷ Pb/ ²³⁵ U	±	Cor. Err.	²⁰⁶ Pb/ ²³⁸ U	±	²⁰⁷ Pb/ ²³⁵ U	±
88-15@1	3.22	52015	0.0582	0.0022	0.082	0.001	0.662	0.008	0.985	511	6	516	5
88-15@2	3.20	255407	0.0580	0.0008	0.085	0.001	0.676	0.007	0.997	523	5	524	4
88-15@3	3.21	274882	0.0582	0.0009	0.087	0.001	0.697	0.007	0.996	537	5	537	4
88-15@5	3.23	54871	0.0583	0.0016	0.083	0.001	0.666	0.007	0.988	513	5	518	4
88-15@6	3.24	203187	0.0581	0.0007	0.084	0.001	0.676	0.007	0.997	522	5	524	4
88-15@7	3.23	230239	0.0580	0.0006	0.086	0.001	0.688	0.007	0.998	532	5	532	4
88-15@8	3.22	187123	0.0580	0.0012	0.086	0.001	0.688	0.007	0.993	532	5	532	4
88-15@9	3.23	106442	0.0580	0.0017	0.084	0.001	0.674	0.007	0.987	521	5	523	4
88-15@10	3.25	231452	0.0579	0.0009	0.086	0.001	0.690	0.007	0.996	534	5	533	4
88-15@11	3.24	248317	0.0580	0.0008	0.086	0.001	0.691	0.007	0.997	534	5	533	4
88-15@13	3.24	263378	0.0580	0.0008	0.086	0.001	0.690	0.007	0.997	534	5	533	4

Table 66: U-Pb measurements on uraninite grains from sample 7703-2. Abbreviations: Ip = Primary intensity; nA = nanoampere; Is = Intensity (in count per second); rel. = relative; Cor. = correlation.

Sample			Corrected ratios		Calibrated ratios				Apparent ages (Ma)				
	Ip (nA)	Is ²⁰⁶ Pb (cps)	²⁰⁷ Pb/ ²⁰⁶ Pb	± rel	²⁰⁶ Pb/ ²³⁸ U	±	²⁰⁷ Pb/ ²³⁵ U	±	Cor. Err.	²⁰⁶ Pb/ ²³⁸ U	±	²⁰⁷ Pb/ ²³⁵ U	±
7703-2@2	3.32	83443	0.0581	0.0021	0.07267	0.00089	0.582	0.007	0.582	452	5	466	5
7703-2@3	3.19	70022	0.0580	0.0020	0.07357	0.00075	0.589	0.006	0.589	458	5	470	4
7703-2@4	3.11	75523	0.0584	0.0013	0.07736	0.00089	0.623	0.007	0.623	480	5	492	4
7703-2@5	3.1	65278	0.0581	0.0019	0.07285	0.00074	0.584	0.006	0.584	453	4	467	4
7703-2@6	3.15	82487	0.0582	0.0018	0.07236	0.00089	0.581	0.007	0.581	450	5	465	5

Table 67: U-Pb measurements on uraninite grains from sample C25. Abbreviations: Ip = Primary intensity; nA = nanoampere; Is = Intensity (in count per second); rel. = relative; Cor. = correlation.

Sample	Corrected ratios		Calibrated ratios				Apparent ages (Ma)						
	Ip (nA)	Is ²⁰⁶ Pb (cps)	²⁰⁷ Pb/ ²⁰⁶ Pb	± rel	²⁰⁶ Pb/ ²³⁸ U	±	²⁰⁷ Pb/ ²³⁵ U	±	Cor. Err.	²⁰⁶ Pb/ ²³⁸ U	±	²⁰⁷ Pb/ ²³⁵ U	±
C25@3	3.25	193626	0.0582	0.0010	0.084	0.001	0.677	0.007	0.995	522	5	525	4
C25@5	3.30	133093	0.0585	0.0010	0.087	0.001	0.702	0.007	0.995	537	5	540	4
C25@6	3.32	242107	0.0583	0.0008	0.084	0.001	0.679	0.007	0.997	522	5	526	4
C25@7	3.32	192369	0.0584	0.0010	0.085	0.001	0.688	0.007	0.995	529	5	532	4
C25@8	3.32	197560	0.0585	0.0008	0.086	0.001	0.695	0.007	0.997	532	5	536	4
C25@9	3.33	43483	0.0588	0.0024	0.086	0.002	0.701	0.012	0.990	534	9	539	7
C25@10	3.34	169455	0.0584	0.0010	0.085	0.001	0.689	0.007	0.996	529	5	532	4
C25@11	3.35	218624	0.0582	0.0007	0.084	0.001	0.676	0.007	0.998	521	5	525	4
C25@12	3.34	230232	0.0585	0.0010	0.087	0.001	0.703	0.007	0.995	539	5	540	4
C25@13	3.33	224682	0.0580	0.0012	0.085	0.001	0.678	0.007	0.994	524	5	526	4
C25@14	3.33	138698	0.0582	0.0013	0.086	0.001	0.686	0.008	0.994	529	6	531	5
C25@15	3.27	75410	0.0586	0.0018	0.084	0.001	0.680	0.007	0.984	522	5	527	4

Table 68: U-Pb measurements on uraninite grains from sample 7703-21. Abbreviations: Ip = Primary intensity; nA = nanoampere; Is = Intensity (in count per second); rel. = relative; Cor. = correlation.

Sample	Corrected ratios		Calibrated ratios				Apparent ages (Ma)						
	Ip (nA)	Is ²⁰⁶ Pb (cps)	²⁰⁷ Pb/ ²⁰⁶ Pb	± rel	²⁰⁶ Pb/ ²³⁸ U	±	²⁰⁷ Pb/ ²³⁵ U	±	Cor. Err.	²⁰⁶ Pb/ ²³⁸ U	±	²⁰⁷ Pb/ ²³⁵ U	±
7703-21@1	3.07	44345	0.0579	0.0021	0.0599	0.0009	0.478	0.007	0.990	375	5	397	5
7703-21@2	3.02	56900	0.0582	0.0022	0.0794	0.0009	0.637	0.007	0.979	492	5	501	4
7703-21@3	2.97	33154	0.0579	0.0026	0.0661	0.0007	0.528	0.006	0.974	413	4	430	4
7703-21@4	2.94	43433	0.0580	0.0015	0.0663	0.0008	0.530	0.006	0.992	414	5	432	4
7703-21@6	2.91	46154	0.0577	0.0022	0.0688	0.0008	0.548	0.007	0.984	429	5	444	4
7703-21@8	2.86	41406	0.0570	0.0014	0.0561	0.0008	0.441	0.007	0.996	352	5	371	5
7703-21@10	2.8	48653	0.0577	0.0018	0.0675	0.0010	0.537	0.008	0.992	421	6	436	5
7703-21@12	2.75	41358	0.0579	0.0024	0.0608	0.0007	0.485	0.006	0.982	381	5	402	4
7703-21@13	2.74	49381	0.0573	0.0036	0.0671	0.0009	0.530	0.007	0.967	419	5	432	5
7703-21@14	2.73	43035	0.0572	0.0027	0.0573	0.0008	0.453	0.006	0.980	359	5	379	4

CONCLUSIONS GENERALES

Dans cette thèse, nous avons couplé des données structurales, pétro-géochimiques, isotopiques, géochronologiques et inclusions fluides afin de (i) déterminer l'évolution crustale de la ceinture Néoprotérozoïque du Lufilien et la nature de l'héritage de croûte, (ii) reconstruire l'évolution *P-T-t* de la ceinture orogénique du Lufilien et définir la nature du contact avec la bordure des cratons Archéens et, enfin, (iii) caractériser le cycle de l'uranium et la genèse des minéralisations uranifères du Lufilien dans le cycle de Wilson. Ces axes d'étude permettent donc de discuter un modèle de croissance crustale tout en intégrant le cycle métallogénique de l'uranium pour ce segment de croûte continentale Lufilien.

1. Croissance crustale et nature de l'héritage de l'Archéen au Mésoprotérozoïque

La ceinture orogénique du Lufilien expose des fenêtres tectoniques dans la région des dômes, en Zambie, où affleurent des unités gneissique et migmatitique au sein de séries néoprotérozoïques métasédimentaires représentées par des micaschistes à disthène±talc et des marbres. Ces unités gneissique et migmatitique représentent des segments de socle dont les âges U-Pb sur zircons magmatiques présentent un enregistrement épisodique entre le Néoarchéen (~2.69 Ga) et le Mésoprotérozoïque (~1.11 Ga) témoignant d'une activité magmatique également épisodique. Les principaux pics d'âge de cristallisation de zircon enregistrés par ces roches gneissique et migmatitique sont datés à ~1.92, 1.89, 1.71, 1.19 et 1.11 Ga (Eglinger et al., à soumettre ; chapitre 2). Ces mêmes grains de zircon présentent des âges modèles T_{DM} compris principalement entre ~2.9 et 2.5 Ga ce qui suggère la formation d'une croûte continentale par fusion partielle du manteau et extraction dès la fin de l'Archéen (Néoarchéen). Les âges modèles T_{DM} Nd entre ~2.9 et 2.3 Ga obtenus sur les roches basiques (amphibolites) corroborent cette contribution juvénile du Néoarchéen. Les valeurs ϵ_{Hf} sur les grains de zircon sont majoritairement comprises entre 0 et -15, et donc inférieures au CHUR, suggérant que la contribution juvénile postérieure au Néoarchéen est peu importante et donc que les différents âges de cristallisation entre le Paléoprotérozoïque et Mésoprotérozoïque correspondent à de la remobilisation d'une croûte plus ancienne (Eglinger et al., à soumettre ; chapitre 2).

Ainsi, la croûte d'âge Néoarchéen aurait été remobilisée durant des événements magmatiques affectant la marge d'un craton, probablement le craton du Bangweulu-Congo. L'intervalle de

temps entre le Paléoprotérozoïque et le Mésoprotérozoïque décrit alors une longue période de métacratonisation (Liégeois et al., 2013) marquée par des épisodes de remobilisation crustale. Des interprétations semblables ont été proposées pour la ceinture orogénique Irumide, décrite comme la marge sud-est du métacraton du Bangweulu-Congo (De Waele et al., 2006). Ainsi, nous proposons que la région des dômes constitue la marge sud-ouest du métacraton du Bangweulu-Congo qui a ensuite été impliquée dans l'orogénèse Pan-Africaine (Eglinger et al., à soumettre ; chapitre 2).

Ces nouvelles données géochronologiques et isotopiques obtenues sur la marge sud du craton du Congo sont en accord avec un modèle de croissance d'une croûte continentale précoce, avant ~2.5 Ga, remobilisée au cours d'orogénèses au Protérozoïque. Cette conclusion partielle s'accorde avec les données récemment publiées par Belousova et al. (2010) basées sur l'analyse d'une volumineuse base de données isotopiques d'Hf de zircons détritiques ($n > 10\ 000$) dont les âges et les provenances sont extrêmement variés. Belousova et al. (2010) concluent que 60 % de la croûte continentale existante a été extrait du manteau avant 2.5 Ga.

2. Evolution *P-T-t* de la ceinture orogénique du Lufilien

Dans cette étude, nous avons redéfini les grands ensembles lithotectoniques décrits dans la littérature. Ainsi, nous distinguons des zones (i) externe et (ii) interne.

(i) La zone externe représentait une marge épicontinentale évoluant en plate-forme carbonatée. Cette série se présente actuellement décollée dans les niveaux évaporitiques du Roan et est caractérisée par des plis-failles à vergence nord. Cette zone externe est bien exprimée en République Démocratique du Congo où la couverture sédimentaire charriée masque le socle, et est connue sous le nom de *External fold-and-thrust belt*.

(ii) La zone interne représentait, au début du Néoprotérozoïque, l'ancienne marge continentale du craton du Congo, une zone à croûte amincie, de plus en plus disloquée aux approches de l'océan Zambezi. On avait donc la présence de blocs plus ou moins basculés, des horsts et des grabens ainsi que de micro-blocs continentaux individualisant

des sous bassins (exemple du bassin du Roan), séparés par des failles normales, pouvant rejouer en failles inverses lors de la convergence continentale. Actuellement, cette zone interne du Lufilien se distingue par des unités de socles gneissique et migmatitique exhumés au sein d'unités composées par des micaschistes et des marbres. Cette zone est bien exprimée en Zambie et est connue dans la littérature sous le nom de *Domes region*.

Les ceintures orogéniques du Lufilien-Zambezi s'inscrivent dans un cycle de Wilson complet. Les premiers épisodes d'amincissement lithosphérique sont contraints par la mise en place de vastes séries volcaniques datées à ~880 Ma. Cet amincissement évolue dans un premier temps en rifting intracontinental entre ~880 et 820 Ma. L'origine de ce rifting reste encore floue ; il pourrait être associé à des manifestations mantelliques profondes, type panache mantellique. Le point important à cette époque est le dépôt de niveaux évaporitiques (les séries sédimentaires du groupe du Roan), précipitant dans des bassins intracontinentaux isolés et bordés au nord par la marge sud du craton du Congo et au sud par des micro-blocs crustaux formés lors de la fragmentation de la Rodinia. Les âges U-Pb obtenus sur des grains détritiques de zircon, extraits de ces séries métasédimentaires, soulignent une source principalement Paléoproterozoïque, dont les âges se distribuent entre ~1.9 et ~1.8 Ga (Eglinger et al., à soumettre ; chapitre 4). Cet amincissement lithosphérique évolue dans le temps, plus au sud, en croûte océanique avec la formation de l'océan Zambezi, comme le confirme la présence de roches basiques avec des affinités de type MORB (John et al., 2003). Au nord, le bassin du Roan-Kundelungu est marqué par la mise en place de séries magmatiques alcalines datées entre ~750-720 Ma par la méthode U-Pb sur zircon magmatique (Barron et al., 2003 ; Eglinger et al., à soumettre ; chapitre 4). Ces séries magmatiques sont exprimées par la mise en place de gabbros, de diorites et de basaltes. Les faibles ratios $^{143}\text{Nd}/^{144}\text{Nd}_{(750-720)}$, compris entre 0.511565 et 0.511782, et les rapports élevés en $^{87}\text{Sr}/^{86}\text{Sr}_{(750-720)}$, compris entre 0.705449 et 0.708408, pourraient être expliqués par le mélange d'une ancienne lithosphère sous-continentale dans le manteau. Ceci serait en accord avec l'amincissement lithosphérique entraînant la fragmentation de la marge sud du craton du Congo. Ainsi, le bassin du Roan-Kundelungu aurait évolué comme un bassin intracontinental alors que plus au sud, l'océan du Zambezi se développait.

Les premiers évènements de convergence lithosphérique par subduction de la croûte océanique sous la marge nord du craton du Kalahari sont datés entre ~640 et 600 Ma, et caractérisés par un gradient HP-BT. Ces âges sont obtenus par la méthode isochrone grenat-roche totale sur des boudins d'éclogite décrits exclusivement dans la ceinture du Zambezi (John et al., 2003). La partie plus interne de la marge du craton du Congo rentre également en subduction, on parle alors de subduction continentale datée entre ~555 et 525 Ma. Une partie de ce matériel subducté enregistre des conditions de moyenne pression de l'ordre de 9 kbar pour des températures de l'ordre de 620 °C (Eglinger et al., à soumettre ; chapitre 4). Enfin, du fait de leur faible densité et de la relaxation thermique, ces roches seront exhumées sous forme de nappes plus ou moins ductiles formant alors un prisme d'accrétion crustal. L'exhumation de l'ensemble socle-couverture est daté entre ~510 et 470 Ma.

3. Cycle de l'uranium et genèse des minéralisations uranifères du Lufilien

L'analyse des grains détritiques de zircon des séries Néoprotérozoïques du Roan, encaissant les minéralisations uranifères, permet de caractériser la nature de l'héritage sédimentaire. Ces séries métasédimentaires ont été principalement alimentées par des roches d'âge Paléoprotérozoïque dont les âges U-Pb se répartissent entre ~1.89 et 1.72 Ga. Les âges modèles Hf de ces mêmes grains de zircon se répartissent entre ~3.16 et 2.55 avec un pic moyen à ~2.70 Ga (Figure 85). Du fait de son affinité hygromagmatophile, c'est-à-dire de son incompatibilité, l'uranium se trouve être principalement concentré dans les liquides silicatés lors des processus de fusion partielle et de cristallisation fractionnée. Ainsi, nous proposons que l'uranium ait été extrait du manteau durant la période Néoarchéenne, lors de l'extraction de ce segment de croûte continentale. Au cours des évènements magmatiques associés à la métacratonisation de cette portion de croûte continentale, notamment au Paléoprotérozoïque où une forte activité magmatique est connue, l'uranium va être remobilisé et concentré par différents événements de différenciation magmatique en marge du craton archéen et par érosion/transport/dépôt (Figure 85).

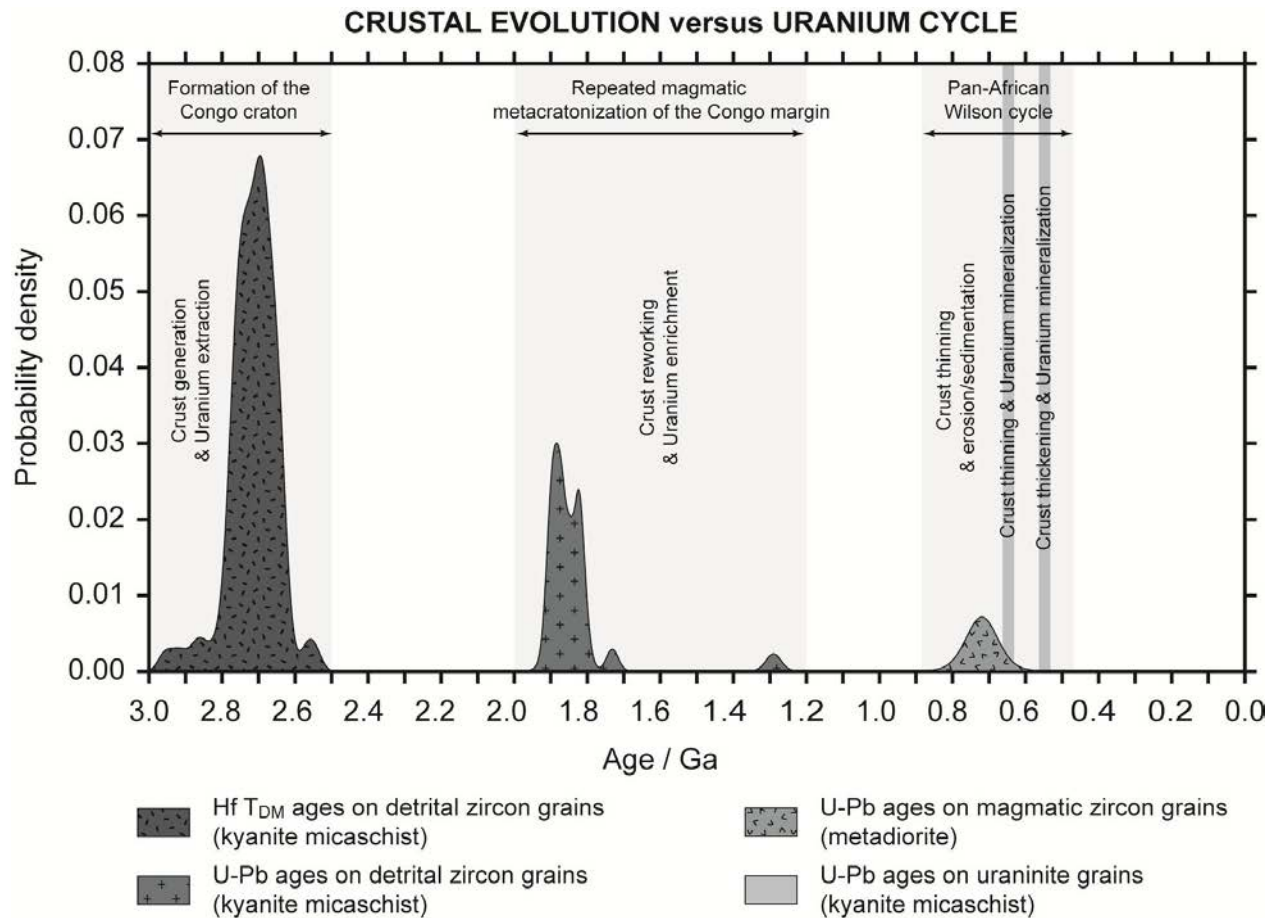


Figure 85: Diagramme de densité de probabilité versus âge. Les données U-Pb et Lu-Hf sur zircon détritique proviennent des séries néoproterozoïques métasédimentaires du groupe du Roan. Les âges obtenus sur grains de zircon magmatique sont obtenus sur les diorites intrusives dans ces séries métasédimentaires du groupe du Roan. Les âges U-Pb obtenus sur les grains d'uraninite datés à 650 Ma (Decrée et al., 2011) et à 530 Ma représentent les deux événements minéralisateurs enregistrés par les métasédiments du groupe du Roan (Eglinger et al., soumis ; chapitre 7).

La dislocation du supercontinent Rodinia au début du Néoproterozoïque favorise l'altération, l'érosion et le transport d'éléments détritiques d'âge paléoproterozoïque dans des bassins intracontinentaux associés au dépôt de séries évaporitiques. Ces niveaux d'évaporites joueront un rôle essentiel dans la (re-)mobilisation et la (re-)concentration de l'élément uranium.

En effet, les premières minéralisations économiques encaissées dans la zone externe de la ceinture du Lufilien sont datées à ~650 Ma (Decrée et al., 2011) et sont associées à des processus tardi-diagénétiques. L'uranium serait transporté par des fluides de bassin salés (Audeoud, 1982), expulsés de niveaux évaporitiques et interprétés comme des saumures dites primaires, circulant à

l'interface socle-couverture. Les signatures en terres rares des uraninites, connues pour refléter les conditions génétiques des minéralisations, sont comparables à celles obtenues sur des uraninites provenant des gisements d'uranium de classe mondiale de type discordance (bassins d'Athabasca au Canada et de Kombolgie en Australie). Ces nouvelles données permettent de décrire le plus jeune gisement de type discordance connu jusqu'alors (Eglinger et al., 2013 ; chapitre 5)! Le second évènement minéralisateur, sub-économique, est daté à ~550-520 Ma et est associé à des processus syn-déformation orogénique. Les signatures en terre rares sont comparables aux signatures pour les uraninites dites syn-métamorphiques. L'uranium est transporté par des fluides aqueux, exceptionnellement salés, issus du métamorphisme des niveaux évaporitiques, on parle alors de saumures dites secondaires (Eglinger et al., accepté 2013 ; chapitre 6). Les conditions P - T enregistrées par les roches encaissantes, $P = 9 \pm 3$ kbar et $T = 610 \pm 30$ °C (Eglinger et al., à soumettre ; chapitre 4), sont en accord avec les données thermométriques obtenues sur rutile et graphite qui donnent une température de cristallisation des oxydes d'uranium entre ~590 et 690 °C (chapitre 7) mais également avec les conditions P - T enregistrées par les fluides minéralisateurs (Eglinger et al., soumis 2013 ; chapitre 7 ; Figure 86). Ces conditions P - T - t sont associées à un contexte de subduction/accrétion continentale. Enfin, un troisième évènement minéralisateur, plus tardif et non-économique, est associé à des fluides aquo-carboniques. Ces fluides circulent durant la période d'exhumation et de relaxation thermique entre ~510 et 470 Ma. Ce troisième évènement marque les dernières remobilisations d'uranium connues dans cette région (Eglinger et al., 2013 soumis ; chapitre 7). Ces deux évènements syn- à tardi-déformation datés entre ~550 et 470 Ma permettent le lessivage de l'élément uranium depuis des phases porteuses telles que l'allanite ou encore la monazite (Eglinger et al., soumis 2013 ; chapitre 7), principalement décrites dans les roches gneissiques-migmatitiques d'âge Paléoproterozoïque, appartenant au socle Pré-Katanga (Eglinger et al., à soumettre ; chapitre 2).

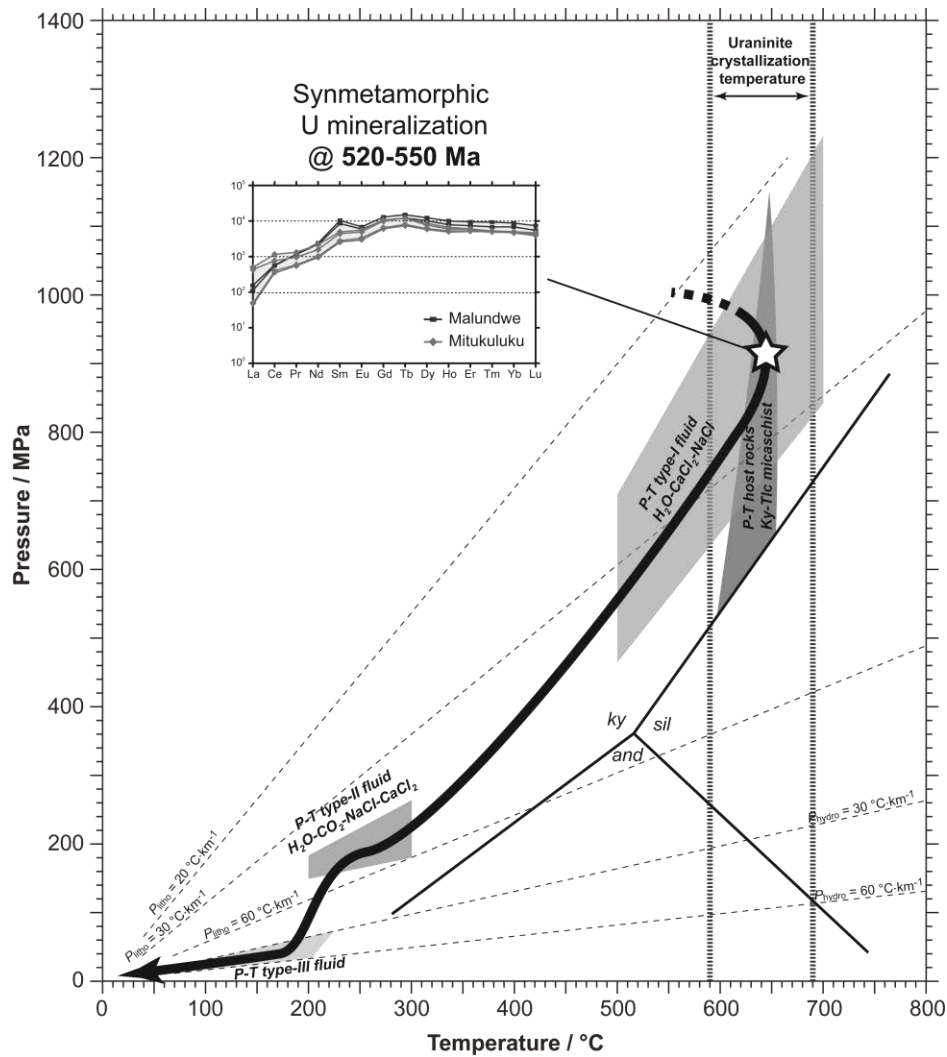


Figure 86: Synthèse de l'évolution *P-T-t* des minéralisations uranifères syn- à tardi-orogéniques et de leur roches encaissantes (métasédiments à kyanite=talc du groupe du Roan) décrites dans la zone interne du Lufilien.

Ainsi, les minéralisations uranifères de la ceinture du Lufilien sont essentiellement liées à l'altération/érosion d'une croûte juvénile Néo-Archéenne qui a été remobilisée à différentes reprises au cours du Protérozoïque. Le dernier cycle de remobilisation/transport/dépôt correspond au cycle Pan-Africain. Dans la zone externe de la ceinture du Lufilien, les minéralisations datées à ~650 Ma sont de type discordance et associées à la circulation de fluides de bassin salés, issus des niveaux évaporitiques du Roan, à l'interface socle/couverture. Dans la zone interne, les minéralisations sont syn- à tardi-métamorphiques et associées à la circulation de fluides issus de la dissolution des évaporites du Roan. Cette circulation et les minéralisations associées sont localisées dans des zones de cisaillement accommodant l'exhumation des nappes de gneiss migmatitiques remobilisant le socle de la série du Katanga.

REFERENCES

BIBLIOGRAPHIQUES

A

- Ague, J.J., 1994a. Mass transfer during Barrovian metamorphism of pelites, south-central Connecticut, I: Evidence for changes in composition and volume. *Am. J. Sci.* 294, 989-1057.
- Ague, J.J., 1994b. Mass transfer during Barrovian metamorphism of pelites, south-central Connecticut, II: Channelized fluid flow and the growth of staurolite and kyanite. *Am. J. Sci.* 294, 1061-1134.
- Ague, J.J., 1997. Crustal mass transfer and index mineral growth in Barrow's garnet zone, northeast Scotland. *Geology* 25, 73-76.
- Ague, J.J., 1997. Thermodynamic calculation of emplacement pressures for batholithic rocks, California: implications for the aluminium-in-hornblende barometer. *Geology* 25, 263-266.
- Albarède, F., 1998. The growth of continental crust. *Tectonophysics* 296, 1-14.
- Alexandre, P., Kyser, K., Polito, P., Thomas, D., 2005a. Alteration Mineralogy and Stable Isotope Geochemistry of Paleoproterozoic Basement-Hosted Unconformity-Type Uranium Deposits in the Athabasca Basin, Canada. *Economic Geology* 100, 1547-1563.
- Alexandre, P., Kyser, T.K., 2005b. Effects of cationic substitutions and alteration in uraninite, and implications for the dating of uranium deposits. *Canadian mineralogist* 43, 1005-1017.
- Allan, M.M., Yardley, B.W.D., Forbes, L.J., Shmulovich K.I., Banks, D.A., Shepherd, T.J., 2005. Validation of LA-ICPMS fluid inclusions analysis with synthetic fluid inclusions. *Am Mineral* 90, 1767-1775.
- Anderson, D.L., 1994. Superplumes or supercontinents? *Geology* 22, 39-42.
- Andersen, L.S., Unrug, R., 1984. Geodynamic evolution of the Bangweulu block, northern Zambia. *Precambrian Res.* 25, 187-212.
- Andersen T., Austrheim A., Burke E.A., Elvevold S., 1993. N₂ and CO₂ in deep crustal fluids: evidence from the Caledonides of Norway. *Chem. Geol.* 108, 113-132.
- Andrews-Speed, C.P., Unrug, R., 1982. Gold in the sedimentary cover of the Bangweulu block, northern Zambia. *Gold* 82, 221-237.
- Annels, A.E., 1989. Ore genesis in the Zambian Copperbelt, with particular reference to the northern sector of the Chambishi basin. In: Boyle, R.W., Brown, A.C., Jefferson, C.W.,

- Jowett, E.C., Kirkham, R.V. (eds.), Sediment-hosted stratiform copper deposits, Geological Association of Canada Special Paper 36, 427-452.
- Arculus, R.J., 1999. Origins of the continental crust. *Journal and Proceedings of the Royal Society of New South Wales* 132, 83-110.
- Armstrong, R.A., Robb, L.J., Master, S., Kuger, F.J., Mumba, P.A.C.C., 1999. New U-Pb age constraints on the Katanga sequence, Central African Copperbelt. *Journal of African Earth Sciences* 28, 6-7.
- Armstrong, R.A., Master, S., Robb, L.J., 2005. Geochronology of the Nchanga Granite, and constraints on the maximum age of the Katanga Supergroup, Zambian Copperbelt. *J. Afr. Earth Sci.* 42, 32-40.
- Armstrong, R.L., 1968. A Model for the Evolution of Strontium and Lead Isotopes in a Dynamic Earth. *Rev. Geophys.* 6, p. 175.
- Armstrong, R.L., 1991. The persistent myth of crustal growth. *American Journal of Earth Sciences* 38, 613-630.
- Artemieva, I.M., Mooney, W.D., 2001. Thermal thickness and evolution of Precambrian lithosphere: A global study. *J. Geophys. Res.* 106, 387-414.
- Artemieva, I.M., 2006. Global $1^\circ \times 1^\circ$ thermal model TC1 for the continental lithosphere: Implications for lithosphere secular evolution. *Tectonophysics* 416, 245-277.
- Artemieva, I.M., 2009. The continental lithosphere: Reconciling thermal, seismic, and petrologic data. *Lithos* 109, 23-46.
- Arthurs, J.W., Legg, C.A., 1974. The Geology of the Solwezi Area: Explanation of Degree Sheets 1126, NW. Quarter, and 1126, Part of SW. Quarter. Government Printer.
- Audeoud, D., 1982. Les mineralizations uranifères et leurs environnement à Kamoto, Kambove et Shinkolobwe (Shaba, Zaïre): pétrographie, géochimie et inclusions fluides. Dissertation, Université Claude Bernard-Lyon 1, France.

B

- Bakker, A.J., Foster, R.P., 1993. Metamorphic fluids and Mineral deposits. *Miner. Mag.* 57, 363-364.
- Bakker, R.J., Diamond L.W., 2006. Estimation of volume fractions of liquid and vapor phases in fluid inclusions, and definition of inclusion shapes. *Am. Mineral.* 91, 635-657.

- Barbey, P., Macaudière, J., Nzenti, J. P., 1990. High-Pressure dehydration melting of metapelites: evidence from the migmatites of Yaounde (Cameroon). *Journal of Petrology* 31, 401-427.
- Barker, A.J., Foster, R.P., 1993. Metamorphic Fluids and Mineral Deposits. *Mineralogy Magazine* 57, 363-364.
- Barron, J.W., 2003. The stratigraphy, Metamorphism and tectonic history of the Solwezi Area, Northwest Province, Zambia: Integrating geological field observations and airborne geophysics in the interpretation of regional geology. Unpublished PhD dissertation, Colorado School of Mines, United States, 233 pp.
- Barron, J.W., Broughton, D.W., Armstrong, R.A., Hitzman, M.W., 2003. Petrology, geochemistry and age of gabbroic bodies in the Solwezi area, northwestern Zambia. In: Contributions presented at the third IGCP-450 Conference, Proterozoic Sediment-hosted Base Metal Deposits of Western Gondwana; Conference and Field Workshop Lubumbashi 2003, Lubumbashi, D.R. Congo, pp. 75-77.
- Barth, M., McDonough, W.F., Rudnick, R.L., 2000. Tracking the budget of Nb and Ta in the continental crust. *Chem. Geol.* 165, 197-213.
- Batumike, M.J., Kampunzu, A.B., Cailteux, J.H., 2006. Petrology and geochemistry of the Neoproterozoic Nguba and Kundelungu Groups, Katanga Supergroup, southeast Congo: Implications for provenance, paleoweathering and geotectonic setting. *J. Afr. Earth Sci.* 44, 97-115.
- Bau, M., 1991. Rare-earth element mobility during hydrothermal and metamorphic fluid-rock interaction and the significance of the oxidation state of europium. *Chemical Geology* 93, 219-230.
- Bau, M., Möller, P., 1992. Rare earth element fractionation in metamorphogenic hydrothermal calcite, magnesite and siderite. *Mineralogy and Petrology* 45, 231-246.
- Baumgartner, M., Bakker, R.J., 2009. CaCl₂-hydrate nucleation in synthetic fluid inclusions. *Chem. Geol.* 265, 335-344.
- Baumgartner, M., Bakker, R.J., 2010. Raman spectra of ice and salt hydrates in synthetic fluid inclusions. *Chem. Geol.* 275, 58-66.

- Bayer, R., Lesquer, A., 1978. Les anomalies gravimétriques de la bordure orientale du craton Ouest-africain: géométrie d'une suture panafricaine. *Bull. Soc. Géol. de France* 6, 868-876.
- Becker, S.P., Fall, A., Bodnar, R.J., 2008. Synthetic Fluid Inclusions. XVII: PVTX Properties of High Salinity H₂O-NaCl Solutions (>30 wt % NaCl): Application to Fluid Inclusions that Homogenize by Halite Disappearance from Porphyry Copper and Other Hydrothermal Ore Deposits. *Econ. Geol.* 103, 539-554.
- Begemann, F., Von Buttlar, H., Houtermans, F.G., Isaac, N., Picciotto, E., 1952. Résultats préliminaires des mesures d'âge de la pechblende de Shinkolobwe par la méthode du RaD. *Bull. Soc. Belge de Géol.* 61, 223-226.
- Begemann, F., Buttlar, H. v., Houtermans, F.G., Isaac, N., Picciotto, E., 1953. Application de la méthode du RaD a la mesure de l'âge "chimique" d'un minerai d'Uranium. *Geochim. Cosmochimi. Acta* 4, 21-35.
- Bekker, A., Holland, H.D., Wang, P.L., Rumble, D., Stein, H.J., Hannah, J.L., Coetzee, L.L., Beukes, N.J., 2004. Dating the rise of atmospheric oxygen. *Nature* 427, 117-120.
- Belousova, E., Kostitsyn, Y.A., Griffin, W.L., Begg, G.C., O'Reilly, S.Y., Pearson, N.J., 2010. The growth of the continental crust: Constraints from zircons Hf-isotope data. *Lithos* 119, 457-466.
- Bernau, R., 2007. The geology and geochemistry of the Lumwana Basement hosted copper-cobalt (uranium) deposits, NW Zambia. PhD dissertation, University of Southampton, England.
- Beyssac, O., Goffe, B., Chopin, C., Rouzaud, J.N., 2002. Raman spectra of carbonaceous material in metasediments: a new geothermometer. *J. Metam. Geol.* 20, 859-871.
- Binda, P.L., Van Eden, J.G., 1972. Sedimentological evidence on the origin of the Precambrian Great Conglomerate (Kundelungu Tillite), Zambia. *Palaeogeo. Palaeoclim. Palaeoeco.* 12, 151-168.
- Bernau, R., Roberts, S., Richards, M., Nisbet, B., Boyce, A., Nowecki, J., 2013. The geology and geochemistry of the Lumwana Cu (\pm Co \pm U) deposits, N.W. Zambia. *Miner Depos.* 48, 137-153.
- Binda, P.L. 1994. Stratigraphy of the Zambian Copperbelt ore body. *J. Afric. Earth Sci.* 19, 251-264.

- Bird, D.K., Helgeson, H.C., 1981. Chemical interaction of aqueous solutions with epidote-feldspar mineral assemblages in geologic systems. II. Equilibrium constraints in metamorphic/geothermal processes. *Am. J. Sci.* 281, 576-614.
- Blichert-Toft, J., Chauvel, C., Albarède, F., 1997. Separation of Hf and Lu for high-precision isotope analysis of rock samples by magnetic sector-multiple collector ICP-MS. *Contrib. Mineral. Petrol.* 127, 248–260.
- Bodnar, R.J., 2003. Reequilibration of fluid inclusions. In: Samson, I., Anderson, A., Marshall, D. (Eds.), *Fluid Inclusions: Analysis and Interpretation*. Mineral. Assoc. Can., Short Course. 32, 213-230.
- Bodnar, R.J., Vityk, M.O., 1994. Interpretation of microthermometric data for H₂O-NaCl fluid inclusions. In: De Vivo, B., Frezzotti, M.L. (Eds.), *Fluid inclusions in Minerals, Methods and Applications*. Virginia Tech, Blacksburg, 117-130.
- Bonhoure, J., 2007. Géochimie des éléments de terres rares et du plomb dans les oxydes d'uranium naturels. Unpublished PhD. Dissertation, Université de Lorraine, France, 390 pp.
- Bonhoure, J., Kister, P., Cuney, M., Deloule, E., 2007. Methodology for Rare Earth Element Determinations of Uranium Oxides by Ion Microprobe. *Geostandards and Geoanalytical Research* 31, 209-225.
- Bonnetti, C., 2013. Genèse des gisements type Roll-Front dans le bassin d'Erlian, Chine. Unpublished PhD. Dissertation Université de Lorraine, France (XXX pp).
- Bouiller, A.M., France-Lanord, C., Dubessy, J., 1991. Linked fluid and tectonic evolution in the High Himalaya mountains (Nepal). *Contrib. Miner. Petro.* 107, 358-372.
- Brems, D., Muchez, P., Sikazwe, O., Mukumba, W., 2009. Metallogenesis of the Nkana copper-cobalt South Orebody, Zambia. *Journal of African Earth Sciences* 55, 185–196.
- Brewer, M.S., Haslam, H.W., Darbyshire, P.F.P., Davis, A.E., 1979. Rb–Sr Age Determinations in the Bangweulu Block, Luapula Province, Zambia, Institute of Geological Sciences, London 79/5.
- Brito Neves, B.B., Cordani, D.G., 1991. Tectonic evolution of South America during the Late Proterozoic. *Precambrian Research* 53, 23-40.

- Brito Neves B.B., Campos Neto M.C., Fuck R.A., 1999. From Rodinia to Western Gondwana: An approach to the Brasiliano-Pan African Cycle and orogenic collage. *Episodes* 22, 155-166.
- Broska, I., Siman, P., 1998. The breakdown of monazite in the West-Carpathian Veporic orthogneisses and Tatric granites. *Geol. Carp.-Bratisl.* 49, 161-167.
- Broska, I., Williams, C.T., Janák, M., Nagy, G., 2005. Alteration and breakdown of xenotime-(Y) and monazite-(Ce) in granitic rocks of the Western Carpathians, Slovakia. *Lithos.* 82, 71-83.
- Brown, M., 2007. Characteristic thermal regimes of plate tectonics and their metamorphic imprint throughout Earth history: When did Earth first adopt a plate tectonics mode of behavior? *Geologic. Soc. Americ* 440, 97-128.
- Budzyń, B., Harlov, D.E., Williams, M.L., Jercinovic, M.J., 2011. Experimental determination of stability relations between monazite, fluorapatite, allanite, and REE-epidote as a function of pressure, temperature, and fluid composition. *Am. Mineral.* 96, 1547-1567.
- Bull, S., Selley, D., Broughton, D., Hitzman, M., Cailteux, J., Large, R., McGoldrick, P., 2011. Sequence and carbon isotopic stratigraphy of the Neoproterozoic Roan Group strata of the Zambian copperbelt. *Precambrian Research* 190, 70-89.
- Burke, E.A.J., 2001. Raman microspectrometry of fluid inclusions. *Lithos.* 55, 139-158.

C

- Caby, R., 1987. The Pan-African belt of West Africa from the Sahara desert to the Gulf of Benin. In Schaer, J.P. and Rodgers, J. (Ed.), *The anatomy of mountain ranges*, Princeton University Press, 129-170.
- Caby, R., Arthaud, M. H., 1987. Petrostructural evolution of the Lagoa Real subalkaline metaplutonic complex (Bahia Brazil). *Rev. Brasil. Geoscienc.* 17, 636.
- Caen-Vachette, M., Vialette, Y., Bassot, J.P., Vidal, P., 1988. Apport de la géochronologie isotopique à la connaissance de la géologie Gabonaise. *Chronique Rech. Min.* 491, 35–54.
- Cagnard, F., Gapais, D., and Barbey, P., 2007. Collision tectonics involving juvenile crust: The example of the southern Finnish Svecofennides. *Precambrian Research*, 154, 125-141.

- Cahen, L., Pasteels, P., Ledent, D., Bourguillot, R., Van Wambeke, L., Eberhardt, P., 1961. Recherche sur l'âge absolu des minéralisations uranifères du Katanga et de Rhodésie du Nord. *Annales Musée royal de l'Afrique centrale* 41, 1–53.
- Cahen, L., François, A., Ledent, D., 1971. Sur l'âge des uraninites de Kambove Ouest et de Kamoto Principal et révision des connaissances relatives aux minéralisations uranifères du Katanga et du Copperbelt de Zambie. *Annales de la Société belge de Géologie* 94, 185–198.
- Cahen, L., Snelling, N.J., 1984. *The geochronology and evolution of Africa*. Clarendon Press, Oxford, 496 pp.
- Cailteux, J.L.H., 1983. Le Roan shabien dans la région de Kambove (Shaba-Zaïre): Etude sédimentologique et métallogénique Unpublished PhD. Dissertation, Université de Liège, Belgium, 232 pp.
- Cailteux, J.L.H., 1994. Lithostratigraphy of the Neoproterozoic Shaba-type (Zaire) Roan Supergroup and metallogenesis of associated stratiform mineralization. *Journal of African Earth Sciences* 19, 279–301.
- Cailteux, J.L.H., 1997. Minéralisations à U-Pb-Se-Mo-Ni dans le gisement stratiforme cupro-cobaltifère de Kampove-Ouest (Shaba, Rép. Zaïre), in: *Colloque International Cornet: Gisements Stratiformes De Cuivre Et Minéralisations Associées*. Belgium, pp. 245–268.
- Cailteux, J.L.H., Binda, P.L., Katekesha, W.M., Kampunzu, A.B., Intiomale, M.M., Kapenda, D., Kaunda, C., Ngongo, K., Tshiauka, T., Wendorff, M., 1983. Lithostratigraphical correlation of the Neoproterozoic Roan Supergroup from Shaba (Zaire) and Zambia, in the central African copper-cobalt metallogenic province. *Journal of African Earth Sciences* 19, 265-278.
- Cailteux, J.L.H., Kampunzu, A.B., 1995. The Katanga tectonic breccias in the Shabe province (Zaïre) and their genetic significance. *Annales de la Société Géologique de Belgique* 101, 63-76.
- Cailteux, J.L.H., Kampunzu, A.B., Lerouge, C., Kaputo, A.K., Milesi, J.P., 2005. Genesis of sediment-hosted stratiform copper–cobalt deposits, central African Copperbelt. *Journal of African Earth Sciences* 42, 134-158.
- Carignan, J., Hild, P., Mévelle, G., Morel, J., Yeghicheyan, D., 2001. Routine analyses of trace elements in geological samples using flow injection and low pressure on-line liquid

- chromatography coupled to ICP-MS: a study of reference materials BR, DR-N, UB-N, AN-G and GH. *Geostandards Newsletter* 25, 187-198.
- Carmichael, D.M., 1969. On the mechanism of prograde metamorphic reactions in quartz-bearing pelitic rocks. *Contrib. Miner. Petro.* 20, 244-67.
- Cathelineau, M., Boiron, M.C., Holliger, P., Poty, B., 1990. Metallogenesis of the French part of the Variscan orogen. Part II: Time-space relationships between U, Au and Sn-W ore deposition and geodynamic events — mineralogical and U-Pb data. *Tectonophysics* 177, 59-79.
- Caumon, M.C., Dubessy, J., Robert, P., Tarantola, A., 2013. Fused-silica capillary capsules (FSCCs) as reference synthetic aqueous fluid inclusions to determine chlorinity by Raman spectroscopy. *Eur. J. Mineral.* doi: 10.1127/0935-1221/2013/0025-2280.
- Cawood, P.A., 2005. Terra Australis Orogen: Rodinia breakup and development of the Pacific and Iapetus margins of Gondwana during the Neoproterozoic and Paleozoic. *Earth-Science Reviews* 69, 249-279.
- Champion, D.C., Smithies, R.H., 2007. Geochemistry of Paleoproterozoic granites of the East Pilbara terrane, Pilbara craton, Western Australia: Implications for Early Archean crustal growth, earth's oldest rocks. *Developments in Precambrian Geology* 15, 369-410.
- Chikhaoui, M., Dupuy, C., Dostal, J., 1980. Geochemistry and Petrogenesis of Late Proterozoic Volcanic Rocks From North-Western Africa. *Contribution to mineralogy and petrology* 73, 375-388.
- Chinner, C.A., 1967. Chloritoid and the isochemical character of Barrow's zones. *J. Petrol.* 8, 1268-1282.
- Cocherie, A., Legendre, O., Peucat, J.J., Kouamelan, A.N. 1998. Geochronology of polygenetic monazites constrained by in situ electron microprobe Th-U-total lead determination: implications for lead behaviour in monazite. *Geochim. Cosmochim. Acta.* 62, 2475-2497.
- Condie, K.C., 1982. *Plate tectonics and Crustal Evolution*. Pergamon Press, Elmsford, N.Y.
- Condie, K.C., 1998. Episodic continental growth and supercontinents: a mantle avalanche connection? *Earth Planet. Sci. Lett.* 163, 97-108.

- Condie, K.C., 2007. Accretionary orogens in space and time, in: Hatcher, R.D., Jr., Carlson, M.P., McBride, J.H., Martinez-Catalan, J.R., eds., 4-D framework of the continental crust. Geological Society of America, Memoir 200, 145-158.
- Condon, D., Zhu, M., Bowring, S., Wang, W., Yang, A., Jin, Y., 2005. U-Pb Ages from the Neoproterozoic Doushantuo Formation, China. *Science* 308, 95-98.
- Connolly, J.A.D., 1990. Multivariable phase diagrams: an algorithm based on generalized thermodynamics. *American Journal of Science* 290, 666-718.
- Connolly, J.A.D., Cesare B., 1993. C-O-H-S fluid compositions and oxygen fugacity in graphitic metapelites. *J. Metamorph. Geol.* 11, 379-388.
- Cordani, D.G., D'Agrella-Filho, M.S., Brito-Neves, B.B., Trindade, R.I.F., 2003. Tearing up Rodinia: the Neoproterozoic palaeogeography of South American cratonic fragments. *Terra Nova* 15, 350-359.
- Corfu, F., Hanchar, J.M., Hoskin, P.W.O., Kinny, P., 2003. Atlas of zircon textures. In: Hanchar, J.M., Hoskin, P.W.O. (Ed.), *Reviews in mineralogy and geochemistry* 53, pp. 469-500.
- Cosi, M., De Bonis, A., Gosso, G., Hunziker, J., Martinotti, G., Moratto, S., Robert, J.P., Ruhlman, F., 1992. Late proterozoic thrust tectonics, high-pressure metamorphism and uranium mineralization in the Domes Area, Lufilian Arc, Northwestern Zambia. *Precambrian Res.* 58, 215-240.
- Coward, I.M., Daly, M.C., 1984. Crustal lineaments and shear zones in Africa: their relationship to plate movements. *Precambrian Res.* 24, 27-45.
- Craw, D., Norris, R. J. 1993. Grain boundary migration of water and carbon dioxide during uplift of garnet-zone Alpine Schist, New Zealand. *J. Metamorph. Geol.* 11, 371-378.
- Crowley, J.L., Ghent, E.D. 1999. An electron microprobe study of the U–Th–Pb systematics of metamorphosed monazite: the role of Pb diffusion versus overgrowth and recrystallization. *Chem. Geol.* 157, 285-302.
- Cuney, M., 2009. The extreme diversity of uranium deposits. *Mineral Dep.* 44, 3-9.
- Cuney, M., 2010. Evolution of Uranium Fractionation Processes through Time: Driving the Secular Variation of Uranium Deposit Types. *Economic Geology* 105, 553-569.
- Cuney, M., Friedrich, M., 1987. Physicochemical and crystal-chemical controls on accessory mineral paragenesis in granitoids: implications for uranium metallogenesis. *Bulletin de Mineralogie* 110, 235-247.

Cuney, M., Kyser, T.K. (Eds.). 2009. Recent and not-so-recent developments in uranium deposits and implications for exploration. Quebec: Mineral. Assoc. Can.

D

D'Agrella-Filho, M. S., Pacca, I. G., Trindade, R. I. F., Teixeira, L. R., Raposo, I. B., Onstott, T. C., 2004. Paleomagnetism and $^{40}\text{Ar}/^{39}\text{Ar}$ ages of mafic dikes from Salvador (Brazil): new constraints on the São Francisco craton APW path between 1080 and 1010 Ma. *Prec. Res.* 132, 55-77.

Daly, M.C., 1986. Crustal shear zones and thrust belts: Their geometry and continuity in central Africa: *Royal Society of London Philosophical Transactions* 317, 111-128.

Dalziel, I. W. D., 1991. Pacific margins of Laurentia and East Antarctica–Australia as a conjugate rift pair: evidence and implications for an Eocambrian supercontinent. *Geology* 19, 598-601.

Dalziel, I. W. D., 1992. On the organization of American plates in the Neoproterozoic and the breakout of Laurentia. *GSA Today* 2, 237-241.

Dalziel, I.W.D., 1997. Neoproterozoic–Paleozoic geography and tectonics; review, hypothesis. *Geological Society of America Bulletin* 109, 16–42.

Darnley, A.G., Horne, J.E.T., Smith, G.H., Chandler, T.R.D., Dance, D.F., Preece, E.R. 1961. Ages of some uranium and thorium minerals from east and central Africa. *Mineral. Mag.* 32, 716-724.

Decrée, S., Deloule, É., De Putter, T., Dewaele, S., Mees, F., Yans, J., Marignac, C., 2011. SIMS U–Pb dating of uranium mineralization in the Katanga Copperbelt: Constraints for the geodynamic context. *Ore Geol. Rev.* 40, 81-89.

Deer, W.A., Howie, R.A., Zussman, J. (Eds.). 1997. *Orthosilicates*. Geol. Soc.

Delhal, J., Ledent, D., 1973. Résultats de quelques mesures d'âges radiométriques par la méthode Rb/Sr dans les pegmatites de la Haute Luanyi, région du Kasai (Zaire). *Rapport Annuel, Mus. Roy. Afr. Centr., Tervuren, Belgique, Dept. Géol. Min.*, 102-103.

Delhal, J., Ledent, D., Torquato, J., 1976. Nouvelles données géochronologiques relatives au complexe gabbro-noritique et charnockitique du bouclier du Kasai et son prolongement en Angola. *Annales Soc. Geol. Belg.* 99, 211–226.

Derome D., Cuney M., Cathelineau M., Fabre C., Dubessy J., Bruneton P. and Hubert A., 2003. A detailed fluid inclusion study in silicified breccias from the Kombolgie sandstones

- (Northern Territory, Australia): inferences for the genesis of middle-Proterozoic unconformity-type uranium deposits. *J. Geochem. Explor.* 80, 259-275.
- Derome, D., Cathelineau, M., Cuney, M., Fabre, C., Lhomme, T., Banks, D.A., 2005. Mixing of Sodic and Calcic Brines and Uranium Deposition at McArthur River, Saskatchewan, Canada: A Raman and Laser-Induced Breakdown Spectroscopic Study of Fluid Inclusions. *Economic Geology* 100, 1529-1545.
- Derome D., Cathelineau M., Fabre C., Boiron M.C., Banks D., Lhomme T. and Cuney M., 2007. Paleo-fluid composition determined from individual fluid inclusions by Raman and LIBS: application to mid-Proterozoic evaporitic Na-Ca brines (Alligator Rivers Uranium Field, Northern territories Australia). *Chemical Geology* 237, 240-254.
- Derriks, J.J., Vaes, J.F., 1956. Le gîte d'uranium de Shinkolobwe: état actuel des connaissances du point de vue géologie et métallogénie, in: *Actes De La Conférence Internationale Sur L'utilisation De L'énergie Atomique à Des Fins Pacifiques*. Geneva, pp. 108-144.
- Derriks, J.J., Oosterbosch, R., 1958. The Swambo and Kalongwe deposits compared to Shinkolobwe: contribution to the study of Katanga uranium, in: *International Conference on the Peaceful Uses of Atomic Energy*. Geneva, pp. 663-695.
- De Swardt, A.M.J., Drysdall, A.R., 1964. Precambrian geology and structure in central Northern Rhodesia. *Memoirs Geological Survey North Rhodesia* 2, 82 pp.
- De Swardt, A.M.J., Garrard, P., Simpson, J.G., 1965. Major zones of transcurrent dislocation and superposition of orogenic belts in part of Central Africa. *Bulletin of Geological Society of America* 76, 89-102.
- De Waele, S., Muchez, P., Vets, J., Fernandez-Alonzo, M., Tack, L., 2006. Multiphase origin of the Cu–Co ore deposits in the western part of the Lufilian fold-and-thrust belt, Katanga (Democratic Republic of Congo). *Journal of African Earth Sciences* 46, 455-469.
- De Waele, B., 2005. The Proterozoic geological history of the Irumide belt, Zambia. Unpublished PhD Dissertation, Curtin University of Technology, Perth, 468 pp.
- De Waele, S., Muchez, P., Vets, J., Fernandez-Alonzo, M., Tack, L., 2006. Multiphase origin of the Cu–Co ore deposits in the western part of the Lufilian fold-and-thrust belt, Katanga (Democratic Republic of Congo). *J. Afr. Earth Sci.* 46, 455-469.
- De Waele, B., Kampunzu, A.B., Mapani, B.S.E., Tembo, F., 2006a. The Irumide Belt of Zambia. *J. Afr. Earth Sci.* 46, 36-70.

- De Waele, B., Liégeois, J.P., Nemchin, A.A., Tembo, F., 2006b. Isotopic and geochemical evidence of Proterozoic episodic crustal reworking within the Irumide Belt of south-central Africa, the southern metacratonic boundary of an Archaean Bangweulu Craton. *Prec. Res.* 148, 225-256.
- De Waele, B., Fitzsimons, I.C.W., 2007. The nature and timing of Palaeoproterozoic sedimentation at the southeastern margin of the Congo Craton. *Prec. Res.* 159, 95–116.
- De Waele, B., Johnson, S.P., Pisarevsky, S.A., 2008. Palaeoproterozoic to Neoproterozoic growth and evolution of the eastern Congo Craton: Its role in the Rodinia puzzle. *Precambrian Research* 160, 127–141.
- Diamond, L.W. 1990. Fluid inclusion evidence for *P-V-T-X* evolution of hydrothermal solutions in late-alpine gold-quartz veins at Brusson, Val d'Ayas, Northwest Italian Alps. *Amer. J. Sci.* 290, 912-958.
- Diamond, L.W. 2001. Reviews of the systematics of the CO₂-H₂O fluid inclusions. *Lithos* 55, 69-99.
- Diamond L.W., Tarantola A., Stünitz H., 2010. Modification of fluid inclusions in quartz by deviatoric stress II: Experimentally induced changes in inclusion volume and composition. *Contributions to Mineralogy and Petrology* 160, 845-864.
- Dodson, M.H., 1979. Theory of cooling ages. In Jager, E., Hunziker, J.C., eds., *Lectures in Isotope Geology*. Springer, p. 194-202.
- Drake, A. A., 1980. Tectonic studies in the Brazilian shield. The Serra de Caldas window, Goiás. *U.S.S Geol. Surv. Prof. Paper* 1119, 1-11.
- Drury, M.R., Urai, J.L., 1990. Deformation-related recrystallisation processes. *Tectonophys.* 172, 235-253.
- Dubessy, J., Audeoud, D., Wilkins, R., Kosztolanyi, C., 1982. The use of the Raman microprobe MOLE in the determination of the electrolytes dissolved in the aqueous phase of fluid inclusions. *Chem. Geol.* 37, 137-150.
- Dubessy, J., Pagel, M., Beny, J.M., Christensen, H., Hickel, B, Kosztolanyi, C., Poty, B., 1988. Radiolysis evidenced by H₂-O₂ and H₂-bearing fluid inclusions in three uranium deposits. *Geochim. Cosmochim. Acta.* 52,1155-1167.
- Dubessy, J., Poty, B., Ramboz, C., 1989. Advances in C-O-H-N-S fluid geochemistry based on micro-Raman spectrometric analysis of fluid inclusions. *Eur.J. Mineral* 1, 517-534.

- Dubessy, J., Ramboz, C., 1996. The history of organic nitrogen from early diagenesis to amphibolite facies: mineralogical, chemical, mechanical and isotopic implications. Extended Abstracts 5th Internat. Symposium Water-Rock Interaction, Reykjavik, Iceland.,170-174.
- Dubessy, J., Lhomme, T., Boiron, M.-C., Rull, F., 2002. Determination of Chlorinity in Aqueous Fluids Using Raman Spectroscopy of the Stretching Band of Water at Room Temperature: Application to Fluid Inclusions. *Appl. Spectrosc.* 56, 99-106.
- Duhamel, I., Cuney, M., Van Lichtervelde, M., 2009. First characterization of uraninite in an Archean peraluminous granitic pegmatite at Tanco (Manitoba, Canada). Inference for uraninite placer deposits. Geological Association of Canada, Mineralogical Association of Canada Conference, Québec, Canada.
- Dupre, B., Allegre, C., 1983. Pb-Sr isotope variation in Indian Ocean and mixing phenomena. *Nature* 303, 142-146.
- Du Toit, A.L., 1937. *Our Wandering Continents, an Hypothesis of Continental Drifting.* Oliver & Boyd, Edinburgh and London. 366 pp.

E

- Eglinger, A., André-Mayer, A.S., Vanderhaeghe, O., Mercadier, J., Cuney, M., Decrée, S., Feybesse, J.L., Milesi, J.P., 2013. Geochemical signatures of uranium oxides in the Lufilian belt: From unconformity-related to syn-metamorphic uranium deposits during the Pan-African orogenic cycle. *Ore Geol. Rev.* 54, 197-213.
- Eglinger, A., Ferraina, C., Tarantola, A., André-Mayer, A.S., Vanderhaeghe, O., Boiron, M.C., Dubessy, J., Richard, A., Brouand, M., (in press). Metamorphic evolution of U-bearing highly saline Ca-Na fluids in syntectonic Pan-African quartz veins in the Domes region (Lufilian belt, Zambia). *Contrib. Mineral. Petrol.* 167, doi: 10.1007/s00410-014-0967-9.
- Eglinger, A., Tarantola, A., Durand, C., Ferraina, C., Vanderhaeghe, O., André-Mayer, A.S., Paquette, J.L., Deloule, E., (submitted). Uranium mobilization by fluids associated with Ca-Na metasomatism: a P-T-t record of fluid-rock interactions during the Pan-African metamorphism (Western Zambien Copperbelt). *Chemical Geology.*
- Eglinger, A., Vanderhaeghe, O., André-Mayer, A.S., Zeh, A., Frémont, F., Durand, C., Poujol, M., Paquette, J.L., (to be submitted). Crustal evolution of the basement inliers in the

internal orogenic Lufilian belt: U-Pb coupled with Hf isotopes of zircon and whole-rock Sm-Nd isotopic data (Domes region, Zambia). *Precambrian Research*.

El Desouky, H.A., Muchez, P., Dewaele, S., Boutwood, A., Tyler, R., 2008. Postorogenic Origin of the Stratiform Cu Mineralization at Lufukwe, Lufilian Foreland, Democratic Republic of Congo. *Economic Geology* 103, 555-582.

El Desouky, H.A., Muchez, P., Cailteux, J., 2009. Two Cu–Co sulfide phases and contrasting fluid systems in the Katanga Copperbelt, Democratic Republic of Congo. *Ore Geology Reviews* 36, 315-332.

El Desouky, H.A., Banks, D., De Clercq, F., Cailteux, J.L.H., Muchez, P., 2012. Chemistry of syn-orogenic copper-cobalt ore-forming fluids in the Katanga copperbelt, Democratic Republic of Congo. *Geofluids VII conference*, June 2012, France.

Elliott, T., Zindler, A., Bourdon, B., 1999. Exploring the kappa conundrum: The role of recycling in the lead isotope evolution of the mantle. *Earth and Planetary Science Letters* 169, 129-145.

Ellis, D.E. 1978. Stability and phase equilibria of chloride and carbonate bearing scapolites at 750 C and 4000 bar. *Geochim. Cosmochim. Acta.* 42, 1271-1281.

Etheridge, M.A., Wall, V.J., Vernon, R.H., 1983. The role of the fluid phase during regional metamorphism and deformation. *J. Metamorph. Geol.* 1, 205-226.

F

Farquhar, J., Wing, B.A., 2003. Multiple sulfur isotopes and the evolution of the atmosphere. *Earth and Planetary Science Letters* 213, 1-13.

Fayek, M., Kyser, T.K., 1997. Characterization of multiple fluid-flow events and Rare-Earth-Element mobility associated with the formation of unconformity-type uranium deposits in the Athabasca Basin, Saskatchewan. *The Canadian Mineralogist* 35, 627-658.

Fernandez, L. A. D., Tommasi, A., Porcher, C. C., 1992. Deformation patterns in the southern Brazilian branch of the Dom Feliciano belt: a reappraisal. *Journal of South American Earth Sciences* 5, 77-96.

Ferry, J.M., 1992. Regional metamorphism of the Waits River Formation, eastern Vermont: delineation of a new type of giant hydrothermal system. *J. Petrol.* 33, 45-94.

- Finger, F., Broska, I., Roberts, M.P., Schermaier, A. 1998. Replacement of primary monazite by apatite-allanite-epidote coronas in an amphibolite facies granite gneiss from the eastern Alps. *Am. Mineral.* 83, 248-258.
- Fontes, J.C., Matray, J.M., 1993. Geochemistry and origin of formation brines from the Paris Basin, France. 1. Brines associated with Triassic salts. *Chem. Geol.* 109, 149-175.
- Förster, H.-J., 1999. The chemical composition of uraninite in Variscan granites of the Erzgebirge, Germany. *Mineralogical Magazine* 63, 239-252.
- Foster, G., Gibson, H.D., Parrish, R., Horstwood, M., Fraser, J., Tindle, A. 2002. Textural, chemical and isotopic insights into the nature and behaviour of metamorphic monazite. *Chem. Geol.* 191, 183-207.
- François, A., 1974. Stratigraphie, tectonique et minéralisations dans l'arc cuprifère du Shaba (Rép. du Zaïre). Centenaire de la Société Géologique de Belgique. Liège, pp. 79-101.
- François, A., Cailteux, J.L.H., 1981. La couverture Katangienne entre les socles de Zilo et de la Kabompo, République du Zaïre, Région de Kolwezi. *Annales Musée royal de l'Afrique centrale* 87.
- Fryer, B.J., Taylor, R.P., 1987. Rare-Earth elements distributions in uraninites: implications for ore genesis. *Chemical Geology* 63, 101-108.
- Frezzotti, M.L., Tecce, F., Casagli, A., 2012. Raman spectroscopy for fluid inclusion analysis. *J. Geochem. Explor.* 112, 1-20.
- Fuck, R.A., Brito Neves, D. B. B., Schobbenhaus, C., 2008. Rodinia descendants in South America. *Precambrian Research* 160, 108-126.
- Fyfe, W.S., 1978. The evolution of Earth's crust: modern plate tectonics to ancient hot spot tectonics? *Chem. Geol.*, 23, 89-114.

G

- Garlick, W.G., Fleischer, V.D., 1972. Sedimentary environment of Zambian copper deposition. *Netherland Journal of Geosciences* 51, 277-298.
- Gasquet, D., Bertrand, J.M., Paquette, J.L., Lehmann, J., Ratzov, G., De Ascençao Guedes, R., Tiepolo, M., Boullier, A.M., Scaillet, S., Nomade, S., 2010. Miocene to Messinian deformation and hydrothermalism in the Lauzière Massif (French Western Alps): New U-Th-Pb and Argon ages. *Bull. Soc. Géol. France* 181, 227-241.

- Gerdes, A., Zeh, A., 2006. Combined U–Pb and Hf isotope LA-(MC)ICP-MS analyses of detrital zircons: comparison with SHRIMP and new constraints for the provenance and age of an Armorican metasediment in Central Germany. *Earth Planet. Sci. Lett.* 249, 47-61.
- Gerdes, A., Zeh, A., 2009. Zircon formation versus zircon alteration—new insights from combined U–Pb and Lu–Hf in-situ LA-ICP-MS analyses, and consequences for the interpretation of Archaean zircon from the Central Zone of the Limpopo Belt. *Chem. Geol.* 261, 230–243.
- Goodwin, A.M., 1981. Archean Plates and Greenstones Belts. In *Precambrian plate tectonics* 5, A. Kröner (Ed.), 105-135.
- Gray, D.R., Foster, D.A., Goscombe, B., Passchier, C.W., Trouw, R.A.J., 2006. $^{40}\text{Ar}/^{39}\text{Ar}$ thermochronology of the Pan-African Damara Orogen, Namibia, with implications for tectonothermal and geodynamic evolution. *Precambrian Res.* 150, 49-72.
- Gray, D.R., Foster, D.A., Meert, J.G., Goscombe, B.D., Armstrong, R.A., Trow, R.A., Passchier, C.W., 2008. A Damara orogen perspective on the assembly of southwestern Gondwana. *Geological Society, London* 294, 257-278.
- Greyling, L.N. 2009. Fluid evolution and characterisation of mineralising solutions in the Central African Copperbelt. Dissertation, University of Witwatersrand, South-Africa.
- Greyling, L.N., Robb, L.J., Master, S., Boiron, M.C., Yao, Y., 2005. The nature of early basinal fluids in the Zambian Copperbelt: A case study from the Chambishi deposit. *Journal of African Earth Sciences* 42, 159-172.
- Günther, D., Heinrich, C.A., 1999. Enhanced sensitivity in laser ablation-ICP mass spectrometry using helium-argon mixtures as aerosol carrier. *J. Anal. Spectrom.*, 1363-1368.

H

- Hammarstrom, J.M., Zen, E.A., 1986. Aluminium in hornblende: an empirical igneous geobarometer. *American Mineralogist* 71, 1297-1313.
- Hanson, G.N., Gast, P.W., 1967. Kinetic studies in contact metamorphic zones. *Geochemica et Cosmochemica Acta* 31, 1119-1153.
- Hanson, R.E., Wilson, T.J., Wardlaw, M.S., 1988. Deformed batholiths in the Pan-African Zambezi Belt, Zambia: age and implications for regional Proterozoic tectonics. *Geology* 16, 1134-1137.

- Hanson, R.E., Wardlaw, M.S., Wilson, T.J., Mwale, G., 1993. U-Pb zircon ages from the Hook granite massif and Mwembeshi dislocation: constraints on Pan-African deformation, plutonism, and transcurrent shearing in Central Zambia. *Precambrian Res.* 63, 189-209.
- Hanson, R.E., Wilson, T.J., Munyanyiwa, H., 1994. Geologic evolution of the neoproterozoic Zambezi orogenic belt in Zambia. *Journal of African Earth Sciences* 18, 135–150.
- Hanson, R.E., 2003. Proterozoic geochronology and tectonic evolution of southern Africa. In: Yoshida, M., Windley, Brian, F., Dasgupta, S. (Eds.) *Proterozoic East Gondwana: Supercontinent Assembly and Breakup*, vol. 206. Geological Society of London Special Publication, London, 427-463 pp.
- Hawkesworth, C.J., Gallagher, K., 1993. Mantle hotspots, plumes and regional tectonics as causes of intraplate magmatism. *Terra Nova* 5, 552-559.
- Hawkesworth, C.J., Dhuime, B., Pietranik, A.B., Cawood, P.A., Kemp, A.I.S., Storey, C.D., 2010. The generation and evolution of the continental crust. *Journal of the Geological Society, London* 167, 229-248.
- Hawkins, D.P., Bowring, S.A. 1997. U-Pb systematics of monazite and xenotime: case studies from the Paleoproterozoic of the Grand Canyon, Arizona. *Contrib. Mineral. Petrol.* 127, 87-103.
- Haynes, F.M., 1985. Determination of fluid inclusion compositions by sequential freezing. *Econ Geol.* 80, 1436-1439.
- Hazen, R.M., Ewintg, R.C., Sverjensky, D.A., 2009. Evolution of uranium and thorium minerals. *American Mineralogist* 94, 1293-1311.
- Hecht, L., Cuney, M., 2000. Hydrothermal alteration of monazite in the Precambrian crystalline basement of the Athabasca Basin (Saskatchewan, Canada): implications for the formation of unconformity-related uranium deposits. *Miner. Deposit.* 35, 791-795.
- Heijlen, W., Banks, D.A., Muchez, P., Stensgard, B.M., Yardley, B.W.D., 2008. The Nature of Mineralizing Fluids of the Kipushi Zn-Cu Deposit, Katanga, Democratic Republic of Congo: Quantitative Fluid Inclusion Analysis using Laser Ablation ICP-MS and Bulk Crush-Leach Methods. *Economic Geology* 103, 1459-1482.
- Henderson, P., 1984. *Rare earth element geochemistry*. Elsevier.
- Hinchey, A.M., Carr, S.D., Rayner, N. 2007. Bulk compositional controls on the preservation of age domains within metamorphic monazite: A case study from quartzite and garnet-

- cordierite-gedrite gneiss of Thor-Odin dome, Monashee complex, Canadian Cordillera. *Chem. Geol.* 240, 85-102.
- Hitzman, M.W., Selley, D., Bull, S., 2010. Formation of Sedimentary Rock-Hosted Stratiform Copper Deposits through Earth History. *Economic Geology* 105, 627–639.
- Hitzman, M.W., Broughton, D., Selley, D., Woodhead, J., Wood, D., Bull, S., 2012. The Central African Copperbelt: Diverse stratigraphic, structural and temporal settings the world's largest sedimentary copper district: in Hedenquist, J.W., Harris, M., Camus, F., 2012. *Geology and genesis of major copper deposits and districts of the world. A tribute to Richard H Sillitoe. Society of economic geologist, special publication 16*, 487-514.
- Hoffman, P.F., 1978. United plates of America, the birth of a craton: early Proterozoic assembly and growth of Laurentia. *Ann. Rev. Earth Planet. Sci.* 16, 543-603.
- Hoffman, P. F., 1991. Did the breakout of Laurentia turn Gondwanaland insideout? *Science* 252, 1409-1412.
- Hoffmann, K.H., Condon, D.J., Bowring, S.A., Crowley, J.L., 2004. U-Pb zircon date from the Neoproterozoic Ghaub Formation, Namibia: Constraints on Marinoan glaciation. *Geology* 32, 817-820.
- Hofmann, A.W., 1988. Chemical differentiation of the Earth: the relationship between mantle, continental crust, and oceanic crust. *Earth and Planetary Science Letters* 90, 297–314.
- Hofmann, A.W., 1997. Mantle geochemistry: the message from oceanic volcanism. *Nature* 385, 219-229.
- Holdaway, M.J., 1971. Stability of andalusite and the alumino-silicate phase diagram. *Am. J. Of Sci.* 271, 97-131.
- Holland, H.D., 2002. Volcanic gases, black smokers, and the great oxidation event. *Geochimica et Cosmochimica Acta* 66, 3811-3826.
- Holloway, J.M., Dahlgren, R.A., 1999. Geologic nitrogen in terrestrial biogeochemical cycling. *Geol.* 27, 567-570.
- Hurley, P.M., Rand, J.R., 1969. Predrift continental nuclei. *Science* 164, 1229–1242.
- Hurrai, V., Paquette, J.L., Huraiova, M., Konecny, P., 2010. Age of deep crustal magmatic chambers in the intra-Carpathian back-arc basin inferred from LA-ICPMS U-Th-Pb dating of zircon and monazite from igneous xenoliths in alkali basalts. *J. Volc. Geo. Res.* 198, 275-287.

Hurrai, V., Paquette, J.L., Huraiova, M., Sabol, M., 2012. U-Pb geochronology of zircons from fossiliferous sediments 1 of the Hajnacka I maar (Slovakia) - type locality of the MN16a biostratigraphic subzone. *Geol. Mag.* 149, 989-1000.

J

Jacob, R.E., Moore, J.M., Armstrong, R.A., 2000. Zircon and titanite age determination from igneous rocks in the Karibib district, Namibia: implications for Navachab vein-style gold mineralization. *Communs Geological Survey of Namibia* 12, 157-166.

Jahn, B.M., 2004. The Central Asian Orogenic Belt and growth of the continental crust in the Phanerozoic, in: Malpas, J., Fletcher, C.J., Aitchison, J.C., eds., *Aspects of the Tectonic Evolution of China*. The Geological Society, London, Special Publication 226, 73-100.

Janeček, J., Ewing, R.C., 1992. Structural formula of uraninite. *Journal of Nuclear Materials* 190, 128-132.

Jayananda, M., Martin, H., Peucat, J.-J., Mahabaleswar, B., 1995. Late Archaean crust–mantle interactions: geochemistry of LREE—enriched mantle derived magmas. Example of the Closepet batholith, southern India. *Contribution to Mineralogy and Petrology* 119, 314-329.

Jedwab, J., 1994. Minéralogie des Métaux du Groupe du Platine au Shaba, Zaïre. In: Charlet, J.-M. (Ed.), *Colloque International Cornet, Gisements stratiformes de cuivre et minéralisations associées*, Mons. Académie Royale des Sciences d'Outre-Mer, pp. 325-355.

Jefferson, C.W., Thomas, D.J., Gandhi, S.S., Ramaekers, P., Delaney, G., Brisbin, D., Cutts, C., Portella, P., Olson, R.A., 2007. Unconformity associated uranium deposits of the Athabasca Basin, Saskatchewan and Alberta, in: *EXTECH IV*. Jefferson C.W. and Delaney G., pp. 23-67.

Jessel, M.W., 1987. Grain-boundary migration microstructures in a naturally deformed quartzite. *J. Struct. Geol.* 9, 1007-1014.

John, T., 2001. Subduction and continental collision in the Lufilian Arc-Zambezi orogen: A petrological, geochemical and geochronological study of eclogites and whiteschists (Zambia). Unpublished PhD. Dissertation, Christian-Albrechts-Universität, Germany, 75 pp.

- John, T., Schenk, V., 2003. Partial eclogitisation of gabbroic rocks in a late Precambrian subduction zone (Zambia): prograde metamorphism triggered by fluid infiltration. *Contributions to Mineralogy and Petrology* 146, 174-191.
- John, T., Schenk, V., Haase, K., Scherer, E., Tembo, F., 2003. Evidence for a Neoproterozoic ocean in south-central Africa from mid-oceanic-ridge-type geochemical signatures and pressure-temperature estimates of Zambian eclogites. *Geology* 31, 243-246.
- John, T., Schenk, V., Mezger, K., Tembo, F., 2004. Timing and PT evolution of whiteschist metamorphism in the Lufilian Arc-Zambezi Belt orogen (Zambia): Implications for the assembly of Gondwana. *The Journal of Geology* 112, 71-90.
- Johnson, E.L., Hollister, L.S., 1995. Syndeformational fluid trapping in quartz: determining the pressure-temperature conditions of deformation from fluid inclusions and the formation of pure CO₂ fluid inclusions during grain-boundary migration. *J. Metam. Geol.* 13, 239-249.
- Johnson, S.P., Oliver, G.J.H., 1998. A second natural occurrence of yoderite. *J. Metamorph. Geol.* 16, 809-818.
- Johnson, S.P., Oliver, G.J.H., 2000. Mesoproterozoic oceanic subduction, island-arc formation and the initiation of back-arc spreading in the Kibaran Belt of central, southern Africa: evidence from the Ophiolite Terrane, Chewore Inliers, northern Zimbabwe. *Precambrian Res.* 103, 125-146.
- Johnson, S.P., Oliver, G.J.H., 2002. High *f*O₂ metasomatism during whiteschist metamorphism. *Journal of petrology* 43, 271-290.
- Johnson, S.P., Oliver, G.J., 2004. Tectonothermal history of the Karouera Arc, northern Zimbabwe. *Precambrian research* 130, 71-97.
- Johnson, S.P., Rivers, T., De Waele, B., 2005. A review of the Mesoproterozoic to early Paleozoic magmatic and tectonothermal history of south-central Africa: implications for Rodinia and Gondwana. *Journal of the Geological Society, London* 162, 433-450.
- Johnson, S.P., De Waele, B., Evans, D., Banda, W., Tembo, F., Milton, J.A., Tani, K., 2007. Geochronology of the Zambezi Supracrustal Sequence, Southern Zambia: A record of Neoproterozoic Divergent Processes along the Southern Margin of the Congo Craton. *The Journal of Geology* 115, 355-374.

Jung, S., Mezger, K., Hoernes, S., 2001. Trace element and isotopic (Sr, Nd, Pb, O) arguments for a mid crustal origin of Pan-African garnet-bearing S-type granites from the Damara orogen (Namibia). *Precambrian Res.* 110, 325-355.

Jung, S., Mezger, K., 2003. Petrology of basement-dominated terranes: I. Regional metamorphic T-t path from U-Pb monazite and Sm-Nd garnet geochronology (Central Damara orogen, Namibia). *Chem. Geol.* 198, 223-247.

K

Kabengele, M., Lubala, R.T., Cabanis, B., 1991. Caractérisation pétrologique et géochimique du magmatisme Ubendien du secteur de Pepa-Lubumba, sur le plateau des Marungu (Nord-Est du Shaba, Zaire). Signification géodynamique dans l'évolution de la chaîne ubendienne. *J. Afr. Earth Sci.* 13, 243-265.

Kampunzu, A.B., Kapenda, D., Manteka, B., 1991. Basic magmatism and geotectonic evolution of the Pan African belt in central Africa: evidence from the Katangan and West Congolian segments. *Tectonophysics* 190, 363-371.

Kampunzu, A.B., Cailteux, J., 1999. Tectonic Evolution of the Lufilian Arc (Central Africa Copper Belt) During the Neoproterozoic Pan-African Orogenesis. *Gondwana Research* 2, 401-421.

Kampunzu, A.B., Tembo, F., Matheis, G., Kapenda, D., Huntsman-Mapila, P., 2000. Geochemistry and Tectonic Setting of Mafic Igneous Units in the Neoproterozoic Katangan Basin, Central Africa: Implications for Rodinia Break-up. *Gondwana Research* 3, 125-153.

Kampunzu, A.B., Cailteux, J.L.H., Kamona, A.F., Intiomale, M.M., Melcher, F., 2009. Sediment-hosted Zn–Pb–Cu deposits in the Central African Copperbelt. *Ore Geology Reviews* 35, 263-297.

Kasch, K.W., 1983. Continental collision, suture progradation and thermal relaxation: A plate tectonic model for the Damara orogen in central Namibia. *Spec. Publ. geol. Soc. S. Afr.*, 423-429.

Katongo, C., Koller, F., Kloetzli, U., Koeberl, C., Tembo, F., De Waele, B., 2004. Petrography, geochemistry and geochronology of granitoid rocks in the Neoproterozoic-Paleozoic Lufilian-Zambezi belt, Zambia: Implications for tectonic setting and regional correlation. *Journal of African Earth Sciences* 40, 219-244.

- Keppler, H., Wyllie, P.J., 1990. Role of fluids in transport and fractionation of uranium and thorium in magmatic provinces. *Nature* 348, 521-533.
- Kerrick, R., 1976. Some effects of tectonic recrystallisation on fluid inclusions in vein quartz. *Contrib. Mineral Petrol* 59, 195-202.
- Key, R. M. and Armstrong, R. A., 2000, Geology and geochronology of pre- Katangan igneous and meta-igneous rocks north of the Lufilian Arc in northwest Zambia: *Journal of African Earth Sciences* 31, p. 36-37.
- Key, R.M., Liyungu, A.K., Njamu, F.M., Somwe, V., Banda, J., Mosley, P.N., Armstrong, R.A., 2001. The western arm of the Lufilian Arc in NW Zambia and its potential for copper mineralization. *Journal of African Earth Sciences* 33, 503-528.
- Killick, A.M., 2000. The Matchless Belt and associated sulphide mineral deposits, Damara Orogen, Namibia. *Communs Geological Survey of Namibia* 12 73–80.
- Kish, L., Cuney, M., 1981. Uraninite-albite veins from the Mistamisk Valley of the Labrador Trough, Québec. *Mineralogical Magazine* 44, 471-483.
- Kohn, M.J., Wieland, M.S., Parkinson, C.D., Upreti, B.N. 2005. Five generations of monazite in Langtang gneisses: implications for chronology of the Himalayan metamorphic core. *J. Metamorph. Geol.* 23, 399-406.
- Kokonyangi, J., Armstrong, R., Kampunzu, A.B., Yoshida, M., Okudaira, T., 2004. U–Pb zircon geochronology and petrology of granitoids from Mitwaba (Katanga, Congo): implications for the evolution of the Mesoproterozoic Kibaran belt. *Precambrian Research* 132, 79-106.
- Kominou, A., Sverjensky, D.A., 1995. Hydrothermal alteration and the chemistry of ore-forming fluids in an unconformity-type uranium deposit. *Geochimica et Cosmochimica Acta* 59, 2709-2723.
- Koziy, L., Bull, S., Large, R., Selley, D., 2009. Salt as a fluid driver, and basement as a metal source, for stratiform sediment-hosted copper deposits. *Geology* 37, 1107-1110.
- Kribek, B., Knesi, I., Pasava, J., Maly, K., Caruthers, H., Sykorova, I., Jehlicka, J., 2005. Hydrothermal alteration of the graphitized organic matter at the Kansanshi Cu-(Au-U) deposit, Zambia. In: Mao J, Bierlein P (eds) *Mineral Deposit Research: Meeting the Global Challenge*. Springer, Heidelberg 278-280.

- Krohn, M.D., Kendall, C., Evans, J.R., Fries, T.L., 1993. Relations of ammonium minerals at several hydrothermal systems in the western US. *J. Volcanol. Geotherm. Res.* 56, 401-413.
- Kröner, A., 1975. Late Precambrian formations in the western Richtersveld, northern Cape Province. *Trans. R. Soc. South Africa* 41, 375-433.
- Kröner, A., 1982. Rb-Sr geochronology and tectonic evolution of the Pan-African Damara Belt of Namibia. Southwestern Africa. *American Journal of Science* 282, 1471-1507.
- Kröner, A., Layer, P., 1992. Crust Formation and Plate Motion in the Early Archean. *Science* 256, 1405-1411.
- Kröner, A., Cordani, U.G., 2003. African, southern Indian and South American cratons were not part of the Rodinia supercontinent: evidence from field relationships and geochronology: *Tectonophysics* 375, 325-352.
- Kukla, P.A., Stanistreet, I.G., 1991. Record of the Damaran Khomas Hochland accretionary prism in central Namibia: Refutation of an “ensialic” origin of a Late Proterozoic orogenic belt. *Geology* 19, 473-476.
- Kyser, K., Cuney, M., 2008. Unconformity-related uranium deposits, in: *Recent and Not-so-recent Developments in Uranium Deposits and Implications for Exploration*. pp. 161-219.

L

- Lach, P., 2012. Signature géochimique des éléments des terres rares dans les oxydes d'uranium et minéraux associés dans les gisements d'uranium: analyse par ablation laser couplée à l'ICP-MS et étude géochronologique. Unpublished PhD. Dissertation, Université de Lorraine, France, 293 pp.
- Lach, P., Mercadier, J., Dubessy, J., Boiron, M.-C., Cuney, M., 2013. In-situ quantitative measurement of rare earth elements in uranium oxides by Laser Ablation-Inductively Coupled Plasma-Mass Spectrometry. *Geostandard and Geoanalytical Research*. 37, 277-296.
- Lagos, M., Scherer, E. E., Tomaschek, F., Münker, C., Keiter, M., Berndt, J., Ballhaus, C., 2007. High precision Lu–Hf geochronology of Eocene eclogite-facies rocks from Syros, Cyclades, Greece. *Chem. Geol.* 243, 16-35.

- Langmuir, D., 1978. Uranium solution-mineral equilibria at low temperatures with application to sedimentary ore deposits. *Geochimica and Cosmochimica Acta* 42, 547-569.
- Lecumberri-Sanchez, P., Steele-MacInnis, M., Bodnar, R.J., 2012. A numerical model to estimate trapping conditions of fluid inclusions that homogenize by halite disappearance. *Geochim. Cosmochim. Acta* 92, 14-22.
- Ledent, D., 1958. Détermination de l'âge absolu de minéraux africains par la méthode du plomb. Unpublished PhD. Dissertation, Université Libre de Bruxelles, Belgium, 352 pp.
- Leisen, M., 2011. Analyse chimique des inclusions fluides par ablation-laser couplée à l'ICPMS et applications géochimiques. Dissertation, Université de Lorraine, France.
- Leisen, M., Dubessy, J., Boiron, M.C., Lach, P., 2012. Improvement of the determination of element concentrations in quartz-hosted fluid inclusions by LA-ICPMS and Pitzer thermodynamic modeling of ice melting temperature. *Geochim. Cosmochim. Acta.* 90, 110-125.
- Lenoir, J.L., Li'égeois, J.-P., Theunissen, K., Klerkx, J., 1994. The Palaeoproterozoic Ubendian shear belt in Tanzania: geochronology and structure. *J. Afr. Earth Sci.* 19, 169–184.
- Leroy, J., 1979. Contribution à l'étalonnage de la pression interne des inclusions fluides lors de leur décrépitation. *Bull. Mineral.* 102, 584-593.
- Lesquer, A., De Almeida, F. F. M., Davino, A., Lachaud, J. C., Maillard, P., 1981. Signification structurale des anomalies gravimétriques de la partie sud du craton de Sao Francisco (Brésil). *Tectonophysics* 3, 273-293.
- Li, Z.X., Li, X.H., Kinny, P.D., Wang, J., Zhang, S., Zhou, H., 2003. Geochronology of Neoproterozoic syn-rift magmatism in the Yangtze Craton, South China and correlations with other continent: evidence for a mantle superplume that broke up Rodinia. *Precambrian Research* 122, 85-109.
- Li, Z. X., Bogdanova, S. V., Collins, A. S., Davidson, A., De Waele, B., Ernst, R. E., Fitzsimons, I. C. W., Fuck, R. A., Gladkochub, D. P., Jacobs, J., Karlstrom, K. E., Lu, S., Natapov, L. M., Pease, V., Pisarevsky, S. A., Thrane, K., Vernikovsky, V., 2008. Assembly, configuration, and break-up history of Rodinia: A synthesis. *Precambrian Research* 160, 179-210.
- Liégeois, J.P., Black, R., Navez, J., Latouche, L., 1994. Early and late Pan-African orogenies in the Air assembly of terranes. *Precambrian Research* 67, 59-88.

- Loewy, S.L., Connelly, J.N., Dalziel, I.W.D., Gower, C.F., 2003. Eastern Laurentia in Rodinia: constraints from whole-rock Pb and U/Pb geochronology. *Tectonophysics* 375, 169-197.
- Longerich, H.P., Jackson, S.E., Günther, D., 1996. Laser ablation inductively coupled plasma mass spectrometric transient signal data acquisition and analyte concentration calculation. *J. Anal. At. Spectrom.* 11, 899-904.
- Loris, N.B.T., 1996. Etude des minéralisations uranifères du gisement cuprocobaltifère de Luiswishi (Shaba, Zaïre): contextes géologiques et géochimiques. Discussion des modèles génétiques. Unpublished PhD. Dissertation, Polytechnic Faculty of Mons, Belgium, 275 pp.
- Loris, N.B.T., Charlet, J.-M., Pechmann, E., Clare, C., Chabu, M., Quinif, Y., 1997. Caractères minéralogiques, cristallographiques, physico-chimiques et âges des minéralisations uranifères de Luiswishi (Shaba, Zaïre), in: Colloque International Cornet. Presented at the Gisements stratiformes de cuivre et minéralisations associées, Mons Académie Royale des Sciences d'Outre-Mer, pp. 285-306.
- Loris, N.B.T., Charlet, J.-M., Okitaudji, R., 2002. La mobilité de l'uranium et des métaux associés en environnement géologique oxydo-réducteur, le cas des minéralisations Cu-Co-Ni-U de Luiswishi (Katanga, RDC). *Académie Royale des Sciences d'Outre-Mer* 48, 165-188.
- Ludwig, K., 2007. Isoplot/Ex version 3.41b, a geochronological toolkit for Microsoft Excel. Berkeley Geochronology Center Special Publication No. 4.
- Lumpkin, G.R., Leung, S.H.F., Colella, M., 2000. Composition, geochemical alteration, and alpha-decay damage effects of natural brannerite. *Scientific Basis for Nuclear Waste Management XXIII, Symposium. Materials Research Society Symposium Proceedings* 608, 359-365.

M

- Maozhong, M., Junqi, W., Xiangyun, W., 1994. Effect of groundwater radiolysis on the wall-rock alteration of uranium ore deposits. *Chin. J. Geochem.* 13, 355-362.
- Marjonon, R.K., 2000. Geology of the Mufulira-Kitwe area: explanation of degree sheet 1228, part of NW quarter and SW quarter: Report of the Geological Survey of Zambia.
- Martin, H., Porada, H., 1977. The intracratonic branch of the Damara Orogen in South West Africa. I. Discussion of geodynamic models. *Precambrian Research* 5, 311-338.

- Master, S., Rainaud, C., Armstrong, R.A., Phillips, D., Robb, L.J., 2005. Provenance ages of the Neoproterozoic Katanga Supergroup (Central African Copperbelt), with implications for basin evolution. *Journal of African Earth Sciences* 42, 41-60.
- McDonough, W.F., McCulloch, M.T., Sun, S.S., 1985. Isotopic and geochemical systematic in Tertiary–Recent basalts from southeastern Australia and implications for the evolution of the subcontinental lithosphere. *Geochimica et Cosmochimica Acta* 49, 2051–2067.
- McDonough, W.F., Sun, S.S., 1995. The composition of the Earth. *Chemical Geology* 120, 223-253.
- McFarlane, C.R., Connelly, J.N., Carlson, W.D. 2006. Contrasting response of monazite and zircon to a high-*T* thermal overprint. *Lithos* 88, 135-149.
- McLennan, S.M., 1989. Rare earth elements in sedimentary rocks; influence of provenance and sedimentary processes. *Reviews in Mineralogy and Geochemistry* 21, 169–200.
- McMenamin, M. A. S., McMenamin, D. L. S., 1990. *The Emergence of Animals: The Cambrian Breakthrough*, 217 pp.
- Meert, J.G., 2001. Growing Gondwana and rethinking Rodinia: a paleomagnetic perspective. *Gondwana Research* 4, 279-288.
- Meert, J.G., 2003. A synopsis events related to the assembly of Eastern Gondwana. *Tectonophysics* 362, 1-40.
- Meert, J. G., Van Der Voo, R., 1997. The assembly of Gondwana 800-550 Ma. *Journal of Geodynamics* 23, 223-235.
- Meert, J.G., van der Voo, R., Ayub, S., 1995. Paleomagnetic investigation of the Neoproterozoic Gagwe lavas and Mbozi complex, Tanzania and the assembly of Gondwana. *Precambrian Res.* 74, 225-244.
- Meert, J.G., Torsvik, T.H., 2003. The making and unmaking of a Supercontinent: Rodinia revisited. *Tectonophysics* 375, 261-288.
- Mendelsohn, F., 1961. *The Geology of the Northern Rhodesian Copperbelt*. Macdonald, London, pp. 523.
- Meneghel, L., 1981. The occurrence of uranium in the Katanga System of northwestern Zambia. *Economic Geology* 76, 56-68.

- Mercadier, J., Richard, A., Boiron, M.-C., Cathelineau, M., Cuney, M., 2010. Migration of brines in the basement rocks of the Athabasca Basin through microfracture networks (P-Patch U deposit, Canada). *Lithos* 115, 121-136.
- Mercadier, J., Cuney, M., Lach, P., Boiron, M.-C., Bonhoure, J., Richard, A., Leisen, M., Kister, P., 2011. Origin of uranium deposits revealed by their rare earth element signature. *Terra Nova* 23, 264-269.
- Mercadier, J., Richard, A., Cathelineau, M., 2012. Boron- and magnesium-rich marine brines at the origin of giant unconformity-related uranium deposits: $\delta^{11}\text{B}$ evidence from Mg-tourmalines. *Geology* 40, 231-234.
- Mernagh, T.P., Wilde, A.R., 1989. The use of the laser Raman microprobe for the determination of salinity in fluid inclusions. *Geochim. Cosmochim. Acta*; 53, 765-771.
- Miller, R.McG., Grote, W., 1988. Geological map of the Damara Orogen of South West Africa/Namibia 1:5.000.000. Geol. Surv. Namibia, Windhoek.
- Moore, E. M., 1991. Southwest U.S. - East Antarctic (SWEAT) connection: A hypothesis. *Geology* 19, 425-428.
- Mossman, D.J., Gauthier-Lafaye, F., Nagy, B., Rigali, M.J., 1998. Chemistry of organic-rich black shales overlying the natural nuclear fission reactors of Oklo, republic of Gabon. *Energy Sources* 20, 521-539.
- Moyen, J.-F., Stevens, G., Kisters, A., 2006. Record of mid-Archaean subduction from metamorphism in the Barberton terrain, South Africa. *Nature* 442, p. 559-562.
- Moyen, J.-F., Van Huene, J., 2012. Short-term episodicity of Archaean plate tectonics. *Geology* 40, 451-454.
- Muchez, P., Vanderhaeghen, P., Desouky, H., Schneider, J., Boyce, A., Dewaele, S., Cailteux, J.L.H., 2008. Anhydrite pseudomorphs and the origin of stratiform Cu–Co ores in the Katangan Copperbelt (Democratic Republic of Congo). *Mineralium Deposita* 43, 575-589.
- Muchez, P., Brems, D., Clara, E., De Cleyn, A., Lammens, L., Boyce, A., De Muynck, D., Mukumba, W., Sikazwe, O., 2010. Evolution of Cu–Co mineralizing fluids at Nkana Mine, Central African Copperbelt, Zambia. *J. Afr. Earth Sci.* 58, 457-474.
- Mullis, J., 1987. Fluid inclusion studies during very low-grade metamorphism. In: M. Frey (Editor), *Low temperature metamorphism*. Blackie, Glasgow, pp. 162-199.

- Munara, A., 2012. Formation des gisements d'uranium de type roll : approche minéralogique et géochimique du gisement uranifère de Muyunkum, Bassin de Chu-Sarysu, Kazakhstan. Unpublished PhD Dissertation Université de Lorraine, France (327 pp).
- Münker, C., Weyer, S., Scherer, E.E., Mezger, K., 2001. Separation of high field strength elements (Nb, Ta, Zr, Hf) and Lu from rock samples for MC-ICPMS measurements. *Geochemistry, Geophysics, Geosystems (G3)*, 2, paper number 10.1029/2001GC000183.
- Murphy, J.B., Pisarevsky, S.A., Nance, R.D., Keppie, J.D., 2004. Neoproterozoic–Early Paleozoic evolution of peri-Gondwanan terranes: implications for Laurentia–Gondwana connections. *International Journal of Earth Sciences* 93, 659-682.
- Nzenti, J. P., Barbey, P., Jegouzo, P., Moreau, C., 1984. Un nouvel exemple de ceinture granulitique dans une chaîne protérozoïque de transition : les migmatites de Yaoundé au Cameroun. *Comptes Rendus de l'Académie des Sciences, Sciences de la Terre et des Planètes* 17, 1197-1199.

N

- Nelson, D.R., McCulloch, M.T., 1989. Enriched mantle components and mantle recycling of sediments. In: Ross, J. (Ed.), *Kimberlites and Related Rocks*, vol 1. Their Composition, Occurrence, Origin and Emplacement. Geological Society of Australia Special Publication, vol. 14, pp. 560-570.
- Newton, R.C., Manning, C.E., 2005. Solubility of Anhydrite, CaSO₄, in NaCl–H₂O Solutions at High Pressures and Temperatures: Applications to Fluid–Rock Interaction. *J. Petrol.* 46, 701-716.
- Ngongo, K., 1975. Sur la similitude entre les gisements uranifères (type Shinkolobwe) et les gisements cuprifères (type Kamoto) au Shaba, Zaïre. *Annales de la Société Géologique de Belgique* 98, 449-462.
- Ngoyi, K., Liégeois, J.-P., Demaiffe, D., Dumont, P., 1991. Age tardi ubendien (Protérozoïque inférieur) des dômes granitiques de l'arc cuprifère zaïro-zambien. *C.R. Acad. Sci.* 313 (II), 83-89.
- Nijland, T.G., Maijer, C., Senior, A., Verschure, R.H., 1993. Primary sedimentary structures and composition of the high-grade metamorphic Nidelva quartzite complex (Bamble,

Norway), and the origin of nodular gneisses. In: Proceedings of the Koninklijke Nederlandse Akademie van Wetenschappen 96, 217-232.

O

Okitaudji, L.R., 1989. Géologie sédimentaire et concentration syndiagénétique du cuivre et du cobalt dans la “Série des Mines” du Shaba, Zaïre. Unpublished PhD. Dissertation, Polytechnic National Institute of Lorraine, France, 476 pp.

Oliver, N.H.S., Wall, V.J., 1987. Metamorphic plumbing system in Proterozoic calc-silicates, Queensland, Australia. *Geol.* 15, 793-796

Oliver, N.H.S., Wall, V.J., Cartwright, I., 1992. Internal control of fluid compositions in amphibolite-facies scapolitic calc-silicates, Mary Kathleen, Australia. *Contrib. Mineral. Petrol.* 111, 94-112.

Oliver, N.H.S., Rubenach, M.J., Valenta, R.K., 1998. Precambrian metamorphism, fluid flow and metallogeny of Australia. *AGSO J. Aust. Geol. Geophys.* 17, 31-53.

Ondrejka, M., Uher, P., Putiš, M., Broska, I., Bačík, P., Konečný, P., Schmiedt, I. 2012. Two-stage breakdown of monazite by post-magmatic and metamorphic fluids: An example from the Veporic orthogneiss, Western Carpathians, Slovakia. *Lithos* 142, 245-255.

P

Pagel, M., Pinte, G., Rotach-Toulhoat, N., 1987. The rare earth elements in natural uranium oxides. *Monogr. Ser. Mineralium Deposita* 27, 81-85.

Pagel, M., Cavellec, S., Forbes, P., Gerbaut, O., Vergely, P., Wagani, I., and Mathieu, R., 2005. Uranium deposits in the Arlit area (Niger): SGA Meeting, Meeting the Global Challenge, 8th, Beijing, China, Proceedings, 303-305.

Pankhurst, R.J., Rapela, C.W., Saavedra, J., Baldo, E., Dahlquist, J., Pascua, I., Fanning, C.M., 1998. The Famatinian magmatic arc in the southern Sierras Pampeanas. In: Pankhurst, R.J., Rapela, C.W. (Eds.), *The Proto-Andean Margin of Gondwana*. Special Publication of the Geological Society, London 142, 343-367.

Parrish, R.R. 1990. U-Pb dating of monazite and its application to geological problems. *Can. J. Earth Sci.* 27, 1431-1450.

Passchier, C.W., Trouw, R.A.J., 2005, *Microtectonics*. Springer.

- Patchett, J.P., Kouvo, O., Hedge, C.E., Tatsumoto, M., 1982. Evolution of continental crust and mantle heterogeneity: Evidence from Hf isotopes. *Contributions to Mineralogy and Petrology* 78, 279-297.
- Pattison, D.R.M., 2006. The fate of graphite in prograde metamorphism of pelites: an example from the Ballachulish aureole, Scotland. *Lithos* 88, 85-99.
- Pearce, J. A., Harris, N. B. W., Tindle, A. G., 1984. Trace element discrimination diagrams for the tectonic interpretation of granitic rocks. *Journal of Petrology* 25, 956-983.
- Pearce, N.J.G., Perkins, W.T., Westgate, J.A., Gorton, M.P., Jackson, S.E., Neal, C.R., Cheney, S.P., 1997. A Compilation of New and Published Major and Trace Element Data for NIST SRM 610 and NIST SRM 612 Glass Reference Materials. *Geostandards and Geoanalytical Research* 21, 115-144.
- Pearson, R.G., 1968. Hard and soft acids and bases, HSAB, part 1: Fundamental principles. *J. Chem. Educ.* 45, 581.
- Penaye, J., Toteu, S. F., Van Schumus, W. R., Nzenti, J. P., 1993. U-Pb and Sm-Nd geochronologic data on the Yaoundé series, Cameroon: reinterpretation of the granulitic rocks as the suture of a collision in the "Centrafrican belt". *Comptes Rendus de l'Académie des Sciences, Sciences de la Terre et des Planètes* 317, 789-794.
- Petrik, I., Konecny, P., Kovacik, M., Holicky, I. 2006. Electron microprobe dating of monazite from Nizke Tatry Mountains orthogneisses (Western Carpathians, Slovakia). *Geol. Carp.-Bratisl.* 57.
- Philpotts, A., Ague, J.J., 2009. Principles of igneous and metamorphic petrology. University Press, Cambridge.
- Pimentel, M. M., Fuck, R. A., 1992. Neoproterozoic crustal accretion in central Brazil. *Geology* 20, 375-379.
- Pisarevsky, S.A., Wingate, M.T.D., Powell, C.M., Johnson, S., Evans, D.A.D., 2003. Models of Rodinia assembly and fragmentation. In: Yoshida, M., Windley, B. & Dasgupta, S. (eds) Proterozoic East Gondwana: Supercontinent Assembly and Breakup. Geological Society, London, Special Publications 206, 35-55.
- Pohl, W., 1992. Defining metamorphogenic mineral deposits-an introduction. *Mineral. Petrol.* 45, 145-152.

- Poidevin, J. L., 1985. Le Protérozoïque supérieur de la République centrafricaine. *Annuaire du Musée Royal d'Afrique Centrale* 91, 75.
- Poitrasson, F., Chenery, S., Bland, D. J., 1996. Contrasted monazite hydrothermal alteration mechanisms and their geochemical implications. *Earth Planet. Sci. Lett.* 145, 79-96.
- Poitrasson, F., Chenery, S., Shepherd, T.J., 2000. Electron microprobe and LA-ICP-MS study of monazite hydrothermal alteration: Implications for U-Th-Pb geochronology and nuclear ceramics. *Geochim. Cosmochim. Acta* 64, 3283-3297.
- Pollack, H.N., 1986. Cratonization and thermal evolution of the Mantle. *Earth and Planetary Science Letters* 80, 175-782.
- Porada, H., Wittig, R., 1983. Turbidites and their significance for the geosynclinal evolution of the Damara Orogen, South West Africa/Namibia. in: Miller, R.McG. (Ed.) *Evolution of the Damara Orogen of South West Africa/Namibia*. Spec. Publ. geol. Soc. S. Afr. 11, 515 pp. 21-36.
- Porada, H., Berhorst, V., 2000. Towards a new understanding of the Neoproterozoic-early palaeozoic Lufilian and northern Zambezi belts in Zambia and the Democratic Republic of Congo. *Journal of African Earth Sciences* 30, 727-771.
- Pöter, B., Gottschalk, M., Heinrich, W., 2004. Experimental determination of the ammonium partitioning among muscovite, K-feldspar and aqueous chloride solutions. *Lithos* 74, 67-90.
- Powell, C. M., Li, Z. X., McElhinny, M. W., Meert, J. G., Park, J. K., 1993. Paleomagnetic constraints on timing of the Neoproterozoic breakup of Rodinia and the Cambrian formation of Gondwana. *Geology* 21, 889-892.
- Putnis, A., 2009. Mineral replacement reactions: from macroscopic observations to microscopic mechanisms. *Miner. Mag.* 66, 689-708.
- Putnis, A., Austrheim, H., 2010. Fluid-induced processes: metasomatism and metamorphism. *Geofluids* 10, 254-269.
- Pyle, J.M., Spear, F.S. 2003. Four generations of accessory-phase growth in low-pressure migmatites from SW New Hampshire. *Amer. Mineral.* 88, 338-351.

R

- Rainaud, C., 2005. Contributions to the geochronology and geological evolution of the Central African Copperbelt. Unpublished PhD. Dissertation, University of the Witwatersrand, South Africa, 221 pp.
- Rainaud, C., Master, S., Armstrong, R.A., Robb, L.J., 2003. A cryptic Mesoarchean terrane in the basement to the central African Copperbelt. *J. Geol. Soc. Lond.* 160, 11-14.
- Rainaud, C., Master, S., Armstrong, R.A., Phillips, D., Robb, L.J., 2005. Monazite U–Pb dating and 40Ar – 39Ar thermochronology of metamorphic events in the Central African Copperbelt during the Pan-African Lufilian Orogeny. *Journal of African Earth Sciences* 42, 183-199.
- Ramsay, C.R., Davidson, L.R., 1970. The origin of scapolite in the regionally metamorphosed rocks of Mary Kathleen, Queensland, Australia. *Contrib. Mineral. Petrol.* 25, 41-51.
- Ramseyer, K., Diamond, L.W., Boles, J.R., 1993. Authigenic K-NH₄-feldspar in sandstones; a fingerprint of the diagenesis of organic matter. *J. Sediment Res.* 6, 1092-1099.
- Rasmussen, B., Muhling, J.R. 2007. Monazite begets monazite: evidence for dissolution of detrital monazite and reprecipitation of syntectonic monazite during low-grade regional metamorphism. *Contrib. Mineral. Petrol.* 154, 675-689.
- Rapp, J.F., Klemme, S., Butler, I.B., Harley, S.L., 2010. Extremely high solubility of rutile in chloride and fluoride-bearing metamorphic fluids: An experimental investigation. *Geology* 38, 323-326.
- Regan, R. D., Marsh, B. D., 1982. The Bangui magnetic anomaly: its geological origin. *Journal of Geophysical Research* 87, 1107-1120.
- Ren, M., Parker, D.F., White, J.C., 2003. Partitioning of Sr, Ba, Rb, Y, and LREE between plagioclase and peraluminous silicic magma. *Am. Mineral.* 88, 1091-1103.
- Renne, P. R., Onstott, T. C., D'Agrella-Filho, M. S., Pacca, I. G. Teixeira, L. R., 1990. $40\text{Ar}/39\text{Ar}$ dating of 1.0–1.1 Ga magnetizations from the Sao Francisco and Kalahari cratons: tectonic implications for Pan-African and Brasiliano. *Earth and Planetary Science Letters* 101, 349-366.
- Reymer, A., Schubert, G., 1986. Rapid growth of some major segments of continental crust. *Geology* 14, 299-302.

- Richard, A., Pettke, T., Cathelineau, M., Boiron, M.C., Mercadier, J., Cuney, M., Derome, D. 2010. Brine–rock interaction in the Athabasca basement (McArthur River U deposit, Canada): consequences for fluid chemistry and uranium uptake. *Terra Nova* 22, 303-308.
- Richard, A., Rozsypal, C., Mercadier, J., Banks, D.A., Cuney, M., Boiron, M.-C., Cathelineau, M., 2012. Giant uranium deposits formed from exceptionally uranium-rich acidic brines. *Nature Geoscience* 5, 142-146.
- Richard, A., Banks, D.A., Mercadier, J., Boiron, M.-C., Cuney, M., Cathelineau, M., 2011. An evaporated seawater origin for the ore-forming brines in unconformity-related uranium deposits (Athabasca Basin, Canada): Cl/Br and $\delta^{37}\text{Cl}$ analysis of fluid inclusions. *Geochimica et Cosmochimica Acta* 75, 2792-2810.
- Richard, A., Cauzid, J., Cathelineau, M., Boiron, M.C., Mercadier, J., Cuney, M., 2013. Synchrotron XRF and XANES investigation of uranium speciation and element distribution in fluid inclusions from unconformity-related uranium deposits. *Geofluids* 13, 101-111.
- Richards, J.P., Cumming, G.L., Krstic, D., Wagner, P.A., Spooner, E.T.C., 1988. Pb isotope constraints on the age of sulfide ore deposition and U-Pb age of late uraninite veining at the Musoshi stratiform copper deposit, Central Africa copper belt, Zaire. *Economic Geology* 83, 724-741.
- Ring, U., Kröner, A., Toulkeredis, T., 1997. Palaeoproterozoic granulite-facies metamorphism and granitoid intrusions in the Ubendian-Usagaran Orogen of northern Malawi, east-central Africa. *Precambrian Res.* 85, 27-51.
- Robb, L. J. and Meyer, F.M., M., 1990. The nature of the Witwatersrand hinterland: conjectures on the source area problem. *Economic Geology* 85, 511-536.
- Robb, L. J., Meyer, F.M., Ferraz, M.F., Drennan, G.K., 1990. The distribution of radioelements in Archaean granites of the Kaapvaal Craton, with implications for the source of uranium in the Witwatersrand Basin. *South African Journal of Geology* 93, 5-40.
- Robb, L.J., Master, S., Greyling, L.N., Yao, Y., Rainaud, C., 2002. Contributions to the geology and mineralization of the central African Copperbelt. V. Speculations Regarding the “Snowball Earth” and Redox Controls on Stratabound Cu-Co and Pb-Zn mineralization.

- In: Anhaeusser, C.R.; (ed.). Economic Geology Research Institute, Information Circular 362. University of the Witwatersrand.
- Robb, L.J., Master, S., Greyling, L.N., Yao, Y., Rainaud, C., 2002. Contribution to the geology and mineralization of the central African Copperbelt., in: Speculations Regarding the “Snowball Earth” and Redox Controls on Stratabound Cu-Co and Pb-Zn Mineralization. Presented at the Proceedings of Geocongress, Namibia, p. 6.
- Roedder, E., 1984. Reviews in Mineralogy: Fluid inclusions. Mineral. Society. of America.
- Rogers, J.J.W., Adams, J.S.S., 1969, Uranium. In: Wedepohl, K.H., (ed.). Handbook of geochemistry: New York, Springer-Verlag.
- Rogers, N.W., Hawkesworth, C.J., Parker, R.J., Marsh, J.S., 1985. The geochemistry of potassic lavas from Vulcini, central Italy and implications for mantle enrichment processes beneath the Roman region. Contributions to Mineralogy and Petrology 90, 244-257.
- Rollinson, H.R., 1993. Using geochemical data: evaluation, presentation, interpretation. Longman Group UK Limited, London.
- Rose, D., 1980. Brabantite, $\text{CaTh}(\text{PO}_4)_2$, a new mineral of the monazite group. N. Jb. Miner. Mh. 6, 247-257.
- Rudnick, R.L., 1995. Making continental crust. Nature 378, 573– 578.
- Rudnick, R.L., Gao, S., 2003. Composition of the continental crust. In: Rudnick, R.L. (Ed.), The Crust, Treatise in Geochemistry 3, pp. 1 – 64.
- S**
- Sarang, A. K., Singh A.S., 2006. Vein type uranium in the Jagunda uranium deposits, Singhbhum, India. Abstract, 12th IAGOD Symposium, Moscow, Russia.
- Shackleton, R. M., 1986. Precambrian plate tectonics of northeast Gondwana: Mem. Soc. Geol. Ital. 31, 139-144.
- Schandelmeier, H., 1980. Regionale gliederung des Prakambriums und aspekte der krustentwicklung um Mambwe/nordost- Zambia. Unpublished Ph.D. Dissertation, Technical University of Berlin, Germany, 134 pp.
- Schandelmeier, H., 1983. The geochronology of post-Ubendian granitoids and dolerites from the Mambwe area, northern province, Zambia. Rep. Inst. Geol. Sci. 83, 40-46.
- Scherer E., Münker C., Mezger K., 2001. Calibration of the lutetium-hafnium clock. Science 293, 683-687.

- Schiffries, C.M., 1990. Liquid-absent aqueous fluid inclusions and phase equilibria in the system CaCl₂-NaCl-H₂O. *Geochim. Cosmochim. Acta* 54, 611-619.
- Schlegel, T.U., Wälle, M., Steele-MacInnis, M., Heinrich, C.A., 2012. Accurate and precise quantification of major and trace element compositions of calcic-sodic fluid inclusions by combined microthermometry and LA-ICPMS analysis. *Chem. Geol.* 334, 144-153.
- Schmidt, M.W., 1992. Amphibole composition in tonalite as a function of pressure: an experimental calibration of the al-in hornblende barometer. *Contributions to mineralogy and petrology* 110, 304-310.
- Schmidt, A., Weyer, S., Mezger, K., Scherer, E. E., Xiao, Y., Hoefs, J., Brey, G. P., 2008. Rapid eclogitisation of the Dabie-Sulu UHP terrane; constraints from Lu-Hf garnet geochronology. *Earth Planet. Sci. Lett.* 273, 203-213.
- Scholl, D.W., Von Huene, R., 2009. Implications of estimated magmatic additions and recycling losses at the subduction zones of accretionary (non-collisional) and collisional (suturing) orogens, in: Cawood, P.A., Kröner, A., eds., *Earth Accretionary systems in space and time*. The Geological Society, London, Special Publication 318, 105-125.
- Schuhmacher, M., Fernandes, F., de Chambost, E., 2004. Achieving high reproducibility isotope ratios with the Cameca IMS 1270 in the multicollection mode. *Appl. Surf. Sci.* 231, 878-882.
- Selley, D., Broughton, D., Scott, R.J., Hitzman, M., Bull, S.W., Large, R.R., McGoldrick, P.J., Croaker, M., Pollington, N., 2005. A New Look at the Geology of the Zambian Copperbelt. *Soc. Economic Geology Inc. 100th anniversary volume*, 965-1000.
- Seydoux-Guillaume, A.M., Paquette, J.L., Wiedenbeck, M., Montel, J.M., Heinrich, W., 2002. Experimental resetting of the U-Th-Pb systems in monazite. *Chem. Geol.* 191, 165-181.
- Shang, C.K., Satir, M., Siebel, W., Nsifa, E.N., Taubald, H., Liégeois, J.-P., Tchoua, F.M., 2004. TTGmagmatism in the Congo Craton; a view from major and trace element geochemistry, Rb-Sr and Sm-Nd systematics: case of the Sangmelima region, Ntem complex, southern Cameroon. *J. Afr. Earth Sci.* 40, 61_79.
- Shannon, R.D., 1976. Revised effective ionic radii and systematic studies of interatomic distances in halides and chalcogenides. *Acta Crystallographica Section A* 32, 751_767.
- Shaw, D., Sturchio, N., 1992. Boron-Lithium Relationships in Rhyolites and Associated Thermal Waters. *Geochim. Cosmochim. Acta* 56, 3723_3731.

- Siebenaller, L., Boiron, M.C., Vanderhaeghe, O., Hibsich, C., Jessel, M.W., Andre-Mayer, A.S., France-Lanord, C., Photiades, A., 2012. Fluid record of rock exhumation across the brittle-ductile transition during formation of a Metamorphic Core Complex (Naxos Island, Cyclades, Greece). *J. Metam. Geol.* doi:10.1111/jmg.12023.
- Skirrow, R., 2009. Uranium mineral systems: processes, exploration criteria and a new deposit framework, Record (Geoscience Australia). Geoscience Australia, Canberra.
- Smith, D.K., 1984. Uranium mineralogy. In: De Vivo B, Ippolito F, Capaldi G, Simpson PR (Eds.) Uranium geochemistry, mineralogy, geology, exploration and resources. The Institution of Mining and Metallurgy, London, England, 43-88.
- Söderlund U., Patchett J. P., Vervoort J. D., Isachsen C. E., 2004. The ^{176}Lu decay constant determined by Lu-Hf and U-Pb isotope systematics of Precambrian mafic intrusions. *Earth Planet. Sci. Lett.* 219, 311-324.
- Span, R., Wagner, W., 1996. A New Equation of State for Carbon Dioxide Covering the Fluid Region from the Triple-Point Temperature to 1100 K at Pressures up to 800 MPa. *J. Phys. Chem. Ref. Data* 25, 1509-1596.
- Spry, P.G., Marshall, B., Vokes, F.M., 2000. Metamorphosed and Metamorphogenic Ore Deposits. *Rev. in Econ. Geol.* 41.
- Steele-MacInnis, M., Bodnar, R.J., Naden, J., 2011. Numerical model to determine the composition of $\text{H}_2\text{O-NaCl-CaCl}_2$ fluid inclusions based on microthermometric and microanalytical data. *Geochim. Cosmochim. Acta* 75, 21-40.
- Steele-MacInnis, M., Lecumberri-Sanchez, P., Bodnar, R.J., 2012. HokieFlincs_H 2O-NaCl : A Microsoft Excel spreadsheet for interpreting microthermometric data from fluid inclusions based on the PVTX properties of $\text{H}_2\text{O-NaCl}$. *Comput. Geosci.* 49, 334-337.
- Steele-MacInnis, M., Bodnar, R.J., 2013. Effect of the vapor phase on the salinity of halite-bearing aqueous fluid inclusions estimated from the halite dissolution temperature. *Geochim. Cosmochim. Acta* 115, 205-216.
- Stern, R. J., 1994. Arc assembly and continental collision in the Neoproterozoic East African Orogen: Implications for the consolidation of Gondwanaland. *Annual Review of Earth and Planetary Sciences* 22, 319-351.

- Sterner, S.M., Hall, D.L., Bodnar, R.J., 1988. Synthetic fluid inclusions. V. Solubility relations in the system NaCl-KCl-H₂O under vapor-saturated conditions. *Geochim. Cosmochim. Acta* 52, 989-1005.
- Stipp, M., Stünitz, H., Heilbronner, R., Schmid, S.M., 2002. The eastern Tonale fault zone: a “natural laboratory” for crystal plastic deformation of quartz over temperature from 250 to 700 °C. *J. Struct. Geol.* 24, 1861-1884.
- Sverjensky, D.A., 1984. Europium redox equilibria in aqueous solution. *Earth and Planetary Science Letters* 67, 70-78.

T

- Tack, L., Fernandez-Alonso, M., Tahon, M., Wingate, M.T.D., Barritt, S., 2002. The “northeastern Kibaran belt” (NKB) and its mineralizations reconsidered: new constraints from a revised lithostratigraphy, a GIS-compilation of existing geological maps and a review of recently published as well as unpublished igneous emplacement ages in Burundi. In: G.S.o. Namibia (Ed.), 11th IAGOD Quadrennial Symposium and Geocongress. Geological Survey of Namibia, Windhoek, Namibia, p. 6.
- Tack, L., Wingate, M.T.D., De Waele, B., Meert, J., Belousova, E., Griffin, B., Tahon, A., Fernandez-Alonso, M., 2010. The 1375 Ma “Kibaran event” in Central Africa: Prominent emplacement of bimodal magmatism under extensional regime. *Precambrian Research* 180, 63-84.
- Tallarico, F.H.B., Figueiredo, B.R., Groves, D.I., Kositcin, N., McNaughton, N.J., Fletcher, I.R., and Rego, J.L., 2005. Geology and SHRIMP U-Pb geochronology of the Igarapé Bahia deposit, Carajás copper-gold belt, Brazil: An Archean (2.57 Ga) example of iron-oxide Cu-Au-(U-REE) mineralization. *Economic Geology*, 100, p. 7-28.
- Tarantola A., Mullis J., Vennemann T., Dubessy J., de Capitani C., 2007. Oxidation of methane at the CH₄ / H₂O-(CO₂) transition zone in the external part of the Central Alps, Switzerland: Evidence from stable isotope investigations. *Chemical Geology* 237, 329-357.
- Tarantola A., Diamond L.W. and Stünitz H., 2010. Modification of fluid inclusions in quartz by deviatoric stress I: Experimentally induced changes in inclusion shapes and microstructures. *Contributions to Mineralogy and Petrology* 160, 825-843.

- Tarantola, A., Diamond, L.W., Stünitz, H., Thust, A., Pec, M., 2012. Modification of fluid inclusions in quartz by deviatoric stress. III: Influence of principal stresses on inclusion density and orientation. *Contributions to Mineralogy and Petrology* 164, 537-550.
- Taylor, S.R., 1967. The origin and growth of continents. *Tectonophysics* 4, 17-34.
- Taylor, S.R., McLellan, S.M., 1985. The continental crust: Its composition and evolution. Oxford, Blackwell, pp. 312.
- Tchameni, R., Mezger, K., Nsifa, N.E., Pouclet, A., 2000. Neoproterozoic crustal evolution in the Congo Craton: evidence from K-rich granitoids of the Ntem Complex, southern Cameroon. *J. Afr. Earth Sci.* 30, 133-147.
- Teertstra, D.K., Sherriff, B.L. 1997. Substitutional mechanisms, compositional trends and the end-member formulae of scapolite. *Chem. Geol.* 136, 233-260.
- Tegtmeyer, A., Kröner, A., 1985. U-Pb zircon ages for granitoid gneisses in northern Namibia and their significance for proterozoic crustal evolution of southwestern Africa. *Precambrian Research* 28, 311-326.
- Tembo, F., Kampunzu, A.B., Porada, H., 1999. Tholeiitic magmatism associated with continental rifting in the Lufilian Fold Belt of Zambia. *Journal of African Earth Sciences* 28, 403–425.
- Toé, W., 2012. Minéralisations uranifères de la ceinture orogénique Pan-Africaine du Damara (Namibie): Implications de la fusion partielle, de la migration et de la mise en place des magmas sur le remaniement de la croûte continentale. Unpublished PhD. Dissertation, Université de Lorraine, France, 349 pp.
- Toé, W., Vanderhaeghe, O., André-Mayer, A.S., Feybesse, J.L., Milesi, J.P., 2013. From migmatites to granites in the Pan-African Damara orogenic belt, Namibia. *Journal of African Earth Sciences* 85, 62-74.
- Tohver, E., D'Agrella-Filho, M.S., Trindade, R.I.F., 2006. Paleomagnetic record of Africa and South America for the 1200–500 Ma interval, and evaluation of Rodinia and Gondwana assemblies. *Precambrian Res.* 147, 193-222.
- Torrealday, H.I., Hitzman, M.W., Stein, H.J., Markley, R.J., Armstrong, R., Broughton, D., 2000. Re-Os and U-Pb dating of the vein-hosted mineralization at the Kansanshi copper deposit, Northern Zambia. *Econ. Geol.* 95, 1165-1170.

- Torsvik, T.H., Smethurst, M.A., Meert, J.G., Van der Voo, R., McKerrow, W.S., Brasier, M.D., Sturt, B.A., Walderhaug, H.J., 1996. Continental break-up and collision in the Neoproterozoic and Palaeozoic: A tale of Baltica and Laurentia. *Earth-Science Reviews* 40, 229-258.
- Touret, J.L.R., Nijland, T.G., 2013. Prograde, peak and retrograde metamorphic fluids and associated metasomatism in Upper Amphibolite to Granulite facies transitions zones. In: Harlov DE, Austrheim H (eds) *Metasomatism and the Chemical transformation of rock*. Springer-Verlag Berlin Heidelberg, 415-469.
- Trompette, R., 1997. Neoproterozoic (600 Ma) aggregation of Western Gondwana: a tentative scenario. *Precambrian Research* 82, 101-112.
- Trompette, R., 2000. Gondwana evolution; its assembly at around 600 Ma. *Comptes Rendus de l'Académie des Sciences, Sciences de la Terre et des Planètes* 330, 305-315.

U

- Unrug, R., 1983. The Lufilian Arc: a microplate in the Pan-African collision zone of the Congo and the Kalahari cratons. *Precambrian Research* 21, 181-196.
- Unrug, R., 1988. Mineralization controls and source of metals in the Lufilian fold belt, Shaba (Zaire), Zambia, and Angola: *Economic Geology*, 83, 1247-1258.
- Unrug, R., 1997. Rodinia to Gondwana: The Geodynamic Map of Gondwana Supercontinent Assembly. *GSA Today*, 7, 1-5.
- Urai, J.L., Means, W.D., Lister, G.S., 1986. Dynamic recrystallization of minerals. In: Heard, H.C., Hobbs, B.E., (Eds.). *Mineral and rock deformation: laboratory studies, the Paterson volume* 36, 161-200.

V

- Van den Kerkhof, A.M., Olsen, S.N., 1990. A natural example of superdense CO₂ inclusions: Microthermometry and Raman analysis. *Geochim. Cosmochim. Acta* 54, 895-901.
- Van den Kerkhof, A.M., Hein, U.F., 2001. Fluid inclusion petrography. *Lithos* 55, 27-47.
- Van Kranendonk, M., Collins, W.J., Hickman, A., Pawley, M., 2004. Critical tests of vertical vs. horizontal tectonic models for the Archaean East Pilbara granite-greenstone terrane, Pilbara Craton, Western Australia. *Precambrian Research* 131, 173-211.

- Vanderhaeghe, O., 1999. Pervasive melt migration from migmatites to leucogranite in the Shuwap metamorphic core complex, Canada: control of regional deformation. *Tectonophysics* 312, 35-55.
- Vanderhaeghe, O., 2009. Migmatites, granites and orogeny: flow modes of partially-molten rocks and magmas associated with melt/solid segregation in orogenic belts. *Tectonophysics* 477, 119-134.
- Vanderhaeghe, O., Ledru, P., Thiéblemont, D., Egal, E., Cocherie, A., Tegye, M., and Milési, J. P., 1998. Contrasting mechanism of crustal growth. Geodynamic evolution of the Paleoproterozoic granite-greenstone belts of French Guiana. *Precambrian Research* 92, 165-193.
- Vanderhaeghe, O., Teyssier, C., 2001. Partial melting and flow of orogens. *Tectonophysics* 342, 451-472.
- Vanko, D.A., Griffith, J.D., Erickson, C.L., 1992. Calcium-rich brines and other hydrothermal fluids in fluid inclusions from plutonic rocks, Oceanographer Transform, Mid-Atlantic Ridge. *Geochim. Cosmochim. Acta* 56, 35-47.
- Vaughan, A.P.M., Storey, B.C., 2000. The eastern Palmer Land shear zone: a new terrane accretion model for the Mesozoic development of the Antarctic Peninsula. *Journal of the Geological Society (London)* 157, 1243-1256.
- Vaughan, A.P.M., Kelley, S.P., Storey, B.C., 2002. Mid-Cretaceous ductile deformation on the Eastern Palmer Land Shear Zone, Antarctica, and implications for timing of Mesozoic terrane collision. *Geological Magazine* 139, 465-471.
- Veizer, J., Jansen, S.L., 1985. Basement and Sedimentary Recycling-2: Time Dimension to Global Tectonics. *The Journal of Geology* 93, 625-643.
- Vaughan, A.P.M., Pankhurst, R.J., 2008. Tectonic overview of the West Gondwana margin. *Gondwana Research* 13, 150-162.
- Vervoort, J. D., Patchett, P. J., Söderlund, U., Baker, M., 2004. Isotopic composition of Yb and the determination of Lu concentrations and Lu/Hf ratios by isotope dilution using MC ICPMS. *Geochemistry, Geophysics, Geosystems (G3)*, 5, paper number 10.1029/2004GC000721.

- Von Huene, R., Scholl, D.W., 1991. Observations at convergent margins concerning sediment subduction, subduction erosion, and the growth of continental crust. *Reviews of Geophysics* 29, 279-316.
- Vrana, S., Kachlik, V., Kroner, A., Marheine, D., Seifert, A.V., Iaaek, V., BabUrek, J., 2004. Ubendian basement and its late Mesoproterozoic and early Neoproterozoic structural and metamorphic overprint in northeastern Zambia. *J. Afr. Earth Sci.* 38, 1-21.

W

- Wagener, A.L., 1915. *Die Entstehung der Kontinente und Ozeane*. Friedr. Vieweg & Sohn Akt.-Ges. (Ed.), 231 pp.
- Walther, J.V., Wood, B.J., 1984. Rate and mechanism in prograde metamorphism. *Contrib. Mineral. Petrol.* 88, 246-259.
- Wasserburg, G.J., Jacobsen, S.B., DePaolo, D.J., McCulloh, M.T., Wen, J., 1981. Precise determinations of Sm/Nd ratios, Sm and Nd isotopic abundances in standard solutions. *Geochimica et Cosmochimica Acta* 45, 2311-2323.
- Weil, A. B., Van Der Voo, R., Niocail, C. M., Meert, J. G., 1998. The Proterozoic supercontinent Rodinia: paleomagnetically derived reconstructions for 1100 to 800 Ma. *Earth and Planetary Science Letters* 154, 13-24.
- Willis, C., Boyd, A.W., Bindner, P.E., 1970. Carbon monoxide yields in the radiolysis of carbon dioxide at very high dose rates. *Can. J. Chem.* 48, 1951-1954.
- Wilson, J.T., 1966. Did the Atlantic close and then re-open? *Nature* 211, 676-681.
- Wilson, T., Hanson, R.E., Wardlaw, M.S., 1993. Late proterozoic evolution of the Zambezi belt, Zambia: Implications for the regional Pan-African and shear displacements in Gondwana. In: Findlay, R.H., Unrug, R., Banks, M.R., Veevers, J.J. (Eds.), *Gondwana Eight: Assembly, Evolution and Dispersal*. Balkema, Rotterdam, pp. 69-82.
- Windley, B. F., 1986. *The evolving continents*. John Wiley & Sons (Ed.), 526 pp.
- Windley, B.F., 2003. Continental growth in the Proterozoic: a global perspective. *Geological Society, London, Special Publications* 206, 23-33.
- Wood, B.J., Walther, J.V., 1983. Rates of hydrothermal reactions. *Science* 222, 413-415.

Y

- Yardley, B.W.D., 2005. 100th Anniversary Special Paper: Metal Concentrations in Crustal Fluids and Their Relationship to Ore Formation. *Econ. Geol.* 100, 613-632.
- Yardley, B.W.D., 2012. The chemical composition of metasomatic fluids in the crust. In: Harlow, D.E., Austrheim, H. (Eds.), *Metasomatism and the Chemical transformation of rock*. Springer-Verlag, pp. 17-51.
- Yardley, B.W.D., Baltatzis, E., 1985. Retrogression of staurolite schists and the sources of infiltrating fluids during metamorphism. *Contrib. Miner. Petro.* 89, 59-68.
- Yardley, B.W.D., Graham, J.T., 2002. The origins of salinity in metamorphic fluids. *Geofluids* 2, 249-256.

Z

- Zack, T., Moraes, R., Kronz, A., 2004. Temperature dependence of Zr in rutile: empirical calibration of a rutile thermometer. *Contributions to Mineralogy and Petrology* 148, 471-488.
- Zeh, A., Gerdes, A., 2012. U-Pb and Hf isotope record of detrital zircons from gold-bearing sediments of the Pietersburg Greenstone Belt (South Africa) – Is there a common provenance with the Witwatersrand Basin? *Precambrian Research* 204-205, 46-56.
- Zindler, A., Hart, S.R., 1986. Chemical geodynamics. *American Reviews of Earth Planetary Science* 14, 493-571.
- Zhao, J.X., Shiraishi, K., Ellis, D.J., Sheraton, J.W., 1995. Geochemical and isotopic studies of syenites from the Yamato Mountains, East Antarctica: implications for the origin of syenite magmas. *Geochimica et Cosmochimica Acta* 59, 1363-1382.
- Zhu, X., O'Nions, R., 1999. Zonation of monazite in metamorphic rocks and its implications for high temperature thermochronology: a case study from the Lewisian terrain. *Earth Planet. Sci. Lett.* 171, 209-220.

LISTE DES FIGURES

Figure 1: Localisation du projet de thèse dans son contexte géologique simplifié	19
Figure 2: Planisphère terrestre représentant la distribution des altitudes (en mètres, échelle de droite) par rapport au niveau de la mer (par référence égale à zero). Les lignes rouges indiquent les limites des différentes plaques tectoniques (carte tirée du SERC : Science Education Resource Center du Carleton College).....	26
Figure 3: Répartition des âges de la croûte continentale à la surface de la Terre (Artemieva, 2006).	27
Figure 4: Histogramme de la distribution volumique de croûte continentale juvénile depuis la formation de la Terre (modifié d'après Condie, 2005). Cette distribution basée sur une compilation des âges U-Pb sur zircons et des âges modèles Nd met en avant le mode épisodique de la croissance continentale. Les modèles de croissance de croûte continentale sont aussi reportés (1 : Fyfe, 1978 ; 2 : Reynet and Schubert, 1984 ; 3 : Armstrong, 1991 ; 4 : Taylor and McLennan, 1985 ; 5 : Hurley and Rand, 1969).	30
Figure 5: Présentation des concentrations moyennes normalisées au manteau primitif des éléments chimiques dans la croûte continentale en comparaison avec les valeurs pour les MORB (modifiée d'après Hofmann, 1988).....	34
Figure 6: Cycle de l'uranium dans les différents contextes de gisements en relation avec les principaux processus de fractionnement au cours d'un cycle géologique (Cuney, 2009). Les réservoirs représentés sont le manteau et la croûte continentale. Les types de gisements sont les caractères rouges gras ; les mécanismes métallogéniques sont en caractères noirs gras. KCa = magma Calco-alcalin potassique ; Pak = magma Peralcalin ; Pal = magma Peralumineux.	35
Figure 7: Tectonic map of central and southern Africa showing the location of the Lufilian-Zambezi belt in relation to the surrounding Archean cratons and Paleo- to Mesoproterozoic belts (modified after De Waele et al., 2008). Abbreviations: Kbp = Kabompo dome; Mbz = Mwombezhi dome; Slz = Solwezi dome; Lwh = Luswishi dome; Kfu = Kafue Anticline; C.-K. = Choma Kalomo block; MSZ = Mwembeshi Shear Zone; Ky = Kyanite; Tlc = Talc.	43
Figure 8: Simplified geological map of the internal and external zones of the Lufilian belt and sample location. References to studied samples: n°1-2-3 = orthogneiss (ZM-10-09, ZM-10-13 and ZM-10-17); n°4 = granite (ZM-10-66); n°5 = paragneiss (ZM-10-62); n°6 = amphibolite (ZM-10-51); n°7 = orthogneiss (ZM-10-53); n°8 = paragneiss (ZM-10-38); n°9 = paragneiss (ZM-39-01); n°10 = amphibolite (ZM-39-04); n°11 = paragneiss (ZM-62-05); n°12 = paragneiss (ZM-66-08); n°13 = orthogneiss (ZM-12-07); n°14 = amphibolite (ZM-12-13); n°15 = amphibolite (ZM-12-16); n°16 = granite (ZM-12-25). Details are in Table 1. Abbreviations: Kbp = Kabompo dome; Mbz = Mwombezhi dome; Slz = Solwezi dome; Lwh = Luswishi dome; Kfu = Kafue Anticline; Bt = Biotite; Gt = Garnet; Ky = Kyanite.	49
Figure 9: Outcrop pictures from the Solwezi dome. a, b, c: Partially migmatitic orthogneiss with feldspar porphyroclasts transposed within foliation. d: Migmatitic paragneiss with concordant syn-migmatitic foliation and discordant granitic veins. e: Garnet porphyroblast within granitic fraction. f: Amphibolite boudins hosted by paragneiss and transposed within the foliation.	50
Figure 10: Outcrop pictures from the Mwombezhi dome. a, b: Orthogneiss with feldspar porphyroclasts transposed within shear bands. c: Garnet amphibolite boudins transposed within syn-migmatitic foliation.	52
Figure 11: Macroscopic pictures, major and traces elements for the orthogneissic rocks from the Solwezi dome.	55
Figure 12: Cathodoluminescence images of some analyzed zircon grains of the orthogneissic and granitic rocks from the Solwezi dome. Dotted circles represent the points of analyses. Italic numbers are the referees label (see table X) and regular numbers are the 207Pb/206Pb ages with concordance >95% and the 176Hf/177Hf(t) ratio.	61
Figure 13: U-Pb concordia diagram for the orthogneissic and granitic rocks from the Solwezi dome....	62

Figure 14: Cathodoluminescence images of some analyzed zircon grains of the paragneissic rocks from the Solwezi dome. Dotted circles represent the points of analyses. Italic numbers are the referees label (see complementary data) and regular numbers are the $^{207}\text{Pb}/^{206}\text{Pb}$ ages with concordance >95% and the $^{176}\text{Hf}/^{177}\text{Hf}(t)$ ratio.	63
Figure 15: U-Pb concordia diagram and probability density plot for the paragneissic rocks from the Solwezi dome.	64
Figure 16: Cathodoluminescence images of some analyzed zircon grains of the paragneissic rocks from the Mwombezhi dome. Dotted circles represent the points of analyses. Italic numbers are the referees label (see complementary data) and regular numbers are the $^{207}\text{Pb}/^{206}\text{Pb}$ ages with concordance >95% and the $^{176}\text{Hf}/^{177}\text{Hf}(t)$ ratio.	67
Figure 17: U-Pb concordia diagram and probability density plot for the paragneissic rocks from the Mwombezhi dome.	68
Figure 18: Cathodoluminescence images of some analyzed zircon grains of the paragneissic rocks from the Mwombezhi dome. Dotted circles represent the points of analyses. Italic numbers are the referees label (see complementary data) and regular numbers are the $^{207}\text{Pb}/^{206}\text{Pb}$ ages with concordance >95% and the $^{176}\text{Hf}/^{177}\text{Hf}(t)$ ratio.	70
Figure 19: U-Pb concordia diagram for the orthogneissic and granitic rocks from the Mwombezhi area.	71
Figure 20: $\varepsilon\text{Hf}(t)$ evolution diagram for all studied samples from (a) the Solwezi dome and (b) the Mwombezhi dome. Dark grey diamonds represent concordant (> 95%) $^{207}\text{Pb}/^{206}\text{Pb}$ ages and light grey squares represent discordant (< 95%) $^{207}\text{Pb}/^{206}\text{Pb}$ ages.	76
Figure 21: Probability density plots versus crystallization $^{207}\text{Pb}/^{206}\text{Pb}$ ages for studied samples.	76
Figure 22: Reconstitutions paléo-géographiques, d'après De Waele et al. (2008) présentant deux modèles possibles de l'évolution du craton du Congo-Sao Francisco à différents intervalles de temps : à 1050 Ma (a et e), à 1020 Ma (b et f), à 880 Ma (c et g) et à 760 Ma (d et h). Abréviations : A = Australia ; Am = Amazonia ; B = Baltica ; C = craton Congo-Sao Francisco; I = India; K = Kalahari; L = Laurentia; M = Mawson Craton (Antarctique); S = Siberia; WA= West-Africa.	121
Figure 23: Reconstitution paléogéographique du supercontinent Rodinia à 750 Ma (Dalziel, 1997). Dans les reconstitutions plus récentes de Torsvik et al. (1996) le bloc West Gondwana est éclaté en plusieurs fragments et les cratons du Kalahari et Congo sont localisés approximativement à la jonction Antarctique-Laurentia (en pointillé sur la figure).	122
Figure 24: Reconstitution du supercontinent Gondwana (d'après Unrug 1997; Vaughan and Pankhurst, 2008). La partie grisée correspond à la limite entre les continents West et East Gondwana. Abréviations : NZ = Nouvelle-Zélande, TAM = Montagnes Trans-antarctiques, ANS = Bouclier Arabo-Nubien, N-N-M = Ceinture du Namaqua-Natal-Maud.	124
Figure 25: Reconstitution du continent West Gondwana (d'après Tohver et al., 2006; Vaughan and Pankhurst, 2008). Cette carte présente les différents cratons ainsi que les ceintures Brasiliano-Pan African. Les cratons sont représentés en jaune clair, on distingue : AM = Amazonia ; ANS = Bouclier Arabo-Nubien ; C = Congo ; GM = Massif du Goiás ; K-G= Kalahari-Grunchogna ; LA = Luis Alves ; P = Parana ; RA = Rio Apa ; SF = Sao Francisco ; SL = Sao Luis ; WA = West Africa. Les ceintures Bresilinao-Pan African sont représentés en traits fins : Ac = Araçuaí ; Ag = Araguaia ; Bo = Borborema ; Br = Brasilia ; Da = Damara ; DF = Dom Feliciano ; Dh/O = Dahomeides/Oubangides ; G = Gariep ; H = Hoggar ou Trans-Sahara ; Ka = Kaoko ; K/Z = Katangan/Zambezi ; LA = Lufilian belt ; M = Mozambique ; P = Paraguay ; R/M = Ribeira/Mantequeira ; Ro = Rokelides ; Ta = Tanzania ; Tu = Tucavaca ; WC = West Congo.	125
Figure 26: Coupe géologique au 1 : 500 000 de la ceinture du Damara (Miller and Grote, 1988).	130
Figure 27: Illustration de l'évolution de la ceinture du Lufilien-Zambezi au cours du cycle Pan-Africain (John, 2001).	130

Figure 28: Tectonic map of central and southern Africa showing the location of the Lufilian-Zambezi belt in relation to the surrounding Archean cratons and Paleo- to Mesoproterozoic belts (modified after De Waele et al., 2008). Black and white diamonds represent the location of moderate to high pressure rocks (John et al., 2004; Vrana and Barr, 1972). Abbreviations: Kbp = Kabompo dome; Mbz = Mwombezhi dome; Slz = Solwezi dome; Lwh = Luswishi dome; Kfu = Kafue Anticline; C.-K. = Choma Kalomo block; MSZ = Mwembeshi Shear Zone; Ky = Kyanite; Tlc = Talc. The black rectangle represents the study area enlarged in Figure 29. **136**

Figure 29: Simplified geological map of the internal and external zones of the Lufilian belt and sample location (modified after Barron, 2003). References to studied samples: n°1 = kyanite micaschists (ZM-10-07, ZM-10-08, ZM-10-24 and ZM-10-41); n°2 = metagabbro (ZM-10-21); n°3 = metagabbro (ZM-10-47); n°4 = metadiorites (ZM-10-45 and ZM-12-18); n°5 = garnet-kyanite amphibolite (ZM-82-14); n°6 = garnet amphibolites (ZM-12-13 and ZM-12-16). Details are in Table 27. Abbreviations: Kbp = Kabompo dome; Mbz = Mwombezhi dome; Slz = Solwezi dome; Lwh = Luswishi dome; Kfu = Kafue Anticline; Bt = Biotite; Gt = Garnet; Ky = Kyanite. **141**

Figure 30: a: Parallel and cross-bedding structures in kyanite micaschist rimming the Pre-Katanga rocks of the Solwezi area. b: Monomictic conglomerate with quartzite pebbles and/or cobbles. c: Mineral lineation marked by kyanite (second generation: K2) porphyroblasts. d: Kyanite micaschist showing C/S fabric. e: Kyanite poikiloblast grain (first generation: K1) wrapped into the schistosity (Sn+1) and containing oriented inclusions of quartz and iron oxide, defining an inherited schistosity (Sn)..... **143**

Figure 31: a, b: Granular and equant texture of metagabbro and metadiorite, respectively. c: Plagioclase-amphibole-epidote matrix of metagabbro showing recrystallized texture with amphibole subgrain formation and one skeletal rutile grain, maybe a pseudomorph of Ti-rich magnetite, surrounded by titanite within amphibole (plane-polarized light). d: K-feldspar-amphibole-plagioclase matrix of metadiorite showing irregular and interlobate boundaries between matrix minerals reflecting a ductile deformation (plane-polarized light). e: Plagioclase-amphibole-epidote matrix of metagabbro showing recrystallized texture with plagioclase subgrains formation (cross-polarized light). f: Plagioclase-feldspar-epidote matrix of metadiorite with magnetite (cross-polarized light). **144**

Figure 32: Major and trace elements geochemistry of the kyanite micaschists from the Solwezi area. Abbreviations: UC = Upper Crust; PAAS = Post Archean Australian shale; LC = Lower Crust; MORB = Mid-Ocean Ridge Basalt. **146**

Figure 33: Major and trace elements geochemistry of the meta-gabbros and the meta-diorites from the Solwezi area. Reference numbers: 12 = quartz diorite/gabbro; 17 = diorite/gabbro. **149**

Figure 34: a. Concordia diagram for U-Pb isotope ratio (a) and probability density plot of 207Pb/206Pb ages (b) for detrital zircon grains from the kyanite micaschist (ZM-10-24)..... **151**

Figure 35: Histogram of Pan-African 232Th-208Pb ages of monazite grains from the kyanite micaschists (dark grey bars => ZM-10-07 and light grey bars => ZM-10-24)..... **152**

Figure 36: Cathodoluminescence images of zircon grains from the metadiorite sample (ZM-10-45). Dotted circles: location and size of laser spots used for U-Pb isotope analyses (207Pb/206Pb ages). Dotted squares: location and size of laser spot used for Lu-Hf isotope analyses (176Hf/177Hf(t) ratios). **152**

Figure 37: Concordia diagram for U-Pb isotope ratio of X individual zircon grains from the meta-diorite sample (ZM-10-45). **153**

Figure 38: a: Mineral equilibria modelling results for the kyanite micaschist (ZM-10-24) rimming the Solwezi basement core. b: T-XFe3+ pseudosection at 10 kbar. In both pseudosections, heavy dashed line underlines the field of the estimated peak assemblage represented by Kyanite-Biotite-Chlorite-Hematite+Quartz. Abbreviations: Bt = Biotite; Chl = Chlorite; Crd = Cordierite; Grt = Garnet; Hem = Hematite; Ky = Kyanite ; Mag = Magnetite ; Ms = Muscovite; Qtz = Quartz; Sa = Sanidine; Sil = Sillimanite ; Tlc = Talc. **155**

- Figure 39:** a: Garnet amphibolite boudins transposed into the metatexite foliation (ZM-12-16: Malundwe mine). b, c: Garnet porphyroblasts in amphibole-rich matrix (samples ZM-12-13 and ZM-12-16). d-e: Rutile inclusions within garnet porphyroblasts in plagioclase-amphibole-biotite matrix. **157**
- Figure 40:** Major and trace elements geochemistry of the amphibolites from the Mwombezhi area. ... **158**
- Figure 41:** Lu-Hf garnet-whole rock isochrons for the garnet-kyanite amphibolite (a) and the garnet amphibolite (b) from the Mwombezhi basement. **160**
- Figure 42:** Mineral equilibria modelling for garnet amphibolite (ZM-12-13) outcropping in the Mwombezhi basement core. a to c: Pseudosections showing the calculated garnet isopleths modelling. Heavy dashed lines represent the calculated composition of garnet grains. Black heavy line represents the limit of the garnet stability field. d: Dashed heavy black lines show the intersection for the measured garnet composition within the field of the stable assemblage. Black heavy line represents the limit of the rutile stability field. Abbreviations: Am = Amphibole; Bt = Biotite; Chl = Chlorite; Cpx = Clinopyroxene; Grt = Garnet; Ilm = Ilmenite; Opx = Orthopyroxene; Pl = Plagioclase; Rt = Rutile; Zo = Zoisite. **161**
- Figure 43:** Provenance ages of the studied Lower Roan Group. a: Location of studied samples from literature and this study (ZM-10-24). b: Probability density plot of $^{207}\text{Pb}/^{206}\text{Pb}$ ages for detrital zircon grains of the Lower Roan Group. **163**
- Figure 44:** $^{143}\text{Nd}/^{144}\text{Nd}$ versus $^{87}\text{Sr}/^{86}\text{Sr}$ isotope correlation diagram showing the main oceanic mantle reservoirs of Zindler and Hart (1986) and the position of the Pan-African magmatic rocks (metagabbros ZM-10-21 and ZM-10-47, metadiorite ZM-12-18 and metabasalt ZM-12-27). Abbreviations: BE = Bulk Silicate Earth; DM = Depleted Mantle; EMI and EMII = Enriched Mantle; HIMU = Mantle with high U/Pb ratio; PREMA = PREvalent MANTle composition. The mantle array is defined by many oceanic basalts and a bulk Earth value of $^{87}\text{Sr}/^{86}\text{Sr}$ can be obtained from this trend. **165**
- Figure 45:** ϵNd versus U-Pb ages and probability density plot of $^{207}\text{Pb}/^{206}\text{Pb}$ intrusion ages and TDM (Sm/Nd and Lu/Hf) model ages for meta-gabbro (ZM-10-21 and ZM-10-47) and meta-diorite (ZM-10-45) intrusive within the Katanga cover. Abbreviations: CHUR = CHondritic Uniform Reservoir; DM = Depleted Mantle. **166**
- Figure 46:** Schematic diagrams showing the Pan-African Wilson cycle of the Lufilian belt. a, b: Rodinia dislocation during two successive rifting stages. c, d: Oceanic followed by continental subduction. e, f: Continental tectonic accretion and high grade rocks exhumation. **169**
- Figure 47:** Geological map of the Pan-African Lufilian belt indicating the main structural trends and mineral occurrences (modified after De Waele et al., 2008). Abbreviations: Kbp = Kabompo Dome; Mbz = Mwombezhi Dome; Slz = Solwezi Dome; Lwh = Luswishi Dome; Kfu = Kafue Anticline; C.-K. = Choma Kalomo block; MSZ = Mwembezhi Shear Zone. (Black rectangle: study area enlarged in Figure 49). **195**
- Figure 48:** Lithostratigraphic correlations for the Katanga supergroup between the External fold-and-thrust belt and the Domes region (modified after Kampunzu and Cailteux, 1999; Porada and Berhorst, 2000; Kampunzu et al., 2009) and uranium occurrences (grey stars). Age constraints are provided by U-Pb geochronology on magmatic zircon grains of volcanic rocks (1 Hanson et al., 1994; 2 Key et al., 2001) and by argon thermochronology on detrital muscovite grains (3 Master et al., 2005). **198**
- Figure 49:** Study area and location of studied uranium occurrences with their ages (from Decrée et al., 2011): Kalongwe, Kolwezi, Swambo, Shinkolobwe and Luiswishi in the External fold-and-thrust belt and Kawanga, Malundwe, Mitukuluku, Musoshi and Nkana in the Domes region. The dashed black line represents the international boundary between Democratic Republic of Congo (DRC) and Zambia. The thick black line is the approximate limit between the External fold-and-thrust belt and the Domes region. **200**
- Figure 50:** SEM images (backscattered electron mode) of all uranium oxides analyzed by LA-ICPMS in this study. a: Altered uranium oxide from the Kalongwe deposit. b: Altered uranium oxide from the Swambo deposit. c: Unaltered uranium oxide from the Shinkolobwe deposit. d: Unaltered uranium oxide from the Kolwezi deposit. e: Unaltered uranium oxide from the Luiswishi deposit. f: Unaltered uranium

- oxide from the Musoshi deposit. g: Unaltered uranium oxide from the Nkana deposit. h: Cogenetic unaltered uranium oxide and molybdenite from Malundwe showing. I: Cogenetic unaltered uranium oxide and brannerite from the Mitukuluku showing. Abbreviations: Br = Brannerite; Chl = Chlorite; Mo = Molybdenite; Phl = Phlogopite; Qtz = Quartz; Ur = Uranium oxide. Black dots represent LA-ICPMS spots with a size ranging from 24 to 60 μm **205**
- Figure 51:** a: Location of uranium oxide samples from nine occurrences and symbol equivalence. Thick dashed black line represents garnet and biotite isograds (after François and Cailteux, 1981). b: Chondrite-normalized REE patterns for uranium oxides from three deposits in the External fold-and-thrust belt dated at ca. 650 Ma. c: Chondrite-normalized REE patterns for uranium oxides from two deposits in the External fold-and-thrust belt dated at ca. 530 Ma. d: Chondrite-normalized REE patterns for uranium oxides from five deposits/showings in the Domes region dated at ca. 530 Ma. See Table 41; Table 42; Table 43 for analytical data. Chondrite values are from McDonough and Sun (1995). **207**
- Figure 52:** Uraninite-normalized REE patterns for uranium oxides dated at ca. 530 Ma from Kolwezi and Luiswishi (upper part), Musoshi and Nkana (middle part), Mitukuluku and Malundwe (lower part) deposits. Values used for normalization are from the Shinkolobwe deposit uraninite dated at ca. 650 Ma (sample: 12048-1', Table 41). **209**
- Figure 53:** Eu^* versus Y_2O_3 contents diagram for uranium oxides, dated at ca. 650 Ma and ca. 530 Ma, from the External fold-and-thrust belt (light grey symbols) and for uranium oxides, dated at ca. 530 Ma, from the Domes region (dark grey symbols). Yttrium content increases with the increasing crystallization temperature of uranium oxides. Abbreviations: Low. Green. = Lower Greenschist metamorphic conditions; Up. Amph. = Upper Amphibolite metamorphic conditions. **210**
- Figure 54:** HREE (Er + Tm + Yb + Lu) versus Yttrium contents diagram for uranium mineralization dated at ca. 530 Ma in the External fold-and-thrust belt (light grey symbols) and in the Domes region (dark grey symbols). The arrow shows the correlation between the increasing HREE and Y contents of uranium oxides and the increasing temperature of uranium oxide crystallization in relation with the metamorphic grade of the host rock. Abbreviations: f.t.b. = Fold-and-thrust belt; d.r. Domes region. **214**
- Figure 55:** REE patterns of uranium oxides from the Lufilian belt compared to ones from known uranium deposits. a: Chondrite-normalized REE patterns for uranium oxides dated at ca. 650 Ma from the External fold-and-thrust belt of the Lufilian belt compared with chondrite-normalized REE patterns for uranium oxides from unconformity-related uranium deposits of the Athabasca Basin (Shea Creek, Eagle Point, Mc Arthur River; data from Bonhoure, 2007; Mercadier et al., 2011) and the Kombolgie Basin (Koongarra, Nabarlek; data from Mercadier et al., 2011). b: Uraninite-normalized REE patterns for uranium oxides from Mistamisk (syn-metamorphic uranium mineralization; Kish and Cuney, 1981) and Shinkolobwe deposits. The uraninite values using for normalization are from Shea Creek deposit (data from Mercadier et al., 2011). c: Chondrite-normalized REE patterns for uranium oxides dated at ca. 530 Ma from the Domes region of the Lufilian belt compared with REE patterns for uranium oxides from the Mistamisk syn-metamorphic uranium deposit (data from Bonhoure, 2007). Chondrite values are from McDonough and Sun, (1995). d: Uraninite-normalized REE patterns for uranium oxides from Mistamisk, Musoshi and Nkana deposits. The uraninite values using for normalization are from Shinkolobwe deposit in External fold-and-thrust belt (sample: 12048-1'). **216**
- Figure 56:** North-South cross section from the External fold-and-thrust belt to the Domes region with uranium mineralization location, their REE patterns and ages, metamorphic grades and their metamorphic index minerals. **220**
- Figure 57:** Geological map of the Pan-African Lufilian belt indicating the main structural trends and HP-HT metamorphic rocks occurrences (modified after De Waele et al., 2008; Eglinger et al., 2013). Abbreviations: Kbp = Kabompo dome; Mbz = Mwombeshi dome; Slz = Solwezi dome; Lwh = Luswishi dome; Kfu = Kafue Anticline; C.-K. = Choma Kalomo block; MSZ = Mwembeshi Shear Zone; Ky = Kyanite; Tlc = Talc. (Black rectangle: study area enlarged in Figure 59). **232**

- Figure 58:** Lithostratigraphy of the Katanga Supergroup in the Domes region in Zambia (modified after Porada and Berhorst, 2000; Kampunzu et al., 2009). Uranium occurrences of Lolwa and Mitukuluku are represented by gray stars within the Lower Roan Group (modified after Meneghel, 1981; Cosi et al., 1992). Age constraints are provided by U-Pb geochronology on magmatic zircon grains of volcanic rocks (1 Hanson et al., 1994; 2 Key et al., 2001), by stratigraphical correlations (3 Robb et al., 2002; 4 Condon et al., 2005) and by argon thermochronology on detrital grains (5 Master et al., 2005). **233**
- Figure 59:** a: Regional geological map of the Lufilian belt with uranium occurrences and metamorphic index minerals (modified after Eglinger et al., 2013). Abbreviations: Kbp = Kabompo domes; Mbz = Mwombezi dome; Slz = Solwezi dome; Lwh = Luswishi dome. Numbers represent uranium occurrences in the high metamorphic grade western part of the Domes region: 1 = Lolwa; 2 = Kawanga; 3 = Malundwe; 4 = Mitukuluku; 5 = Kansanshi; 6 = Kimale; 7 = Dumbwa; 8 = Nkana; 9 = Musoshi; 10 = Luiswishi; 11 = Shinkolobwe; 12 = Swambo; 13 = Kolwezi; 14 = Kalongwe. b: Schematic cross section along the line of Figure 59a showing the spatial and structural location of synmetamorphic uranium mineralizations (black dashed rectangle). **237**
- Figure 60:** Microphotographs of thick sections showing the relationships between metamorphic minerals. a: LPNA optical microscopic image of the kyanite-talc micaschist with brannerite mineralization. Schistosity (Sn+1) is underlined by phlogopite and talc minerals. b: Schematic sketch showing the relationships between metamorphic minerals of the kyanite-talc micaschist. c: LPNA optical microscopic image of the kyanite micaschist with uraninite and brannerite mineralization. Schistosity (Sn+1) is underlined by phlogopite minerals. Two generations of kyanite are observed (Ky1 and Ky2). d: Schematic sketch showing the relationship between metamorphic minerals of the kyanite micaschist. Abbreviations: Ap = Apatite; Br = Brannerite; Chl = Chlorite; Ky = Kyanite; Ms = Muscovite; Phl = Phlogopite; Qtz = Quartz; Tlc = Talc. **242**
- Figure 61:** General paragenetic sequence of the kyanite±talc micaschist from Lolwa (Kabompo dome) and Mitukuluku (Solwezi dome) occurrences in the internal zone. Abbreviations: Up. Amp. = Upper Amphibolite; G.S. = Greenschist; GBM = Grain boundary migration. **243**
- Figure 62:** SEM images (backscattered electron mode) of all types of uranium minerals analyzed by EMP. a: Syn-tectonic porphyroblast of brannerite. b: Iron oxide halo surrounding metamict brannerite grain. c: Totally metamict brannerite grain. d: Uraninite porphyroblasts with cogenetic brannerite grains within phlogopite-chlorite minerals. e: Brannerite porphyroblast within phlogopite. f: Secondary coffinite around brannerite grain. Abbreviations: Ap = Apatite; Br = Brannerite; Cal = Calcite; Chl = Chlorite; Cof = Coffinite; Fe-ox = Iron oxide; Gn = Galena; Ky = Kyanite; Ms = Muscovite; Phl = Phlogopite; Pl = Plagioclase; Qtz = Quartz; Tlc = Talc; Ur = Uraninite. **245**
- Figure 63:** Schematic sketch of quartz veins showing the different quartz grain typologies, fluid inclusion types and the relationship between quartz-scale deformation and chronology of fluid circulations. **246**
- Figure 64:** Microphotographs showing the different generations of fluids inclusions. Detailed description of each fluid inclusion generation is given in the text. a: trails of fluid inclusions type-I, deviated by subgrains boundaries. b: multiphase fluid inclusion of type-I. c: trails of fluid inclusions type-IIA. d: multiphase fluid inclusion of type-IIA. e: trails of fluid inclusions type-IIB. f: CO₂-rich fluid inclusion of type-IIB. g: trails of fluid inclusions of type-III. The arrows point to a two-phase inclusion. h: one-phase type-III fluid inclusion. Abbreviations: Cal = Calcite; H = Halite; Hem = Hematite; Hyd = Hydrate; L_{aq} = Aqueous Liquid; V = N₂-H₂ Vapor; L_{car} = Carbonic Liquid; V_{car} = Carbonic Vapor; S = Unidentified Solid. **249**
- Figure 65:** Vapor-saturated phase equilibria in the H₂O-NaCl-CaCl₂ system showing isotherms (in degrees Celsius) of halite solubility and ice-melting (modified after Steele-MacInnis et al., 2011). Diamond symbols represent data for type-I fluid inclusions (dark grey diamond => Lolwa occurrence; light grey diamond => Mitukuluku occurrence) and square symbols for type-IIA fluid inclusions (dark grey square => Lolwa occurrence; no type-IIA fluid inclusions were found in Mitukuluku occurrence). Abbreviations: E = H₂O-CaCl₂-NaCl eutectic (-52.0 °C); E' = H₂O-NaCl eutectic (-21.2 °C); E'' = H₂O-

- CaCl₂ eutectic (-49.9 °C); P1 = H₂O-CaCl₂-NaCl first peritectic (-22.4 °C); P2 = H₂O-CaCl₂-NaCl second peritectic (29.0 °C); P3 = H₂O-CaCl₂-NaCl third peritectic (45.0 °C); P' = H₂O-NaCl peritectic (0.1 °C); P1'' = H₂O-CaCl₂ first peritectic (30.1 °C); P2'' = H₂O-CaCl₂ second peritectic (45.1 °C). **251**
- Figure 66:** Box diagram of Ca, Na, K, Mg, Ba, Sr, Cu, Ti, U and Mo element concentrations in Lolwa (dark grey) and Mitukuluku (light grey) fluid inclusions. Lower whiskers, bottoms of boxes, central lines, tops of boxes and upper whiskers represent 5th, 25th, 50th, 75th and 95th percentiles, respectively. **254**
- Figure 67:** Shape factor ($P^2/4\pi A$; P = Perimeter; A = Area; Bakker and Diamond, 2006) of type-I fluid inclusions versus the distance to the closest grain or subgrain boundary. The external shape of fluid inclusions with various shapes (1, perfect circle, 2 and 6) are schematized on the vertical axes. Symbols in dark grey represent data of fluid inclusions from Lolwa and in light grey from Mitukuluku occurrences. Data in italic represent bulk homogenization temperature by halite melting and, data in bold italic, by vapor disappearance. The horizontal dashed line at 1.75 delimits the inclusions with regular or irregular shapes (Bakker and Diamond, 2006). The vertical dashed line is shown at 100 μm, arbitrary distance to the closest grain/subgrain boundary to which the inclusions are less deformed. The resulting light grey field is the domain where inclusions are less affected by dynamic recrystallization. **257**
- Figure 68:** Geological map of the Pan-African Lufilian belt indicating the main structural trends (modified after De Waele et al., 2008; Eglinger et al., 2013). Abbreviations: Kbp = Kabompo dome; Mbz = Mwombeshi dome; Slz = Solwezi dome; Lwh = Luiswishi dome; Kfu = Kafue Anticline; C.-K. = Choma Kalomo block; MSZ = Mwembeshi Shear Zone; Ky = Kyanite; Tlc = Talc. The black rectangle represents the study area enlarged in Figure 69b. **280**
- Figure 69:** a: Lithostratigraphy of the Katanga Supergroup in the Domes region in Zambia (modified after Porada and Berhorst, 2000; Kampunzu et al., 2009). Uranium occurrences (stars) are found within the Lower Roan Group (modified after Meneghel, 1981; Cosi et al., 1992). Age constraints are provided by U-Pb geochronology on magmatic zircon grains of volcanic rocks (1Hanson et al., 1994; 2Key et al., 2001), by stratigraphical correlations (3Robb et al., 2002; 4Condon et al., 2005) and by argon thermochronology on detrital grains (5Master et al., 2005). b: Geological map of the Solwezi dome showing the sample localizations associated with the structural measurements (lineation and schistosity/foliation). Star symbols represent the uranium occurrences intersected by drilling. References to studied samples: n°1 = ZM-10-07; n°2 = ZM-10-24; n°3 = 7703-29; n°4 = ZM-10-09; n°5 = ZM-10-17; n°6 = ZM-10-62. Details are found in Table 56. **284**
- Figure 70:** a: Parallel and cross-bedding structures in kyanite micaschist. b: Micaschist showing oriented kyanite porphyroblasts. c: Augen gneiss with recrystallized and transposed feldspar porphyroclasts. d: Migmatitic rock with concordant leucosome and discordant granitic veins. **286**
- Figure 71:** a: Kyanite micaschist with quartz pebble (sample ZM-10-07). b: Kyanite micaschist showing shear bands marked by phlogopite and sigmoidal schistosity (sample ZM-10-24). c: Kyanite poikiloblast grain wrapped into the schistosity and containing oriented inclusions of quartz and iron oxide, defining an inherited schistosity (sample ZM-10-24). d: Sub-automorphic metamorphic monazite within the cleavage plane of phlogopite blasts (sample ZM-10-24). e: Uraninite porphyroblasts with cogenetic brannerite grains within phlogopite-chlorite schistosity (sample 7703-29). Abbreviations: Br = Brannerite; Chl = Chlorite; Ky = Kyanite; Mnz = Monazite; Phl = Phlogopite; Qtz = Quartz; Ur = Uraninite. **289**
- Figure 72:** BSE images and X-ray maps of monazite from the Solwezi dome. Images a to d: monazite grain within Qtz-Phl matrix from sample ZM-10-07, and images e to h: monazite grain within phlogopite from sample ZM-10-24. BSE images show the location of ICPMS laser ablation pits (11 μm) and their corresponding ²³²Th-²⁰⁸Pb ages (2σ level). Numbers shown on yttrium maps correspond to electronic microprobe analysis reported in Table 59 and Table 60. Abbreviations: Mnz = Monazite; Phl = Phlogopite; Qtz = Quartz. **290**
- Figure 73:** a: U + Th + Pb versus Ca-Si diagram (per formula for 4 oxygens) showing the relative proportions of brabantite and huttonite substitutions from the monazite end-members (dark grey diamonds => ZM-10-07 and light grey diamonds => ZM-10-24). **291**

- Figure 74:** a: Macroscopic view of gneissic rock showing strong scapolite alteration overprinting the gneissic fabric. b: Photomicrograph of scapolite porphyroblasts with Qtz-Pl-rich matrix and epidote inclusions (sample ZM-10-09); epidote-muscovite assemblage is also visible in the lower part of the picture (sample ZM-10-09). c: Macroscopic view of gneiss showing boudinaged and folded leucosome within gneissic fabric (sample ZM-10-17). d: Photomicrograph of large poikilitic scapolite porphyroblasts (sample ZM-10-17). Abbreviations: Ep = Epidote; Pl = Plagioclase; Qtz = Quartz; Scp = Scapolite. **292**
- Figure 75:** BSE images of accessory minerals observed in Pre-Katanga rocks from Solwezi dome. a: Metamict allanite grain surrounding by epidote. Allanite is filled by REE-rich silicate (sample ZM-10-09). b: Metamict allanite grain with newly formed apatite and (REE, Th)-rich minerals (sample ZM-10-17). c and d: Replacement of primary monazite by allanite and then by epidote-apatite. Some fractures are filled by newly REE-rich carbonates (sample ZM-10-62). Numbers shown on images b, c and d correspond to electronic microprobe analysis reported in Table 61. Abbreviations: Aln = Allanite; Ap = Apatite; Ep = Epidote; Mnz = Monazite; Ox = Iron oxide ; Zrn = Zircon. **293**
- Figure 76:** Al₂O₃ vs. SiO₂ diagram for electron microprobe analyses of altered monazite grains (dark grey diamonds). The linear trend toward the allanite compositional field defined after 30 analyses reported in Deer et al. (1997), suggests that the monazite alteration leads to allanite replacement. **294**
- Figure 77:** Cl atoms (per formula for Si + Al = 12) versus EqAn (equivalent anorthite content) diagram showing the range of scapolite compositions from two samples of Solwezi dome. Dotted lines show the stoichiometry of marialite-meionite and marialite-mizzonite coupled substitutions. **295**
- Figure 78:** Histogram of Pan-African monazite ²³²Th-²⁰⁸Pb ages (dark grey bars => ZM-10-07 and light grey bars => ZM-10-24; Table 63). **296**
- Figure 79:** ²³²Th-²⁰⁸Pb ages, obtained by LA-ICPMS (Table 63), versus brabantite substitution, determined by electronic microprobe analyses (Table 59; Table 60; Table 63), diagram showing different clusters interpreted as related to episodic dissolution/recrystallization events recorded during the growth of monazite grains (dark grey diamonds => ZM-10-07 and light grey diamonds => ZM-10-24; vertical bars represent the age error at 2σ level). **297**
- Figure 80:** Concordia plots of U-Pb data (n = 9) for uraninite grains from Mitukuluku occurrence with an upper intercept at 532±18 Ma associated with a lower intercept anchored at 0±100 Ma. **298**
- Figure 81:** P-T trapping conditions of the three types of fluid inclusions. The age at ca.530 Ma, U-Pb on monazite, represents the P-T conditions at the temperature peak of metamorphism of the internal zone of the Lufilian belt, obtained by John et al. (2004) on kyanite-talc assemblage. **299**
- Figure 82:** Fluid evolution, with respective P-T trapping conditions, related to fluid-rock alteration and uranium mineralization. Minerals on brackets represent the dating material and ages are from this study and from John (2001). Abbreviations: Br = Brannerite; Bt = Biotite; Mnz = Monazite; Ms = Muscovite; Ur = Uraninite. **304**
- Figure 83:** In-situ thermometry on minerals using the LA-ICPMS on rutile grains (a) and the Raman spectroscopy on graphite (b). **322**
- Figure 84:** Concordia plots of U-Pb data for uraninite grains from Malundwe (a, b, c) and Kawanga (d) occurrences. a = sample #88-15; b = sample 7703-2; c = sample C025; d = sample 7703-21. **323**
- Figure 85:** Diagramme de densité de probabilité versus âge. Les données U-Pb et Lu-Hf sur zircon détritique proviennent des séries néoproterozoïques métasédimentaires du groupe du Roan. Les âges obtenus sur grains de zircon magmatique sont obtenus sur les diorites intrusives dans ces séries métasédimentaires du groupe du Roan. Les âges U-Pb obtenus sur les grains d'uraninite datés à 650 Ma (Decrée et al., 2011) et à 530 Ma représentent les deux événements minéralisateurs enregistrés par les métasédiments du groupe du Roan (Eglinger et al., soumis ; chapitre 7). **332**
- Figure 86:** Synthèse de l'évolution P-T-t des minéralisations uranifères syn- à tardi-orogéniques et de leur roches encaissantes (métasédiments à kyanite±talc du groupe du Roan) décrites dans la zone interne du Lufilien. **334**

LISTE DES TABLEAUX

Table 1: Sampling details. Abbreviations: Am = Amphibole, Ap = Apatite, Bt = Biotite, Cal = Calcite, Chl = Chlorite, Ep = Epidote, Kfs = Feldspar, Grt = Garnet, Ilm = Ilmenite, Mnz = Monazite, Ms = Muscovite, Ox = Iron oxide, Pl = Plagioclase, Qtz = Quartz, Rt = Rutile, Ttn = Titanite, Zrn = Zircon. ...	77
Table 2: Major element composition of whole-rock by ICP-OES samples from the Solwezi dome.	78
Table 3: Major element composition of whole-rock by ICP-OES samples from the Mwombezhi dome.	80
Table 4: Whole rock Nd and Sr isotopic data for samples from Solwezi and Mwombezhi domes.	81
Table 5: U-Pb isotope analyses of magmatic zircon grains from orthogneiss (ZM-10-09; Solwezi Dome)	82
Table 6: U-Pb isotope analyses of magmatic zircon grains from orthogneiss (ZM-10-13; Solwezi dome)	84
Table 7: U-Pb isotope analyses of magmatic zircon grains from orthogneiss (ZM-10-53; Solwezi dome)	85
Table 8: U-Pb isotope analyses of magmatic zircon grains from granite (ZM-10-66; Solwezi dome)	86
Table 9: U-Pb isotope analyses of detrital zircon grains from paragneiss (ZM-10-38; Solwezi dome) ...	87
Table 10: U-Pb isotope analyses of detrital zircon grains from paragneiss (ZM-10-62; Solwezi dome).	90
Table 11: U-Pb isotope analyses of detrital zircon grains from paragneiss (ZM-39-01; Mwombezhi dome).....	92
Table 12: U-Pb isotope analyses of detrital zircon grains from paragneiss (ZM-62-05; Mwombezhi dome).....	96
Table 13: U-Pb isotope analyses of detrital zircon grains from paragneiss (ZM-66-08; Mwombezhi dome).....	99
Table 14: U-Pb isotope analyses of magmatic zircon grains from orthogneiss (ZM-12-07; Mwombezhi dome).....	101
Table 15: U-Pb isotope analyses of magmatic monazite grain from orthogneiss (ZM-12-07; Mwombezhi dome).....	104
Table 16: U-Pb isotope analyses of magmatic zircon grains from granite (ZM-12-25; Mwombezhi dome)	104
Table 17: Lu-Hf isotope analyses of magmatic zircon grains from orthogneiss (ZM-10-09; Solwezi Dome).....	106
Table 18: Lu-Hf isotope analyses of magmatic zircon grains from orthogneiss (ZM-10-13; Solwezi Dome).....	107
Table 19: Lu-Hf isotope analyses of magmatic zircon grains from orthogneiss (ZM-10-53; Solwezi Dome).....	108
Table 20: Lu-Hf isotope analyses of magmatic zircon grains from granite (ZM-10-66; Solwezi Dome)	109
Table 21: Lu-Hf isotope analyses of detrital zircon grains from paragneiss (ZM-10-38; Solwezi Dome)	109
Table 22: Lu-Hf isotope analyses of detrital zircon grains from paragneiss (ZM-39-01; Mwombezhi Dome).....	111
Table 23: Lu-Hf isotope analyses of detrital zircon grains from paragneiss (ZM-62-05; Mwombezhi Dome).....	112
Table 24: Lu-Hf isotope analyses of detrital zircon grains from paragneiss (ZM-66-08; Mwombezhi Dome).....	113
Table 25: Lu-Hf isotope analyses of magmatic zircon grains from orthogneiss (ZM-12-07; Mwombezhi Dome).....	114

Table 26: Lu-Hf isotope analyses of magmatic zircon grains from granite (ZM-12-25; Mwombezi Dome).....	116
Table 27: Sampling details. Abbreviations: Am = Amphibole, Ap = Apatite, Bt = Biotite, Chl = Chlorite, Ep = Epidote, Fsp = Feldspar, Grt = Garnet, Hem = Hematite, Ilm = Ilmenite, Ky = Kyanite, Mag = Magnetite, Mnz = Monazite, Ms = Muscovite, Phl = Phlogopite, Pl = Plagioclase, Qtz = Quartz, Rt = Rutile, Ttn = Titanite, Zrn = Zircon.....	172
Table 28: Major element composition of whole-rock samples from the Solwezi area analyzed by ICP-OES.....	173
Table 29: Major element composition of whole-rock samples from Mwombezi area analyzed by ICP-OES.....	174
Table 30: Average mineral compositions with confidence interval of 95% in brackets (n = number of samples) from samples ZM-10-07 and ZM-10-24.....	175
Table 31: Representative mineral analyses by electronic microprobe.....	176
Table 32: Representative mineral analyses by electronic microprobe.....	176
Table 33: Representative mineral analyses by electronic microprobe.....	177
Table 34: Representative mineral analyses by electronic microprobe.....	177
Table 35: Whole rock Nd and Sr isotopic data for samples from Solwezi and Mwombezi areas (Abbreviations: Metagab. = metagabbro; Amphib. = amphibolite).....	178
Table 36: U-Pb isotope analyses of detrital zircon from kyanite micaschist (ZM-10-24).....	179
Table 37: Lu-Yb-Hf isotope analyses of detrital zircon grains from the kyanite micaschist (ZM-10-24).....	182
Table 38: U-Pb isotope analyses of magmatic zircon grains from the metadiorite (ZM-10-45).....	185
Table 39: Lu-Yb-Hf isotope analyses of magmatic zircon grains from the metadiorite (ZM-10-45)....	187
Table 40: Overview of the different uranium occurrences in the Lufilian belt: External fold-and-thrust belt (Abbreviation: Ext. f. & t.) and Domes region (Abbreviation: Domes r.; Derricks and Vaes, 1956; Derricks and Oosterbosch, 1958; Ngongo, 1975; Meneghel, 1981; Cosi et al., 1992; Bernau, 2007). Temperature estimates based on fluid inclusion analysis and/or on metamorphic paragenesis (François, 1974; Audeoud, 1982; Meneghel, 1981; Cosi et al., 1992). Abbreviations: Ab = Albite ; Ap = Apatite; Br = Brannerite ; Bt = Biotite; Cal = Calcite ; Chl = Chlorite; Cof = Coffinite; Dol = Dolomite; Gt = Garnet; Qtz = Quartz; Ky = Kyanite ; Mns = Magnesite; Mnz = Monazite ; Mo = Molybdenite ; Msc = Muscovite; Ox = Oxides; Py = Pyrite ; Rt = Rutile ; Ser = Sericite; Tlc = Talc; Tur = Tourmaline ; Zr = Zircon.	223
Table 41: Electron microprobe data expressed in weight percent oxides and LA-ICPMS data expressed in ppm (with a 1 σ uncertainty of 15-35 %) for uranium oxides from the External fold-and-thrust belt. Abbreviations: Loc. = location; Occ. = Occurrences; N $^{\circ}$ = Measurement label; N = normalized. Ages are from Decrée et al., (2011).....	224
Table 42: Electron microprobe data expressed in weight percent oxides and LA-ICPMS data expressed in ppm (with a 1 σ uncertainty of 15-35 %) for uranium oxides from the External fold-and-thrust belt. Abbreviations: Loc. = location; Occ. = Occurrences; N $^{\circ}$ = Measurement label; N = normalized. Ages are from Decrée et al., (2011).....	225
Table 43: Electron microprobe data expressed in weight percent oxides and LA-ICPMS data expressed in ppm (with a 1 σ uncertainty of 15-35 %) for uranium oxides from the Domes region. Abbreviations: Loc. = location; Occ. = Occurrences; N $^{\circ}$ = Measurement label; N = normalized. Ages are from Decrée et al., (2011).....	226
Table 44: Chemical composition of phlogopite from the Lolwa occurrence analyzed by electron microprobe.....	268
Table 45: Chemical composition of talc and chlorite from the Lolwa occurrence analyzed by electron microprobe.....	268

Table 46: Chemical composition of phlogopite from the Mitukuluku occurrence analyzed by electron microprobe.....	269
Table 47: Chemical composition of chlorite and muscovite from the Mitukuluku occurrence analyzed by electron microprobe.....	269
Table 48: Chemical composition of brannerite from the Lolwa occurrence analyzed by electron microprobe.....	270
Table 49: Chemical composition of uraninite and brannerite from the Mitukuluku occurrence analyzed by electron microprobe.....	270
Table 50: Results of microthermometry for type-I fluid inclusions of the Lolwa and Mitukuluku occurrences.....	270
Table 51: Results of microthermometry for type-IIA fluid inclusions of the Lolwa occurrence.....	270
Table 52: Results of microthermometry for type-IIB fluid inclusions of the Lolwa and Mitukuluku occurrences.....	271
Table 53: Results of microthermometry for type-III fluid inclusions of the Lolwa and Mitukuluku occurrences.....	271
Table 54: Results of Raman spectroscopy for all fluid inclusions of the Lolwa and Mitukuluku occurrences.....	271
Table 55: Chemical compositions obtained by LA-ICPMS of 20 fluid inclusions from the Lolwa and Mitukuluku occurrences. The element concentration for each fluid inclusion is expressed in $\mu\text{g.g}^{-1}$ and as molar ratios.....	272
Table 56: Sample location. Abbreviations: Aln = Allanite, Ap = Apatite, Br = Brannerite, Bt = Biotite, Chl = Chlorite, Ep = Epidote, Kfs = K-Feldspar, Grt = Garnet, Hem = Hematite, Ky = Kyanite, Mc = Microcline, Mnz = Monazite, Ms = Muscovite, Phl = Phlogopite, Pl = Plagioclase, Qtz = Quartz, Rt = Rutile, Scp = Scapolite, Tlc = Talc, Ur = Uraninite, Zrn = Zircon.....	311
Table 57: Whole rock geochemistry of investigated samples.....	312
Table 58: Average mineral compositions with confidence interval of 95% in brackets (n = number of samples) for samples ZM-10-07, ZM-10-24 and 7703-29.....	313
Table 59: Representative monazite analyses from sample ZM-10-07.....	314
Table 60: Representative monazite analyses from sample ZM-10-24.....	315
Table 61: Representative monazite, allanite and epidote analyses from sample ZM-10-62 using for uranium mass balance calculation.....	316
Table 62: Representative scapolite analyses from sample ZM-10-09 and ZM-10-17.....	317
Table 63: Th-Pb results on monazite grains from kyanite micaschists.....	318
Table 64: U-Pb measurements on uraninite grains from sample 7703-29. Abbreviations: Ip = Primary intensity; nA = nanoampere; Is = Intensity (in count per second); rel. = relative; Cor. = correlation.	320
Table 65: U-Pb measurements on uraninite grains from sample #88-15. Abbreviations: Ip = Primary intensity; nA = nanoampere; Is = Intensity (in count per second); rel. = relative; Cor. = correlation.	324
Table 66: U-Pb measurements on uraninite grains from sample 7703-2. Abbreviations: Ip = Primary intensity; nA = nanoampere; Is = Intensity (in count per second); rel. = relative; Cor. = correlation.	324
Table 67: U-Pb measurements on uraninite grains from sample C25. Abbreviations: Ip = Primary intensity; nA = nanoampere; Is = Intensity (in count per second); rel. = relative; Cor. = correlation.	325
Table 68: U-Pb measurements on uraninite grains from sample 7703-21. Abbreviations: Ip = Primary intensity; nA = nanoampere; Is = Intensity (in count per second); rel. = relative; Cor. = correlation.	325

Résumé: L'uranium, du fait de ses propriétés chimiques (lithophile, incompatible) représente un traceur de choix dans le suivi de la formation et de l'évolution de la croûte continentale. Il peut être utilisé pour discuter des différents modèles de formation, de croissance et d'évolution de la croûte continentale débattus ces dernières décennies. Ce travail de thèse, ciblé sur la ceinture Pan-Africaine du Lufilien en Zambie, s'appuie sur une approche multi-méthodes combinant géologie structurale, pétro-géochimie, géochronologie et inclusions fluides dans le but de caractériser le cycle de l'U et les minéralisations uranifères pour ce segment de croûte continentale. Les séries silicoclastiques/évaporitiques de la ceinture du Lufilien, encaissant les minéralisations uranifères, se sont déposées en contexte de rift (bassin du Roan) lors de l'amincissement lithosphérique et de la dislocation du supercontinent Rodinia au Néoprotérozoïque inférieur. Les âges U-Pb des grains de zircon détritique de ces séries métasédimentaires soulignent une source principalement Paléoprotérozoïque. Ces mêmes grains de zircon présentent des signatures isotopiques ϵ_{Hf} inférieures au CHUR (entre 0 et -15) et des âges modèles $T_{\text{DM}} \text{ Hf}$, compris entre ~2.9 et 2.5 Ga. Ces données suggèrent donc la formation d'une croûte continentale précoce, et donc une extraction mantellique de l'uranium dès la fin de l'Archéen (< 2.5 Ga) puis une remobilisation par déformation et métamorphisme au cours du Protérozoïque. L'uranium aurait donc été remobilisé et reconcentré au cours d'orogènes successives jusqu'au cycle Pan-Africain. Durant ce cycle Pan-Africain, la datation U-Pb et la signature REY (REE et Yttrium) des cristaux d'uraninite caractérisent un premier événement minéralisateur, daté vers 650 Ma, associé à la circulation de fluides de bassin expulsés des évaporites du Roan, circulant à l'interface socle/couverture, dans ce contexte de rift continental. Un second événement minéralisateur, daté vers 530 Ma et contemporain du pic métamorphique ($P=9\pm 3$ kbar ; $T=610\pm 30$ °C), est assuré par des fluides métamorphiques issus de la dissolution des évaporites, en contexte de subduction/accrétion continentale. Quelques remobilisations tardives de l'uranium sont observées lors de l'exhumation des roches métamorphiques et leur accrétion tectonique dans la zone interne de la ceinture orogénique du Lufilien. L'analyse pétrographique indique que durant ces interactions fluides/roches syn- à tardi-métamorphiques, l'uranium est lessivé des minéraux hôtes (allanite, monazite), des gneiss formant le socle de la série du Katanga remobilisé et partiellement fondu au cours de l'orogène Pan-Africain.

Abstract: Uranium is an incompatible and lithophile element, and thus more concentrated in silicate melt produced by the partial melting of the mantle related to continental crust formation. Uranium can be used as a geochemical tracer to discuss the generation and the evolution of continental crust. This thesis, focused on the Pan-African Lufilian belt in Zambia, combines structural geology, metamorphic petrology and thermobarometry, fluid inclusions, geochemistry and geochronology in order to characterize the uranium cycle for this crustal segment. Silici-clastic and evaporitic sediments have been deposited within an intracontinental rift during the dislocation of the Rodinia supercontinent during the early Neoproterozoic. U-Pb ages on detrital zircon grains in these units indicate a dominant Paleoproterozoic provenance. The same zircon grains show subchondritic ϵ_{Hf} (between 0 and -15) and yield Hf model ages between ~2.9 and 2.5 Ga. These data suggest that the continental crust was generated before the end of the Archean (< 2.5 Ga) associated with uranium extraction from the mantle. This old crust has been reworked by deformation and metamorphism during the Proterozoic. Uranium has been remobilized and reconcentrated during several orogenic cycles until the Pan-African orogeny. During this Pan-African cycle, U-Pb and REY (REE and Yttrium) signatures of uranium oxides indicate a first mineralizing event at ca. 650 Ma during the continental rifting. This event is related to late diagenesis hydrothermal processes at the basement/cover interface with the circulation of basinal brines linked to evaporites of the Roan. The second stage, dated at 530 Ma, is connected to metamorphic highly saline fluid circulations, synchronous to the metamorphic peak of the Lufilian orogeny ($P=9\pm 3$ kbar ; $T=610\pm 30$ °C). These fluids are derived from the Roan evaporite dissolution. Some late uranium remobilizations are described during exhumation of metamorphic rocks and their tectonic accretion in the internal zone of the Lufilian orogenic belt. During these synmetamorphic fluid-rock interactions, uranium has been leached from U-bearing minerals such as allanite or monazite hosted by the reworked and partially molten gneissic basement.